UNIVERSIDAD COMPLUTENSE DE MADRID
FACULTAD DE CIENCIAS FÍSICAS

TESIS DOCTORAL

Dispersive study of light mesons

Estudio dispersivo de mesones ligeros

MEMORIA PARA OPTAR AL GRADO DE DOCTOR

PRESENTADA POR

Arkaitz Rodas Bilbao

Director

José Ramón Peláez Sagredo

Madrid

Dispersive Study of Light Mesons

Estudio Dispersivo de Mesones Ligeros

by

Arkaitz Rodas Bilbao

under the supervision of

Dr. José Ramón Peláez Sagredo

thesis submitted to
Universidad Complutense de Madrid
for the degree of Doctor in Physics

Universidad Complutense de Madrid
Facultad de Ciencias Físicas
Departamento de Física Teórica
Instituto de Física de Partículas y del Cosmos

Octubre 2019

UNIVERSIDAD COMPLUTENSE MADRID

DECLARACIÓN DE AUTORÍA Y ORIGINALIDAD DE LA TESIS PRESENTADA PARA OBTENER EL TÍTULO DE DOCTOR

D./Dña. Arkaitz Rodas Bilbao,
estudiante en el Programa de Doctorado de Física,
de la Facultad de Ciencias Físicas de la Universidad Complutense de Madrid, como autor/a de la tesis presentada para la obtención del título de Doctor y titulada:

Estudio Dispersivo de Mesones Ligeros

Dispersive Study of Light Mesons

y dirigida por: José Ramón Peláez Sagredo

DECLARO QUE:

La tesis es una obra original que no infringe los derechos de propiedad intelectual ni los derechos de propiedad industrial u otros, de acuerdo con el ordenamiento jurídico vigente, en particular, la Ley de Propiedad Intelectual (R.D. legislativo 1/1996, de 12 de abril, por el que se aprueba el texto refundido de la Ley de Propiedad Intelectual, modificado por la Ley 2/2019, de 1 de marzo, regularizando, aclarando y armonizando las disposiciones legales vigentes sobre la materia), en particular, las disposiciones referidas al derecho de cita.

Del mismo modo, asumo frente a la Universidad cualquier responsabilidad que pudiera derivarse de la autoría o falta de originalidad del contenido de la tesis presentada de conformidad con el ordenamiento jurídico vigente.

En Madrid, a 2 de julio de 2019

Fdo.: Arkaitz Rodas

Esta DECLARACIÓN DE AUTORÍA Y ORIGINALIDAD debe ser insertada en la primera página de la tesis presentada para la obtención del título de Doctor.

Acknowledgements

To alcohol!, the cause of, and solution to all life's problems.

– Homer Jay Simpson

Me gustaría comenzar agradeciendo a todos aquellos profesores que tanto se esforzaron para inculcarme un poco de su sabiduría.

Este doctorado ha sido una mezcla de emociones y sentimientos que se han alargado durante años. Muchos de los momentos vividos han sido gratos, aunque el camino ha sido duro y largo a veces. El apoyo y compañía de muchas personas durante este tiempo es una de esas cosas que merecen ser recordadas.

En primer lugar me gustaría darle las gracias a mi director y amigo José Ramón. De él he aprendido el que mas. Su guía y ayuda han sido cruciales durante este arduo camino. Su perseverancia conmigo, lo que se has esforzado por cambiar mis malas manías, y lo que le queda.... Muchos son los recuerdos coleccionados durante estos años, y los hay de todo tipo, incluidas las discusiones que tanto han entretenido a los despachos vecinos. Me llevo conmigo muchos buenos momentos vividos como estudiante. Muchas gracias por ayudarme a ser mejor físico, mejor speaker, y mucho más trabajador.

En segundo lugar me gustaría agradecerle a Jacobo su ayuda durante esta tesis. De él he aprendido mucho durante y fuera de los trabajos llevados a cabo, y espero seguir haciéndolo en el futuro. Por todas la charlas, por la ayuda prestada y la compañia, por ser mi colaborador más optimista. Muchas gracias.

En tercer lugar me gustaría agradercele a Adam, a Alessandro, a César, a Vincent y a todos los miembros de JPAC por su acogida, por la motivación y alegría que me transmitieron desde el primer día, por haber cumplido el papel de una familia de físicos para mí. Lo que he aprendido con ellos y lo bien que lo he pasado trabajando desde entonces es inconmensurable. En aquella época estaba falto de motivación y me devolvisteis la ilusión. Muchas gracias.

Me gustaría agradecer a Jianwei y a todos los miembros del Jefferson Laboratory por su cálida acogida durante mi estancia de investigación. Son muchas las discusiones

y mucho lo que aprendí durante esos meses, además de los deliciosos “cake seminars”. Fue toda una experiencia, muchas gracias, Raul, Jozef, Christian, José, Josh, Andrea, Carlotta, Ishara, Kemal, Carlota, por hacer de Newport News un lugar fantástico.

Quiero también recordar a aquellas personas a las que conocí en ese pequeño lugar, y que son parte de mi familia de amigos desde entonces. A Carlos, por su compañía, apoyo y alegría. A Juan, mi compañero de piso, el único con el que he aguantado y que volvería a repetir, mi confidente y un gran amigo. A Alessandro, uno de mis mejores amigos, por tu ambición, tu pasión, por ser uno de los cerebros más brillantes que conozco y a la vez un poco desastre. Todo aquello que he aprendido de tí no se puede pagar en unas pocas palabras. Muchas gracias a todos vosotros.

No podrían faltar en estas líneas todos los compañeros de trabajo, que son demasiados para mencionarlos a todos. A Dani, David, Hector, Miguel, Jose Manuel A y Jose Manuel B, Santiago, Mercedes, José Alberto, Juan Miguel, Alvarito, Domi, Juanjo, Adolfo, Roberto, Pablo, Prado, Andrea, Adrián, Raquel, Vincent, Alejandro, Jose, Luis y un largo etc... Por las discusiones, las risas y las cervezas compartidos. También me quiero acordar de todos aquellos que ya no están en la facultad, pero que tuvieron que aguantarme en un momento u otro. En especial me acuerdo de Oscar, al que le auguro un gran futuro, y Santos, aunque a este le doy un regulín regulag.

No mucha gente tiene la suerte de tener una koadrilla proveniente de su lugar natal, mucho menos provenientes de la misma clase del colegio, yo la tuve. Por todas las fiestas, los viajes, la amistad atemporal, y las personas que se anexaron para disfrutar de la noche madrileña. Muchas gracias Gorka, Javi, Roberto, Arkaitz, Ekain, Diego y Sergio.

Los amigos son la familia que elegimos, y yo tuve suerte de elegir el mejor grupo del mundo. Toda la ayuda y compañía que se dan por concedias provienen de las mejores amistades, que en unos pocos casos se vuelven eternas. A Luis, Raul, Mario, Jagoba, porque vosotros tenéis el poder de transformar un día horrible en algo inolvidable. A Alex, Alexis, Aingeru, Guille, Kevin, Ekintza, Aitor, Gari, y un largo etc que se me olvida, y a la Berrea. Porque mi hogar siempre estará a vuestro lado.

Me gustaría agradecer a la que fue mi alma gemela y mi mejor compañera durante gran parte de esta tesis. A Melissa, porque tú si que eres la que ha hecho posible que yo escriba este trabajo. No podría explicar ni en un millón de líneas todo lo que hemos vivido juntos y lo afurtando que fui de tenerte. Por todo, muchas gracias.

Me gustaría agradecer enormemente a mi familia y a mi tío Melchor por todo lo vivido, los buenos recuerdos y todo el cariño.

Finalmente, esta tesis va dedicada a mis padres, por todo el esfuerzo, por la confianza, por todo su amor, su dedicación y su apoyo incondicional. Nunca podré devolveros todo lo recibido, pero espero haceros sentir orgullosos de mi.

List of Publications

The research activity performed in this thesis has given rise to the following list of publications:

1. J. R. Peláez and A. Rodas, "Pion-kaon scattering amplitude constrained with forward dispersion relations up to 1.6 GeV," **Phys. Rev. D 93, no. 7, 074025 (2016)**

2. J. R. Peláez, A. Rodas and J. Ruiz de Elvira, "Strange resonance poles from $K\pi$ scattering below 1.8 GeV," **Eur. Phys. J. C 77, no. 2, 91 (2017)**

3. J. R. Peláez and A. Rodas, "The non-ordinary Regge behavior of the $K_0^*(800)$ or κ-meson versus the ordinary $K_0^*(1430)$," **Eur. Phys. J. C 77, no. 6, 431 (2017)**

4. J. R. Peláez and A. Rodas, "$\pi\pi \to K\bar{K}$ scattering up to 1.47 GeV with hyperbolic dispersion relations," **Eur. Phys. J. C 78, no. 11, 897 (2018)**

5. M. Mikhasenko *et al.* [JPAC Collaboration], "Pole position of the $a_1(1260)$ from τ-decay," **Phys. Rev. D 98, no. 9, 096021 (2018)**

6. A. Rodas *et al.* [JPAC Collaboration], "Determination of the pole position of the lightest hybrid meson candidate," **Phys. Rev. Lett. 122, no. 4, 042002 (2019)**

7. J. R. Peláez, A. Rodas and J. Ruiz de Elvira, "Global $\pi\pi$ scattering parameterization,", **In preparation**

8. J. R. Peláez, A. Rodas and J. Ruiz de Elvira, "Determination of the lightest strange resonance $K_0^*(700)$ or κ, from a dispersive data analysis,", **In preparation**

included in different sections of this volume.

Also, the research activity performed during this thesis has been presented by the student in the following international conferences:

1. 1st Hadron Spanish Network Days and Spanish-Japanese JSPS workshop
   Title of the talk: Forward dispersion relations applied to πK scattering.
   Valencia, Spain June 2015.

2. VII CPAN DAYS
   Title of the talk: Forward dispersion relations in πK scattering.
   Segovia, Spain December 2015.

3. Excited QCD 2016
   Title of the talk: Forward dispersion relations for πK scattering.
   Caparica, Portugal March 2016.

4. 2nd Hadron Spanish Network Days
   Title of the talk: Regge trajectories of strange resonances and the non-ordinary nature of the κ.
   Madrid, Spain September 2016.

5. VIII CPAN DAYS
   Title of the talk: Regge trajectories of strange resonances and the non-ordinary nature of the κ.
   Zaragoza, Spain December 2016.

6. PWA 9/ ATHOS 4
   Title of the talk: $K\pi$ scattering with Forward Dispersion Relations and other analytic methods.
   Bad Honnef, Spain March 2017.

7. Excited QCD 2017
   Title of the talk: Analityc approach to pion-kaon scattering and strange resonances.
   Sintra, Portugal May 2017.

8. HADRON 2017
   Title of the talk:Calculation of strange resonances from $K\pi$ scattering.
   Salamanca, Spain September 2017.

9. 2nd Workshop on Future Directions in Spectroscopy Analysis
   Title of the talk: Dispersive analysis of pion-kaon scattering.
   Ciudad de México, México November 2017.

10. XIIIth Quark Confinement and the Hadron Spectrum
    Title of the talk: Review of phenomenological analyzes of $\eta\pi$ resonances through data measured at the COMPASS experiment.
    Maynooth University, Ireland August 2018.

11. Ninth International Workshop on Chiral Dynamics
    Title of the talk: Dispersive study of low energy pi-K scattering.
    Duke University, USA September 2018.

12. X CPAN DAYS
    Title of the talk: Determination of the lightest hybrid meson pole.
    Salamanca University, Spain October 2018.

13. Excited QCD 2019
    Title of the talk: Determination of the lightest hybrid meson candidate.
    Schladming, Austria January 2019.

14. JPAC/BESIII: A Workshop on theory-experiment collaboration
    Title of the talk: Hunting Glueballs with BESIII.
    Beijin, China April 2019.

15. 8th Workshop of the APS Topical Group on Hadronic Physics
    Title of the talk: New determination of the lightest hybrid meson.
    Denver, USA April 2019.

As a result, several works included in this thesis have contributed producing the following list of conference proceedings

1. A. Rodas, "Calculation of Regge trajectories of strange resonances and identification of the $K_0^*(800)$ as a non-ordinary meson," **Acta Phys. Polon. Supp. 9, 453 (2016)**

2. A. Rodas and J. R. Peláez, "Forward dispersion relations for πK scattering and the $K_0^*(800)$ resonance," **Acta Phys. Polon. Supp. 9, 459 (2016)**

3. A. Rodas, "Analytic Approach to πK Scattering and Strange Resonances," **Acta Phys. Polon. Supp. 10, 1037 (2017)**

4. J. R. Peláez and A. Rodas, "Dispersive analysis tools for $\pi\pi$ and πK scattering," **PoS Hadron 2017, 139 (2018)**

5. A. Rodas, J. R. Peláez and J. Ruiz de Elvira, "Calculation of strange resonances from $K\pi$ scattering," **PoS Hadron 2017, 043 (2018)**

6. A. Rodas, A. Pilloni and A. Szczepaniak, "Review of phenomenological analyses of $\eta^{(\prime)}\pi$ resonances," **PoS Confinement 2017, 043 (2019)**

7. J. R. Peláez, A. Rodas and J. Ruiz de Elvira, "Dispersive analysis of the $\kappa/K_0^*(700)$ meson and other light strange resonances," **EPJ Web Conf. 212, 03003 (2019).**

Contents

Resumen

La Cromodinámica Cuántica (QCD) es la teoría fundamental que explica la interacción fuerte entre quarks y gluones. Sin embargo, el hecho de que (QCD) muestra una libertad asintótica a distancias muy pequeñas también implica que quarks y gluones se encuentran confinados a baja energía, formando los conocidos hadrones, por tanto estos pasan a ser los grados de libertad a traves de los cuales extraer información. Es por esto que Weinberg introdujo en 1979 [1] la Teoría de Perturbaciones Quiral (ChPT). Esta es una teoría efectiva que considera el octete de pseudo-bosones goldstone (piones, kaones y eta) producidos por la ruptura espontánea de la simetría Qiral como grados de libertad y proporciona una expansión sistemática de los observables a baja energía. Sin embargo, esta no puede determinar con la precisión necesaria las constantes de baja energía, a parte de no respetar principios fundamentales como la unitariedad, por lo que en principio sólo puede ser aplicada a energías en torno al umbral de interacción.

En esta tesis estudiamos las interacciones entre mesones mediante el uso de las llamadas relaciones de dispersión, provenientes de los conocidos fundamentos de la matriz S analítica, como las relaciones de cruce, unitariedad y causalidad. Estas nos proveen de una serie de heramientas independientes de los modelos que como se verá son extremadamente útiles en la determinación de los procesos de dispersión. El resumen de la estructura y contenidos de la tesis se presenta a continuación.

Chapter 1: Introduction

En esta primera parte de la tesis se introduce el desarrollo de la Teoría de Perturbaciones Qiral, un breve resumen sobre sus predicciones para el sector escalar, y se señalan algunos de sus puntos débiles para determinar la interacción entre mesones. También se comparan ciertos resultados con aquellos provenientes de cáculos de QCD en el retículo, mostrando la incompatibilidad entre ambos métodos.

Tras esta introducción los conceptos fundamentales de la matriz S analítica son presentados, prestando especial atención a la hipótesis de Mandelstam, de la cual se derivan las relaciones de dispersión empleadas en la tesis. El capítulo finaliza con una breve introducción general a la teoría de Regge.

Chapter 2: Dispersion relations

En este capítulo estudiamos de manera dispersiva las interacciones entre mesones ligeros, en particular nos hemos centrado en diversos estudios de las interacciones πK y $\pi\pi \to K\bar{K}$, ampliando y generalizando un antiguo trabajo en el tema [2]. Además hemos extendido las relaciones de dispersión GKPY [3] a todo su región de convergencia en el plano complejo, construyendo una serie de parametrizaciones que describen todas las propiedades analíticas de la dispersión $\pi\pi$ en el límite de isospin.

- En la sección 2.2 obtenemos y presentamos un sistema de relaciones de dispersión para las amplitudes del proceso $\pi K \to \pi K$. Al emplear para estas una energía nula en el canal cruzado ($t = 0$), su convergencia en el eje real es ilimitada. Se realiza especial énfasis en la descripción del umbral del proceso, para determinar con precisión las longitudes de dispersión.

- Se presentan los ajustes a todos los sets de datos, y un posterior análisis de cuan bien describen estos sets cada relación de dispersión es llevado a cabo. Se encuentran desviaciones importantes que deben ser corregidas. Como resultado se obtienen un conjunto de ondas parciales que describen los datos a la vez que respetan los principios de analiticidad, cruce y unitariedad del proceso.

- En la sección 2.2 se derivan y optimizan por primera vez las relaciones de dispersión hiperbólicas para ambos procesos $\pi K \to \pi K$ y $\pi\pi \to K\bar{K}$, y su región de aplicación es optimizada por primera vez. Estas nos permiten estudiar las ondas parciales hasta $\sqrt{s} \sim 1$ GeV y $\sqrt{t} \sim 1.5$ GeV, respectivamente. Tras estudiar el sistema $\pi\pi \to K\bar{K}$ se obtienen dos soluciones distintas compatibles con las relaciones de dispersión para la onda parcial $g_0^0(t)$, además de una solución para $g_1^1(t)$ y $g_2^0(t)$.

- Se incluye en la sección 2.3 por primera vez como resultado parte del análisis conjunto de ambos procesos, el cual será publicado tras la tesis. Se reobtienen por medio de 3 distintitas familias y un total de 18 relaciones de dispersión, todas las constantes de baja energía, los parámetros de Regge, y las ondas parciales de ambas interacciones.

- Finalizamos el capítulo con la sección 2.4, en la cual proporcionamos una parametrización global de los resultados obtenidos por las ecuaciones GKPY en [3], tanto en el eje real, como en su región de aplicación en el plano complejo. Además de describir con precisión las constantes de baja energía, las posciones de cada una de las resonancias relevantes, en particular la $\sigma/f_0(500)$, los datos experimentales hasta 2 GeV y las relaciones de dispersión en el eje real y plano complejo.

Chapter 3: Meson spectroscopy

En esta segunda parte estudiamos las resonancias relevantes en distintos procesos. Centrándonos en la $\kappa/K_0^*(700)$, que aparece en πK, o en la $\pi_1(1600)$ que decae en $\eta^{(\prime)}\pi$. Finalmente extendemos los análisis a un proceso de desintegración a tres cuerpos en 3.4.3.

- En 3.1 desarrollamos y explicamos el método de las secuencias de Padés al estudio de resonancias elásticas, e inelásticas en πK. Este método analítico nos permite extraer con gran estabilidad y precisión los parámetros de hasta 6 estados distintos, y propició el cambio de nombre de la κ de $K_0^*(800)$ a $K_0^*(700)$ en el Review of Particle Phypics (RPP) publicado por el Particle Data Group (PDG) [4].
- Extendemos las relaciones de dispersión hiperbólicas al plano complejo, determinando con gran precisión los parámetros de la $\kappa/K_0^*(700)$ y de la $K^*(892)$, donde la primera se muestra compatible con resultados analíticos previos.
- Tras esto, en 3.2 determinamos la existencia de un único meson híbrido, rebatiendo la hipótesis del RPP de dos mesones distintos y extraemos sus parámetros.
- Finalmente, estudiamos la desintegración de la $a_1(1260)$ a tres piones como aplicación de la unitariedad a tres cuerpos. Determinando sus parámetros y comparando estos con modelos más simples que no incluyen todas las propiedades fundamentales.

Chapter 4: Nature of the lightest strange scalar meson

Finalmente, en la sección 4.1 realizaremos un estudio de las propiedades de los mesones $\kappa/K_0^*(700)$ y $K_0^*(1430)$ por medio de la teoría de Regge.

- Extendemos el método del cálculo dispersivo de trayectorias de Regge al sistema πK. Con el cual estudiamos dos resonancias: el mesón escalar con extrañeza más ligero, la $\kappa/K_0^*(700)$, y el mesón escalar perteneciente al nonete más pesado, la $K_0^*(1430)$
- Mientras que la más pesada de ellas $K_0^*(1430)$ se muestra como un meson ordinario $q\bar{q}$, la $\kappa/K_0^*(700)$ tiene una trayectoria que es claramente no ordinaria, mostrando un comportamiento atípico.
- Tras compararlo con ciertas soluciones en la literatura, concluimos que este compartamiento bien podría ser descrito por un estado quasi-molecular a baja energía, y el resultado es comparado con el obtenido para la $\sigma/f_0(500)$ [5].

Conclusions

El objetivo principal de esta tesis es el estudio dispersivo de mesones ligeros. Hemos visto primero como las llamadas relaciones de dispersión son útiles para constreñir los datos experimentales provenientes de las interacciones entre mesones, produciendo resultados precisos y que respetan los principios fundamentales de la matriz S. Tras esto hemos aplicado técnicas basadas en estos principios para extraer de manera robusta los parámetros de hasta un total de 8 mesones distintos, incluyendo la conocida $\kappa/K_0^*(700)$ y el meson híbrido más ligero $\pi_1(1600)$. Finalmente, las relaciones de dispersión se han aplicado para determinar las trayectorias de Regge de dos resonancias extrañas, donde se encuentra un compartamiento no ordinario para la $\kappa/K_0^*(700)$.

Abstract

Quantum Chromodynamics (QCD) is the fundamental theory that explains the strong interactions between quarks and gluons. Unfortunately, the fact that QCD is asymptotically free at short distances produces the confinement of quarks at low energies, creating the well known hadrons, which are then appropriate the degrees of freedom to extract information from. In order to overcome this difficulty, Weinberg introduced in 1979 [1] Chiral Perturbation Theory (ChPT). This is an effective field theory that considers the octet of pseudo-goldstone bosons (pions, kaons and eta) produced by the chiral symmetry breaking as the degrees of freedom and provides a systematic low-energy expansion for the observables. Nevertheless, ChPT is not able to determine with high accuracy the low energy parameters of the meson-meson interactions, besides, its series expansion does not respect unitarity, and hence can only be applied very close to threshold.

In this thesis we study the interactions between mesons by using the so-called dispersion relations, derived from the well known S-matrix principles of crossing, unitarity and causality. These provide us with a series of model independent tools that, as we will see, are extremely powerful for the determination of scattering processes. The structure and summary of the contents of the thesis are summarized next.

Chapter 1:Introduction

In this first part of thesis the Chiral Perturbation Theory is introduced, together with a brief summary on its predictions for the scalar sector of $SU(3)$, and we point out some of its weakness to determine the interaction between mesons. We also compare certain results with those from Lattice QCD calculations, showing the incompatibility between both predictions.

After this introduction, the concepts of the analytic S matrix are explained in a comprehensive manner, paying special attention to the Mandelstam hypothesis, from which the dispersion relations used in the thesis are derived. This chapter ends with a general introduction to Regge theory.

Chapter 2: Dispersion relations

In this chapter we study the interactions between light mesons by means of dispersion relations, in particular we have focused on several studies of the interactions πK and $\pi\pi \to K\bar{K}$, extending an old previous work in the topic [2]. We have also extended the dispersion relations called GKPY [3] to the entire complex plane, constructing a series of parameterizations that describe all the analytical properties of $\pi\pi$ scattering in the isospin limit.

- In section 2.2 we present a system of dispersion relations for the $\pi K \to \pi K$ scattering amplitude. By setting the crossed channel variable $t = 0$, their convergence on the real axis has no upper bound. Special emphasis is given to the threshold description, in order to determine the scattering lengths with high precision.
- We present a series of fits to the process, and a subsequent analysis on how well the data sets describe each dispersion relation is performed. There are severe deviations that must be corrected. As a result, a set of partial waves that describe the data while fulfilling the principles of analyticity, crossing and unitarity are obtained.
- In section 2.2 we derive the hyperbolic dispersion relations for both processes $\pi K \to \pi K$ and $\pi\pi \to K\bar{K}$ and we also optimize its applicability region for the first time. They allow us to study the partial waves up to $\sqrt{s} \sim 1$ GeV and $\sqrt{t} \sim 1.5$ GeV, respectively. After performing a dispersive analysis of $\pi\pi \to K\bar{K}$ two different solutions are obtained for the $g_0^0(t)$ partial wave, as well as one solution for each $g_1^1(t)$ and $g_2^0(t)$.
- A first part of the combined analysis of both $\pi K \to \pi K$ and $\pi\pi \to K\bar{K}$ processes is included in section 2.3 as an original result. Where we obtain the low-energy constants, Regge parameters, and the partial waves of both interactions by means of 3 different families of dispersion relations which make a total of 18 constraints.
- In the last section 2.4 we present a global parameterization of the results from the system of GKPY equations in [3], which allows us to accurately describe the low-energy expansion, the position of all relevant resonances, in particular the $\sigma/f_0(500)$, the experimental data up to 2 GeV and the dispersion relations in the real axis and their applicability region in the complex plane.

Chapter 3: Meson spectroscopy

In this second part of the thesis we study the relevant resonances decaying to different processes. With special attention to the $\kappa/K_0^*(700)$ that appears in πK, or the $\pi_1(1600)$ that decays in $\eta^{(\prime)}\pi$. Finally, we extend these analyses to a 3-body decay process.

- In 3.1 we implement the method of the Padé sequences to the study of elastic and inelastic resonances for πK. This analytic method allows us to extract the parameters of up to 6 different states with great accuracy. This work triggered the denomination change of the κ from $K_0^*(800)$ to $K_0^*(700)$ in the RPP [4].
- We extend the hyperbolic dispersion relations to the complex plane, determining with great precision the parameters of the $\kappa/K_0^*(700)$ and the $K^*(892)$.
- After this, we study in section 3.2 the reliability of the existence of a single hybrid meson, thus questioning the RPP actual status with two different mesons, and we determine its parameters.
- Finally, we study the decay of the $a_1(1260)$ to three pions as an application of 3-body unitarity. We determine its parameters and compare this result with simpler approximations which do not fulfill all analytic requirements.

Chapter 4: Nature of the lightest strange scalar meson

In this final chapter, we carry out a study of the properties of the $\kappa/K_0^*(700)$ and $K_0^*(1430)$ mesons by means of Regge theory.

- We extend the dispersive calculation of Regge trajectories performed in [5] to πK scattering in order to study two resonances: the lightest strange scalar meson $\kappa/K_0^*(700)$, and its heavier partner, lying on the next heavier octet the $K_0^*(1430)$.
- While for the later the Regge trajectory shows an ordinary $q\bar{q}$ behavior, the $\kappa/K_0^*(700)$ trajectory is clearly not ordinary, with a weird curvature and slope parameters.
- This behavior could well be described by a quasi-molecular state at low energy, as shown by its similarity to the Yukawa potentials. This result is compared with the one obtained for the $\sigma/f_0(500)$ [5].

Conclusions

The aim of this thesis is the dispersive study of light mesons. In the first part we have seen how the dispersion relations, as a result of the S-matrix principles, provide accurate, model independent constraints for meson-meson interactions. We have applied several analytic techniques to extract in a robust way the parameters of up to 8 different resonances, including the much debated $\kappa/K_0^*(700)$ and the lightest hybrid meson candidate $\pi_1(1600)$. Finally, dispersion relations have also been applied to the determination of Regge trajectories, where we have found a non-ordinary behavior of the $\kappa/K_0^*(700)$ meson.

Chapter 1

Introduction

Four fundamental interactions in nature are known: the Electromagnetic force, the Weak force, the Strong force and the Gravity force, of which the first three ones are described by the Standard Model of Particle Physics, developed during the 20^{th} century, who evolved from the first principles of Quantum Mechanics, to include the special relativity constraints, becoming what we call a quantum field theory. The elementary blocks of these three interactions are the quarks and leptons, spin 1/2 structureless particles, *aka* fermions, which interact by exchanging force-mediating particles called bosons. Out of these three interactions, the weak and strong forces only appear at very short distances, mediated by the W, Z and gluon bosons respectively. The strong interaction is described by Quantum Chromodynamics (QCD), a name that enlightens the fact that it describes the interactions between colored particles, quarks and anti-quarks. The fundamental gauge symmetry through which the strong interactions are described implies that gluons interact with each other, causing as a consequence that quarks are strongly binded, "glued" at low energies, confined as hadrons. As a result, no quarks are found in nature, and all hadrons interact through a residual force coming from QCD, just like neutral molecules interact as a consequence of the electromagnetic force.

The purpose of this thesis is to study the properties of hadronic interactions, in particular low-energy interactions between mesons, and the compositeness of the excited states appearing as a result of the rich QCD dynamics.

In this chapter we briefly introduce the motivation of the thesis, together with the basic tools and concepts necessary for the understanding of the works included here. In section 1.1 we review the historical introduction of quarks and their symmetries. Next, in section 1.2 a comprehensive introduction to the Chiral Perturbation Theory (ChPT) Lagrangian is presented. We will follow with the explanation of the main tools used in this thesis in section 1.3, and we will finish with a brief summary of Regge theory in section 1.4.

1.1 Hadrons

The constituents of matter can be divided into two groups, the ones that do not interact by the strong force (photon, electron,muons,...) and the hadrons, which are central to this thesis. Nowadays we know that QCD has a rich spectrum, as can be seen in the Review of Particle Physics (RPP) [4] by the Particle Data Group (PDG).

Nevertheless in this introductory chapter it is convenient to briefly review the discovery and classification of hadrons in terms of quarks, and the basic properties of the naive quark model. The quest for the discovery of the constituents of the observed matter is a really old one and it has been pursued by scientists since ancient civilizations. We will pay attention only to the past century, when almost all our hadrons where discovered. By 1932 the list of elementary particles was tiny, the photon, the electron, the positron, the proton, and the neutron, of which only the last two ones interact through nuclear forces. However, Yukawa had already predicted the pion as the force carrier between the proton and the neutron, causing this short range nuclear interactions. By that time, an elementary particle could be uniquely classified by its angular momentum J, its parity P, its charge conjugation C and its electric charge. Soon it was realized that both protons and neutrons interacted similarly through nuclear forces. Hence this interaction cannot depend on the charge of the particle, and a new quantum number, called the isospin (I) was born. The relation between the proton and the neutron is the SU(2) symmetry group, and it was later discovered [6] that nuclear interactions must preserve this symmetry, apart from the total charge and the baryon number B (+1 for baryons, -1 for anti-baryons, and 0 for mesons). The hadrons, as explained above, will correspond to irreducible representations of their symmetry group, described by the quantum numbers I or Q. With the discovery of the kaons and lambdas, another quantum number, called strangeness S was introduced, actually, there is a relation between Q, B and S

$$Q = I_3 + \frac{1}{2}(B + S) \tag{1.1}$$

The most important discovery regarding hadron classification was made by Gell-Mann and Ne'eman in 1961 [7, 8]. They considered the strangeness with the other isospin classifications to gather the spin-half baryons and pseudo-scalar mesons in octets and decuplets, as representations of the $SU(3)$ group. This new representation makes use of two quantum numbers, I_3, Y to classify hadrons with the same angular momentum and parity. Soon after, the naive quark picture was introduced [9], where hadrons are considered non-elementary particles, but constituted of quarks, spin-half elementary particles with a characterizing quantum number, their flavor, up, down or strange at that time. These quarks lie in the fundamental representation of $SU(3)$ whereas the anti-quarks lie in the conjugate representation. Hereby, the mesons, defined now as $q\bar{q}$ states can be classified following the next representation

$$3 \otimes 3^* = 1 \oplus 8, \tag{1.2}$$

which corresponds to an octet plus a singlet. While baryons, considered qqq states

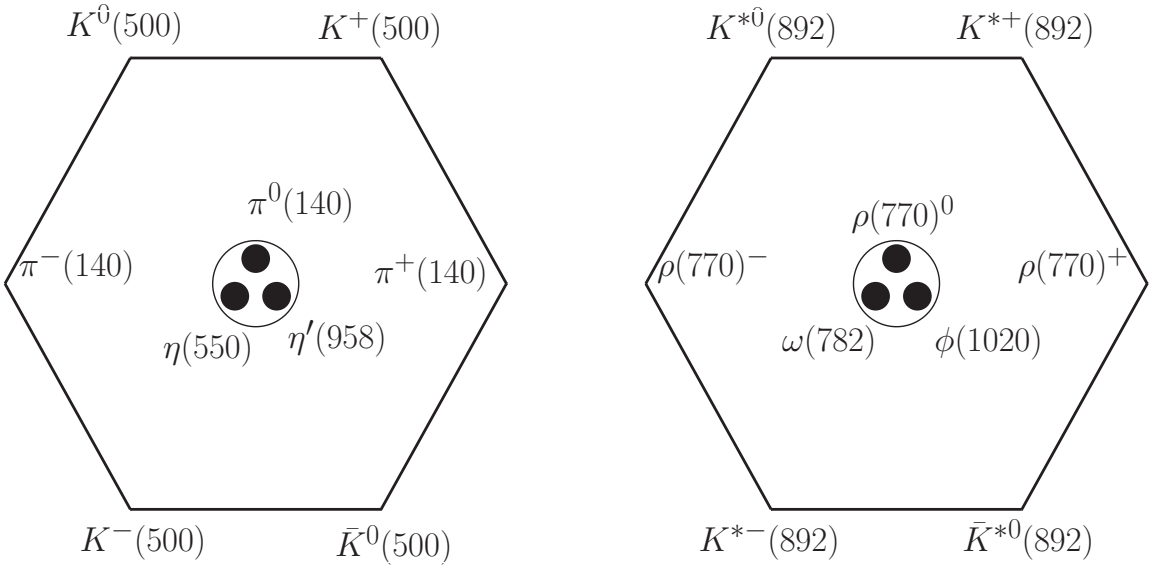

Figure 1.1: Nonet of pseudoscalars (left) and vectors (right).

come from the next product

$$3 \otimes 3 \times 3 = 1 \oplus 8 \oplus 8 \oplus 10, \tag{1.3}$$

which means that for baryons the octet and anti-octet coexist, together with the singlet and decuplet. This representation was successful in predicting the Ω^-. Unfortunately, the model was not complete, as there were several drawbacks. In particular it could not explain the wave function of the $\Delta^{++}(1232)$. Therefore, another gauge symmetry, exact, was introduced, the color, which could take 3 different possible values, red, green and blue, and hadrons were postulated to be colorless.

More quarks where later discovered, the charm quark, the bottom quark, and the top quark, but none of them are relevant in this thesis, as their masses are way out of the region where chiral symmetry is spontaneously broken.

1.1.1 Mesons

As introduced above, mesons in the quark model are constituted by a $q\bar{q}$ pair, which may have different flavors. They are classified by the three quantum numbers introduced before J^{PC}, parity $P = (-1)^{\ell+1}$, charge conjugation $C = (-1)^{\ell+s}$ and total angular momentum $|\ell - s| \leq J \leq |\ell + s|$, where ℓ is the orbital angular momentum of the $q\bar{q}$ system.

The states corresponding to $\ell = 0$ are called pseudoscalars 0^{-+} and vectors 1^{--}, whereas their excitations $\ell = 1$ are called scalars 0^{++}, axial-vectors 1^{++}, 1^{+-} and tensors 2^{++}. As shown in Fig. 1.1 this classification leads to an octet and a singlet, which mixes with the elements of the octet.

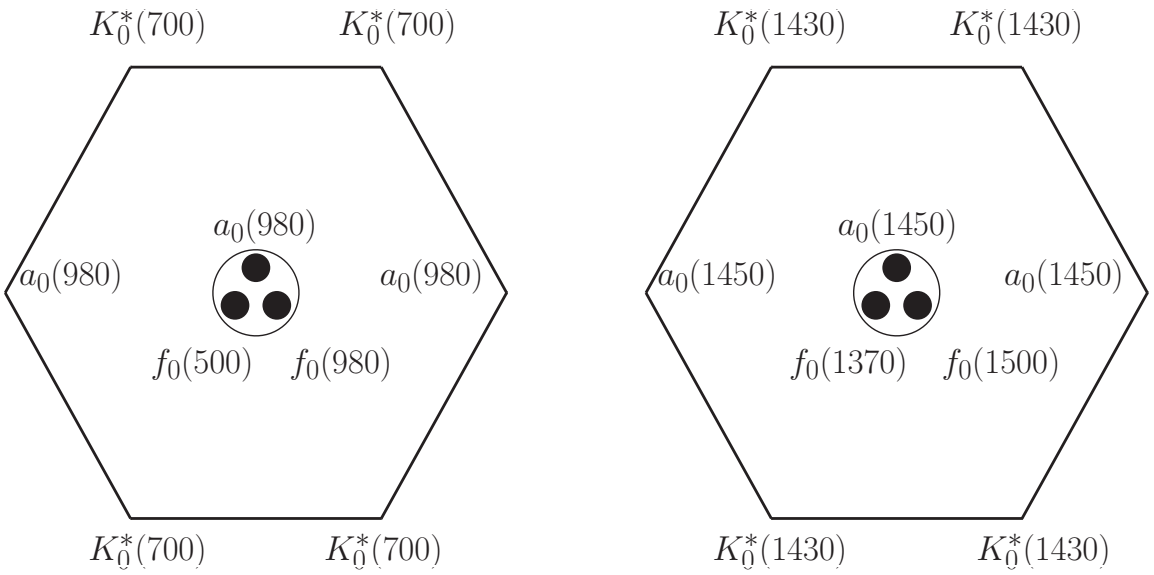

Figure 1.2: Nonet of scalars below 1 GeV (left) and above (right).

While the quark model describes this vector mesons very well, the pseudoscalar ones cannot be accommodated within this naive model. Actually, the mass of the pions would be similar to the one of the $\rho(770)$. Fortunately, this is not the case for the rest of the mesons, which have almost degenerated masses for those formed by u, d quarks. The strange quark is way heavier and thus the strange mesons will always be around $100 - 300$ MeV heavier than its non-strange partners. During the years, more sophisticated models, including QCD approximations [10] have shown even better agreement. Lately, the study of hadron spectroscopy has been gaining weight amongst Lattice QCD practitioners, there have been crucial developments during the last years. However, although several promising results have been published in the topic [11] (see Fig. 1.3), their meson masses are not yet the physical ones.

Unfortunately, the picture regarding scalar mesons is not so clear even today (Fig. 1.2), in particular, those states below 1 GeV. They cannot be considered pure $q\bar{q}$ states, or they would violate the mass hierarchy [12–15], so that there are clear indications that these states are non-ordinary [16–24]. In particular, the $\sigma/f_0(500)$ and $\kappa/K_0^*(700)$ mesons have been a fierce subject of debate for several decades. The status of the $\kappa/K_0^*(700)$ is "still needs confirmation" according to the PDG. Even though their existence and non-ordinary nature are widely accepted, there are still several controversies surrounding these mesons, in which we will focus on the study of their fundamental parameters in next sections.

Another interesting feature is that some of the states lying on this nonet and the one above 1 GeV share the same quantum numbers of the vacuum. In addition, the $\sigma/f_0(500)$ was long considered to have a non-negligible glueball component. Nowadays we know that the ground state glueball, expected at around 1.5 GeV [25], should mix with some of the pure $q\bar{q}$ f_0's, hence it will have some mixing with the $f_0(1370)$, $f_0(1500)$ and the $f_0(1710)$.

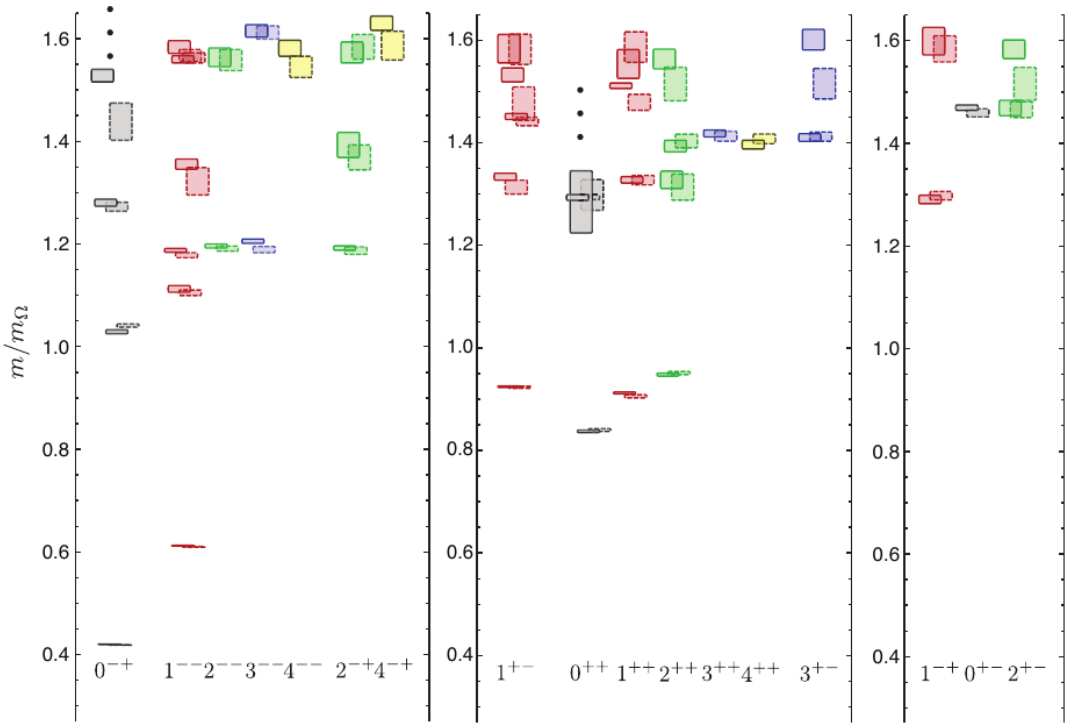

Figure 1.3: Figure from [11] (Jozef J.Dudek et al.), showing the isovector meson spectrum obtained from Lattice QCD.

As seen before, a crucial quest of QCD is the one for exotica, *i.e.*, those states that do not fit in the $q\bar{q}$ quantum numbers picture. In particular, in the light mesonic sector, the 0^{+-} and the 1^{-+} are forbidden within the quark model, and so any state sharing this quantum numbers must be constituted by different structures. This field has been a subject of debate, with several different approaches, mainly in the heavy quark sector [26–30]. The searches for different exotic hadrons have motivated several experimental programs, like those of COMPASS, LHCb, BaBar, CLAS12,GlueX, etc...

The main part of this thesis is devoted to the study of meson interactions and the determination of non-ordinary mesons, in particular the light scalars, and the lightest hybrid π_1. Our goal is to study their properties in a model independent way, enlightening some unclear aspects in this low-energy region.

1.2 Chiral Perturbation Theory

The study of effective field theories is out of the scope of this thesis. Nevertheless, the pseudoscalar mesons, considered as degrees of freedom rather than objects constituted by quarks and gluons, cannot be well understood without the effective Lagrangian that describes their main features. Furthermore, along this thesis we will make use of several properties, constraints and predictions coming from this low-energy effective theory. Therefore, this section is dedicated to briefly introduce the central concepts of such theory, and also to include some predictions and tensions as a motivation.

The Effective Lagrangian method is a powerful tool to incorporate in a delimited energy region the symmetries of the underlying theory. The basic assumption in this case is that dynamics at small distances do not depend on the large ones, thus neglecting all degrees of freedom relevant outside the low-energy region. In particular, the spontaneous chiral symmetry breaking of QCD gives rise to eight pseudo-goldstone bosons, whose masses are much smaller than the typical hadronic scale. These bosons can be used as the degrees of freedom of a Lagrangian built as a low-energy expansion, called Chiral Perturbation Theory (ChPT). Now, let us recall that the QCD coupling constant:

$$\alpha_s(\mu) = \frac{g^2(\mu)}{4\pi} = \frac{12\pi}{(11N_c - 2N_f)\log\left(\frac{\mu^2}{\Lambda^2_{QCD}}\right)},$$
$$\beta(\mu) = \mu\frac{g(\mu)}{d\mu} = -\frac{g^3(\mu)}{(4\pi)^2}\left(\frac{11}{3}N_c - \frac{2}{3}N_f\right) + O(g^5). \tag{1.4}$$

which was first derived by Gross, Wilczek and Politzer [31–34]. Note that when $N_c = 3$ and $N_f \leq 16$ then the β function is negative, so that the coupling decreases as μ increases. This property, called asymptotic freedom means that the QCD interactions are weaker at higher energies. Hence the strong interactions can be perturbatively studied in a systematic way at high energies. In contrast, at low energies the coupling constant increases which intuitively explains the binding of quarks and gluons, confined into hadrons, which will be the degrees of freedom at low energies.

Let us focus on the fermionic QCD Lagrangian

$$\mathcal{L} = \bar{\psi}(i\not{D} - M)\psi, \tag{1.5}$$

where ψ is a vector containing the N_f quark flavors, M is the diagonal mass matrix and D_μ the covariant derivative. We will now pay attention to the limit $M \to 0$ as the masses of the three lightest quarks are of the order of few MeV. If one decomposes the fermionic field into its chiral components

$$\psi_L = \frac{(1+\gamma_5)}{2}\psi, \qquad \psi_R = \frac{(1-\gamma_5)}{2}\psi, \tag{1.6}$$

then the Lagrangian is invariant under chiral $SU_R(N_f) \times SU_L(N_f)$ transformations.

$$\psi_{L,R}(x) \to \exp\left(-i\alpha^a_{L,R}\tau^a\right)\psi_{L,R}(x), \tag{1.7}$$

where τ^a are the generators of the flavor group. It is convenient to introduce here the vector V transformation where $\alpha_R = \alpha_L$, and the axial A transformations with $\alpha_R = -\alpha_L$.

The difference between the masses of multiplets with different parity is of the order of 500 MeV, much larger than the difference between the quark masses. Therefore, there must be a spontaneous symmetry breaking with the following pattern:

$$SU_R(N_f) \times SU_L(N_f) \to SU_V(N_f), \tag{1.8}$$

which according to the Goldstone theorem [35–39] produces a massless boson for each generator spontaneously broken. In the case of interest, where the u, d and s quarks are considered massless there will be eight pseudoscalar bosons, due to the breaking of the 8 A_a generators. However, the symmetry is only an approximation as quarks have mass, and that is the reason why these bosons have a very small mass.

According to the representations of the $SU(3)$ group there should be a singlet partner to the pseudoscalar octect, but the lightest meson that can fit this description, the η', is almost 1 GeV. The axial $U(1)$ anomaly is the responsible for its mass [40–42], which produces a non-conserved current and thus it could not be spontaneously broken.

As explained above, these pseudo-Goldstone bosons will be the relevant degrees of freedom at low energies, with whom we can build an effective lagrangian to describe their interactions.

The resultant effective theory is called Chiral Perturbation Theory (ChPT), was first introduced by Weinberg in 1979 [1] and respects by construction the symmetries of QCD, such as invariance under Lorentz transformations, parity and charge conjugation, and the same chiral symmetry breaking pattern. At lowest order the Lagrangian reads

$$\mathcal{L}_{LO} = \frac{F^2}{4}\left\langle \partial_\mu U \partial^\mu U^\dagger + 2B_0 \mathcal{M}\left(U + U^\dagger\right)\right\rangle, \tag{1.9}$$

where $U(\phi) = \exp(i\sqrt{2}\phi/F)$ is a unitary matrix, $\langle\cdot\rangle$ is the trace in flavor space, and in the $SU(3)$ theory the pseudo-goldstone bosons are collected through the $SU(N_f)$ ϕ matrix

$$\phi(x) = \begin{pmatrix} \frac{1}{\sqrt{2}}\pi^0 + \frac{1}{\sqrt{6}}\eta & \pi^+ & K^+ \\ \pi^- & -\frac{1}{\sqrt{2}}\pi^0 + \frac{1}{\sqrt{6}}\eta & K^0 \\ K^- & \overline{K}^0 & -\frac{2}{\sqrt{6}}\eta \end{pmatrix}. \tag{1.10}$$

Now, the chiral invariance of the Lagrangian under $SU_R(3) \times SU_L(3)$ transformations demands

$$U \to L U R^\dagger, \tag{1.11}$$

where both L, R are in $SU(3)$. This transformation produces the axial and vector conserved currents

$$
\begin{aligned}
V_a^\mu &= R_a^\mu + L_a^\mu = -i\frac{F^2}{4}\left\langle \lambda_a \left(U^\dagger \partial^\mu U + U \partial^\mu U^\dagger\right)\right\rangle, \\
A_a^\mu &= R_a^\mu - L_a^\mu = i\frac{F^2}{4}\left\langle \lambda_a \left(U^\dagger \partial^\mu U - U \partial^\mu U^\dagger\right)\right\rangle,
\end{aligned}
\tag{1.12}
$$

with which calculate the matrix element of the axial current between a one-boson state and the vacuum. Since the A_a generators are broken they no longer annihilate the vacuum, so that:

$$
\langle 0 \left| A_a^\mu \right| \pi_b \rangle = i p^\mu F \delta_{ab}, \tag{1.13}
$$

where F can be identified as the meson decay constant in the chiral limit.

Higher orders can be constructed, the only demand is that they obey chiral symmetry breaking pattern depicted above. They are ordered by the dimensionality of their operators, organized in a momentum and quark mass expansion. According to Weinberg's power counting rule, the order D of a diagram is

$$
D = 2 + 2L + \sum_{K=1} V_{2K}(2K-2), \tag{1.14}
$$

where V_{2K} is the number of vertices of $\mathcal{L}_{2K}$, and L is the number of loops. It is then clear that a tree diagram with couplings of higher order will match the order of a given loop with coupling from a lower order Lagrangian. The most general $\mathcal{L}_4$ $SU(3)$ Lagrangian is

$$
\begin{aligned}
\mathcal{L}_4 = \quad & L_1 \left\langle \partial_\mu U^\dagger \partial^\mu U \right\rangle^2 + L_2 \left\langle \partial_\mu U^\dagger \partial_\nu U \right\rangle \left\langle \partial^\mu U^\dagger \partial^\nu U \right\rangle \\
+ \quad & L_3 \left\langle \partial_\mu U^\dagger \partial^\mu U \partial_\nu U^\dagger \partial^\nu U \right\rangle + L_4 \left\langle \partial_\mu U^\dagger \partial^\mu U \right\rangle \left\langle U^\dagger M_0 + M_0^\dagger U \right\rangle \\
& + L_5 \left\langle \partial_\mu U^\dagger \partial^\mu U \left(U^+ M_0 + M_0^+ U\right)\right\rangle + L_6 \left\langle U^\dagger M_0 + M_0^+ U \right\rangle^2 \\
+ \quad & L_7 \left\langle U^\dagger M_0 - M_0^\dagger U \right\rangle^2 + L_8 \left\langle M_0^\dagger U M_0^\dagger U + U^\dagger M_0 U^\dagger M_0 \right\rangle.
\end{aligned}
\tag{1.15}
$$

Higher orders also absorb the divergences of the lower ones through the renormalization of the low-energy constants (LECs). That is the reason why these effective theories must be renormalized order by order. The role of the LECs is to encode the contributions of heavier particles and higher energy scales. Even though there are some qualitative predictions [43, 44], they are usually fitted to experimental data [45–48]. In principle, higher order Lagrangians could be constructed as [49, 50]

$$
\mathcal{L}_{\text{eff}} = \mathcal{L}_2 + \mathcal{L}_4 + \mathcal{L}_6 + \mathcal{L}_8 + \cdots, \tag{1.16}
$$

however, the huge amount of new free parameters, together with the lack of data make it very complicated to extract relevant information from these higher order contributions.

1.2.1 πK predictions

Since its early years, most of the efforts from the community of ChPT practitioners were devoted to the actual study of the data on meson-meson interactions, with particular emphasis on $\pi\pi \to \pi\pi$ scattering. In such case, $SU(2)$ is a simpler and more accurate representation of the spontaneous chiral symmetry breaking than $SU(3)$.

Regarding the $SU(3)$ case, most particularly πK scattering, the low-energy expansion does not converge very rapidly. Of particular interest are the πK scattering lengths, which represent the strength of the interaction at threshold. These low energy parameters illustrate the convergence of the $SU(3)$ expansion, and some experimental, dispersive and Lattice results exist for them. Therefore, in figure 1.4 we shown a comparison between ChPT calculations at tree level (triangle), NLO (square) and NNLO (circle). Not only do higher order results separate from Lattice QCD predictions (in red), but the NNLO is far away from the tree level current algebra prediction [51]:

$$a_0^+ = \frac{a^{1/2} + 2a^{3/2}}{3} = 0. \tag{1.17}$$

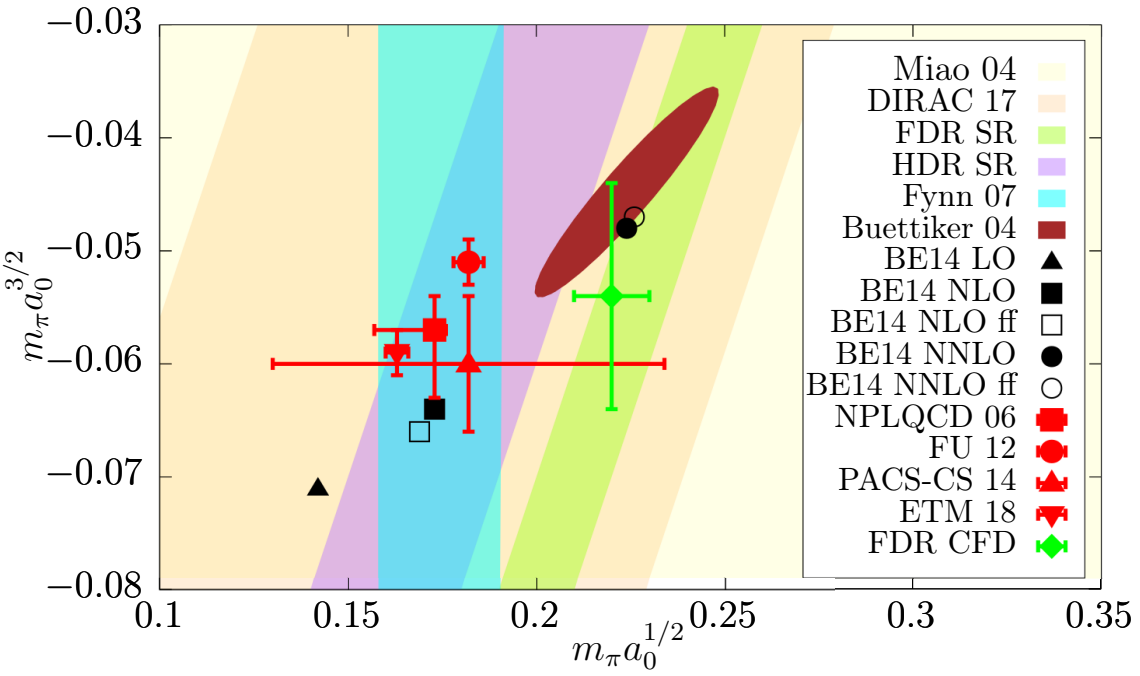

Figure 1.4: Comparison between various sum rules and determinations coming from different Roy-Steiner equations compared with both Lattice predictions and ChPT based calculations.

These scattering lengths will be central in this thesis. They not only provide an estimation on how well does the expansion converge, but also dominate the extraction of the LECs, the scattering process close to threshold, the form factors, the lifetime of mesonic atoms, etc...

Reference	$m_\pi a_0^{1/2}$	$m_\pi a_0^{3/2}$	Description
Büttiker et al. (2004) [2]	0.224±0.022	-0.0448±0.0077	Dispersive Roy-Steiner
Peláez-Rodas (2016) [52]	0.220±0.010	$-0.0540^{+0.010}_{-0.014}$	Fit constrained with FDR
Bijnens-Ecker (2014) [53]	0.142	-0.071	ChPT LO
Bijnens-Ecker (2014) [53]	0.173(0.169)	-0.064(-0.066)	ChPT NLO fit 14(free fit)
Bijnens-Ecker (2014) [53]	0.224(0.226)	-0.048(-0.047)	ChPT NNLO fit 14(free fit)
Miao et al.(2004) [54]	-	-0.056±0.023	Lattice, Wilson quenched
NPLQCD (2006) [55]	$0.1725\pm0.0017^{+0.0023}_{-0.0156}$	$-0.0574\pm0.016^{+0.0024}_{-0.0058}$	Lattice. Domain-wall
Flynn-Nieves (2007) [56]	0.175±0.017	-	Lattice+Omnés DR
Fu (2012) [57]	0.1819±0.0035	-0.0512±0.0018	Lattice, moving wall source
PACS-CS (2014) [58]	0.182±0.053	-0.060±0.006	Lattice, improved Wilson
ETM (2018) [59]	0.163±0.003	-0.059±0.002	Lattice, twisted mass.

Table 1.1: Determinations of πK scalar scattering lengths from various approaches.

Another interesting possibility is the study of the properties of resonances, particularly their compositeness, which is a long-standing problem (see [60] for a recent review on the $\sigma/f_0(500)$).

Unfortunately, the main feature of the formulation of ChPT is also a huge drawback on itself. The perturbative nature of the expansion, together with the definition of the Lagrangian order by order does not fulfil unitarity, *i.e.*, probability is not conserved. This behavior is not an unexpected one, as the amplitudes would be described by no more than a expansion, only valid really close to their thresholds. Furthermore, resonance are usually defined when unitarity is saturated, which is the indication of a strong interaction. Thus, in order to describe resonances unitarity is a key ingredient. In addition, resonances correspond to poles in the complex plane and a perturbative expansion will never reproduce a pole, at most it could reporduce the tail of the resonance. One could then include the resonances explicitly [44], but hence the approach would not be able to predict anything about their dynamical generation from ChPT.

This problem was partially solved in the 90's when two different unitarization methods were combined with ChPT [61–65]. These unitarization methods, known as the Inverse Amplitude Method (IAM) and the N/D method respectively, introduced a new systematic way of describing meson-meson interactions. Nevertheless, by means of analytic methods the partial waves of the processes are unitarized, hence, they can be used at a given order to describe resonances. One of their interesting properties is the dynamical generation of resonances, *i.e.*, excited states that do not appear explicitly in the Lagrangian are generated by meson-meson interactions. This was the case for the much debated $\sigma/f_0(500)$ and $\kappa/K_0^*(700)$ resonances [66–70], together with several predictions for the f_0, a_0 [71], the $\Lambda(1405)$ states [72], or even KN interactions [73, 74]. As for the study of their compositeness, unitarized Chiral Perturbation Theory (UChPT) has been shown to be effective, with several predictions for relevant resonances [70, 75–77].

Although fruitful for phenomenological analyses of resonance properties, this de-

scription fails to achieve the high accuracy nowadays demanded for the low-energy sector, since it is hard to estimate reliable uncertainties. However, it is possible to obtain reliable pole determination by means of dispersive approaches (complemented or not with ChPT). These are the ones that dominate present determinations as shown in Fig. 1.5 (see note on the scalars at the RPP). Most of the thesis is dedicated to the study of meson interactions from the point of view of such dispersive approaches, that we will introduce in the next section. However, basic properties and definitions coming from ChPT phenomenology will be extensively used.

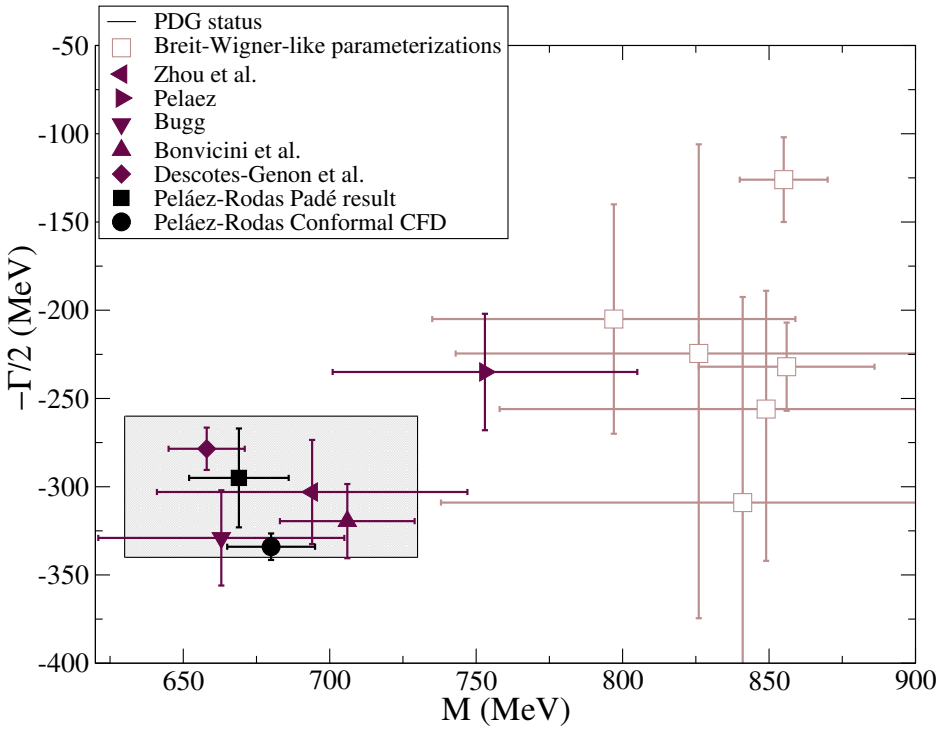

Figure 1.5: Present status of the $\kappa/K_0^*(700)$ in the Review of Particle Physics [4].

1.3 The S-matrix

We review in this section the main ideas that result from the implementation of the S-matrix principles. First, it is worth stating that several of the results presented in this sections will be extensively used throughout almost all chapters of this thesis. For a more pedagogical, while also more detailed explanation of the S-matrix principles we refer to the reader to [78–80].

It was already pointed out that, although fruitful for many purposes, ChPT cannot fully solve the longstanding problem of low-energy strong interactions. Unfortunately, no ideal description for the hadronic sector has been found yet, and many of the phenomena produced at low energies are still a challenge.

The S-matrix theory, introduced more than half a century ago is still one of the most powerful tools in hadronic physics, in particular in the study of meson-meson interactions. This formalism, based on first principles, provides model independent, robust, and precise results and at the same time it can be easily implemented. Thus we will take advantage of its simplicity and ability to provide accurate predictions when applied to hadronic physics.

As explained in the previous section, experimental scattering data analyses are crucial for our understanding of light particles. In particular, strong interactions have been understood during the years thanks to the enormous experimental efforts, always evolving towards higher energies and more sophisticated analyses. Unfortunately , a precise theoretical formulation is rather complicated, depending on the number of particles and the energies involved. In the rest of the thesis we will restrict ourselves to strong interactions and two or at most three particles in the initial or final state.

The main feature of the QCD coupling constant α_s, entails the confining interaction between quarks, producing the short distance strong interaction between hadrons. As a result, hadrons move freely after a very short interaction time. If we take into account that all other interactions are much weaker, we can, in most cases, safely neglect their formulation when describing strong interactions between hadrons. In this picture, several beams of non interacting particles are created, they collide an interact which each other while at very short distances, and the final beams are produced and then measured provided the time of flight is sufficiently long after the collision.

Taking into account these processes, we define the matrix element $\langle j|S|i\rangle$ as the amplitude produced by an initial state of particles $|i\rangle$ which interact and create the final state $|j\rangle$. The resultant matrix is the so called S matrix. Its very first proposition is that, if our interaction respects some symmetry principles, the matrix must be invariant under the corresponding symmetry transformations. For example, the S matrix must be Lorentz invariant, which means that the matrix elements $\langle j|S|i\rangle$ must be scalars. Hence if the particle states are described by their 4-momenta, the amplitude can depend only on scalar variables such as $p_i^\mu p_{j\mu}$. On top of that, if the interactions preserve some quantity, then the matrix will commute with its operator, and, if the

states are eigenvectors of that operator X hence

$$\langle j|S|i\rangle = \delta_{j\,i}\,\langle j\,|S_x|\,i\rangle\,. \tag{1.18}$$

In particular, due to the translational invariance of the theory, the total 4-momentum must be preserved

$$\langle j|S|i\rangle = \delta^4\,(p_j - p_i)\,\langle j\,|S_p|\,i\rangle\,. \tag{1.19}$$

If the state is composed of more particles, then it will be described as the direct product, creating the so called Fock space

$$|p_1, \cdots, p_n\rangle = |p_1\rangle \otimes |p_2\rangle \otimes \cdots \otimes |p_n\rangle\,. \tag{1.20}$$

As particles may or may not interact at all, we should take care of this condition in order to extract the irrelevant information from the S matrix, we define instead

$$S = \mathbb{1} + iT, \tag{1.21}$$

where T is known as the interaction matrix.

Finally, there is always the possibility that the particles cannot be fully described by just their 4-momentum, as they may exhibit different quantum numbers as spin, isospin, etc... In this cases, more "labels" will be included as a direct product in the definition of the one particle states, hence producing

$$|i\rangle = |p_\mu\rangle \otimes |\alpha_i\rangle, \tag{1.22}$$

so that

$$\langle j|S|i\rangle = \delta^4\,(p_j - p_i)\,(\langle\alpha_j|\alpha_i\rangle + i\langle\alpha_j|T|\alpha_i\rangle)\,. \tag{1.23}$$

Finally, let us introduce the most crucial observable in particle physics. In practice, experimental results are expressed in terms of cross sections. Imagine we have an incoming beam of density $\rho_1(x)$ that collides with a target of density $\rho_2(x)$ and we want to measure the scattering from the given initial state to the final state, hence, if the number of sets of outgoing particles $|f\rangle$ per unit time is n the cross section takes the form

$$\sigma_f = n/\left(v\int \rho_1(x)\rho_2(x)\mathrm{d}^3x\right) \tag{1.24}$$

This formula takes the dimensions of an area and in the particular case of $12 \to 34$ scattering it can be proved that the total cross section takes the form

$$\sigma_{12} = \frac{1}{4\,|p_1|\,\sqrt{s}}\sum_j (2\pi)^4\delta^4\left(p^j - p^i\right)\,|\langle j|T|i\rangle|^2. \tag{1.25}$$

This expression is key to hadronic physics, as all two-body scattering measurements are expressed through this observable, and most of the resonances we are interested in will produce the characteristic form of peaks or bumps in this cross sections. In the next sections we will study some relations between unitarity and the cross sections.

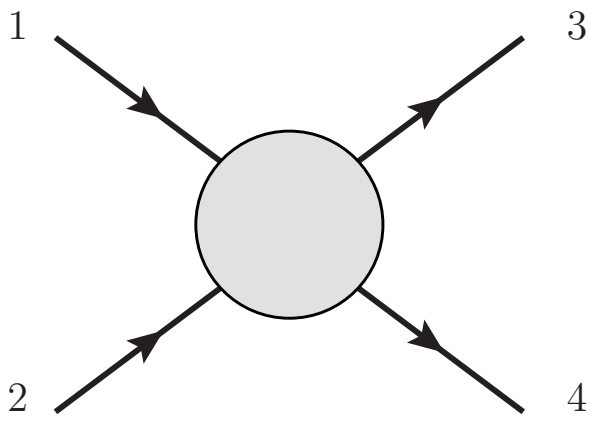

Figure 1.6: $12 \to 34$ scattering process.

1.3.1 Kinematics and Crossing

In this section we will discuss the kinematics of the scattering process $12 \to 34$ depicted in Fig. 1.6. The masses of the particles are allowed to be different, and we will restrict ourselves to spinless particles. This diagram also describes the scattering processes $1\bar{3} \to \bar{2}4$ and $1\bar{4} \to \bar{2}3$, where $\bar{2}, \bar{3}, \bar{4}$ are the antiparticles of $2, 3, 4$. Concerning one-particle states, spinless particles are characterized by their 4-momentum, apart from different possible quantum numbers (λ), relating their isospin, compositeness, etc.... , therefore, the irreducible representations of the one particles states are $|m, \mathbf{p}, \lambda\rangle$. They are normalized so that

$$\langle p|p'\rangle = \langle m, \mathbf{p}, \lambda|m', \mathbf{p}', \lambda'\rangle = (2\pi)^3 2E_{\mathbf{p}}\delta^{(3)}(\mathbf{p} - \mathbf{p}')\,\delta_{mm'}\delta_{\lambda\lambda'}. \tag{1.26}$$

Concerning two-particle scattering, one could build up to 10 different Lorentz scalars $p_i^\mu p_{j\mu}$, but only two are independent as the first four of them are related through

$$p_i^2 = m_i^2, \tag{1.27}$$

and the 4-momentum conservation

$$\sum_i p_i^\mu = 0, \tag{1.28}$$

relates another four of them. Thus we choose these two variables to be

$$s = (p_1 + p_2)^2, \quad t = (p_1 - p_3)^2, \tag{1.29}$$

which correspond to the $12 \to 34$ and $1\bar{3} \to \bar{2}4$ center of mass squared energies respectively. Analogously we can define $u = (p_1 - p_4)^2$ and the three of them, known as the Mandelstam variables, are related through the equation

$$s + t + u = \sum_{i=1} m_i^2. \tag{1.30}$$

Therefore, as scattering amplitudes behave as scalars under Lorentz transformations, they can be described by two Mandelstam variables. In the particular case of the s-channel center of mass frame they can be recast as

$$\begin{aligned} s &= m_1^2 + m_2^2 + 2\left(E_1 E_2 + |\mathbf{p}|^2\right), \\ t &= m_1^2 + m_3^2 + 2\left(E_1 E_3 - |\mathbf{p}|\,|\mathbf{p}'|\cos\theta_s\right), \\ u &= m_1^2 + m_4^2 + 2\left(E_1 E_4 + |\mathbf{p}|\,|\mathbf{p}'|\cos\theta_s\right), \end{aligned} \tag{1.31}$$

where the momenta are defined as

$$\begin{aligned} p &= \frac{1}{2\sqrt{s}}\sqrt{\left(s-(m_1+m_2)^2\right)\left(s-(m_1-m_2)^2\right)}, \\ p' &= \frac{1}{2\sqrt{s}}\sqrt{\left(s-(m_3+m_4)^2\right)\left(s-(m_3-m_4)^2\right)}, \end{aligned} \tag{1.32}$$

and θ_s is the angle between the first and third momenta, customarily called the center of mass scattering angle. We can thus define the energies in the center of mass frame as

$$\begin{aligned} E_1 &= \frac{1}{\sqrt{2}}\left(s + m_1^2 - m_2^2\right), \quad E_2 = \frac{1}{\sqrt{2}}\left(s + m_2^2 - m_1^2\right) \\ E_3 &= \frac{1}{\sqrt{2}}\left(s + m_1^3 - m_2^4\right), \quad E_4 = \frac{1}{\sqrt{2}}\left(s + m_4^2 - m_1^3\right), \end{aligned} \tag{1.33}$$

which yields

$$\cos\theta_s = \frac{s(t-u) + (m_1^2 - m_2^2)(m_3^2 - m_4^2)}{4spp'}. \tag{1.34}$$

As explained above, only two scalars are needed to describe the scattering process, in our particular case the most convenient choices are the modulus of the incoming momentum p and the angle θ_s. If we restrict ourselves to the elastic case where $m_1 = m_3$ and $m_2 = m_4$ then

$$\begin{aligned} s &= (E_1 + E_2)^2, \\ t &= -2|\mathbf{p}|^2\left(1 - \cos\theta_s\right), \\ u &= -2|\mathbf{p}|^2\left(1 + \cos\theta_s\right). \end{aligned} \tag{1.35}$$

The s-channel physical region is defined through the next condition

$$s \geq (m_1 + m_2)^2, \tag{1.36}$$

so that

$$t \leq 0. \tag{1.37}$$

The last condition implies $\cos\theta_s \geq -1$ and forces the physical region to be the interior of the hyperbola defined by

$$u \leq \frac{(m_1^2 - m_2^2)^2}{s}. \tag{1.38}$$

The very same derivation can be applied for both the t and the u-channels, with similar results. For the simpler case of equal mass elastic scattering, the physical regions are

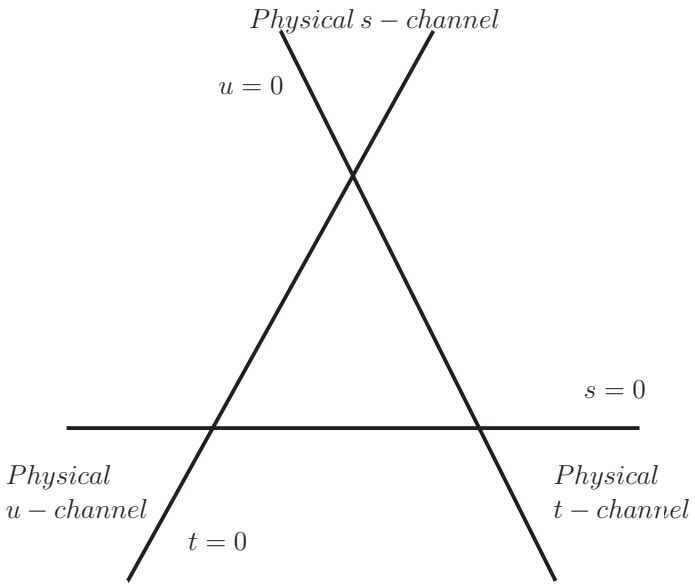

Figure 1.7: Physical regions for the scattering of equal mass particles.

shown in Fig. 1.7 , defined by the relations

$$\begin{array}{lllll} s-\text{channel}: & s \geqslant 4M^2, & t \leqslant 0, & u \leqslant 0, \\ t-\text{channel}: & t \geqslant 4M^2, & s \leqslant 0, & u \leqslant 0, \\ u-\text{channel}: & u \geqslant 4M^2, & s \leqslant 0, & t \leqslant 0. \end{array} \tag{1.39}$$

Therefore, a $12 \to 34$ scattering process like the one shown in Fig. 1.6 will always be described by two of the three s, t, u Mandelstam variables. For example, for the case of equal masses we choose for the s-channel

$$\langle p_3 p_4 | T | p_1 p_2 \rangle \equiv T_{12\to 34}(s,t), \tag{1.40}$$

where the physical region is the one described in Eq. (1.39).

Let us now consider the three Mandelstam variables in a two dimensional plane, deriving from Eq. (1.30). In such case, the analytic continuation from the physical s-channel region to the one of the t-channel

$$t-\text{channel}: \quad t \geqslant 4M^2, \quad s \leqslant 0, \quad u \leqslant 0, \tag{1.41}$$

would describe the amplitude of the process $1\bar{4} \to \bar{2}3$, that is

$$\langle p_3 p_{\bar{2}} | T | p_1 p_{\bar{4}} \rangle \equiv T_{1\bar{4}\to 3\bar{2}}(t,s). \tag{1.42}$$

In the same way, the variables could be continued into the u-channel physical region

$$u-\text{channel}: \quad u \geqslant 4M^2, \quad s \leqslant 0, \quad t \leqslant 0, \tag{1.43}$$

now describing the u-channel physical amplitude

$$\langle p_{\bar{2}} p_4 | T | p_1 p_{\bar{3}} \rangle \equiv T_{1\bar{3}\to \bar{2}4}(u,t). \tag{1.44}$$

Finally we can collect all these amplitudes under the same function, which can be analytically continued from one region to another

$$T(s,t,u) = \begin{cases} T_{12\to34}(s,t,u) & s \geq 4m^2, \quad t \leq 0, \quad u \leq 0, \\ T_{1\bar{3}\to\bar{2}4}(t,s,u) & t \geq 4m^2, \quad s \leq 0, \quad u \leq 0, \\ T_{1\bar{4}\to3\bar{2}}(u,t,s) & u \geq 4m^2, \quad s \leq 0, \quad t \leq 0. \end{cases} \tag{1.45}$$

This property, called Mandelstam hyphotesis [81, 82], is crucial in the description of hadronic processes, and although no general proof is known, it is fulfilled diagram by diagram [78] in QFT perturbation theory.

We shall see later how crossing affects analyticity. It is clear however, that there must be some analytical relation between the different physical regions, as they are just different regions in the very same plane.

1.3.2 Partial wave projection

Invariance under rotations entails the conservation of the total angular momentum in all scattering processes. Therefore, the amplitudes can be decomposed as a sum of scalar functions with well defined angular momentum, known as partial waves. One of the most interesting features is that resonances have a defined spin, so that they will appear only on one of these partial waves, which makes the analysis of partial waves crucial for the determination of their parameters.

It is worth remembering that the scattering amplitude is described by two scalars, in particular we choose s and $\cos\theta_s$. If we define z_s as the cosine in the physical region, then the amplitude of spinless particles can be described as

$$T(s,t,u) = 16\pi N \sum_\ell (2\ell+1) f_\ell(s) P_\ell(z_s), \tag{1.46}$$

where $N = 2$ for equal particle scattering and 1 otherwise. The functions $P_\ell(z_s)$ are the first kind Legendre polynomials, which are normalized as follows

$$\int_{-1}^{1} P_\ell(x) P'_\ell(x) dx = \frac{2}{2\ell+1}\delta_{\ell\ell'}. \tag{1.47}$$

We can now extract the partial waves by projecting the amplitude using

$$f_\ell(s) = \frac{1}{32\pi N} \int_{-1}^{1} dz_s P_\ell(z_s) T\left(s, t\left(z_s\right), u\right). \tag{1.48}$$

From the point of view of the partial waves $f_\ell(s)$ we have projected an amplitude that depends on two variables s, θ_s using a suitable orthogonal basis of Legendre polynomials so that the final result is a set of functions that depend only on one variable, s.

The same approach can be applied to the other physical channels, for example, for the t-channel the projection reads

$$g_\ell(t) = \frac{1}{32\pi N} \int_{-1}^{1} dz_t P_\ell(z_t) T(t, s(z_t), u), \tag{1.49}$$

where, in the t-channel case it is customary to factorize out the momenta ($g_\ell(t) \propto (q_{12}(t)q_{34}(t))^\ell$) from the integrand. The region of convergence of these partial-wave projections is called the Lehmann ellipse [83], which will be discussed in Appendix B.

1.3.3 Unitarity

Interactions must always satisfy that the total probability of finding any of the possible final states must be one. If we start in a given sate $|i\rangle$, then, the total probability of finding the state within a closed set of $|n\rangle$ possible states is always one

$$\sum_n P_n = 1, \tag{1.50}$$

where the probability of producing a $|n\rangle$ state from $|i\rangle$ reads

$$P_n = |\langle n|S|i\rangle|^2, \tag{1.51}$$

hence, Eq. (1.50) is just

$$\sum_n |\langle n|S|i\rangle|^2 = 1, \tag{1.52}$$

which, together with the completeness condition $\sum_n |n\rangle\langle n| = \mathbb{1}$ yields

$$\left\langle i \left| S^\dagger S \right| i \right\rangle = 1. \tag{1.53}$$

If we now take two different orthonormal vectors $|a\rangle$ and $|b\rangle$ and define a mixture vector by

$$\frac{\alpha|a\rangle + \beta|b\rangle}{\sqrt{|\alpha|^2 + |\beta|^2}}, \tag{1.54}$$

after inserting it in Eq. (1.53) we get the formula

$$1 = \frac{1}{|\alpha|^2 + |\beta|^2}\left(|\alpha|^2 + |\beta|^2 + \alpha^*\beta \left\langle a \left| S^\dagger S \right| b \right\rangle + \alpha\beta^* \left\langle b \left| S^\dagger S \right| a \right\rangle\right), \tag{1.55}$$

which, after a simple algebraic manipulation yields

$$\alpha^*\beta \left\langle a \left| S^\dagger S \right| b \right\rangle + \alpha\beta^* \left\langle b \left| S^\dagger S \right| a \right\rangle = 0. \tag{1.56}$$

Since α, β are arbitrary complex numbers, the off-diagonal terms must obey

$$\left\langle a \left| S^\dagger S \right| b \right\rangle = \left\langle b \left| S^\dagger S \right| a \right\rangle = 0. \tag{1.57}$$

Together with Eq. (1.53) we arrive at the unitarity condition

$$S^\dagger S = \mathbb{1} = S S^\dagger. \tag{1.58}$$

Now, the unitarity relation for $T = (S - \mathbb{1})/i$ reads

$$T - T^\dagger = iTT^\dagger, \tag{1.59}$$

or, equivalently

$$\langle j|T|i\rangle - \left\langle j\left|T^{\dagger}\right|i\right\rangle = (2\pi)^4 i \sum_n \delta^4\left(p^n - p^i\right)\left\langle j\left|T^{\dagger}\right|n\right\rangle\langle n|T|i\rangle. \tag{1.60}$$

Let us now focus our attention to elastic scattering, where $|j\rangle = |i\rangle$. In such case we get

$$\langle i|T|i\rangle - \left\langle i\left|T^{\dagger}\right|i\right\rangle = 2\mathrm{Im}\,\langle i|T|i\rangle. \tag{1.61}$$

On top of that, we will also take advantage of the time reversal invariance of strong interactions to write down $\langle n|T|i\rangle = \langle i|T|n\rangle$. Finally Eq. (1.60) can be rewritten as

$$2\mathrm{Im}\,\langle i|T|i\rangle = (2\pi)^4 \sum_n \delta^4\left(p^n - p^i\right)|\langle n|T|i\rangle|^2. \tag{1.62}$$

If one makes use of the previously defined Eq. (1.25), and compares it with Eq. (1.62) the cross section takes the following form

$$\sigma_{tot} = \frac{1}{2\,|p|\,\sqrt{s}}\mathrm{Im}\,T(s, t=0). \tag{1.63}$$

This means that the total cross section of a scattering process $1+2$ is proportional to the imaginary part of the forward amplitude, this relation is known as the Optical Theorem. It will be relevant in this thesis because total cross sections are easier to measure than other observables and therefore forward amplitudes become particularly relevant.

Now, a well defined angular momentum partial wave fulfills a similar relation

$$\mathrm{Im}\, f_\ell^{ji}(s) = \sum_n \sigma_n(s) f_\ell^{jn}(s) f_\ell^{ni}(s)^*, \tag{1.64}$$

where $\sigma_n(s) = 2p_n(s)/\sqrt{s}$ is just the phase space of the channel n.

We will define a partial wave projected S-matrix as

$$S_\ell^{ji}(s) = 1 + 2i\sigma(s) f_\ell^{ji}(s), \tag{1.65}$$

which fulfills

$$S_\ell S_\ell^{\dagger} = \mathbb{1}. \tag{1.66}$$

As the probability must be conserved, any given channel will have an absolute upper bound of one, which would be the case for elastic scattering, where

$$|S_\ell(s)|^2 = 1. \tag{1.67}$$

Otherwise, every entry of the matrix must have a modulus smaller or equal to one, obeying a more general relation

$$|S_\ell^{ji}(s)|^2 = \eta(s), \quad \eta(s) \leq 1. \tag{1.68}$$

Following Eq. (1.68) we can always write down a partial wave as

$$f_\ell^{ji}(s) = \frac{\eta_\ell^{ji}(s)\mathrm{e}^{2i\delta_\ell^{ji}(s)} - 1}{2i\sigma^{ji}(s)}, \tag{1.69}$$

which, in the elastic case reduces to a simpler formula

$$f_\ell(s) = \frac{e^{i\delta_\ell(s)}\sin\delta_\ell(s)}{\sigma(s)}. \tag{1.70}$$

The function $\delta_\ell(s)$ is known as the phase shift, whose analytic properties entails that the partial wave can be expanded for low momentum as follows:

$$\frac{2}{\sqrt{s}}\mathrm{Re}\, f_\ell(s) \simeq q^{2\ell}\left(a_\ell + b_\ell q^2 + \cdots\right), \tag{1.71}$$

where the first term of the expansion is the scattering length a_ℓ. This low-energy coefficients of this expansion are key to the understanding of meson-meson interactions and central to the ChPT low-energy constants determination. For these reasons, they will be one of the main topics of this thesis.

An interesting phenomenological description of the elastic region can be achieved by means of a conformal mapping in the complex plane. It is easy to rewrite Eq. (1.70) as

$$f_\ell(s) = \frac{1}{\Psi(s) - i\sigma(s)}, \tag{1.72}$$

where the function $\Psi(s) = \sigma(s)\cot\delta_\ell(s)$ must be an analytical function with a branch point starting at the inelastic threshold, together with a left and circular cuts corresponding to the crossed channel contributions, all consequences of unitarity.

We could now exploit the analytic features of the partial wave (section 1.3.4) by writing a new variable $\omega(s)$, called conformal variable, which in the case of equal masses reads

$$\omega(s) = \frac{\sqrt{s} - \alpha\sqrt{s_0 - s}}{\sqrt{s} + \alpha\sqrt{s_0 - s}}. \tag{1.73}$$

This new variable describes by construction the analytic structures of the partial wave, the parameter α centers the new variable, while s_0 describes the highest s value for which the infinite expansion of the function $\Psi(s)$ converges. Therefore, the function $\cot\delta_\ell(s)$ is expanded as

$$\cot\delta_\ell(s) = \sum_n B_n\omega(s)^n. \tag{1.74}$$

If α is chosen wisely, the data can be centered around the zero in both directions, giving rise to a fairly more stable fit. In practice, the series are truncated up to a given order, so that the whole expression could be used beyond s_0 for purely phenomenological purposes, to describe the inelastic region.

The case of unequal masses is more complicated, due to different analytic structures that appear in the partial wave, the main difference is that now the conformal variable

would be defined by

$$y(s) = \left(\frac{s-(M^2-m^2)}{s+(M^2-m^2)}\right)^2,$$
$$\omega(s) = \frac{\sqrt{y(s)}-\alpha\sqrt{y(s_0)-y(s)}}{\sqrt{y(s)}+\alpha\sqrt{y(s_0)-y(s)}}, \tag{1.75}$$

where the $y(s)$ mapping is introduced to describe the circular cut derived in section 1.3.4.

Finally, let us introduce the coupled channel formulation, imagine we have two channels whose unitary relation is in matrix form

$$\text{Im}\, f_\ell(s) = f_\ell(s)\Sigma(s)f_\ell(s)^*, \tag{1.76}$$

where $\Sigma(s)$ is the diagonal matrix containing the phase spaces. Then, such a set of partial waves can be written as

$$S_\ell(s) = \begin{pmatrix} \eta(s)e^{2i\delta_1(s)} & i\sqrt{1-\eta^2(s)}e^{i(\delta_1(s)+\delta_2(s))} \\ i\sqrt{1-\eta^2(s)}e^{i(\delta_1(s)+\delta_2(s))} & \eta(s)e^{2i\delta_2(s)} \end{pmatrix}. \tag{1.77}$$

This formula could be extended to more than two channels, although the algebraic manipulations would be more complicated. In section 3.2 we will study in detail a more suitable formula for the phenomenological description of several coupled channels and this particular description will not play a relevant role in this thesis.

Some of these general formulas will be used in sections 2.2.3, 2.2.4, 2.4.3, 3.1.3 and section 4.1.3. Therefore, unitarity, one of the key S-matrix principles will be implemented on the partial waves by construction.

1.3.4 Analyticity

Now that the main kinematic and unitary features of the S-matrix have been introduced, the next step is to study the origin of its analytic structure. We shall consider the amplitude $T(s,t,u)$ of a given elastic scattering process of unequal mass particles m, M. This amplitude, in order to respect causality, must be analytic [84] except where the dynamics or first principles demand it to behave otherwise.

We will pay attention to the s-channel complex plane once t is fixed. Let us first recall the unitary relation of Eq. (1.62)

$$2\text{Im}\,\langle i|T|i\rangle = (2\pi)^4 \sum_n \delta^4\left(p^n - p^i\right) |\langle n|T|i\rangle|^2, \tag{1.78}$$

which produces a non-vanishing imaginary part above the first threshold, in particular, in the case of unequal masses m, M the threshold starts at $s = (m+M)^2$, and it continues until infinity. In addition, the opening of more intermediate inelastic channels

will also create more and more imaginary parts, each one corresponding to its own inelastic threshold.

Remember that the amplitude $T(s,t,u)$ is defined through the Mandelstam hypothesis. It is the combined amplitude that relates all physical regions by means of analytic continuation. Therefore, the imaginary parts of the crossed channels will also arise in the s-plane, as they are part of the amplitude when the variables move from the s-channel physical region to the t or u-channel physical regions. Now by recalling again the relation between the Mandelstam variables:

$$s + t + u = 2(m^2 + M^2), \tag{1.79}$$

it is clear that the u-channel threshold $u = (m+M)^2$ opens at $s = (m-M)^2 - t$, and goes in the opposite direction as the s-channel one. Again, more imaginary parts would be produces once the crossed channels start creating different final states. On top of that, and despite the fact that it would not be the case for meson-meson scattering, there could also be bound states, if the dynamics does not prohibit two particles creating a third stable one. It can be proven that this bound states correspond to poles in the real axis between the thresholds.

We now know that the imaginary part does not vanish from $(m+M)^2$ to ∞ due to the s-channel cut, and also from $(m-M)-t$ to $-\infty$ due to the u-channel unitarity condition. Therefore, the amplitude is real in the real axis between the thresholds. There is an important theorem in complex variable analysis known as the Schwarz reflection principle, which states that if a function satisfies the following conditions:

(i) $f(z)$ is analytic in a domain C in the complex plane,

(ii) $f(z)$ is real in a segment in C,

then the function must satisfy the equation

$$f(z^*) = f(z)^*. \tag{1.80}$$

It follows from this result that the scattering amplitude satisfies

$$T(s^*,t,u) = T(s,t,u^*)^*, \tag{1.81}$$

where we have also conjugated u to satisfy the condition of Eq. (1.30).

Provided that the relation of Eq. (1.81) holds in the complex plane, the unitarity relation produces an interesting feature, the amplitude cannot be analytic in the entire complex plane, or it would also be real in the entire real axis. The imaginary parts produce branch cuts, discontinuities between the $s+i\epsilon$ and $s-i\epsilon$ values of the amplitude, using both unitary and Schwarz reflection equations we get

$$2\mathrm{Im}\, T(s,t) = \lim_{\epsilon\to 0}\left[T(s+i\epsilon,t) - T(s-i\epsilon,t)\right] = (2\pi)^4 \sum_n \delta^4\left(p^n - p^i\right)\left|\langle n|T|i\rangle\right|^2. \tag{1.82}$$

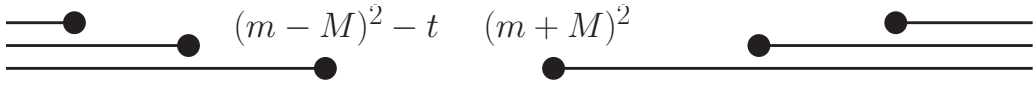

Figure 1.8: Analytic structure of meson-meson scattering amplitudes with fixed t.

Hence, for meson-meson scattering, the amplitude will have two different branch cuts, associated to the s-channel and u-channel dynamics, and it will be analytic elsewhere, producing the analytic structure depicted in Fig. 1.8.

As we now have two different limits of the amplitude, one above and one below the branch cut, it has to be clarified which limit gives the correct physical value. Taking into account the $i\epsilon$ perturbative description of Feynman diagrams, it is clear that the physical amplitude would be the limit from above the real axis

$$T(s,t,u) \equiv \lim_{\epsilon\to 0} T(s+i\epsilon,t,u), \tag{1.83}$$

whereas for the u-channel the same condition reads:

$$T(s,t,u) \equiv \lim_{\epsilon\to 0} T(s,t,u+i\epsilon) = \lim_{\epsilon\to 0} T(s-i\epsilon,t,u). \tag{1.84}$$

Finally, let us detail the analytic structure of partial waves, as they will be the main topic of this thesis. It is clear from the projection formula Eq. (1.48) that the s-channel partial waves of a given process share the same s-channel structures as the amplitude. Apart from the right hand cut, the projection itself will produce two additional branch cuts due to the singularities that would be produced inside the amplitude for t or u values, when the variable z_s moves from -1 to 1. In order to study these singularities in detail one would first need to introduce the double variable dispersive representation of the amplitudes [80]. However, it will not be discussed here as it goes beyond the scope of this introduction. We will just summarize the main properties instead. The double variable dispersive representation is based on the dispersive description of the projection of the amplitudes, so that it will produce terms proportional to $P_\ell(x')/(x-x')$ coming from the projection formula Eq. (1.48). Now these circular branch cuts are associated to the branch point singularities of the Legendre polynomials of the second kind

$$Q_\ell(x) = \frac{1}{2}\int_{-1}^{1} \frac{P_\ell(x')}{x-x'}dx', \tag{1.85}$$

whose branch cuts start at

$$\begin{aligned} 1+\frac{t}{2q^2} &= \pm 1, \\ 1+\frac{2M^2+2m^2-s-u}{2q^2} &= \pm 1. \end{aligned} \tag{1.86}$$

Finally, these equations can be translated into two different conditions

1. Left hand cut when $-\infty \leq s \leq (m-M)^2$,

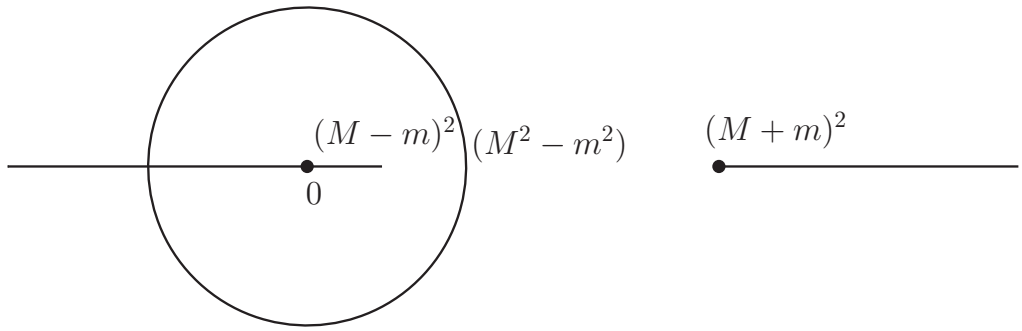

Figure 1.9: Analytic structure of the meson-meson partial waves of the scattering of two particles with different masses m and M.

2. Another cut when $s^2 - 2\beta s + (M^2 - m^2)^2 = 0$,

where β lies within

$$-\infty < \beta \leqslant M^2 - m^2. \tag{1.87}$$

This second condition comes from the fact that q^2 must be real in the region $-\infty \leq s \leq m^2$. For values $-(M^2 - m^2) \leq \beta \leq (M^2 - m^2)$ it produces a circle with radius $(M^2 - m^2)$, while for $\beta < -(M^2 - m^2)$ the solution for s lies in the very same left hand cut. Thus we conclude that the analytic structure of a partial wave is the one shown in Fig. 1.9. Note that for equal masses the circular cut disappears and the left cut starts at $s = 0$.

1.3.5 Dispersion relations

Dispersion relations are the central tool of this thesis, as they allow us to constrain and extract information from partial wave analyses in a model independent way, on top of many other features that this formalism provides us. Even though the next chapter is entirely devoted to the topic of dispersion relations, applied to meson-meson scattering, including some detailed derivations of advanced formalisms, we include here a brief general introduction, as they will be implemented in all results of this thesis.

In the previous section we have obtained the analytic structures of the scattering amplitudes, derived from first principles, *i.e.*, unitarity, analyticicty, and crossing. As a result, the amplitude of a given process will have a particular branch cut structure and it is analytic elsewhere. Hence, after fixing t we can make use of the Cauchy theorem and write

$$T(s,t,u) = \frac{1}{2\pi i} \oint ds' \frac{T\,(s',t,u)}{s'-s}. \tag{1.88}$$

This simple formula could be applied in many different situations, not only scattering but also form factors, finite energy sum rules, Feynman diagrams, etc... .

If we restrict ourselves to the $\pi K \to \pi K$ scenario as an illustrative example, the analytic structure of the amplitude is depicted in Fig. 1.10. This contour must be

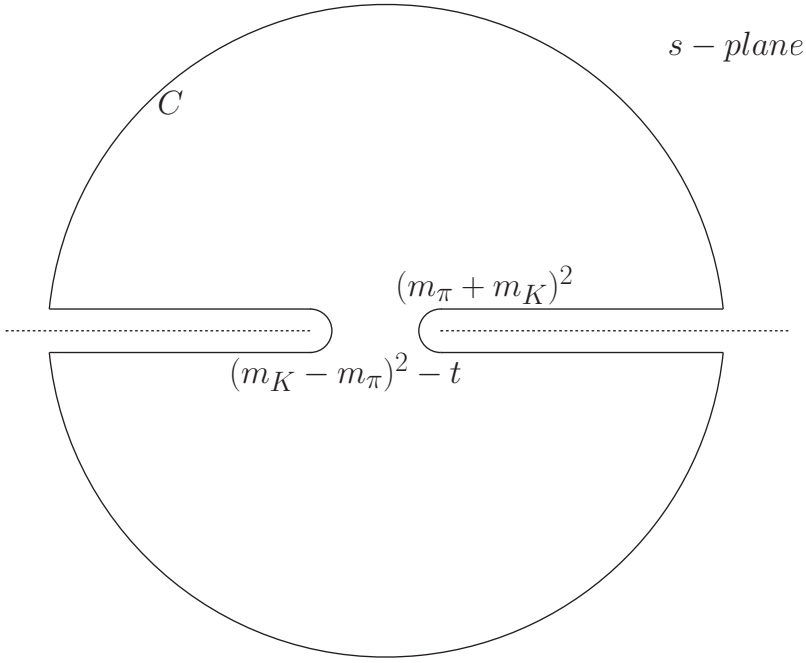

Figure 1.10: Analytic structure of the $\pi K \to \pi K$ amplitude for fixed t, together with a customary dispersion relation path before sending its radius to infinity.

splited into two different pieces. The semicircular paths, where $|s| = R$, and the straight paths around the branch cuts. First we will suppose that the amplitude goes to zero faster than $1/s$ as $s \to \infty$, so that the circular paths do not contribute for large enough radius R, and the integrals over the branch cuts converge. Second, if we take into account the Schwartz reflection principle, which states that $T(s^*, t, u) = T(s, t, u)^*$, the difference between the upper and lower parts over the branch cuts is proportional to the imaginary part. Therefore Eq. (1.88) reads

$$T(s,t,u) = \frac{1}{\pi}\int_{(m_K+m_\pi)^2}^{\infty} ds' \frac{\mathrm{Im}\, T\,(s',t,u)}{s'-s} + \frac{1}{\pi}\int_{-\infty}^{(m_K-m_\pi)^2-t} ds' \frac{\mathrm{Im}\, T\,(s',t,u)}{s'-s}. \tag{1.89}$$

Finally, the amplitude for real values of the variable s can be obtained by using the relation

$$\frac{1}{s'-s-i\epsilon} = PV\frac{1}{s'-s} + i\pi\delta\left(s'-s\right), \tag{1.90}$$

where PV means that the principal value prescription must be taken, hence, the amplitude in the physical region ($(m_\pi+m_K)^2 \le s \le \infty$) reads

$$\begin{aligned}\mathrm{Re}\, T(s,t,u) = \frac{1}{\pi} PV \int_{(m_K+m_\pi)^2}^{\infty} ds' \frac{\mathrm{Im}\, T\,(s',t,u)}{s'-s} \\ + \frac{1}{\pi}\int_{-\infty}^{(m_K-m_\pi)^2-t} ds' \frac{\mathrm{Im}\, T\,(s',t,u)}{s'-s}.\end{aligned} \tag{1.91}$$

The only assumption is that of the asymptotic behavior of the amplitude. Now, the imaginary parts can be obtained from experimental data up to a given s_{max}. In practice,

they are described with Regge parameterizations that will be briefly introduced in section 1.4. The asymptotic behavior of the Regge phenomenological description at high energies will tell us if the assumption about the asymptotics is valid. Let us imagine that $\mathrm{Im}\, T(s,t,u)/s \to constant$ as $s \to \infty$, hence, the integral written above does not converge, however, we could always subtract the function at a known value and obtain the following dispersion relation

$$T(s,t,u) - T\left(s_0,t,u\right) = \frac{1}{2\pi i}\left(s-s_0\right)\oint ds' \frac{T\left(s',t,u\right)}{\left(s'-s\right)\left(s'-s_0\right)}. \tag{1.92}$$

Now, this integral does converge and we can again rewrite the formula so that it matches with the branch cut description of Fig. 1.10

$$\begin{aligned}\mathrm{Re}\, T(s,t,u) = \mathrm{Re}\, T\left(s_0,t,u\right) &+ \frac{s-s_0}{\pi}\int_{(m_K+m_\pi)^2}^{\infty} ds' \frac{\mathrm{Im}\, T\left(s',t,u\right)}{\left(s'-s\right)\left(s'-s_0\right)} \\ &+ \frac{s-s_0}{\pi}\int_{-\infty}^{(m_K-m_\pi)^2-t} ds' \frac{\mathrm{Im}\, T\left(s',t,u\right)}{\left(s'-s\right)\left(s'-s_0\right)}.\end{aligned} \tag{1.93}$$

More subtractions may be necessary, or convenient, for which two different approaches can be implemented. The first one would be subtracting the amplitude at a different value of s as:

$$\begin{aligned}&T(s,t,u) - T\left(s_0,t,u\right)\frac{\left(s-s_1\right)}{s_0-s_1} - T\left(s_1,t,u\right)\frac{\left(s-s_0\right)}{s_1-s_0} \\ &= \frac{1}{2\pi i}\left(s-s_0\right)\left(s-s_1\right)\oint ds' \frac{T\left(s',t,u\right)}{\left(s'-s\right)\left(s'-s_0\right)\left(s'-s_1\right)}.\end{aligned} \tag{1.94}$$

The second would be to subtract the amplitude and its derivative at the same energy

$$\begin{aligned}T(s,t,u) =& T\left(s_0,t,u\right) + \left(s-s_0\right)T'\left(s_0,t,u\right) \\ &+ \frac{1}{2\pi i}\left(s-s_0\right)^2\oint ds' \frac{T\left(s',t,u\right)}{\left(s'-s\right)\left(s'-s_0\right)^2}.\end{aligned} \tag{1.95}$$

If the asymptotic region is not well known, or the integral must be truncated, subtractions can be helpful. However, the price to pay is the addition of subtraction constants that need to be determined as input. In practice, a balance must be found between including more subtractions and suppressing the asymptotic regions. In particular, as our Regge descriptions fit the high energy data nicely, so that their input is trustworthy, we will not introduce within our amplitudes more subtractions that the necessary ones to obtain a reliable and robust result.

Let us remark that all dispersion relations, as written in this section, depend on two different branch cuts. The first one is the s-channel physical cut, produced by its own unitarity condition and where data can be found to describe the imaginary part, while there is a second branch cut, whose values are unphysical. It is then that crossing symmetry plays a crucial role, as we will always be able to rewrite this cut over the physical regions of different channels, thus depending only on direct meson-meson scattering measurements.

1.3.6 Resonance poles

One of the most salient features of the scattering between particles are the peaks or bumps in cross sections. In the case of non-relativistic Quantum Mechanics, the quasi-bound states that create peaks also produce a dramatic increase of the phase shift $\delta(s)$, which customarily defines the mass of the particle when it crosses 90^o. This scenario partially translate into relativistic scattering, however we will focus here on a model independent definition of what a resonance is.

It is worth remembering that no poles exist in the first Riemann sheet of the s-plane, except for possible bound states in the real axis. Otherwise either unitarity or causality would be violated [78]. However, poles can appear in the second Riemann sheet, and under certain circumstances they can describe resonances. Let us clarify this situation by the introduction of the simple Breit-Wigner formula [85] in the S wave

$$f_0(s) \sim \frac{\Gamma/2}{s-(M-i\Gamma/2)^2}. \tag{1.96}$$

This formula has a pole when $s_p = (M - i\Gamma/2)^2$, which is seen in the real axis as a peak whose width depends on how far or close the pole is from the real axis. This width has direct relation with the lifetime of the particle. Hence such a resonance could in principle be characterized by the narrowness and position of the peak in the real axis.

In the formula above the prescription $s \equiv s + i\epsilon$ has been taken, the physical amplitude $T(s,t,u)$ is defined as the limit when $\epsilon \to 0$. This prescription ensures that the positive imaginary parts lie in the first Riemann sheet, while we can cross the unitarity cut continuosly to the second Riemann sheet. The Breit-Wigner formula thus gives a direct analytical continuation into the second Riemann sheet across the unitarity cut, valid only in a small region around the peak.

Nonetheless, relativistic Breit-Wigner formulas do not have simple interpretations, as barrier factors and other kinematic structures may be included to describe the partial wave, thus varying the position of the pole for the same input in the real axis. On top of that, as we will see in next sections, broad resonances, cusp effects, or overlapping resonances can distort the shape when seen in different processes. Nevertheless all amplitudes with the same quantum numbers should have the same singularities.

That is the reason why we will adopt the convention of the position of the pole in the next continuous Riemann sheet, $\sqrt{s_p} = M - i\Gamma/2$, as the definition of the parameters of a resonance. Another relevant parameter is the coupling of a given resonance to a particular final state, which is proportional to the residue of the pole through the relation

$$g^2 = -16\pi \lim_{s\to s_{pole}} (s - s_{pole}) \frac{t_\ell^{II}(s)(2\ell+1)}{q(s)^{2\ell}}, \tag{1.97}$$

where $t_\ell^{II}(s)$ is the partial wave in the second Riemann sheet for the scattering of that state. This coupling is usually related to the width for narrow resonances, however, when there are overlapping states, cusps, or broad resonances it becomes a new degree of freedom of the particle.

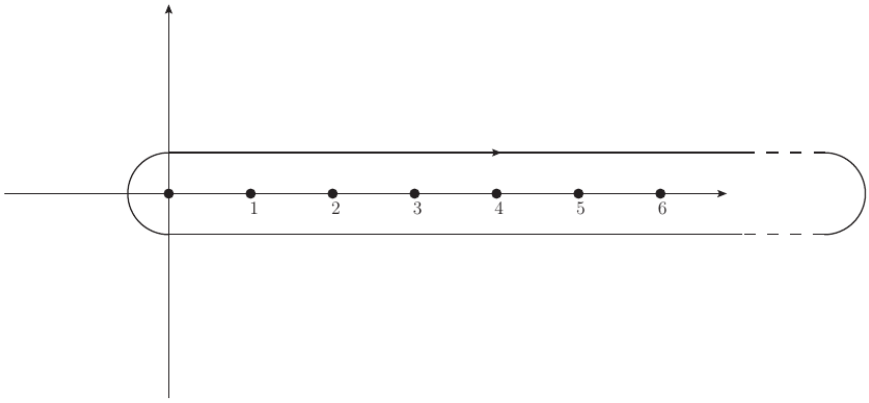

Figure 1.11: Integration contour in the complex angular momenta plane surrounding the poles at integer ℓ values.

1.4 Regge theory

Is in 1959 when T. Regge [86] first introduced the concept of what nowadays is a fruitful theoretical tool in High Energy Physics. He studied the theory of complex angular momenta to discuss solutions of the non-relativistic Schroedinger equation. There it was proved that, for a broad class of potentials, the only singularities appearing in the scattering amplitude complex ℓ plane were poles, of which the ones appearing for positive integer values of ℓ were identified as resonances. In fact, these Regge poles are relevant for the determination of the analytical and dispersive properties of the relativistic scattering amplitudes. In the QCD case, there is also a relevant cut singularity, dominant at higher energies, known as the Pomeron, which is not defined with a resonance exchange. In practice however, it is parameterized as if it were a pole.

In this section we briefly introduce the reader to the theory of complex angular momenta, deriving the formula for high energy hadron scattering amplitudes that we will use in several sections of this thesis, together with an introduction to the concept of factorization of a Regge exchange. Finally, we will also include an introduction to the Pomeron exchange, which plays a relevant role in sections 2.2.3, 2.2.4 and 3.3.3. For a detailed and pedagogical introduction we refer the reader to [79, 87, 88].

In this section we will consider the scattering of equal mass spinless particles for simplicity, so that one could write a partial wave expansion for the t-channel scattering as:

$$T(s,t) = 32\pi \sum_{\ell} (2\ell+1) P_\ell(z_t) f_\ell(t), \tag{1.98}$$

where the scattering angle reads:

$$z_t = 1 + \frac{2s}{t-4m^2}. \tag{1.99}$$

As detailed in appendix B partial wave expansions are only valid in a limited region, known as the Lehmann ellipse [83], driven by the value of s in this particular case. If one wants to get a general description, applicable also for large values of the Mandelstam variable, an analytic continuation is needed. It is here where the extension to complex values of ℓ play an important role, as the new partial wave expansion will be valid in the entire s plane.

We first start by replacing the sum over ℓ in Eq. (1.98) by an integral over the contour of Fig. 1.11,

$$T(s,t) = 16\pi i \int_C \frac{(2\ell+1) f(\ell,t) P_\ell(-z_t)}{\sin \pi\ell} d\ell, \tag{1.100}$$

where we use Cauchy's theorem, and $f(\ell,t)$ is the analytical continuation to complex ℓ values of the original partial wave. The next step would be to deform the contour of Fig. 1.11 into the one in Fig. 1.12. However, we must first study the definition of $f(\ell,t)$, as it is not unique. Fortunately, due to Carlson's Theorem, a unique definition can be achieved by imposing an upper bound for $f(\ell,t)$ when $\ell \to \infty$. The theorem states that if:

(i) $f(z)$ is analytic in Re $z > C$, where C is a real constant.

(ii) $f(z) < e^{K|z|}$, where $K < \pi$ in Re $z > C$.

(iii) $f(z) = 0$ at an infinite sequence of positive integers.

Then $f(z) = 0$, which is equivalent to the uniqueness of $f(\ell,t)$ if it satisfies the first two conditions. Unfortunately, if one uses the partial wave projection formula

$$f_\ell(t) = \frac{1}{32\pi} \int_{-1}^{1} P_\ell(z_t) T(s(z_t),t) dz_t, \tag{1.101}$$

then, due to the asymptotic behavior in ℓ of $P_\ell(z) \to \ell^{-1/2}(C_1 e^{i\theta} + C_2 e^{-i\theta})$ and the fact that $-1 < \cos\theta < 1$, it implies that $f(\ell,t)$ does not satisfy the second condition.

Nevertheless, this problem can be avoided by defining a new set of partial waves called $f^+(\ell,t)$ defined as the even $f(\ell,t)$ partial waves, and $f^-(\ell,t)$ defined as the odd partial waves. These two sets satisfy Carlson's Theorem, thus allowing us to use the well-defined amplitudes

$$T^\pm(s,t) = 16\pi \sum_\ell (2\ell+1) f^\pm(\ell,t)(P_\ell(z_t) \pm P_\ell(-z_t)), \tag{1.102}$$

where the physical amplitude is defined through the addition of both amplitudes

$$T(s,t) = T^+(s,t) + T^-(s,t). \tag{1.103}$$

As explained above, we use the Cauchy Theorem, together with the contour of Fig. 1.11 to rewrite the partial wave expansion of Eq. (1.102) as

$$T^\pm(s,t) = 16\pi i \int_C \frac{(2\ell+1) f^\pm(\ell,t)(P_\ell(-z_t) \pm P_\ell(z_t))}{\sin \pi\ell} d\ell, \tag{1.104}$$

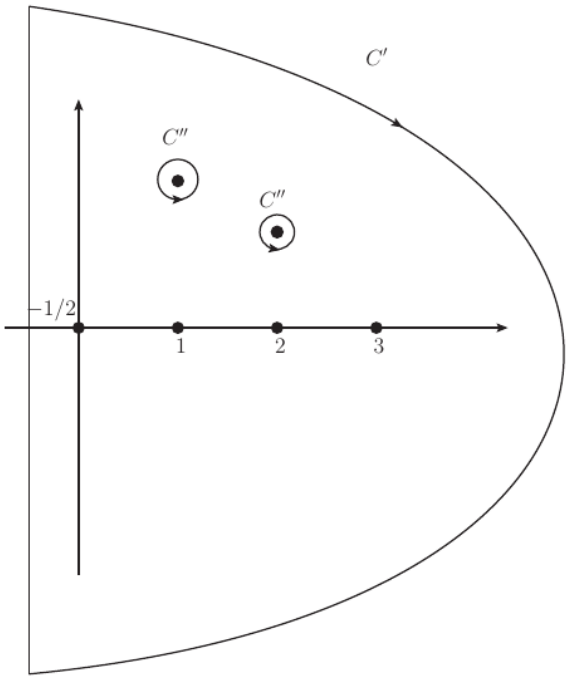

Figure 1.12: Deformation of the original contour in the complex angular momenta plane.

now let us deform the original contour into the one shown in Fig. 1.12, which apart from a semicircle enclosed with a line at $\mathrm{Re}\,\ell = -1/2$ it also includes the contours around the Regge poles appearing in the complex ℓ-plane.

We will denote the positions of these poles in $f^{\pm}(\ell, t)$ as $\alpha^{\pm}(t)$, while the residues will be denoted as $\beta^{\pm}(t)$. This function $\alpha^{\pm}(t)$ will also be called Regge trajectory, as the position of such poles describes a path parameterized by t in the ℓ-plane.

The contribution from the semicircle of the contour C' is zero, due to the convergent behavior of the $f^{\pm}(\ell, t)$ partial waves. While the contributions coming from the Regge poles can be directly evaluated using their parameters, the result reads:

$$T^{\pm}(s,t) = 16\pi^2 \sum_i \frac{(2\alpha_i^{\pm}(t)+1)\beta_i^{\pm}(t)}{\sin \pi\alpha_i^{\pm}(t)} (P_{\alpha_i^{\pm}(t)}(-z_t) \pm P_{\alpha_i^{\pm}(t)}(z_t)) + 8\pi i \int_{-1/2-i\infty}^{-1/2+i\infty} \frac{(2\ell+1) f^{\pm}(\ell,t)(P_\ell(-z_t) \pm P_\ell(z_t))}{\sin \pi\ell} d\ell. \tag{1.105}$$

Finally, for large values of s, z_t is large and negative. Taking into account the asymptotic behavior of the Legendre Polynomials, the second integral of Eq. (1.105) vanishes, and the final formula reads:

$$T^{\pm}(s,t) \simeq -\pi \sum_i \beta_i^{\pm}(t) \frac{1 \pm e^{-i\pi\alpha_i^{\pm}(t)}}{\Gamma(\alpha_i^{\pm}(t)+1)\sin(\pi\alpha_i^{\pm}(t))} s^{\alpha_i^{\pm}(t)}. \tag{1.106}$$

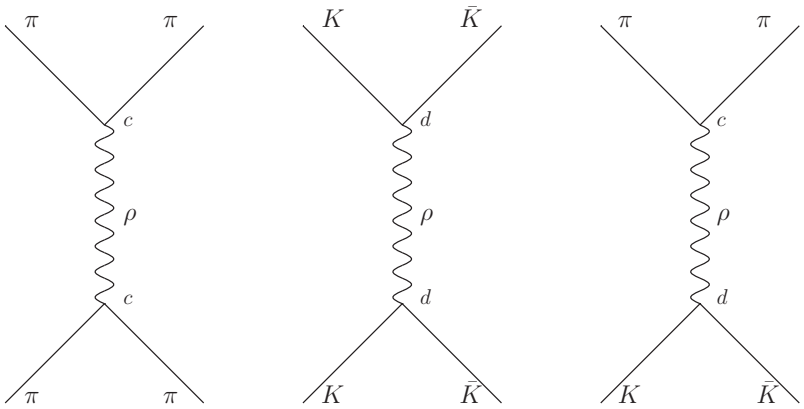

Figure 1.13: Exchanges of the ρ resonance between different states.

As we will see in more detail in section 4.1 for most hadrons, there is a one to one correspondence between a Regge trajectory and a family of resonances of given parity and other quantum numbers. Phenomenologically, it is observed that most hadrons can be grouped in linear Regge trajectories which are characterized by a positive slope $\alpha'(0) \sim 1$ GeV^{-2}, which is universal and an intercept $\alpha(0)$ that greatly depends on the family of resonances. As a result the trajectory $\alpha(t)$ varies linearly depending on the crossed-channel energy t.When $\alpha(t)$ reaches a positive integer number the value of the t variable will be considered the mass of the relevant exchanged particle.

In this thesis, we will make use of the Regge theory for several works, in particular, an explicit parameterization describing all $\pi\pi \to \pi\pi$, $\pi K \to \pi K$ and $\pi N \to \pi N$ processes [89], compatible with more recent results in [90] is used. All processes of a given isospin and strangeness in the t-channel are related through the well known factorization property. It states that Reggeon exchanges, *i.e.*, the crossed channel exchanged resonances couple to every vertex with a given constant $\beta(t)$, which produces the desired factorization effect as shown in Fig. 1.13.

Another interesting property we will take advantage of is the so called degeneracy. In principle Regge trajectories could be completely different one from another, there is no dispersive property that relates all of them, however, as explained above. All hadronic slopes $\alpha'(0)$ are similar. Furthermore, one would expect close intercepts for resonances that are almost degenerated within multiplets. This is the case for example of ρ and K^* families, which would be the degenerated if $SU(3)$ was an exact symmetry. Therefore, the parameters used to describe the later for $\pi\pi \to K\bar{K}$ scattering in section 2.2.4 can be initially taken from the ones of the ρ from $\pi\pi \to \pi\pi$. There exist a well known formulation, called the Veneziano model [91–94], that implements all these features, together with crossing. This model is compatible with the Regge asymptotic formulas, while it is also applicable at intermediate crossed energy values, where both the s and t variables are large. Therefore we will make use of it in sections 2.2.4 and 2.3, when the t dependence is needed.

1.4.1 The Pomeron

There is an interesting phenomenon that was discovered during the early years of strong interactions, even before Regge theory was applied to high energy interactions. All hadronic cross sections were remarkably constant at high energies. As a result of the optical theorem, it means that for $\sigma^{tot}(s) \sim C$ to occur then a Regge trajectory of positive parity with $\alpha_P^+(0) \sim 1$ is needed [95]. Its name, Pomeron, comes from I.Ya. Pomeranchuk, who showed in 1958 that the total cross sections of the scattering of a particle and its antiparticle off the same target must be asymptotically equal, if these are constant at high energies. Indeed, as the Pomeron trajectory is forced to have the quantum numbers of the vacuum due to its properties, then cross sections of particles and antiparticles must be equal at high energies $\sigma^{ab}(s) = \sigma^{a\bar{b}}(s)$. Nowadays we know that this is no longer the case, since hadronic cross sections grow like $s \log^2 s$ (see RPP review on cross-sections). This is actually understood from QCD as the exchange of gluon ladders, but this is well beyond our scope (see [80, 84, 87]). Note however that the Pomeron exchange does not correspond to the exchange of a family of resonances in the S-channel. Nonetheless, for simplicity and phenomenological purposes it is parameterized as if it were a pole, with an $s^{\alpha(t)}$ behavior with a trajectory $\alpha(t)$ slightly bigger than one.

1.4.2 Regge $\pi K \to \pi K$ formula

The $\pi K \to \pi K$ scattering process cannot be fully addressed dispersively without describing its behavior at high energies. However, even though data on cross sections for several other processes like $\pi\pi \to \pi\pi$ exist [96–100], there is no data on this reaction. That is the reason why we will take advantage of the factorization property detailed above to extract this amplitude from the $\pi\pi \to \pi\pi$ one as it was done in [89].

It is worth noticing first that the $\pi\pi$ system has three different independent amplitudes according to the three different isospins $I = 0, 1, 2$, and the same happens in the crossed channels since they are $\pi\pi \to \pi\pi$ again. However, the πK system which only has two different isospins $I = 1/2, 3/2$, becomes the $\pi\pi \to K\bar{K}$ channel when crossed , which may have $I = 0, 1$ could produce isospin $I = 0, 1$.

As factorization relates processes with the same quantum numbers, there will be no mix between different isospins, and we will have

$$\mathrm{Im}\, T_{\pi K}^{I_t=0}(s,t) = f_{K/\pi} \mathrm{Im}\, T_{\pi\pi}^{I_t=0}(s,t), \tag{1.107}$$

where $f_{K/\pi} = f_K^{(P)}(0)/f_\pi^{(P)}(0)$ and I_t is the isospin in the t-channel. Similarly

$$\mathrm{Im}\, T_{\pi\pi}^{I_t=0}(s,t) = P(s,t) + P'(s,t). \tag{1.108}$$

In this equation, $P(s,t), P'(s,t)$ are the Regge contributions of the Pomeron and f_2 respectively. For convenience even for the Pomeron, these formulas take the form

derived in Eq. (1.106). Whereas for isospin one we have

$$\mathrm{Im}\, T_{\pi K}^{I_t=1}(s,t) = g_{K/\pi}\mathrm{Im}\, T_{\pi\pi}^{I_t=1}(s,t), \tag{1.109}$$

where now $g_{K/\pi} = g_K^{(\rho)}(0)/g_\pi^{(\rho)}(0)$. Note that in this case the isospin one $\pi\pi \to \pi\pi$ amplitude is dominated by the $\rho(770)$ resonance.

Chapter 2

Dispersion relations

Several concepts related to the application of the S-matrix principles where already introduced in section 1.3, including a brief summary of dispersion relations. In this section, we will make use of the Mandelstam hypothesis, together with some convenient paths described by the Mandelstam variables, which lead us to closed sets of dispersion relations for meson-meson scattering processes. In this chapter we will particularly focus on $\pi\pi \to \pi\pi$ and $\pi K \to \pi K$ scattering, paying special attention to the convenient amplitudes and dispersion relations that maximize our applicability region. For a more general and pedagogical introduction to dispersion relations applied to meson-meson scattering see [79, 80, 101].

Nonetheless, dispersion relations could and are indeed applied to many other areas apart from meson-meson scattering within hadronic physics. Although they were first derived BY Kramers and Kronig in 1926 and 1927 in the field of Optical Physics, nowadays they are a widespread, powerful phenomenological tool in Hadron Physics. In particular, but not only, dispersion relations have also been successfully applied to Regge physics, as we will see in section 4.1.3. They have also been applied to many different production process, of which section 3.3.3 is an example, they could also be implemented for studies of Lattice QCD results as pointed in [102], to study form factors [103] or even devoted to the precision measurements regarding the anomalous magnetic dipole moment of the muon [104–107]. Finally, they are also crucial to study 3-body interactions [108–111].

In this chapter we will first extend the analyticity concepts, with a detailed description of how dispersion relations are built in section 2.1 for meson-meson scattering. Two different original results on the application of these techniques to $\pi K \to \pi K$ and $\pi\pi \to K\bar{K}$ scattering are presented in sections 2.2.3 and 2.2.4 respectively. Next, some original results on the joint analysis of the πK system are presented for the first time in section 2.3. Finally, in section 2.4.3 a set of parameterizations describing both the real axis and complex plane of the Roy-Steiner and GKPY equations analysis for $\pi\pi \to \pi\pi$

scattering made in [3, 112] is included.

2.1 Meson-meson scattering

The central topic of this thesis is the study of pion and kaon interactions, together with the determination of the parameters of strange resonances. The following sections will introduce the main dispersive tools for $\pi K \to \pi K$ scattering, although a few remarks on $\pi\pi \to \pi\pi$ scattering will also be presented.

For simplicity, we suppose isospin symmetry for pions and kaons, which is a valid approximation within a 3% error, which is the relative difference between the charged and neutral pion masses. Therefore, for the case of two-particle scattering the amplitudes will be described in terms of the total isospin of each reaction. Otherwise, one would regard any possible reaction as different, producing a large system that is not doable in practice.

In this particular case, pions have total isospin 1, while kaons have isospin 1/2. Pions are then classified in an isotriplet

$$\begin{aligned} |\pi^+\rangle &= |u\bar{d}\rangle = |I=1, I_3=1\rangle, \qquad |\pi^-\rangle = |\bar{u}d\rangle = -|I=1, I_3=-1\rangle, \\ |\pi^0\rangle &= \frac{1}{\sqrt{2}}|d\bar{d} - u\bar{u}\rangle = |I=1, I_3=0\rangle. \end{aligned} \tag{2.1}$$

In contrast, kaons are classified in two different isodoublets

$$\begin{aligned} |K^+\rangle &= |u\bar{s}\rangle = |I=1/2, I_3=1/2\rangle, \qquad |K^0\rangle = |d\bar{s}\rangle = |I=1/2, I_3=-1/2\rangle, \\ |K^-\rangle &= |\bar{u}s\rangle = |I=1/2, I_3=-1/2\rangle, \qquad |\bar{K}^0\rangle = |\bar{d}s\rangle = |I=1/2, I_3=1/2\rangle. \end{aligned} \tag{2.2}$$

Taking the isospin decomposition into account, together with the conservation of isospin by strong interactions, it is clear that $\pi K \to \pi K$ scattering will be classified by isospin $1/2, 3/2$ amplitudes, while its crossed channel $\pi\pi \to K\bar{K}$ will form amplitudes with possible isospins 0 and 1.

Let us now relate the different isospin amplitudes of a process through the isospin crossing matrices. Imagine we have a set of well defined isospin amplitudes in the s-channel, so that every process can be expanded as follows

$$\langle I_3, m_3; I_4, m_4 \,|T|\, I_1, m_1; I_2, m_2\rangle = \sum_I \langle m_3 m_3 | I, m\rangle \, \langle m_1 m_2 | I, m\rangle \, T^I(s,t,u), \tag{2.3}$$

where I is the isospin of the particle and m its projection over the z axis. In this formula, $\langle m_i m_j | I, m\rangle$ are no more than the well-known Clebsch-Gordan coefficients, so that every amplitude can be directly described as the sum of the well defined isospin ones. If we invoke crossing symmetry, the amplitude in the s-channel can be rewritten

as the one in the t-channel for particles $1\bar{3} \to \bar{2}4$ as

$$\left\langle \overline{I_2, m_2}; I_4, m_4 \left| T^t \right| I_1, m_1; \overline{I_3, m_3} \right\rangle = \sum_I \langle m_4 m_2 | I, m \rangle \langle m_1 m_3 | I, m \rangle T^{I_t = I}(s,t,u). \tag{2.4}$$

As both Eqs. (2.3) and (2.4) represent the same amplitude we have

$$T^{I_t}(s,t,u) = \sum_{I_s} C_{st} T^{I_s}(s,t,u), \tag{2.5}$$

where the isospin crossing matrix C_{st} relates the s and t-channels. In particular, in $\pi K \to \pi K$ and $\pi\pi \to K\bar{K}$ scattering the crossing matrices read

$$C_{st} = \begin{pmatrix} \frac{1}{\sqrt{6}} & 1 \\ \frac{1}{\sqrt{6}} & -\frac{1}{2} \end{pmatrix}, C_{su} = \begin{pmatrix} -\frac{1}{3} & \frac{4}{3} \\ \frac{2}{3} & \frac{1}{3} \end{pmatrix}, C_{tu} = \begin{pmatrix} 1 & 0 \\ 0 & -1 \end{pmatrix}, \tag{2.6}$$

whereas for $\pi\pi \to \pi\pi$ scattering, where three different isospin combinations are possible $(0, 1, 2)$, the matrices read

$$C_{st} = \begin{pmatrix} \frac{1}{3} & 1 & \frac{5}{3} \\ \frac{1}{3} & \frac{1}{2} & -\frac{5}{6} \\ \frac{1}{3} & -\frac{1}{2} & \frac{1}{6} \end{pmatrix}, C_{su} = \begin{pmatrix} \frac{1}{3} & -1 & \frac{5}{3} \\ -\frac{1}{3} & \frac{1}{2} & \frac{5}{6} \\ \frac{1}{3} & \frac{1}{2} & \frac{1}{6} \end{pmatrix}, C_{tu} = \begin{pmatrix} 1 & 0 & 0 \\ 0 & -1 & 0 \\ 0 & 0 & 1 \end{pmatrix}. \tag{2.7}$$

We define the inverse of the matrix C_{ij} as the crossing matrix C_{ji}, so that they fulfill

$$C_{st} C_{tu} = C_{tu} C_{us} = C_{us} C_{st} \quad C_{su} C_{ut} = C_{ts} C_{su} = C_{ut} C_{ts}, \tag{2.8}$$

and they are orthogonal projectors. In particular, in $\pi K \to \pi K$ scattering crossing relates both isospins

$$T^{1/2}(s,t,u) = \frac{1}{2}\left[3T^{3/2}(u,t,s) - T^{3/2}(s,t,u)\right], \tag{2.9}$$

where $T^{3/2}(s,t,u)$ is the amplitude of the process $\pi^+K^+ \to \pi^+K^+$. Instead, for $\pi\pi \to \pi\pi$ scattering we define the amplitude of the process $\pi^+\pi^- \to \pi^0\pi^0$ as $A(s,t,u)$ so that we get

$$\begin{aligned} T^0(s,t,u) &= 3A(s,t,u) + A(t,s,u) + A(u,t,s), \\ T^1(s,t,u) &= A(t,s,u) - A(u,t,s), \\ T^2(s,t,u) &= A(t,s,u) + A(u,t,s). \end{aligned} \tag{2.10}$$

Isospin decomposition is key for the construction of dispersion relations as we will see in next sections. Precisely, we will make use of it to build two different amplitudes T^+ and T^- for the $\pi K \to \pi K$ process, which are symmetric or anti-symmetric under $s \leftrightarrow u$ exchange respectively, and are also related to $\pi\pi \to K\bar{K}$ through isospin crossing factors

$$\begin{aligned} T^+(s,t,u) = T^+(u,t,s) &= \frac{T^{I_s=1/2}(s,t,u) + 2T^{I_s=3/2}(s,t,u)}{3} = \frac{T^{I_t=0}(t,s,u)}{\sqrt{6}}, \\ T^-(s,t,u) = -T^-(u,t,s) &= \frac{T^{I_s=1/2}(s,t,u) - T^{I_s=3/2}(s,t,u)}{3} = \frac{T^{I_t=1}(t,s,u)}{2}. \end{aligned} \tag{2.11}$$

Let us remember that the unsubtracted fixed-t dispersion relation Eq. (1.91) for $\pi K \to \pi K$ scattering reads

$$\begin{aligned} T(s,t,u) &= \frac{1}{\pi}\int_{(m_K+m_\pi)^2}^{\infty} ds' \frac{\mathrm{Im}\, T\,(s',t,u)}{s'-s} + \frac{1}{\pi}\int_{-\infty}^{(m_K-m_\pi)^2-t} ds' \frac{\mathrm{Im}\, T\,(s',t,u)}{s'-s} \\ &= \frac{1}{\pi}\int_{(m_K+m_\pi)^2}^{\infty} ds' \frac{\mathrm{Im}\, T\,(s',t,u)}{s'-s} + \frac{1}{\pi}\int_{(m_K+m_\pi)^2}^{\infty} du' \frac{\mathrm{Im}\, T\,(s,t,u')}{u'-u}, \end{aligned} \tag{2.12}$$

where we have rewritten s' as $s' = 2\Sigma - t - u'$, so that the integral runs over the physical region of the u' dummy variable.

Now, it is clear that, by taking into account the symmetry relations of Eq. (2.11) for the $\pi K \to \pi K$ amplitudes, the last integrand of Eq. (2.12) can be rewritten as an integral over the s-channel, for every amplitude of the process. The input is thus fixed by data on the physical region. One could follow the same steps for every amplitude of the $\pi\pi \to \pi\pi$ process, yielding a similar result.

2.1.1 Fixed-t Dispersion relations

In previous sections, the analytic structure of the amplitudes has been derived by fixing t as an intermediate step. With this structure in mind we will derive a simple, yet powerful set of dispersion relations for the amplitudes that are convenient for our analysis.

Let us remember that due to the optical theorem the total cross sections of a process is proportional to the imaginary part of the amplitude

$$\sigma_{tot} = \frac{1}{2\,|p|\,\sqrt{s}} \mathrm{Im}\, T(s, t=0). \tag{2.13}$$

Now, if one substitutes the imaginary part by its Regge expression at high energies Eq. (1.106), it is clear that the parameters of the Regge asymptotic formula are fixed by the experimental results. Furthermore, at $t = 0$ all Legendre polynomials are equal to 1, so that they do not produce any singular structure when increasing s. Therefore, if we write down a dispersion relation at $t = 0$, called Forward Dispersion Relation (FDR), the input will be directly determined by the cross sections, for which reliable data exist, while in principle the output can be calculated up to arbitrary high energies.

Regarding subtractions, the number will depend on how fast the Regge trajectory growths . According to the Froissart bound [113], a twice-subtracted dispersion relation for T^+ and a once-subtracted for T^- will always converge for fixed-t. In practice however, it is enough to include a once subtracted for T^+, while the T^- amplitude does converge without any subtraction, just because the growing parts coming from the Regge formula on the left and right integrals cancel each other due the the anti-symmetric nature of this amplitude.

Thus, if we use T^- and T^+ respectively in Eqs. (1.91) and (1.93) and we substitute $t=0, s_0=s_{th}$ we get

$$\begin{aligned}
\mathrm{Re}\,T^-(s) &= \frac{(2s-2\Sigma_{\pi K})}{\pi} PV\int_{(m_\pi+m_K)^2}^{\infty} ds' \frac{\mathrm{Im}\,T^-(s')}{(s'-s)(s'+s-2\Sigma_{\pi K})},\\
\mathrm{Re}\,T^+(s) &= T^+\left((m_\pi+m_K)^2\right)\\
&+\frac{(s-(m_\pi+m_K)^2)}{\pi} PV\int_{(m_\pi+m_K)^2}^{\infty} ds'\left[\frac{\mathrm{Im}\,T^+(s')}{(s'-s)(s'-(m_\pi+m_K)^2)}\right.\\
&\left.-\frac{\mathrm{Im}\,T^+(s')}{(s'+s-2\Sigma_{\pi K})(s'+(m_\pi+m_K)^2-2\Sigma_{\pi K})}\right],
\end{aligned} \tag{2.14}$$

where we have defined $T^+(s,0,u)=T^+(s)$. In the case of $\pi\pi\to\pi\pi$ scattering we use the amplitudes

$$T^{00}=\frac{1}{3}\left(T^0+2T^2\right),\quad T^{0+}=\frac{1}{2}\left(T^1+T^2\right),\quad T^{I_t=1}=\frac{1}{3}T^0+\frac{1}{2}T^1-\frac{5}{6}T^2, \tag{2.15}$$

which yield the equations listed below

$$\begin{aligned}
\mathrm{Re}\,T^{00}(s) &= T^{00}\left(4m_\pi^2\right)+\frac{(s-4m_\pi^2)}{\pi} PV\int_{4m_\pi^2}^{\infty} ds'\frac{(2s'-4m_\pi^2)\,\mathrm{Im}\,T^{00}(s')}{s'(s'-s)(s'-4m_\pi^2)(s'+s-4m_\pi^2)},\\
\mathrm{Re}\,T^{0+}(s) &= T^{0+}\left(4m_\pi^2\right)+\frac{(s-4m_\pi^2)}{\pi} PV\int_{4m_\pi^2}^{\infty} ds'\frac{(2s'-4m_\pi^2)\,\mathrm{Im}\,T^{0+}(s')}{s'(s'-s)(s'-4m_\pi^2)(s'+s-4m_\pi^2)},\\
\mathrm{Re}\,T^{I_t=1}(s) &= \frac{2s-4m_\pi^2}{\pi} PV\int_{4m_\pi^2}^{\infty} ds'\frac{\mathrm{Im}\,T^{I_t=1}(s',0)}{(s'-s)(s'+s-4m_\pi^2)}.
\end{aligned} \tag{2.16}$$

Besides calculating dispersion relations for these amplitudes, we can always combine them and evaluate them at a given energy point, the result is known as a sum rule, and they are usually evaluated at the threshold or sub-threshold. They are particularly interesting when the integral over the whole physical region can be related to a given low-energy parameter, thus producing a robust and model-independent extraction of its value. On top of that, if at a given energy value the amplitude is well known, a sum rule can always be implemented to relate the low-energy data to the high-energy contribution.

Actually, fixed-t partial-wave dispersion relations where first derived in Hadron physics to get an accurate description of low-energy parameters. The two first applications, $\pi\pi$ and πN scattering were obtained by Roy [114] and Steiner [115], respectively. These fixed-t relations are a fairly simple group of dispersion relations that fulfill the following practical requirements

1. Inputs come from the experimental data.
2. The kernels inside the integrals are analytic and simple.
3. They can be applied in a considerable energy range in the physical region

The set of equations described above are obtained through the implementation of crossing, once projected into partial waves they read

$$\mathrm{Re}\, f_l^{(I)}(s) = C_l^{(I)} a_0^{(0)} + C_l'^{(I)} a_0^{(2)} + \sum_{l',I'} PV \int_{4M_\pi^2}^{\infty} \mathrm{d}s' K_{l,l';I,I'}(s',s)\, \mathrm{Im}\, f_{l'}^{(I')}(s')\,, \quad (2.17)$$

where the constants $C_\ell^{(\prime)(I)}$ are known. A detailed derivation, including its region of applicability is given in Appendix A.

Thus, as proved in [116, 117], depending on the number of free parameters coming from subtractions and the values of the phase shifts at a given matching point s_m, a unique solution for the system of Roy-Steiner equations can be obtained just by including as input the imaginary parts above s_m. The price to pay however, is that the input above s_m is fixed and thus any systematic effect produced by deviations of the input is neglected. This approach has been used by several groups applied to $\pi\pi \to \pi\pi$ scattering [118–120], $\pi K \to \pi K$ scattering [2, 121], $\gamma\gamma \to \pi\pi$ [122, 123] and also to πN scattering [124, 125].

A different approach, more data driven, is the one performed in a series of works by the Madrid-Krakow group [3, 112, 126–128]. It consists on constraining the fits to partial waves by means of dispersion relations, while they are also forced to describe the data. We will follow this very same approach for the study of both $\pi K \to \pi K$ and $\pi\pi \to K\bar{K}$ systems. In such a case, it was shown [129] that the lower the number of subtractions, the smaller are the uncertainties produced, thus we will also take advantage of this fact to implement dispersion relations that are as less subtracted as possible. In particular, the fixed-t amplitude dispersion relations we will use for $\pi K \to \pi K$ read

$$\begin{aligned} T^-(s,t) &= \frac{1}{\pi}\int_{(m_\pi+m_K)^2}^{\infty} ds'\, \mathrm{Im}\, T^-(s',t)\left[\frac{1}{s'-s} - \frac{1}{s'-u}\right], \\ T^+(s,t) &= c^+(t) + \frac{1}{\pi}\int_{(m_\pi+m_K)^2}^{\infty} ds' \frac{\mathrm{Im}\, T^+(s',t)}{s'^2}\left[\frac{s^2}{s'-s} + \frac{u^2}{s'-u}\right], \end{aligned} \quad (2.18)$$

where the constant $c^+(t)$ is obtained by means of a hyperbolic dispersion relation, as explained in detail in Appendix A. After projecting this system of equation one gets

$$\begin{aligned} f_l^+(s) &= \frac{m_+ a_0^+}{2} + \frac{1}{\pi}\sum_\ell \int_{m_+^2}^{\infty} ds' L_{l,\ell}^+(s,s')\mathrm{Im}\, f_\ell^+(s') + \frac{1}{\pi}\sum_{\ell\geq 0}\int_{4m_\pi^2}^{\infty} dt' L_{l,2\ell}^0(s,t')\mathrm{Im}\, g_{2\ell}^0(t'), \\ f_l^-(s) &= \frac{1}{\pi}\sum_\ell \int_{m_+^2}^{\infty} ds' L_{l,\ell}^-(s,s')\mathrm{Im}\, f_\ell^-(s'), \end{aligned} \quad (2.19)$$

where the kernels are known functions given in Appendix D, and the only input apart from the data is the scattering length a_0^+. For the anti-symmetric partial wave however, the scattering length will be produced as a sum rule, dominated by the input of the $S^{1/2}$ partial wave at low energies. We thus expect this value to be really precise and trustworthy.

While a system of fixed-t dispersion relations could be derived also for $\pi\pi \to K\bar{K}$, it is explained in Appendix 2.2.4 how their applicability region is restricted below the physical threshold. An alternative formulation, obtained by means of a different mathematical relation between the Mandelstam variables is thus needed. Such a system will be described in next section.

2.1.2 Hyperbolic Dispersion relations

As pointed out above, even though fixed-t dispersion relations are fairly advantageous to study low-energy meson-meson scattering, the crossed-channel physical regions produced by two-particle states with different masses cannot be studied using this approach. A different scheme must be followed instead. Hyperbolic dispersion relations (HDR) were first introduced by Hite and Steiner [130] to solve the problem of the reduced validity region of fixed-t dispersion relations for πN scattering. The approach was extended later to $\pi\pi \to K\bar{K}$ [131] and πK [132] scattering in the 70's. Unfortunately, data was scarce, with crude results and small statistics. Furthermore, just a few partial waves had been measured. Hence no accurate results for these reactions were found.

Instead of considering the analytic structure when t is fixed, we will use a family of hyperbolae $(s-a)(u-a) = b$, where a will be used to maximize the analyticity domain as detailed in Appendix B. In previous works [2, 121, 131–133] the parameter defining the various families of hyperbolas a was set equal to zero for simplicity, however, we will take advantage of the approach described in [122, 124] to enlarge the physical region of applicability in the t-channel roughly a 70% by optimizing this parameter. At the same time we also increase the region of applicability of the s-channel up to the first inelastic threshold, which is key for a more stable extrapolation to obtain the $\kappa/K_0^*(700)$ pole.

Taking into account the hyperbola defined above, the Mandelstam variables s, u can be written as

$$\begin{aligned} s_b \equiv s_b(t) &= \tfrac{1}{2}\left(2\Sigma - t + \sqrt{(t+2a-2\Sigma)^2 - 4b}\right) \quad , \\ u_b \equiv u_b(t) &= \tfrac{1}{2}\left(2\Sigma - t - \sqrt{(t+2a-2\Sigma)^2 - 4b}\right) \quad . \end{aligned} \tag{2.20}$$

The analytic structure of the amplitude will thus be the same as before, however, we will express the Cauchy Theorem in terms of the t variable and then rewrite it using the relations above. Let us remark that all amplitudes must be even under $s \leftrightarrow u$ exchange if one wants to build a hyperbolic system of dispersion relations. Thus we will use two functions, the symmetric amplitude $T^+(s,t)$ and $T^-(s,t)/(s-u)$ which is symmetric by construction. It is worth noticing that $s-u$ goes to infinity as s increases, so that the latter does not need any subtraction to converge and hence it reads

$$\frac{T^-(s_b,t)}{s_b-u_b} = \frac{1}{2\pi}\int_{4m_\pi^2}^{\infty} dt' \frac{\mathrm{Im}\, T^{I_t=1}(t',s_b')}{(t'-t)(s_b'-u_b')} + \frac{1}{\pi}\int_{m_+^2}^{\infty} ds' \frac{\mathrm{Im}\, T^-(s',t_b')}{(s'-s_b)(s'-u_b)}, \tag{2.21}$$

where

$$s'_b \equiv s_b(t'), \quad u'_b \equiv u_b(t'),$$
$$t'_b = 2\Sigma - s' - \frac{b}{s'-a} + a. \tag{2.22}$$

For the symmetric amplitude however, one subtraction is needed, thus yielding the following equation

$$T^+(t,b,a) = h(b,a) + \frac{t}{\pi}\int_{4m_\pi^2}^{\infty} \frac{\mathrm{Im}\, T^{I_t=0}(t',s'_b)}{\sqrt{6}\, t'(t'-t)} dt' + \frac{1}{\pi}\int_{m_+^2}^{\infty} ds' \frac{\mathrm{Im}\, T^+(s',t'_b)}{s'}\Big(\frac{s}{s'-s} + \frac{u}{s'-u}\Big). \tag{2.23}$$

The relation between the subtraction constant $h(b,a)$ and the low-energy scattering length a_0^+ is detailed in Appendix A. Let us write the final equation

$$\begin{aligned} T^+(s_b,t) = 8\pi m_+ a_0^+ &+ \frac{t}{\pi}\int_{4m_\pi^2}^{\infty} \frac{\mathrm{Im}\, T^{I_t=0}(t',s'_b)}{\sqrt{6}\, t'(t'-t)} dt' \\ &+ \frac{1}{\pi}\int_{m_+^2}^{\infty} ds' \frac{\mathrm{Im}\, T^+(s',t_b)}{s'} \left[h(s',t,b,a) - h(s',0,b,a)\right] \\ &+ \frac{1}{\pi}\int_{m_+^2}^{\infty} ds' \frac{\mathrm{Im}\, T^+(s',0)}{s'^2} \left[g(s',b,a) - g(s',\Delta^2,0)\right], \end{aligned} \tag{2.24}$$

where the kernels $h(s',t,b,a)$ and $g(s',b,a)$ are also given in Appendix A. The advantage of hyperbolic dispersion relations is that they do not produce complicated integrands, while they are more useful than most of the alternative paths defined during the years.

Later on, in section 2.3 it will be explained how a once-subtracted dispersion relation for $T^-(s,t)/(s-u)$ is also of interest. As a brief remark, such an equation will depend way less on the crossed input, thus producing a more reliable result, barely affected by the uncertainties coming from $\pi\pi \to K\bar{K}$. This equation reads

$$\begin{aligned} \frac{T^-(s_b,t)}{s_b-u_b} = \frac{8\pi m_+ a_0^-}{m_+^2-m_-^2} &+ \frac{t}{2\pi}\int_{4m_\pi^2}^{\infty} dt' \frac{\mathrm{Im}\, T^{I_t=1}(t',s'_b)}{t'(t'-t)(s'_b-u'_b)} \\ &+ \frac{1}{\pi}\int_{m_+^2}^{\infty} ds' \mathrm{Im}\, T^-(s',t'_b) \left[d(s',t,b,a) - d(s',0,b,a)\right] \\ &+ \frac{1}{\pi}\int_{m_+^2}^{\infty} ds' \mathrm{Im}\, T^-(s',0) \left[f(s',b,a) - f(s',\Delta^2,0)\right], \end{aligned} \tag{2.25}$$

where once again the integrands $d(s',t,b,a)$ and $f(s',b,a)$ are known functions, listed in Appendix A.

Now let us recall the formulas for the s-channel and t-channel partial-wave projec-

tions, which in the particular case of πK scattering read

$$f_l^I(s) = \frac{1}{16\pi}\int_{-1}^{1} dz_s P_l(z_s) T^I(s,t),$$
$$g_\ell^I(t) = \frac{\sqrt{2}}{32\pi(q_\pi q_K)^\ell}\int_0^1 dz_t P_\ell(z_t) T^{I_t=I}(t,s). \tag{2.26}$$

Introducing these projection formulas into Eqs. (2.21), (2.24) and (2.25), the partial-wave dispersion relations for the s-channel read:

$$\begin{aligned}
f_l^+(s) &= \frac{m_+ a_0^+}{2} + \frac{1}{\pi}\sum_\ell + \frac{1}{\pi}\sum_{\ell\geq 0}\int_{4m_\pi^2}^\infty dt' K^0_{l,2\ell}(s,t')\mathrm{Im}\, g^0_{2\ell}(t'), \int_{m_+^2}^\infty ds' K^+_{l,\ell}(s,s')\mathrm{Im}\, f^+_\ell(s'),\\
f_l^-(s) &= \frac{1}{\pi}\sum_\ell \int_{m_+^2}^\infty ds' K^-_{l,\ell}(s,s')\mathrm{Im}\, f^-_\ell(s') + \frac{1}{\pi}\sum_{\ell\geq 1}\int_{4m_\pi^2}^\infty dt' K^1_{l,2\ell-1}(s,t')\mathrm{Im}\, g^1_{2\ell-1}(t'),\\
f_l^-(s) &= \delta_{l,0}\frac{m_+ a_0^-}{2}\frac{3s^2-2s\Sigma-\Delta^2}{8sm_\pi m_K} + \delta_{l,1}\frac{m_+ a_0^-}{2}\frac{m_\pi^4+(m_K^2-s)^2-2m_\pi^2(m_K^2+s)}{24sm_\pi m_K}\\
&\quad + \frac{1}{\pi}\sum_\ell \int_{m_+^2}^\infty ds' \hat{K}^-_{l,\ell}(s,s')\mathrm{Im}\, f^-_\ell(s') + \frac{1}{\pi}\sum_{\ell\geq 1}\int_{4m_\pi^2}^\infty dt' \hat{K}^1_{l,2\ell-1}(s,t')\mathrm{Im}\, g^1_{2\ell-1}(t'),
\end{aligned} \tag{2.27}$$

where all kernels are known functions, listed in Appendix D, and the scattering lengths come from the fits to the data. Note that we use a hat for the kernels of the once-subtracted T^- dispersion relation. On the other hand, the partial-wave expansion for the t-channel reads:

$$\begin{aligned}
g_0^0(t) =& \frac{\sqrt{3}}{2} m_+ a_0^+ + \frac{t}{\pi}\int_{4m_\pi^2}^\infty \frac{\mathrm{Im}\, g_0^0(t')}{t'(t'-t)}dt' + \frac{t}{\pi}\sum_{\ell\geq 2}\int_{4m_\pi^2}^\infty \frac{dt'}{t'} G^0_{0,2\ell-2}(t,t')\mathrm{Im}\, g^0_{2\ell-2}(t')\\
&+ \frac{1}{\pi}\sum_\ell \int_{m_+^2}^\infty ds' G^+_{0,\ell}(t,s')\mathrm{Im}\, f^+_\ell(s'),\\
g_2^0(t) =& \frac{t}{\pi}\int_{4m_\pi^2}^\infty \frac{\mathrm{Im}\, g_2^0(t')}{t'(t'-t)}dt' + \frac{t}{\pi}\sum_{\ell\geq 2}\int_{4m_\pi^2}^\infty \frac{dt'}{t'} G'^0_{2,4\ell-2}(t,t')\mathrm{Im}\, g^0_{4\ell-2}(t')\\
&+ \frac{1}{\pi}\sum_\ell \int_{m_+^2}^\infty ds' G'^+_{2,\ell}(t,s')\mathrm{Im}\, f^+_\ell(s'),\\
g_1^1(t) =& \frac{1}{\pi}\int_{4m_\pi^2}^\infty \frac{\mathrm{Im}\, g_1^1(t')}{t'-t}dt' + \frac{1}{\pi}\sum_{\ell\geq 2}\int_{4m_\pi^2}^\infty dt' G^1_{1,2\ell-1}(t,t')\mathrm{Im}\, g^1_{2\ell-1}(t')\\
&+ \frac{1}{\pi}\sum_\ell \int_{m_+^2}^\infty ds' G^-_{1,\ell}(t,s')\mathrm{Im}\, f^-_\ell(s'),\\
g_1^1(t) =& \frac{2\sqrt{2} m_+ a_0^-}{3(m_+^2-m_-^2)} + \frac{t}{\pi}\int_{4m_\pi^2}^\infty \frac{\mathrm{Im}\, g_1^1(t')}{t'(t'-t)}dt' + \frac{t}{\pi}\sum_{\ell\geq 2}\int_{4m_\pi^2}^\infty \frac{dt'}{t'} \hat{G}^1_{1,2\ell-1}(t,t')\mathrm{Im}\, g^1_{2\ell-1}(t')\\
&+ \frac{1}{\pi}\sum_\ell \int_{m_+^2}^\infty ds' \hat{G}^-_{1,\ell}(t,s')\mathrm{Im}\, f^-_\ell(s'),
\end{aligned} \tag{2.28}$$

Note that, once again, we use a hat for the kernels of the once-subtracted T^- dispersion relation. In practice, these integrals will be evaluated up to some maximum value s_{max} or t_{max} up to which we know all relevant partial waves. Above s_{max}, t_{max} we will make use of Regge theory, sometimes in the form of a simple Veneziano formula [80, 91], or as a more sophisticated description through a pure asymptotic formula [89].

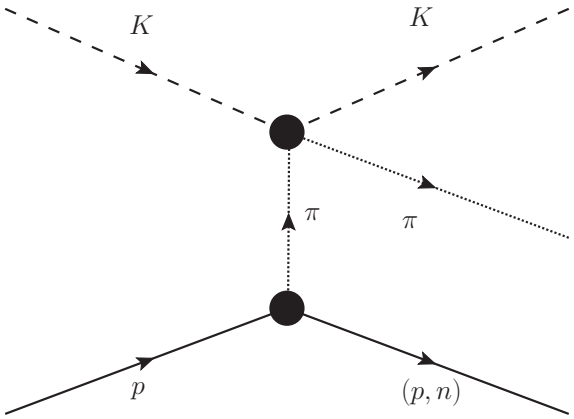

Figure 2.1: Production process $Kp \to \pi Kp$ in the one-pion exchange approximation.

2.2 Dispersive study of $\pi K \to \pi K$ and $\pi\pi \to K\bar{K}$

2.2.1 Motivation

As reviewed in previous sections, a precise determination of the scattering amplitudes of all $\pi\pi \to \pi\pi$, $\pi K \to \pi K$, and $\pi\pi \to K\bar{K}$ processes is crucial for the understanding of Chiral Perturbation Theory, the properties of relevant resonances, like the $\sigma/f_0(500)$ or $\kappa/K_0^*(700)$, and even for the precise determination of the Regge asymptotic parameters. Furthermore, the $\kappa/K_0^*(700)$ plays a central role in this thesis. It is the partner of the $\sigma/f_0(500)$, and whose status according to the PDG [134] is "still needs confirmation". On top of all the above, these hadronic processes appear as final states in many different experiments, in particular, they play a role in CP violating effects at the LHCb [135], they appear as final states in several COMPASS analyses [136], BESIII [137, 138], BaBaR [139–141] or in many others like E791, BELLE, ALEPH etc... .

These hadronic processes have been extensively studied throughout the years from the experimental point of view, however, the experimental information can not be determined directly, as there is no feasible experiment where two collimated meson beams collide, not at least with enough luminosity. As a result all determinations rely on some kind of approximations, depending on whether the original reaction was a production process, a strong decay, or a semileptonic one. In particular, the production process measured in [142–147] to determine the $\pi K \to \pi K$ interactions is shown in Fig. 2.1, a similar production process, $\pi p \to KKp$ was used in [148–151] to measure $\pi\pi \to K\bar{K}$.

In order to extract the upper subprocess of Fig. 2.1 the one pion exchange approximation has to be assumed (see [80] for a pedagogical introduction). Even though the pion pole lies relatively close to the zero of the physical transferred momentum to the protons, the latters cannot be measured below typically 100 MeV of transferred momentum. Otherwise they would not leave the target. As a result, the approximation carries a systematic effect,as the extrapolation of a pole in the real axis is not that

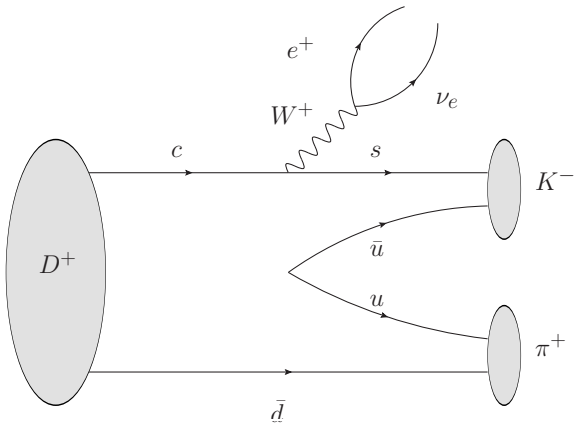

Figure 2.2: D^+ semileptonic decay studied in [155, 156].

precise anymore. These extrapolations are what causes most of the deviations from one experiment to another, creating conflicting data sets with no clear constraint. This was for example the case of $\pi\pi \to \pi\pi$ Cern-Munich experiments [152–154], where the very same measurement produced several conflicting extrapolations due to different exchanges and rescattering effects that are not taken into account. On top of that, the statistics of some of the $\pi K \to \pi K$ production experiments is small at best compared to more modern standards, with such a low statistic, the uncertainties are expected to be bigger.

More experimental results come into play if one considers different reactions, like the ones in Figs. 2.2, and 2.3. Unfortunately, and although the statistics is much bigger, these experimental results are not appropriate to extract scattering phases and poles with precision, as shown in section 2.2.3 due to their large systematic uncertainties, coming mostly from hadronic and unitarity approximations.

This situation has given rise to poorly constrained scattering amplitudes, and basically no data close to the $\pi K \to \pi K$ threshold, so that the low-energy expansion of $SU(3)$ ChPT cannot be accurately determined [157]. Moreover, the region where the $\kappa/K_0^*(700)$ plays a role in the real axis is plagued with systematic effects, which does not help to study its properties, still debated nowadays. Furthermore, all non-dispersive determinations of the $\kappa/K_0^*(700)$ pole will be unstable due to how far it is from the real axis.

A completely different approach, based on Lattice QCD, has shown to be effective nowadays when computing scattering lengths and phase shifts for this processes. Interesting results for both of them have been published recently by well-known collaborations [55, 57–59, 102, 158]. Unfortunately, even though their results are promising, they are not using the physical masses of the pseudo-scalar mesons yet, and extrapolations of the masses, carried out by means of UChPT are necessary to compare with results at the physical point.

In a previous series of works [2, 121, 133] the dispersive formalism was applied to the study of $\pi K \to \pi K$ interactions, with special emphasis on the low-energy expansion,

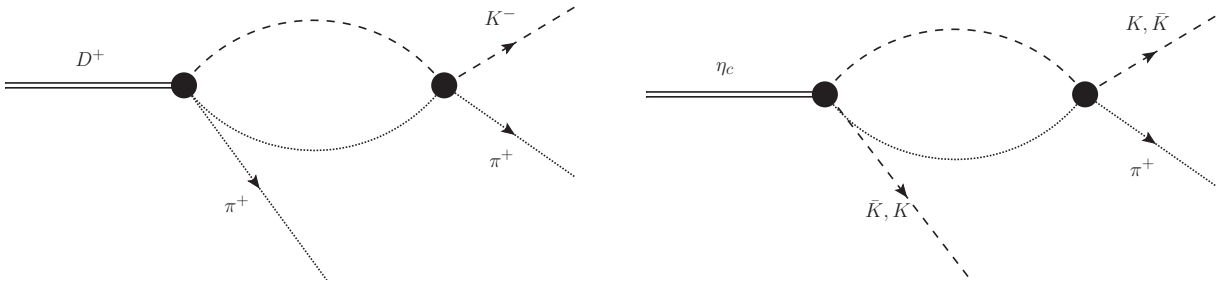

Figure 2.3: D^+ decay measured in [159] (left) and η_c decay measured in [160] (right).

where the $\pi\pi \to K\bar{K}$ scattering was considered as input. As a final result, partial waves for $\pi K \to \pi K$ below 1 GeV where predicted, without using any data input in that region. Nevertheless, several systematic uncertainties have not been taken into account, like the matching condition they use to match the solution with the input above 1 GeV, or the high energies inputs for $\pi K \to \pi K$ and $\pi\pi \to K\bar{K}$, which could be deviated from the dispersive constraints, and the obtained P wave is at odds with the data. This result is surprising taking into account that it is dominated by a very well known resonance, the $K^*(892)$. In addition, no study of the $\pi\pi \to K\bar{K}$ physical region was performed. On top of all the above, the use of a different approach towards the implementation of dispersion relations, driven by the data, like the one of the Madrid-Krakow group [89, 126–128] is of interest, as it offers more control over several conflicting regions.

It is then timely to give rise to a complete, precise, and model independent dispersive analysis of the $\pi K \to \pi K$ and $\pi\pi \to K\bar{K}$ scattering data.

2.2.2 Outline of the main results

In this subsection, two published research papers are presented in sections 2.2.3 and 2.2.4. As detailed in several sections of this thesis, πK was already studied dispersively in [2], together with some other more simple, partial calculations [121,161,162]. However, the system of Roy-Steiner equations used by the authors can solve the partial waves only up to $\sqrt{s} \sim 0.95$ GeV, so the data in between that lower bound and 2.5 GeV was fixed as mere input. In the first publication 2.2.3 we analyze $\pi K \to \pi K$ scattering by means of forward dispersion relations, as introduced in section 2.1.1. With this new analysis we were able not only to determine a similar parameterization to the data for the S waves in the elastic region, while our P wave is compatible with the data, but we also constrained the higher energy regions for the first time. In section 2.2.4 we present a published work devoted to the study of $\pi\pi \to K\bar{K}$. We determine for the first time the g_0^0,g_1^1 and g_2^0 partial waves within a dispersive formalism in the physical region. The main results of the publications are summarized as follows:

- In the first place, we obtain unconstrained fits to all $\pi K \to \pi K$ relevant partial waves for both isospins, that is, the S, P, D and F-waves. We fit all possible data

sets up to 1.8 GeV, playing special care on how to treat systematic uncertainties.

- We derive the system of dispersion relations, together with two different sum rules applied at the threshold. We then check the fulfillment of said equations, finding sizable deviations at all energies.

- We constrain the set of partial waves by minimizing the distance between the input and output of the DR while describing the data. We find a constrained parameterization that describes the data while fulfilling all the dispersion relations and threshold sum rules. The scattering lengths are then obtained with high accuracy, and the factorization constants of the Regge theory are constrained by these system of equations.

- We then evaluate the analytic parameterizations in the complex plane, finding the pole positions of both the $\kappa/K_0^*(700)$ and $K^*(892)$ resonances, although these still are not completely model-independent results, which will be obtained in section 3.1.4.

- In 2.2.4 we present a generalized system of hyperbolic dispersion relations, where the parameter a determining the hyperbola $(s-a)(u-a) = b$ is used to maximize the applicability domain in both the s and t-channels. All necessary kernels to evaluate the disperson relations up to tensor partial waves in the t-channel are also included.

- We obtain a system of unconstrained fits to data for g_0^0,g_1^1 and g_2^0, where special emphasis for the former is paid. It has two incompatible data sets, that will be studied separately.

- As the g_2^0 has no data points for its phase, we solve some caveats within the literature on parameterizations for this partial wave. By imposing unitarity for the phase of the g_2^0 partial wave a different description from these customarily considered in the literature is obtained, in particular it differs from the experimental one of the Brookhaven collaboration [149]. Not only does it differ from the experimental solution in the low-energy region, but also in the high energy one, producing a new phase for the g_0^0 as both are determined using data on $\phi(g_0^0) - \phi(g_2^0)$.

- After imposing the set of dispersion relations, parameterizations for all these partial waves are found, these equations are consistent with the inputs coming from $\pi K \to \pi K$ while the fulfill the analytic requirements. As a final remark, two different parameterizations, both compatible with dispersion relations, related to the two different compatible data sets for g_0^0 are found.

2.2.3 Publication: *Pion-kaon scattering amplitude constrained with forward dispersion relations up to 1.6 GeV*

PHYSICAL REVIEW D **93,** 074025 (2016)

Pion-kaon scattering amplitude constrained with forward dispersion relations up to 1.6 GeV

J. R. Pelaez and A. Rodas

Departamento de Física Teórica II, Universidad Complutense de Madrid, 28040 Madrid, Spain

(Received 26 February 2016; published 20 April 2016)

In this work we provide simple and precise parametrizations of the existing πK scattering data from threshold up to 1.6 GeV, which are constrained to satisfy forward dispersion relations as well as three additional threshold sum rules. We also provide phenomenological values of the threshold parameters and of the resonance poles that appear in elastic scattering.

DOI: 10.1103/PhysRevD.93.074025

I. INTRODUCTION

Pion-kaon scattering is a very relevant process for our understanding of hadron physics and the strong interaction. The motivation to study it is threefold.

First of all, because pions and/or kaons appear in the final states of all hadronic processes. In particular kaons do so if the process involves net strangeness. Since pions and kaons interact strongly, final state πK rescattering effects are essential to describe and understand such hadronic processes.

Second, the reaction is interesting by itself, because even though we cannot solve QCD at low energies, the identification of pions and kaons as pseudo Goldstone bosons of the QCD spontaneous chiral symmetry breaking allows for a rigorous formulation in terms of a low-energy effective theory known as chiral perturbation theory (ChPT) [1]. In turn, ChPT provides πK scattering amplitudes which have been calculated first to one loop [2] and then to two loops [3]. Relevant constraints on the ChPT low-energy constants can be obtained from sum rules and dispersion relations applied to πK scattering [4]. In addition, πK scattering was subsequently unitarized to one loop [5,6] or within the chiral unitary approach [7], providing a simultaneous description of the low-energy and resonant regimes. Moreover, there is a renewed interest in πK scattering in lattice QCD, where the main features, like threshold parameters [8], scattering phases and resonances [9], have already been calculated. Although the pion mass used for these lattice calculations is not physical, one can expect physical values to be within reach soon. Alternative lattice strategies that calculate πK scattering from unitarized chiral Lagrangians have also been followed recently in [10].

Third, in pion-kaon scattering appear some of the still controversial light scalar mesons, like the $K_0^*(800)$ or κ resonance and the $K_0^*(1430)$. The former has been the subject of a long-standing debate about its very existence and nature. Actually, it is a firm candidate to form the lightest nonet of scalar mesons together with the $f_0(500)$ or σ meson, the $f_0(980)$ and the $a_0(980)$. There is strong evidence that these states might form a nonet of non-ordinary mesons [7,11], i.e., mesons not predominantly made of a quark and an antiquark. The κ resonance has been obtained within different variants of unitarized ChPT in [6,7]. It has also been shown to have a mass smaller than 900 MeV [12] and has been found [13] from a rigorous *solution* [14] of the Roy-Steiner dispersion relations [15], which is the best determination so far. However, those pieces of evidence are still not considered enough by the Review of Particle Physics (RPP) [16], which still lists the $K_0^*(800)$ resonance under the "needs confirmation" label. Thus, the κ meson is a further motivation for our present study, since any rigorous resonance determination from data (not a solution of dispersion relations or lattice) requires first a consistent knowledge of πK scattering, which, in order to control all uncertainties, should reach beyond the pure elastic regime. Incidentally, the latter region is also of direct interest for the $K_0^*(1430)$ resonance.

Hence, the goal of this work is to perform an analysis of the existing πK scattering data constrained to satisfy forward dispersion relations. The advantage of these relations is that, contrary to other kinds of dispersion relations (like Roy-Steiner equations in their simplest form), they can be easily implemented up to arbitrarily high energies. Here we will apply to πK scattering an approach that has been recently followed [17] to obtain a precise description of $\pi\pi$ scattering data, consistent with dispersion relations. Namely, on a first stage one obtains simple fits to different, even conflicting, sets of data for each partial wave up to 1.74 GeV, without any further constraint apart from unitarity. The resulting parametrizations form a set of simple "unconstrained fits to data" that could be easily modified wave by wave in case new data would appear. However, we check later to see that this set is not consistent with forward dispersion relations up to 1.74 GeV. Then, using this set as a starting point, one refines its parameters by imposing the dispersion relations without spoiling the data description. The resulting "constrained fits to data" will be the main result of this work and will provide precise parametrizations describing

the existing data, while being simultaneously consistent with forward dispersion relations up to 1.6 GeV as well as with three threshold sum rules. Since these parametrizations are rather simple, we expect that they will become a useful tool for further studies, either theoretical or experimental, involving πK scattering at some stage and particularly for the precise determination of resonance parameters. This was indeed the case of the parametrizations resulting from a similar analysis of $\pi\pi$ scattering.

II. KINEMATICS AND NOTATION

As is customary we will use the partial wave decomposition of the πK scattering amplitudes

$$T^I(s,t,u) = \frac{4}{\pi}\sum_l (2l+1)P_l(\cos\theta)t_l^I(s), \qquad (1)$$

where s, t, u are the standard Mandelstam variables, satisfying $s+t+u = 2(m_\pi^2+m_K^2)$ and $\sigma(s) = 2q_{K\pi}/\sqrt{s}$. The center of mass momentum of two particles with mass m_1 and m_2 is

$$q_{12}(s) = \frac{1}{2\sqrt{s}}\sqrt{(s-(m_1+m_2)^2)(s-(m_1-m_2)^2)}. \qquad (2)$$

For later convenience we also define $\Sigma_{12} = m_1^2+m_2^2$ and $\Delta_{12} = m_1^2-m_2^2$. Unless explicitly stated, $m_1 = m_K$ and $m_2 = m_\pi$ and $q = q_{K\pi}$ in this work. Note that we are working in the isospin limit of equal masses for all pions $m_\pi = 139.57$ MeV and equal masses for all kaons $m_K = 496$ MeV. We also use $m_\eta = 547$ MeV.

The elastic unitarity condition $\mathrm{Im}t(s) = \sigma(s)|t(s)|^2$ implies that the elastic partial wave can be recast in terms of a real phase shift

$$t_l(s) = \frac{\hat{t}(s)}{\sigma(s)} = \frac{e^{i\delta_l(s)}\sin\delta_l(s)}{\sigma(s)} = \frac{1}{\sigma(s)}\frac{1}{\cot\delta(s)-i}, \qquad (3)$$

where we have introduced the "Argand" partial wave $\hat{t}(s)$ for later convenience.

In contrast, in the inelastic regime an inelasticity function is also introduced to write

$$t_l(s) = \frac{\hat{t}(s)}{\sigma(s)} = \frac{\eta_l(s)e^{2i\delta_l(s)}-1}{2i\sigma(s)}. \qquad (4)$$

Later on we will also study the scattering at very low energies through the threshold parameters defined as

$$\mathrm{Re}\hat{t}_l^I(s) \sim q^{2l+1}(a_l^I + b_l^I q^2 + O(q^4)). \qquad (5)$$

Throughout this work we will also use the traditional spectroscopic notation, naming the partial waves with isospin I and angular momentum $l = 0,1,2,3\ldots$ as S^I, P^I, D^I and F^I waves …, respectively.

III. UNCONSTRAINED FITS TO DATA

A. The data

Data on πK scattering were obtained mostly during the 1970s and the 1980s, measured indirectly from $KN \to K\pi N$ reactions, assuming they are dominated by the exchange of a single pion.

On the one hand, data on the $I = 3/2$ πK scattering cross sections was isolated in the early 1970s using different reactions: early experiments provided cross sections by studying $K^-d \to K^-\pi^- pp$ in Cho *et al.* [18] and $K^-n \to K^-\pi^- p$ in Bakker *et al.* [19] as well as $K^\pm p \to K^\pm\pi^-\Delta^{++}$ in Jongejans *et al.* [20]. Since this πK channel seems elastic up to at least 1.8 GeV, it is straightforward to obtain the phase shift. Actually, this was done explicitly by Linglin *et al.* in [21] from their $K^-p \to K^-\pi^-\Delta^{++}$ analysis. In general, the experiments in the earlier 1970s have low statistics, which were improved by later experiments. In particular, in 1977 Estabrooks *et al.* [22] performed a relatively high statistics analysis of $K^\pm p \to K^\pm\pi^+ n$ and $K^\pm p \to K^\pm\pi^-\Delta^{++}$ at 13 GeV to obtain the $I = 3/2$ πK component, also with no evidence of inelasticity up to 1.8 GeV in πK scattering. We will see that the differences between experiments are larger than the statistical uncertainties they quote, which points to the existence of a sizable systematic uncertainty that we will have to estimate separately for each wave.

On the other hand, isospin $I = 1/2$ scattering waves have always been obtained in combination with those with $I = 3/2$. This was done for instance by Mercer *et al.* in [23] using the $K^+p \to K^+\pi^-\Delta^{++}$ and $K^+p \to K^0\pi^0\Delta^{++}$ reactions. Due to low statistics, in order to separate different isospins, they needed to combine their results with the so-called world data summary tape, a heterogeneous and not very precise collection of data that existed at that time. As a consequence, the results for their $I = 1/2$ and $3/2$ waves have huge uncertainties, which is why they are usually neglected against later and more precise experiments.

As a matter of fact, what was really measured in scattering experiments was the $t_l = t_l^{1/2} + t_l^{3/2}/2$ combination. This was already studied with relatively high statistics in [22] up to 1.85 GeV, but also in the experiment with the highest statistics so far that was performed in the 1980s by Aston *et al.* at the LASS spectrometer [24] at SLAC. This LASS experiment studied the $K^-p \to K^-\pi^+ n$ reaction at 11 GeV and obtained the same πK partial wave combination up to 2.6 GeV.

The analysis needed to extract πK scattering amplitudes from $KN \to K\pi N$ has several sources of systematic uncertainties, like corrections to the on-shell extrapolation of the exchanged pion or rescattering effects. However, most experimental works only quote statistical uncertainties for

each solution and for this reason conflicting data exist. This will be clearly seen in the figures below. Thus, in our fits we sometimes add a systematic uncertainty to different sets or to certain data points which are in conflict with other data points in the same region. In the case of the most delicate and controversial wave, which is the $S^{1/2}$, we have checked to see that the resulting data set and the fit are consistent with certain statistical tests explained in Appendix B.

In addition some ambiguities occur in the determination of the phase that sometimes lead to different solutions for πK scattering even within the same $KN \to K\pi N$ experiment. In the case of Aston *et al.* [24] these ambiguities appear above the region of interest for this work. In contrast, Estabrooks *et al.* [22] do have four solutions above 1.5 GeV, but we only consider solution B since it is the one qualitatively closer to Aston *et al.*

So far we have been discussing scattering data where the $I = 1/2$ state has always been obtained in combination with the $I = 3/2$ one. However, it is also possible to obtain information on πK scattering from the decays of heavier particles. In particular, when πK's are the only strongly interacting particles in the decay, the Watson theorem implies that, in the πK elastic region, the phase of the global process should be the same as the scattering phase shift. In particular, the phase-shift difference between S and P waves with $I = 1/2$ have been measured from $D^+ \to K^-\pi^+e^+\nu_e$ by the *BABAR* Collaboration [25] and recently by the BESIII Collaboration [26]. The results are very consistent with the LASS experiment, but their uncertainties are too large and will not be included in our fits, although we will show them for completeness.

Moreover, there are measurements of the $I = 1/2$ phase of the $K\pi S$-wave amplitude obtained from Dalitz plot analyses of $D^+ \to K^-\pi^+\pi^+$ by the E791 [27], FOCUS [28] and CLEO-c [29] collaborations, as well as a recent similar analysis of $\eta_c \to K\bar{K}\pi$ by the *BABAR* Collaboration [30]. These phases (and amplitudes) are not necessarily those of πK scattering due to the presence of a third strongly interacting particle, which invalidates the use of Watson's theorem. However, *a posteriori* comparison with the scattering data has shown that, within the large uncertainties and at least in the elastic region, the resulting phase (but not the amplitude) is very similar to that of LASS. This means that the effect of the third particle on the phase is rather constant and almost amounts to a global shift. But these data cannot really be interpreted as a scattering phase beyond this qualitative agreement and are therefore not included in our fits. Nevertheless we will show and discuss them in comparison with our results.

B. General form of our parametrizations

Each partial wave will now be fitted to the existing data up to ~1.7 GeV, which means that we will only fit S, P, D and F waves, since there are no data for G, H and higher waves below 1.8 GeV. In this first stage, the fit to a wave with a given angular momentum will be performed independently of other waves with different angular momentum, by means of simple functions, without imposing any dispersive constraint. For this reason the resulting set of partial waves will be called an unconstrained fit to data (UFD). When possible, as in waves which are elastic in the whole energy range, a single functional form will be used throughout the whole energy region. However, for more complicated waves different functional forms will be used in different regions. Typically these piecewise functions will be matched at thresholds demanding continuity.

We would like to add a word of caution here. The data are not precise nor numerous enough to exclude large fluctuations between successive data points, particularly in certain energy regions. One could devise complicated parametrizations that would pass through every single data point, or even produce fluctuations between points. In this work we are assuming that such fluctuations do not occur and that the data can be correctly fitted with simple and relatively smooth parametrizations. The size of the uncertainties thus depends on this assumption. The parametrizations we describe below are the ones we have finally chosen because they satisfy the above assumption and yield uncertainty bands which do not show wild fluctuations or become too large in a region where the data spread does not require so. In particular, we have explored different kinds of conformal parametrizations (with different centers and more terms in the expansion, see Appendix A), we have tried simple polynomials in different variables, including orthogonal polynomials in a given region, adding or removing resonant shapes, etc. Since all of them fit the data, their central result is not too different from our final choice. Except in a few relevant cases, we spare the reader from explaining the caveats that affect the many other parametrizations we tried. We just present below our final choice. Moreover, for a given parametrization, and once the systematic uncertainty that affects the data has been estimated, we decide to stop adding parameters when the χ^2/dof is close to or less than one. Of course, the size of the final uncertainties depends on our educated guess of systematic uncertainties, which, as we will see, dominate the final error bands in many cases.

1. Partial waves in elastic regions

For the elastic regions, in which a partial wave can be recast in terms of just a phase shift, we will use a conformal expansion of the type

$$\cot\delta_l(s) = \frac{\sqrt{s}}{2q^{2l+1}}F(s)\sum_n B_n\omega(s)^n, \tag{6}$$

where $F(s) = 1$ except for scalar waves that have an Adler zero at $s_{\rm Adler}$, in which case $F(s) = 1/(s - s_{\rm Adler})$, or for waves that exhibit a clear narrow resonance and whose phase shift crosses $\pi/2$ at m_r, in which case

$F(s) = (s - m_r^2)$. In addition, the conformal variable is defined as

$$\omega(y) = \frac{\sqrt{y} - \alpha\sqrt{y_0 - y}}{\sqrt{y} + \alpha\sqrt{y_0 - y}}, \quad y(s) = \left(\frac{s - \Delta_{K\pi}}{s + \Delta_{K\pi}}\right)^2. \quad (7)$$

This change of variables, which maps the complex s plane into the unit circle, is relatively similar to those used for $\pi\pi$ scattering in [17] or πK scattering in [12], and is explained in detail in Appendix A. It suffices here to say that, by taking full advantage of the analytic properties of the partial waves in the complex plane, such a conformal expansion ensures a rapid convergence of the series and no more than three B_i coefficients are needed for the fits to each wave in the elastic region. The $y_0 \equiv y(s_0)$ and α constants are fixed, not fitted, for each partial wave. The s_0 parameter sets the maximum energy at which this mapping is applicable on the real axis, whereas α fixes the energy where the expansion is centered.

2. Partial waves in inelastic regions

The parametrizations of partial waves in the inelastic region have to accommodate several resonant structures that have been observed and ensure a continuous matching with the elastic parametrization. Note that for the $D^{1/2}$ and $F^{1/2}$ waves, since data only exist in the inelastic region, we will use a unified inelastic formalism in the whole energy region, which reduces to the elastic case below the $K\eta$ threshold.

We have tried different parametrizations, like polynomial fits in powers of the πK, $K\eta$ momenta, or the s or $\sqrt{s}$ variables. However such fits tend to have small uncertainties close to the elastic region and very large as the energy increases, which does not necessarily reproduce the uncertainty observed in the data and leads to huge correlations. As other authors before [14], we have found that it is more efficient to describe this region with products of exponential or rational functions, which are more flexible to accommodate resonant structures and whose resulting uncertainty bands are more uniform throughout the fit region. Moreover, the use of products of functions allows for a straightforward implementation of unitarity, which is done as follows:

$$t_l(s) = \frac{1}{2i\sigma(s)}\left(\prod_n S_n(s) - 1\right). \quad (8)$$

The S_n could either have the form of a nonresonant background

$$S_n = S_n^b = \exp\left[2iq_{ij}^{2l+1}(\phi_0 + \phi_1 q_{ij}^2 + \cdots)\right], \quad (9)$$

with ϕ_k real parameters, or a resonantlike form

$$S_n = S_n^r = \frac{s_{rn} - s + i(P_n(s) - Q_n(s))}{s_{rn} - s - i(P_n(s) + Q_n(s))}, \quad (10)$$

where s_{rn} are real parameters and $P_n(s)$ and $Q_n(s)$ are polynomials that have the same sign over the inelastic region. Using the equations above, $|S_n| \leq 1$ and inelastic unitarity is satisfied. If these polynomials were constant, one would recover the simplest Breit-Wigner formula for S_n^r. We will explain in the following subsections the choice of polynomials for different waves. Continuity with the elastic region is imposed by fixing the $P_n(s)$ polynomial of the S_n that has a pole with the lowest s_{rn}. This formalism is a modification of the parametrizations used in [14] for the high energy region [31]. When reducing this parametrization to the elastic case, Q_n is set to zero, which as commented above is of relevance for the $D^{1/2}$ and $F^{1/2}$ waves.

Note that close to a resonance, each of the S_n^r functions bear some resemblance to a Breit-Wigner form, but the actual parameters of a resonance have to be calculated with the full partial wave and not obtained from an individual S_n^r. Let us remark once again that when combining the S_n's in the complete functional form of t_l, unitarity has been enforced exactly. This would not occur in a simple sum of Breit-Wigner amplitudes, which would violate unitarity.

We will use partial waves to describe data up to ~1.7 GeV. Beyond that energy we will use Regge theory to describe the amplitudes, as we will see in Sec. III G below.

C. S waves

1. $I = 3/2$ S wave

Let us then start by describing our simple fit to the $I = 3/2$ S wave, since data for this wave exist independently of other waves. Once again, we emphasize that there is no evidence so far of inelasticity up to ~1.8 GeV, and thus we will consider this wave as elastic up to that energy. Hence, as commented above and explained in more detail in the Appendix A, we will use the following simple functional form to describe the phase shift:

$$\cot\delta_0^{3/2}(s) = \frac{\sqrt{s}}{2q(s_{\rm Adler} - s)}(B_0 + B_1\omega(s) + B_2\omega(s)^2). \quad (11)$$

Note that we have explicitly factorized the Adler zero, which we will set to its leading order within chiral perturbation theory, i.e., $s_{\rm Adler} = \Sigma_{K\pi}$. For this wave, the constants that define the conformal variable ω in Eq. (7) are fixed to

$$\alpha = 1.4, \qquad s_0 = (1.84\ \text{GeV})^2. \quad (12)$$

The existing data are shown in Fig. 1. There is a relatively fair agreement between different experiments

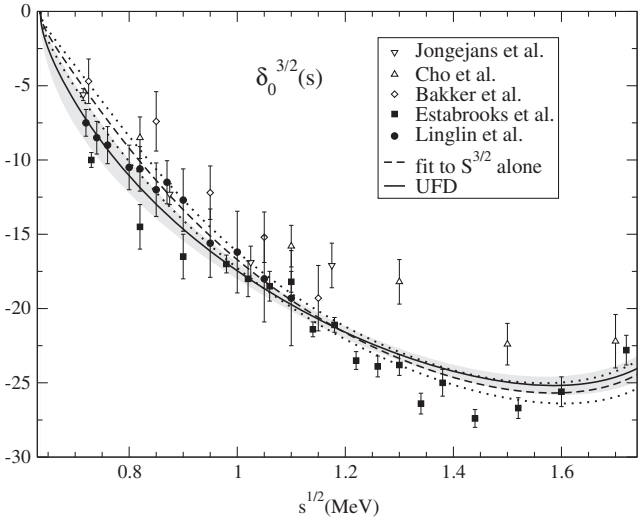

FIG. 1. Experimental data on the $S^{3/2}$ phase shift, $\delta_0^{3/2}(s)$. The data come from [18] (Cho *et al.*), [19] (Bakker *et al.*), [20] (Jongejans *et al.*), [21] (Linglin *et al.*) and [22] (Estabrooks *et al.*). The dashed line shows our fit to these data and the dotted lines enclose its uncertainty band. The continuous line represents our unconstrained fit including also the data on $t_0^{1/2} + t_0^{3/2}/2$, whose uncertainty is represented by the gray band.

below 1.1 GeV. However we can already notice some incompatible points between the Bakker *et al.* [19] and Estabrooks *et al.* [22] data sets, mostly due to the very small uncertainty of some points in the latter set. Note also the large variations between the uncertainties of successive data points in the Estabrooks *et al.* set. Above 1.1 GeV the two data sets that exist are largely incompatible. It is clear that some systematic uncertainty exists.

Therefore, we have fitted the data in Fig. 1 in two ways, either adding a constant systematic uncertainty of 1° or multiplying the existing statistical uncertainties by a factor of 2, which is chosen so that the resulting χ^2/d.o.f. is slightly less than one. The resulting fits are rather similar, but we have preferred the uncertainty band of the first because the systematic uncertainty is not correlated to the statistical one. In addition, the second approach satisfies much worse the threshold sum rules that we will check in the next sections. The result of our fit, with the estimate of systematic uncertainty added to the statistical uncertainties, is $\chi^2/\text{d.o.f.} = 37/(44-3+1)$.

Had we considered only two B_k parameters, the fit would yield an 80% larger χ^2/d.o.f, whereas with four it would decrease by 15%. Since three parameters as in Eq. (11) already provide a $\chi^2/\text{d.o.f.} < 1$, we do not consider it necessary to have a fourth parameter. We show this fit as a dashed line in Fig. 1, where the uncertainty band is delimited by the dotted lines.

Still this is not our final fit because there is also experimental information on the $t_S \equiv t_0^{1/2} + t_0^{3/2}/2$ combination. In the next subsection we will explain how the fit to the t_S data produces a small modification on the $S^{3/2}$ wave. The result provides the final $S^{3/2}$ parametrization, which is also shown in Fig. 1 as a thick continuous line whose uncertainties are covered by the gray band. Since no dispersion relation has been imposed yet, this result will be called an UFD, whose parameters are found in Table I. The constrained fit to data (CFD) in that table will be discussed later in Sec. V. In the figure it can be noticed that this UFD result is similar to the fit to the $S^{3/2}$-wave data alone that has been described in this subsection.

TABLE I. Parameters of the $S^{3/2}$ wave.

Parameter	UFD	CFD
B_0	2.25 ± 0.04	2.27 ± 0.04
B_1	4.21 ± 0.17	3.94 ± 0.17
B_2	2.45 ± 0.50	3.36 ± 0.50

2. $I = 1/2$ S wave

For this wave, inelasticity has been measured above 1.3 GeV and for the most part it is due to the $K\eta$ state rather than to states with more than two mesons. Hence, we are going to parametrize the amplitude using the elastic formalism of Sec. III B 1 below the $K\eta$ threshold, and with the inelastic formalism of Sec. III B 2 above that threshold.

Thus, for $(m_K + m_\pi)^2 \le s \le (m_K + m_\eta)^2$ we will use a conformal expansion of the type in Eq. (6), namely,

$$\cot\delta_0^{1/2}(s) = \frac{\sqrt{s}}{2q(s - s_{\text{Adler}})}(B_0 + B_1\omega). \tag{13}$$

Once again we have explicitly factorized the Adler zero, which we have set to its leading order within chiral perturbation theory value:

$$s_{\text{Adler}} = \left(\Sigma_{K\pi} + 2\sqrt{\Delta_{K\pi}^2 + m_K^2 m_\pi^2}\right)/5 \simeq 0.236\ \text{GeV}^2. \tag{14}$$

As explained in Appendix A, for this wave it is convenient to fix the constants that define the center of the conformal variable ω in Eq. (7) to the following values:

$$\alpha = 1.15, \qquad s_0 = (1.1\ \text{GeV})^2. \tag{15}$$

The parameters obtained for the best UFD are given in the first column of Table II.

TABLE II. Parameters of the elastic $S^{1/2}$ wave.

Parameter	UFD	CFD
B_0	0.411 ± 0.007	0.411 ± 0.007
B_1	0.181 ± 0.034	0.162 ± 0.034

In contrast, in the $s \geq (m_K + m_\eta)^2$ region we will implement the inelastic formalism of Eqs. (8), (9), (10) as follows:

$$t_0^{1/2}(s) = \frac{S_0^b S_1^r S_2^r - 1}{2i\sigma(s)}, \tag{16}$$

where

$$S_0^b = \exp[2iq_{\eta K}(\phi_0 + \phi_1 q_{\eta K}^2)]. \tag{17}$$

For S_1^r we use Eq. (10) with

$$P_1(s) = (s_{r1} - s)\beta + e_1 G_1 \frac{p_1(q_{\pi K})}{p_1(q_{\pi K}^r)} \frac{q_{\pi K} - \hat{q}_{\pi K}}{q_{\pi K}^r - \hat{q}_{\pi K}}, \tag{18}$$

$$Q_1(s) = (1 - e_1) G_1 \frac{p_1(q_{\pi K})}{p_1(q_{\pi K}^r)} \frac{q_{\eta K}}{q_{\eta K}^r} \Theta_{\eta K}(s), \tag{19}$$

where $p_1(x) = 1 + ax^2 + bx^4$, $q_{ij}^r = q_{ij}(s_r)$, $\hat{q}_{ij} = q_{ij}((m_\eta + m_K)^2)$ and $\Theta_{\eta K}(s) = \Theta(s - (m_K + m_\eta)^2)$ is the step function at the $K\eta$ threshold. In addition, for S_2^r we use Eq. (10) with

$$P_2(s) = e_2 G_2 \frac{p_2(q_{\pi K})}{p_2(q_{\pi K}^r)} \frac{q_{\pi K} - \hat{q}_{\pi K}}{q_{\pi K}^r - \hat{q}_{\pi K}}, \tag{20}$$

$$Q_2(s) = (1 - e_2) G_2 \frac{p_2(q_{\pi K})}{p_2(q_{\pi K}^r)} \frac{q_{\eta K}}{q_{\eta K}^r} \Theta_{\eta K}(s), \tag{21}$$

with $p_2(x) = 1 + cx^2$.

By matching the elastic and inelastic parametrizations at the $K\eta$ threshold we only need to demand continuity, which is ensured by defining $\beta \equiv 1/\cot\delta_0^{1/2}((m_K + m_\eta)^2)$, where $\delta_0^{1/2}$ is calculated here with the elastic parametrization in Eq. (13).

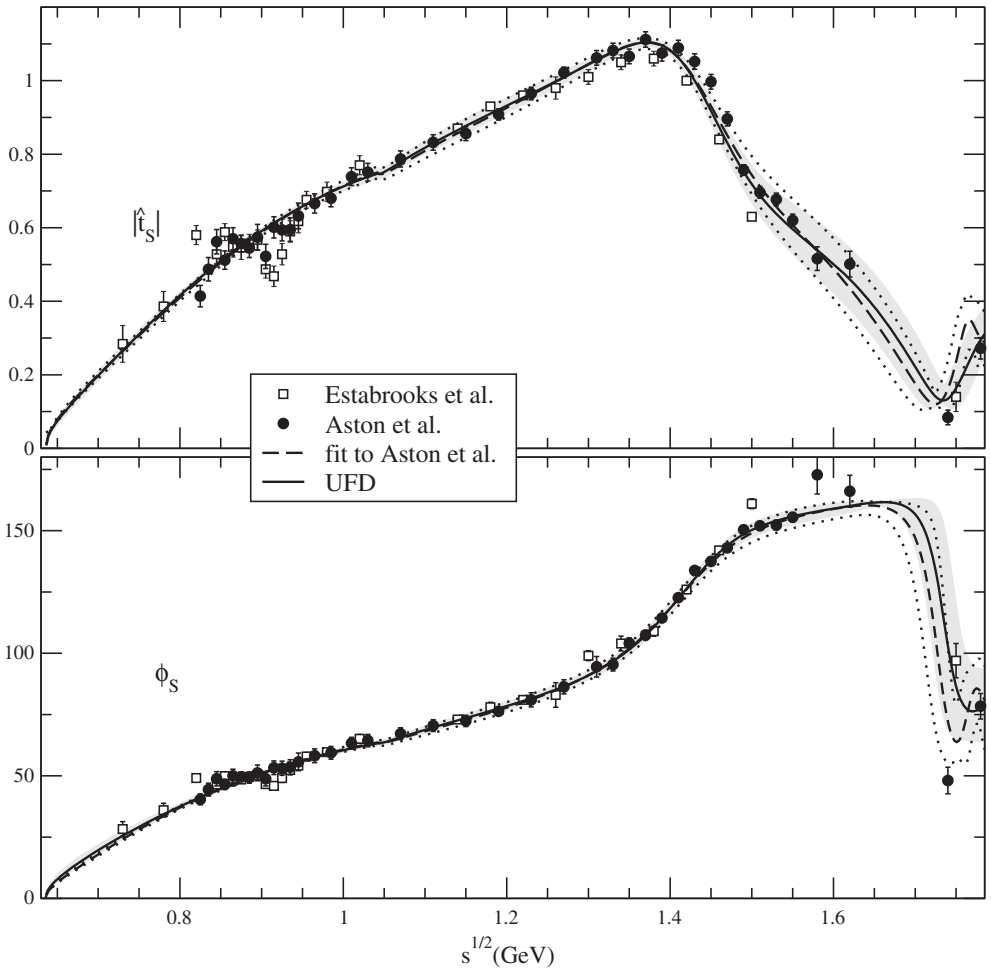

FIG. 2. Data on $\hat{t}_S(s)$ from Estabrooks *et al.* [22] and Aston *et al.* [24]. The upper panel shows $|\hat{t}_S(s)|$, whereas the lower one shows $\phi_S(s)$, which were measured independently. The continuous line is our unconstrained fit (UFD), whose uncertainties are covered by the gray band. For comparison we show, as a dashed line, a fit only to the data in [24], whose corresponding uncertainties are delimited by the dotted lines.

3. t_S wave

Nevertheless, as already explained above, we do not fit the $S^{1/2}$ wave alone, but in the $t_S \equiv t_0^{1/2} + t_0^{3/2}/2$ combination that was originally measured. Let us then define

$$t_S(s) = |t_S(s)|e^{i\phi_S(s)}, \tag{22}$$

and remark that, since $|t_S|$ and ϕ_S were measured independently, we will fit them both. In order to compare with data is convenient to use the normalization

$$\hat{t}_S(s) = t_S(s)\sigma(s). \tag{23}$$

Thus, in Fig. 2 we show the data on $\hat{t}_S$ and the result of our UFD. The upper panel shows $|\hat{t}_S|$, whereas the lower one shows ϕ_S. The combined χ^2/d.o.f. of the $S^{1/2}$ and $S^{3/2}$ data fits is $\chi^2/\text{d.o.f.} = 168/(182-15+1)$ with the UFD parameters provided in Table III. The e_1 parameter was initially left free but it comes out practically indistinguishable from 1, with tiny uncertainties, and has been fixed later to 1 for practical purposes.

From Fig. 2 it can be easily noted that there are data points which are largely incompatible with one another, not only between the two different experiments [22,24], but even among the successive data points of Estabrooks *et al.* [22]. Thus, it seems clear that there are some systematic errors not covered by the experimental uncertainties. Since these are the most controversial waves, here we have followed a more elaborate procedure to estimate the uncertainties of the resulting fit. In particular, we follow one of the techniques suggested in [32], which, in brief, consists of running Gaussianity tests on the data with respect to the fit and enlarge the uncertainties of those data points that spoil the test. This yields a new fit upon which the procedure is iterated until the Gaussianity test is satisfied. The details of this method are given in Appendix B. We show in Fig. 2, as a gray band, the resulting uncertainty of our fit to those data and the $I = 3/2$ data already discussed in the previous section.

TABLE III. Parameters of the $S^{1/2}$ inelastic fit.

Parameters	UFD	CFD
ϕ_0	-0.20 ± 0.04 GeV^{-1}	-0.19 ± 0.04 GeV^{-1}
ϕ_1	4.76 ± 0.25 GeV^{-3}	5.03 ± 0.25 GeV^{-3}
a	-5.22 ± 0.04 GeV^{-2}	-5.20 ± 0.04 GeV^{-2}
b	7.57 ± 0.13 GeV^{-4}	7.60 ± 0.13 GeV^{-4}
c	-1.72 ± 0.07 GeV^{-2}	-1.73 ± 0.07 GeV^{-2}
$\sqrt{s_{r1}}$	1.399 ± 0.006 GeV	1.401 ± 0.006 GeV
$\sqrt{s_{r2}}$	1.815 ± 0.017 GeV	1.817 ± 0.017 GeV
e_1	1	1
e_2	0.184 ± 0.033	0.184 ± 0.033
G_1	0.499 ± 0.017 GeV	0.497 ± 0.017 GeV
G_2	0.29 ± 0.12 GeV	0.28 ± 0.12 GeV

In the literature it is rather usual [14,33–35] to neglect the Estabrooks *et al.* data, although it is not always the case [36]. To be able to compare with this choice, we have thus considered a fit to the $I = 3/2$ data together with only the $I = 1/2$ data set of Aston *et al.* [24], which is much smoother than that of Estabrooks *et al.* [22], particularly below 1.5 GeV. In this case we have not added any systematic uncertainty and the result is shown in Fig. 2 as a dashed line, which almost overlaps with our previous fit up to 1.5 GeV, and has a very similar uncertainty band represented as the area between dotted lines. However, above 1.5 GeV and up to 1.7 GeV, the Aston *et al.* [24] set is not so consistent. For instance, it is well known that two of its points violate unitarity [36] (which we have always removed from our fits). Nevertheless, it is still compatible with our previous fit within uncertainties. Since here we want to stay on the conservative side, we have decided not to neglect the Estabrooks *et al.* data. Thus, from now on we will consider our UFD result only, which describes both sets. We will repeat this comparative exercise for other waves, but in all cases we will keep the UFD result obtained by fitting both sets when they exist.

With the combined fit to the $I = 1/2$ and $I = 3/2$ data we can separate the results for each isospin partial wave. The UFD result for the $I = 3/2$ S wave was already shown in its elastic region in Fig. 1, whereas we show now in Fig. 3 the resulting $I = 1/2$ S-wave phase shift. Note once

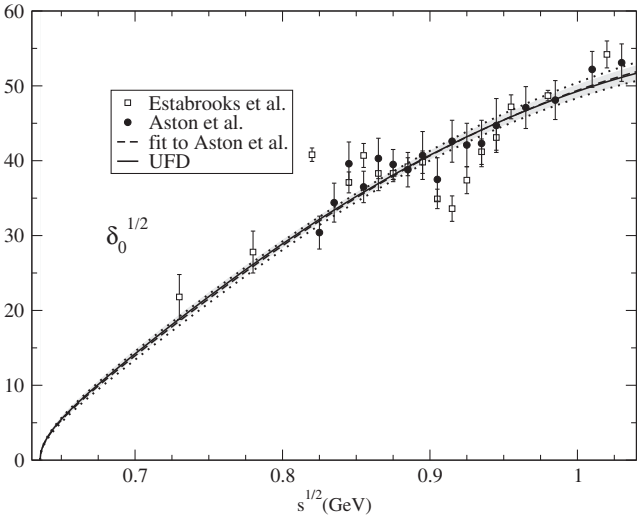

FIG. 3. $S^{1/2}$-wave phase shift below the $K\eta$ threshold. In this region the amplitude is elastic in practice. The continuous line is our UFD result, whose uncertainty is covered by the gray band. Data points extracted from Estabrooks *et al.* [22] and Aston *et al.* [24]. As explained in the text, we do not fit this wave individually, but in combination with the $I = 3/2$, as it was originally measured. The dashed curve is the fit to Aston *et al.* [24] data alone and the dotted lines cover the corresponding uncertainty band.

TABLE IV. S-wave scattering lengths from our UFD and CFD sets, in m_π^{-1} units, compared to other values in the literature.

	$m_\pi a_0^{1/2}$	$m_\pi a_0^{3/2}$
Büttiker *et al.*, Ref. [14]	0.224 ± 0.022	-0.0448 ± 0.0077
Dobado and Peláez, Ref. [37]	0.155 ± 0.012	-0.049 ± 0.004
Jamin *et al.*, Ref. [36]	0.18	-0.12
Bugg, Ref. [33]	0.195 ± 0.006	...
Zhou and Zheng, Ref. [34]	0.219 ± 0.034	-0.042 ± 0.002
UFD, this work	0.22 ± 0.01	$-0.10^{+0.03}_{-0.05}$
CFD, this work	$\mathbf{0.22 \pm 0.01}$	$\mathbf{-0.054^{+0.010}_{-0.014}}$

again that in the elastic region our UFD result is almost identical to the fit to Aston *et al.* data alone.

4. S-wave scattering lengths

Once we have fitted the data on the two S waves, we can use our UFD parametrizations to obtain the scattering lengths defined in Eq. (5), which we show in Table IV. Note that they are in fair agreement with other existing values in the literature, also provided in the table.

There is a renewed interest towards these quantities due to recent lattice calculations [8] and also due to the experimental measurement by the DIRAC Collaboration [38],

$$\frac{1}{3}(a_0^{1/2} - a_0^{3/2}) = 0.11^{+0.09}_{-0.04} m_\pi^{-1} \quad \text{(DIRAC)}, \tag{24}$$

which was not determined from scattering experiments, but from the formation of πK atoms. From our UFD set we find

$$\frac{1}{3}(a_0^{1/2} - a_0^{3/2}) = 0.108^{+0.018}_{-0.010} m_\pi^{-1} \quad \text{(UFD)}. \tag{25}$$

Note that our uncertainties are smaller, by roughly an order of magnitude, than the present direct experimental knowledge. We have explicitly checked to see that including the DIRAC value or not does not change the result of our fits.

D. P waves

1. $I = 3/2$ P wave

Only Estabrooks *et al.* [22] provide data for the $I = 3/2$ P-wave phase shift up to 1.74 GeV, which we show in Fig. 4. As can be noticed in the figure, this wave is rather small. Namely, below 1.1 GeV its phase shift is less than 1°, below 1.4 GeV it is less than 2° and below 1.74 GeV it is less than 3°. There is no inelasticity measured up to 1.74 GeV so that we will parametrize this partial wave with a conformal expansion as in Eqs. (6) and (7):

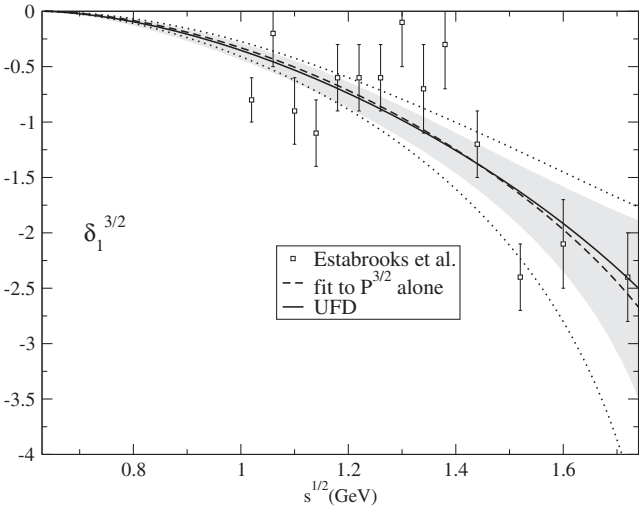

FIG. 4. Data on the $I = 3/2$ P wave from Estabrooks *et al.* [22]. We also show our UFD result as solid line with a gray uncertainty band, which is obtained by fitting these data together with the data on the $t_P = t_1^{1/2} + t_1^{3/2}/2$ combination. For comparison we show with a dashed line a fit only to the data in this figure, whose uncertainty is delimited by the dotted lines.

$$\cot \delta_1^{3/2}(s) = \frac{\sqrt{s}}{2q^3}(B_0 + B_1 \omega). \tag{26}$$

Let us remark that the α parameter that defines the conformal variable ω [see Eq. (7)] has been chosen so that the center of the conformal expansion lies on the center of the region where data exists. Thus, for this wave we have set

$$\alpha = 1.45, \qquad s_0 = (1.84\ \text{GeV})^2. \tag{27}$$

The existence of systematic uncertainties is evident from Fig. 4. If we make a naive fit without taking these systematic effects into account, the resulting $\chi^2/\text{d.o.f.} \simeq 2$. Hence, we have included an estimation of the systematic uncertainty in our fits by multiplying the data statistical uncertainties by $\sqrt{2}$. Two conformal parameters are enough to describe this wave and no significant improvement is obtained by considering a third one.

As happened with the $S^{3/2}$ wave, our final fit for the $I = 3/2$ P wave is obtained by fitting simultaneously the data for this wave alone together with the data on the $t_P \equiv t_1^{1/2} + t_1^{3/2}/2$ combination obtained by Estabrooks *et al.* [22] and Aston *et al.* [24]. The resulting UFD is shown in Fig. 4, where the gray band covers its uncertainty. The corresponding UFD parameters are listed in Table V.

Also in Fig. 4 we show, as a dashed line, the result when fitting only the data on that wave. Its corresponding uncertainty band is delimited by dotted lines. As we can

TABLE V. Parameters of the $P^{3/2}$ wave.

Parameter	UFD	CFD
B_0	-14.8 ± 2.6	-15.6 ± 2.6
B_1	2.7 ± 7.4	-2.2 ± 7.4

see, it is almost indistinguishable from our UFD result, for which we have also fitted data on $t_P \equiv t_1^{1/2} + t_1^{3/2}/2$, as we will see next.

2. $I = 1/2$ P wave

The $I = 1/2$ wave is only measured in scattering experiments together with the $I = 3/2$ wave in the t_P combination defined just above. Although in the literature it is frequent to neglect the $P^{3/2}$ wave, because as we have just seen it is very small, we will keep it in our fits for completeness.

Let us then discuss the $P^{1/2}$ wave in the elastic region, i.e., $s \leq (m_\eta + m_K)^2$, for which we use a conformal fit to describe the data, namely,

$$\cot\delta_1^{1/2}(s) = \frac{\sqrt{s}}{2q^3}(m_r^2 - s)(B_0 + B_1\omega + B_2\omega^2). \quad (28)$$

Note that we have explicitly extracted an $(m_r^2 - s)$ factor so that the phase crosses $\pi/2$ at the energy of the peak associated with the $K^*(892)$ resonance, which is the dominant feature of this wave in the elastic region. As explained in Appendix A, the α and s_0 parameters, which define the conformal variable ω in Eq. (7), are fixed from the choice of the center of the expansion and the highest energy of the fit to be

$$\alpha = 1.15, \qquad s_0 = (1.1\ \text{GeV})^2. \quad (29)$$

For $s \geq (m_\eta + m_K)^2$, we will use once more the inelastic formalism of Eqs. (8) and (10). Thus, we write

$$t_1^{1/2}(s) = \frac{S_1^r S_2^r S_3^r - 1}{2i\sigma(s)}, \quad (30)$$

where all the S_k^r's are of the form in Eq. (10), with

$$P_1 = (s_{r1} - s)\beta + e_1 G_1 \frac{p_1(q_{\pi K})}{p_1(q_{\pi K}^r)} \frac{q_{\pi K}^2 - \hat{q}_{\pi K}^2}{(q_{\pi K}^r)^2 - \hat{q}_{\pi K}^2} \frac{q_{\pi K}}{q_{\pi K}^r},$$
$$P_{2,3} = e_{2,3} G_{2,3} \frac{p_{2,3}(q_{\pi K})}{p_{2,3}(q_{\pi K}^r)} \frac{q_{\pi K}^2 - \hat{q}_{\pi K}^2}{(q_{\pi K}^r)^2 - \hat{q}_{\pi K}^2} \frac{q_{\pi K}}{q_{\pi K}^r},$$
$$Q_{1,2,3} = (1 - e_{1,2,3}) G_{1,2,3} \frac{p_{1,2,3}(q_{\pi K})}{p_{1,2,3}(q_{\pi K}^r)} \left(\frac{q_{\eta K}}{q_{\eta K}^r}\right)^3 \Theta_{\eta K}(s). \quad (31)$$

In addition,

$$p_i(q_{\pi K}) = 1 + a_i q_{\pi K}^2, \quad (32)$$

and $\Theta_{\eta K}(s) = \Theta(s - (m_K + m_\eta)^2)$ is the step function at the $K\eta$ threshold. Again, in order to impose continuity at $K\eta$ threshold we have defined $\beta \equiv 1/\cot\delta_1^{1/2}((m_K + m_\eta)^2)$, with $\delta_1^{1/2}$ calculated from the elastic expression in Eq. (28).

3. t_P wave

Thus, now that we have the functional forms for the $I = 1/2$ and $I = 3/2$ P waves, we can perform the fit to all the P-wave data. As we did for the S wave we first define

$$t_P(s) = |t_P(s)|e^{i\phi_P(s)}, \quad (33)$$

which is sometimes used with the alternative normalization

$$\hat{t}_P(s) = t_P(s)\sigma(s). \quad (34)$$

As commented before, we fit simultaneously the $I = 3/2$ data in Fig. 4 and the data on both $|\hat{t}_P|$ and ϕ_P that we show in Figs. 5 and 6. Note that once again there are clear systematic deviations of certain points, particularly from the Estabrooks *et al.* data set [22]. In this case we have proceeded as follows: we have performed a first fit, then we have added a systematic uncertainty to the isolated incompatible data points, which is half of their distance to the central value of the fit. In regions where the two sets of data are incompatible a systematic uncertainty is also added to each set, which corresponds to half of the average

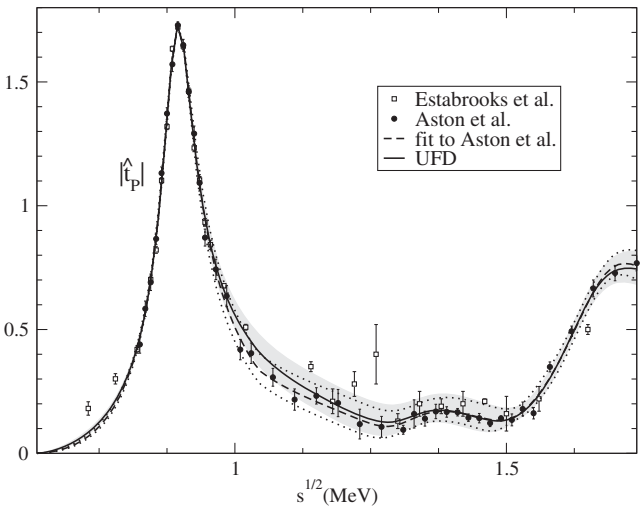

FIG. 5. Data on $|\hat{t}_P(s)|$ from [22,24]. The continuous line is our unconstrained fit (UFD), whose uncertainties are covered by the gray band. For comparison we show as a dashed line a fit only to the data from [24], whose corresponding uncertainties are delimited by the dotted lines.

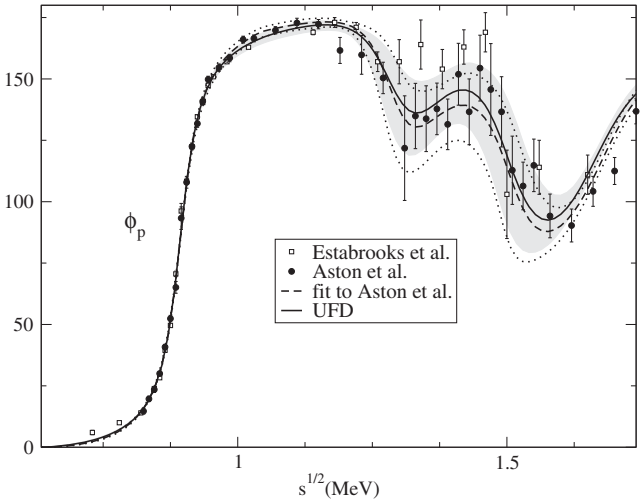

FIG. 6. Data on $\phi_P(s)$ from Estabrooks *et al.* [22] and Aston *et al.* [24]. The continuous line is our unconstrained fit (UFD), whose uncertainties are covered by the gray band. For comparison we show as a dashed line a fit only to the data from [24], whose corresponding uncertainties are delimited by the dotted lines.

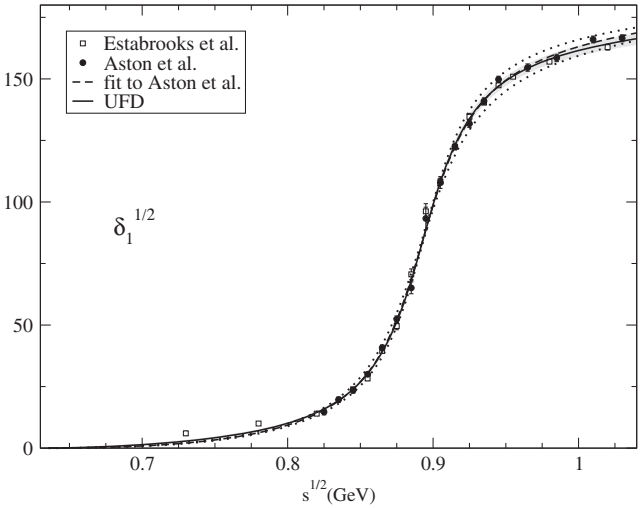

FIG. 7. $P^{1/2}$-wave phase shift below the $K\eta$ threshold. The continuous line is our UFD parametrization, whose uncertainty is covered by the gray band. Data from Estabrooks *et al.* [22] and Aston *et al.* [24]. The dashed curve is the fit to Aston *et al.* data alone and the dotted lines cover its corresponding uncertainty.

difference from the fit to the data set in that region. With these additional systematic uncertainties we have performed a final fit, which we call an UFD, with $\chi^2/\text{d.o.f.} = 76.4/(78-12+1)$. The resulting curves are also shown in Figs. 5 and 6, together with a fit in which we have only fitted the Aston *et al.* data for the $I=1/2$ wave. It can be noticed that in such a case the result would still be compatible with our UFD.

Once all P-wave data have been fitted, we can separate the different isospin components. The $I=3/2$ UFD result was already discussed in Sec. III D 1 and its parameters were given in Table V.

Concerning the $P^{1/2}$ wave, let us first look at the elastic region. When restricted below the $K\eta$ threshold the UFD result has $\chi^2/\text{d.o.f.} = 27/(34-4+1)$ and the corresponding parameters are listed in Table VI. The resulting curve for the $P^{1/2}$ wave can be seen in Fig. 7, where the distinct shape of the $K^*(892)$ is nicely observed. We are also showing a fit where only the data of Aston *et al.* has been fitted and how the results are hard to distinguish from our UFD line, except for the somewhat larger uncertainty band of the latter, particularly at higher energies.

The UFD parameters for the $P^{1/2}$-wave inelastic parametrization are given in Table VII. Note that to describe the inelastic region we still need to take into account the high energy tail of the $K^*(892)$ resonance, which is elastic, so that we set $e_1=1$. In addition its mass is fixed to the neutral case, 896 MeV, since this is the one measured in the LASS [24] and Estabrooks *et al.* [22] experiments. The other resonance shapes of the $K^*(1410)$ and $K^*(1680)$ are also very nicely described.

Let us remark that there is a recent fit to the t_P data [39], neglecting the $I=3/2$ wave as usual, in which the authors also consider three poles for the $I=1/2$ partial wave within a two-channel K-matrix approach, the channels being πK and $\pi K^*(892)$. In [39] only the central value of the fit is given and, since it is a fit to basically the same data we fit here, the results are relatively similar to ours within uncertainties—actually, around 1 GeV it is slightly closer to our CFD result, which we will discuss later on,

TABLE VI. $P^{1/2}$-wave parameters in the elastic region.

Parameter	UFD	CFD
B_0	0.97 ± 0.02	0.97 ± 0.02
B_1	0.98 ± 0.30	0.55 ± 0.30
B_2	0.79 ± 0.95	0.75 ± 0.95
m_r	0.8957 ± 0.0004 GeV	0.8957 ± 0.0004 GeV

TABLE VII. $P^{1/2}$-wave parameters in the inelastic region.

Parameters	UFD	CFD
a_1	-1.90 ± 0.10 GeV^{-2}	-1.76 ± 0.10 GeV^{-2}
a_2	-2.14 ± 0.23 GeV^{-2}	-2.33 ± 0.23 GeV^{-2}
a_3	-1.34 ± 0.07 GeV^{-2}	-1.41 ± 0.07 GeV^{-2}
$\sqrt{s_{r1}}$	0.896 GeV (fixed)	0.896 GeV (fixed)
$\sqrt{s_{r2}}$	1.346 ± 0.012 GeV	1.347 ± 0.012 GeV
$\sqrt{s_{r3}}$	1.644 ± 0.005 GeV	1.645 ± 0.005 GeV
e_1	1 (fixed)	1 (fixed)
e_2	0.052 ± 0.007	0.055 ± 0.007
e_3	0.295 ± 0.016	0.306 ± 0.016
G_1	0.044 ± 0.003 GeV	0.044 ± 0.003 GeV
G_2	0.217 ± 0.041 GeV	0.231 ± 0.041 GeV
G_3	0.295 ± 0.018 GeV	0.306 ± 0.018 GeV

than to the UFD result discussed here. Note also that the parametrization in [39] is a fit to data up to 1.8 GeV and that, in principle, it could be extrapolated up to 2.3 GeV.

E. D waves

1. $I = 3/2$ D wave

Once again, only Estabrooks *et al.* [22] provide data for the $I = 3/2$ D-wave phase shift up to 1.74 GeV, which we show in Fig. 8. Note it is very small in the whole energy region. No inelasticity has been measured so that we can use the elastic formalism parametrized with the conformal expansion in Eqs. (6) and (7), as follows:

$$\cot\delta_1^{3/2}(s) = \frac{\sqrt{s}}{2q^5}(B_0 + B_1\omega + B_2\omega^2). \tag{35}$$

Three conformal parameters are enough to describe this wave. As we did for the $P^{3/2}$ wave, the α parameter that defines the conformal variable ω in Eq. (7) has been chosen so that the center of the conformal expansion lies at the center of the region where data exists. Thus, for this wave we have set

$$\alpha = 1.45, \qquad s_0 = (1.84\ \text{GeV})^2. \tag{36}$$

As can be noticed in Fig. 8, there are sizable systematic uncertainties, which can be simply taken into account by multiplying the statistical uncertainties by $\sqrt{2}$. The resulting fit yields a $\chi^2/\text{d.o.f} \simeq 1.1$. However, as happened with the $S^{3/2}$ and $P^{3/2}$ waves, our final fit for the $I = 3/2$ D wave is obtained from a simultaneous fit to the data for this wave alone together with the data on the $t_D \equiv t_2^{1/2} + t_2^{3/2}/2$ combination obtained by Estabrooks *et al.* [22] and Aston *et al.* [24]. The parameters of such an UFD are given in Table VIII and we show the resulting phase shift as a continuous line in Fig. 8, where the gray band covers the corresponding uncertainty.

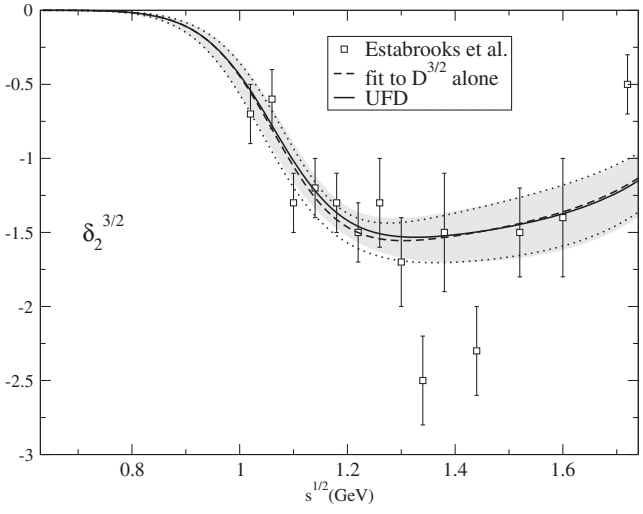

FIG. 8. Data on the $I = 3/2$ D wave from Estabrooks *et al.* [22]. We also show our UFD result as a solid line with a gray uncertainty band, which is obtained by fitting this data in a simultaneous fit with the data on the $t_2^{1/2} + t_2^{3/2}/2$ combination. For comparison we show with a dashed line a fit only to the data in this figure.

TABLE VIII. Parameters of the $D^{3/2}$ wave.

Parameter	UFD	CFD
B_0	-1.70 ± 0.12	-1.67 ± 0.12
B_1	-6.5 ± 1.7	-7.0 ± 1.7
B_2	-36 ± 9	-38 ± 9

In Fig. 8 we also show, as a dashed line, the result when fitting only the data in that figure and not the data on the t_D combination. The corresponding uncertainty band is delimited by dotted lines. As we can see it is very similar to our UFD curve.

2. $I = 1/2$ D wave

As happened with the S and P waves, the $I = 1/2$ D wave is only measured together with the $I = 3/2$ wave in the $t_D \equiv t_2^{1/2} + t_2^{3/2}/2$ combination. In the literature it is usual to neglect the $D^{3/2}$ wave, because as we have just seen it is very small, but we will keep it in our fits for completeness.

Let us then describe our fit to the $D^{1/2}$ wave, which is dominated by the $K_2^*(1430)$ resonance, whose branching ratio to πK is approximately 50%, so that we have to use an inelastic formalism as in Eqs. (8), (9), (10). In practice, it is enough to consider a nonresonant background and a resonantlike form, as follows:

$$t_2^{1/2} = \frac{S_0^b S_1^r - 1}{2i\sigma(s)}, \tag{37}$$

with a background term

$$S_0^b = e^{2i(p(s))}, \tag{38}$$

where

$$p(s) = \phi_0 q_{\eta K}^5 \Theta_{\eta K}(s) + q_{\eta' K}^5 \phi_1 \Theta_{\eta' K}(s),$$

and $\Theta_{ab} = \Theta(s - (m_a + m_b)^2)$. A resonant term is also considered in order to describe easily the $K_2^*(1430)$ shape, namely,

$$S_1^r = \frac{s_{r1} - s + i(P_1 - Q_1)}{s_{r1} - s - i(P_1 + Q_1)},$$
$$P_1 = e_1 G_1 \frac{p_1(q_{\pi K})}{p_1(q^r_{\pi K})}\left(\frac{q_{\pi K}}{q_{\pi K,r}}\right)^5,$$
$$Q_1 = (1-e_1) G_1 \frac{p_1(q_{\pi K})}{p_1(q^r_{\pi K})}\left(\frac{q_{\eta K}}{q_{\eta K,r}}\right)^5 \Theta_{\eta K}(s), \quad (39)$$

with $p_1(q_{\pi K}) = 1 + a q^2_{\pi K}$.

3. t_D wave

Once more we define

$$t_D(s) \equiv |t_D(s)| e^{i\phi_D(s)}, \qquad \hat{t}_D(s) = t_D(s)\sigma(s). \quad (40)$$

Thus, in Figs. 9 and 10 we show the data on $|\hat{t}_D|$ and Φ_D, respectively. As we did for the P wave, we have treated the systematic uncertainties as follows: we have performed a first fit and added a systematic uncertainty to those isolated data points that are incompatible with it. This systematic uncertainty is half of their distance to the central value of the fit. In regions where the two sets of data are incompatible the systematic uncertainty is half of the average difference from the fit to each set in that region. With these additional systematic uncertainties we have performed a final fit, called an UFD, which is shown as a continuous line in Figs. 9 and 10. The UFD uncertainty is represented by a gray band. The total χ^2/d.o.f. is $49/(44-6+1)$. In addition, we show as a dashed line the result that is obtained if only the data on $\hat{t}_D$ from Aston *et al.* [24] is fitted. The central values are almost indistinguishable

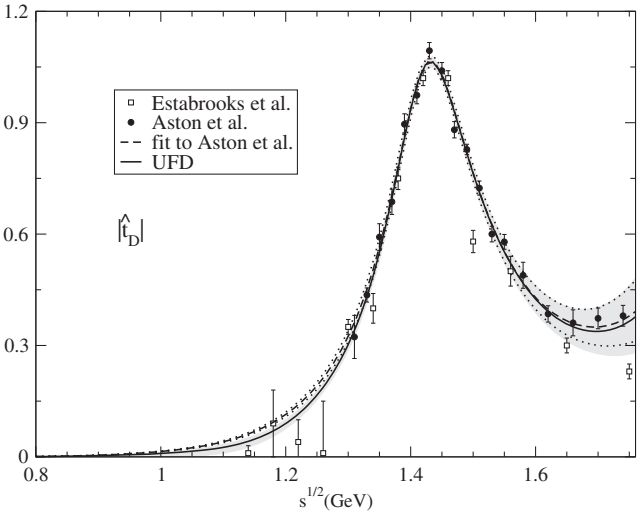

FIG. 9. Data on $|\hat{t}_D(s)|$ from [22,24]. The continuous line is our unconstrained fit (UFD), whose uncertainties are covered by the gray band. For comparison we show, as a dashed line, a fit only to the data from [24], whose corresponding uncertainties are delimited by the dotted lines.

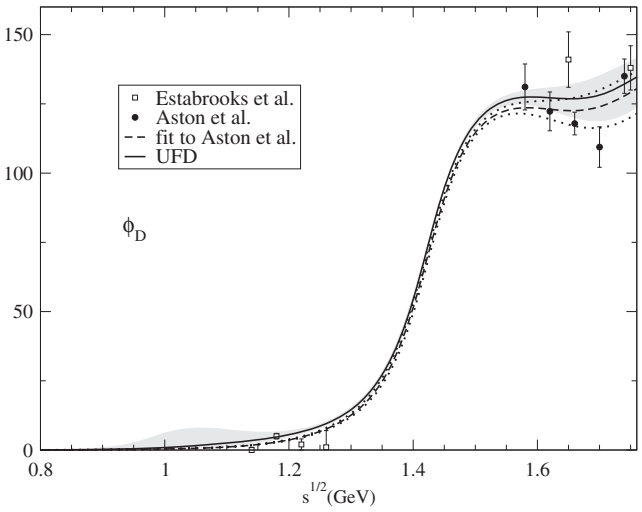

FIG. 10. Data on $\phi_D(s)$ from [22,24]. The continuous line is our unconstrained fit (UFD), whose uncertainties are covered by the gray band. For comparison we show, as a dashed line, a fit only to the data from [24], whose corresponding uncertainties are delimited by the dotted lines.

but the uncertainties are smaller. We still prefer our UFD parametrization because it contains more experimental information, although the uncertainties come larger due to the systematic uncertainties that we have taken into account in our UFD set. The UFD parameters are shown in Table IX.

F. $F^{1/2}$ wave

Once more we define

$$t_F(s) \equiv |t_F(s)| e^{i\phi_F(s)}, \qquad \hat{t}_F(s) = t_F(s)\sigma(s). \quad (41)$$

For this wave there are no observations of an $I = 3/2$ channel, which is neglected in the literature as will be done here too. In addition, the threshold suppression is so large that there are no data below 1.5 GeV, as can be seen in Figs. 11 and 12. In the latter we can observe that there are only two data points with very large uncertainties for the phase ϕ_F below 1.85 GeV. Thus, in order to stabilize our fit we will extend our data sample to 2 GeV, although later on

TABLE IX. Parameters of the $D^{1/2}$ fit.

Parameters	UFD	CFD
ϕ_0	2.17 ± 0.26 GeV^{-5}	3.00 ± 0.26 GeV^{-5}
ϕ_1	-12.1 ± 1.7 GeV^{-5}	-9.3 ± 1.7 GeV^{-5}
$\sqrt{s_{r1}}$	1.446 ± 0.002 GeV	1.445 ± 0.002 GeV
e_1	0.466 ± 0.006	0.465 ± 0.006
G_1	0.220 ± 0.009 GeV	0.222 ± 0.009 GeV
a	-0.53 ± 0.16 GeV^{-2}	-0.72 ± 0.16 GeV^{-2}

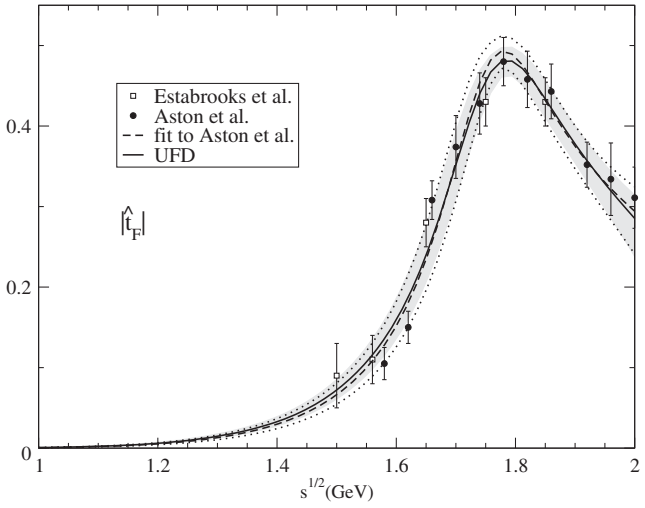

FIG. 11. Data on $|\hat{t}_F(s)|$ from [22,24]. The continuous line is our unconstrained fit (UFD), whose uncertainties are covered by the gray band. For comparison we show, as a dashed line, a fit to the data from [24], whose corresponding uncertainties are delimited by the dotted lines.

we will only make use of our partial wave parametrizations up to 1.74 GeV.

The most salient feature of this wave is the $K_3^*(1780)$ resonance, whose branching ratio to πK is slightly less than 20%. Therefore we will need the usual inelastic formalism explained in the Introduction to this section:

$$t_3^{1/2} = \frac{S_1^r - 1}{2i\sigma(s)}, \tag{42}$$

with

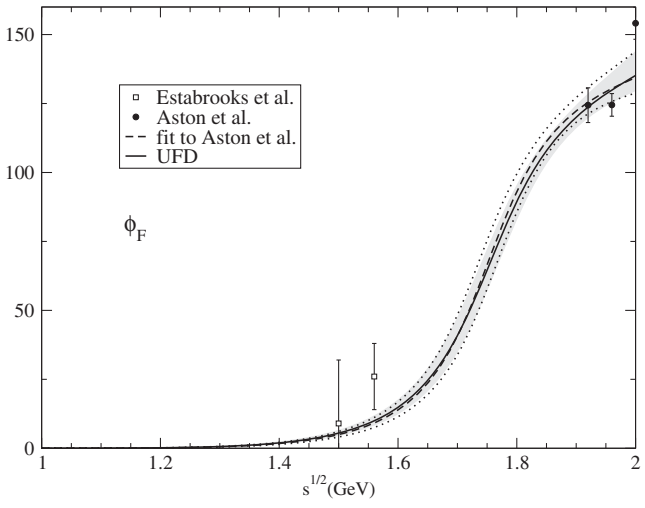

FIG. 12. Data on $\phi_F(s)$ from [22,24]. The continuous line is our unconstrained fit (UFD), whose uncertainties are covered by the gray band. For comparison we show, as a dashed line, a fit to the data from [24], whose corresponding uncertainties are delimited by the dotted lines.

TABLE X. Parameters of the $F^{1/2}$ wave.

Parameters	UFD	CFD
$\sqrt{s_{r1}}$	1.801 ± 0.013 GeV	1.804 ± 0.013 GeV
e_1	0.181 ± 0.006	0.184 ± 0.006
G_1	0.47 ± 0.05 GeV	0.50 ± 0.05 GeV
a	-0.88 ± 0.10 GeV^{-2}	-0.97 ± 0.10 GeV^{-2}

$$S_1^r = \frac{s_{r1} - s + i(P_1 - Q_1)}{s_{r1} - s - i(P_1 + Q_1)},$$
$$P_1 = e_1 G_1 \frac{p_1(q_{\pi K})}{p_1(q_{\pi K}^r)} \left(\frac{q_{\pi k}}{q_{\pi k,r}}\right)^7,$$
$$Q_1 = (1 - e_1) G_1 \frac{p_1(q_{\pi K})}{p_1(q_{\pi K}^r)} \left(\frac{q_{\eta k}}{q_{\eta k,r}}\right)^7 \Theta_{\eta K}(s). \tag{43}$$

In addition, $p_1(q_{\pi K}) = 1 + a q_{\pi K}^2$ and $\Theta_{\eta K}(s) = \Theta(s - (m_\eta + m_K)^2)$.

No background term is needed for this wave because its behavior is well described using the resonantlike form only, as can be observed in Figs. 11 and 12. The fit yields $\chi^2/\text{d.o.f.} = 16/(21 - 4 + 1)$ and the UFD parameters listed in Table X.

G. Regge parametrization

There are no data on $I = 3/2$ above 1.74 GeV, thus above that energy we will make use of the Regge parametrization for πK scattering in [17,40], which was obtained from factorization after fitting data on NN, $N\pi$, NK and $\pi\pi$ high energy scattering. Note that for πK scattering only the exchange of isospin 0 and 1 can occur in the t channel.

For the isoscalar exchange there are two contributions: the Pomeron, called $P(s)$ here, and the subleading f_2 trajectory, called $P'(s)$, so that we write

$$\text{Im}T_{\pi K}^{(I_t=0)}(s,t) = f_{K/\pi}[P(s,t) + rP'(s,t)], \tag{44}$$

where

$$P(s,t) = \beta_P \psi_P(t) \alpha_P(t) \frac{1 + \alpha_P(t)}{2} e^{bt} \left(\frac{s}{s'}\right)^{\alpha_P(t)},$$
$$P'(s,t) = \beta_{P'} \psi_{P'}(t) \frac{\alpha_{P'}(t)(1 + \alpha_P(t))}{\alpha_{P'}(0)(1 + \alpha_P(0))} e^{bt} \left(\frac{s}{s'}\right)^{\alpha_{P'}(t)},$$
$$\alpha_P(t) = 1 + t\alpha_P', \qquad \psi_P = 1 + c_P t,$$
$$\alpha_{P'}(t) = \alpha_{P'}(0) + t\alpha_{P'}', \qquad \psi_P = 1 + c_{P'} t. \tag{45}$$

Note that, by using factorization, the substitution of the $\pi\pi$-Pomeron vertex by the KK-Pomeron vertex is taken into account by the $f_{K/\pi}$ constant, whereas $rf_{K/\pi}$ takes care of the similar factorization for P'.

Since in this work we are interested in forward dispersion relations, we will only use the above Regge formulas with $t = 0$, but we provide the full expressions for completeness.

For the isovector exchange only the ρ trajectory is needed and we use

$$\mathrm{Im}T_{\pi K}^{(I_t=1)}(s,t) = g_{K/\pi}\mathrm{Im}T_{\pi\pi}^{(I_t=1)}(s,t), \tag{46}$$

with

$$\mathrm{Im}T_{\pi\pi}^{(I_t=1)}(s,t) = \beta_\rho \frac{1+\alpha_\rho(t)}{1+\alpha_\rho(0)}\varphi(t)e^{bt}\left(\frac{s}{s'}\right)^{\alpha_\rho(t)},$$
$$\alpha_\rho(t) = \alpha_\rho(0) + t\alpha'_\rho + \frac{1}{2}t^2\alpha''_\rho,$$
$$\varphi(t) = 1 + d_\rho t + e_\rho t^2. \tag{47}$$

Once again, the replacement of the $\pi\pi\rho$ vertex by the $KK\rho$ one is described by the $g_{K/\pi}$ constant, assuming factorization. Note that in [17] the value of $g_{K/\pi} = 1.1 \pm 0.1$ was used together with $\beta_\rho = 0.94 \pm 0.20$ to provide a description of πK. However, the same group [40] updated their $\pi\pi$ scattering analysis using dispersion relations and $\pi\pi$ scattering data at high energies to find $\beta_\rho = 1.48 \pm 0.14$. Consequently, if we want to use this latter value, we also have to update $g_{K/\pi} = 0.70 \pm 0.07$. One should nevertheless take into account that the information on this parameter is relatively scarce, since, in contrast to $\pi\pi$ scattering, there are no high energy data on πK scattering.

TABLE XI. Values of Regge parameters obtained in [17,40]. Since these could be fixed using reactions other than πK scattering, they will be fixed in both our UFD and CFD parametrizations.

Regge parameters	Used for both UFD and CFD
s'	1 GeV^2
b	2.4 ± 0.5 GeV^{-2}
α'_ρ	0.9 GeV^{-2}
α''_ρ	-0.3 GeV^{-4}
d_ρ	2.4 ± 0.5 GeV^{-2}
e_ρ	2.7 ± 2.5
α'_P	0.2 ± 0.1 GeV^{-2}
$\alpha'_{P'}$	0.9 GeV^{-2}
c_P	0.6 ± 1 GeV^{-2}
$c_{P'}$	-0.38 ± 0.4 GeV^{-2}
β_ρ	1.48 ± 0.14
$\alpha_\rho(0)$	0.53 ± 0.02
β_P	2.50 ± 0.04
$c_P(0)$	0 ± 0.04
$\beta_{P'}$	0.80 ± 0.05
$c_{P'}(0)$	-0.4 ± 0.4
β_2	0.08 ± 0.2
$\alpha_{P'}(0)$	0.53 ± 0.02

TABLE XII. Values of Regge parameters directly related to πK scattering. In practice r does not change from the UFD to the CFD parametrization.

Parameters	UFD	CFD
$f_{K/\pi}$	0.67 ± 0.01	0.66 ± 0.01
r	5×10^{-2}	5×10^{-2}
$g_{K/\pi}$	0.70 ± 0.07	0.53 ± 0.07

Thus it has to be determined only from factorization of KN scattering. Note that β_ρ, which is the equivalent value for $\pi\pi$, suffered a large revision when taking into account dispersion relations. Thus, large deviations in $g_{K/\pi}$ should not come as a surprise and they actually do occur when imposing our dispersive constraints on πK scattering.

The set of Regge parameters used before imposing any πK dispersion relation will be labeled as UFD values, similar to what we have been doing so far with our partial wave parametrizations. Correspondingly, we will refer to CFD values when in the next sections forward dispersion relations will be imposed on our fits. Those Regge parameters that could be determined without $K\pi$ input are shown in Table XI and their values are fixed both for the UFD and CFD parametrizations. They just correspond to the values in the original works [17,40].

In contrast, the values $f_{K/\pi}$, $g_{K/\pi}$ and r, which are directly related to πK scattering, are listed in Table XII and in this work they are allowed to vary from the UFD to the CFD parametrization, although in practice r stays the same.

IV. FORWARD DISPERSION RELATIONS AND SUM RULES

The aim of this work is to provide a simple set of partial waves which are consistent with basic requirements of analyticity (or causality) and crossing. These features impose stringent constraints on the scattering amplitude, which translate into integral equations that relate the πK scattering amplitude at a given energy with an integral over the whole physical energy region. In this section we introduce a complete set of forward dispersion relations that will be used first to check the consistency of our parametrizations and next as constraints on our fits.

A. Forward dispersion relations

Forward dispersion relations (FDRs), i.e., those calculated at $t = 0$, are useful because forward scattering is relatively easy to measure in the whole energy region, since it is related to the total cross section by the optical theorem. Moreover, this is the only fixed value of t for which the integrands in the dispersion relation will be given directly in terms of the imaginary part of a physical amplitude. They are applicable at any energy, in contrast to Roy-like equations, which, in practice, have a limited applicability energy range due to the projection in partial waves.

Fixed-t dispersion relations for πK have been frequently used in the literature as an intermediate step for the derivation of more elaborate dispersion relations for partial waves [14,15,41–43], or of sum rules for low-energy parameters [4], but not directly as constraints on the amplitudes, as will be done here.

For the sake of simplicity, given that $s+t+u=2(m_K^2+m_\pi^2)$ and $t=0$, it is customary to use an abbreviated notation $T(s,t=0,u)=T(s)$. It is also very convenient to make use of $s\leftrightarrow u$ crossing to change the amplitudes from the isospin basis to the $s\leftrightarrow u$ symmetric and antisymmetric amplitudes. These are defined, respectively, as

$$T^+(s)=\frac{T^{1/2}(s)+2T^{3/2}(s)}{3}=\frac{T^{I_t=0}(s)}{\sqrt{6}},$$
$$T^-(s)=\frac{T^{1/2}(s)-T^{3/2}(s)}{3}=\frac{T^{I_t=1}(s)}{2}. \quad (48)$$

In the last step we have indicated that T^+ and T^- correspond, by crossing, to the exchange of isospin 0 or 1 in the t channel, respectively. This is relevant because it means that T^+ is dominated at high energies by the t-channel exchanges of the Pomeron and P' trajectories, with no ρ trajectory contribution, whereas the opposite occurs for T^-.

Since dispersive integrals extend to infinity, naively one would need two subtractions to ensure the convergence of the Pomeron contribution and one for that of the ρ trajectory. For this reason, even if only used as intermediate steps for the derivation of other dispersion relations, the fixed-t dispersion relations for T^+ are customarily written with two subtractions and those for T^- with at least one. However, this is not necessary, because the $T^\pm$ FDRs have integrals over the right-hand and left-hand cuts whose leading terms multiplying the Regge trajectories cancel against each other due to the symmetry properties. As a consequence, one subtraction is enough to ensure the convergence of the T^+ FDR and no subtraction is needed for the T^- FDR. These kinds of cancellations have been recently used for $\pi\pi$ scattering FDRs in [17,40,44,45]. Having more subtractions implies that the dispersion relation is determined up to a polynomial of higher order. Thus, generically, fewer subtractions are convenient to avoid the propagation of the uncertainties in the subtraction constants to become too large in the resonance region, whereas more subtractions are useful when concentrating on the threshold region. Since in this work we will deal with scattering up to 1.74 GeV, we will make use of FDRs with the minimum number of subtractions needed, which also makes the equations slightly simpler.

Thus, for T^+ the once-subtracted FDR reads

$$\mathrm{Re}T^+(s)=T^+(s_{\rm th})+\frac{(s-s_{\rm th})}{\pi}P\int_{s_{\rm th}}^{\infty}ds'\left[\frac{\mathrm{Im}T^+(s')}{(s'-s)(s'-s_{\rm th})}-\frac{\mathrm{Im}T^+(s')}{(s'+s-2\Sigma_{\pi K})(s'+s_{\rm th}-2\Sigma_{\pi K})}\right], \quad (49)$$

where $s_{\rm th}=(m_\pi+m_K)^2$ and P stands for the principal part of the integral. In contrast, the unsubtracted FDR for T^- reads

$$\mathrm{Re}T^-(s)=\frac{(2s-2\Sigma_{\pi K})}{\pi}P\int_{s_{\rm th}}^{\infty}ds'\frac{\mathrm{Im}T^-(s')}{(s'-s)(s'+s-2\Sigma_{\pi K})}. \quad (50)$$

We have evaluated these two FDRs at 50 values of $\sqrt{s_i}$ equally spaced between a minimum energy $\sqrt{s_{\rm min}}$ and 1.74 GeV, using as input for the integrals our UFD partial waves at $s'\leq 1.74$ GeV and the Regge UFD parametrizations above. At each of these $\sqrt{s_i}$'s we have also calculated the difference d_i between the left- and right-hand sides of each FDR as well as its corresponding uncertainty Δd_i. When $d_i\lesssim\Delta d_i$ we can consider that the FDR is satisfied within uncertainties at the energy $\sqrt{s_i}$.

As a word of caution, let us remark that the uncertainties Δd_i are calculated as the quadratic addition of the uncertainties due to the error bar of each parameter in the UFD parametrization. Note however that in the full physical amplitude, being a solution of the FDRs, all these parameters would be correlated. Our parametrizations are just a fit to partial waves, many of which have been measured independently from one another, and these correlations may be lost. Therefore our FDR error bands only reflect the propagation of the uncertainties from our data parametrizations, without the possible correlations between parameters that may exist.

The results of the above calculation for T^+ are shown in the upper panel of Fig. 13. We plot $\mathrm{Re}T^+$ calculated directly from the UFD parametrization (input UFD) versus $\mathrm{Re}T^+$ calculated from the dispersive representation in Eq. (49) above (dispersive UFD). The gray area corresponds to adding $\pm\Delta d_i$ to the "dispersive UFD" curve. Note that for this symmetric amplitude we have set $\sqrt{s_{\rm min}}$ at $K\pi$ threshold. We can see that the input UFD lies slightly beyond the uncertainty band up to 1.2 GeV, but that it is much more separated beyond 1.55 GeV. The consistency of the data with the T^+ FDR is therefore not very satisfactory, particularly at higher energies.

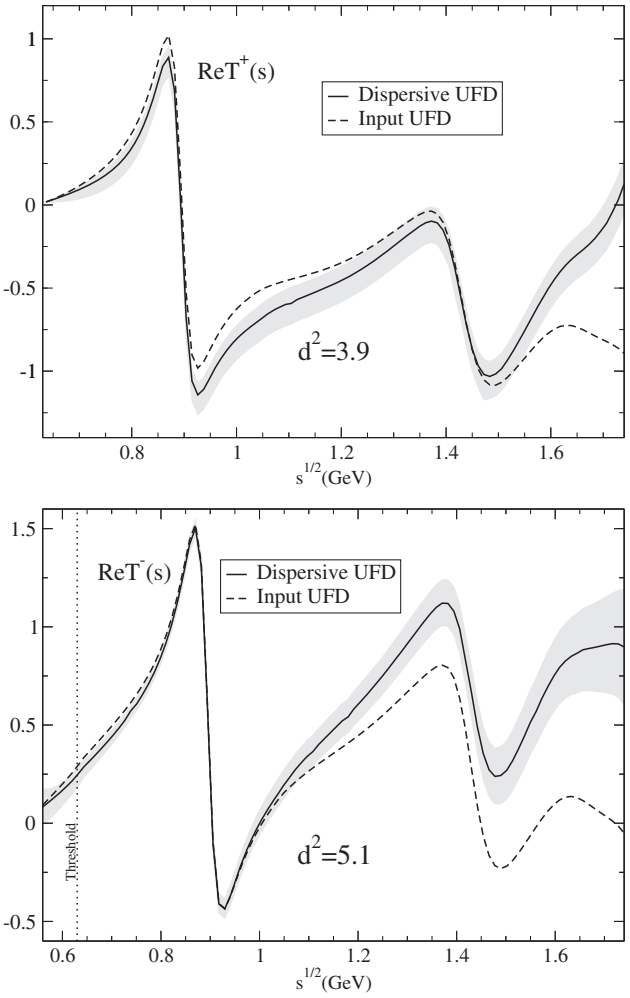

FIG. 13. Comparison between the input (dashed lines) and the output for the T^+ (top panel) and T^- (bottom panel) FDRs when using the UFD set. These correspond to the left-hand side versus the right-hand side in Eqs. (49) and (50). The gray bands describe the uncertainty of the difference.

The results for T^- are plotted in the lower panel of Fig. 13, using the same conventions. In this case we have set $\sqrt{s_{\rm min}} = 0.56$ GeV, below threshold, because the T^- FDR has no subtractions and thus provides strong constraints on a combination of scalar scattering lengths. The figure shows that the separation between both calculations is slightly above Δd_i up to 0.8 GeV. Above this energy, the T^- FDR is nicely satisfied within uncertainties up to 1.2 GeV, where the difference between the two curves starts growing, becoming much larger than Δd_i. As we will see, the deviation at energies above 1.2 GeV is mainly caused by the ρ-exchange Regge contribution.

In order to provide a quantitative measure of the fulfillment of each FDR, we have defined an averaged squared distance for each FDR,

TABLE XIII. Fulfillment of forward dispersion relations (FDRs) in different energy regions. We provide the averaged square distance divided by relative error between the left- and right-hand sides of each FDR. Note the remarkable improvement from the UFD to the CFD parametrization.

	UFD		CFD	
	$d^2_{T^+}$	$d^2_{T^-}$	$d^2_{T^+}$	$d^2_{T^-}$
$\sqrt{s_{\rm min}} \le \sqrt{s} \le m_K + m_\eta$	3.35	0.97	0.39	0.13
$m_K + m_\eta \le \sqrt{s} \le 1.6$ GeV	1.3	6.8	0.17	0.70
1.6 GeV $\le \sqrt{s} \le 1.74$ GeV	14.6	12.8	8.0	0.5
$\sqrt{s_{\rm min}} \le \sqrt{s} \le 1.74$ GeV	3.9	5.1	1.3	0.44

$$d^2_{T\pm} = \frac{1}{N}\sum_{i=1}^{N}\left(\frac{d_i}{\Delta d_i}\right)^2_{T^\pm}, \tag{51}$$

which is rather similar to the usual definition of a χ^2 function. Consistency of the data parametrizations with FDRs would demand $d^2_{T\pm} \lesssim 1$.

In Table XIII we show the values of $d^2_{T\pm}$ in different energy regions. For the UFD set it is clear that the consistency with FDRs is not very satisfactory, particularly in the inelastic region, and very inconsistent above 1.6 GeV. There is room for the considerable improvement that will be achieved in Sec. V, to the point of obtaining a constrained set of parametrizations (CFD) remarkably consistent with both FDRs up to 1.6. However, we will see that above that energy we are only able to improve the agreement but not achieve consistency within uncertainties.

B. Sum rules for threshold parameters

Threshold parameters of partial waves, defined in Eq. (5), are of interest for our understanding of the lowest energy physics and particularly for studies within ChPT [1]. In this section we present three sum rules (SRs) that provide a more accurate determination of certain combinations of threshold parameters, in terms of integrals, than would be achieved directly from the partial wave parametrizations. These SRs will be used first as tests of our UFD parametrizations and in Sec. V will be used as constraints.

Other sum rules have been derived for determining the ChPT low-energy constants [4], but here we will use our own sum rules for threshold parameters. In [14] a sum rule for a combination of scattering lengths is given, but it needs $\pi\pi \to K\bar{K}$ scattering input, and here we only want to use data on πK scattering.

Thus, the first of our sum rules yields precisely the combination of scalar scattering lengths measured at DIRAC [38], see Eq. (24) above. It is basically the T^- FDR evaluated at threshold and for convenience we will write it as follows:

TABLE XIV. Sum rules in m_π units. We show results for the UFD and CFD parametrizations. Note that since $a_1^{3/2}$ is more than 30 times smaller than $b_0^{3/2}$, then $D_{3/2} \sim b_0^{3/2}$.

	UFD	CFD
D_a	$0.108^{+0.018}_{-0.010}$	$0.091^{+0.006}_{-0.005}$
SR_a	0.093 ± 0.004	0.091 ± 0.003
Δ_a	$0.015^{+0.020}_{-0.012}$	$0.000^{+0.006}_{-0.005}$
$D_{1/2}$	$0.205^{+0.039}_{-0.024}$	$0.187^{+0.023}_{-0.016}$
$SR_{1/2}$	$0.186^{+0.006}_{-0.006}$	$0.182^{+0.006}_{-0.005}$
$\Delta_{1/2}$	$0.019^{+0.038}_{-0.024}$	$0.005^{+0.022}_{-0.016}$
$D_{3/2}$	$-0.051^{+0.037}_{-0.005}$	$-0.047^{+0.005}_{-0.005}$
$SR_{3/2}$	$-0.046^{+0.003}_{-0.011}$	$-0.041^{+0.002}_{-0.002}$
$\Delta_{3/2}$	$-0.005^{+0.048}_{-0.007}$	$-0.006^{+0.006}_{-0.006}$

$$0 = \Delta_a \equiv D_a - SR_a, \tag{52}$$

where

$$D_a \equiv \frac{1}{3}(a_0^{1/2} - a_0^{3/2}) \tag{53}$$

is calculated "directly" from our parametrizations. In principle it should be equal to the following integral expression:

$$SR_a \equiv \frac{2m_\pi m_K}{\sqrt{s_{th}}} P \int_{s_{th}}^{\infty} \frac{\mathrm{Im}T^-(s')}{s'(s'-s_{th})} ds'.$$

In practice, since D_a and SR_a are obtained from data the sum rule will not be exactly zero, but consistency requires it to cancel within uncertainties.

In Table XIV we show the results of this sum rule calculation using our UFD parametrizations. Note that it is not very well satisfied, since the Δ_a is slightly above 1.2 deviations from zero. This small disagreement suggests that there is room for improvement at low energies in the S waves. Both the direct and integral results are compatible with the experimental value obtained in DIRAC, Eq. (24), but this is not surprising given the very large experimental uncertainties.

Let us remark that a sum rule involving only scalar scattering lengths cannot be derived from the T^+ FDR because it has one subtraction. However, from once-subtracted FDRs it is possible to obtain sum rules involving scalar slope parameters and vector scattering lengths. Actually, by combining the T^+ FDR in Eq. (49) and the once-subtracted version of the T^- FDR, we can obtain two independent sum rules. Once again we will write them as

$$0 = \Delta_I \equiv D_I - SR_I, \tag{54}$$

with $I = 1/2, 3/2$. On the one hand,

$$D_I \equiv b_0^I + 3a_1^I \tag{55}$$

will be calculated directly from the parametrizations. Note that $a_1^{3/2}$ is more than 30 times smaller than $b_0^{3/2}$, so that $D_{3/2} \sim b_0^{3/2}$ is a very good approximation. On the other hand, the SR_I's are calculated with the following integral expressions:

$$SR_{1/2} \equiv \frac{\sqrt{s_{\mathrm{th}}}}{2m_\pi m_K} \times P \int_{s_{\mathrm{th}}}^{\infty} ds' \left[\frac{\mathrm{Im}T^+(s') + 2\mathrm{Im}T^-(s')}{(s'-s_{\mathrm{th}})^2} - \frac{\mathrm{Im}T^+(s') - 2\mathrm{Im}T^-(s')}{(s'+s_{\mathrm{th}}-2\Sigma_{\pi K})^2} \right], \tag{56}$$

and

$$SR_{3/2} \equiv \frac{\sqrt{s_{\mathrm{th}}}}{2m_\pi m_K} \times P \int_{s_{\mathrm{th}}}^{\infty} ds' \left[\frac{\mathrm{Im}T^+(s') - \mathrm{Im}T^-(s')}{(s'-s_{\mathrm{th}})^2} - \frac{\mathrm{Im}T^+(s') + \mathrm{Im}T^-(s')}{(s'+s_{\mathrm{th}}-2\Sigma_{\pi K})^2} \right]. \tag{57}$$

In Table XIV we show the results of these sum rules when the UFD set is used as input. As expected, the integral result, SR_I, is more accurate than the direct evaluation, D_I, for both sum rules. Although the fulfillment of these sum rules by our UFD set is fairly good, this is mostly due to the large and very asymmetric uncertainties in D_I, to not very good agreement in the central values.

In summary, the UFD set leaves room for improving the fulfillment of the sum rules just discussed. Hence in Sec. V they will be considered, together with the FDRs, as constraints for our parametrizations.

V. CONSTRAINED FITS TO DATA

So far we have used the FDRs and sum rules as checks of our UFD set. We have seen that there is room for improvement and therefore in this section we will use them as constraints to obtain a new set of parametrizations, that we will call the CFD set. In particular we will minimize the following quantity:

$$W^2(d_{T^+}^2 + d_{T^-}^2) + \sum_{I=\frac{1}{2},\frac{3}{2}} \left(\frac{\Delta_I}{\delta\Delta_I} \right)^2 + \sum_k \left(\frac{p_k^{UFD} - p_k}{\delta p_k^{UFD}} \right)^2, \tag{58}$$

where $d_{T^\pm}^2$ are the average square distances between the FDR input and output defined in Eq. (51), Δ_I are the sum rules defined in Eq. (54) and $\delta\Delta_I$ are their associated

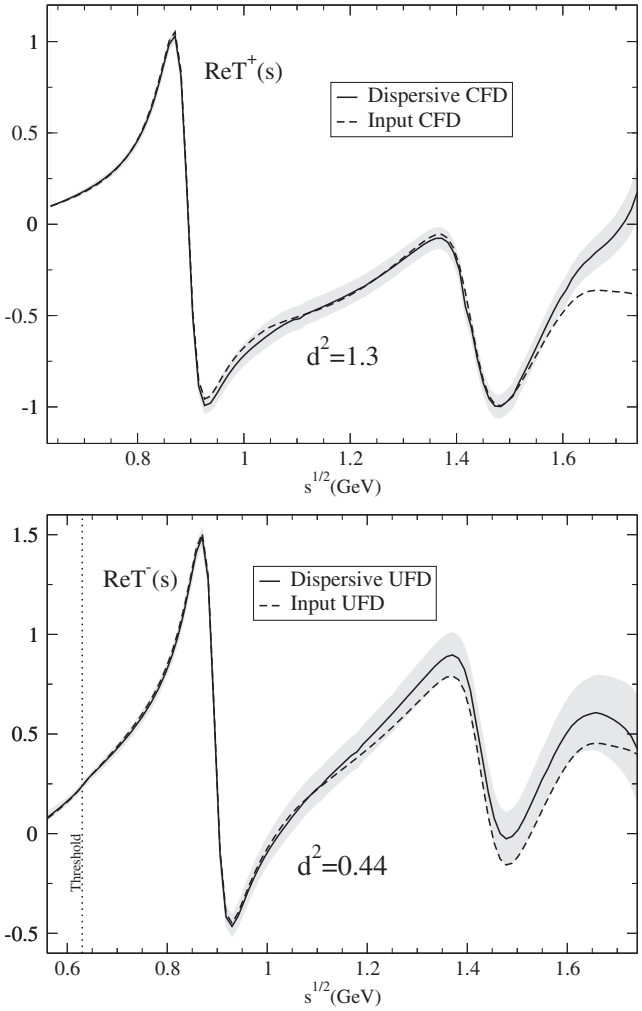

FIG. 14. Comparison between the input (dashed line) and the output for the T^+ (top panel) and T^- (bottom panel) FDRs when using the CFD set. These correspond to the left-hand side versus the right-hand side, respectively, in Eqs. (49) and (50). The gray bands describe the uncertainty of the difference. Note the dramatic improvement below 1.6 GeV compared to the results in Fig. 13 using the UFD set. Actually, the input and dispersive CFD calculations are consistent within uncertainties up to 1.6 GeV.

uncertainties. Note that the Δ_a sum rule of Eq. (52) is included in the $d^2_{T^-}$ term. Finally, to avoid large deviations from the UFD data description, we add a χ^2-like penalty function for each UFD parameter. Generically we have denoted these UFD parameters by p_k^{UFD} and their uncertainty by δp_k^{UFD}. The $W^2 = 12$ constant stands for the number of degrees of freedom observed naively from the shape of Re$T^{\pm}$, which as seen in Fig. 14 is roughly 12. This approach is the same already followed for $\pi\pi$ scattering in [17,40,44,45].

With this minimization procedure we have arrived to a CFD set, whose parameters can be found in Tables I–III and V–X. Most CFD parameters are consistent within one deviation with their UFD counterparts. Actually, we have allowed 46 parameters to vary, of which 38 lie within 1 deviation, and only three lie beyond 1.6 deviations. These are the Φ_0 parameter of the $D^{1/2}$ wave, which changes by 3 deviations, the Regge $g_{K/\pi}$ parameters, changing by 2.5 deviations, and the B_2 parameter of the $S^{3/2}$ wave that changes by 1.8 deviations.

Before discussing in detail the changes from the UFD to the CFD set, let us discuss first how well this new CFD set satisfies the FDRs and sum rules.

A. FDRs and sum rules for the CFD set

In Fig. 14 we show the FDR results for the T^+ and T^- amplitudes using the CFD set as input. These have to be compared with the corresponding results for the UFD set in Fig. 13. Note that, in contrast to what happened when using the UFD set as input, the CFD input and its dispersive output now agree within uncertainties. The only exception is still the T^+ FDR above 1.6 GeV, where the agreement has nevertheless improved compared to the UFD result. For this reason in this work we only claim to have precise and consistent parametrizations up to 1.6 GeV. It seems that improving the agreement above this region would require our parametrizations to depart from data. This could be due to the existence of some large systematic uncertainties in some waves or to the fact that the whole tower of higher partial waves may start to play a more relevant role.

The results for the averaged distances $d^2_{T^\pm}$ of the two FDRs for this CFD set are shown in Table XIII. Let us remark that they are much smaller than 1 below 1.6 GeV. The CFD set is therefore remarkably consistent up to that energy, which is a dramatic improvement over the UFD set. In addition, from 1.6 to 1.74 GeV the antisymmetric FDR is also well satisfied. However, although the CFD improves on the fulfillment of the symmetric FDR above 1.6 GeV, it is still quite inconsistent. It has not been possible to fulfill the T^+ FDR above 1.6 GeV with an acceptable data description.

In Table XIV we have also provided the CFD result for the sum rules. The central value of all Δ_I's are now closer to zero and the uncertainties are much smaller and much more symmetric.

Thus, once we have seen that the consistency of the description has improved, let us study in detail the changes in the partial waves from the UFD to the CFD set, and check to see that they still provide a good description of data up to 1.6 GeV.

B. S waves

1. $S^{3/2}$ wave

The $S^{3/2}$-wave CFD parameters can be found in Table I. In Fig. 15 we show as a continuous line the CFD phase shift whose uncertainties are covered by the gray band,

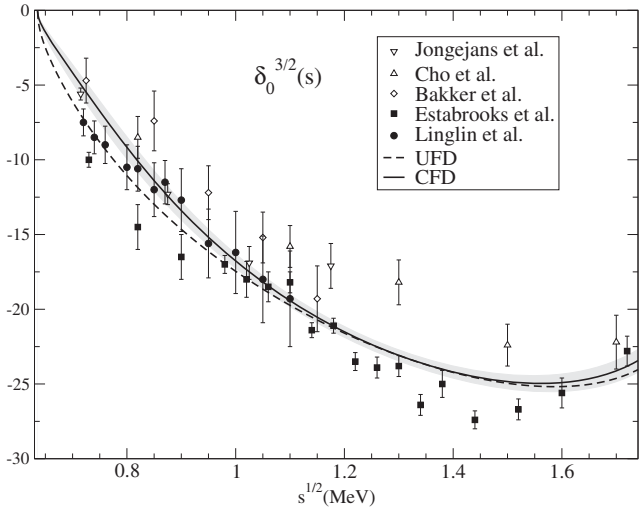

FIG. 15. The CFD parametrization of the $S^{3/2}$ wave is shown as a continuous line and its uncertainty as a gray band. For comparison the UFD parametrization is shown as a dashed line. See Fig. 1 for data references.

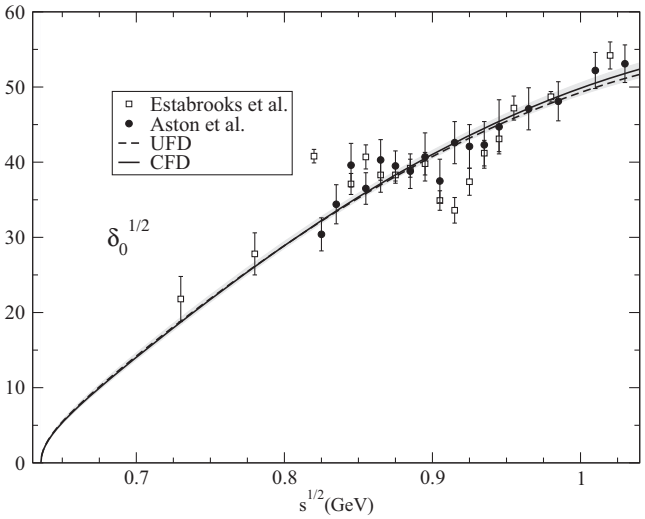

FIG. 16. CFD parametrization of the $S^{1/2}$-wave phase shift in the elastic region, shown as a continuous line whose uncertainty is covered by the gray band. For comparison we also show as a dashed line the UFD result. Note that in this case the UFD and CFD parametrizations are almost indistinguishable. See Fig. 3 for data references.

whereas the UFD phase is represented by a dashed line. We do not plot the uncertainty band of the UFD curve because it was already given in Fig. 1 and it overlaps with the CFD band. From 1 to 1.74 GeV, the UFD and CFD fits are almost identical, although they differ at lower energies. In particular the central value of the CFD scattering length is about half of that obtained for the UFD, as seen in Table IV.

That some changes were needed at low energies in the scalar waves was to be expected since we already saw that the Δ_a sum rule was not satisfied very well by the UFD set. Moreover, in Fig. 13 a deviation in the low-energy region of the FDRs was also observed for the UFD set.

It turns out that the FDRs and sum rule constraints tend to correct these small deviations by modifying only the $S^{3/2}$ wave at low energies. Actually, note that both the B_1 and B_2 parameters of the $S^{3/2}$ wave change from their UFD values by 1.5 and 1.8 deviations, respectively. In contrast, imposing the FDR and sum rule constraints barely changes the $S^{1/2}$ wave in the elastic region, as we will see next. Note also that the CFD result strongly disfavors the Estabrooks *et al.* data at low energies. This may serve as *a posteriori* justification for those works that neglect these data from the start.

2. $S^{1/2}$ wave

As can be seen in Fig. 16 the CFD $S^{1/2}$ wave in the elastic region (the continuous line) is almost indistinguishable from the UFD parametrization. Actually, as seen in Table II, the B_0 parameter does not change at all, whereas the CFD B_1 central value lies within less than one deviation of the UFD parameter.

3. t_S wave

As explained in previous sections, the data in the inelastic region are presented in terms of the modulus and phase of the $\hat{t}_S$ amplitude. As seen now in Fig. 17, in the inelastic region the UFD and CFD descriptions are quite compatible up to 1.5 GeV. However, above that energy the CFD parametrization starts deviating from the UFD result. The UFD central value (the dashed line) lies slightly outside the uncertainty band of the CFD set, although both uncertainty bands would always overlap and therefore the CFD still provides a fairly good description of the data. Actually, it can be checked in Table III that the parameter of the CFD inelastic fit that varies the most with respect to its UFD value is ϕ_1, which changes by merely 1.1 deviations. Around 1.7 GeV the CFD result prefers the solution of Aston *et al.* [24] for the phase. This deviation of the CFD set from the UFD one reflects the fact that forward dispersion relations are not well satisfied by the UFD set in this region, as we already saw in Fig. 13. As a matter of fact, the S waves and the $D^{1/2}$ wave are the ones that change most to improve the consistency of the FDRs above 1.5 GeV.

C. P waves

1. $P^{3/2}$ wave

The CFD solution for this wave is shown as a continuous line in Fig. 18, where its uncertainty is covered by the gray band. Note that the UFD solution is compatible in the whole energy region with the new CFD parametrization. Moreover, in Table V it can be seen that the two CFD B_k

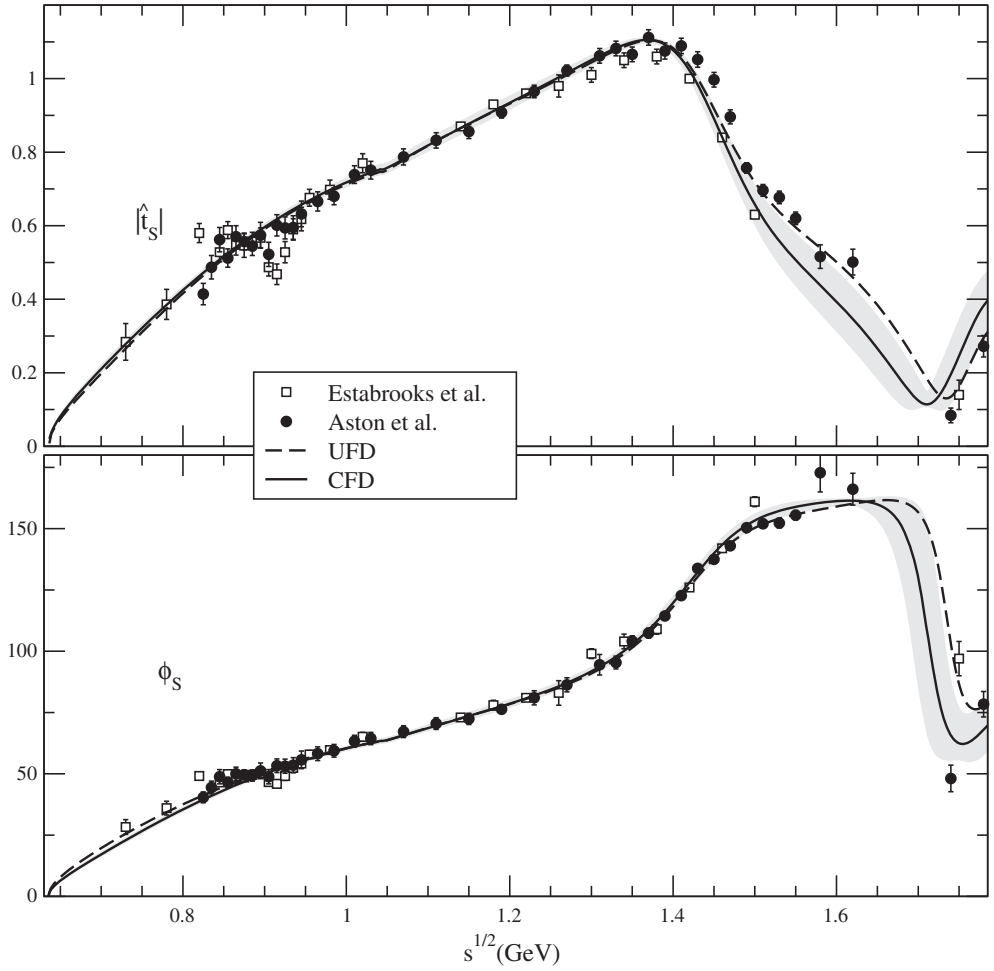

FIG. 17. CFD parametrization of the $\hat{t}_S$ wave in the whole energy region. On the upper panel we show $|\hat{t}_S(s)|$, whereas in the lower one we show $\phi_S(s)$. The continuous line is our constrained fit (CFD), whose uncertainties are covered by the gray band. For comparison we show the UFD result as a dashed line. Data references are as in Fig. 2.

parameters lie well within the uncertainties of their UFD counterparts. Therefore the data description is still acceptable.

Let us recall that although the absolute value of this phase shift is smaller than 2.5° in the whole energy region, this wave still has a sizable effect on our calculations. This is partly due to the $(2l+1)$ factors in Eq. (1), but particularly because all other waves become relatively small around 1.5 GeV.

2. $P^{1/2}$ wave

As seen in Fig. 19 the CFD (continuous line) and UFD (dashed) fits are almost indistinguishable up to 930 MeV despite the very small uncertainty (the gray band). Around that energy, the CFD result starts deviating towards slightly lower values of the phase, although it is still compatible with the UFD thanks to the fact that the uncertainty band becomes larger in that region.

This means that describing the data around the $K^*(892)$ resonance, whose mass is $\simeq$896 MeV and width is $\simeq$49 MeV, requires the phase in the 930 MeV to 1 GeV region to be somewhat below the existing data. We emphasize this remark because in the solution of the Roy-Steiner equations in [14], the $K^*(892)$ phase comes out somewhat incompatible with the data (we show the result as a dotted line in Fig. 19). To obtain such a solution the authors use as a boundary condition the value of the phase (and its derivative) at $\sqrt{s} = \sqrt{0.935\ \text{GeV}^2} \simeq 0.967$ GeV, which they take to be $155.8 \pm 0.4°$. However, at that energy, our CFD result yields $152.5 \pm 2.0°$. This could suggest that the mismatch between the Roy-Steiner solution of [14] and the scattering data around the $K^*(892)$ resonance could be due in part to the choice of matching phase and that it might be improved by lowering it by roughly 3°, as our CFD prefers.

In the threshold region we have calculated the scattering length directly from the CFD parametrization:

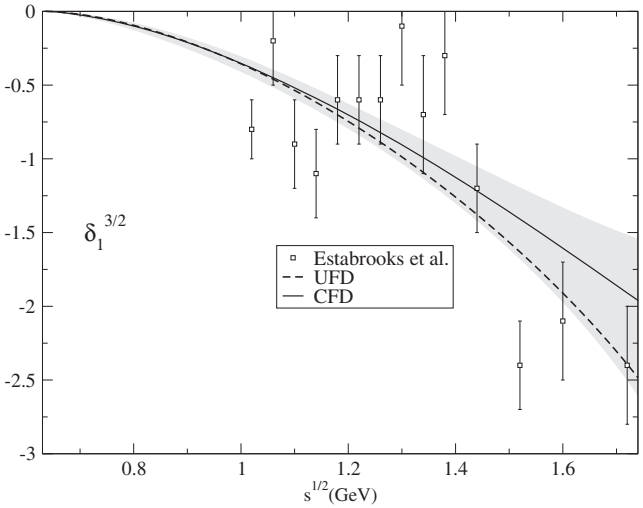

FIG. 18. Phase shift of the $P^{3/2}$ wave. Data are from [22]. We show as a continuous line the CFD fit and the gray band covers its uncertainties. The UFD result lies right on the border of this uncertainty band. Note that this phase is rather small up to 1.74 GeV.

$$m_\pi a_1^{1/2} = 0.024^{+0.008}_{-0.005}, \tag{59}$$

to be compared with the UFD result $m_\pi a_1^{1/2} = 0.031^{+0.013}_{-0.008}$. Note that since our UFD and CFD fits describe the data in Fig. 19, the resulting scattering lengths are larger than the one obtained in [14], $m_\pi a_1^{1/2} = 0.019 \pm 0.001$.

3. t_P wave

Once we have described both the isospin $1/2$ and $3/2$ P waves, we show the modulus and phase of the $t_P = t_1^{1/2} + t_1^{3/2}/2$ amplitude in Figs. 20 and 21, respectively. In the inelastic region both the phase and the modulus obtained for the CFD solution are compatible with the UFD parametrizations. Actually, by looking at Table VII one can check to see that the CFD parameters are almost identical to their UFD counterparts, varying by less than one deviation, except the a parameter, which changes by 1.4 deviations.

Our CFD solution describes fairly well the three resonances observed in this partial wave, namely, the $K^*(892)$, the $K^*(1410)$ and the $K^*(1680)$.

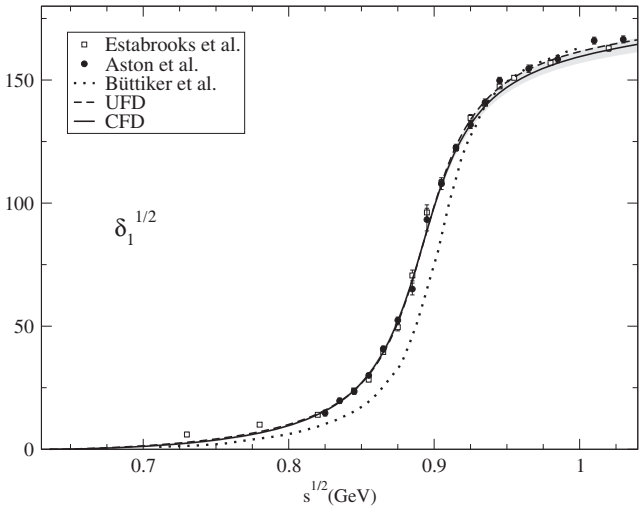

FIG. 19. Phase shift of the $P^{1/2}$ wave. The CFD and UFD results are almost indistinguishable up to 950 MeV, where the CFD phase becomes somewhat smaller. Note however that the UFD results still lie inside the uncertainty band. In addition we show the solution in [14]. Data are from [22,24].

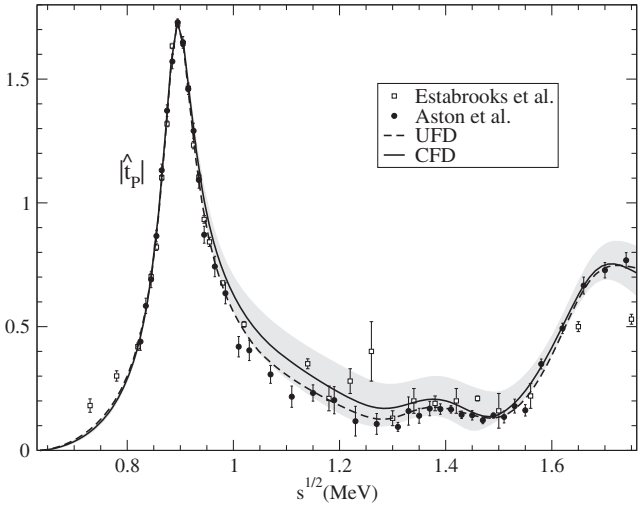

FIG. 20. Modulus of the $\hat{t}_P = \hat{t}_1^{1/2} + \hat{t}_1^{3/2}/2$ amplitude. We show the CFD fit as a continuous line and its uncertainty as a gray band. Note that the UFD result (dashed line) is also compatible within the CFD uncertainties. Data are from [22,24].

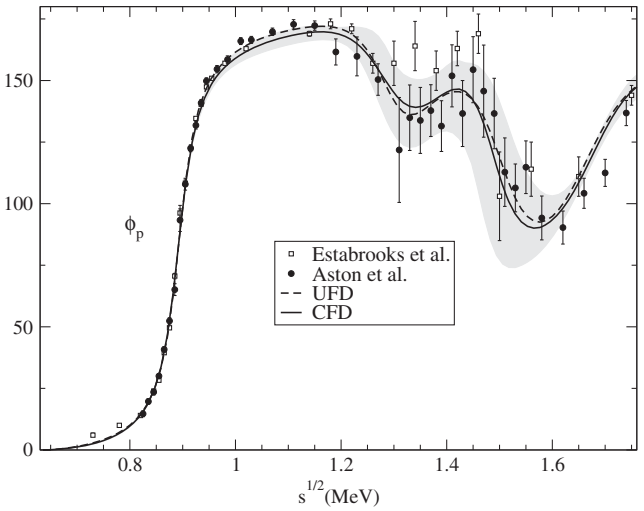

FIG. 21. Phase of the $t_P = t_1^{1/2} + t_1^{3/2}/2$ amplitude. We show the CFD fit as a continuous line and its uncertainty as a gray band. Note that the UFD result (the dashed line) is also very compatible within the CFD uncertainties. Data are from [22,24].

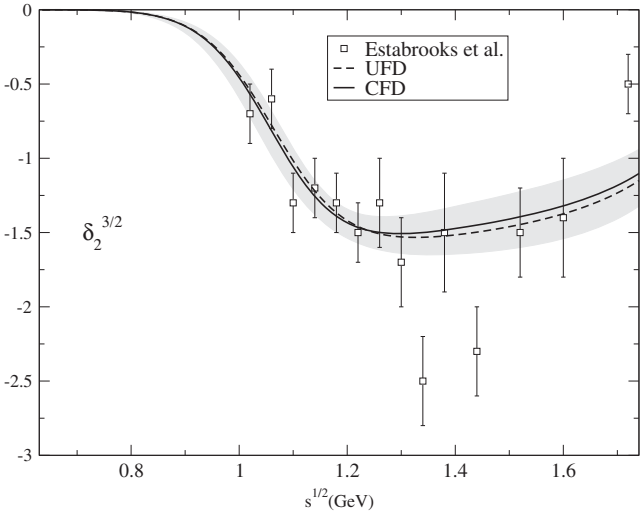

FIG. 22. $D^{3/2}$ phase shift. Data are from [22]. We show the CFD result as a continuous line and its uncertainty as a gray band. Note that it deviates very slightly from the UFD result (the dashed line) and only above 1.2 GeV.

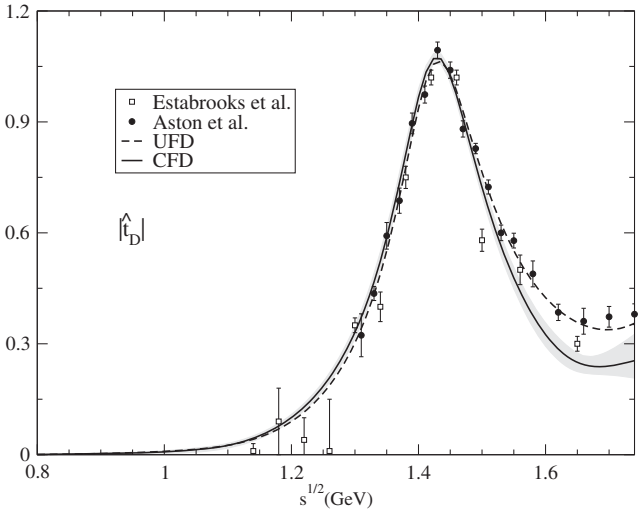

FIG. 23. Modulus of the $\hat{t}_D$ wave. Data are from [22,24]. Note the clear peak of the $K_2^*(1430)$ resonance and that above 1.6 GeV the UFD central result (the dashed line) is incompatible with the CFD result (the continuous line) within its uncertainties (the gray band).

Let us remark that although the two parametrizations are compatible, the CFD result prefers, for the modulus, the data of Estabrooks *et al.* [22] between 1 and 1.5 GeV.

D. D waves

1. $D^{3/2}$ wave

In Fig. 22 we show the CFD result for the $D^{3/2}$ wave, whose structure is relatively simple and whose size and influence are rather small, but not completely negligible, particularly in the inelastic regime. As seen in the figure, the CFD solution we obtain is almost the same as the UFD parametrization. In Table VIII it can be observed that the CFD parameters change by less than one third of a deviation from their UFD counterparts.

2. t_D wave

Since there are no data in the elastic region for the $I = 1/2$ D-wave partial wave, we directly show the modulus and phase of the $t_D = t_2^{1/2} + t_2^{3/2}/2$ combination in Figs. 23 and 24, respectively. For the modulus, the CFD solution is almost indistinguishable from the UFD curve up to 1.6 GeV. However, above that energy the central UFD value lies typically 2 to 3 deviations away from the central CFD value. Nevertheless, both fits are still compatible due to the rather large uncertainty band of the UFD set, shown in Fig. 9. Concerning the phase, this is the curve where, above 1.6 GeV, we find the largest deviation from the data and the UFD set. By comparing the CFD versus the UFD parameters for this wave, given in Table IX, we find that the ϕ_0 parameter changes by more than 3 deviations. This is the only parameter that changes so dramatically from its UFD to its CFD value. Note it is closely related to the background produced by the opening of the $K\eta$ channel.

This deviation is not too worrisome since it occurs at the very end of our parametrizations and outside the peak of the $K_2^*(1430)$, whose width is roughly 100 MeV. Therefore, the amplitude in that region is relatively small. At this point it is important to recall that the symmetric FDR, shown in Fig. 14, is well satisfied by the CFD set only up to 1.6 GeV. Above that energy, it improves the UFD result, but it is not enough to consider it satisfactory. As already commented,

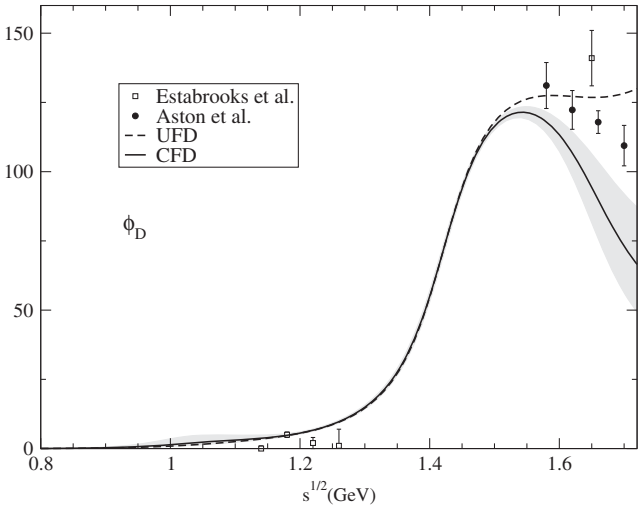

FIG. 24. Phase of the t_D wave. Data are from [22,24]. Note the sharp phase rise due to the $K_2^*(1430)$ resonance and that above 1.6 GeV the existing data and the UFD central result (the dashed line) are both incompatible with the CFD result (the continuous line) within its uncertainties (the gray band).

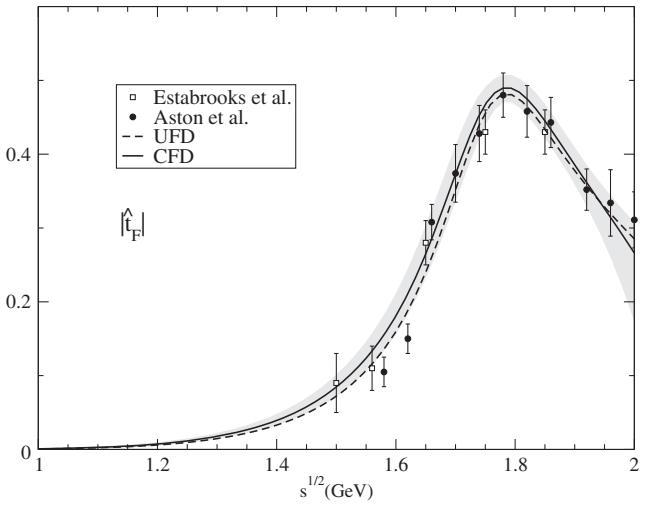

FIG. 25. Modulus of the $F^{1/2}$ wave. Data are from [22,24]. Note that the peak of the $K_3^*(1780)$ resonance is well described by both the CFD and UFD curves, which are very compatible. The gray band stands for the CFD uncertainty.

this is one of the reasons why in this work we claim to have precise and consistent data parametrizations up to 1.6 GeV and not beyond. Above that region the measured data is hard to reconcile with the dispersive constraints. This might be due to the existence of further systematic uncertainties, not necessarily in this wave, or to the increasingly important contribution from the tower of partial waves to the partial wave expansion.

E. $F^{1/2}$ wave

The CFD result for the $F^{1/2}$ wave is almost indistinguishable from our previous UFD result and describes nicely the $K_3^*(1780)$. This can be seen in Figs. 25 and 26,

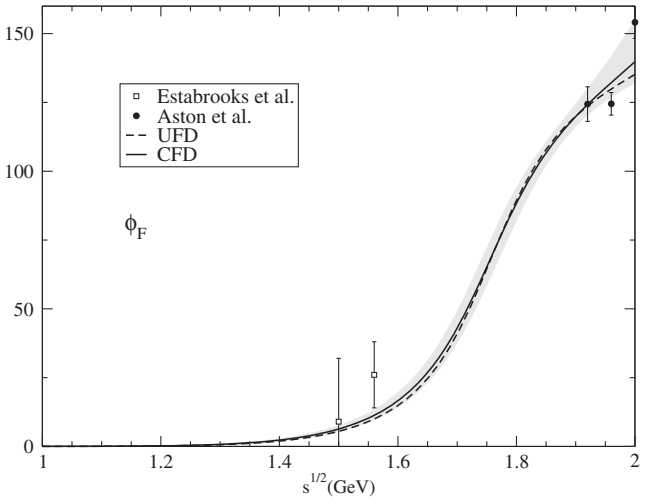

FIG. 26. Phase of the $F^{1/2}$ wave. Data are from [22,24]. Note that the CFD and UFD curves are very compatible. The gray band stands for the CFD uncertainty.

where we show the modulus and the phase of the partial wave, respectively.

F. CFD Regge parametrizations

When imposing dispersive constraints on the amplitude, we have also allowed the $f_{K/\pi}$, r and $g_{K/\pi}$ Regge parameters to vary. The rest of the Regge parameters have been kept fixed to the values in the literature, also used for the UFD set and given in Table XI. The reason is that, in principle, these other parameters can be determined without using processes involving kaons or πK scattering.

In Table XII we can observe that, in the end, the $f_{K/\pi}$ and r parameters barely change. However the CFD value of $g_{K/\pi}$ changes by 2.5 deviations from its UFD counterpart and is responsible for more than half of the reduction in $d_{T^-}^2$, particularly at high energies. As we commented before, it is not very surprising that this parameter suffers a large change, since there is little information to determine it reliably. It can be considered that in this work we are making a dispersive determination of this parameter.

VI. DISCUSSION

Before concluding, let us discuss our results in relation to data obtained from the decay of heavier particles, as well as regarding poles of resonances in the elastic regime and particularly the controversial $K_0^*(800)$ or κ meson.

A. Data from decays of heavier particles

As was already commented in Sec. III A, further information on the πK system has been obtained from the decays of heavier particles.

The semileptonic $D^+ \to K^-\pi^+e^+\nu_e$ decays have been analyzed by the *BABAR* [25] and BESIII [26] collaborations providing data on the phase difference between the S and P components. Since only the πK's interact strongly in the final state, Watson's theorem applies and in the elastic region this measurement is nothing but the difference between the S and P scattering phase shifts. In Fig. 27 we show the results for the $I = 1/2$ S-wave phase obtained from semileptonic D decays, compared to those from scattering experiments. Note that the uncertainties from decays are much larger than those obtained from scattering. Although what is actually measured in these decays is the phase-shift difference between the P and S waves, the experimental collaborations provide tables for the S wave alone, by using a simple P-wave description, whose uncertainty is much smaller and can be neglected. A similar procedure has been followed with the LASS scattering data of Aston *et al.* [24] shown in Fig. 27 for comparison, where the $I = 3/2$ component has been separated with the Estabrooks *et al.* model [22]. The above caveats and the very large uncertainties justify our not including data from decays in our fits. All in all, there is a nice qualitative agreement between different data sources and also with our

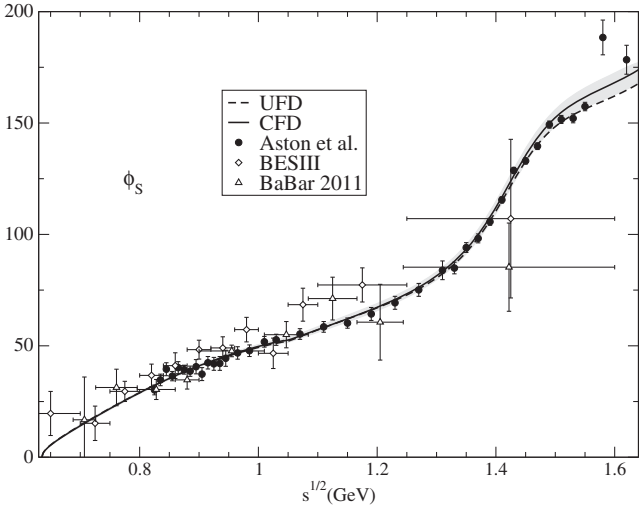

FIG. 27. Phase of the $I = 1/2$ πK S wave obtained from the semileptonic decay $D^+ \to K^-\pi^+e^+\nu_e$ by the *BABAR* Collaboration [25] and recently by the BESIII Collaboration [26]. These phases are compared to the LASS scattering phase shift of Aston *et al.* (using their $I = 3/2$ parametrization to separate the $I = 1/2$). Note that the experiments are in fairly good agreement up to 1.6 GeV.

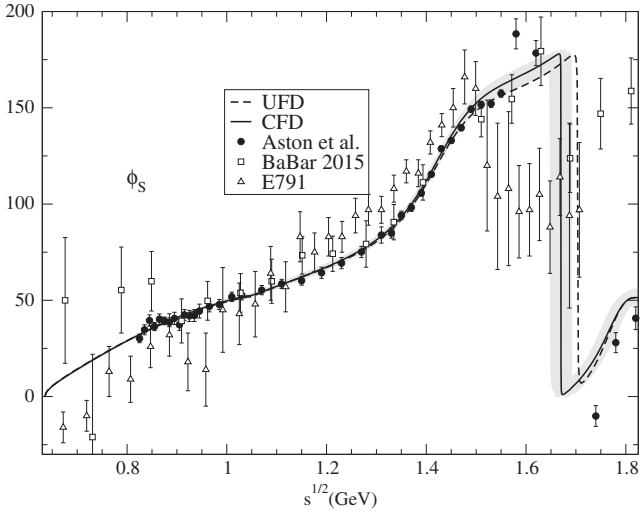

FIG. 28. Phase of the $I = 1/2$ πK S wave obtained from Dalitz plot analyses of $D \to K\pi\pi$ by the E791 Collaboration [27] and of $\eta_c \to K^0_S K^\pm\pi^\mp$ by the *BABAR* Collaboration [30]. We have plotted the systematic plus the statistical uncertainties for [27]. These phases are compared to the LASS scattering phase shift of Aston *et al.* (using their $I = 3/2$ parametrization to separate the $I = 1/2$). The data from *BABAR* are displaced by 34° while those from E791 are displaced by 86°. Note that the qualitative agreement with the scattering phase only reaches up to 1.5 GeV and is not particularly good at low energies.

UFD and CFD results that we also show in the figure. Moreover it is reassuring to see the good agreement between our parametrizations and the decay data in the near threshold region, where no scattering data exist.

In addition, from Dalitz plot analyses it has been possible to extract the $I = 1/2$ amplitude and phase of the πK S-wave component in $D^+ \to K^-\pi^+\pi^+$ by the E791 [27], FOCUS [28] and CLEO-c [29] collaborations, as well as in $\eta_c \to K\bar{K}\pi$ by the *BABAR* Collaboration [30]. As was already commented in Sec. III A, in this case Watson's theorem does not imply that the phase thus measured should be the same as that of scattering. The reason is the presence of another strongly interacting particle in the final state. This is particularly obvious by noting that the measured amplitudes and phases do not satisfy the elastic scattering unitarity condition. Nevertheless, it has also been noticed in these works that the measured phase shows a qualitative agreement with the scattering phase shift in the elastic region, once it is appropriately displaced by a constant. We show this qualitative agreement in Fig. 28, where once again the data from scattering has been extracted using the simple $I = 3/2$ model suggested by the experimental authors, which is a good enough description for a qualitative comparison. Once more, our UFD and CFD parametrizations describe well all these data.

Note, however, that the agreement disappears in the region above 1.6 GeV, which is where we have also found that the scattering data are largely incompatible with forward dispersion relations. It is then tempting to fit in this region the phase from decays instead of the phase from scattering, in the hope that the FDRs may be better satisfied. However, note that we can only try to fit the phase from decays, based on its similarity to the scattering phase, but not the modulus, since the energy dependence observed for the latter is very different from that of scattering. We have performed this exercise and we have verified that the FDRs are satisfied even more poorly.

B. Pole parameters of elastic resonances

Our partial waves are constructed as piecewise parametrizations which are matched continuously in the real axis. As a consequence, the resulting global amplitude does not provide a rigorous analytic continuation to the whole complex plane. Each one of the pieces may have an analytic continuation of its own, but at most it may only be a good approximation to the amplitude near the part of the real axis where that particular function is used, far from the other pieces of functions. Nevertheless, in the elastic region we have used a conformal mapping which has a well-defined analytic continuation to the complex s plane. As explained in Appendix A, the interesting feature of this mapping is that it places the inelastic singularities at the boundary of the unit circle. Therefore one can expect that it will provide a relatively good representation of the partial wave for complex values of s which are not close to that boundary.

With these caveats in mind, we can obtain a determination of the pole positions of resonances that appear in the elastic region by considering the analytic continuation of

just the elastic conformal parametrizations. Two such resonances exist, both with $I = 1/2$, namely, the controversial $K_0^*(800)$, or κ meson, and the $K^*(892)$ in the scalar and vector partial waves, respectively. Their associated poles are located in the second Riemann sheet of the partial wave, defined as

$$t^{II}(s) = \frac{t(s)}{1 + 2i\sigma(s)t(s)}, \tag{60}$$

where in the upper half complex s plane $\sigma(s)$ is defined as in Sec. II, whereas in the lower half plane $\sigma(s) = -\sigma(s^*)^*$. Therefore the second sheet pole position is a solution of

$$\cot\delta_l^I(s_{\rm pole}) = -i, \tag{61}$$

where the analytic continuation of the cotangent of the phase shift is obtained through the conformal expansion in Eqs. (13) and (28) for the $K_0^*(800)$ and the $K^*(892)$, respectively.

Customarily, since for narrow resonances isolated from other poles or thresholds the Breit-Wigner formula applies, one identifies the pole position of a resonance with its mass and width as follows: $s_R = (M_R - i\Gamma_R/2)^2$. Despite the $K_0^*(800)$ being a very wide resonance, we keep this convention and the resulting pole parameters for this resonance can be found in Table XV, both for the UFD and the CFD parametrization. This is also the convention used in the Review of Particle Physics (RPP) [16]. The values we obtain are very compatible with the averaged mass in the RPP, $M_{K_0^*(800)} = 682 \pm 29$ MeV. In contrast, the width is somewhat larger than the value quoted there, $\Gamma_{K_0^*(800)} = 547 \pm 24$ MeV. Actually, the most rigorous derivation is that in [13] by means of a Roy-Steiner analysis, where it is found that $M_{K_0^*(800)} = 658 \pm 13$ MeV and $\Gamma_{K_0^*(800)} = 557 \pm 24$ MeV. Nevertheless, there is a large spread of values listed in the RPP and several other determinations find a width very similar to ours. As a word of caution, when making a comparison to the RPP one should take into account that our numbers correspond to a pole position, whereas many values there correspond to peak parametrizations through Breit-Wigner formalisms or its variations, whose applicability is dubious due to the large width of this resonance.

The corresponding poles for the vector $K^*(892)$ are found in Table XVI. In this case the pole mass is very similar to the values provided in the RPP, typically obtained from Breit-Wigner parametrizations. In contrast our pole width is about 10 MeV higher that the ones listed in the RPP or those found in $\tau^- \to K_S\pi^-\nu_\tau$ decays by the Belle Collaboration [46] and on $D^+ \to K^-\pi^+e^+\nu_e$ decays by the *BABAR* Collaboration [25]. It has been pointed out in [47] that this shift may occur on the width when fitting the LASS Collaboration [24] phase shift due to the fact that those data have been given before unfolding the detector mass resolution, yielding 56 MeV instead of the 50.8 MeV quoted in the original LASS publication [24]. A similar caveat is pointed out by Estabrooks *et al.* [22], who estimate a ± 5 MeV systematic uncertainty in their width determination for this reason. In both cases it is pointed out that this effect barely affects the mass determination. Of course, all these experimental poles have been extracted by using Breit-Wigner parametrizations modified with Blatt-Weiskopf barrier factors, which are also model dependent.

For the future, we plan to impose consistency with partial wave dispersion relations starting from the parametrizations we have obtained in this work. Those dispersion relations will provide a rigorous analytic continuation to the complex plane and a rigorous and precise determination of the resonance poles. In addition, we plan to use a simpler but model-independent method, recently proposed to extract the poles from the knowledge of scattering data in the real axis by means of Padé approximants and Montessus's theorem [48]. These two approaches are beyond the scope of the present work, which is only focused on obtaining a data description consistent with FDRs.

TABLE XV. Pole parameters of the $K_0^*(800)$ from the analytic continuation of the elastic parametrization only.

Poles	Mass (MeV)	Width (MeV)	Coupling
UFD	673 ± 15	674 ± 15	5.01 ± 0.07
CFD	680 ± 15	668 ± 15	4.99 ± 0.08

TABLE XVI. Pole parameters of the $K^*(892)$ from the analytic continuation of the elastic parametrization only.

Poles	Mass (MeV)	Width (MeV)	Coupling
UFD	893 ± 1	56 ± 2	5.95 ± 0.07
CFD	892 ± 1	58 ± 2	6.02 ± 0.06

VII. CONCLUSIONS AND OUTLOOK

In this work we have presented a set of pion-kaon scattering parametrizations, which up to 1.6 GeV describe data and simultaneously satisfy a complete set of forward dispersion relations as well as three sum rules for threshold parameters. Our aim has been to make the parametrizations relatively simple and easy to implement in future theoretical or experimental applications.

As a first step we have obtained a set of UFD, in which partial waves with different angular momenta are fitted independently. Waves with different isospins are fitted together because that is how data was originally obtained. We have paid particular attention to the estimation of uncertainties, particularly to those of a systematic nature, which are not always taken into account in the literature. In addition, for the most controversial wave we have checked some statistical tests for the consistency of our uncertainty

estimates. Above 1.74 GeV, since no data on all partial waves exist, we have used Regge parametrizations that were obtained in previous works by applying factorization to other processes involving nucleons, pions and kaons.

However, it is shown that, even within uncertainties, this UFD set does not satisfy well forward dispersion relations and also shows some tension when used inside the threshold sum rules. In particular, above the $K\eta$ threshold the dispersive results lie typically 2 deviations or more away from the direct calculation when using the UFD parametrizations. Throughout the elastic region the agreement is somewhat better, but still only at the level of 1.5 deviations.

Thus, as a second step, we have imposed the forward dispersion relations and the sum rules as constraints on the fit parameters. Note that the parametrizations stay the same and we only change the values of the parameters. Our final result is a set of CFD that satisfies forward dispersion relations remarkably well up to 1.6 GeV while still describing the data. In particular, the deviations between the CFD and UFD results have been shown to be relatively small and within the uncertainties of the UFD fit. As a consequence, the CFD set still provides a good description of the data. Above 1.6 GeV, we have found that the fulfillment of the dispersive constraints would require large modifications of the fits that would spoil the data description. Thus our parametrizations describe the data and are simultaneously consistent with dispersive constraints only up to 1.6 GeV.

Using this CFD set we have provided a precise determination of three combinations of scattering lengths and slope parameters. In addition, given that the conformal map parametrization chosen for the elastic region has very good analytic properties in the complex plane we have obtained the pole parameters of the resonances that appear in that region, namely the vector $K^*(892)$ and the controversial scalar $K_0^*(800)$ or κ meson. The poles and residues come in reasonably good agreement with previous determinations, although, of course, the analytic continuation is dependent on our choice of conformal mapping, which is very reasonable, but not entirely model independent. Nevertheless, we plan to use our CFD results in the real axis as input to extract pole parameters using model-independent analytic approaches.

For the future we also plan to constrain further our parametrizations with a complete set of equations of the Roy-Steiner type. These are much more complicated relations written in terms of partial waves but they are very relevant to imposing crossing in addition to analyticity. Also, being formulated in terms of partial waves, they allow for a rigorous continuation to the complex plane, independent of the parametrizations used in the real axis. Thus they can provide a rigorous determination of the parameters of the resonances. Nevertheless, unlike the forward dispersion relations used here, they are limited in practice to roughly the elastic region. Moreover, equations of the Roy-Steiner type use as input the amplitudes in the whole energy region, for which it is important to use as input the CFD set obtained here.

We also expect that the simple parametrization of all the relevant partial waves can be of use in present and future experimental and theoretical analysis involving pions and kaons in the final state.

ACKNOWLEDGMENTS

J. R. P. and A. R. are supported by Spanish Projects No. FPA2011-27853-C02-02 and No. FPA2014-53375-C2-2 and Red de Excelencia de Física Hadrónica FIS2014-57026-REDT. We are very grateful to B. Moussallam for kindly providing us with his parametrizations as well as for his instructive comments and discussions.

APPENDIX A: CONFORMAL EXPANSION FOR ELASTIC WAVES

Let us recall that elastic partial waves can be written as

$$t_l(s) = \frac{1}{\sigma(s)} \frac{1}{\cot \delta_l(s) - i}, \tag{A1}$$

where $\sigma(s) = 2q/\sqrt{s}$ and q is the center of mass momentum. In the complex s plane, partial waves for the scattering of two particles with different masses m_1 and m_2 have a distinct analytic structure in the first Riemann sheet, shown in Fig. 29(a). First of all, there is a right-hand or physical cut extending from the opening of the elastic threshold to infinity. In addition, due to the thresholds in the crossed channels, there is a left-hand cut extending from $(m_1 - m_2)^2$ to $-\infty$, as well as a circular cut at $|s|^2 = (m_1^2 - m_2^2)^2$. Other singularities may appear on the real axis when bound states exist in the direct or crossed channels, but this is not the case in πK scattering. Let us emphasize that there are no poles in the first Riemann sheet. The cut singularities are reproduced in the second Riemann sheet, where poles can now occur anywhere in the complex plane. When poles are sufficiently close to the real axis, they give rise to resonant phenomena.

Now, in order to describe the amplitude in the complex s plane, it is customary to recast the partial wave as

$$t_l(s) = \frac{q^{2l}}{\Phi(s) - iq^{2l}\sigma(s)}, \tag{A2}$$

so that, as shown in Fig. 29(b), the effective range function $\Phi(s)$ does not have elastic cuts, but only the left-hand and circular ones, as well as the inelastic cuts. Depending on the dynamics, it might also have poles at the zeros of the amplitude, as we will discuss below. In our case, it has no singularity from the πK threshold to the next inelastic

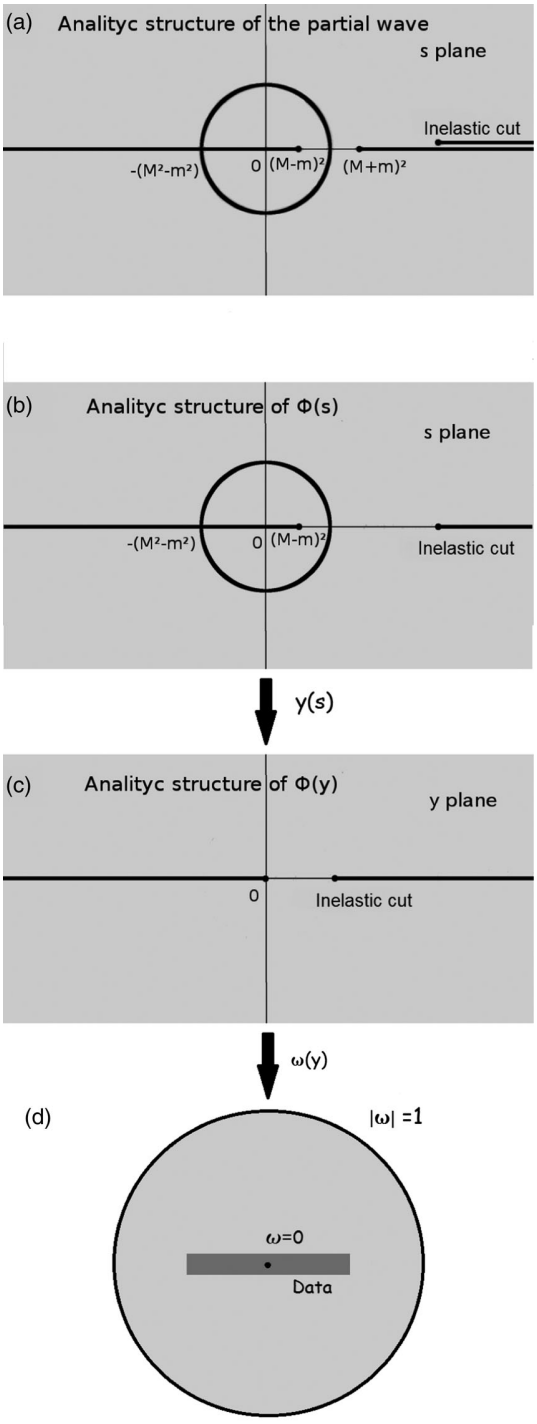

FIG. 29. Analytic structure in different variables of a πK scattering partial wave $t(s)$ and effective range function $\Phi(s)$: (a) $t(s)$ in the complex s plane. Note the elastic, inelastic, left-hand and circular cuts. (b) $\Phi(s)$ in the s plane has the same structure as $t(s)$ except for the absence of the elastic cut. (c) In the $y(s)$ plane the circular cut disappears. (d) The conformal variable $\omega(y)$ maps the whole analyticity domain of $\Phi(y)$ inside the unit circle, whereas the cut singularities are confined to $|\omega| = 1$. Note that ω is defined so that the data region is roughly centered around $\omega = 0$ and not too close to the border.

threshold s_0. When the expansion of $\Phi(s)$ is made in terms of the powers of q, the coefficient of the first term of the expansion is known as the scattering length, the second is the slope, etc. But the radius of convergence of this series, centered at $s = (m_K + m_\pi)^2$, is small, since the circular cut singularity lies rather close. The best way to use the largest possible domain of analyticity is by changing variables by means of a conformal transformation. In this case, however, it is convenient to perform first another change of variable which maps the circular cut into the left real axis:

$$y(s) = \left(\frac{s - \Delta_{K\pi}}{s + \Delta_{K\pi}}\right)^2, \tag{A3}$$

where $\Delta_{K\pi} = m_K^2 - m_\pi^2$. The resulting $\Phi(y(s))$ function now only has a right-hand "inelastic" cut and a left-hand cut, as shown in Fig. 29(c), and then we can use the conformal variable

$$w(y) = \frac{\sqrt{y} - \alpha\sqrt{y_0 - y}}{\sqrt{y} + \alpha\sqrt{y_0 - y}}, \tag{A4}$$

to map the cut y plane into the unit circle in the ω plane.

With the exception of the minute $P^{3/2}$ and $D^{3/2}$ waves, in this work we have chosen α for each wave so that the center of the conformal expansion $\omega = 0$ corresponds to the intermediate point between the πK threshold and the energy of the last data point that is fitted with the conformal formula. The reason for this choice is to ensure that the region where data is to be fitted lies well inside the ω circle, roughly centered around $\omega = 0$, as shown in Fig. 29(d). Actually, for the $S^{1/2}$ and $P^{1/2}$ waves, the data fitted with the elastic formalism lie at $|\omega| < 0.45$. However for the $S^{3/2}$ wave the data lie at $|\omega| < 0.6$. The $P^{3/2}$ and $D^{3/2}$ waves are an exception, because their data starts at 1 GeV, far from the πK threshold. Thus we have chosen their α parameters so that the center of the conformal expansion corresponds to the intermediate point where data exists. With this choice, the data fitted with this conformal expansion lies at $|\omega| < 0.6$.

Since with these changes of variable the singularities now lie at $|\omega| = 1$, the function has an analytic expansion $\Phi(s) = \sum_n B_n w(s)^n$ convergent in the whole $|\omega| < 1$ circle. In this way, and in terms of s, the domain of analyticity of the conformal mapping extends to the whole complex plane outside the circular cut, with a left-hand cut and a right-hand cut above the first inelastic threshold. Thus on the elastic region of the real axis

$$\cot\delta_l(s) = \frac{\sqrt{s}}{2q^{2l+1}}\Phi(s) = \frac{\sqrt{s}}{2q^{2l+1}}\sum_n B_n w(s)^n, \tag{A5}$$

which are the expressions we have used for our elastic fits.

Finally, let us recall that due to chiral symmetry, scalar partial waves have a so-called Adler zero below threshold,

which is easily implemented in the partial waves by writing a pole factor in front of the $\Phi(s)$ expansion, as follows:

$$\Phi(s) = \frac{1}{s - s_{\rm Adler}} \sum_n B_n w(s)^n. \tag{A6}$$

In addition, when there is a narrow well-established resonance and the phase crosses $\pi/2$ at m_r it is also convenient to extract a factor out of the conformal expansion as

$$\Phi(s) = (s - m_r^2) \sum_n B_n w(s)^n, \tag{A7}$$

to accelerate the convergence of the fit.

APPENDIX B: STATISTICAL TEST ON THE S WAVE

Since the $S^{1/2}$ wave is the most controversial one, we have used some statistical tests to check the consistency of our fits and the data obtained from [22] and [24] for the $t_S \equiv t_0^{1/2} + t_0^{3/2}/2$ amplitude. As has been explained in the main text, the problem with the data is the existence of large systematic uncertainties that we necessarily had to estimate. Once we had these systematic uncertainties added to the statistical ones, we have performed the fits and obtained, by minimizing the χ^2, the fit parameters and their uncertainties. The χ^2 is based on a Gaussianity assumption and one would like to test to see that the resulting fit and the data are still consistent with it. For this reason we will check the consistency of our fits by means of the central moment statistical test, which in rather similar conditions was suggested for $\pi\pi$ scattering in [32].

Let N be the number of data points, measured at energies $\sqrt{s_i}$, $i = 1 \ldots N$. We then introduce a set of N residuals $R_i = (P_i - f(\alpha, s_i))/(\Delta P_i)$. Here P_i is the experimental value of the ith measurement, ΔP_i its uncertainty (experimental and systematic) associated with that value, and $f(\alpha, s_i)$ is the theoretical model evaluated at s_i. The set of UFD parameters is called α.

By assumption, this set of residuals must obey a standardized normal distribution. For this purpose we study the central moments of the residual distribution

$$\mu_{UFD,n} = \frac{1}{N} \sum_{i=1}^{N} (R_i - R_{\rm mean})^n, \tag{B1}$$

where $R_{\rm mean} = \sum R_i/N$.

We would like to compare these $\mu_{UFD,n}$ with the expected value of a set of N data standardized Gaussian points. Thus, we generate M samples of distributions of N data points R_{ik}, $k = 1, \ldots M$ that follow a normal Gaussian distribution, and calculate the central moments μ_{nk} of each sample. We then define the average central moment $\langle \mu_n \rangle = \sum_k^M \mu_{nk}/M$. Similarly, we define the uncertainty in this distribution of residuals as the usual standard deviation: $\Delta\mu_n \equiv \sqrt{\langle \mu_n^2 \rangle - \langle \mu_n \rangle^2}$.

In order to compare the moments of our UFD result with those of the generated distributions, we have to recall that we have parametrized the S wave into two regions with different functional forms, and we have fitted two sets of observables, $|\hat{t}_S|$ and ϕ_S. Therefore we have four different tests, which are presented in Tables XVII, XVIII, XIX and XX.

Actually, our procedure to estimate uncertainties has made use of these tests. At first we introduce as systematic uncertainties half of the distance between those points measured at the same energy which are incompatible. Then, we modify the systematic uncertainties of the few data points that cause deviations from the Gaussian behavior of the tests. With these modified systematic uncertainties the fit is performed again, the tests are checked once more and the systematic uncertainties of points that cause deviations from the test are changed again. The procedure is iterated until the Gaussianity tests are well satisfied.

TABLE XVII. Normality condition for Φ_S in the elastic region.

n	1	2	3	4	5	6
$\mu_{\rm UFD},n$	0	0.8	−0.3	1.6	−1.1	4.2
$\mu_{\rm random},n$	0 ± 0	1.0 ± 0.2	0 ± 0.4	2.8 ± 1.6	0 ± 4	14 ± 17

TABLE XVIII. Normality condition for $|\hat{t}_S|$ in the elastic region.

n	1	2	3	4	5	6
$\mu_{\rm UFD},n$	0	1.1	0.1	2.4	0.8	6.7
$\mu_{\rm random},n$	0 ± 0	1.0 ± 0.2	0 ± 0.4	2.8 ± 1.6	0 ± 4	14 ± 17

TABLE XIX. Normality condition for the Φ_S in the inelastic region.

n	1	2	3	4	5	6
$\mu_{\rm UFD},n$	0	1	0.2	3.3	−2.1	18.1
$\mu_{\rm random},n$	0 ± 0	1.0 ± 0.2	0 ± 0.4	2.8 ± 1.6	0 ± 4	14 ± 16

TABLE XX. Normality condition for the $|\hat{t}_S|$ in the inelastic region.

n	1	2	3	4	5	6
$\mu_{\rm UFD},n$	0	0.9	0.09	1.6	0.6	3.6
$\mu_{\rm random},n$	0 ± 0	1.0 ± 0.2	0 ± 0.4	2.8 ± 1.6	0 ± 4	14 ± 16

[1] J. Gasser and H. Leutwyler, Chiral perturbation theory: Expansions in the mass of the strange quark, Nucl. Phys. **B250**, 465 (1985).

[2] V. Bernard, N. Kaiser, and U. G. Meissner, πK scattering in chiral perturbation theory to one loop, Nucl. Phys. **B357**, 129 (1991).

[3] J. Bijnens, P. Dhonte, and P. Talavera, πK scattering in three flavor ChPT, J. High Energy Phys. 05 (2004) 036.

[4] B. Ananthanarayan, P. Büttiker, and B. Moussallam, πK sum rules and the SU(3) chiral expansion, Eur. Phys. J. C **22**, 133 (2001); B. Ananthanarayan and P. Büttiker, Comparison of pion kaon scattering in SU(3) chiral perturbation theory and dispersion relations, Eur. Phys. J. C **19**, 517 (2001).

[5] A. Dobado and J. R. Pelaez, A global fit of $\pi\pi$ and πK elastic scattering in ChPT with dispersion relations, Phys. Rev. D **47**, 4883 (1993); A. G. Nicola and J. R. Pelaez, Meson-meson scattering within one-loop chiral perturbation theory and its unitarization, Phys. Rev. D **65**, 054009 (2002).

[6] J. R. Pelaez, Light scalars as tetraquarks or two-meson states from large N_c and unitarized chiral perturbation theory, Mod. Phys. Lett. A **19**, 2879 (2004).

[7] J. A. Oller and E. Oset, Chiral symmetry amplitudes in the S-wave isoscalar and isovector channels and the σ, $f_0(980)$, $a_0(980)$ scalar mesons, Nucl. Phys. **A620**, 438 (1997); **A652**, 407(E) (1999); N/D description of two meson amplitudes and chiral symmetry, Phys. Rev. D **60**, 074023 (1999); J. A. Oller, E. Oset, and J. R. Pelaez, Nonperturbative Approach to Effective Chiral Lagrangians and Meson Interactions, Phys. Rev. Lett. **80**, 3452 (1998); Meson-meson interaction in a nonperturbative chiral approach, Phys. Rev. D **59**, 074001 (1999); **60**, 099906(E) (1999); **75**, 099903(E) (2007).

[8] S. R. Beane, P. F. Bedaque, T. C. Luu, K. Orginos, E. Pallante, A. Parreño, and M. J. Savage, πK scattering in full QCD with domain-wall valence quarks, Phys. Rev. D **74**, 114503 (2006); J. Nagata, S. Muroya, and A. Nakamura, Lattice study of $K\pi$ scattering in $I = 3/2$ and $1/2$, Phys. Rev. C **80**, 045203 (2009); **84**, 019904(E) (2011); Z. Fu, Lattice study on πK scattering with moving wall source, Phys. Rev. D **85**, 074501 (2012); K. Sasaki, N. Ishizuka, M. Oka, and T. Yamazaki (PACS-CS Collaboration), Scattering lengths for two pseudoscalar meson systems, Phys. Rev. D **89**, 054502 (2014).

[9] C. B. Lang, L. Leskovec, D. Mohler, and S. Prelovsek, $K\pi$ scattering for isospin $1/2$ and $3/2$ in lattice QCD, Phys. Rev. D **86**, 054508 (2012); S. Prelovsek, L. Leskovec, C. B. Lang, and D. Mohler, $K\pi$ scattering and the K^* decay width from lattice QCD, Phys. Rev. D **88**, 054508 (2013); Z. Fu and K. Fu, Lattice QCD study on $K^*(892)$ meson decay width, Phys. Rev. D **86**, 094507 (2012); J. J. Dudek, R. G. Edwards, C. E. Thomas, and D. J. Wilson (Hadron Spectrum Collaboration), Resonances in Coupled $\pi K - \eta K$ Scattering from Quantum Chromodynamics, Phys. Rev. Lett. **113**, 182001 (2014); D. J. Wilson, J. J. Dudek, R. G. Edwards, and C. E. Thomas, Resonances in coupled $\pi K, \eta K$ scattering from lattice QCD, Phys. Rev. D **91**, 054008 (2015).

[10] M. Doring and U. G. Meissner, Finite volume effects in pion-kaon scattering and reconstruction of the $\kappa(800)$ resonance, J. High Energy Phys. 01 (2012) 009; M. Doring, U. G. Meissner, E. Oset, and A. Rusetsky, Scalar mesons moving in a finite volume and the role of partial wave mixing, Eur. Phys. J. A **48**, 114 (2012).

[11] R. L. Jaffe, Multiquark hadrons. I. Phenomenology of Q^2Q^{-2} mesons, Phys. Rev. D **15**, 267 (1977); M. D. Scadron, Spontaneous breakdown and the scalar nonet, Phys. Rev. D **26**, 239 (1982); E. van Beveren, T. A. Rijken, K. Metzger, C. Dullemond, G. Rupp, and J. E. Ribeiro, A low lying scalar meson nonet in a unitarized meson model, Z. Phys. C **30**, 615 (1986); R. Kaminski, L. Lesniak, and B. Loiseau, Three channel model of meson meson scattering and scalar meson spectroscopy, Phys. Lett. B **413**, 130 (1997); D. Black, A. H. Fariborz, F. Sannino, and J. Schechter, Putative light scalar nonet, Phys. Rev. D **59**, 074026 (1999); F. E. Close and N. A. Tornqvist, Scalar mesons above and below 1 GeV, J. Phys. G **28**, R249 (2002); A. H. Fariborz, E. Pourjafarabadi, S. Zarepour, and S. M. Zebarjad, Chiral nonet mixing in πK scattering, Phys. Rev. D **92**, 113002 (2015); T. Wolkanowski, M. Soltysiak, and F. Giacosa, $K_0^*(800)$ as a companion pole of $K_0^*(1430)$, arXiv:1512.01071.

[12] S. N. Cherry and M. R. Pennington, There is no $\kappa(900)$, Nucl. Phys. **A688**, 823 (2001).

[13] S. Descotes-Genon and B. Moussallam, The $K_0^*(800)$ scalar resonance from Roy-Steiner representations of πK scattering, Eur. Phys. J. C **48**, 553 (2006).

[14] P. Büttiker, S. Descotes-Genon, and B. Moussallam, A new analysis of πK scattering from Roy and Steiner type equations, Eur. Phys. J. C **33**, 409 (2004).

[15] F. Steiner, Partial wave crossing relations for meson-baryon scattering, Fortschr. Phys. **19**, 115 (1971).

[16] K. A. Olive (Particle Data Group), Review of particle physics, Chin. Phys. C **38**, 090001 (2014) and 2015 update.

[17] J. R. Pelaez and F. J. Yndurain, Pion-pion scattering amplitude, Phys. Rev. D **71**, 074016 (2005).

[18] Y. Cho *et al.*, Study of $K^-\pi^-$ scattering using the reaction $K^-d \to K^-\pi^- pp_s$, Phys. Lett. B **32**, 409 (1970).

[19] A. M. Bakker *et al.*, A determination of the $I = 3/2$ $K\pi$ elastic-scattering cross section from the reaction $K^-n \to pK^-\pi^-$ at 3 GeV/c, Nucl. Phys. **B24**, 211 (1970).

[20] B. Jongejans, R. A. van Meurs, A. G. Tenner, H. Voorthuis, P. M. Heinen, W. J. Metzger, H. G. J. M. Tiecke, and R. T. Van de Walle, Study of the $I = 3/2$ $K^-\pi^-$ elastic scattering from the reaction $K^-p \to K^-\pi^- p\pi^+$ at 4.25 GeV/c incident K^- momentum, Nucl. Phys. **B67**, 381 (1973).

[21] D. Linglin *et al.*, $K^-\pi^-$ elastic scattering cross-section measured in 14.3 GeV/c K^-p interactions, Nucl. Phys. **B57**, 64 (1973).

[22] P. Estabrooks, R. K. Carnegie, A. D. Martin, W. M. Dunwoodie, T. A. Lasinski, and D. W. G. S. Leith, Study of $K\pi$ scattering using the reactions $K^{+-}p \to K^{+-}\pi^+ n$ and $K^{+-}p \to K^{+-}\pi^-\Delta^{++}$ at 13 GeV/c, Nucl. Phys. **B133**, 490 (1978).

[23] R. Mercer *et al.*, $K\pi$ scattering phase shifts determined from the reactions $K^+p \to K^+\pi^-\delta^{++}$ and $K^0\pi^0\Delta^{++}$, Nucl. Phys. **B32**, 381 (1971).

[24] D. Aston *et al.*, A study of $K^-\pi^+$ scattering in the reaction $K^-p \to K^-\pi^+ n$ at 11 GeV/c, Nucl. Phys. **B296**, 493 (1988).

[25] P. del Amo Sanchez *et al.* (*BABAR* Collaboration), Analysis of the $D^+ \to K^-\pi^+e^+\nu_e$ decay channel, Phys. Rev. D **83**, 072001 (2011).

[26] M. Ablikim *et al.* (BESIII Collaboration), Study of $D^+ \to K^-\pi^+e^+\nu_e$, arXiv:1512.08627.
[27] E. M. Aitala *et al.* (E791 Collaboration), Model independent measurement of S-wave $K^-\pi^+$ systems using $D^+ \to K\pi\pi$ decays from Fermilab E791, Phys. Rev. D **73**, 032004 (2006); **74**, 059901(E) (2006).
[28] J. M. Link *et al.* (FOCUS Collaboration), Dalitz plot analysis of the $D^+ \to K^-\pi^+\pi^+$ decay in the FOCUS experiment, Phys. Lett. B **653**, 1 (2007); The $K^-\pi^+$ S-wave from the $D^+ \to K^-\pi^+\pi^+$ decay, Phys. Lett. B **681**, 14 (2009).
[29] G. Bonvicini *et al.* (CLEO Collaboration), Dalitz plot analysis of the $D^+ \to K^-\pi^+\pi^+$ decay, Phys. Rev. D **78**, 052001 (2008).
[30] J. P. Lees *et al.* (*BABAR* Collaboration), Measurement of the $I = 1/2$ $K\pi\mathcal{S}$-wave amplitude from Dalitz plot analyses of $\eta_c \to K\bar{K}\pi$ in two-photon interactions, Phys. Rev. D **93**, 012005 (2016).
[31] We thank B. Moussallam for kindly providing us with his parametrizations.
[32] R. N. Pérez, E. R. Arriola, and J. R. de Elvira, Self-consistent statistical error analysis of $\pi\pi$ scattering, Phys. Rev. D **91**, 074014 (2015).
[33] D. V. Bugg, Update on the kappa, Phys. Rev. D **81**, 014002 (2010).
[34] Z. Y. Zhou and H. Q. Zheng, An improved study of the kappa resonance and the non-exotic s wave πK scatterings up to $\sqrt{s} = 2.1$ GeV of LASS data, Nucl. Phys. **A775**, 212 (2006).
[35] S. Ishida, M. Ishida, T. Ishida, K. Takamatsu, and T. Tsuru, Analysis of $K\pi$ scattering phase shift and existence of $\kappa(900)$ particle, Prog. Theor. Phys. **98**, 621 (1997).
[36] M. Jamin, J. A. Oller, and A. Pich, S wave $K\pi$ scattering in chiral perturbation theory with resonances, Nucl. Phys. **B587**, 331 (2000).
[37] A. Dobado and J. R. Pelaez, Inverse amplitude method in chiral perturbation theory, Phys. Rev. D **56**, 3057 (1997).
[38] B. Adeva *et al.* (DIRAC Collaboration), First πK atom lifetime and πK scattering length measurements, Phys. Lett. B **735**, 288 (2014).
[39] P. Guo, R. Mitchell, M. Shepherd, and A. P. Szczepaniak, Amplitudes for the analysis of the decay $J/\psi \to K^+K^-\pi^0$, Phys. Rev. D **85**, 056003 (2012).
[40] R. Garcia-Martin, R. Kaminski, J. R. Pelaez, J. Ruiz de Elvira, and F. J. Yndurain, Pion-pion scattering amplitude. IV. Improved analysis with once subtracted Roy-like equations up to 1100 MeV, Phys. Rev. D **83**, 074004 (2011).
[41] J. P. Ader, C. Meyers, and B. Bonnier, General features of low energy $K\pi$ scattering from physical region method, Phys. Lett. B **46B**, 403 (1973).
[42] F. P. Palou, J. L. Sanchez Gomez, and F. J. Yndurain, Low-energy parameters for scattering of pions and kaons, Z. Phys. A **274**, 161 (1975).
[43] F. P. Palou and F. J. Yndurain, Low-energy $\pi\pi$ scattering parameters, Nuovo Cimento Soc. Ital. Fis. **19A**, 245 (1974).
[44] R. Kaminski, J. R. Pelaez, and F. J. Yndurain, Pion-pion scattering amplitude. II. Improved analysis above $\bar{K}K$ threshold, Phys. Rev. D **74**, 014001 (2006); **74**, 079903(E) (2006).
[45] R. Kaminski, J. R. Pelaez, and F. J. Yndurain, Pion-pion scattering amplitude. III. Improving the analysis with forward dispersion relations and Roy equations, Phys. Rev. D **77**, 054015 (2008).
[46] D. Epifanov *et al.* (Belle Collaboration), Study of $\tau^- \to K_S\pi^-\nu_\tau$ decay at Belle, Phys. Lett. B **654**, 65 (2007).
[47] V. Bernard, First determination of $f_+(0)|V_{us}|$ from a combined analysis of $\tau \to K\pi\nu_\tau$ decay and πK scattering with constraints from $K_{\ell 3}$ decays, J. High Energy Phys. 06 (2014) 082.
[48] P. Masjuan and J. J. Sanz-Cillero, Padé approximants and resonance poles, Eur. Phys. J. C **73**, 2594 (2013); P. Masjuan, J. Ruiz de Elvira, and J. J. Sanz-Cillero, Precise determination of resonance pole parameters through Padé approximants, Phys. Rev. D **90**, 097901 (2014); I. Caprini, P. Masjuan, J. Ruiz de Elvira, and J. J. Sanz-Cillero, On the uncertainty estimates of the σ-pole determination by Padé approximants, Phys. Rev. D **93**, 076004 (2016); I. Caprini, Finding the σ pole by analytic extrapolation of $\pi\pi$ scattering data, Phys. Rev. D **77**, 114019 (2008).

2.2.4 Publication: $\pi\pi \to K\bar{K}$ *scattering up to 1.47 GeV with hyperbolic dispersion relations*

Eur. Phys. J. C (2018) 78:897
https://doi.org/10.1140/epjc/s10052-018-6296-9

THE EUROPEAN PHYSICAL JOURNAL C

Regular Article - Theoretical Physics

$\pi\pi \to K\bar{K}$ scattering up to 1.47 GeV with hyperbolic dispersion relations

J. R. Pelaez[a], **A. Rodas**

Departamento de Física Teórica, Universidad Complutense de Madrid, 28040 Madrid, Spain

Received: 23 July 2018 / Accepted: 28 September 2018 / Published online: 5 November 2018

Abstract In this work we provide a dispersive analysis of $\pi\pi \to K\bar{K}$ scattering. For this purpose we present a set of partial-wave hyperbolic dispersion relations using a family of hyperbolas that maximizes the applicability range of the hyperbolic dispersive representation, which we have extended up to 1.47 GeV. We then use these equations first to test simple fits to different and often conflicting data sets, also showing that some of these data and some popular parameterizations of these waves fail to satisfy the dispersive analysis. Our main result is obtained after imposing these new relations as constraints on the data fits. We thus provide simple and precise parameterizations for the S, P and D waves that describe the experimental data from $K\bar{K}$ threshold up to 2 GeV, while being consistent with crossing symmetric partial-wave dispersion relations up to their maximum applicability range of 1.47 GeV. For the S-wave we have found that two solutions describing two conflicting data sets are possible. The dispersion relations also provide a representation for S, P and D waves in the pseudo-physical region.

1 Introduction

The scattering of pions and kaons is interesting for several reasons: First, by itself, in order to test and understand the dynamics of these particles, which are the pseudo-Goldstone Bosons of the QCD spontaneous chiral symmetry breaking. Second, because these scattering processes are one of the main sources of information on the existence and parameters of several meson resonances. In particular, this is the case of light scalar mesons, whose very existence, nature and classification are still a matter of debate (see the note on light scalars in the review of particle properties (RPP) [1]). These resonances are very relevant for the identification of glueballs, tetraquaks or molecular states that lie beyond the ordinary meson states of the naive quark model. Finally, being the lightest mesons, final state interactions (FSI) of pions and kaons play an essential role in the description of many hadronic processes. The unprecedented statistical samples obtained in the last years on different hadronic experiments and the even more ambitious plans for future facilities have provoked a renovated interest for precise and rigorous analyses of existing meson-meson scattering data, superseding simple model descriptions.

Unfortunately, most of the data on meson-meson scattering [2–10] are extracted indirectly from meson-nucleon to meson-meson-nucleon reactions. This extraction is complicated, relying on some model assumptions, and for this reason it is affected with large systematic uncertainties, which can be estimated from the differences between data sets from different experiments (and for $\pi\pi$ scattering even within data sets from the same experiment [2,3]). Moreover, the description of these data is frequently done in terms of meson-meson models which can lead to artifacts and unreliable determinations of resonances and their parameters. It is for these reasons that dispersive techniques are required.

Dispersion relations are the mathematical expression of causality and crossing. They relate the amplitude at a given energy to integrals of the amplitude and can be used as consistency tests of the experimental data or as constraints on the fits. We will make both uses here. For dispersive integrals to be evaluated just over the physical region, crossing must be used and two main kinds of dispersion relations appear then: Forward Dispersion Relations (FDRs) and those for partial waves generically know as Roy or Roy–Steiner equations [11–13], depending on whether the scattering occurs among particles with equal or different masses. FDRs are rather simple and easily extended to arbitrary energies. They have been recently applied to constrain $\pi\pi$ [14–17] and $K\pi$ [18] scattering amplitudes that will be used as input in some stages of the present work. Roy-like equations are a complicated system of coupled equations, limited in practice to energies of $\mathcal{O}(1\,\text{GeV})$ for meson-meson scattering. However, they pro-

[a] e-mail: jrpelaez@fis.ucm.es

vide a rigorous continuation to the complex plane that allows for a precise and model independent determination of resonances. Actually, it was only in 2012 that the RPP [1] considered settled the issue of the existence and parameters of the much debated scalar $f_0(500)$ resonance [19], traditionally known as σ-meson, and to a very large extent this was due to the results of dispersive analyses of $\pi\pi$ scattering amplitudes with versions of Roy equations [20–22]. Similarly, the scalar $K_0^*(800)$ or κ-meson has also been obtained from πK scattering using unitarization and dispersive methods [23–25], the most reliable value [26] being the Roy–Steiner method based on hyperbolic dispersion relations [27], but according to the RPP this resonance still "needs confirmation" [1]. Roy–Steiner equations have also been applied recently to πN scattering [28] and for $\gamma\gamma \to \pi\pi$ [29]. For meson-resonances beyond ∼1 GeV, Roy-like equations are not used in practice, but other analytic tools have been recently applied [30–32] to extract resonance poles from the description of amplitudes in the physical region constrained with dispersion relations, thus minimizing the model-dependence.

The purpose of this paper is to obtain a set of simple $\pi\pi \to K\bar{K}$ scattering parameterizations satisfying Roy–Steiner dispersion relations that can be easily used later on both by theoreticians and experimentalists, as has already been the case of previous works for $\pi\pi$ and πK scattering. The motivations to study $\pi\pi \to K\bar{K}$ are the ones explained above for meson-meson scattering in general: (i) a rigorous $\pi\pi \to K\bar{K}$ description is a necessary input for further studies of resonances (like scalars in the 1–1.6 GeV, range), in particular in order to compare their $\pi\pi$ and $K\bar{K}$ couplings, (ii) it is also an essential ingredient in the Roy–Steiner study of $K\pi$ scattering and the determination of the controversial $K_0^*(800)$-meson (whose determination is one of the goals of a recent proposal at JLab [33]) (iii) the $\pi\pi \to K\bar{K}$ amplitude also influences, via unitarity, the $\pi\pi \to \pi\pi$ and $\pi\pi \to N\bar{N}$ amplitudes, and consequently those of KN and $\bar{K}N$ scattering. Finally $\pi\pi \to K\bar{K}$ is a very relevant ingredient in the FSI of numerous hadron decays. For instance, the role of $\pi\pi \to K\bar{K}$ re-scattering has gained a renewed interest due to the recent observation of a large CP violation in recent studies at LHCb [34–36], although the amplitude used for such studies has been approximated with simple models and the amplitudes obtained here could be used to avoid such assumptions in further studies which are under way. Finally, lattice calculations of the coupled channel $\pi\pi$, $K\bar{K}$, $\eta\eta$ scattering have appeared very recently [37]. Although these calculations are performed still at relatively high pion masses, the physical point where one can compare with our actual $\pi\pi \to K\bar{K}$ parameterizations could be accessible soon.

Dispersive studies of $\pi\pi \to K\bar{K}$ scattering and its relation to $\pi K \to \pi K$ scattering were first performed in the seventies [38–41]. It was soon clear that the formalism of fixed-t dispersion relations combined with hyperbolic dispersion relations (HDR) for partial waves [12,13] was best suited to study the physical regions of both channels simultaneously [39,41]. However, $\pi\pi \to K\bar{K}$ data was scarce and these analyses only allowed for crude checks of low-energy scalar partial waves, frequently focusing on threshold parameters and the non-physical region between the two-pion and the two-kaon thresholds (or at most up to 1100 MeV). For a review of the theoretical and experimental situation until 1978 we refer to [42].

The main experimental results on $\pi\pi \to K\bar{K}$ partial waves, that will be thoroughly analyzed in this work, were obtained in the early eighties [7,8], indirectly from $\pi N \to K\bar{K}N'$ reactions. They extend from energies very close to the $K\bar{K}$ threshold up to 1.6 GeV. Several models exist in the literature describing these $\pi\pi \to K\bar{K}$ data [43–48], in particular with unitarized chiral Lagrangians [23,24,49,51,53]. These works are of relevance for studies of f_0 resonances and glueballs in that range.

A renewed interest on dispersive analysis of $\pi\pi \to K\bar{K}$ at the turn of the century was triggered by the need for precise determinations of threshold parameters and chiral perturbation theory low energy constants. Actually, sum rules for πK were obtained from a Roy–Steiner type of equations from HDR [52,53] in which the $\pi\pi \to K\bar{K}$ amplitude in the unphysical region was obtained as a solution of a dispersive Mushkelishvili–Omnés problem. The $\pi\pi \to K\bar{K}$ partial-wave data of [7,8] was used as input. However, no dispersive analysis of these data has been carried out beyond the $K\bar{K}$ threshold, mostly due to the relatively low applicability limit of the HDR along the $su = b$ hyperbolas used in those works. It was nevertheless shown that an extrapolation of the HDR solutions beyond their applicability region was fairly close to the data. Finally, in [27] a Roy–Steiner type of analysis was performed to obtain solutions for the πK elastic amplitudes, using once again as input the $\pi\pi \to K\bar{K}$ amplitudes in the physical region. This study was the basis for confirming the existence of the $K_0^*(800)$ meson through a dispersive analysis [26].

The aim of this work is then to provide a simple set of $\pi\pi \to K\bar{K}$ parameterizations that describe the data up to 2 GeV while also satisfying dispersive constraints in the whole region from $\pi\pi$ threshold up to 1.47 GeV. To this end, we will derive a new set of hyperbolic dispersion relations, along $(s-a)(u-a) = b$ hyperbolas, choosing the a parameter to maximize the applicability range which allows us to use them up to 1.47 GeV. This will also allow us to test different and often conflicting data sets and popular parameterizations.

The plan of the work is as follows: in Sect. 2 we will introduce the notation, in Sect. 3 we will present simple unconstrained fits to the different $\pi\pi \to K\bar{K}$ data as well as a Regge formalism for the high energy part, taking particular care on the determination of uncertainties. In Sect. 4 we will derive our new set of HDR, i.e. Roy–Steiner like equa-

tions for partial waves, and formulate the Mushkelishvili–Omnés problem used for both the unphysical region below $K\bar{K}$ threshold and the physical region up to 1.47 GeV. In Sect. 5 we will first use these equations as checks for the unconstrained parameterizations. Finally, in Sect. 6 we will impose the new relations on the data fits. This will lead to the desired constrained fits to data satisfying the analyticity requirements, which are the main results of this work. In Sect. 7 we will summarize our findings and conclude.

2 Kinematics and notation

Throughout this work we will be working in the isospin limit of equal mass for all pions, $m_\pi = 139.57\,\text{MeV}$, and equal mass for all kaons, $m_K = 496\,\text{MeV}$.

Crossing symmetry relates the $\pi\pi \to K\bar{K}$ amplitudes to those of πK scattering. It is then customary to use the standard Mandelstam variables s, t, u for πK scattering, satisfying $s+t+u = 2(m_\pi^2 + m_K^2)$ and write

$$\begin{aligned} G^0(t,s,u) &= \sqrt{6}F^+(s,t,u), \\ G^1(t,s,u) &= 2F^-(s,t,u), \end{aligned} \tag{1}$$

where G^I are the fixed isospin $I = 0, 1$ amplitudes of $\pi\pi \to K\bar{K}$ whereas the $F^\pm$ are the $s \leftrightarrow u$ symmetric and antisymmetric πK amplitudes, respectively. The latter are defined as

$$\begin{aligned} F^+(s,t,u) &= \frac{1}{3}F^{1/2}(s,t,u) + \frac{2}{3}F^{3/2}(s,t,u), \\ F^-(s,t,u) &= \frac{1}{3}F^{1/2}(s,t,u) - \frac{1}{3}F^{3/2}(s,t,u), \end{aligned} \tag{2}$$

where now F^I are the fixed isospin $I = 1/2, 3/2$ amplitudes of πK scattering. These satisfy:

$$F^{1/2}(s,t,u) = \frac{3}{2}F^{3/2}(u,t,s) - \frac{1}{2}F^{3/2}(s,t,u), \tag{3}$$

from where the $s \leftrightarrow u$ symmetry properties of $F^\pm$ follow.

In this work we will also use the partial-wave decompositions of the πK and $\pi\pi \to K\bar{K}$ scattering amplitudes, defined as follows:

$$\begin{aligned} F^I(s,t,u) &= 16\pi \sum_\ell (2\ell+1) P_\ell(z_s) f_\ell^I(s), \\ G^I(t,s,u) &= 16\pi\sqrt{2} \sum_\ell (2\ell+1)(q_\pi q_K)^\ell P_\ell(z_t) g_\ell^I(t), \end{aligned} \tag{4}$$

where $q_\pi = q_{\pi\pi}(t)$, $q_K = q_{KK}(t)$ are the CM momenta of the respective $\pi\pi$ and $K\bar{K}$ states, namely

$$q_{12}(s) = \frac{1}{2\sqrt{s}}\sqrt{(s-(m_1+m_2)^2)(s-(m_1-m_2)^2)}. \tag{5}$$

Note the $(q_\pi q_K)^\ell$ factors in the partial waves of the t-channels, which are customarily introduced to ensure good analytic properties for $g_\ell(t)$ (see [54] in the $\pi\pi \to N\bar{N}$ context). The scattering angles in the s and t channels are given by:

$$z_s = \cos\theta_s = 1 + \frac{2st}{\lambda_s}, \quad z_t = \cos\theta_t = \frac{s-u}{4q_\pi q_K}, \tag{6}$$

where $\lambda_s = (s-(m_\pi+m_K)^2)(s-(m_K-m_\pi)^2) = 4s\,q_{K\pi}^2(s)$.

It is also convenient to define $m_\pm = m_K \pm m_\pi$, $\Sigma_{12} = m_1^2 + m_2^2$ and $\Delta_{12} = m_1^2 - m_2^2$, as well as $t_\pi = 4m_\pi^2$, $t_K = 4m_K^2$. In the rest of this work, and unless stated otherwise, $m_1 = m_K$, $m_2 = m_\pi$, $\Delta = \Delta_{K\pi}$, $\Sigma = \Sigma_{K\pi}$ and $q = q_{K\pi}(s)$. For later use we define the $K\pi$ scattering lengths as follows:

$$a_0^I = \frac{2}{m_+} f_0^I(m_+^2) \tag{7}$$

and similarly for $a_0^\pm$.

Let us recall that in the case when we have two identical particles in the initial state, as it happens with two pions in the isospin limit formalism, we define

$$g_\ell^I(t) = \frac{\sqrt{2}}{32\pi(q_\pi q_K)^\ell}\int_0^1 dz_t\, P_\ell(z_t) G^I(t,s). \tag{8}$$

For later use we also write here the explicit expressions for the $\ell = 0, 1, 2$ partial waves:

$$\begin{aligned} g_0^0(t) &= \frac{\sqrt{3}}{16\pi}\int_0^1 dz_t\, F^+(s,t), \\ g_1^1(t) &= \frac{\sqrt{2}}{16\pi q_\pi q_K}\int_0^1 dz_t z_t\, F^-(s,t), \\ g_2^0(t) &= \frac{\sqrt{3}}{16\pi(q_\pi q_K)^2}\int_0^1 dz_t \frac{3z_t^2-1}{2} F^+(s,t). \end{aligned} \tag{9}$$

Finally, the relation with the S-matrix partial waves, which allows for straightforward comparison with some experimental works, is:

$$\begin{aligned} S_\ell^I(s)_{\pi\pi\to\pi\pi} &= 1 + i\frac{4q}{\sqrt{s}} f_\ell^I(s)\theta(s-m_+^2), \\ S_\ell^I(t)_{\pi\pi\to K\bar{K}} &= i\frac{4(q_\pi q_K)^{\ell+1/2}}{\sqrt{t}} g_\ell^{I,}(t)\theta(t-t_K). \end{aligned} \tag{10}$$

3 Unconstrained fits to data

3.1 The data

As we have already emphasized in the introduction we will explicitly choose very simple parameterizations to fit the data, so that they can be used easily later on. In this section we will just describe the data without imposing dispersion relations. These will be called unconstrained fits to data (UFD). In this way the fits to each wave are independent from

each other. Later on we will impose the dispersion relations as constraints and obtain the constrained fits to data (CFD). This will correlate different waves.

The data we will fit are of four types. First, we will use data on the phases and modulus of the g_0^0, g_1^1 partial waves extracted from $\pi^- p \to K^- K^+ n$ and $\pi^+ n \to K^- K^+ p$ at the Argonne National Laboratory [7] and from $\pi^- p \to K_s^0 K_s^0 n$ at the Brookhaven National Laboratory in a series of three works [8–10], that we will call Brookhaven-I, Brookhaven-II and Brookhaven-III, respectively. Second, for the tensor g_2^0 wave, data for its modulus was given in Brookhaven-II and Brookhaven-III, although as we will see the old experimental parameterizations are not quite compatible with the present resonance parameters listed in the RPP. Third, for higher partial waves, which play a very minor role in the numerics, we use simple resonance parameterizations with their parameters as quoted in the RPP. Finally, for the high-energy range above 2 GeV we rely on recent updates [17,18,26], of Regge parameterizations [55] based on factorization and the phenomenological observations about Regge trajectories or the Veneziano model [56–59].

3.2 Partial wave fits from $K\bar{K}$ threshold to 2 GeV

We now describe our partial-wave parameterizations in the region from $K\bar{K}$ threshold to 2 GeV. For all of them we define a modulus and a phase $t_\ell^I = |t_\ell^I| e^{i\phi_\ell^I}$. We will start with the waves that have less controversy on the data sets and that, as we will see later, satisfy best our Roy–Steiner-like equations, leaving for the end the most difficult one, which is that with $\ell = 0, I = 0$. Note that since in the isospin limit all pions are identical particles, Bose statistics applies and $\ell + I$ must be even.

3.2.1 $\ell = 1, I = 1$ partial wave

For the g_1^1 partial wave there is only data from the Argonne Collaboration (Cohen et al. [7]), extending up to around 1.6 GeV for both the modulus $|g_1^1|$ and its phase ϕ_1^1. Although there is no data on the 1.6–2 GeV region, which is the starting energy of our Regge parameterizations, we will see that a rather simple functional form covering the whole range from $\pi\pi$ threshold up to 2 GeV satisfies fairly well the Roy–Steiner equations even before imposing them as constraints. In particular we will use a phenomenological parameterization similar to that in [27]:

$$g_1^1(t) = \frac{C}{\sqrt{1 + r_1 \hat{q}_\pi^2(t)}\sqrt{1 + r_1 \hat{q}_K^2(t)}} \times \Big\{ \overline{BW}(t)_\rho + (\beta + \beta_1 \hat{q}_K^2(t)) \overline{BW}(t)_{\rho'} + (\gamma + \gamma_1 \hat{q}_K^2(t)) \overline{BW}(t, m)_{\rho''} \Big\}, \tag{11}$$

Table 1 Parameters of the g_1^1 wave. Masses and widths are given in GeV whereas, C, β_1, γ_1 and r_1 are given in GeV^{-2}

Parameter	UFD	CFD
m_ρ	0.7757 ± 0.0010	0.7749 ± 0.0010
Γ_ρ	0.152 ± 0.001	0.153 ± 0.001
$m_{\rho'}$	1.440 ± 0.015	1.438 ± 0.015
$\Gamma_{\rho'}$	0.310 ± 0.029	0.309 ± 0.029
$m_{\rho''}$	1.72	1.72
$\Gamma_{\rho''}$	0.25	0.25
C	1.21 ± 0.11	1.23 ± 0.11
r_1	3.95 ± 0.76	3.43 ± 0.76
β	-0.168 ± 0.007	-0.172 ± 0.007
β_1	0.37 ± 0.02	0.38 ± 0.02
γ	0.10 ± 0.02	0.14 ± 0.02
γ_1	-0.06 ± 0.06	-0.17 ± 0.06

where the three vector resonances $\rho(770)$, $\rho' = \rho(1450)$, $\rho'' = \rho(1700)$ have been parameterized by a combination of three Breit–Wigner-like shapes:

$$\overline{BW}(t)_V = \frac{m_V^2}{m_V^2 - t - i\Gamma_V \sqrt{t}\, \frac{2G_\pi(t) + G_K(t)}{2G_\pi(m_V^2)}},$$
$$G_P(t) = \sqrt{t}\left(\frac{2q_P(t)}{\sqrt{t}}\right)^3, \tag{12}$$

and m_V, Γ_V correspond to the masses and widths of the resonances given in Table 1. Note that $\hat{q}_P^2(t) \equiv q_P^2(t)\Theta(t - 4m_P^2)$ vanishes below the $2m_P$ threshold. In particular, Eq. (11) below $K\bar{K}$ threshold is similar to the widely used Kuhn and Santamaría form in [60]. In this region, since the coupling to the 4-pion state is negligible and $\pi\pi$ scattering is elastic, Watson's Theorem implies that $\phi_1^1(t)$ should be equal to the phase shift of the $I = 1, \ell = 1$ partial wave of $\pi\pi$ scattering. Since C and r_1 are real, they do not contribute to the phase, nor β_1 nor γ_1, being multiplied by $\hat{q}_K^2$, so that the parameters $m_\rho, \Gamma_\rho, \beta, \gamma$ are obtained from a fit to the dispersive analysis [17] of the $\pi\pi$ phase shift in the elastic region. Indeed, in the lower panel of Fig. 1 it can be seen that our parameterization describes remarkably well the $\pi\pi$ scattering data on the phase below $K\bar{K}$ threshold.

The parameters of the ρ'' resonance are fixed for simplicity to those of the RPP [1], whereas those for the ρ' are allowed to vary within 1.5 standard deviations within the values listed in the PDG. Note that the ones determined by the CLEO Collaboration [61] are not compatible with our best fit, if one tries to fix those parameters to reproduce the $\pi\pi \to K\bar{K}$ data the χ^2 is increased by almost a factor of 2. Then we fit the rest of the parameters to describe the data in the physical and pseudophysical regions, the best result is shown in Fig. 1 and the parameters are given in Table 1. The fit has a total

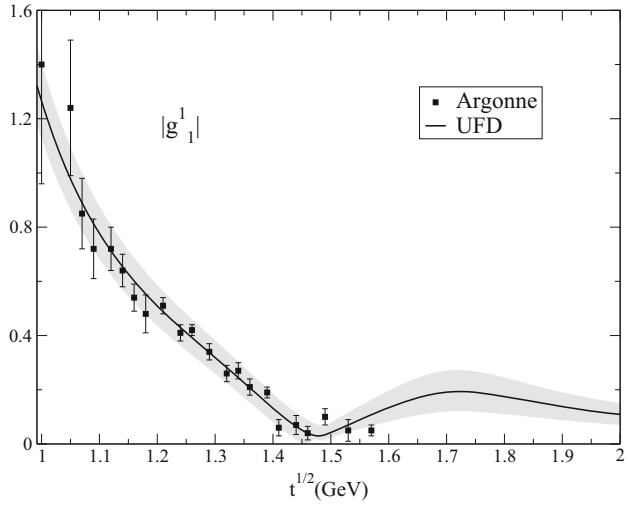

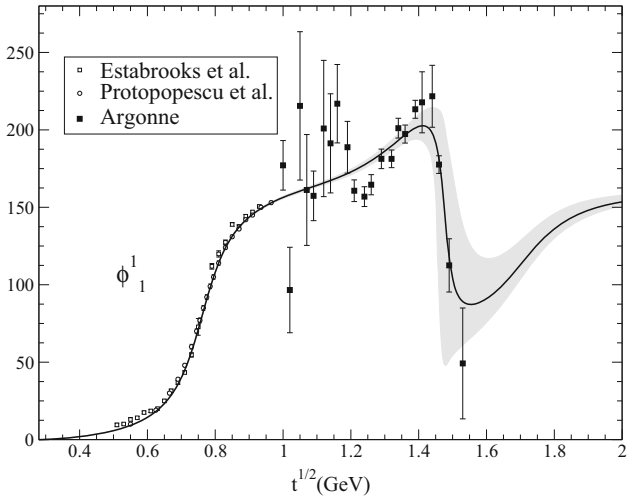

Fig. 1 Modulus and phase of the $g^1_1(t)$ $\pi\pi \to K\bar{K}$ partial wave. The continuous line and the uncertainty band correspond to the UFD parameterization described in the text. Note that the phase below $K\bar{K}$ follows that of $I = 1, \ell = 1$ elastic $\pi\pi$ scattering [17]. The white circles and squares come from the $\pi\pi$ scattering experimental analyses of Protopopescu et al. [2] and Estabrooks et al. [4], respectively

$\chi^2/dof = 1.7$, but a slightly larger $\chi^2/dof = 2.2$ is found in the physical region. Conservatively we use the square root of the latter to rescale the fit parameter uncertainties in the table.

The data and the results of our unconstrained fit to data (UFD) are shown in Fig. 1. Note that we plot the modulus from $K\bar{K}$ threshold and that, as already commented, data only reaches up to 1.57 GeV. The shape above that energy is almost entirely given by the ρ'' resonance. Concerning the phase, from the two-pion threshold to the $K\bar{K}$ threshold it is indistinguishable from that obtained from the $\pi\pi$ dispersive analysis in [17]. In Fig. 1 our result below threshold can be compared to the data from elastic $\pi\pi$ scattering [2,4]. Note also the large uncertainty of both the data and the error bands in the region around 1.5 GeV, which is due to the fact that

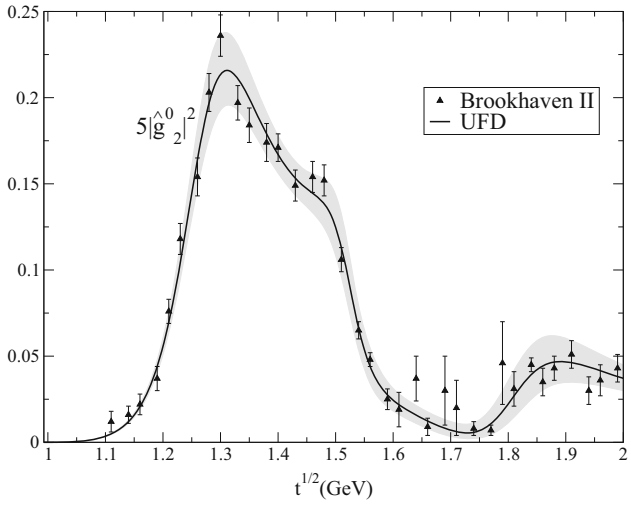

Fig. 2 Data on the modulus of $\hat{g}^0_2(t)$ from the Brookhaven-II analysis [9] together with our UFD fit, described in the text

the modulus almost vanishes there. Fortunately, this will also make the contribution of that region to the dispersive integrals almost negligible.

3.2.2 $\ell = 2, I = 0$ *partial wave*

The data in Fig. 2 that we use for this wave in the physical region were obtained in the Brookhaven-II analysis [9], published 6 years after Brookhaven-I. The Brookhaven-II work was a study of the $I = 0$, $J^{PC} = 2^{++}$ channel of $\pi\pi \to K\bar{K}$ scattering within a coupled channel formalism, which included data from other reactions. The latest Brookhaven-III re-analysis by some members of that collaboration, including even further information on other processes can be found in [10]. Note that our normalization differs from that in the experimental works and this is why we are plotting $|\hat{g}^0_2|$, defined as:

$$\hat{g}^0_2(t) \equiv \frac{2(q_\pi q_K)^{5/2}}{\sqrt{t}} g^0_2(t) \equiv |\hat{g}^0_2(t)| \exp(i\phi^0_2(t)). \tag{13}$$

Contrary to the previous $\ell = 1, I = 1$ case, where the $\rho(770)$ resonance dominates the unphysical region, now the lowest resonance is well above the $K\bar{K}$ threshold and therefore it does not dominate the unphysical region. Thus our $\ell = 2, I = 0$ parameterization will have two pieces: one above $K\bar{K}$ threshold and another one below.

Concerning the physical region, $t \geq t_K$, note that there are only data for the modulus $|\hat{g}^0_2|$, Fig. 2. Therefore, since we also need to have a phase we use a phenomenological description in terms of resonances similar to that in [10], which is a sum of usual Breit–Wigner shapes, although since they overlap significantly we include some interference phases. We thus use:

$$\hat{g}_2^0(t) = \frac{C\sqrt{(q_\pi(t)q_K(t))^5}}{\sqrt{t}\sqrt{1+r_2^2\hat{q}_\pi^4(t)}\sqrt{1+r_2^2\hat{q}_K^4(t)}} \times\left\{e^{i\phi_1}BW(t)_1+\beta e^{i\phi_2}BW(t)_2+\gamma e^{i\phi_3}BW(t)_3\right\}, \tag{14}$$

with

$$BW(t)_T = \frac{m_T^2}{m_T^2-t-im_T\Gamma_T(t)},$$
$$\Gamma_T(t) = \Gamma_T\left(\frac{q_T(t)}{q_T(m_T^2)}\right)^5\frac{m_T}{\sqrt{t}}\frac{D_2(r\,q_T(m_T^2))}{D_2(r\,q_T(t))}, \tag{15}$$

where $D_2(x) = 9+3x^2+x^4$ provides the usual Blatt–Weisskopf barrier factor for $\ell = 2$, with a typical $r = 5\,\text{GeV}^{-1} \simeq 1\,\text{fm}$.

In Eq. (15) above, $T = 1,2,3$ stands for the tensor $f_2(1270)$, $f_2'(1525)$ and $f_2(1810)$ resonances, respectively. Since they decay predominantly to $\pi\pi$, $\bar{K}K$ and $\pi\pi$, respectively, we have set $q_1(t) = q_3(t) = q_\pi(t)$, whereas $q_2(t) = q_K(t)$. The mass M_T and width Γ_T of each resonance after the fit are given in Table 2. As can be seen in the Brookhaven-II and III fits in [9,10], the $f_2'(1525)$ was at odds with the present knowledge about this resonance parameters. Moreover, the parameters of the $f_2(1810)$ vary within a huge range even when using almost the same data. As we have no data for the phase of the partial wave it is not possible to fix the position of the masses with accuracy, however, performing a coupled-channel analysis for the tensor partial wave is out of the scope of this work, mostly because we have no dispersive control over other channels apart from $\pi\pi \to K\bar{K}$. For that reason we have included the masses of both the $f_2(1270)$ and the $f_2'(1525)$ as additional data for our fit. In particular, we take as input for the fit $m_{f_2} = 1.2755 \pm 0.0035\,\text{GeV}$ which is the average and standard deviation of the values used in the RPP's own average [1]. This we do to have a more conservative estimate of the systematic uncertainty. For the f_2' we take directly the RPP average $m_{f_2'} = 1.525 \pm 0.005\,\text{GeV}$. The inclusion of the $f_2(1810)$ is purely phenomenological, following [9,10], just to describe the final rise seen in the modulus, but this resonance still "needs confirmation" according to the RPP. We could have described this raise equally well with another functional form, although it is also clear that there exist some enhancements of the amplitudes and phases for $\pi\pi \to \pi\pi$ and $\pi\pi \to \eta\eta$. Its numerical effect on our dispersive integrals is rather small. In Table 2 we also provide the phases ϕ_T resulting from the fit to data.

Concerning the unphysical region, $t < t_K$, since the contribution of the four pion state is negligible, we have assumed that $\pi\pi$ scattering is elastic. Hence we can use Watson's Theorem to identify $\phi_2^0 = \delta_2^{(0)}$, where $\delta_2^{(0)}$ is the $\pi\pi$-scattering phase shift. Then we have fitted $\delta_2^{(0)}$ to the result obtained in [17] from a dispersive analysis of $\pi\pi$ scattering data. For this we have used a conformal expansion similar to that in [17] but with one more parameter B_2 fixed to ensure a continuous matching of g_2^0 at threshold. Namely:

$$\cot\phi_2^0(t) = \frac{t^{1/2}}{2q_\pi^5}(m_{f_2(1270)}^2-t)m_\pi^2 \times\left\{B_0+B_1w(t)+B_2w(t)^2\right\},$$
$$w(t) = \frac{\sqrt{t}-\sqrt{t_0-t}}{\sqrt{t}+\sqrt{t_0-t}},\quad t_0^{1/2} = 1.05\,\text{GeV}, \tag{16}$$

where

$$B_2\,\omega(t_K)^2 = \frac{q_\pi^5(t_K)\cot(\phi_2^0(t_K))}{m_K(m_{f_2(1270)}^2-t_K)m_\pi^2} - B_0 - B_1\,\omega(t_K), \tag{17}$$

has been fixed by continuity with the piece above t_K in Eq. (14). In Table 2 we provide values of B_0, B_1 after fitting the CFD phase-shift in [17]. With this parameterization we obtain a final $\chi^2/dof = 1.4$. Thus we rescale our uncertainties by a factor of ~ 1.2. We have checked that this phase is also compatible within uncertainties with the dispersive analysis of the $\pi\pi$ D-wave using Roy and GKPY equations in [62].

Neither Brookhaven-I nor Argonne provide data for this wave, nor the models they used to parameterize it. Nevertheless Brookhaven-I shows a plot with the central value of their phase for this channel, which is later used to extract the g_0^0 phase. As seen in Fig. 3 our phase is fairly compatible with the Brookhaven-I model between 1.25 and 1.54 GeV. However, also in that figure it can be seen that the Brookhaven-I

Table 2 Parameters of the g_2^0 wave

Parameter	UFD	CFD
$m_{f_2(1270)}$	1.271 ± 0.0035 GeV	1.271 ± 0.0035 GeV
$m_{f_2'(1525)}$	1.522 ± 0.005 GeV	1.522 ± 0.005 GeV
$m_{f_2(1810)}$	1.806 ± 0.017 GeV	1.802 ± 0.017 GeV
$\Gamma_{f_2(1270)}$	0.187 ± 0.009 GeV	0.191 ± 0.009 GeV
$\Gamma_{f_2'(1525)}$	0.108 ± 0.016 GeV	0.107 ± 0.016 GeV
$\Gamma_{f_2(1810)}$	0.201 ± 0.028 GeV	0.198 ± 0.028 GeV
$\phi_{f_2(1270)}$	-0.049 ± 0.014	-0.078 ± 0.014
$\phi_{f_2'(1525)}$	2.62 ± 0.16	2.59 ± 0.16
$\phi_{f_2(1810)}$	-0.72 ± 0.16	-0.82 ± 0.16
B_0	12.5 ± 0.4	12.4 ± 0.4
B_1	10.3 ± 1.0	12.3 ± 1.0
C	1.82 ± 0.09 GeV^{-2}	1.86 ± 0.09 GeV^{-2}
r_2^2	6.68 ± 0.72 GeV^{-4}	6.78 ± 0.72 GeV^{-4}
β	0.070 ± 0.016	0.066 ± 0.016
γ	0.093 ± 0.02	0.094 ± 0.02

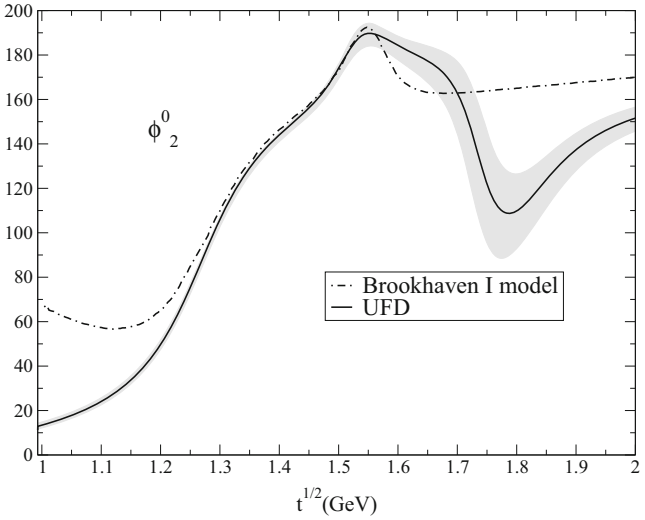

Fig. 3 Comparison between the UFD g_2^0 phase and the one obtained with the Brookhaven-I model. Note that the latter violates Watson's Theorem at $K\bar{K}$ threshold. Also, the former includes an $f_0(1810)$ resonance whereas the latter uses a flat background. As explained in the text, the latter is strongly disfavored when fitting Brookhaven II data on the modulus

model violates Watson's Theorem at low energies, which our phase fully satisfies. In addition, above 1.6 GeV our phase, obtained by fitting the Brookhaven-II data [9] on the modulus with modern values for the f_2 family of resonances, is rather different from the flat behavior of the Brookhaven-I model [8] up to 1.9 GeV. The reason is that the Brookhaven-I model used a simple smooth background to describe the 1.6–1.9 GeV region, instead of the $f_2(1810)$ used in this work. Actually, we have checked that if we impose the phase of the Brookhaven-I model on our fit to the Brookhaven-II modulus, the resulting χ^2/dof is ~ 5, and thus strongly disfavored with respect to our phase. Even by deforming our fits by including more parameters, the best we have been able to achieve when imposing the phase of the Brookhaven-I model above 1.6 GeV, is $\chi^2/dof \sim 3$, but at the price of introducing contributions difficult to interpret in terms of resonance parameters. Both the violation of Watson's Theorem and the use of such non-resonant background make the Brookhaven-I solution suspicious.

Unfortunately the Brookhaven-I model was used to extract the phase of the g_0^0, which therefore also becomes suspicious below 1.2 GeV and above 1.6 GeV. Nevertheless, and with this caveats in mind we will still study the g_0^0 phase coming from the Brookhaven-I collaboration above 1.6 GeV. The reason is that this region lies outside the applicability range of Roy–Steiner equations, so that for our purposes is just input. Fortunately, the modulus there is very small, so that the contribution from this region to the Roy–Steiner equations below 1.6 GeV is very suppressed. In Appendix A, we have checked that either with our g_0^0 phase or the Brookhaven-I phase, the difference lies within our uncertainties in the region up to 1.47 GeV, which is the one of interest for this work since it is the one where partial-wave dispersion relations can be applied.

3.2.3 $\ell = 0, I = 0$ *partial wave*

This wave is the most complicated but also the most interesting one for hadron spectroscopy, since here we can find the much debated scalar-isoscalar resonances. For the $g_0^0(t)$ partial wave there are data in the whole region of interest on both the modulus $|g_0^0|$ and the phase ϕ_0^0, which we show in Fig. 4. The data sets extend up to 2.4 GeV, but we do not fit that region because from 2 GeV we will use Regge parameterizations. It is then convenient to split into two regions the data description below 2 GeV:

I. Region I: From $\sqrt{t_{min,I}} = 2m_K$ up to $\sqrt{t_{max,I}} = 1.47$ GeV, where data from Argonne [7] and Brookhaven-I [8] coexist. Note that this region will lie within the applicability of Roy–Steiner equations and will be later constrained to satisfy dispersion relations.
Concerning the phase ϕ_0^0, it is clearly seen in Fig. 4 that from $2m_K$ up to 1.2 GeV, the Argonne [7] and Brookhaven-I [8] sets are incompatible. Let us now recall that, by Watson's Theorem, ϕ_0^0 at $K\bar{K}$ threshold should match the scalar-isoscalar $\pi\pi \to \pi\pi$ phase shift $\delta_0^{(0)}$. However, the $\pi\pi$ scattering analyses with Roy and GKPY equations that extend up to or beyond $K\bar{K}$ threshold [17,63] find $\delta_0^{(0)} > 200°$, which is consistent with the Argonne [7] phase, but much higher than the phase of Brookhaven-I [8]. In addition we have just seen that this phase was extracted using a g_2^0 wave that also violates Watson's Theorem. Therefore, for our fits we have discarded the phase of Brookhaven-I [8] below ~ 1.15 GeV, i.e. until it agrees with that of Argonne [7].
Concerning the data on $|g_0^0|$, shown in Fig. 4, the Argonne and Brookhaven-I sets are consistent among themselves but not with the Brookhaven-II. However, the latter is consistent up to 1.2 GeV with the dip solution for the inelasticity favored from dispersive analyses of $\pi\pi \to \pi\pi$ scattering [17,63] (assuming that only $\pi\pi$ and $K\bar{K}$ states are relevant). Finally, the "dip" solution from $\pi\pi$ scattering in the 1.2 GeV to 1.47 region has such large uncertainties that is roughly consistent with the three data sets.

II. In the region from $\sqrt{t_{min,II}} = 1.47$ GeV to $\sqrt{t_{max,II}} = 2$ GeV Roy–Steiner equations will not be applicable and thus this region will only be used as input for our dispersive calculations for lower energies. Note that here all experiments are roughly consistent, although the Argonne set only reaches up to ~ 1.5 GeV, Brookhaven-I up to ~ 1.7 GeV and only Brookhaven-II reaches up to 2 GeV.

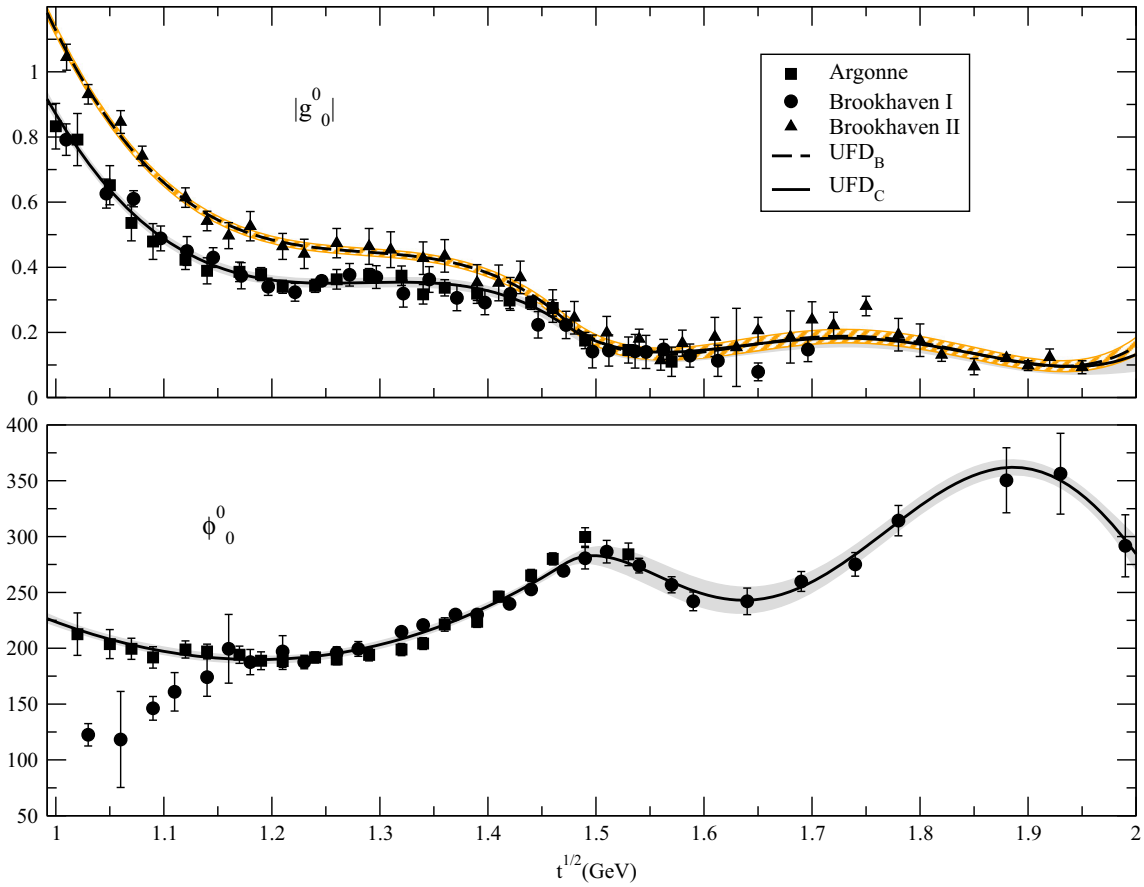

Fig. 4 Upper panel: modulus of the scalar-isoscalar $\pi\pi \to K\bar{K}$ scattering. The continuous line represents the UFD_C parameterization while the dashed line represents the UFD_B fit to the Brookhaven-II data only. Lower panel: scalar-isoscalar UFD phase for $\pi\pi \to K\bar{K}$ scattering, which is common for both UFD_B and UFD_C. Note that the Brookhaven-I phase close to threshold lies around 150° or below, at odds with all dispersive analysis of $\pi\pi$ scattering, which find a phase around or above 200°

Therefore in order to test different data sets independently and to be able to impose later Roy–Steiner equations as constraints below 1.5 GeV using as input the region above, we have decided to parameterize our amplitudes by piecewise functions. Actually, each piece will be parameterized by Chebyshev polynomials, because they are rather simple and, in practice, tend to reduce the correlation between the small number of parameters needed to obtain a good fit. They are given by:

$$p_0(x) = 1, \quad p_1(x) = x,$$
$$p_{n+1}(x) = 2xp_n(x) - p_{n-1}(x). \tag{18}$$

Thus we first map each energy region $i = I, II$ into the $x \in [-1, 1]$ interval through the lineal transformation

$$x_i(t) = 2\frac{\sqrt{t} - \sqrt{t_{min,i}}}{\sqrt{t_{max,i}} - \sqrt{t_{min,i}}} - 1. \tag{19}$$

Note that for any n, $p_n(1) = 1$ and $p_n(-1) = (-1)^n$, which is useful for matching the different pieces smoothly up to the first derivative.

Since for the ϕ_0^0 phase we have already selected a single set on each region, our unconstrained fit to data (UFD) will be given in just two pieces:

$$\phi_0^0(t) = \begin{cases} \sum_{n=0}^{3} B_n p_n(x_I(t)), & \text{Region I,} \\ \sum_{n=0}^{5} C_n p_n(x_{II}(t)), & \text{Region II.} \end{cases} \tag{20}$$

Note that we set:

$$B_0 = \delta_0^{(0)}(t_K) + B_1 - B_2 + B_3, \tag{21}$$
$$C_0 = \phi_0^0(t_{max,I}) + C_1 - C_2 + C_3 - C_4 + C_5, \tag{22}$$

in order to impose continuity at $K\bar{K}$ threshold and between the two energy regions, respectively. In addition, we fix C_1 to have a continuous derivative for the central value of the curve and we take $\delta_0^{(0)}(t_K) = (226.5 \pm 1.3)°$ from [16]. The rest of the parameters of the fit are given in Table 3. The total $\chi^2/dof = 1.47$, which comes slightly larger than one due to some incompatibilities between data sets. Consequently, the

Table 3 Parameters of ϕ_0^0

Parameter	UFD	CFD_B	CFD_C
B_1	23.6 ± 1.3	22.1 ± 1.3	22.9 ± 1.3
B_2	29.4 ± 1.3	27.7 ± 1.3	28.4 ± 1.3
B_3	0.6 ± 1.6	1.8 ± 1.6	1.1 ± 1.6
C_1	34.3932 fixed	35.3450 fixed	34.51593 fixed
C_2	4.4 ± 2.6	4.3 ± 2.6	4.3 ± 2.6
C_3	-32.9 ± 5.2	-33.3 ± 5.2	-32.6 ± 5.2
C_4	-16.0 ± 2.2	-16.5 ± 2.2	-16.0 ± 2.2
C_5	7.4 ± 2.4	7.2 ± 2.4	7.2 ± 2.4

Table 4 Parameters of the UFD_B and CFD_B fits to $|g_0^0|$

Parameter	UFD_B	CFD_B
D_0	0.59 ± 0.01	0.60 ± 0.01
D_1	-0.38 ± 0.01	-0.35 ± 0.01
D_2	0.12 ± 0.01	0.13 ± 0.01
D_3	-0.09 ± 0.01	-0.12 ± 0.01
F_1	-0.04329 fixed	-0.04078 fixed
F_2	-0.008 ± 0.009	-0.007 ± 0.009
F_3	-0.028 ± 0.007	-0.035 ± 0.007
F_4	0.026 ± 0.007	0.037 ± 0.007

uncertainties of the parameters in Table 3 have been rescaled by a factor $\sqrt{1.5}$.

In contrast, for the modulus we want to test different sets of data. Thus, we have performed two Unconstrained Fits to Data (UFD) in Region I: (i) A UFD_B fitting the data of Brookhaven-II [9]. (ii) A UFD_C fitting the "Combined" data of Argonne [7] and Brookhaven-I [8]. Both use the same data in Region II. Thus we will use the following functional form:

$$|g_0^0(t)| = \begin{cases} \sum_{n=0}^{3} D_n p_n(x_I(t)), & \text{Region I,} \\ \sum_{n=0}^{4} F_n p_n(x_{II}(t)), & \text{Region II,} \end{cases} \tag{23}$$

where we now set:

$$F_0 = |g_0^0(t_{max,I})| + F_1 - F_2 + F_3 - F_4, \tag{24}$$

in order to ensure continuity between the two regions and we fix F_1 to ensure a continuous derivative for the central value.

Both the UFD_B and UFD_C fits, whose parameters are given in Tables 4 and 5, respectively, have $\chi^2/dof \sim 1$ and are shown in the upper panel of Fig. 4.

3.2.4 Partial waves with $\ell > 2$

For higher partial waves we just use Breit–Wigner descriptions associated to the poles listed in the PDG. In particular, for the $g_3^1(t)$ we include a single $\rho_3(1690)$ resonance. The $\ell = 4$ partial wave, parametrized as an $f_4(2050)$ Breit–Wigner resonance, is only included in the $g_2^0(t)$ dispersive calculation due to its negligible contribution below 2 GeV for the $g_0^0(t)$.

Table 5 Parameters of the UFD_C and CFD_C fits to $|g_0^0|$

Parameter	UFD_C	CFD_C
D_0	0.46 ± 0.01	0.46 ± 0.01
D_1	-0.27 ± 0.01	-0.25 ± 0.01
D_2	0.11 ± 0.01	0.11 ± 0.01
D_3	-0.078 ± 0.009	-0.087 ± 0.009
F_1	-0.04153 fixed	-0.03738 fixed
F_2	-0.010 ± 0.008	-0.013 ± 0.008
F_3	-0.023 ± 0.007	-0.025 ± 0.007
F_4	0.021 ± 0.006	0.025 ± 0.006

3.3 Higher energies

There is no high-energy experimental information on $\pi\pi \to \bar{K}K$ nor $\pi K \to \pi K$. However, the high energy behavior of both processes can be confidently modeled by applying factorization to Regge amplitudes obtained for other processes. In this work we will use, for the s-channel above 1.74 GeV the Regge model description presented in [55] and updated in [17,18], whereas for the t-channel we will use the asymptotic forms of the Veneziano model [56–59], with the updated parameters in [27], to describe the process above 2 GeV. The reasons to choose 2 GeV in this work are twofold: on the one hand data for the g_0^0 and g_2^0 waves reach above that energy, on the other hand, even if the g_1^1 data end at 1.6 GeV, the $\rho''(1720)$ is well established in the RPP and with its 250 MeV width, reaches well above 2 GeV. Thus we rely on our partial-wave parameterizations up to 2 GeV, but not much more.

In what follows we provide the detail of these descriptions using the notation of this work.

For the symmetric amplitude we have the Pomeron $P(s,t)$ contribution and the f_2 or $P'(s,t)$ exchange:

$$\begin{aligned} \text{Im}\, F_{\pi K}^{+}(s,t) &= \frac{\text{Im}\, F_{\pi K}^{(I_t=0)}(s,t)}{\sqrt{6}} \\ &= \frac{4\pi^2}{\sqrt{6}} f_{K/\pi} \left[P(s,t) + r P'(s,t) \right], \end{aligned} \tag{25}$$

where, as explained in [55], $f_{K/\pi}$ is the factorization that allows to convert one $\pi\pi$-Reggeon into a KK-Reggeon vertex, whereas r is related to the branching ratio of the $f_2(1270)$ resonance to $\bar{K}K$. In addition

$$P(s,t) = \beta_P \psi_P(t) \alpha_P(t) \frac{1+\alpha_P(t)}{2} e^{\hat{b}t} \left(\frac{s}{s'}\right)^{\alpha_P(t)},$$

$$P'(s,t) = \beta_{P'} \psi_{P'}(t) \frac{\alpha_{P'}(t)(1+\alpha_P(t))}{\alpha_{P'}(0)(1+\alpha_P(0))} e^{\hat{b}t} \left(\frac{s}{s'}\right)^{\alpha_{P'}(t)},$$

$$\alpha_P(t) = 1 + t\alpha'_P,\ \psi_P = 1 + c_P t,$$
$$\alpha_{P'}(t) = \alpha_{P'}(0) + t\alpha'_{P'},\ \psi_P = 1 + c_{P'} t. \quad (26)$$

In contrast, the antisymmetric amplitude is dominated by just one contribution coming from the exchange of a Reggeized ρ:

$$\text{Im}\, F^{-}_{\pi K}(s,t) = \frac{\text{Im}\, F^{(I_t=1)}_{\pi K}(s,t)}{2} = 2\pi^2 g_{K/\pi}\, \text{Im}\, T^{(I_t=1)}_{\pi\pi}(s,t), \quad (27)$$

where now $g_{K/\pi}$ is the factorization constant to change a $\pi\pi \to \rho$ Regge vertex into $K\bar{K} \to \rho$, and

$$\text{Im}\, T^{(I_t=1)}_{\pi\pi}(s,t) = \beta_\rho \frac{1+\alpha_\rho(t)}{1+\alpha_\rho(0)} \varphi(t) e^{\hat{b}t} \left(\frac{s}{s'}\right)^{\alpha_\rho(t)},$$
$$\alpha_\rho(t) = \alpha_\rho(0) + t\alpha'_\rho + \frac{1}{2}t^2\alpha''_\rho,$$
$$\varphi(t) = 1 + d_\rho t + e_\rho t^2. \quad (28)$$

All the parameters in Eqs. (26) and (28) correspond to Regge exchanges without strangeness (the Pomeron, f_2 and ρ) and can be determined [55] from processes that do not involve kaons. Therefore in this work we fix them, both for the unconstrained (UFD) and constrained fits (CFD) here, to their updated values of the CFD fits given in [17], which are listed in Table 6. Let us remark that with these parameters our asymptotic value of the Pomeron πK cross section is $\simeq 10.3$ mb. This is about twice the $\simeq 5 \pm 2.5$ mb value used in [27]. This value was inspired by the work in [20], which asymptotically yielded 6 ± 5 mb for $\pi\pi$ scattering. However, this $\pi\pi$ value has been revisited recently by members of the same group [64] yielding 12.2 ± 0.1 mb for $\pi\pi$ scattering, thus supporting our larger value for πK rather than 5 ± 2.5 mb.

In contrast, the determination of the parameters $f_{K/\pi}$, r and $g_{K/\pi}$ needs input from kaon interactions. In principle all them were determined in [55] from KN factorization and we take the $f_{K/\pi}$ and r values from that reference. Concerning $g_{K/\pi}$ we take the updated value from the forward dispersion relation study of πK scattering in [18] (we use the value from the CFD there). Their values can be found in Table 7. Since their determination involves kaon interactions, we will allow them to vary when constraining our fits with dispersion relations, i.e. from the UFD to the CFD sets. However, in the table it is seen that the change is minute.

For the t-channel, $\pi\pi \to K\bar{K}$, we also need the exchange of strange Reggeons, for which we will assume that the dominant trajectories $K_1^*(892)$ and $K_2^*(1430)$ are degenerate, Thus we use for them a common trajectory $\alpha_{K^*}(s) = \alpha_{K^*} + \alpha'_{K^*} s$ whose parameters, listed in Table 7, are obtained from the linear Regge trajectories for strange resonances and therefore are kept fixed for both our UFD and CFD sets.

Table 6 Values of Regge parameters obtained in [14,17]. Since these could be fixed using reactions other than πK scattering, they will be fixed both in our UFD and CFD parameterizations

Regge parameters	Used both for UFD and CFD
s'	1 GeV^2
$\hat{b}$	2.4 ± 0.5 GeV^{-2}
α'_P	0.2 ± 0.1 GeV^{-2}
$\alpha'_{P'}$	0.9 GeV^{-2}
c_P	0.6 ± 1 GeV^{-2}
$c_{P'}$	-0.38 ± 0.4 GeV^{-2}
β_P	2.50 ± 0.04
$c_P(0)$	0 ± 0.04
$\beta_{P'}$	0.80 ± 0.05
$c_{P'}(0)$	-0.4 ± 0.4
$\alpha_{P'}(0)$	0.53 ± 0.02
$\alpha_\rho(0)$	0.53 ± 0.02
α'_ρ	0.9 GeV^{-2}
α''_ρ	-0.3 GeV^{-4}
d_ρ	2.4 ± 0.5 GeV^{-2}
e_ρ	2.7 ± 2.5
β_ρ	1.47 ± 0.14

All these features are nicely incorporated in the dual-resonance Veneziano–Lovelace model [56–59,65], which was already used in the Roy–Steiner context for πK scattering [52,53]. Here we are only interested in the asymptotic behavior [27]:

$$\frac{\text{Im}\, G^0(t,s_b)}{\sqrt{6}}\Big|_{\text{Regge}} = \frac{\text{Im}\, G^1(t,s_b)}{2}\Big|_{\text{Regge}} = \frac{\pi\lambda(\alpha'_{K^*}t)^{\alpha_{K^*}+a\alpha'_{K^*}}}{\Gamma(\alpha_{K^*}+a\alpha'_{K^*})} \times \left[1 + \frac{\alpha'_{K^*}b}{t}\left(\psi(\alpha_{K^*}+a\alpha'_{K^*}) - \log(\alpha'_{K^*}t)\right)\right], \quad (29)$$

where ψ is the polygamma function. Note that the a, b parameters in the above equation will be those defining the hyperbola $(s-a)(u-a) = b$ along which we will define our hyperbolic dispersion relations in the next section. For a given t, s_b is the value of s that lies in the previous hyperbola. In order to compare with the expressions in [27], where $a = 0$, we have kept just the first order in the b/t expansion, although its numerical effect is rather small.

We estimate the remaining λ parameter from exact degeneracy between the ρ and K^* families. We thus match Eq. (27) at 2 GeV with the expression from the degenerate Veneziano model with its original parameter $\alpha^V_\rho = 0.475$. In this way we find

Table 7 Values of Regge parameters involving strangeness. They are all allowed to vary from our UFD to our CFD sets with the exception of α_{K^*} and α'_{K^*}, since they are both determined from linear Regge trajectory fits to strange resonances

Regge	UFD	CFD
$f_{K/\pi}$	0.66 fixed	0.66 fixed
$g_{K/\pi}$	0.53 fixed	0.53 fixed
r	0.05 ± 0.010	0.052 ± 0.010
α_{K^*}	0.352	0.352
α'_{K^*}	0.882 GeV^{-2}	0.882 GeV^{-2}
λ	11.0 ± 5.0	10.7 ± 5.0

$$\lambda \simeq \frac{2\pi\,\Gamma(\alpha_\rho^V)}{\alpha_{K^*}^{\prime\alpha_\rho^V}} 4^{\alpha_\rho - \alpha_\rho^V} \simeq 10.6 \pm 2.5, \tag{30}$$

which is compatible with the value used in [27], $\lambda = 14 \pm 5$. Conservatively we also add a 25% uncertainty due to the breaking of degeneracy and thus we arrive to our final estimate

$$\lambda \simeq 11 \pm 5, \tag{31}$$

which for completeness is also listed in Table 7. Given that it is a crude estimate we will allow this value to vary when constraining our fits to obtain the CFD sets. We will see that after imposing the dispersive constraints we obtain $\lambda = 10.7$, which due to the degeneracy between the ρ and K^* families, suggests $g_{K/\pi} \sim 0.55$, in perfect agreement with the value used here that comes from a dispersive πK study.

A final remark on the size of Regge contributions is in order. As commented in the introduction, in the next sections we will obtain partial-wave dispersion relations by integrating hyperbolic dispersion relations. This is an integral over b for a family of $(s-a)(u-a) = b$ hyperbolas, while $a = -10.8 M_\pi^2$ is fixed to the value that maximizes the applicability region (see Appendix D). This means that the exponent $\alpha_{K^*} + a\alpha'_{K^*} < \alpha_{K^*}$ and thus the Regge contribution to $\pi\pi \to \bar{K}K$ in this work, for the same number of subtractions, is suppressed with respect to its size in [27], where $a = 0$. This will allow us to consider less subtractions without Regge contributions growing large.

4 Hyperbolic dispersion relations and sum rules

Our goal is to calculate a set of parameterizations that describe the data up to 1.47 GeV consistently with hyperbolic dispersion relations (HDR). As already advanced in the introduction, in this work we will consider a set of hyperbolas $(s-a)(u-a) = b$ and use a to maximize the energy domain where the hyperbolic dispersion relations hold. Note that the phenomenology of the $\pi\pi \to K\bar{K}$ $a = 0$ case has been studied in detail in [27,52,53]. Moreover, HDR with $a = 0$ were also used for the study of the $K_0^*(800)$ resonance [26].

In addition, we will use the smallest number of subtractions needed for each channel. This has the advantage that our equations for g_0^0 and g_1^1 are independent from one another. In contrast, in [27] they use more subtractions and the subtraction constants are constrained by means of sum rules that mix the dispersive representations of both waves.

4.1 Hyperbolic dispersion relations

For their derivation we basically follow the same steps described in [39] but using $a \neq 0$, or more recently the steps in [28] but applied here to for $\pi\pi \to K\bar{K}$ instead of πN scattering. Recall that in this work we use hyperbolas $(s-a)(u-a) = b$, which with $s+t+u = 2\Sigma$, implies that s and u on these hyperbolas are the following functions of t:

$$\begin{aligned} s_b \equiv s_b(t) &= \frac{1}{2}\left(2\Sigma - t + \sqrt{(t+2a-2\Sigma)^2 - 4b}\right), \\ u_b \equiv u_b(t) &= \frac{1}{2}\left(2\Sigma - t - \sqrt{(t+2a-2\Sigma)^2 - 4b}\right) \end{aligned} \tag{32}$$

Let us remark that we do not need any subtraction for the antisymmetric amplitude

$$\begin{aligned} \frac{F^-(s_b,t)}{s_b - u_b} &= \frac{1}{2\pi}\int_{4m_\pi^2}^\infty dt' \frac{\mathrm{Im}\, G^1(t', s'_b)}{(t'-t)(s'_b - u'_b)} \\ &\quad + \frac{1}{\pi}\int_{m_+^2}^\infty ds' \frac{\mathrm{Im}\, F^-(s', t'_b)}{(s'-s_b)(s'-u_b)}, \end{aligned} \tag{33}$$

where

$$\begin{aligned} &s'_b \equiv s_b(t'), \quad u'_b \equiv u_b(t'), \\ &t'_b = 2\Sigma - s' - \frac{b}{s'-a} + a. \end{aligned} \tag{34}$$

Whereas for the symmetric one:

$$\begin{aligned} F^+(t,b,a) &= h(b,a) + \frac{t}{\pi}\int_{4m_\pi^2}^\infty \frac{\mathrm{Im}\, G^0(t', s'_b)}{\sqrt{6}\, t'(t'-t)} dt' \\ &\quad + \frac{1}{\pi}\int_{m_+^2}^\infty ds' \frac{\mathrm{Im}\, F^+(s', t'_b)}{s'} \left(\frac{s}{s'-s} + \frac{u}{s'-u}\right). \end{aligned} \tag{35}$$

With these numbers of subtractions the convergence is fast enough so that the asymptotic amplitude contribution is relatively small (recall it starts at $t = 4\,\mathrm{GeV}^2$ and $s \simeq 3\,\mathrm{GeV}^2$ in this work). In the above equations s_b and u_b are the values of s and u that lie in the hyperbola $(s-a)(u-a) = b$ for a given value of t. Now, we want to rewrite the subtraction constant

$h(b,a)$ and for this we follow the procedure in [39,52,53]. We thus introduce the following fixed-t dispersion relation

$$F^+(s,t) = c(t) + \frac{1}{\pi}\int_{m_+^2}^{\infty} ds' \frac{\text{Im}\, F^+(s',t)}{s'^2}\left(\frac{s^2}{s'-s} + \frac{u^2}{s'-u}\right). \tag{36}$$

Note that two subtractions are needed to ensure the convergence of this fixed-t dispersion relation, due to the Pomeron contribution. Next, recall that $G^0(t,s,u) = \sqrt{6}F^+(s,t,u)$, so that by equating Eqs. (35) and (36) at $t = 0$, $b = a^2 - 2\Sigma a + \Delta^2$, the values of $c(t)$ and $h(b,a)$ are determined. Actually, Eq. (35) can be rewritten as:

$$\begin{aligned} F^+(s_b,t) = {} & 8\pi m_+ a_0^+ + \frac{t}{\pi}\int_{4m_\pi^2}^{\infty} \frac{\text{Im}\, G^0(t',s_b')}{\sqrt{6}\,t'(t'-t)}dt' \\ & + \frac{1}{\pi}\int_{m_+^2}^{\infty} ds' \frac{\text{Im}\, F^+(s',t_b)}{s'} \\ & \times \left[h(s',t,b,a) - h(s',0,b,a)\right] \\ & + \frac{1}{\pi}\int_{m_+^2}^{\infty} ds' \frac{\text{Im}\, F^+(s',0)}{s'^2} \\ & \times \left[g(s',b,a) - g(s',\Delta^2,0)\right], \end{aligned} \tag{37}$$

where

$$\begin{aligned} h(s',t,b,a) &= \frac{s'(2\Sigma - t) - 2[b - a^2 + (2\Sigma - t)a]}{s'^2 - s'(2\Sigma - t) + [b - a^2 + (2\Sigma - t)a]}, \\ g(s',b,a) &= \frac{s'(2\Sigma)^2 - 2[b - a^2 + 2\Sigma a](s' + \Sigma)}{s'^2 - s'2\Sigma + [b - a^2 + 2\Sigma a]}. \end{aligned} \tag{38}$$

We have explicitly checked that in the $a = 0$ case we recover the HDR in [39,41,52,53]. However, with our HDR above we can now choose the a parameter to maximize the applicability region of the HDR once projected into partial waves, which we will do in the next subsection.

Before finishing this subsection, a comment on the high energy region is in order. We have three different kinds of contributions above 2 GeV, the first one is $G^I(t',s_b')$, which can be calculated from Eq. (29). The second kind is the evaluation of $F^{\pm}(s',0)$: for the symmetric amplitude we just use Eq. (25), while for the anti-symmetric one we use Eq. (27). The last kind is for $F^{\pm}(s',t_b')$, which corresponds to an exotic exchange, so that its contribution is negligible.

4.2 Partial-wave hyperbolic dispersion relations

In this work we want to obtain parameterizations of the $\ell = 0, 1, 2$ partial waves which are consistent with data and the hyperbolic dispersive representation. Thus, we project Eqs. (33) and (37) into partial waves using Eq. (9) to obtain a set of Roy–Steiner-like equations:

$$\begin{aligned} g_0^0(t) = {} & \frac{\sqrt{3}}{2} m_+ a_0^+ + \frac{t}{\pi}\int_{4m_\pi^2}^{\infty} \frac{\text{Im}\, g_0^0(t')}{t'(t'-t)}dt' \\ & + \frac{t}{\pi}\sum_{\ell\geq 2}\int_{4m_\pi^2}^{\infty} \frac{dt'}{t'} G^0_{0,2\ell-2}(t,t')\text{Im}\, g^0_{2\ell-2}(t') \\ & + \frac{1}{\pi}\sum_{\ell}\int_{m_+^2}^{\infty} ds' G^+_{0,\ell}(t,s')\text{Im}\, f_\ell^+(s'), \\ g_1^1(t) = {} & \frac{1}{\pi}\int_{4m_\pi^2}^{\infty} \frac{\text{Im}\, g_1^1(t')}{t'-t}dt' \\ & + \frac{1}{\pi}\sum_{\ell\geq 2}\int_{4m_\pi^2}^{\infty} dt' G^1_{1,2\ell-1}(t,t')\text{Im}\, g^1_{2\ell-1}(t') \\ & + \frac{1}{\pi}\sum_{\ell}\int_{m_+^2}^{\infty} ds' G^-_{1,\ell}(t,s')\text{Im}\, f_\ell^-(s'), \\ g_2^0(t) = {} & \frac{t}{\pi}\int_{4m_\pi^2}^{\infty} \frac{\text{Im}\, g_2^0(t')}{t'(t'-t)}dt' \\ & + \frac{t}{\pi}\sum_{\ell\geq 2}\int_{4m_\pi^2}^{\infty} \frac{dt'}{t'} G^0_{2,4\ell-2}(t,t')\text{Im}\, g^0_{4\ell-2}(t') \\ & + \frac{1}{\pi}\sum_{\ell}\int_{m_+^2}^{\infty} ds' G^+_{2,\ell}(t,s')\text{Im}\, f_\ell^+(s'). \end{aligned} \tag{39}$$

The explicit expressions of the $G^I_{\ell\ell'}(t,t')$, $G^{\pm}_{\ell\ell'}(t,s')$ integration kernels are given in Appendix B. Since so far in this work we have left free the a parameter, we can now use it to maximize the applicability of the equations right above. Note there are constraints coming from the applicability of the HDR in Eqs. (33) and (37) as well as from the convergence of the partial-wave expansion. As shown in Appendix D, by setting $a = -10.8 m_\pi^2$ the applicability range of these equations is $-0.286\,\text{GeV}^2 \leq t \leq 2.19\,\text{GeV}^2$. In other words, we can study the physical region from the $K\bar{K}$ threshold $\simeq 0.992$ GeV up to $\simeq 1.47$ GeV. In contrast, the usual HDR projected into partial waves are only valid up to $\simeq 1.3$, GeV. Thus, with our choice of a, the applicability of the dispersive approach in the physical region, where we can test or use data as input, has been extended by 55% in terms of the $\sqrt{t}$ variable, or 67% in terms of t.

As can be directly seen in Eq. (39) the $g_1^1(t)$ partial wave does not have any scattering length as input parameter and its dominant contribution to the integral comes from its own imaginary part. Since it is not subtracted, the Regge contribution is not negligible, but we have already attached a conservatively large uncertainty to its residue and we will see that it barely changes when using the dispersive representation as a constraint on data. In the case of even partial waves, one subtraction is necessary to ensure the convergence, and hence the output is always influenced by the scattering lengths coming from πK scattering. In this work we fix them to the values obtained in [18], which are also compatible with the Roy–Steiner prediction in [27]. As already

commented, an important advantage of using HDR with the smaller possible number of subtractions is to decouple odd and even partial waves. For example in [27] the Roy–Steiner equation for g_0^0 uses g_1^1 as input.

Finally, we want to remark that, as usual, the high energy part of the integrals in Eq. (39) is obtained by projecting into the corresponding partial-wave the high-energy part of the integrals in Eqs. (33) and (37), where Regge theory was used as input as explained in previous sections.

4.3 The unphysical region and the Muskhelishvili–Omnès problem

As can be observed in Eq. (39), the integration region actually starts at $\pi\pi$ threshold. This means that the integrals extend over an "unphysical" regime where $\pi\pi \to K\bar{K}$ scattering does not occur and thus cannot be described with data parameterizations. Nevertheless, below $K\bar{K}$ threshold the inelasticity to more than two-pion states is completely negligible. Since $\pi\pi$ is the only available state in that region Watson's Theorem implies that the $g_\ell^{I_t}$ phase below $K\bar{K}$ threshold is just that of $\pi\pi$ scattering and thus we write $\phi_\ell^{I_t}(t) = \delta^{I_t}_{\ell,\pi\pi\to\pi\pi}(t)$. Note that Watson's Theorem does not provide any direct information on $|g_\ell^{I_t}|$. But once the phase is known, determining the modulus in the unphysical region is nothing but the standard Muskhelishvili–Omnès problem [66,67], that we describe next following similar steps as in [27–29,39,52]. Recalling that partial waves have a right- and left-hand cut we can re-write Eq. (39) as follows:

$$\begin{aligned} g_\ell^0(t) &= \Delta_\ell^0(t) + \frac{t}{\pi}\int_{4m_\pi^2}^{\infty} \frac{dt'}{t'}\frac{\mathrm{Im}\, g_\ell^0(t)}{t'-t}, \quad \ell = 0, 2, \\ g_1^1(t) &= \Delta_1^1(t) + \frac{1}{\pi}\int_{4m_\pi^2}^{\infty} dt' \frac{\mathrm{Im}\, g_1^1(t)}{t'-t}, \end{aligned} \tag{40}$$

where the $\Delta_\ell^I(t)$ contain the left-hand cut contributions and subtraction terms. Note that $\Delta_\ell^I(t)$ does not depend on g_ℓ^I itself, but on other $g_{\ell'}^I$ with $\ell' \geq \ell + 2$, which in the unphysical region are much more suppressed than g_ℓ^I, due to the centrifugal barrier.

Now we define the Omnès function

$$\Omega_\ell^I(t) = \exp\left(\frac{t}{\pi}\int_{4m_\pi^2}^{t_m} \frac{\phi_\ell^I(t')dt'}{t'(t'-t)}\right), \tag{41}$$

which satisfies

$$\Omega_\ell^I(t) \equiv \Omega_{l,R}^I(t) e^{i\phi_\ell^I(t)\theta(t-4m_\pi^2)\theta(t_m-t)}, \tag{42}$$

where, in the real axis, $\Omega_{l,R}^I(t)$ can be written as:

$$\begin{aligned} \Omega_{l,R}^I(t) = &\left|\frac{t_m}{t_\pi}(t-t_\pi)^{-\phi_\ell^I(t)/\pi}(t_m-t)^{\phi_\ell^I(t)/\pi}\right| \\ &\times \exp\left(\frac{t}{\pi}\int_{4m_\pi^2}^{t_m} dt' \frac{\phi_\ell^I(t') - \phi_\ell^I(t)}{t'(t'-t)}\right). \end{aligned} \tag{43}$$

In the real axis, $\Omega_{l,R}^I$ is nothing but the modulus of Ω_l^I and therefore a real function.

Note that from $4m_\pi^2$ to t_m the Omnés function has the same cut as $g_\ell^I(t)$. Thus, we can define a function

$$F_\ell^I(t) = \frac{g_\ell^I(t) - \Delta_\ell^I(t)}{\Omega_\ell^I(t)}, \tag{44}$$

which is analytic except for a right hand cut starting at t_m. Hence we can write dispersion relations for $F_\ell^I(t)$, which in terms of $g_\ell^I(t)$ read:

$$\begin{aligned} g_0^0(t) = &\Delta_0^0(t) + \frac{t\Omega_0^0(t)}{t_m - t} \\ &\left[\alpha + \frac{t}{\pi}\int_{4m_\pi^2}^{t_m} dt' \frac{(t_m-t')\Delta_0^0(t')\sin\phi_0^0(t')}{\Omega_{0,R}^0(t')t'^2(t'-t)}\right. \\ &\left. + \frac{t}{\pi}\int_{t_m}^{\infty} dt' \frac{(t_m-t')|g_0^0(t')|\sin\phi_0^0(t')}{\Omega_{0,R}^0(t')t'^2(t'-t)}\right], \end{aligned} \tag{45}$$

$$\begin{aligned} g_1^1(t) = &\Delta_1^1(t) + \Omega_1^1(t)\left[\frac{1}{\pi}\int_{4m_\pi^2}^{t_m} dt' \frac{\Delta_1^1(t')\sin\phi_1^1(t')}{\Omega_{1,R}^1(t')(t'-t)}\right. \\ &\left. + \frac{1}{\pi}\int_{t_m}^{\infty} dt' \frac{|g_1^1(t')|\sin\phi_1^1(t')}{\Omega_{1,R}^1(t')(t'-t)}\right], \end{aligned} \tag{46}$$

$$\begin{aligned} g_2^0(t) = &\Delta_2^0(t) + t\Omega_2^0(t)\left[\frac{1}{\pi}\int_{4m_\pi^2}^{t_m} dt' \frac{\Delta_2^0(t')\sin\phi_2^0(t')}{\Omega_{2,R}^0(t')t'(t'-t)}\right. \\ &\left. + \frac{1}{\pi}\int_{t_m}^{\infty} dt' \frac{|g_2^0(t')|\sin\phi_2^0(t')}{\Omega_{2,R}^0(t')t'(t'-t)}\right]. \end{aligned} \tag{47}$$

When t lies in the real axis above the $\pi\pi$ threshold, a principal value must be understood on each integral. In addition, between $\pi\pi$ threshold and t_m on the left hand sides the amplitude is reduced to its modulus (since by construction the Omnés function removes the phase), whereas above t_m it is reduced to its real part.

Since in the next sections we will choose t_m with $\phi_0^0(t_m) \geq \pi$ we have introduced one subtraction for the $g_0^0(t)$ Omnès solution in order to ensure the convergence when $t \to t_m$. The subtraction constant α will be obtained by imposing numerically a no-cusp condition on t_m for $g_0^0(t)$.

The interest of these equations is that for a given $g_\ell^I(t)$, the integrals *in the unphysical region* only make use of the phases and the Δ_ℓ^I. But thanks to Watson's Theorem the former are known from $\pi\pi$ scattering, which we take from the dispersive analysis of [17], and the latter do not involve $g_\ell^I(t)$ itself, but

only partial waves with $\ell' - \ell \geq 2$. These higher partial waves are suppressed in the unphysical region with respect to that with ℓ. We also need input from $K\pi$ scattering that is known and we take it from our recent dispersive data analysis in [18]. Thus we can directly solve $g_1^1(t)$ and $g_2^0(t)$, for which we have explicitly checked that the $\ell = 3$ and $\ell = 4$ contributions are small and negligible, respectively. Once we have $g_2^0(t)$ we can use it as input to solve Eq. (45) for $g_0^0(t)$.

It is worth noticing here that, in purity, for the Regge contributions to $\Delta_\ell^I(t)$, one has to subtract the projection of the Regge amplitude itself into the desired I, ℓ partial wave. Fortunately this projection is negligible, and our solutions do not depend on this procedure.

We still have to discuss the choice of t_m, which is always above the $K\bar{K}$ threshold. It is important to recall that the derivation of the above equations implies that $g_{output}(t_m) = g_{input}(t_m)$. This condition will always be forced into the output no matter if the data at that energy is in good or bad agreement with dispersion relations. If the data at that energy region were not close to the dispersive solution, the output would be forced to describe it and the result could be strongly distorted in other regions. In particular the g_0^0 wave is the most sensitive to this instability, the effect is more moderate on the g_2^0 and negligible for the g_1^1 because it is already very consistent for any t_m choice. Thus, we have studied what energy region is the most consistent for g_0^0 when changing t_m and we have found that there are two regions that yield systematically rather consistent results between input and output: one around $\sqrt{t_m} = 1.2\,\text{GeV}$, which is also valid for g_2^0, and another one around $\sqrt{t_m} = 1.47\,\text{GeV}$. However, if we chose the latter, we find that the uncertainty in the dispersive result between $K\bar{K}$ and 1.2 GeV is so large that there is no dispersive constraint in practice, having larger uncertainties could even produce both $g_0^0(t)$ solutions to be compatible between them. Moreover by looking at Eqs. (45), (46) and (47) one can notice that t_m marks the energy above which $|g_\ell^I|$ is used as input for its own equation. Since we are actually trying to test the data parameterizations, within our approach we would like to maximize that region and choose the smaller possible t_m. All in all, we have made the final choice $\sqrt{t_m} = 1.2\,\text{GeV}$ for all partial waves. This is a point above $K\bar{K}$ threshold where there are no cusps coming from the two most important inelasticities ($K\bar{K}$, $\eta\eta$). In particular, the g_2^0 is well controlled at this energy since its largest contribution comes from the $f_2(1270)$, a very well-known resonance very close to t_m.

5 Consistency check of unconstrained fits

In order to study in a systematic way the consistency of the unconstrained data parameterizations of Sect. 3 with respect to dispersion relations, we first define a "distance-square"

$$d^2 = \frac{1}{N}\sum_{i=1}^{N}\left(\frac{d_i}{\Delta d_i}\right)^2, \tag{48}$$

for each dispersion relation. Note its similarity to a χ^2/dof function, although we are still not fitting or imposing the dispersion relations. Here d_i is the difference between the "input" and "output" of each dispersion relation at the energy $\sqrt{t_i}$. We use thirty energy points $\sqrt{t_i}$ equally spaced from threshold up to 1.47 GeV. In addition, Δd_i is the uncertainty in the d_i difference, which is obtained by varying the parameters of our unconstrained fits to data (UFD) within their errors.

As we explained before, Eqs. (45), (46), (47) yield the modulus of the partial wave below t_m and the real part above. However, in order to simplify our plots and calculations, we will just display the modulus. In particular by "input" we will understand the modulus of the partial wave on the left hand side of Eqs. (45), (46), (47), i.e. as obtained directly from our fits. Similarly, by "output" we will always mean the modulus of the dispersive representation. Note that for $t < t_m$ this modulus is obtained from the right hand side of those equations with principal values on each integral. However, for $t > t_m$ only the real part is obtained from the integrals and the modulus is reconstructed by adding the imaginary part from the direct parameterizations.

With the above definition we can study the consistency of each partial-wave dispersion relation. It will be well satisfied on the average if its corresponding $d^2 \leq 1$. In case of disagreement it is also relevant to check whether it comes from a particular energy region and for this we will show figures comparing the input and output as a function of $\sqrt{t}$.

5.1 g_1^1 UFD check

Let us study first the consistency of g_1^1. We see in Eq. (46) that its partial wave dispersion relation is decoupled from even partial waves. The highest partial wave we have considered in Δ_1^1 is the $\ell = 3$ contribution. Actually, by using the simple model dominated by the $\rho(1690)$ resonance described in Sect. 3.2.4, we have explicitly checked that its contribution is very small and barely affects our results for g_1^1 below 1.47 GeV.

As can bee seen in Fig. 5 the dispersion relation in Eq. (46) is remarkably well satisfied, with a total $d^2 = 1$. Such a nice agreement was expected since it has a large contribution from the $\rho(770)$ that dominates $\pi\pi$ scattering in this channel below $K\bar{K}$ threshold, and our input from [18] is already consistent with $\pi\pi$ data and dispersion relations. Let us now recall that the $\pi\pi \to K\bar{K}$ data we use as input show large uncertainties and fluctuations (see Fig. 1). Our UFD description does not follow visually all these fluctuations but, roughly speaking, it averages them and rises softly and

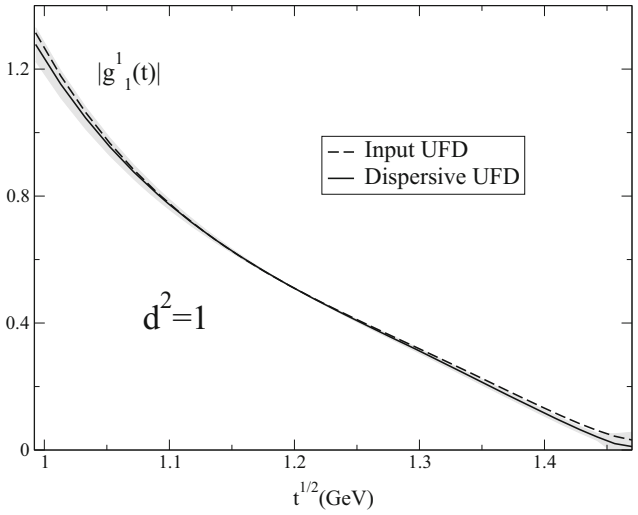

Fig. 5 Comparison between the input (dashed line) and the dispersive output (continuous line) for the modulus of the g_1^1 dispersion relation in Eq. (46). The gray band covers the uncertainty of the difference

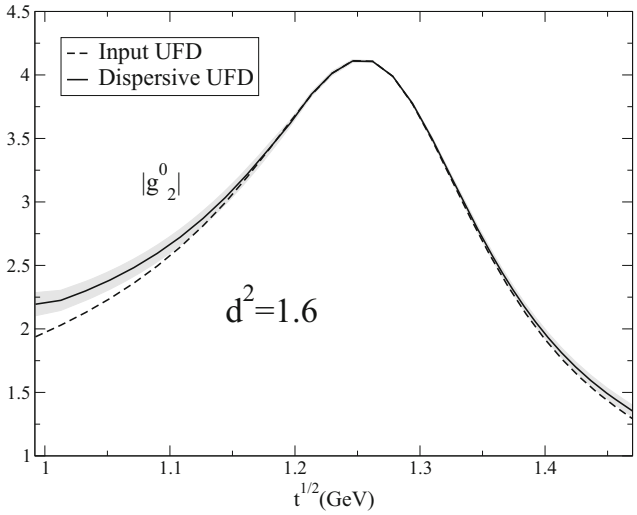

Fig. 6 Comparison between the input (dashed line) and the dispersive output (continuous line) for the modulus of the g_2^0 dispersion relation in Eq. (47) using as input the UFD set. The gray band covers the uncertainty of the difference

monotonously. Still, our UFD is remarkably consistent with the dispersive representation. Actually we have checked that parameterizations with more oscillations may describe the central values of the data points better, but satisfy worse the dispersive representation than our UFD fit. In the $\pi\pi \to K\bar{K}$ physical region we had also included resonant shapes for the ρ' and ρ'' resonances in our UFD. As seen from our results, the parameters and shape of the ρ', which for a good part lies within the applicability region of our equations, are fairly consistent with dispersion relations. As commented in Sect. 3.2.1 the ρ'' was used just as a simple form to parameterize the amplitude at energies beyond the reach of our dispersive representation where scattering data do not exist.

One could also be worried that, since the g_1^1 dispersion relation has no subtractions, it may require some tuning on the Regge asymptotics and the λ parameter we estimated with the Veneziano model and degeneracy in Sect. 3.3. However the nice fulfillment of the dispersion relation yields strong support for our λ estimations.

5.2 g_2^0 UFD check

In the case of the $g_2^0(t)$ dispersion relation, Eq. (47), it involves even partial waves with $\ell \geq 4$, but they are almost negligible below 2 GeV. As seen in Fig. 6, when using the UFD parameterizations, the $g_2^0(t)$ dispersion relation is clearly not well satisfied right above $K\bar{K}$ threshold and this incompatibility fades away near 1.1 GeV. At threshold, the deviation is $\simeq 3\sigma$. Very naively one could have expected this region to be dominated by the $f_2(1270)$ resonance tail, since the threshold is merely 1.5 widths away from the resonance peak. However, if one tries to use a simple Breit–Wigner description instead of our UFD parameterization, then $d^2 \geq 6$. Thus, such naive expectation does not hold, which justifies the elaborated form of our parameterization in Eq. 14. Nevertheless, there is still room for improvement that will be achieved when imposing the dispersion relations as constraints in Sect. 6.

5.3 g_0^0 UFD check

Finally, for the scalar-isoscalar dispersion relation in Eq. (45), we need both the $g_0^0(t)$ and $g_2^0(t)$. In this case, partial waves with $\ell \geq 4$ are totally negligible below 2 GeV. In Fig. 7 we show the results of the $g_0^0(t)$ dispersion relation when using either the UFD_B or UFD_C parameterizations as input. In both cases the agreement is poor, particularly due to the results in the region 10–20 MeV above $K\bar{K}$ threshold, where the dispersive solution increases rapidly. This feature is common to both the UFD_B and UFD_C and is due to the influence of the $f_0(980)$. The respective $d^2 = 5.6$ and $d^2 = 2.7$ are dominated by this near threshold region. There is a clear need for improvement, that we will achieve by imposing dispersion relations as constraints in the next section, although in both cases the disagreement in the region very near threshold will linger on. However, we will see that for both solutions a very good consistency with dispersion relations can be achieved except for the very near threshold region.

Finally, let us remark that the g_0^0 partial-wave dispersion relation in Eq. (45) depends on the πK scattering length a_0^+. We have checked that the dispersion relation would be better satisfied if we used a somewhat lower value of a_0^+ than that obtained in our previous work [18] (which was also compatible with Roy–Steiner determinations [27]). Since in this work we are considering πK scattering amplitudes as

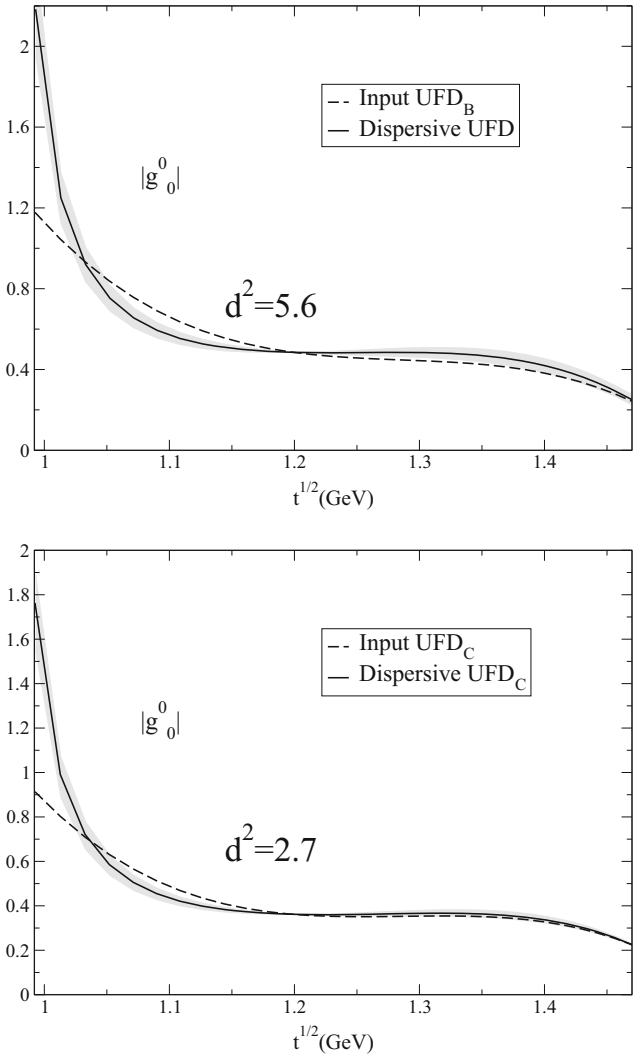

Fig. 7 Comparison between the input (dashed line) and the dispersive output (continuous line) for the modulus of the g_0^0 dispersion relation in Eq. (45). In the upper panel we show the results using as input the UFD_B parameterization and in the lower panel those from the UFD_C. The gray bands cover the uncertainty of the difference between the input and the respective dispersive result

fixed input, we keep the value from the πK constrained fit, but this result could be relevant for future re-analysis of πK scattering data.

6 Constrained fits to data

Therefore, we have just seen that the data on the g_2^0 and even more so on the g_0^0 do not satisfy very well the dispersive representation. There is clear room for improvement. Thus, in this section we will impose the dispersion relations in Eqs. (45), (46), (47) as constraints of the fits. In this way we will obtain a set of constrained fits to data (CFD) which fulfillment of the dispersive representation will be much improved. In this section we use the same functional forms for the amplitudes that we used in Sect. 3, but the parameters change from the UFD to the CFD sets. In general the difference between the UFD and CFD parameters is small, with a few exceptions. Nevertheless, due to large correlations in the parameters, even if some CFD parameters deviate from the UFD set, the resulting UFD and CFD curves are typically consistent with one another at the 1 or 1.5 σ level. Only for the constrained analysis of the UFD_C, the CFD_C g_0^0 partial wave deviates by about 2 σ in the region from 1.25 to 1.45 GeV, but it still compatible with the upper error bars of the data. Hence the CFD description of data is still rather good.

To minimize the discrepancy between the fit used as input in the dispersion relation and the output obtained from the dispersion relation, without deviating much from the data, one first defines a χ^2-like function

$$W_1^2 d^2_{g_\ell^I} + \frac{W_2^2}{N}\sum_k^N \left(\frac{|g_\ell^I|_{exp,k} - |g_\ell^I(s_k)|}{\delta|g_\ell^I|_{exp,k}}\right)^2 + \frac{W_3^2}{N'}\sum_k^{N'} \left(\frac{(\phi_\ell^I)_{exp,k} - \phi_\ell^I(s_k)}{\delta(\phi_\ell^I)_{exp,k}}\right)^2, \tag{49}$$

where $|g_\ell^I|_{exp,k}$, $(\phi_\ell^I)_{exp,k}$ are the experimental values of the kth data point for the modulus and the phase, respectively, and $\delta|g_\ell^I|_{exp,k}$, $\delta(\phi_\ell^I)_{exp,k}$ are their corresponding errors. The weights W_1^2, $W_2^2 = W'^2 N/(N+N')$, $W_3^2 = W'^2 N'/(N+N')$ are used to roughly take into account the degrees of freedom needed to parameterize the curves that describe the modulus and the phase. For simplicity we have chosen the same $W_1^2 = 5$ and $W'^2 = 12$ value for all partial waves as an average value of their degrees of freedom. Note that we actually minimize the sum of this function over the three partial waves of interest $(I,\ell) = (0,0), (1,1)$ and $(0,2)$. In addition, recall that, as explained in Sect. 3.2.2, we have added two points to the χ^2-function to take into account the experimental mass of the f_2 and f_2' resonances.

Let us remark that in previous works our procedure was slightly different: we defined a similar χ^2-like function but in terms of the unconstrained fit parameters, which were not allowed to vary much from their unconstrained best values. In contrast, in Eq. (49) we define our χ^2-like function directly in terms of data, not the unconstrained fit parameters. The reason is that in this work the onset of Regge parameterizations is 2 GeV and thus we use our partial-wave parameterizations to describe data from $K\bar{K}$ threshold up to 2 GeV. However, the dispersion relations are only applicable up to 1.47 GeV. If we constrained only the fit parameters with the dispersion relations, which affect only the lower-energy data, we would obtain large artificial deviations in the description of the higher-energy data. With the procedure we use here, and contrary to what happened in previous works, if

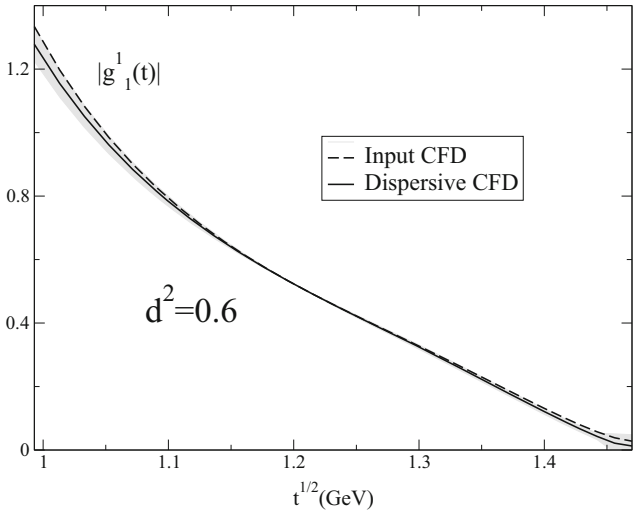

Fig. 8 Comparison of the modulus and the dispersion relation after the minimization procedure. The gray band covers the uncertainty of the difference between the input and dispersive results

there are some strongly correlated parameters, we can see that their constrained values can deviate appreciably from their unconstrained best values but still the constrained and unconstrained curves look very similar. As the uncertainty variation is of second order, and parameters that are not compatible with old values deviate by a small number of sigmas at most, we still maintain their uncertainties as they are a reliable and almost unchanged estimate of the error, as one can see in the final uncertainty band plotted in the figures for the CFD parameterizations.

6.1 Constrained $g_1^1(t)$ partial wave

Let us recall that the UFD $I = 1, \ell = 1$ wave from $K\bar{K}$ threshold up to 1.47 was already consistent with the dispersive representation. By imposing our dispersion relations d^2 decreases just from 1 to 0.6. The difference between the constrained input and dispersive output for the g_1^1 wave can be seen in Fig. 8.

Actually, as seen in Fig. 9 imposing the dispersive constraints barely changes this wave, i.e. the UFD and CFD curves are almost indistinguishable both for the modulus and the phase of g_1^1. Note also that, as shown in Fig. 10, the dispersive CFD output perfectly describes the data. In that Figure we also show the CFD modulus in the unphysical region and the continuous matching at threshold.

The new CFD parameters can be found in Table 1 where it can be checked that the CFD values are remarkably consistent with the UFD ones: only two are beyond one standard deviation but not more than $2\,\sigma$. As we are using a non-subtracted HDR to study the odd angular momentum partial waves, the small improvement in the description of this partial wave comes mostly from the slight variation of the Regge parameters. Nevertheless, as it can be seen in Table 7, our CFD result for the λ Regge parameter is compatible with its UFD value, thus supporting the degeneracy between the ρ and K^* families.

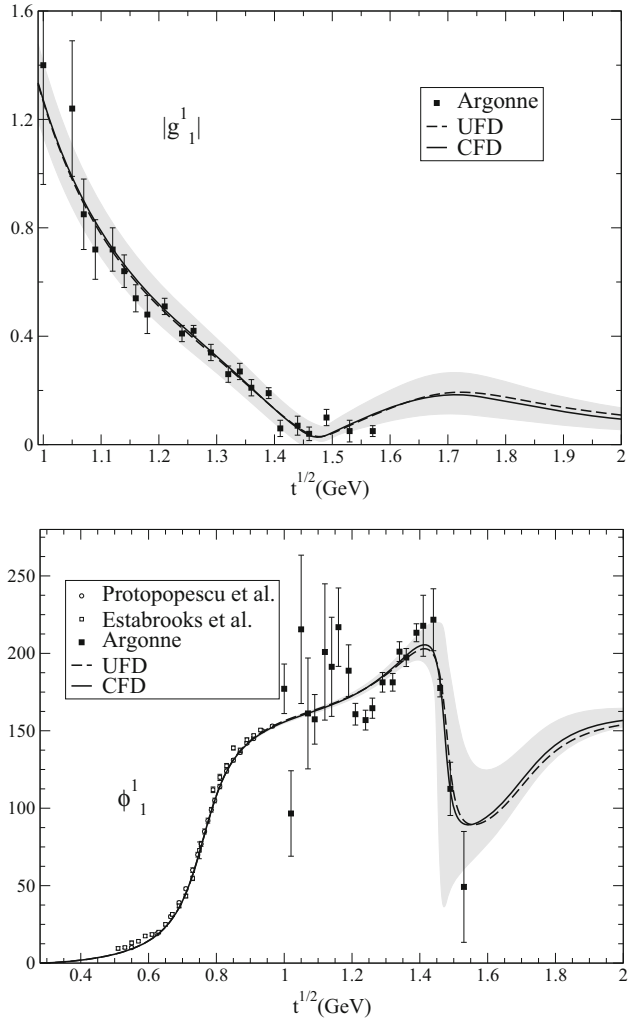

Fig. 9 Modulus and phase of the $g_1^1(t)$ $\pi\pi \to K\bar{K}$ partial wave. The continuous line and the uncertainty band corresponds to the CFD whereas the dashed line corresponds to the UFD. The white circles and squares come from the $\pi\pi$ scattering experimental analyses of Protopopescu et al. [2] and Estabrooks et al. [4], respectively.

It is worth noticing that, as we are using no subtractions, the value of the $\pi\pi \to K\bar{K}$ amplitude at $t = 0$, $b = \Delta^2$ can be related to the a_0^- $\pi K \to \pi K$ scattering length $a_0^- = (a^{1/2} - a^{3/2})/3$, using Eq. (33), to obtain the following sum rule [27,68]:

$$\frac{8\pi m_+ a_0^-}{m_+^2 - m_-^2} = \frac{1}{2\pi}\int_{4m_\pi^2}^{\infty} \frac{dt'}{t'} \frac{\mathrm{Im}\, G^1(t', s'_{\Delta^2})}{\sqrt{(t'-4m_\pi^2)(t'-4m_K^2)}} + \frac{1}{\pi}\int_{m_+^2}^{\infty} ds' \frac{\mathrm{Im}\, F^-(s', t'_{\Delta^2})}{\lambda_{s'}} \tag{50}$$

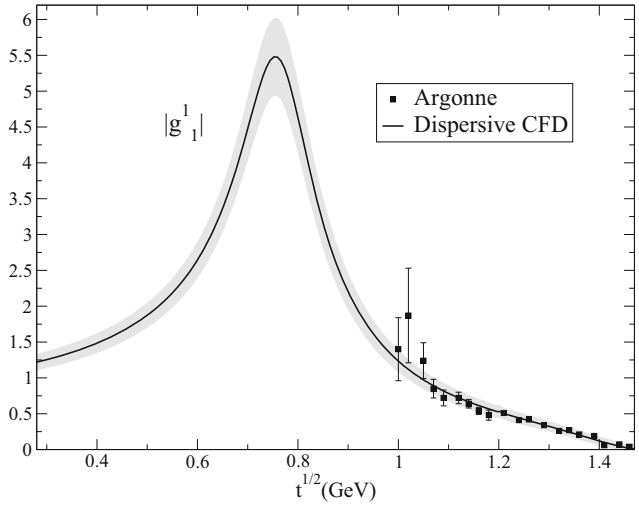

Fig. 10 Dispersive output for the modulus of the $g_1^1(t)$ $\pi\pi \to K\bar{K}$ partial wave obtained from the CFD set. The continuous line and the uncertainty band corresponds to the CFD dispersive result

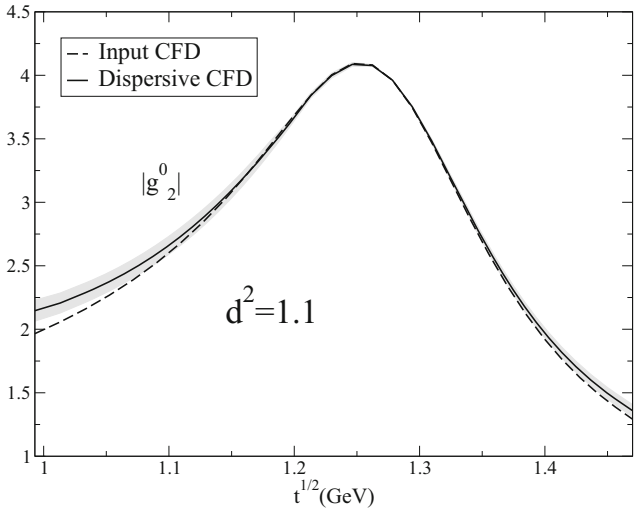

Fig. 11 Comparison between the input (dashed line) and the dispersive output (continuous line) for the modulus of the g_2^0 dispersion relation in Eq. (47) using as input the CFD set. The gray band covers the uncertainty of the difference

Note that the scattering length results from the integration over both $\pi K \to \pi K$ and $\pi\pi \to K\bar{K}$ channels. Using as input for G^1 our constrained parameterizations just calculated and our the CFD parameterizations for $K\pi$ scattering in [18], we find

$$m_\pi(a^{1/2} - a^{3/2}) = 0.249 \pm 0.032, \quad \text{(sum rule+CFD)}. \tag{51}$$

To be compared with

$$m_\pi(a^{1/2} - a^{3/2}) = 0.251 \pm 0.014, \quad \text{(sum rule in [20])}$$

obtained in [27] using this same sum rule with their unconstrained input from $\pi\pi \to K\bar{K}$ and the $K\pi$ solutions from their Roy–Steiner analysis of $K\pi$. We obtain a larger uncertainty since we use the Regge asymptotics from 2 GeV instead of 2.5 GeV as in [27] and because, in contrast to [27], we also include uncertainties in all partial-waves.

Those two values obtained using the sum rule can also be compared with direct calculations from the $K\pi$ amplitudes:

$$m_\pi\left(a^{1/2} - a^{3/2}\right) = 0.273^{+0.018}_{-0.015}, \quad \text{(CFD [14])}$$
$$m_\pi\left(a^{1/2} - a^{3/2}\right) = 0.269^{+0.015}_{-0.015}. \quad \text{(Roy–Steiner [20])}.$$

The first is obtained from our recent dispersive analysis using Forward Dispersion Relations as constraints on fits to $K\pi$ data [18] and the second from the solutions of Roy–Steiner equations in [27].

6.2 Constrained $g_2^0(t)$ partial wave

For this wave the agreement was not as good as for the $I = 1$ and $\ell = 1$ partial wave, particularly in the threshold region.

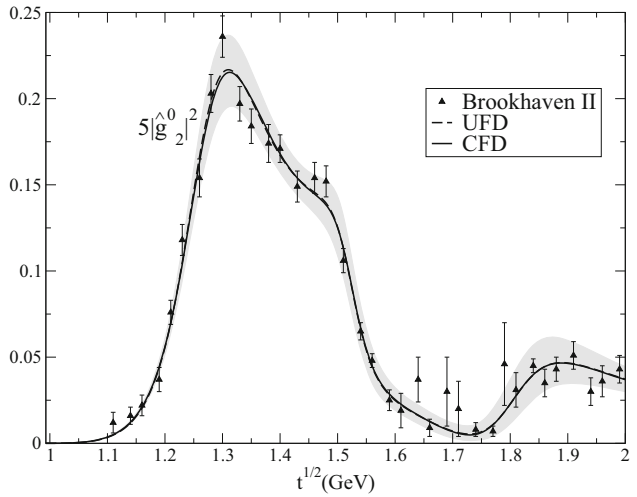

Fig. 12 The continuous line is our final CFD parameterization of the data on the modulus of $\hat{g}_2^0(t)$ from the Brookhaven-II analysis [9]. The gray band stands for the uncertainty from the CFD parameters.The dashed line is the UFD parameterization. The difference between the UFD and CFD parameterization near threshold is imperceptible due to the q^5 factor

After minimization the overall agreement has improved considerably, from $d^2 = 1.6$ down to 1.1. However, as seen in Fig. 11, our CFD parameterization still shows some small discrepancy with its dispersive output near threshold, although the deviation has improved substantially in that region compared to the unconstrained case.

This improvement is achieved without changing much the CFD parameterization with respect to the UFD. The CFD parameters change little from their previous UFD values, as seen in Table 2. In addition, in Fig. 12 we can see that the deviations from the UFD to the CFD modulus are almost

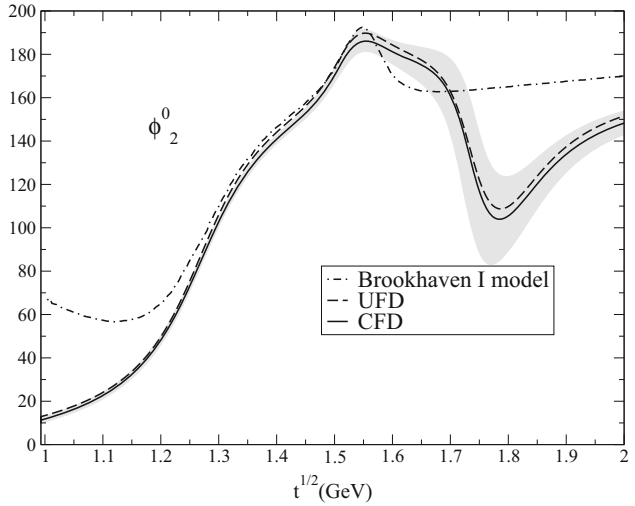

Fig. 13 Comparison between the UFD and CFD g_2^0 phases obtained with a model including an $f_2(1810)$ resonance and the one obtained with the Brookhaven model without it, using a flat background

imperceptible. There are some differences near threshold but, unfortunately, when plotting the modulus together with data, the resulting curves look almost identical due to a $q(s)^5$ factor. In contrast, we can see in Fig. 13 some small difference between the UFD and CFD phase ϕ_2^0. This change is actually the one mostly responsible for the improvement in the d^2.

We have also checked that the values obtained at the $K\bar{K}$ threshold still fulfill Watson's Theorem when using the $\pi\pi$ scattering values obtained from dispersion relations [17,62]. One should be careful not to force too much the fit in the threshold region because, as commented in the UFD case, this could spoil the $f_2(1270)$ mass, which is very well established from different experiments, not just scattering. That is why we considered the f_2 and f_2' masses as additional data points when fitting the $\pi\pi \to K\bar{K}$ data. We have also added this extra contribution when minimizing the χ^2 to obtain the CFD set.

We have tried different parameterizations, including additional flexibility upon Breit–Wigner-like parameterizations, but we have not been able to find a solution that satisfies better the dispersion relation near threshold without spoiling severely the data description.

Finally, let us note that this dispersion relation has some sensitivity to πK scattering, in particular to the scalar partial wave. A more thorough study would require allowing the πK scattering amplitude to vary when imposing the hyperbolic dispersion relations as constraints, but that is well beyond the scope of this work dedicated to $\pi\pi \to K\bar{K}$, where we have taken πK scattering as fixed input.

6.3 Constrained $g_0^0(t)$ partial wave

The scalar partial wave g_0^0 is the most interesting in this work, given that we are dealing with two incompatible sets of experimental data for the modulus and also because neither of them are consistent with the dispersive representation.

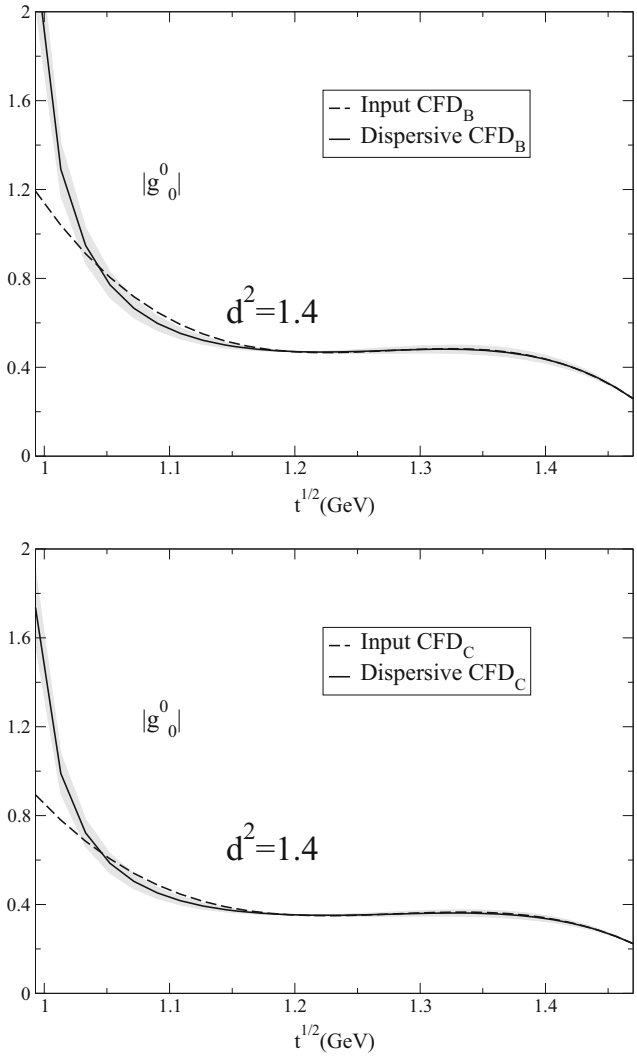

Fig. 14 Comparison between the input (dashed line) and the dispersive output (continuous line) for the modulus of the g_0^0 dispersion relation in Eq. (45). In the upper panel we show the results using as input the CFD_B parameterization and in the lower panel those from the CFD_C. The gray bands cover the uncertainty in the difference between the input and dispersive results. By comparing with Fig. 7 we see that the fulfillment of the dispersion relation by the CFD set has improved considerably with respect to the UFD parameterization. Also, there is no significant difference in the consistency of the CFD_B and CFD_C sets

As seen in Sect. 3, on the one hand we have the Brookhaven-II [9] data and, on the other hand, the data of Brookhaven-I [8] and Argonne [7]. From these two sets we obtained the UFD_B and UFD_C parameterizations, respectively. For the phase we had a single UFD parameterization. Let us recall that the overall UFD_C agreement with its dispersive output up to 1.47 GeV is poor, with $d^2 = 2.7$, whereas the UFD_B is even more inconsistent with $d^2 = 5.6$. In that respect the UFD_B parameterization may seem disfavored.

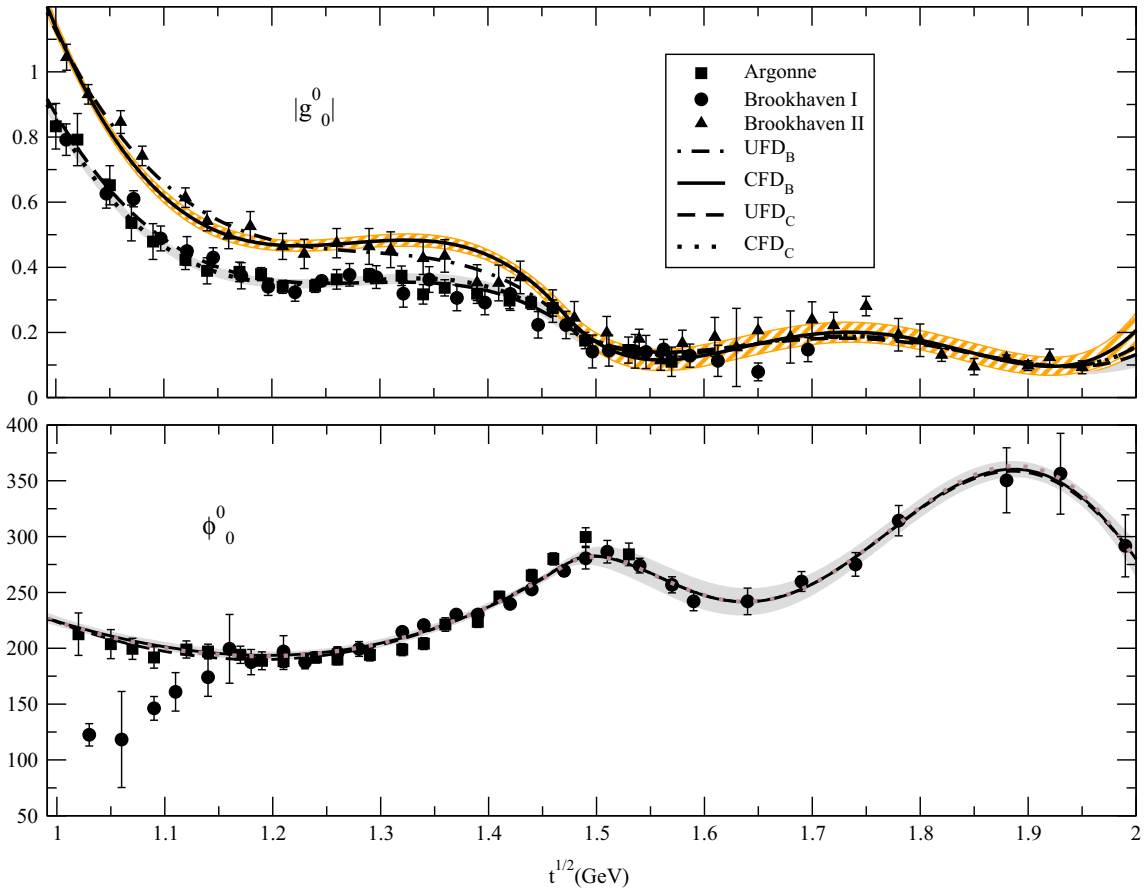

Fig. 15 Comparison between the UFD and CFD parameterizations for $g_0^0(t)$. The bands cover the uncertainties of the CFD solutions. Upper panel: modulus of the scalar-isoscalar $\pi\pi \to K\bar{K}$ scattering. The dotted line represents the CFD combined fit while the continuous line represents the CFD fit to the Brookhaven-II data only. The only significant change is in the 1.25–1.45 GeV between UFD_B to CFD_B. Lower panel: scalar-isoscalar phase for $\pi\pi \to K\bar{K}$ scattering. Note that the UFD, CFD_B and CFD_C phases are almost indistinguishable

However, the UFD_C modulus is clearly incompatible with the value that would be obtained from the inelasticity of $\pi\pi$ scattering obtained from dispersion relations [17] assuming two coupled channels, $\pi\pi$ and $K\bar{K}$. For that reason we will study here both UFD_B and UFD_C and will obtain a fit to each data set constrained with our dispersion relation in Eq. (45). We will see that after this process both constrained solutions will be equally acceptable with respect to their consistency regarding dispersion relations.

Let us note that we now use as input the g_2^0 CFD parameterization obtained in the previous subsection. The consistency test of the constrained g_0^0 results can be found in Fig. 14. It can be seen that we obtain an equally good consistency for both the CFD_B and CFD_C parameterizations except for the region very close to threshold. The behavior in this region is controlled by the $f_0(980)$ shape in the elastic region of $\pi\pi$ scattering and thus is out of the scope of this work, since we consider it input. The rest of the energy region up to 1.47 GeV has values of d^2 below one.

In Fig. 15 we also compare both CFD parameterizations against their respective UFD parameterizations and the data. There one can see that the UFD and CFD phases are almost identical, except in the 1.1–1.2 GeV region where the CFD is higher by more than one standard deviation, and in the 1.9 GeV region where the CFD phase is again higher but well within uncertainties. Actually there are two CFD_B and CFD_C phases but they are totally indistinguishable.

Concerning the modulus, the UFD_C and CFD_C are compatible, whereas the CFD_B is slightly lower than the UFD_B in the 1.05–1.15 region, but clearly higher in the 1.3–1.45 region. These differences go above the 2-σ level, so that they lie still reasonable close to the data, but prefer to cross the top of the experimental uncertainty bars.

Note that the "dip" structure in the inelasticity from $\pi\pi$ scattering occurs around 1.1 GeV, whereas the biggest difference between the in UFD_B and the CFD_B is found above 1.25 GeV, so that we conclude that such a dip is not the cause of the deviation for the UFD_B set. The dip structure favored by $\pi\pi$ scattering dispersive analyses can therefore be accommodated also with the hyperbolic dispersive representation of $\pi\pi \to K\bar{K}$.

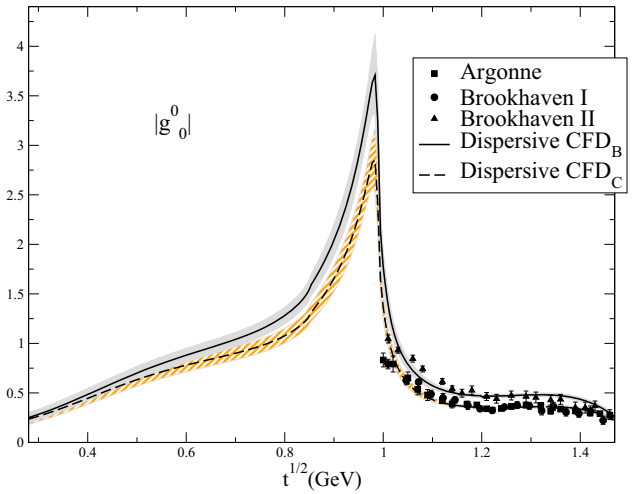

Fig. 16 Dispersive output for the modulus of the $g_0^0(t)$ $\pi\pi \to K\bar{K}$ partial wave obtained from the CFD sets. Note how they differ also below the $K\bar{K}$ threshold

Therefore we conclude that the data most commonly used in the literature (Argonne [7]) is not necessarily the only acceptable solution and that one does not have to ignore the Brookhaven-II data. Actually, we have shown that with the CFD_B solution the Brookhaven-II data can also be fairly well described while being consistent with $\pi\pi \to K\bar{K}$ dispersion relations and with the dispersive determination of the inelasticity in $\pi\pi$ scattering that, in contrast, is not consistent with the Argonne data. In this sense the CFD_C is disfavored against the CFD_B set.

Finally, in Fig. 16 we also show the CFD_B and CFD_C parameterizations in the unphysical region. There one can observe that their respective pseudo-threshold behaviors are quite different. Namely, the modulus of the CFD_B around the $f_0(980)$ peak is larger than that of the CFD_C. Such different behaviors may have a sizable impact for future studies of $\pi K \to \pi K$ dispersion relations.

7 Conclusions and outlook

In this work we have performed a dispersive study of $\pi\pi \to K\bar{K}$ scattering by means of partial-wave dispersion relations of the Roy–Steiner type, i.e. based on hyperbolic dispersion relations. While other studies with similar equations used dispersion theory to obtain information on the sub-threshold region, we have also used them for the first time in the physical region. Moreover, we have derived a set of equations based on $(s-a)(u-a) = b$ hyperbolae in which we have obtained the value of a that maximizes the applicability range of these hyperbolic dispersion relations. Compared to the existing $a = 0$ case we have increased the applicability range of the hyperbolic partial-wave dispersion relations in the physical region by 67% in the t variable. This has allowed us to study dispersively the existing data sets on $\pi\pi \to K\bar{K}$ up to 1.47 GeV.

In particular, on a first step we have obtained a set of unconstrained fits to data (UFD) for each partial wave $g_\ell^I(t)$, where ℓ and I are the angular momentum and isospin, respectively. For the case of the scalar-isoscalar wave g_0^0 we have provided two alternative fits, called UFD_B and UFD_C, to differentiate between fits to two conflicting sets of data. In addition, we have provided high energy parameterizations for $\pi\pi \to K\bar{K}$ scattering, based on factorization and Regge theory, that we need for the high energy part of our dispersive integrals. We have then tested these UFD parameterizations against our dispersion relations. We have found that the P wave UFD is very consistent with dispersion relations. Also, the D wave is crudely consistent with these equations, although there is clear room for improvement. In contrast, we have found that the unconstrained fits to both solutions of the scalar-isoscalar wave show a significant inconsistency with the dispersive representation, particularly, but not only, near threshold. These deviations are not related to the high energy input, and thus they become a first warning to the phenomenological use of simple fits to the existing data.

Next, we have provided a new set of fits to data using the hyperbolic partial-wave dispersion relations as constraints. For the P and D waves, these constrained fits to data (CFD) satisfy their dispersion relations within uncertainties while describing very well the experimental data. There is only some relatively small tension in the D-wave threshold region. In particular we have shown that a simple description of the D-wave threshold region with a simple Breit–Wigner parameterization of the nearby $f_2(1270)$ resonance is not acceptable.

We have also found that, with the exception of the region very close to threshold, both constrained parameterizations of the g_0^0 wave, labeled CFD_B and CFD_C, satisfy well the dispersion relations, while still describing reasonably well their respective sets of data. Nevertheless some systematic deviations from the data central values are needed in order to satisfy the dispersive representation, particularly for the UFD_B in the region between 1.25 and 1.45 GeV. This becomes a second warning towards considering only the most popular data set described by UFD_C: the data on which the UFD_C set is based can be also described consistently with hyperbolic partial-wave dispersion relations, and is favored by previous $\pi\pi$ scattering dispersive analysis. This second set should definitely not be discarded, if not directly favored against the most popular one.

In conclusion, our constrained data fits provide reliable, precise and simple parameterizations of data on S, P and D partial waves up to 2 GeV, which are consistent with the hyperbolic dispersive representation up to its maximum applicability limit of 1.47 GeV.

As an outlook for this work, our constrained parameterizations could be used by both the theoretical and experimental hadron communities as input for other processes. Actually, in the near future we plan to use them for further studies. For example: to implement re-scattering effects in CP violating decays involving pions and kaons, or to study the much debated $f_0(1370)$ and $f_0(1500)$ resonance by means of model-independent methods based on analyticity, or combined with $\pi\pi$ scattering determinations, to obtain a precise determination of the $a_0^{\pm}$ scattering lengths from sum rules. Finally, we will use them as input for a similar dispersive analysis of $K\pi$ scattering data and the rigorous and precise determination of light-strange resonance parameters. In particular, this input will be very useful for a precise determination of the elusive $K_0^*(800)$, by analyzing data using hyperbolic partial-wave dispersion relations of the type derived here.

Note Added in Proof While completing the publication of this manuscript we have become aware that the $K_0^*(800)$ resonance it is now called $K_0^*(700)$ in the new edition of the Review of Particle Physics [71].

Acknowledgements JRP and AR are supported by the Spanish project FPA2016-75654-C2-2-P. AR would also like to acknowledge the financial support of the Universidad Complutense de Madrid through a predoctoral scholarship. We would also like to thank B. Moussallam and J. Ruiz de Elvira for fruitful discussions, as well as J. Miranda for her comments and corrections.

Funded by SCOAP[3].

Appendix A: Modified $g_0^0(t)$ data extraction above 1.6 GeV

In the main text we have included a third pole for the $f_2(1810)$ in the $g_2^0(t)$ partial wave, since it is listed in the RPP, although it claims that "Needs confirmation". As we already commented, this produces a large oscillation of the phase above 1.6 GeV different from the almost flat parameterization used in [8], as can be seen in Fig. 3.

However, in [8] the $g_2^0(t)$ wave is used as input to extract the $g_0^0(t)$. Hence, if one now assumes the existence of the $f_2(1810)$, the extraction of the $g_0^0(t)$ phase above 1.6 GeV no longer corresponds to the one given in the paper. The "New UFD" $g_0^0(t)$ phase we obtain is shown in Fig. 17, which parameters can be found in Table 8. Let us recall that above 1.6 GeV the modulus is rather small, so that its contribution to the dispersion relation below 1.47 GeV is also very small. However, one may still wonder if this new UFD S-wave phase above 1.6 GeV could change significantly the results for the modulus after analyzing the dispersion relations.

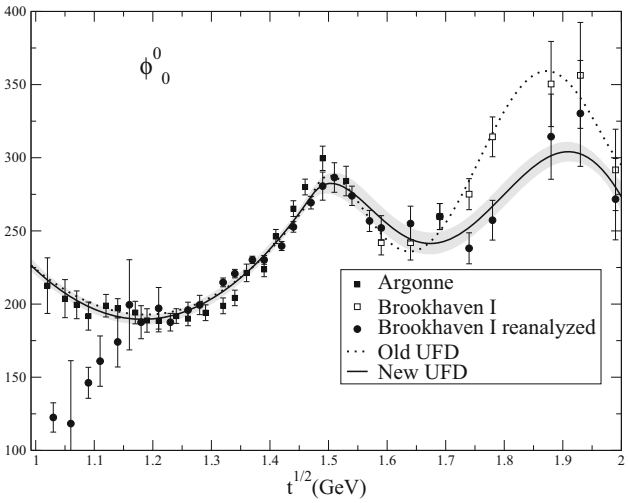

Fig. 17 New ϕ_0^0 phase obtained after extracting the data from [8] by using our UFD for the g_2^0 partial wave

Table 8 Parameters of the new ϕ_0^0

Parameter	New UFD	New CFD_B	New CFD_C
B_1	23.5 ± 1.3	21.8 ± 1.3	22.5 ± 1.3
B_2	29.0 ± 1.3	27.3 ± 1.3	27.9 ± 1.3
B_3	0.01 ± 1.60	1.49 ± 1.60	0.81 ± 1.60
C_1	12.0890 fixed	12.4388 fixed	12.1076 fixed
C_2	13.6 ± 2.6	13.6 ± 2.6	13.3 ± 2.6
C_3	-12.9 ± 2.3	-13.0 ± 2.3	-13.1 ± 2.3
C_4	-13.1 ± 2.2	-13.3 ± 2.2	-13.4 ± 2.2
C_5	4.0 ± 2.4	4.2 ± 2.4	4.0 ± 2.4

Hence, we have run again our whole procedure to obtain a "New CFD" phase for $g_0^0(t)$ and we show in Fig. 18 the final result of the new analysis. As expected, since the input is small above 1.6 GeV, the values obtained for the modulus are almost equal to the ones calculated with the old phase and we do not plot them.

However, as a matter of fact the $g_0^0(t)$ phase above 1.6 GeV is different if one assumes the presence of the $f_2(1810)$ in the $g_2^0(t)$. If one wants to be consistent with that assumption, which at present in the RPP seems to be favored versus the flat solution used in [8], then one should use our "New UFD" rather than the main one in the text. Of course, the difference below 1.47 GeV is negligible.

Appendix B: Kernels

In this section we provide the explicit expressions for the $G^I_{\ell\ell'}(t,t')$ and $G^{\pm}_{\ell\ell'}(t,s')$ kernels needed in the partial-wave dispersion relations in Eq. (39). Recall that $\ell \leq 2$ corre-

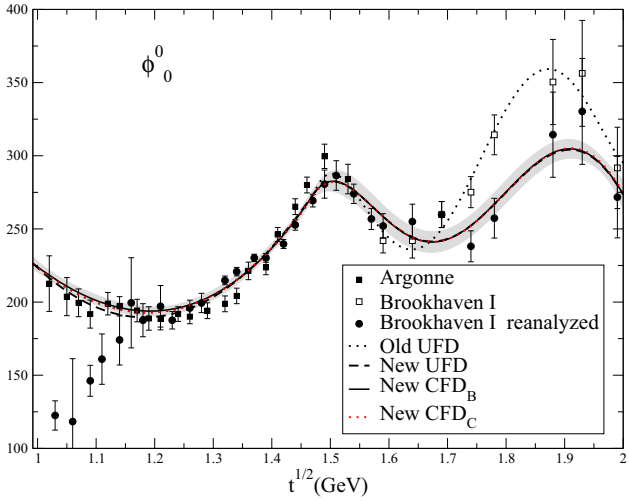

Fig. 18 New CFD ϕ_0^0 phase obtained after extracting the data from [8] by using our model for the g_2^0 partial wave

sponds to the angular momentum of the partial-wave dispersion relation, i.e. the "output" partial wave, whereas ℓ' corresponds to the angular momentum of the "input" wave in the integrand of the dispersion relation. Similarly, s' and t' are the integration variables, whereas t is the variable of the "output" partial wave coming out of the dispersion relation. Note that, in the input, partial waves with $\ell' > 2$ can be safely neglected, except for the $\ell' = 4$ partial wave needed for the g_2^0 equation, which nevertheless gives a rather small contribution.

Let us first recall some previous definitions:

$$z_{s'} = 1 + \frac{2s't}{\lambda_{s'}},$$
$$\lambda_{s'} = \left(s' - (m_\pi + m_K)^2\right)\left(s' - (m_\pi - m_K)^2\right).$$

We start by listing the kernels of the $g_1^1(t)$ partial wave:

$$\begin{aligned}
G^1_{1,3}(t,t') &= \frac{7}{48}(t + t' - 4\Sigma + 10a),\\
G^-_{1,0}(t,s') &= 4\sqrt{2}\left[\frac{(2s' - 2\Sigma + t)A(t,s') - 4q_K(t)q_\pi(t)}{16(q_K(t)q_\pi(t))^3}\right],\\
G^-_{1,1}(t,s') &= 12\sqrt{2}\left[P_1(z_{s'})\frac{(2s' - 2\Sigma + t)A(t,s') - 4q_K(t)q_\pi(t)}{16(q_K(t)q_\pi(t))^3}\right.\\
&\quad \left. - \frac{2s'}{3(s'-a)\lambda_{s'}}\right],\\
G^-_{1,2}(t,s') &= 20\sqrt{2}\left[P_2(z_{s'})\frac{(2s' - 2\Sigma + t)A(t,s') - 4q_K(t)q_\pi(t)}{16(q_K(t)q_\pi(t))^3}\right.\\
&\quad - \frac{2s'z'_s}{(s'-a)\lambda_{s'}} + \frac{s'^2(2s' + t - 2\Sigma)^2}{2(s'-a)^2\lambda^2_{s'}}\\
&\quad \left. - \frac{24s'^2(q_K(t)q_\pi(t))^2}{5(s'-a)^2\lambda'^2_s}\right],
\end{aligned} \tag{B1}$$

where $P_l(z_{s'})$ are the Legendre polynomials, a is one of the parameters that defines the hyperbola $(s-a)(u-a) = b$ and we have defined for convenience

$$A(t,s') = \mathrm{Arcth}\left(\frac{4q_K(t)q_\pi(t)}{2s' + t - 2\Sigma}\right).$$

For the g_2^0 we first define for convenience

$$x(t,s') = \frac{4q_K(t)q_\pi(t)}{2s' + t - 2\Sigma}.$$

By using the same definitions as above one obtains

$$\begin{aligned}
G^0_{2,4}(t,t') &= \frac{3}{8}(t + t' - 4\Sigma + 7a),\\
G^+_{2,0}(t,s') &= \frac{\sqrt{3}(2s' + t - 2\Sigma)^2}{32q_K(t)^5q_\pi(t)^5}\\
&\quad \times\left[(3 - x(t,s')^2)A(t,s') - 3x(t,s')\right],\\
G^+_{2,1}(t,s') &= \frac{3\sqrt{3}(2s' + t - 2\Sigma)^2}{32q_K(t)^5q_\pi(t)^5}P_1(z_{s'})\\
&\quad \times\left[(3 - x(t,s')^2)A(t,s') - 3x(t,s')\right],\\
G^+_{2,2}(t,s') &= 5\sqrt{3}\left[\frac{(2s' + t - 2\Sigma)^2}{32q_K(t)^5q_\pi(t)^5}P_2(z_{s'})\right.\\
&\quad \times\left((3 - x(t,s')^2)A(t,s') - 3x(t,s')\right)\\
&\quad \left. - \frac{16s'^2t}{5(s'-a)^2\lambda^2_{s'}}\right].
\end{aligned} \tag{B2}$$

Finally, for the $g_0^0(t)$ dispersion relation the kernels we need are

$$\begin{aligned}
G^0_{0,2}(t,t') &= \frac{5}{16}(t + t' - 4\Sigma + 6a),\\
G^+_{0,0}(t,s') &= \sqrt{3}\left[\frac{A(t,s')}{q_K(t)q_\pi(t)} + \frac{2(\Sigma - s')}{\lambda_{s'}}\right],\\
G^+_{0,1}(t,s') &= 3\sqrt{3}\left[\frac{A(t,s')}{q_K(t)q_\pi(t)}P_1(z_{s'}) - \frac{(2s' + 2t - 2\Sigma)}{\lambda_{s'}}\right.\\
&\quad \left. - \frac{2at}{(s'-a)\lambda_{s'}}\right],\\
G^+_{0,2}(t,s') &= 5\sqrt{3}\left[\frac{A(t,s')}{q_K(t)q_\pi(t)}P_2(z_{s'}) - \frac{2s - 2\Sigma}{\lambda_{s'}}\right.\\
&\quad - \frac{6st(\Delta^2 + s'(3s' + 2t - 4\Sigma)}{(s'-a)\lambda^2_{s'}}\\
&\quad + \frac{3s'^2t(2s' + t - 2\Sigma)^2}{2(s'-a)^2\lambda'^2_s}\\
&\quad \left. - \frac{8s'^2t(q_K(t)q_\pi(t))^2}{(s'-a)^2\lambda^2_{s'}}\right].
\end{aligned} \tag{B3}$$

All these kernels produce smooth integrable inputs in the physical region. They also produce the left and circular cut structures required by partial wave projection.

Appendix C: t-channel numerical solution

In order to calculate numerically the Omnès integrals it is convenient to make a change of variables to facilitate the integration near t_m. For concreteness we explain the $g_1^1(t)$ dispersion relation, following closely the method explained in [27,29] although in our case it has one less subtraction. The other waves are similar. We start by separating within the integrals the regions above and below t_m,

$$g_1^1(t) = \Delta_1^1(t) + \frac{\Omega_1^1(t)}{\pi} \times \left[\int_{4m_\pi^2}^{t_m-\tau} dt' \frac{\Delta_1^1(t')\sin\phi_1^1(t')}{\Omega_{1,R}^1(t')(t'-t)} + \int_{t_m-\tau}^{t_m} dt' \frac{\Delta_1^1(t')\sin\phi_1^1(t')}{\Omega_{1,R}^1(t')(t'-t)} + \int_{t_m+\tau}^{\infty} dt' \frac{|g_1^1(t')|\sin\phi_1^1(t')}{\Omega_{1,R}^1(t')(t'-t)} + \int_{t_m}^{t_m+\tau} dt' \frac{|g_1^1(t')|\sin\phi_1^1(t')}{\Omega_{1,R}^1(t')(t'-t)} \right]. \tag{C1}$$

We now introduce the variable $v(t') = (t'-t_m)/(t_m-t)$ and write:

$$\frac{\Omega(t)}{\pi}\int_{t_m-\tau}^{t_m} dt' \frac{\Delta_1^1(t')\sin\phi_1^1(t')}{\Omega_{1,R}^1(t')(t'-t)} = \frac{\Delta_1^1(t_m)\exp(i\phi_1^1(t_m))\sin\phi_1^1(t_m)}{\pi}\int_0^{\tau(t)} \frac{dv}{v^{\phi_1^1(t_m)/\pi}(1-v)},$$

$$\frac{\Omega(t)}{\pi}\int_{t_m}^{t_m+\tau} dt' \frac{|g_1^1(t')|\sin\phi_1^1(t')}{\Omega_{1,R}^1(t')(t'-t)} = \frac{g_1^1(t_m)\sin\phi_1^1(t_m)}{\pi}\int_0^{\tau(t)} \frac{dv}{v^{\phi_1^1(t_m)/\pi}(1+v)}. \tag{C2}$$

As shown in [27] this equation also implies the continuity of the partial waves at the matching point t_m. Since $\tau(t_m) = \infty$ and using

$$\frac{1}{\pi}\int_0^\infty \frac{dv}{v^{\phi_1^1(t_m)/\pi}(1-v)} = -\frac{\exp(-i\phi_1^1(t_m))}{\sin(\phi_1^1(t_m))},$$

$$\frac{1}{\pi}\int_0^\infty \frac{dv}{v^{\phi_1^1(t_m)/\pi}(1+v)} = \frac{1}{\sin(\phi_1^1(t_m))}, \tag{C3}$$

inside Eqs. (45), (46), (47) one recovers the matching values $|g_0^0(t_m)|$, $|g_1^1(t_m)|$, $|g_2^0(t_m)|$. In addition, for g_0^0, and due to the introduction of the free parameter α, one has to impose a smooth continuity condition at t_m to fix α, which is done numerically in this work. Otherwise spurious cusps would be produced for the modulus of the amplitude at $t = t_m$, spoiling the analytic structure and its behavior at different values of t.

Appendix D: Applicability range

Let us recall that in this work our aim is to maximize the applicability range of the partial-wave hyperbolic dispersion relations in the real axis, by choosing the a parameter appropriately. Our approach will be similar to that in [28,29] and we will study the applicability range both for the s-channel $\pi K \to \pi K$ and for the t-channel $\pi\pi \to K\bar{K}$.

First of all we have to calculate the double spectral regions, where the imaginary part of the amplitude becomes also imaginary and therefore the Mandelstam hypothesis does not hold (see [69] for a textbook introduction). For this we use the πK scattering box diagrams that we show in Fig. 19 (see also [26]). Then we obtain the restrictions needed to avoid these regions when projecting into partial waves for all the s, t and u channels. In addition, one has to ensure that the partial-wave projection is used only inside the so-called Lehmann ellipse [70–72], where its convergence is guaranteed. Finally by considering the strongest restriction we maximize the domain of applicability by fixing a.

Double spectral regions

The equations that describe the boundary of the support of the spectral function ρ_{st} are:

$$b_I(s,t) : (t-16m_\pi^2)\lambda_s - 64m_\pi^4 s = 0,$$
$$b_{II}(s,t) : (t-4m_\pi^2)(s-(m_K+3m_\pi)^2) - 32m_\pi^3 m_+ = 0. \tag{D1}$$

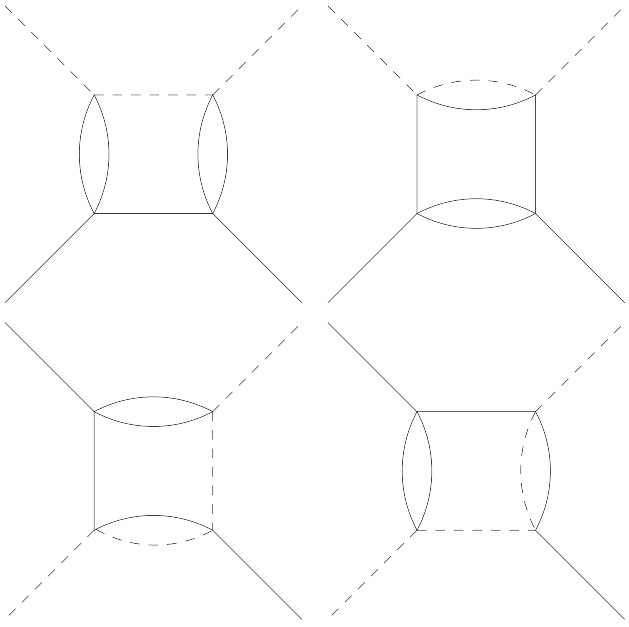

Fig. 19 Box diagrams for πK scattering. Continuous lines denote pions while dashed lines denote kaons

By means of $s \leftrightarrow u$ crossing, similar equations are obtained for ρ_{ut}. The equations that describe the boundary of the support of ρ_{us} are

$$
\begin{aligned}
&b_{III}(s,u): \qquad (D2)\\
&(s-(m_K-m_\pi)^2)(t+s-(m_K+m_\pi)^2)\\
&\times((m_K^2+2m_Km_\pi+5m_\pi^2-s)^2\\
&+t(s-(m_K+3m_\pi)^2))=0,\\
&b_{IV}(s,u):\\
&(s-(m_K-m_\pi)^2)(t+s-(m_K+m_\pi)^2)\\
&\times(((3m_\pi-m_K)(m_K+m_\pi)+s)^2\\
&+t(s-(m_K+m_\pi)^2))=0, \qquad (D3)
\end{aligned}
$$

where $\lambda(x,y,z)=x^2+y^2+z^2-2xy-2xz-2yz$.

Out of these three possible spectral regions, the most restrictive boundary is that of the ρ_{st} support. Thus, by solving Eq. (D1) for t as a function of s one obtains

$$T_{st}(s)=16m_\pi^2+\frac{64m_\pi^4 s}{\lambda_s}, \quad \forall s\le s_0, \qquad (D4)$$

$$T_{st}(s)=4m_\pi^2+\frac{32m_\pi^3(m_K+m_\pi)}{(s-(m_K+3m_\pi)^2)}, \quad \forall s\ge s_0, \qquad (D5)$$

where

$$
\begin{aligned}
s_0 &= m_K^2+4m_Km_\pi+5m_\pi^2\\
&\quad +2m_\pi\sqrt{5m_K^2+12m_Km_\pi+8m_\pi^2}. \qquad (D6)
\end{aligned}
$$

As shown in [12,13], the most simple set of curves in the Mandelstam plane that combine both crossed channels, do not introduce complicated kernels and are suitable to study partial waves in a wide range, are hyperbolas defined trough the relation $(s-a)(u-a)=b$.

In the next subsection we will combine the double spectral region constraints with those restrictions arising from the partial wave projection.

Lehmann ellipse

We now have to consider the projection of $T(s,t,u)$ into partial waves for the two different channels that appear in the hyperbolic dispersion relations.

Thus, on the one hand, for a fixed value of a, the family of hyperbolas $(s-a)(u-a)=b$ must not enter any double spectral region for all values of b needed to perform the partial-wave projection. On the other hand, for a fixed a, we now calculate the restriction on b implied by requiring to stay within the Lehmann ellipse. This depends on what channel we perform the partial-wave projection.

s-channel

The partial-wave expansion for the s-channel converges for angles $z_{s'}(s',t')=1+2s't'/\lambda_{s'}$ inside the Lehmann ellipse [3,70,71]

$$\frac{(\mathrm{Re}\, z_{s'})^2}{A_s^2}+\frac{(\mathrm{Im}\, z_{s'})^2}{B_s^2}=1, \qquad (D7)$$

where the foci are located at $z_{s'}=\pm 1$. The maximum value of $z_{s'}$ that does not enter inside the double spectral region is obtained for $t'=T_{st}(s')$, namely

$$z_{s'}^{max}=1+\frac{2s'T_{st}(s')}{\lambda_{s'}}=A_s, \quad \forall s'\ge m_+^2, \qquad (D8)$$

with the constraint given by the ellipse

$$-z_{s'}^{max}\le z_{s'}\le z_{s'}^{max}. \qquad (D9)$$

This relation translates into a restriction on t'

$$-\frac{\lambda_{s'}}{s'}-T_{st}(s')\le t'\le T_{st}(s'). \qquad (D10)$$

Now, by using $b(s,t,a)=(s-a)(2\Sigma-s-t-a)$ we obtain the following set of bounds for b:

$$
\begin{aligned}
&b_s^-(s',a)\le b\le b_s^+(s',a),\\
&b_s^-(s',a)=(s'-a)(2\Sigma-s'-T_{st}(s')-a),\\
&b_s^+(s',a)=(s'-a)(2\Sigma-s'+\frac{\lambda_{s'}}{s'}+T_{st}(s')-a). \qquad (D11)
\end{aligned}
$$

Thus, the final range of values allowed for b to avoid touching any boundary are

$$b_s^-(a)\le b\le b_s^+(a), \qquad (D12)$$

where

$$
\begin{aligned}
&b_s^-(a)=\min b_s^-(s',a),\\
&b_s^+(a)=\max b_s^+(s',a). \qquad (D13)
\end{aligned}
$$

t-channel

The argument is now more complicated due to the non-linear relation between the scattering angle and t' for the t-channel partial wave projection

$$z_{t'}^2=\frac{(t'-2\Sigma+2a)^2-4b(s',t',a)}{16q_\pi(t')^2q_K(t')^2}, \qquad (D14)$$

so we use the ellipse for $z_{t'}^2$

$$\frac{(\mathrm{Re}\, z_{t'}^2-\frac{1}{2})^2}{\hat{A}_t^2}+\frac{(\mathrm{Im}\, z_{t'}^2)^2}{\hat{B}_t^2}=1, \qquad (D15)$$

where $\hat{A}_t = (A_t^2 + B_t^2)/2$ and $\hat{B}_t = A_t B_t$ are the axes of the ellipse for $z_{t'}^2$ and A_t, B_t the ones for $z_{t'}$. Then, the geometrical restrictions for $z_{t'}^2$ are

$$1 - A_t^2 \leq z_{t'}^2 \leq A_t^2. \tag{D16}$$

As shown in Eq. (6) the relation between z_t and $s - u$ is really simple, calling $\nu = s - u$ and rewriting Eq. (D5) in terms of ν we obtain

$$\begin{aligned} \nu_{st}(t) &= \frac{-16m_\pi^3 m_K - 12m_\pi m_+ t - t^2}{4m_\pi^2 - t}, \quad \forall t \geq t_\pi, \\ \nu_{st}(t) &= \frac{1}{t - 16m_\pi^2} \times \Big[(t - 8m_\pi^2)^2 \\ &\quad + 4m_\pi \sqrt{t}\sqrt{(t - 16m_\pi^2)m_K^2 + 16m_\pi^4}\Big], \quad \forall t \geq 4t_\pi, \end{aligned} \tag{D17}$$

Defining now the upper bound as

$$N_{st}(t) = \min \nu_{st}(t), \tag{D18}$$

we obtain that

$$z_{t'}^{\max}(t') = \frac{N_{st}(t')}{4q_\pi(t')q_K(t')} = A_t \quad \forall t' \geq t_K, \tag{D19}$$

now using Eq. (D16) together with (D18) we obtain the restriction for ν

$$16[q_\pi(t')q_K(t')]^2 - N_{st}(t')^2 \leq \nu^2 \leq N_{st}(t')^2, \tag{D20}$$

finally, the restriction for b is obtained just by translating the $\nu^2 = (t' - 2\Sigma + 2a)^2 - 4b$ constraint into

$$b_t^-(t', a) \leq b \leq b_t^+(t', a), \tag{D21}$$

with

$$\begin{aligned} b_t^-(t', a) &= \frac{(t' - 2\Sigma + 2a)^2 - N_{st}(t')^2}{4}, \\ b_t^+(t', a) &= \frac{(t' - 2\Sigma + 2a)^2 - 16(q_\pi(t')q_K(t'))^2 + N_{st}(t')}{4}. \end{aligned} \tag{D22}$$

Defining again the bounds

$$\begin{aligned} b_t^-(a) &= \max b_t^-(t', a), \\ b_t^+(a) &= \min b_t^+(t', a), \end{aligned} \tag{D23}$$

we have finally obtained the allowed values of b for a fixed a that do not touch any boundary while projecting t-channel partial waves

$$b_t^-(a) \leq b \leq b_t^+(a), \quad \forall t \geq t_\pi \geq a. \tag{D24}$$

Partial-wave projection

s-channel

Hence, to perform the partial-wave projection for the s-channel we must require $b \in [b_{s,t}^-(a), b_{s,t}^+(a)]$. For this to occur, we need $s \leq s_{max}$, where s_{max} is the value of s for which the region of projection touches the support of the double spectral region. Since the integration range $-1 \leq z_s \leq 1$ translates into

$$-\frac{\lambda_s}{s} \leq t \leq 0, \tag{D25}$$

then, given a fixed a, the limits on b due to the s-channel projection are

$$\begin{aligned} &b^{min}(s, a) \leq b \leq b^{max}(s, a), \\ &b^{min}(s, a) = (s - a)(2\Sigma - s - a), \\ &b^{max}(s, a) = (s - a)(2\Sigma - s + \frac{\lambda_s}{s} - a). \end{aligned} \tag{D26}$$

Now, s_{max} is reached when touching the Lehmann ellipse, namely

$$\begin{aligned} b^{min}(s_{max}, a) &= b_{s,t}^-(a), \\ b^{max}(s_{max}, a) &= b_{s,t}^+(a). \end{aligned} \tag{D27}$$

We can now choose a to obtain the largest s_{max} and thus maximize the projection region. For the s-channel projection the strongest restriction comes from the t-channel Lehmann ellipse and therefore

$$\begin{aligned} a &= -13.9\, m_\pi^2, \quad s_{max} = 0.98\,\text{GeV}^2, \\ b_t^-(a) &= -592\, m_\pi^4, \quad b_t^+(a) = 1070\, m_\pi^4. \end{aligned} \tag{D28}$$

t-channel

To perform the t-channel projection we need to consider the scattering angle

$$0 \leq z_t^2 = \frac{(t - 2\Sigma + 2a)^2 - 4b}{16q_\pi^2 q_K^2} \leq 1. \tag{D29}$$

To maximize the domain using a we search for the value $t = t_{max}$ where both the maximum and minimum values of b coincide with $b_{s,t}^-(a)$ and $b_{s,t}^+(a)$. Using Eq. (D29) and taking into account that the projection is made between $z_t^2 = 0$ and $z_t^2 = 1$ this means

$$\begin{aligned} z_t^2(t_{max}, b_{s,t}^-(a)) &= 1, \\ z_t^2(t_{max}, b_{s,t}^+(a)) &= 0. \end{aligned} \tag{D30}$$

Once again, the restriction of the t-channel is stronger than the one of the s-channel, and therefore

$$a = -10.9 m_\pi^2, \quad -0.286\,\text{GeV}^2 \leq t \leq 2.19\,\text{GeV}^2,$$
$$b_t^-(a) = -672\, m_\pi^4, \quad b_t^+(a) = 1010\, m_\pi^4. \tag{D31}$$

Note that the upper limit for $t \simeq \sqrt{2.19}\,\text{GeV} \simeq 1.47\,\text{GeV}$, which is the value we have been using throughout this work as the maximum applicability range of our partial-wave hyperbolic dispersion relations. Taking these values into account one can proceed to study the physical region of both processes. Note that HDR are a very useful tool to study the crossed channel and extend as much as possible the applicability range in its real axis. However their convergence in the real axis of the s-channel is worse than for fixed-t dispersion relations. Nevertheless, the scope of this work is precisely the study of the t-channel partial waves, and therefore HDR are best suited for our purposes.

References

1. C. Patrignani et al. (Particle Data Group), Chin. Phys. C **40**, 100001 (2016)
2. S.D. Protopopescu et al., Phys. Rev. D **7**, 1279 (1973)
3. G. Grayer et al., Nucl. Phys. B **75**, 189 (1974)
4. P. Estabrooks, A.D. Martin, Nucl. Phys. B **79**, 301 (1974)
5. P. Estabrooks, R.K. Carnegie, A.D. Martin, W.M. Dunwoodie, T.A. Lasinski, D.W.G.S. Leith, Nucl. Phys. B **133**, 490 (1978)
6. D. Aston et al., Nucl. Phys. B **296**, 493 (1988)
7. D.H. Cohen, D.S. Ayres, R. Diebold, S.L. Kramer, A.J. Pawlicki, A.B. Wicklund, Phys. Rev. D **22**, 2595 (1980)
8. A. Etkin et al., Phys. Rev. D **25**, 1786 (1982)
9. R.S. Longacre et al., Phys. Lett. B **177**, 223 (1986)
10. S.J. Lindenbaum, R.S. Longacre, Phys. Lett. B **274**, 492 (1992)
11. S.M. Roy, Phys. Lett. **36B**, 353 (1971)
12. F. Steiner, Fortsch. Phys. **19**, 115 (1971)
13. G.E. Hite, F. Steiner, Nuovo Cim. A **18**, 237 (1973)
14. J.R. Pelaez, F.J. Yndurain, Phys. Rev. D **71**, 074016 (2005)
15. R. Kaminski, J.R. Pelaez , F.J. Yndurain, Phys. Rev. D **74**, 014001 (2006). [Phys. Rev. D **74**, 079903 (2006)]
16. R. Kaminski, J.R. Pelaez, F.J. Yndurain, Phys. Rev. D **77**, 054015 (2008)
17. R. Garcia-Martin, R. Kaminski, J.R. Pelaez, J. Ruiz de Elvira, F.J. Yndurain, Phys. Rev. D **83**, 074004 (2011)
18. J.R. Pelaez, A. Rodas, Phys. Rev. D **93**(7), 074025 (2016)
19. J.R. Pelaez, Phys. Rep. **658**, 1 (2016)
20. B. Ananthanarayan, G. Colangelo, J. Gasser, H. Leutwyler, Phys. Rep. **353**, 207 (2001)
21. I. Caprini, G. Colangelo, H. Leutwyler, Phys. Rev. Lett. **96**, 132001 (2006)
22. R. Garcia-Martin, R. Kaminski, J.R. Pelaez, J. Ruiz de Elvira, Phys. Rev. Lett. **107**, 072001 (2011)
23. J.A. Oller, E. Oset, J.R. Pelaez, Phys. Rev. D **59**, 074001 (1999). Erratum: [Phys. Rev. D **60**, 099906 (1999)]. Erratum: [Phys. Rev. D **75**, 099903 (2007)]
24. J.R. Pelaez, Mod. Phys. Lett. A **19**, 2879 (2004)
25. H.Q. Zheng, Z.Y. Zhou, G.Y. Qin, Z. Xiao, J.J. Wang, N. Wu, Nucl. Phys. A **733**, 235 (2004)
26. S. Descotes-Genon, B. Moussallam, Eur. Phys. J. C **48**, 553 (2006)
27. P. Buettiker, S. Descotes-Genon, B. Moussallam, Eur. Phys. J. C **33**, 409 (2004)
28. C. Ditsche, M. Hoferichter, B. Kubis, U.-G. Meissner, JHEP **1206**, 043 (2012)
29. M. Hoferichter, D.R. Phillips, C. Schat, Eur. Phys. J. C **71**, 1743 (2011)
30. P. Masjuan, J.J. Sanz-Cillero, Eur. Phys. J. C **73**, 2594 (2013)
31. P. Masjuan, J. Ruiz de Elvira, J.J. Sanz-Cillero, Phys. Rev. D **90**(9), 097901 (2014)
32. J.R. Pelaez, A. Rodas, J. Ruiz de Elvira, Eur. Phys. J. C **77**(2), 91 (2017)
33. S. Adhikari et al. [GlueX Collaboration], arXiv:1707.05284 [hep-ex]
34. S. Adhikari et al. Phys. Rev. D **89**(9), 094013 (2014)
35. R. Aaij et al. [LHCb Collaboration], Phys. Rev. D **90**(11), 112004 (2014)
36. J.H. Alvarenga Nogueira, I. Bediaga, A.B.R. Cavalcante, T. Frederico , O. Loureno, Phys. Rev. D **92**(5) 054010 (2015)
37. R.A. Briceno, J.J. Dudek, R.G. Edwards, D.J. Wilson, Phys. Rev. Lett. **118**(2), 022002 (2017)
38. H. Nielsen, G.C. Oades, Nucl. Phys. B **55**, 301 (1973)
39. N. Johannesson, G. Nilsson, Nuovo Cim. A **43**, 376 (1978)
40. F.P. Palou, J.L. Sanchez Gomez , F.J. Yndurain, Z. Phys. A **274**, 161 (1975)
41. N.O. Johannesson, J.L. Petersen, Nucl. Phys. B **68**, 397 (1974)
42. C.B. Lang, Fortsch. Phys. **26**, 509 (1978)
43. D.H. Cohen et al., Phys. Rev. D **22**, 2595 (1980)
44. K.L. Au, D. Morgan, M.R. Pennington, Phys. Rev. D **35**, 1633 (1987)
45. R. Kaminski, L. Lesniak, J.P. Maillet, Phys. Rev. D **50**, 3145 (1994)
46. D.V. Bugg, B.S. Zou, A.V. Sarantsev, Nucl. Phys. B **471**, 59 (1996)
47. R. Kaminski, L. Lesniak, B. Loiseau, Phys. Lett. B **413**, 130 (1997)
48. M.P. Locher, V.E. Markushin, H.Q. Zheng, Eur. Phys. J. C **4**, 317 (1998)
49. J.A. Oller , E. Oset, Nucl. Phys. A **620**,438 (1997).Erratum: [Nucl. Phys. A **652**,407 (1999)]. J.A. Oller, E. Oset, J.R. Pelaez, Phys. Rev. D **59**, 074001 (1999). Erratum: [Phys. Rev. D **60**, 099906 (1999)]. Erratum: [Phys. Rev. D **75**, 099903 (2007)]
50. A. Gomez Nicola , J.R. Pelaez, Phys. Rev. D **65**, 054009 (2002)
51. M. Albaladejo, J.A. Oller, Phys. Rev. Lett. **101**, 252002 (2008)
52. B. Ananthanarayan, P. Büttiker, B. Moussallam, Eur. Phys. J. C **22**, 133 (2001)
53. B. Ananthanarayan, P. Büttiker, Eur. Phys. J. C **19**, 517 (2001)
54. W.R. Frazer, J.R. Fulco, Phys. Rev. **117**, 1603 (1960)
55. J.R. Pelaez, F.J. Yndurain, Phys. Rev. D **69**, 114001 (2004)
56. G. Veneziano, Nuovo Cim. A **57**, 190 (1968)
57. C. Lovelace, Phys. Lett. **28B**, 264 (1968)
58. J.A. Shapiro, Phys. Rev. **179**, 1345 (1969)
59. K. Kawarabayashi, S. Kitakado, H. Yabuki, Phys. Lett. **28B**, 432 (1969)
60. J.H. Kuhn , A. Santamaria, Z. Phys. C **48**, 445 (1990)
61. S. Anderson et al. [CLEO Collaboration], Phys. Rev. D **61**, 112002 (2000)
62. P. Bydovsky, R. Kaminski , V. Nazari, Phys. Rev. D **94**(11), 116013 (2016)
63. B. Moussallam, Eur. Phys. J. C **71**, 1814 (2011)
64. I. Caprini, G. Colangelo, H. Leutwyler, Eur. Phys. J. C **72**, 1860 (2012)
65. B.R. Martin, D. Morgan, G. Shaw, *Pion-Pion Interactions in Particle Physics* (Academic, London, 1976)
66. N.I. Muskhelishvili, *Singular Integral Equations* (P. Noordhooff, Groningen, 1953)
67. R. Omnès, Nuovo Cim. **8**, 316 (1958)
68. A. Karabarbounis, G. Shaw, J. Phys. G **6**, 583 (1980)

69. A.D. Martin, T.D. Spearman, *Elementary particle theory* (North-Holland Pub. Co., Amsterdam, 1970)
70. H. Lehman, Nuovo Cim. **10**, 579 (1958)
71. A. Martin, Nuovo Cim. **42**, 930 (1966)
72. A. Martin, Nuovo Cim. **44**, 1219 (1966)
73. M. Tanabashi et al., Particle data group. Phys. Rev. D **98**, 030001 (2018)

2.3 Joint πK and $\pi\pi \to K\bar{K}$ analysis

In this section we present our final, combined study of both πK and $\pi\pi \to K\bar{K}$ channels. For this purpose we use two closed systems of Steiner like Hyperbolic Dispersion Relations and a Roy-like Fixed-t set of dispersion relations, previously introduced in section 1.3.5, together with a system of Forward Dispersion relations. We will first present a new set of fits, with slight modifications from those detailed in sections 2.2.3 and 2.2.4. Later on, we will compare them with the dispersion relations and sum rules for the scattering lengths, paying also particular attention to the contribution coming from the crossed channel and asymptotic regions. Next we will impose all dispersion relations for both channels. Finally, we will provide the constrained results for the most relevant partial waves, *i.e.*, the $S^{1/2}$, $S^{3/2}$, and $P^{1/2}$. In addition, low-energy parameters and sum rules are provided.

2.3.1 Introduction

It was already pointed out throughout this thesis how relevant $\pi K \to \pi K$ and $\pi\pi \to K\bar{K}$ interactions are to low-energy Hadron physics, with a detailed introduction to the topic, and several possible applications. Henceforth, we will focus on the phenomenological description, and later analysis of both systems as a whole.

Even though we have included within these lines several separated results published in [52, 163] and that there exists a previous dispersive solution for $\pi K \to \pi K$ scattering [2], a combined dispersive analysis, including both physical regions, has never been performed. One might wonder if the processes are related in such a way that crossed contributions play an non negligible role. This correlation between both channels will be studied in next sections, with emphasis on the low-energy region.

Up to now, we have introduced the dispersive equations and their kernels and applicability regions have been explained in sections 2.2.4 and Appendixes B and D. These will complete the closed system of dispersion relations implemented within this analysis.

While Forward Dispersion Relations may be applicable up to arbitrary energies, the main drawback of partial-wave dispersion relations is their limited applicability region. This domain of validity depends on the singularities of box diagrams like those depicted in the appendix of section 2.2.4, where the internal particles could be on shell, thus producing imaginary parts inside the imaginary parts of the amplitude. Such result would break the Mandelstam double spectral representation, and hence it creates a series of boundaries in the Mandelstam plane, which cannot be accessed if one wants to perform a dispersive analysis.

Fortunately, different families of dispersion relations are known, and some of them are more adequate to study a given process or energy region. Of all these families we will

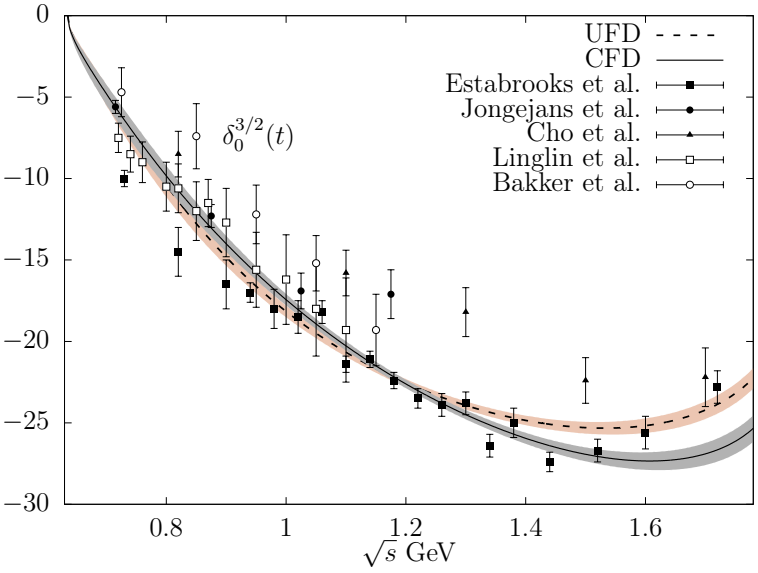

Figure 2.4: $S^{3/2}(s)$ $\pi K \to \pi K$ partial wave, whe show the UFD fit as a dashed line, compared to the final CFD result as a continuos line. The data shown comes from [146] (solid squares), [144] (solid circles), [142] (colid triangles), [145] (empty squares) and [143] (empty circles).

just pay attention to either fixed-t or Hyperbolic Dispersion Relations defined through the equation $(s-a)(u-a)=b$. The former usually reaches greater applicable energies in the real axis [2], whereas the later is convenient if one wants to perform crossed channels studies, or to analytically continue the partial wave into the complex plane as in section 3.1.4. In order to do so, a choice on a must be made. The most appealing one is to maximize the region as done in [124]. In our case of interest, $\pi K \to \pi K$ scattering, we will set $a_s = -13.9\, m_\pi^2$ for the Hyperbolic Dispersion relations, reaching up to $s_{max} = 0.98\,\text{GeV}^2$. For the t-channel $\pi\pi \to K\bar{K}$ we will set $a_t = -10.9\, m_\pi^2$ instead, providing us with up to $t = 2.19\,\text{GeV}^2$ of applicable energy in the physical region. Although we will set $a = -9m_\pi^2$ later on to study the $\kappa/K_0^*(700)$ pole.

On top of all the above relations we will also make use of two different sum rules, the one of Eq. (53) in section 2.2.3, and Eq. (50) in section 2.2.4. The main reason is that both should produce the very same value for a_0^-. However, the former is controlled by the inputs coming from $\pi K \to \pi K$ scattering itself, whereas the later depends on a large contribution coming from the crossed $\pi\pi \to K\bar{K}$ partial wave g_1^1. All in all we think that the difference between these predictions shows how well crossing is being described within our dispersive analysis.

2.3.2 Fits to data

All relevant partial waves needed to describe this processes both at low and high energies have been revised and explained in sections 2.2.3 and 2.2.4. However, some slight modifications, convenient for our combined analysis will be included here. Of

all relevant partial waves, we have only modified the original $S^{1/2}$, $S^{3/2}$,$P^{1/2}$ and the g_1^1 fits. Our main goal with the modifications is to improve the description of the uncertainties associated with the data.

The main data to be fitted in the $\pi K \to \pi K$ interaction come from the SLAC experiments, either from [146] or from [147], several other smaller data sets play an important role in the determination of the $S^{3/2}$ partial wave and are shown in Fig. 2.4. While both partial waves can be isolated from one another, the main data are measured in the given combination of isospins $f_\ell^{1/2}+f_\ell^{3/2}/2$. While this result is not a complication for vector and higher ℓ partial waves, where the $I = 3/2$ is almost negligible, it is relevant to the scalar partial waves determination. In what follows we will focus on the scalar and vector partial waves of the $\pi K \to \pi K$ interaction, the unconstrained fits to the data will be referred to as UFD, while the final constrained results will be called CFD.

Let us comment briefly on each modified partial wave:

$S^{3/2}$ partial wave.— Regarding the isospin 3/2 partial wave, there are several data sets coming from different experiments from the 70's. As shown in Fig. 2.4 most of them look incompatible from one another. Unfortunately, this wave plays a crucial role for our understanding of low energy $\pi K \to \pi K$ interactions, as it dominates the $T^{3/2}$ amplitude, from where the $T^{1/2}$ can be obtained by means of crossing $T^{1/2}(s,t) = \left(T^{3/2}(u,t) - T^{3/2}(s,t)\right)/2$. Furthermore, these data sets would produce different values for the scattering length $a_0^{3/2}$, which would yield a wide spread of results. This motivates our goal, which is the accurate determination of the low-energy region. On top of all the above, even though they have different isospins, the $S^{3/2}$ enters as input for the determination of the $S^{1/2}$ dispersion relation and its contribution is considerable. That is the reason why its uncertainties would be propagated into the determination of the $\kappa/K_0^*(700)$ pole. In addition, as stated above, the only way to extract the $S^{1/2}$ partial wave is through the data on the $S^{1/2} + S^{3/2}/2$ combination, so that both partial waves will be correlated from the very first fit.

For all these reasons we have tried to avoid overstimating the systematic uncertainties. Let us first recall that we added in 2.2.3 systematic uncertainties while also respecting gaussianity, so that the final result produces the required $\chi^2/d.o.f. \sim 1$ result, but no artifacts nor any artificial uncertainty has been added. The approach was supported by the methods detailed in [164,165], where several statistical tests were applied to NN and $\pi\pi \to \pi\pi$ interactions respectively, in order to select a consistent data set.

Table 2.1: Parameters of the $S^{3/2}$-wave.

Parameter	UFD	CFD
B_0	2.14 $\pm$0.03	2.16 $\pm$0.03
B_1	4.08 $\pm$0.14	3.53 $\pm$0.14
B_2	3.43 $\pm$0.38	2.30 $\pm$0.38

However, the formalism applied in section 2.2.3 will no longer be used here, where we will simply discard all data points deviated from the best fit to the whole set by more than 3.5 sigmas. There are several reasons why we think this simpler approach could be an improvement. First, taking into account the number of data points we are fitting for the S wave, deviations above 3.5 sigmas are extremely unlikely, which is also motivated by [165]. Second, after removing these inconsistent values, the $\chi^2/d.o.f.$ obtained for the different regions of the $S^{3/2}$ and $S^{1/2}+S^{3/2}/2$ combinations get immediately reduced below 2, with an almost normal distribution of the residues of the fit. Therefore it is enough to multiply the fit coefficients by a given factor to normalize the errors and thus the $\chi^2/d.o.f.$ to one. In particular, after removing the conflicting points we get $\chi^2_{S^{3/2}}/d.o.f. = 1.8$, $\chi^2_{e\,S^{1/2}+S^{3/2}/2}/d.o.f. = 1.3$ and $\chi^2_{in\,S^{1/2}+S^{3/2}/2}/d.o.f. = 1.5$, where the $\chi^2_{e\,S^{1/2}+S^{3/2}/2}$ combination is the result of the fit in the elastic region, whereas the later corresponds to the inelastic one, above the $\pi\eta$ threshold.

Let us then recall our simple fit to the $I = 3/2$ S-wave, since It is worth noticing that there is no evidence so far of inelasticity up to ∼1.8 GeV, we will thus consider this wave as elastic. Hence, as detailed in section 2.2.3 we will make use of a conformal parameterization to fit the phase shift

$$\cot\delta_0^{3/2}(s) = \frac{\sqrt{s}}{2q(s_{Adler}-s)}(B_0 + B_1\omega(s) + B_2\omega(s)^2). \tag{2.29}$$

Note we have explicitly extracted the Adler zero, which is fixed to its leading order within Chiral Perturbation Theory: $s_{Adler} = \Sigma_{K\pi}$. Now, in this particular case the conformal variable

$$\omega(y) = \frac{\sqrt{y} - \alpha\sqrt{y_0 - y}}{\sqrt{y} + \alpha\sqrt{y_0 - y}}, \quad y(s) = \left(\frac{s - \Delta_{K\pi}}{s + \Delta_{K\pi}}\right)^2, \tag{2.30}$$

will be defined through the following values:

$$\alpha = 1.4, \quad s_0 = (1.84\,\text{GeV})^2. \tag{2.31}$$

The parameters of the new fit are shown in Table 2.1. If one compares this result with the original fit of 2.2.3 there is a clear difference between both scattering lengths. As we will see in the forthcoming sections, the new UFD produces a much closer result to the dispersion relations than the original one from section 2.2.3, at the same time as its uncertainties have been reduced.

$S^{1/2}$ partial wave.— For the $I = 1/2$ S wave inelasticity has been measured only above 1.3 GeV. Taking into account that this region is dominated by the $K_0^*(1430)$ resonance, the most appealing approach is to split the energy region to be fitted into two parts, where the one up to $s = 4m_K^2$ will be considered elastic. Once again we will take advantage of the conformal mapping to fit the phase shift as:

$$\cot\delta_0^{1/2}(s) = \frac{\sqrt{s}}{2q(s-s_{Adler})}(B_0 + B_1\omega). \tag{2.32}$$

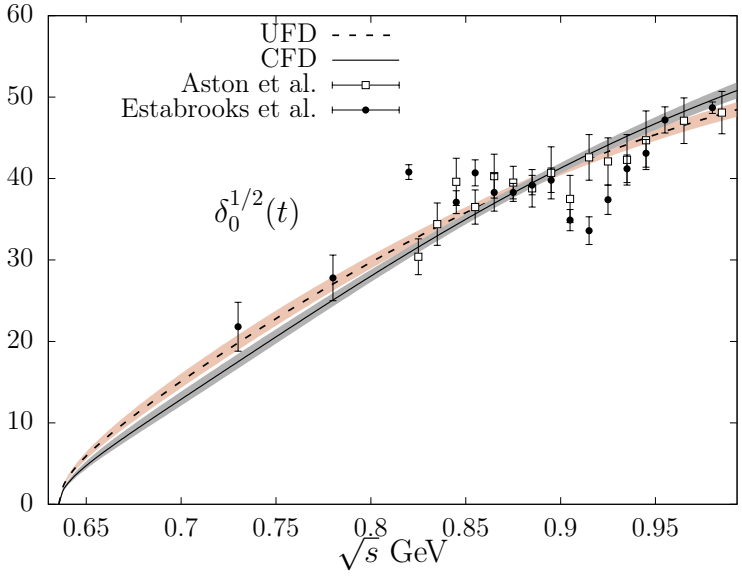

Figure 2.5: $S^{1/2}(s)$ $\pi K \to \pi K$ partial wave. We show the UFD fit as a dashed line, compared to the final CFD result as a continuous line. The data shown comes from [147] (empty squares) and [146] (solid circles).

Table 2.2: Parameters of the elastic $S^{1/2}$-wave.

Parameter	UFD	CFD
B_0	0.403 ±0.006	0.418 ±0.006
B_1	0.223 ±0.032	0.064 ±0.032

Once more we have explicitly factorized the Adler zero, which we have set to its leading order within Chiral Perturbation Theory:

$$s_{Adler} = \left(\Sigma_{K\pi} + 2\sqrt{\Delta_{K\pi}^2 + m_K^2 m_\pi^2}\right)/5 \simeq 0.236\,\text{GeV}^2. \tag{2.33}$$

As explained in section 2.2.3, for this wave it is convenient to fix the constants that define the center of the conformal variable ω to the following values

$$\alpha = 1.15, \quad s_0 = (1.1\,\text{GeV})^2. \tag{2.34}$$

The values of the new fit are given in Table 2.2, and the are pretty similar to the original fit of section 2.2.3.

$P^{1/2}$ partial wave.— Let us then discuss the $I = 1/2$ P wave. We will slightly modify the data choice in the elastic region, while the inelastic region will remain as in the original fit. There are three reasons to take a closer look to the region surrounding the $K^*(892)$. First, as seen in [2], the solution of the Roy-Steiner equations clearly deviates from all data, furthermore, the mass and width associated to the $K^*(892)$ coming from this solution would be at odds with all determinations listed in the PDG, by several standard deviations. But even describing the data, as we did in [52] the $K^*(892)$ poles extracted with Padé sequences [166] are a few MeV off. This is the

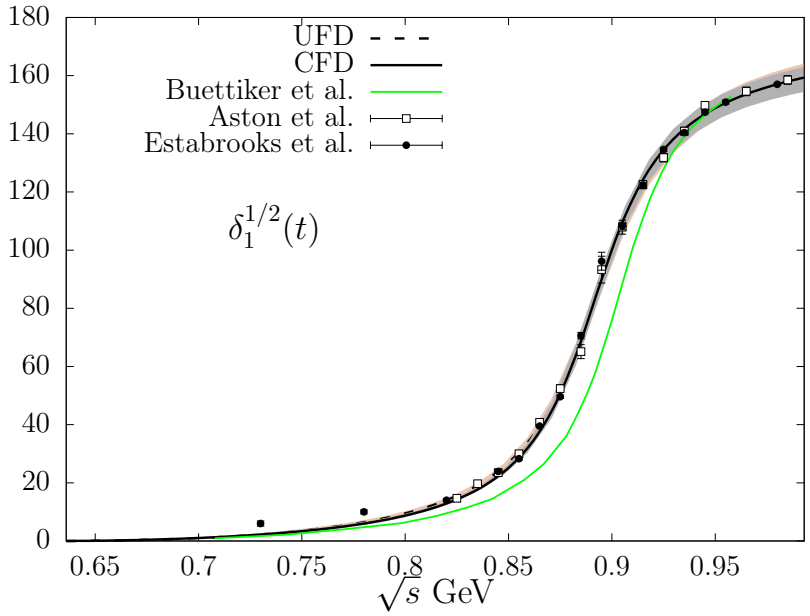

Figure 2.6: $P^{1/2}(s)$ $\pi K \to \pi K$ partial wave, we show the UFD fit as a dashed line, compared to the final CFD result as a continuous line. The data shown comes from [147] (empty squares) and [146] (solid circles).

reason why an averaged systematic uncertainty between both data sets will be included. Second, isospin violating effects should be considered, as they would be at least of the same order of the statistical uncertainties coming from the experimental data. Thus we will include an explicit systematic uncertainty of 2 MeV to the parameter that produces the corresponding "Breit-Wigner mass" of the $K^*(892)$, called m_r. Finally, the two first bins coming from Estabrooks et al. [146] will be discarded, as they are clearly incompatible with our fit (see section 2.2.3) and also because they would produce a too large scattering length, at odds with all dispersive checks, forcing an output similar to the one in [2], going back to the first reason. The rest of the data will be fitted as in section 2.2.3.

Then, in the elastic region, i.e. $s \leq (m_\eta + m_K)^2$, we use again a conformal fit to describe the data, namely,

$$\cot \delta_1^{1/2}(s) = \frac{\sqrt{s}}{2q^3}(m_r^2 - s)(B_0 + B_1\omega + B_2\omega^2). \tag{2.35}$$

Note we have explicitly factorized $(m_r^2 - s)$ so that the phase crosses $\pi/2$ at the energy of the peak associated to the $K^*(892)$ resonance. As explained in section 2.2.3, the α and s_0 parameters, are fixed from the choice of the center of the expansion and the highest energy of the fit to be

$$\alpha = 1.15, \quad s_0 = (1.1\,\text{GeV})^2. \tag{2.36}$$

The parameters of the unconstrained fit are listed in Table 2.3, where in this case, the low-energy region is incompatible with the one of section 2.2.3.

Table 2.3: Parameters of the $P^{1/2}$-wave.

Parameter	UFD	CFD
B_0	0.98 ±0.02	1.07 ±0.02
B_1	0.48 ±0.28	0.39 ±0.28
B_2	2.66 ±0.78	0.95 ±0.78
m_r	0.8955 ±0.0020GeV	0.8950 ±0.0020GeV

Finally, minor changes have been introduced to the g_1^1 partial wave, although we do not modify the data choice, the way we added systematic uncertainties in the original fit of section 2.2.4 was improvable. On the one hand, we included these uncertainties by means of an overall factor multiplying the errors, so that we got a global $\chi^2/d.o.f. \sim 1$. On the other hand, there were two relevant regions where the original $\chi^2/d.o.f.$ was already acceptable, which after multiplying by that factor yielded too large uncertainties where they were not needed. We have just modified the region where we include this factor to match those data points where a high $\chi^2/d.o.f.$ is produced.

The rest of the partial waves will remain unchanged and thus their formulas and UFD parameters are given either in section 2.2.3 for $\pi K \to \pi K$ scattering, or in section 2.2.4 for $\pi\pi \to K\bar{K}$ scattering partial waves.

2.3.3 Dispersion relations: checks and constraints

The aim of our works is to provide a simple set of parameterizations which are consistent with basic requirements as analyticity, unitarity and crossing. These features impose stringent constraints on the scattering amplitudes and partial waves, which translate into integral equations that relate the value of a given amplitude at values of s, t over the whole physical energy region. In this section we briefly review the main checks and constraints imposed by means of amplitude and partial-wave dispersion relations.

Of the whole list of dispersive equations detailed in this thesis, we will make use of Forward Dispersion relations in Eq. (2.14), fixed-t Roy-like equations [114, 121, 167] taken from Eq. (2.19) and Hyperbolic [130, 132], Steiner-like equations Eqs. (2.27) and (2.28). These systems add up to 18 integral equations to be satisfied within our analysis, that is, two FDR, two HDR and one fixed-t for every S and P wave, together with 4 HDR for the crossed channel g_0^0, g_1^1 and g_2^0. Let us remember that we will make use of two different HDR to described the T^- amplitude. The main reason is that while the unsubtracted T^- amplitude is powerful to obtain a sum rule at threshold, so that it constrains even more the low-energy parameters, the Regge contribution is not negligible. On top of that, the crossed channel contribution, in particular the one of the g_1^1 partial wave plays an important role at low energies, which entails the correlated fulfillment of both dispersion relations for $\pi K \to \pi K$ and $\pi\pi \to K\bar{K}$. In order to get a different constraint, where the Regge asymptotic region is almost negligible and the partial waves are dominated by their own input, we will include a once-subtracted T^- HDR. It is worth noticing, however, that we are not following this same approach for

the fixed-t dispersion relations, since in this case both the higher energy region and the crossed channel are more suppressed, and their UFD check shows how well described this equation is compared to the HDRs.

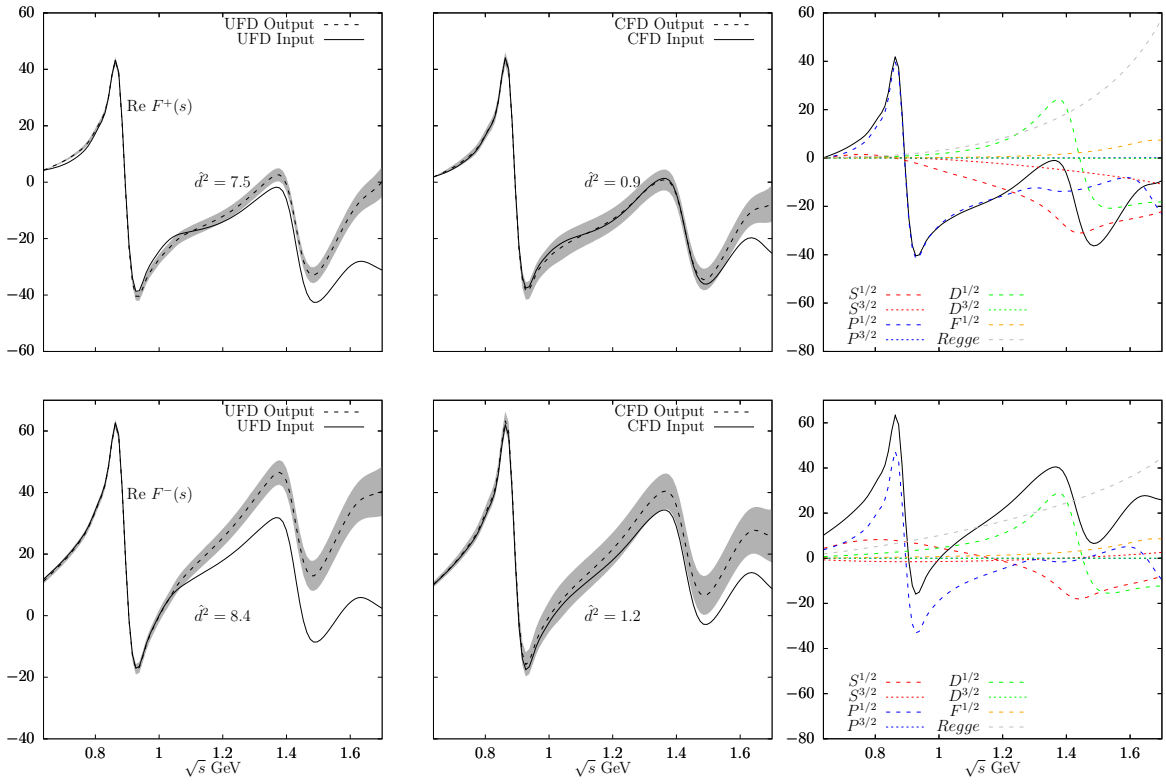

Figure 2.7: Checks of the $T^+(s), T^-(s)$ Forward Dispersion Relations. Note the large inconsistencies between input and output for the UFD and the clear improvement of the CFD. In the last column we show the size of different contributions for each dispersion relation.

Following a similar approach to what we did in [52, 163] let us now first introduce a quantitative measurement of the deviation between the input coming from the fits to the data and the output of a given dispersion relation

$$d^2 = \frac{1}{N}\sum_{i=1}^{N}\left(\frac{d_i}{\Delta d_i}\right)^2, \tag{2.37}$$

where d_i are the differences between input and output at a set of discrete energies and Δd_i are the uncertainties of the output, obtained from the errors of the initial parameters.

Every dispersion relation will then have an associated distance which provides a fair estimate of its fulfilment. We consider that a given dispersive equation is satisfied if this $\chi^2/d.o.f.$-like function is below 1, and that it violates analyticity otherwise. A different approach, where the partial waves at low energy are solved depending on a given matching condition and the low-energy parameters, was successfully applied

[2,118,119,124,125] to different processes in the past. However, in this particular system we consider it is appealing to use a more data driven approach, as the matching condition is not so clear due to the systematic effects, and there is no accurate determination of the low-energy parameters.

Hence, in order to constrain the parameterizations we will weight every distance by the degrees of freedom they are roughly describing. Thus, we have chosen a weight (W_i) equal to 3 for every dispersion relation regarding the $S^{1/2}$, $S^{3/2}$ and $P^{1/2}$ partial waves, together with a weight equal to 8 for the Forward Dispersion Relations. In addition, we will define a second distance (Δ_p^2) between the starting parameters and the final ones of the high-energy asymptotic formulas, both for the Regge description from [89] and for the Veneziano formula used in section 2.2.4. The weight of this parameters will be simply their total number. Finally we will add these distances on top of a modification of the χ^2 of the data, where every partial wave has been weighted by its degrees of freedom ($W_{pw\,i}$). Thus, the final formula to be minimized reads

$$\sum_i \left(W_{pw\,i}\chi_i^2 + \Delta_{p\,i}^2 + W_i d_i^2\right) + W_{FDR}\, d_{FDR}^2. \tag{2.38}$$

In Fig. 2.7 the checks to the FDR are shown (first column), together with the CFD final results (middle), and a partial decomposition into the relevant contributions (right). It is worth noticing first that there is no hierarchy between partial waves above 1.6 GeV, and that the Regge contributions are way bigger than any other input. This, together with the fact that above 1.8 GeV the experimental data violates dispersion relations by more than 5 sigmas make us conclude that the partial wave expansion is not converging well in this region. Hereby we do not fit, nor we do impose any dispersive constraints above roughly 1.8 GeV.

Now, compared to the previous analysis done in section 2.2.3 the low-energy region is better described. There are two reasons, both related to the new fits of the S and P waves, whose unconstrained scattering lengths are now much closer to the final result, which supports our decision of modifying these fits. Unfortunately, the relative deviations are equal if not worse at higher energies, as now our uncertainties have been shrank due to the new fits. Nonetheless, these uncertainties are produced by the high energy region fits and as we see in the CFD result, they look similar to those of section 2.2.3, with minor deviations above 1.6 GeV.

Let us now focus on the main partial waves, *i.e.*, the $\pi K \to \pi K$ S waves and the $P^{1/2}$ wave. Although we also study the $P^{3/2}$ wave for completeness, its phase shift is almost compatible with zero at all values of s, hereby it is almost negligible for our purposes.

We will detail first the analysis over the fixed-t dispersion relations. Let us first recall that this system of equations is applicable up to $s \sim 1.1\text{GeV}^2$, however, for simplicity and the sake of comparison we will only impose all dispersion relations up to $s = 0.98\text{GeV}^2$, which is the highest allowed value for the Hyperbolic ones. Now, as can be seen in Fig. 2.8, the deviations between input and output do not look worrisome, as

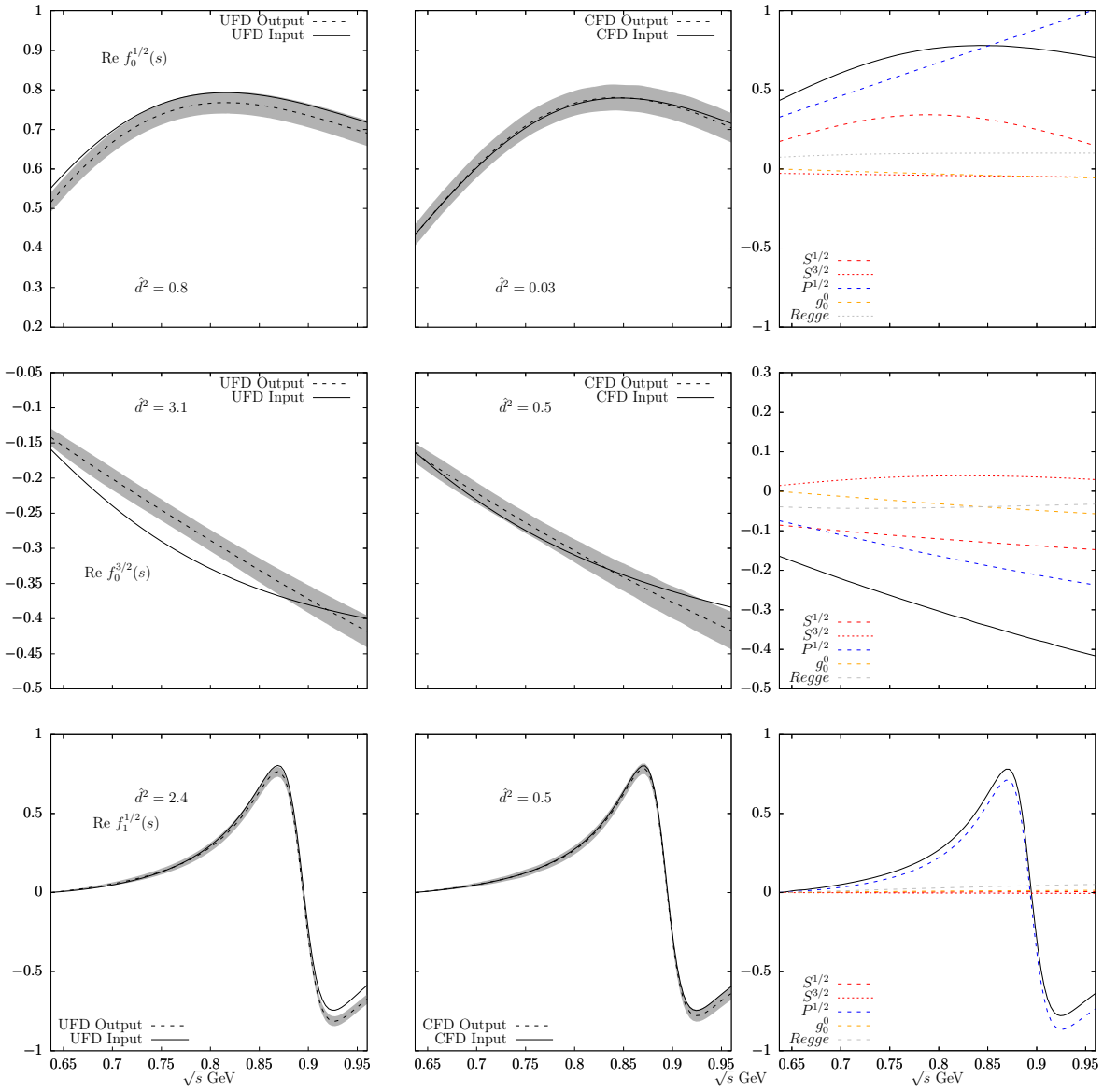

Figure 2.8: Checks of the $f_0^{1/2}(s)$, $f_0^{3/2}(s)$ and $f_1^{1/2}(s)$ fixed-t partial-wave dispersion relations. Note the large deviations between input and output in the UFD and the remarkable agreement of the three CFD partial waves. In the last column we show the size of different contributions to each dispersion relation.

no partial wave deviates by more than 1.8 sigmas, which is a pretty consistent system. The main reason is, as shown in the right panels of the figure, that the partial wave which dominates the input is the $P^{1/2}$. Even though the $P^{1/2}$ wave is slightly deviated from its own output, this difference is small as it is due to a tiny uncertainty. Therefore, we conclude that this system is very robust against crossed channel and higher-energy contributions.

Let us remark that this check would be much worse in case we had used the original fits of section 2.2.3 instead of the new ones. The main reason is the previous large

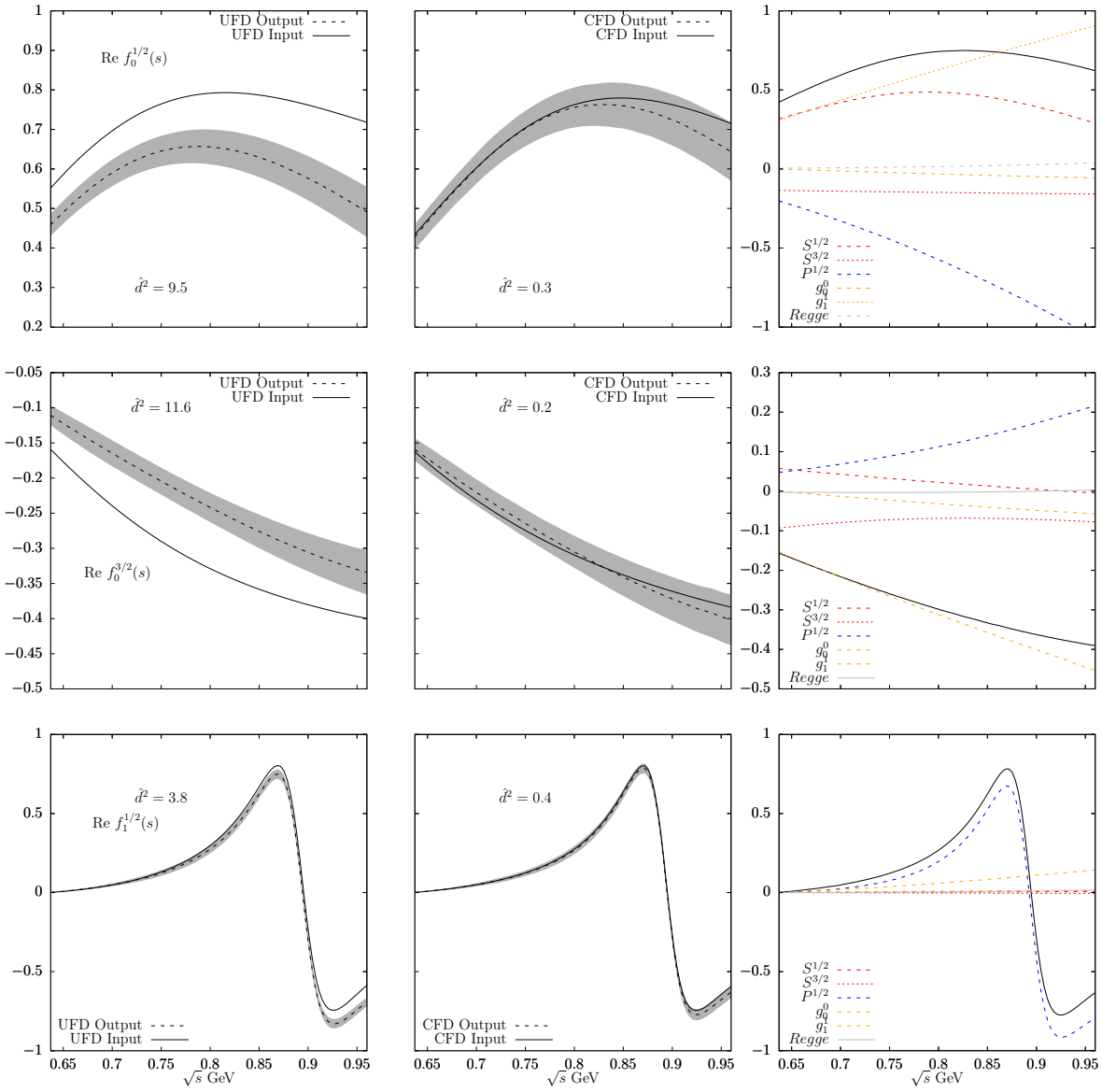

Figure 2.9: Checks of the $f_0^{1/2}(s)$, $f_0^{3/2}(s)$ and $f_1^{1/2}(s)$ non-subtracted hyperbolic partial-wave dispersion relations. Note the large deviations between input and output in the UFD and the remarkable agreement of the three CFD partial waves. In the last column we show the size of different contributions to each dispersion relation.

deviation between the UFD $S^{3/2}$ partial waves, which are now much closer to the final constrained result. Therefore this comparison supports our new choice and thus produces a more robust starting point.

After imposing the dispersion relations we get a final system which is fairly compatible up to ~ 1GeV, where basically no inconsistencies larger than the error band are found. At the same time, the fulfillment of dispersion relations at threshold is remarkable, which ensures that the sum rule of the T^- amplitude is well reproduced by the input.

The situation regarding the Hyperbolic Dispersion Relations is different however. In particular the system coming from the unsubtracted T^- amplitude, shown in Fig. 2.9. There is a large, homogeneous deviation of all UFD partial waves, which in the case of the S waves reaches more than 3 sigmas. Such a strong violation is related also to the deviation from the dispersive T^- sum rule [52] at low energies, and this energy region is, as shown in the right panels, dominated by the g_1^1 partial wave, in particular by the pseudo-physical region included as input between $4m_\pi^2$ and $4m_K^2$. This behavior is unexpected, as the phase in that region is the one coming from the $\pi\pi \to \pi\pi$ P wave, taken from the dispersive study of [3], and the modulus is obtained by means of a Muskhelishvili-Omnès dispersion relation. One may wonder if the dispersive extrapolation to the pseudo-physical region was not that stable, and as we will see in the following, it is indeed the favored scenario.

Fortunately, the CFD result is well described, where again all dispersion relations lie well within the uncertainties, and the low-energy region is perfectly compatible. Nevertheless, this solution has been obtained thanks to the introduction of a once-subtracted T^- amplitude, which shows a deviation within the g_1^1 partial wave that remains hidden in the unsubtracted case. The system is way more unstable if the later is not imposed, and that is the reason why we include two different families of Hyperbolic Dispersion Relations.

Now, the situation regarding the last set of $\pi K \to \pi K$ dispersion relations is pretty similar to the first one, where the UFD inputs are relatively close to the dispersive output, and a fairly good qualitative result, as shown in Fig. 2.10, is found. This scenario would be again worse if the original fits of section 2.2.3 were used instead of the new ones. The g_1^1 partial wave is now less dominant, albeit big, and there are several cancellations that produce a way more stable result, almost dominated by its own input. On the one hand the Regge contributions have been suppressed, on the other hand however, the a_0^- scattering length is much more relevant now.

The final result, shown in the middle column of Fig. 2.10 is compatible with the previous systems. No partial wave is incompatible below 1 GeV. However the threshold does not offer any information now, as it is a mere input due to the subtraction constants.

Finally, let us summarize why a once-subtracted dispersion relation for T^- was added to the previous analysis of section 2.2.4. As shown in Fig. 2.11, the deviation of the unsubtracted UFD result is pretty small and it is due to a smooth, homogeneous separation between input and output around 1.1 GeV. In contrast, the once-subtracted is way more deviated, and thus needs to be imposed. One may wonder why in this case the unsubtracted dispersion relation is the one closer to the input. As can be seen in the right panels, in the unsubtracted case the input is clearly dominated by its own fit to the data, while the once subtracted has non-negligible contributions coming from the crossed $\pi K \to \pi K$ channel.

Actually, this is the reason why in section 2.2.4 we decided to use only an unsubtracted dispersion relation, as we though the result would be more stable. Unfortunately,

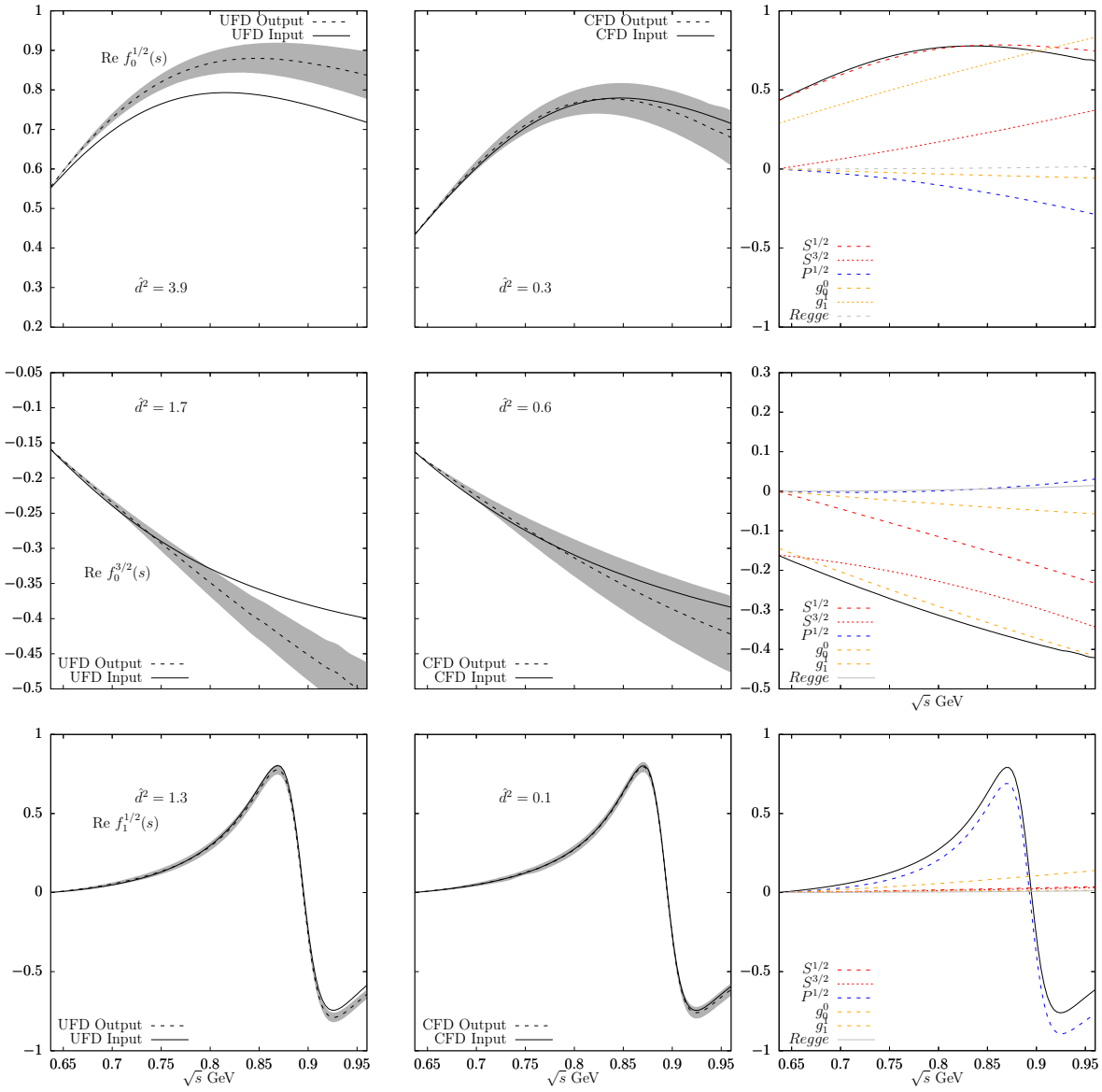

Figure 2.10: Checks of the $f_0^{1/2}(s), f_0^{3/2}(s)$ and $f_1^{1/2}(s)$ once-subtracted hyperbolic partial-wave dispersion relations. Note the large deviations between input and output in the UFD and the remarkable agreement of the three CFD partial waves. In the last column we show the size of different contributions to each dispersion relation.

the right panels of Figs. 2.11, 2.9 and 2.10 illustrate how correlated the values close to threshold are between both channels. Furthermore, as explained above, the contribution of the pseudo-physical region coming from the g_1^1 is central to the description of the $\pi K \to \pi K$ Hyperbolic Dispersion Relations. This scenario disfavors the unsubtracted g_1^1 equation, as it is almost unaffected by other waves and thus a deviation within his pseudo-physical region would remain hidden, but it would produce large systematic effects in the $\pi K \to \pi K$ channel. In order to have control both over the physical region and below the $K\bar{K}$ threshold, while we also maintain the sum rule coming from the unsubtracted T^- amplitude, we will make use of both dispersion relations

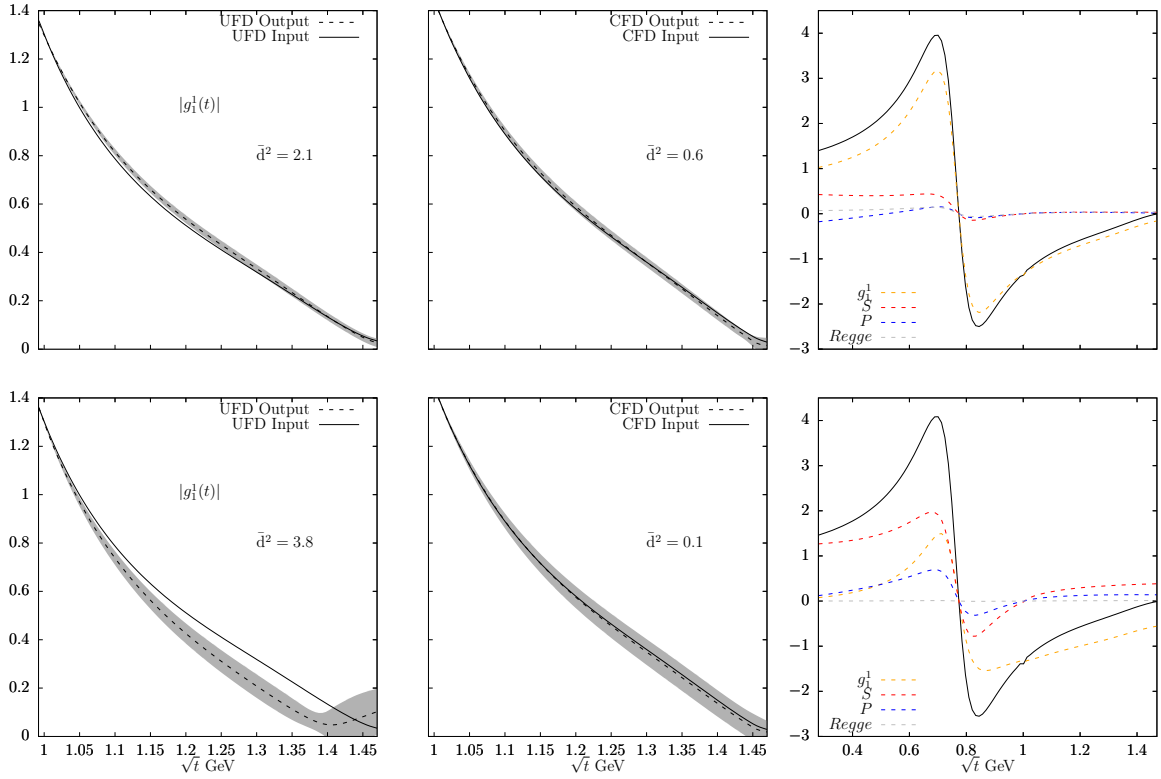

Figure 2.11: Checks of the $g_1^1(t)$ partial waves with none and with one subtraction for the T^- amplitude.

for g_1^1. On top of that, we have slightly changed the value of the matching point of the Muskhelishvili-Omnès equations from the previous value $\sqrt{t_m} = 1.2$GeV used in section 2.2.4 to the new one $\sqrt{t_m} = 1$GeV. The reason is that this new point makes the pseudo-physical region more sensitive to changes occurring in the low-energy physical region, thus allowing us to have more room for improvement.

Again, after imposing the dispersive constraints, both input and output are fairly compatible, with a remarkable description of the physical region, although the unphysical peak of the $\rho(770)$ appearing below the $K\bar{K}$ threshold is now higher than in [163]. Also, we list in Table 2.5 the values of the sum rule of the T^- Hyperbolic Dispersion Relation in [163], which in the case of the CFD result describes perfectly the one coming from $\pi K \to \pi K$, together with the input.

We thus conclude that our final CFD result describes the whole system of 18 dispersion relations constraining $\pi K \to \pi K$ and $\pi\pi \to K\bar{K}$ scattering, where the parameterizations fulfill well the dispersive equation up to 1.6 GeV, with minor violations up to roughly 1.8 GeV. The scattering lengths, in particular the combination $a_0^- = (a_0^{1/2} - a_0^{3/2})/3$ have been also constrained due to the unsubtracted dispersive equations. All in all, we think that our CFD values are a robust determination of the interactions between both systems and at the same time we are able to calculate the low-energy constants with a high degree of accuracy.

Low-energy parameters.— We pay special attention to the low-energy parameters of meson-meson interactions across this thesis. In particular, we included in section 1.2 the Fig. 1.4 where the situation regarding the scattering lengths of the $\pi K \to \pi K$ interaction is depicted. As explained in several introductory sections, our central goal is to perform a model-independent analysis and determination of this scattering process. The system of equations derived in section 2.2 and in the Appendix A provide us with the necessary tools to reach our final goal.

Once the CFD parameterizations are determined, we can easily evaluate the low-energy parameters. In this section we briefly discuss the values of the scattering lengths, listed in Table 2.4. It seems that our new value is slightly deviated from the previous dispersive prediction of [2], and it prefers to lie within the Lattice QCD calculations.

Table 2.4: Low-energy parameters after constraining the fits to data with the full set of DR. In customary m_π units.

	UFD	CFD	Buettiker et al. [2]
$a_0^{1/2}$	0.241±0.013	0.192±0.008	0.224±0.022
$a_0^{3/2}$	-0.066±0.014	-0.067±0.014	-0.0448± 0.0077

Let us finally remark that part of the deviation between our low-energy results and the ones obtained in [2] is due to the constraint coming from two different sum rules for the a_0^- scattering length, coming from different channels as shown in Table 2.5. There are other constraints coming from high energy, different channels, larger applicability regions that are an extension of the previous works and thus produces a slightly different determination.

Table 2.5: Comparison of the value a_0^- obtained directly from the parameterization versus the value obtained from two different sum rules, the first one coming from the Hyperbolic Dispersion Relations (HDR), and a second one calculated from Forward Dispersion Relations (FDR), which is shown in boldface as it is our most precise determination.

	UFD	CFD
Direct a_0^-	0.306 ±0.019	0.259 ±0.018
HDR a_0^-	0.253 ±0.015	0.261 ±0.017
FDR a_0^-	0.290 ± 0.009	**0.262 ± 0.012**

2.4 $\pi\pi \to \pi\pi$ scattering global analytic parameterization

2.4.1 Motivation

As shown in section 2.2 the use of dispersive approaches constraints the partial waves of the scattering processes in a model independent way. In particular all the uncertainties are reduced, and the inconsistencies dissappear. In the previous works done by the Madrid-Krakow group [3, 112] a longstanding debate on the conflicting data sets on $\pi\pi \to \pi\pi$ interactions and the determination of the $\sigma/f_0(500)$ resonance was solved. In addition, several results are also compatible with a different analysis carried out by the Bern group [118, 120] within a different approach. Since their publication, these works have been widely used by phenomenologists working on $\pi\pi \to \pi\pi$ interactions. At the same time, experimental collaborations have taken advantage of these parameterizations to exploit all their nice analytic features within their analyses, producing more constrained uncertainties, and thus smaller systematic effects in their final results.

Nevertheless, the dispersive formalism cannot be applied to the whole energy region where data exist. Even more, the determination of the resonances is performed by means of dispersion relations, so that the parameterizations only play the role of inputs here. This is of relevance since in many different processes the use of the $\sigma/f_0(500)$ and the $\rho(770)$ as isobars is crucial to extract further information. Such implementations could only be doable if the resonances were included within simple parameterizations. This is the reason why there are several groups that are still relying on old, model-dependent descriptions of these processes, in order to keep their inputs as simple as possible. In the last years, some approaches to obtain a powerful, yet simple description of these processes, including some analytical features have been published [168–170].

Considering the situation described above our goal is to provide a set of global but simple parameterizations to mimick the S and P partial waves as obtained in the dispersive analysis [3, 112], both in the real axis and complex plane in order to describe the position of the relevant resonances, their couplings, and the low-energy parameters. These parameterizations will now extend also up to 2 GeV by fitting there the existing data.

2.4.2 Outline of the main results

In section 2.4.3 we describe a new set of global parameterizations for the $I = 0$ S and $I = 1$ P partial waves of the $\pi\pi \to \pi\pi$ scattering process. The main results of such work are summarized as follows:

- We build a new global parameterization for the escalar-isoscalar partial wave.

To do so we implement an analytic conformal mapping in the elastic region, combined with a simple inelastic parameterization that respects analyticity and unitarity. This parameterization reproduces the dispersive $\sigma/f_0(500)$ values and at the same time it includes an explicit pole for the $f_0(980)$ resonance with the most precise values determined in [112]. This parameterization will be used up to 1.4 GeV in the real axis. A simple phenomenological parameterization of both the inelasticity and phase shift will be used above 1.4 GeV, imposing continuity and derivability at the matching point, which describes the data up to roughly 2 GeV.

- For the vector partial wave, a conformal parameterization, elastic up to 1.1 GeV is preferred, above which we will include an explicit inelasticity. First, up to 1.4 GeV we will just multiply the conformal formula by an inelastic S-matrix, thus preserving unitarity. Above 1.4 GeV a phenomenological fit like the one for the scalar wave will be used, also fulfilling continuity and derivability.

- For both waves we fit the result of the system of GKPY partial-wave dispersion relations both in the real axis up to 1.1 GeV, and in the complex plane inside the large Lehman ellipse, together with the result of Forward Dispersion Relations up to 1.4 GeV. Above that energy we will fit the available data coming from [152–154].

- The parameterizations also describe the low-energy parameters, in particular scattering lengths and intercepts. The Adler zero of the scalar partial wave has also been imposed. The final result is a simple set of global parameterizations that describe the whole dispersiveanalysis of [3, 112] in the region of maximal analyticity, including the resonances and the low-energy parameters, but in addition it also describes the data up to roughly 2 GeV.

2.4.3 Preprint: *Global parameterization of $\pi\pi$ scattering*

Global parameterization of $\pi\pi$ scattering

J. R. Pelaez,[1,*] A. Rodas,[1,†] and J. Ruiz de Elvira[2,‡]

[1] *Departamento de Física Teórica and IPARCOS, Universidad Complutense de Madrid, E-28040 Madrid, Spain*
[2] *Albert Einstein Center for Fundamental Physics, Institute for Theoretical Physics, University of Bern, Sidlerstrasse 5, 3012 Bern, Switzerland*

We provide a global parameterization of $\pi\pi \to \pi\pi$ scattering $S0$ and P partial wave data, both in the elastic and inelastic regions, up to 2 GeV, for phenomenological use. The parameterization describes the output and uncertainties of previous partial-wave dispersive analyses of $\pi\pi \to \pi\pi$, both in the real axis up to 1.12 GeV and in the complex plane, while also fulfilling forward dispersion relations up to 1.43 GeV. Moreover, the analytic continuation of this global parameterization also describes the dispersive determinations of the $\sigma/f_0(500)$, $f_0(980)$ and $\rho(770)$ poles in the complex plane.

I. INTRODUCTION

The unprecedented high statistics on hadronic observables attained at experiments like LHCb, Belle or Babar require rigorous and precise parameterizations of final state interactions. Future Hadronic facilities (Fair, Panda, etc..) will be even more demanding. One of the most needed parameterizations is that of $\pi\pi \to \pi\pi$ scattering below 2 GeV, since two or more pions appear very frequently as final products of many hadronic interactions. Also a renewed interest on $\pi\pi \to \pi\pi$ scattering is coming from lattice calculations, which have been recently able to to obtain scattering partial waves with almost realistic masses.

Data on $\pi\pi \to \pi\pi$ scattering was obtained in the 70's [1–5] indirectly from the $\pi N \to \pi\pi N$ reaction. Unfortunately, this technique leads to conflicting data sets. For decades, crude models were enough to describe such data. The exception is the very low-energy region, both in the experimental and theoretical fronts. On the one hand, there is very precise data below the kaon mass coming from K_{l4} decays [6, 7], particularly after the NA48/2 results [8]. On the other hand, Chiral Perturbation Theory (ChPT) provides a systematic and accurate low-energy expansion in terms of pion masses and momenta.

However, for most phenomenological applications the low-energy region is not enough since the production of pions is generically more copious around resonances. ChPT can be successfully extended to the resonance region by means of unitarization. Different versions of this method generate or reconstruct all resonances in $\pi\pi \to \pi\pi$ up to 1.2 GeV: the $\sigma/f_0(500)$ the $\rho(770)$ and the $f_0(980)$. However, the prize to pay is the loss of a controlled systematic expansion, which hinders the calculation of uncertainties and the length of the analytic expressions once one deals with coupled channels above $K\bar{K}$ threshold. Above 1.2 GeV one can introduce by hand other resonances, with the same caveats as before, but with expressions even more elaborated. Nevertheless, the interest of these unitarized approaches is that they can connect with QCD through the chiral parameters and provide a good semi-quantitative approximation, including values of resonance poles, which are much better than the usual description of two pions in terms of a superposition of simple resonant shapes, like Breit Wigner formulas in different versions, Isobar models, etc...

The interest of those popular models is, on the one hand, their simplicity, since for most applications just the phase and the inelasticity functions are needed, not an elaborated model of the interactions with other channels. On the other hand, they can be fairly reasonable for narrow isolated resonances, like the $\rho(770)$. However, such models provide an incorrect description of the scalar-isoscalar partial wave, particularly for the very broad $\sigma/f_0(500)$ pole and its interplay with the very narrow $f_0(980)$, together with the singularity structure in terms of cuts in the complex s plane. Actually, the rescattering of two pions in this channel is frequently described with some sort of Breit-Wigner parameterization for the $\sigma/f_0(500)$, which might be able to describe a wide bump in the data, but it fails to describe the phase shift in that channel or the chiral constraints in the threshold region. Recall that by Watson's Theorem [9] any strong elastic rescattering of two pions must have the very same phase of the $\pi\pi \to \pi\pi$ partial-wave with the same isospin and angular momentum.

In general, modern Hadron Physics demands more precise and model-independent meson-meson scattering parameterizations. This has been achieved over the last two decades by means of dispersion relations, not only for $\pi\pi$ [10–12], but also for πN [13, 14] or πK scattering [15] Unfortunately, we have found that for the hadron community these results are not always so easy to implement or do not cover a sufficiently large energy region. Hence, the purpose of this work is to provide a relatively simple and ready to use parameterization of the phase and inelasticity of the scalar-isoscalar and vector $\pi\pi \to \pi\pi$ scattering partial waves up to 2 GeV, consistent with data and with the dispersive analysis in [12], which extends up to 1.43 GeV. Moreover, we will impose that this

* jrpelaez@fis.ucm.es
† arodas@ucm.es
‡ elvira@itp.unibe.ch

parameterization will provide a simple analytic continuation to the complex plane, consistent with the dispersive representation and the values for the pole positions and residues of the $\sigma/f_0(500)$, $\rho(770)$ and $f_0(980)$ resonances. In addition, both the dispersive results for the threshold and subthreshold regions are also described, thus providing the scattering lengths, slope parameters and $S0$ wave Adler zero values obtained in [12].

II. THE INPUT TO BE DESCRIBED

As we already commented, there are many $\pi\pi \to \pi\pi$ scattering data sets extending up to 2 GeV [1–5]. However, all of them are often incompatible among one another and, moreover, simple fits to each separated set or to averaged data sets do not satisfy well dispersion relations [12, 16–19]. Nevertheless, it is possible to use dispersion relations as constraints to obtain a Constrained Fit to Data (CFD) [12] that still describes the $\pi\pi \to \pi\pi$ data on partial-waves but satisfies dispersion relations within uncertainties. This CFD parameterization will thus be part of our input.

One might wonder why not using directly this CFD parameterization and why in this work we are trying to obtain another one. After all, this parameterization has become quite popular and used in many phenomenological applications. There are several reasons.

First, the dispersion relations used in [12] are of two types and they were applied up to different energies, always below 2 GeV. One set consists of Forward Dispersion Relations, which were studied up to 1.43 GeV. These equations are rather simple, but unfortunately cannot be extended to the complex plane in search for poles. They are only useful as constraints on the real axis. The other set consists of partial-wave dispersion relations, usually referred to as Roy equations [10, 11, 20] (with two subtractions) or GKPY equations [12] (with one subtraction). The former are more stringent in the low-energy region and the latter in the resonance region. Unfortunately, these partial-wave equations are limited to 1.12 GeV, although they can be rigorously continued to the complex plane in search for resonance poles. The existence of these different energy regions motivated the authors in [12] to describe the data with a piecewise parameterization, which in principle cannot be extended rigorously to the complex plane. Therefore, our first aim is to provide a rather simple and global analytic parameterization, with realistic uncertainties, that can be used from $s = 0$ to 1.43 GeV. It will mimic the CFD piecewise parameterization *in the real axis*, which will be used as the first of our inputs to be described.

Second, the $\sigma/f_0(500)$ pole lies so deep in the complex plane that a careful dispersive determination is needed in order to extract its precise parameters rigorously [21–23]. Using the CFD parameterization as input in the GKPY equations, it was obtained numerically that its pole lies at $\sqrt{s_\sigma} = (457^{+14}_{-13}) - i(279^{+11}_{-7})\,\text{MeV}$ with a residue $|g| = 3.57^{+0.11}_{-0.13}$. Now, the low-energy piece of the CFD parameterization [12] was constructed as a conformal expansion valid up to 850 MeV, which lies within the elastic $\pi\pi \to \pi\pi$ region. This CFD conformal piece can be continued to the complex plane finding $\sqrt{s_\sigma} = (474 \pm 6) - i(254 \pm 4)\,\text{MeV}$, which is fairly close, but it is not the pole obtained from the dispersive representation. This illustrates how trying to obtain the $f_0(500)$ pole from a data fit that only reaches 850 MeV is not precise enough. Actually, the effects of the $f_0(980)$ and other singularities, like the left hand cut, are significant at this level of precision. Hence, our second aim is to provide a simple analytic parameterization that reproduces simultaneously the dispersive poles of the $f_0(500)$ and $f_0(980)$ and their interference. Thus, the numerical results of the GKPY dispersion relations in the complex plane, including the numerical values of the $f_0(500)$ and $f_0(980)$ poles, will be the second input to be described. For the P-wave we will do something similar, but just for the $\rho(770)$ pole.

Finally, the CFD parameterization and the dispersive data analysis from which it was obtained only reach 1.43 GeV, but there are more data up to 2 GeV. However, the data at those high energies have many well-known caveats. Some of them were already discussed in detail in [24] and in appendix C of [16], but we summarize them here. First, in that energy region we have to rely on a single scattering experiment, the CERN-Munich Collaboration, so that systematic uncertainties relative to other experiments are not available. Second, this collaboration has many different solutions for the $\pi\pi$ scattering partial waves. Of these, the most popular one for the S-wave is the one published in 1973 [1], also called "solution b" in the collaboration compilation of Grayer et al. [2]. This solution is also consistent with a later reanalysis with polarized targets [4],. In addition, there is the "solution (- - -)", which was the most favored in the 1975 collaboration reanalysis [3]. This is also the most used solution for the P-wave, which we will use in what follows. Note that both "b" and "(- - -)"solutions are consistent below 1.43 GeV. Other solutions for both waves were already disfavored in that very same analysis. Third, both solutions have caveats. On the one hand, the inelastic contribution to all hadronic cross sections are expected to dominate over the elastic ones (something that has been verified for πN, KN and NN scattering). However, this is not the case of"solution b". It is hard to understand why this should be different for pions. On the other hand, if the inelasticity is large, then it can be proved theoretically [25, 26] that the solution in terms of phase and inelasticity is not unique. Solution b is an example of an almost elastic case and solution (- - -) of an strong inelastic effect. Finally, the very same convergence of the partial-wave expansion could be questioned at those energies, since around 1.7 GeV the F-wave is as large as the P-wave, the D0 wave as large as the S0 and the D2 actually larger than the S2. Nevertheless, and with these words of caution, we have extended our fit beyond 1.43

GeV using as our third source of input, either the data of [1, 2, 4] to obtain a "solution I" or the (- - -) data of [3] to obtain a "solution II". Below 1.43 GeV the input is the same for both our solutions and they agree within uncertainties. As a technical remark, we have ensured that the central value and the first derivative of both the phase and inelasticity are continuous at the matching point, which is chosen at 1.4 GeV, to avoid fitting the very end of the CFD parameterization. In any case, one should keep in mind that neither one of these two solutions has been checked against dispersion relations above 1.43 GeV. Thus, above that energy they should be considered purely phenomenological fits.

III. ANALYTIC PARAMETERIZATIONS

In this section we present the parameterizations used to describe the scalar and vector $\pi\pi \to \pi\pi$ partial waves. Below the $K\bar{K}$ threshold the process will be considered elastic and thus it is uniquely described by its phase shift. Above the inelastic region two different parameterizations will be implemented. In the case of the scalar partial wave, up to 1.4 GeV, we will include on top of the conformal parameterization, the inelasticity produced by the $f_0(980)$ resonance, who is located very near the $K\bar{K}$ threshold and hence must be studied carefully. Above 1.4 GeV we will match a second phenomenological parameterization, that will be fitted to the data up to 1.9 GeV. In the case of the vector partial wave, a phenomenological inelasticity will be included from 1.1 to 1.4 GeV, at which we will match with a pure phenomenological parameterization fitted to the data up to 1.8 GeV.

In the elastic region, we will make use of the customary definition of the partial wave

$$t_\ell^I(s) = \frac{\hat{t}_\ell^I(s)}{\sigma(s)} = \frac{e^{i\delta_\ell^I(s)}\sin\delta_\ell^I(s)}{\sigma(s)} = \frac{1}{\sigma(s)}\frac{1}{\cot\delta_\ell^I(s) - i}, \tag{1}$$

where $\sigma(s) = 2q(s)/\sqrt{s} = \sqrt{1-4m_\pi^2/s}$. The explicit formulas we use to describe the phase shift in the elastic region are

$$\cot\delta_0^0(s) = \frac{\sqrt{s}}{2q(s)}\frac{m_\pi^2}{s - z_0^2/2}\left(\frac{z_0^2}{m_\pi\sqrt{s}} + \sum_{n=0}^{N} B_n\omega(s)^n\right),$$
$$\cot\delta_1^1(s) = \frac{\sqrt{s}}{2q^3(s)}(m_\rho^2 - s)\left(\frac{2m_\pi^3}{m_\rho^2\sqrt{s}} + \sum_{n=0}^{N} B_n\omega(s)^n\right), \tag{2}$$

where in our particular case we will set $N = 5$ for the scalar and $N = 4$ for the vector partial waves. As we will see below, no more parameters need to be included in the elastic region to obtain a good overall χ^2. The conformal variable is defined as follows

$$\omega(s) = \frac{\sqrt{s} - \alpha\sqrt{s_0 - s}}{\sqrt{s} + \alpha\sqrt{s_0 - s}}, \tag{3}$$

where the parameters s_0 and α locate the last point where the expansion is real, and the center of the conformal expansion, respectively. Now, the vector partial wave will be fitted using $s_0 = 1.43^2\,\text{GeV}^2$ to describe the whole region, while α is choosen so that the center is close to the threshold, in order to get a more accurate error band, values ranging from 0.2 to 0.5 make a suitable parameterization, of which we use $\alpha = 0.3$. However, the scalar partial wave is better described if the conformal expansion introduces some inelasticity above the $K\bar{K}$ threshold, so that we chose $s_0 = 4m_K^2$ with $\alpha = 1$ for simplicity. In the inelastic region however, we will always multiply the conformal parameterization by an inelastic formula, which in the case of the vector partial wave will be described by a simple polynomial introduced above 1.12 GeV

$$\eta_1^1(s) = 1 - k_0\left(1 - \frac{s_m}{s}\right)^2, \tag{4}$$

where s_m is the point where the inelasticity is introduced. Fortunately, this partial wave is almost and always compatible with $\eta_1^1 = 1$, so that by introducing this phenomenologiacal parameterization at $\sqrt{s_m} = 1.12\,\text{GeV}$ we are able to analytically describe just with the conformal expansion the whole dispersive real axis and complex plane, while nicely describing the inelasticity above until 1.43 GeV.

However, the description of the inelastic region of the scalar partial wave is much more complicated, we will first factorize the conformal expansion from the inelastic contribution as

$$t_0^0(s) = t_{0,conf}^0(s) + t_{f_0}(s) + 2i\sigma(s)t_{0,conf}^0 t_{f_0}^0(s), \tag{5}$$

where the formula $t_{f_0}^0$ will be inspired in the used in [27]

$$t_{f_0}^0(s) = \frac{k_1 s + k_2 s^2}{k_0 - s - (k_1 s + k_2 s^2)\bar{J}(s, m_\pi) - (k_3 + k_4 s + k_5 s^2)\bar{J}(s, m_K)}, \tag{6}$$

where the loop functions are

$$\bar{J}(s,m) = \frac{2}{\pi} + \frac{\sigma(s)}{\pi}\log\left(\frac{\sigma(s)-1}{\sigma(s)+1}\right). \tag{7}$$

However, even though this parameterization suits very

well our fit in the inelastic region, the pole obtained for the $f_0(980)$ is incompatible with the most accurate dispersive results [22, 23], and is also quite unstable. The position and coupling of the $f_0(980)$ to both $\pi\pi$ and $K\bar{K}$ is crucial to our understanding of the first inelasticity of $\pi\pi \to \pi\pi$ scattering, so that a precise determination is a must. To this end, we will build a new inelastic formula, including an explicit pole in the second Riemann sheet as done in [28]. Unfortunately, a parameterization like the one later mentioned would modify our low energy parameters, which is not acceptable as they will be explicitly included from a precise dispersive result in [12]. In order to overcome this problem a modification of Eq. (6) will be necessary, and modifying the formula described above looks appealing. We need to analytically constrain Eq. (6) to include an explicit pole in the second Riemann sheet, while it also maintains the same structure so that the low energy parameters are not modified.

Both the $\sigma/f_0(500)$ and $f_0(980)$ resonances appear in the second Riemann sheet, below the $K\bar{K}$ threshold in the form of poles of the partial wave. They drive the behavior of the partial wave. In particular, the $f_0(980)$ resonance describes a dip destructive interference, partially due to its proximity to the inelastic threshold, which in practice is complicated to describe with simple models.

According to the S-matrix unitary relation $SS^\dagger = \mathbb{1}$, now taking into account the Schwartz reflection principle of the partial waves $t_\ell^I(s+i\epsilon) = t_\ell^I(s-i\epsilon)^*$, the partial wave in the second Riemann sheet is algebraically related to the first Riemann sheet through the equation

$$t_\ell^{2,I}(s) = \frac{t_\ell^{1,I}(s)}{1 + 2i\sigma(s) t_\ell^{1,I}(s)}, \tag{8}$$

where $\sigma(s)$ must be defined so that $\sigma(s^*) = -\sigma(s)^*$ and hence the partial wave satisfies the reflection principle also in the second sheet

$$t_\ell^{2,I}(s^*) = t_\ell^{2,I}(s)^* \tag{9}$$

We can thus constrain Eq. (8) so that it has a zero in the denominator, corresponding to a pole at $s_p = s_R + is_I$. The derivation is as follows. First, instead of Eq. (6) we will start by writing an alternative inelastic formula

$$t_{f_0}^0(s) = \frac{s\,G}{M - s - i\bar{J}(s, m_\pi)\, s\, G - \bar{J}(s, m_K) f(s)}, \tag{10}$$

where $f(s)$ could in principle be any real, analytic function. Notice that in [27] the numerator was always multiplied by s in order to cancel the pole of the phase space at $s = 0$, also, this formula is convenient as the contribution close to threshold is suppressed by this factor. The $f(s)$ function will then be built as an expansion of the well known Chebyshev polynomials. The main advantage of such a parameterization is the reduced correlation between the parameters, which produces better error estimates. The variable of the expansion however will not be $\sqrt{s}$, but a linear transformation that maps the fitted energy region into the $[-1, 1]$ segment, where the Chebyshev polynomials are orthogonal. Given the initial and final energy values as e_{min}, e_{max} the new variable reads

$$\omega_1(s) = 2\frac{\sqrt{s} - e_{min}}{e_{max} - e_{min}} - 1. \tag{11}$$

Thus, the real function $f(s)$ can be expanded as

$$f(s) = \sum_{i=0}^{N} k_i x_i(\omega_1(s)), \tag{12}$$

where $x_i(s)$ are the Chebyshev polynomials of order i.

In the elastic region, obtained by setting all $k_i \to 0$, if we want to include a pole at $s_p = s_R + is_I$ in the second sheet we must set

$$\begin{aligned} M_e &= s_R + s_I \frac{\text{Im}\ (s_p\, \sigma(s_p))}{\text{Re}\ (s_p\, \sigma(s_p))}, \\ G_e &= \frac{s_I}{\text{Re}\ (s_p\, \sigma(s_p))}. \end{aligned} \tag{13}$$

In the inelastic region instead, the k_i parameters would shift the pole position to a new location, depending on the explicit values of the parameters. In order to avoid this outcome we will rewrite the M and G parameters so that the position of the pole remains fixed. By using Eq. (8), imposing a pole at $s_p = s_R + is_I$, the final explicit solution reads

$$\begin{aligned} M &= \frac{(f_I J_{KR} + f_R J_{KI})(s_I(J_{\pi I} - 2\sigma_R) - s_R(J_{\pi R} + 2\sigma_I)) - (f_I J_{KI} - f_R J_{KR})(J_{\pi I} s_R + J_{\pi R} s_I + 2(\sigma_I s_I - s_R \sigma_R))}{J_{\pi I} s_R + J_{\pi R} s_I + 2\sigma_I s_I - 2 s_R \sigma_R} \\ &\quad + \frac{(J_{\pi I} - 2\sigma_R)\left(s_I^2 + s_R^2\right)}{J_{\pi I} s_R + J_{\pi R} s_I + 2(\sigma_I s_I - s_R \sigma_R)}, \\ G &= -\frac{f_I J_{KR} + f_R J_{KI} + s_I}{J_{\pi I} s_R + J_{\pi R} s_I + 2\sigma_I s_I - 2 s_R \sigma_R} \end{aligned} \tag{14}$$

where, for simplicity, all of the $\bar{J}(s, m)$, $\sigma(s)$ terms have been evaluated at the $f_0(980)$ pole position $s_{pole} = s_R +$

is_I. The terms above thus read

$$\begin{aligned} f_I &= \mathrm{Im}\, f(s_p), \quad f_R = \mathrm{Re}\, f(s_p), \\ J_{KI} &= \mathrm{Im}\, \bar{J}(s_p, m_K), \quad J_{KR} = \mathrm{Re}\, \bar{J}(s_p, m_K), \\ J_{\pi I} &= \mathrm{Im}\, \bar{J}(s_p, m_\pi), \quad J_{\pi R} = \mathrm{Re}\, \bar{J}(s_p, m_\pi), \\ \sigma_I &= \mathrm{Im}\, \sigma(s_p), \quad \sigma_R = \mathrm{Re}\, \sigma(s_p). \end{aligned} \tag{15}$$

Thus, we will use Eq. (5) with this new $t^0_{f_0}(s)$ parameterization as our final formula. Take into account that due to the conformal mapping used in Eq. (2) the cotangent acquires an imaginary part above the $K\bar{K}$ threshold. Two scenarios are then possible, the one where we no longer use the conformal mapping above the inelastic threshold, fitting the whole inelastic region by means of $t^0_{f_0}(s)$, and the one where we allow this formula to become imaginary in order to develop an inelasticity. The second option seems favored, as the imaginary part helps with a much better description of the inelastic region, and is thus the solution adopted in this work.

Above 1.43 GeV we will introduce a simple phenomenological description

$$t^I_\ell(s) = \frac{\eta^I_\ell(s) e^{2i\delta^I_\ell(s)} - 1}{2i\sigma(s)}, \tag{16}$$

where the inelasticity and phase shift will be described by two different functions. They will be matched to the previous formula at $s_m = 1.4^2\,\mathrm{GeV}^2$, so that the continuity of the value and first derivative are ensured, and the parameterizations will be fitted to data up to $\sqrt{s} = 1.9\,\mathrm{GeV}$.

In order to perform the matching, the values of the phase shift and inelasticity and their derivatives are needed at s_m. These inputs will be taken from the parameterizations above, where the derivative is understood with respect to the energy squared. To reduce the number of parameters we will again make use of a second order Chebyshev polynomial to describe the phase shift above s_m. However, the inelasticity will be fitted through an exponential function to ensure unitarity, which in the case of the P-wave will be described using Chebyshev polynomials again. Unfortunately, in the case of the S-wave, Chebyshev polynomials would produce unwanted oscillations, so that a simple phenomenological expansion in terms of the energy will be used instead. As for the vector-channel inelasticity, a simple Chebyshev polynomial expansion will be enough. All in all, the final formulas for the phenomenological parameterizations are as follows

$$\begin{aligned} \delta^I_\ell(s) &= \delta^I_\ell(s_m) + \Delta^I_\ell(x_1(\omega_2(s)) + 1) + d_0(x_2(\omega_2(s)) - 1) \\ &\quad + d_1(x_3(\omega_2(s)) - 1), \\ \Delta^I_\ell &= \frac{\delta'^I_\ell(s_m) - d_0 x'_2(\omega_{2\,m}) - d_1 x'_3(\omega_{2\,m})}{x'_1(\omega_{2\,m})}, \\ \eta^0_0(s) &= \exp - \left(\sqrt{-\log(\eta^0_0(s_m))} \right. \\ &\quad + 8\frac{q_m(q(s) - q_m)\eta^{0\,\prime}_0(s_m)}{-2\sqrt{-\log(\eta(s_m))}\eta(s_m)} + e_0 \left(\frac{q(s)}{q_m} - 1 \right)^2 \\ &\quad \left. + e_1 \left(\frac{q(s)}{q_m} - 1 \right)^3 + e_2 \left(\frac{q(s)}{q_m} - 1 \right)^4 \right)^2, \\ \eta^1_1(s) &= \exp - \left(\sqrt{-\log(\eta^1_1(s_m))} \right. \\ &\quad + H^1_1(x_1(\omega_2(s)) + 1) + e_0(x_2(\omega_2(s)) - 1) \\ &\quad \left. + e_1(x_3(\omega_2(s)) - 1) + e_2(x_4(\omega_2(s)) + 1) \right)^2, \\ H^1_1 &= \frac{\eta'^1_1(s_m) - e_0 x'_2(\omega_{2\,m}) - e_1 x'_3(\omega_{2\,m}) - e_2 x'_4(\omega_{2\,m})}{x'_1(\omega_{2\,m})}, \end{aligned} \tag{17}$$

where x_i are again the Chebyshev polynomials of order i and the new inelastic variable is

$$\begin{aligned} \omega_2(s) &= 2\frac{\sqrt{s} - \sqrt{s_m}}{e_{max} - \sqrt{s_m}} - 1, \\ \omega_{2\,m} &= \omega_2(s_m). \end{aligned} \tag{18}$$

Note that the logarithms in Eq.(17) appear in the constants needed for the smooth matching, they do not introduce any spurious analytic structure.

We will not make use of e_1 when fitting solution I, as its behavior is pretty smooth and the uncertainties of the data are so large the χ^2 of both phase shift and inelasticity are always below 1.

IV. S-WAVE FIT

The aim of this work is to perform a global fit that describes all analytic constrains at low energies, while also describing the existing data above the energy region where dispersion relations can be implemented. To this end we have developed a set of parameterizations that are flexible enough to incorporate all our requirements.

As shown in [12], the partial waves of $\pi\pi \to \pi\pi$ scattering fulfil the dispersive constrains fairly well up to 1.43 GeV. These set consist on a group of forward dispersion relations for the amplitudes, together with the more sophisticated Roy and GKPY equations for the partial waves, applicable up to roughly 1.1 GeV.

If one would like to mimic this dispersive result, an exact constrain should be imposed over our parameterizations so that they fully describe the central dispersive values, however, several sources of uncertainty come into

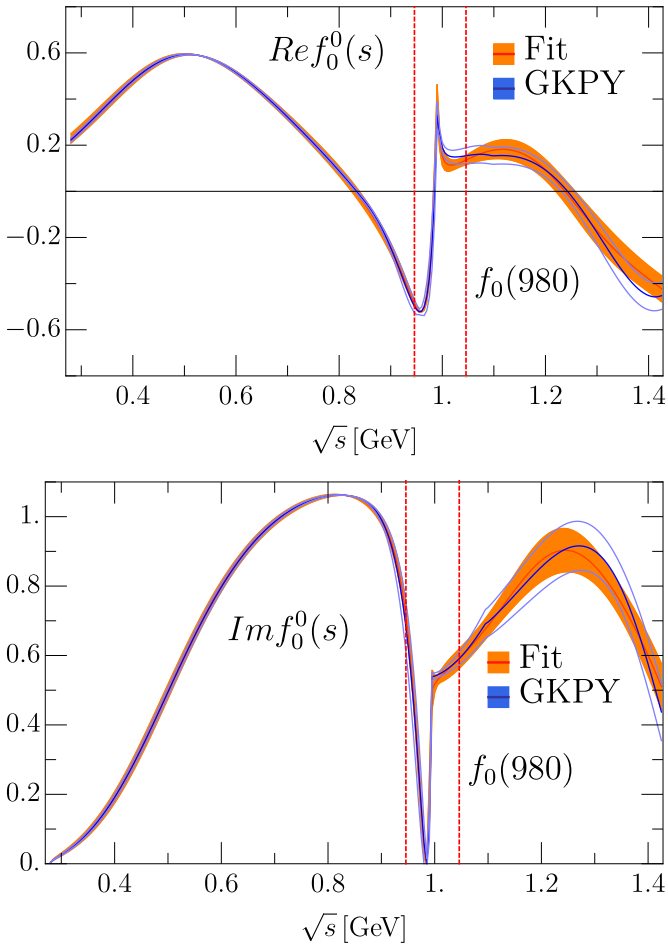

FIG. 1: Comparison between the CFD fit in [12] (blue) and solution I (Table II (orange band). The energy region dominated by the $f_0(980)$ pole is delimited between the red dashed lines.

play, so that we will impose all dispersive results through a χ^2 function as follows. In the real axis, the solution coming from the constrained parameterizations of [12] will be fitted, where the uncertainties are the error bands, which are at the same time related to the initial fits of [12] up to 1.43 GeV. This solution has way smaller uncertainties than the dispersion relations themselves, and thus is preferred to build a more accurate result. We will impose just the phase shift up to the inelastic $K\bar{K}$ threshold, and both the phase shift and inelasticity above it.

Below the elastic threshold, and in the complex plane, we will make use of the GKPY equations, which produce narrower errors than those of Roy equations, while both are compatible in the whole complex plane and real axis. The fit will run from about $\mathrm{Re}\, s \sim (0\,\mathrm{GeV})^2$ to $\mathrm{Re}\, s \sim (1.12\,\mathrm{GeV})^2$, and, as the data points must remain inside the applicability region of the dispersion relations [10, 20, 21], the imaginary parts will never go above it. Using such a vast region we force the fit to have a well rounded description of the scattering lengths, the Adler zero, and the $\sigma/f_0(500)$ pole position and coupling. Due to the large number of points, and the tiny uncertainties in the real axis, the errors obtained in the complex plane are smaller than the dispersive ones, however, comparable errors in the complex plane would produce a huge mismatch in the real axis, which is our mayor source of information.

TABLE I: Results in terms of the χ^2 function of the fits

	χ^2_1	χ^2_2	χ^2_{com}	χ^2_{pha}	χ^2_{ine}
Solution I [1, 2, 4, 29]	0.2	0.5	0.4	0.5	0.4
Solution II [3]	0.2	0.5	0.3	1.0	1.0

These constrains will be imposed by means of a χ^2 function, although they are not data points, the reason is that the least squares solution provides an stiff bind to the parameterization, while also weighting the results depending on whether they have large or small uncertainties. Nevertheless, the statistical meaning of the $\chi^2 \sim 1$ looses part of its purpose, as the results coming from dispersion relations are smooth functions instead of normally distributed points, and their uncertaintites are totally correlated between bins. As a result, a value lower than 1 is expected, and we will consider all results below 1 as good descriptions of our dispersion relations.

We show in Fig. 1 the comparison between the constrained fit of [12] and our best result of solution I. Both parameterizations look almost equal below the $K\bar{K}$ threshold, and are also well compatible above it, the error bands are of the same order, although there is a small region where the solution I has smaller uncertainties. Taking into account that we are explicitly including the $f_0(980)$ parameters coming from the most precise GKPY determination of [22], it is clear the the region close to its nominal mass will no longer be dominated by the CFD parameterization, as the $f_0(980)$ uncertainties are tiny there. All in all this new parameterization is able to fulfil the GKPY dispersion relations in the low energy region, together with the low energy parameters, the Adler zero, the positions of both $\sigma/f_0(500)$ and $f_0(980)$ poles, and the inelastic region up to 1.43 GeV. While also producing similar uncertainties to those of the CFD parameterization in [12].

Above 1.43 GeV no dispersive result exist, thus we will make use of the available experimental data. The only sources of data in this energy region produce two different plausible solutions. The first one, called solution I in this work comes from [1, 2, 4, 29]. Whereas there is a second one, called solution II, also coming from the CERN-Munich experiment [3]. The parameters of the fits are listed in Tables II and III, both results are almost equivalent in the elastic region, while exhibiting some almost negligible deviation in the inelastic region below 1.4 GeV. Above this splitting point the solutions are fairly different, in particular the inelasticities depict a clearly different pattern, with a sharp falloff in solution

TABLE II: Parameters resultant of the fits of the Global parameterization for solution I.

Elastic		$\sqrt{s} < 1.43$ GeV		$\sqrt{s} > 1.43$ GeV	
B_0	12.2±0.3	K_0	1.29±0.07	d_0	-5.4±3.7
B_1	-0.9±1.1	K_1	-1.08±0.04		
B_2	15.9±2.7	K_2	-0.043±0.038	e_0	10.3±4.0
B_3	-5.7±3.1	K_3	-0.068±0.015		
B_4	-22.5±3.7				
B_5	6.9±4.8				
z_0	0.137±0.028				

II, while solution I has a smooth decreasing inelasticity close to 1.9 GeV.

It is worth noticing (see Fig. 2) that the uncertainties of the solution II are larger for the phase shift, due to the scarcity of data above 1.5 GeV. Furthermore, even though we included some data points coming from [1, 2] for the inelasticity, the solution II is fairly unstable. Such a behavior could not be interpreted in terms of a resonance, or any known cusp, so that we favored the solution fitted to [1, 2].

Finally, let us recall that all data points above 1.43 GeV (dashed red line Fig. 2) have been included for completeness, as there is no unique solution, and no dispersive analysis has been performed in this region yet. However, solution I looks fairly compatible and stable, which, together with the conservative error band associated to it, could provide a fair estimate of the phase shift and inelasticity up to roughly 4 GeV [2].

TABLE III: Parameters resultant of the fits of the Global parameterization for solution II.

Elastic		$\sqrt{s} < 1.43$ GeV		$\sqrt{s} > 1.43$ GeV	
B_0	12.2±0.3	K_0	1.22±0.02	d_0	-16.5±6.2
B_1	-1.2±0.8	K_1	-1.16±0.02		
B_2	15.5±1.5	K_2	-0.010±0.044	e_1	160.8±2.5
B_3	-6.0±1.5	K_3	-0.075±0.010	e_1	-715.5±8.5
B_4	-21.4±1.3			e_2	-937.3±25.0
B_5	6.3±4.5				
z_0	0.135±0.031				

A. Poles, Couplings and Low Energy Parameters

TABLE IV: Poles and residues of both $f_0(500)$ and $f_0(980)$ resonances.

	$\sqrt{s_{pole}}$ (MeV)	$\lvert g\rvert$
$f_0(500)$	$(457 \pm 9) - i(279 \pm 7)$	3.47 ± 0.07
$f_0(980)$	$(996 \pm 7) - i(25 \pm 8)$	2.28 ± 0.06

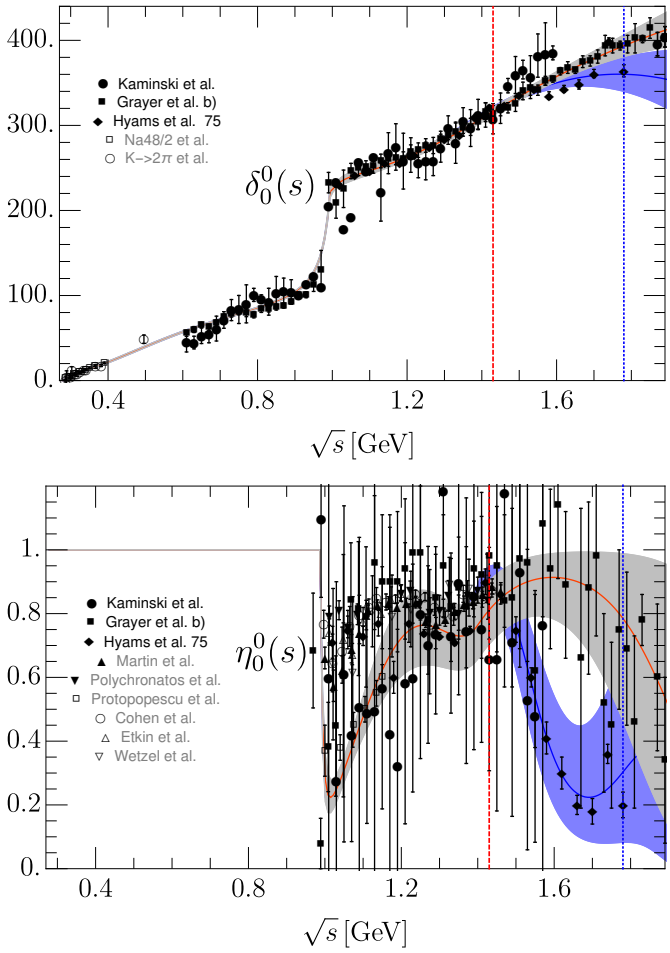

FIG. 2: Comparison of solutions I and II (Tables II and III) with the data sets that they are compatible with. The red dashed line splits the region below where the fits are obtained by means of imposing dispersion relations, and the region above where the two different solutions are shown. The blue dotted line depicts the energy of the last data point for solution II. Solution I fits the data of [4, 29] (solid circles) and [1, 2] (solid squares), whereas solution II fits [3] (solid diamonds). The data coming from [8] (empty squares), [30] (empty circles), [31] (triangle up), [32](triangle down), [5] (empty squares), [30] (empty circles), [33] (empty triangle up) and [34] (empty triangle down) are shown for comparison. The gray band corresponds to the fit of solution I and the blue band is solution II.

As explained above, the fit is also constrained to describe the $\sigma/f_0(500)$ resonance, which together with the fact that we are also imposing the whole complex energy plane, produces a stable and accurate description of its parameters. In Fig.3 we show our parameterization and its uncertainties in the first Riemann sheet of complex plane, which reproduces the output of GKPY equations. In addition, we list in Table IV the parameters of both the $\sigma/f_0(500)$ and $f_0(980)$ resonances. It

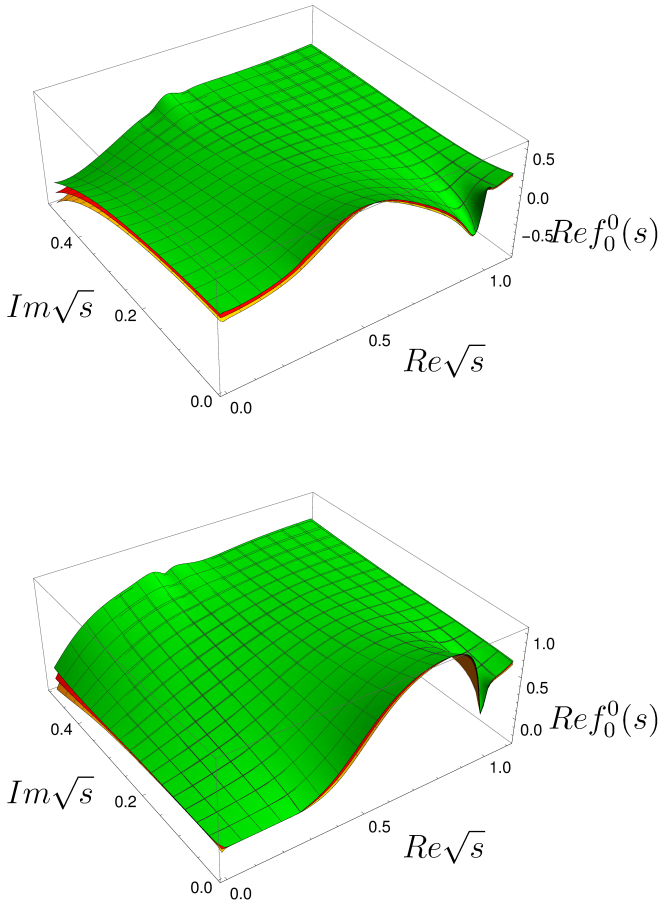

FIG. 3: Real (top) and imaginary (bottom) parts of the scalar-isoscalar partial wave in a vast region in the complex plane in the first Riemann Sheet. Notice that the behavior of the solution is smooth and the uncertainties are small even deep in the complex plane.

is worth noticing that the uncertainties of the $\sigma/f_0(500)$ resonance associated to this fit are a bit smaller than the GKPY determination [22]. This behavior is caused due to the large statistic we have fitted in the region where the pole exists.

As for the $f_0(980)$ resonance, we have imposed its pole position to be the one obtained by means of the GKPY equations in [22]. The main reason is that no phenomenological fit can extract its parameters in a stable way. In particular, the CFD fit of [12] cannot provide a decent estimate of its position. With this improved fit, the $f_0(980)$ is no longer a problem, as both the data, the cusp effect and the pole position are nicely incorporated into a simple, yet powerful functional form. As a result of this constrains, the coupling of the $f_0(980)$ to $\pi\pi$ has smaller uncertainties than the GKPY determination, which can be related to the smaller uncertainty seen in this region in Fig. 1.

TABLE V: Adler zero and threshold parameters. The latter in customary $m_\pi = 1$ units.

	This work	Dispersive result [12]
$\sqrt{s_{Adler}}$	96±20 MeV	85±34 MeV
a_0^0	0.227±0.020	0.220±0.008
b_0^0	0.266±0.009	0.278±0.005

Last, but not the least, the results of these fits produce compatible low energy parameters with thus of the Madrid-Krakow group [12] and the Bern group [10, 11]. The description of the partial wave in the real axis both above and below the $\pi\pi$ threshold produces a well compatible result for all this quantities, although the dispersive low energy constants will always be more constrained. The reason is that there is a direct correlation between the values of scattering lengths, slope parameters and the output coming from the dispersive integral, thus providing a way bigger constrain that a simple fit.

V. P-WAVE FIT

The $\pi\pi$-scattering P wave is completely dominated by the $\rho(770)$ meson, which is customarily described using simple resonant descriptions. However, even though the $\rho(770)$ is usually considered as the prototype of narrow resonance, its width is relatively large as compared with its mass, which explains that the ρ-meson shape cannot be fully described with precision using a simple Breit-Wigner function or within an Isobar model, but requires additional shape parameters [35, 36]. Let us also recall that the $\rho(770)$ is the main player of vector meson dominance, and therefore it saturates the most common hadronic observables, like, for instance, the hadronic total cross section $\sigma(e^+e^- \to \text{hadrons})$ [37], which implies applications well beyond low-energy meson physics. Thus, given its relevance for Hadron physics, we will provide in this section an analytic parameterization to describe the pion-pion vector-isovector channel up to 2 GeV.

Following the same procedure considered for the scalar-isoscalar channel, in the physical region and below 1.43 GeV we will impose the constrained parameterization of [12]. Note that this P-wave parameterization describes both $\pi\pi$ scattering [3, 5, 38] and pion-vector form factor [39, 40] data, while fulfilling at the same time the dispersive constraints described in the Introduction. Once more, in the subthreshold region and in the complex plane we will fit the GKPY-equation dispersive results. Like for the scalar channel, we will only consider the energy region within the Lehmann ellipse, where both Roy and GKPY equations are formally valid.

Above 1.43 GeV there are no further dispersive results and hence we will only describe the available experimental data, which rely on a single scattering experiment from the CERN-Munich Collaboration. In addition, in

the vector case there is a relevant difference between the best solution of the original CERN-Munich result published in 1973 [1] and the (- - -) solution of the 1975 collaboration reanalysis [3]. Nevertheless, the behavior of the original P-wave result shows a large interference in the region between 1.6 and 1.8 GeV. Namely, the phase shift changes in more than 20° and the inelasticity goes down below 0.5 to return back to 1 in around 200 MeV. This behavior could only be explained if the ρ' and ρ'' resonances and the $K\bar{K}$ channel would interfere strongly, which is in contradiction with the experimental values for the width and couplings of these two resonances [41, 42]. Thus, the solution (- - -) of Hyams 75 [3] is the one customarily used in the literature. However, we will fit both solutions for completeness, as we have done for the S-wave. The original CERN-Munich result [1] will be called solution I, whereas the fit to the updated reanalysis of [3] will be called solution II.

Once more, even when our fit does not have a well-defined statistical meaning, we impose all constraints by means of a χ^2 function, which ensures compatible results within uncertainties. Using the parameterizations described in Section III we obtain a nice description of the input. Namely, the χ^2 values, given in Tables VI and VII, are all below or close to 1. The fit parameters are collected in Tables VIII and IX for solutions I and II, respectively. The fit results for the P-wave phase shift and inelasticity are plotted in Fig. 4. The uncertainties are described by the gray band for solution I and blue band for solution II, and they are consistent with those given in [12]. Note that they are extremely small in the low-energy region. Actually, in order to ensure an accurate description of the error band in this region, we choose the center of the conformal parameterization, i.e. the α parameter in (2), to be close to the threshold. In this way, the uncertainties are dominated by the lowest conformal parameters B_0 and B_1, ensuring that the value of the scattering length and slope parameter, given in Table XI, are consistent with the dispersive values in [12]. On the contrary, the fit result errors close to 1.4 GeV are smaller than those quoted in [12], which is consequence of describing simultaneously the experimental data up to 2 GeV. The P-wave inelasticity in [12] is compatible with 1 below 1.12 GeV and very small below 1.4 GeV. Thus, it is reproduced by the simple polynomial parameterization given in (4) for simplicity.

Finally, the $\rho(770)$ pole- parameteres are given in Table X. Central values and uncertainties are nicely compatible with the dispersive results in [22].

TABLE VI: Results in terms of the $\chi^2/d.o.f.$ function of the fits of Solution I.

	χ^2_1	χ^2_2	χ^2_{com}	χ^2_{pha}	χ^2_{ine}
Best Solution [3]	0.6	0.4	0.6	1.2	0.6

Above the matching point at 1.4 GeV the two solutions coming from the CERN-Munich experiment are incompatible among themselves. The behavior of solution I looks compatible with a strong interference between the ρ' and ρ'', with a phase movement around 1.6 GeV and a dip structure in the inelasticity at the same energy. Nevertheless, as explained above, we will fit these data by using purely phenomenological parameterizations.

TABLE VII: Results in terms of the $\chi^2/d.o.f.$ function of the fits of Solution II. We have added roughly 1 degree of systematic uncertainty to the phase shift data above 1.4 GeV.

	χ^2_1	χ^2_2	χ^2_{com}	χ^2_{pha}	χ^2_{ine}
Best Solution [3]	0.6	0.5	0.7	0.9	0.9

In contrast, solution II looks smoother, with a phase that rises slowly above 180°, and an inelasticity with a less pronounced dip, which, together with the smaller uncertainties quoted in [3] produces a way more constrained result.

TABLE VIII: Fit parameters of the Global parameterization for solution I.

Elastic		$\sqrt{s} < 1.43$ GeV		$\sqrt{s} > 1.43$ GeV	
B_0	0.97±0.01	K_0	0.33±0.16	d_0	11.1±1.6
B_1	0.12±0.04			d_1	5.7±0.5
B_2	-0.18±0.08				
B_3	0.41±0.20			e_0	-0.132±0.031
B_4	1.64±0.40			e_1	0.353±0.011
m_ρ	0.7752±0.0014			e_2	0.205±0.064

TABLE IX: Fit parameters of the Global parameterization for solution II.

Elastic		$\sqrt{s} < 1.43$ GeV		$\sqrt{s} > 1.43$ GeV	
B_0	0.97±0.01	K_0	0.17±0.06	d_0	3.4±1.2
B_1	0.11±0.04			d_1	2.4±0.3
B_2	-0.13±0.08				
B_3	0.47±0.20			e_0	-0.16±0.02
B_4	1.38±0.36			e_1	0.042±0.005
m_ρ	0.7752±0.0014			e_2	0.059±0.003

TABLE X: Pole and residue of the $\rho(770)$.

	$\sqrt{s_{pole}}$ (MeV)	$\lvert g\rvert$
$\rho(770)$	$(763.1 \pm 1.6) - i(73.3 \pm 1.4)$	5.99 ± 0.06

VI. SUMMARY

In this work we have provided a global parameterization of the data on S0 and P-waves of $\pi\pi \to \pi\pi$ up to 2

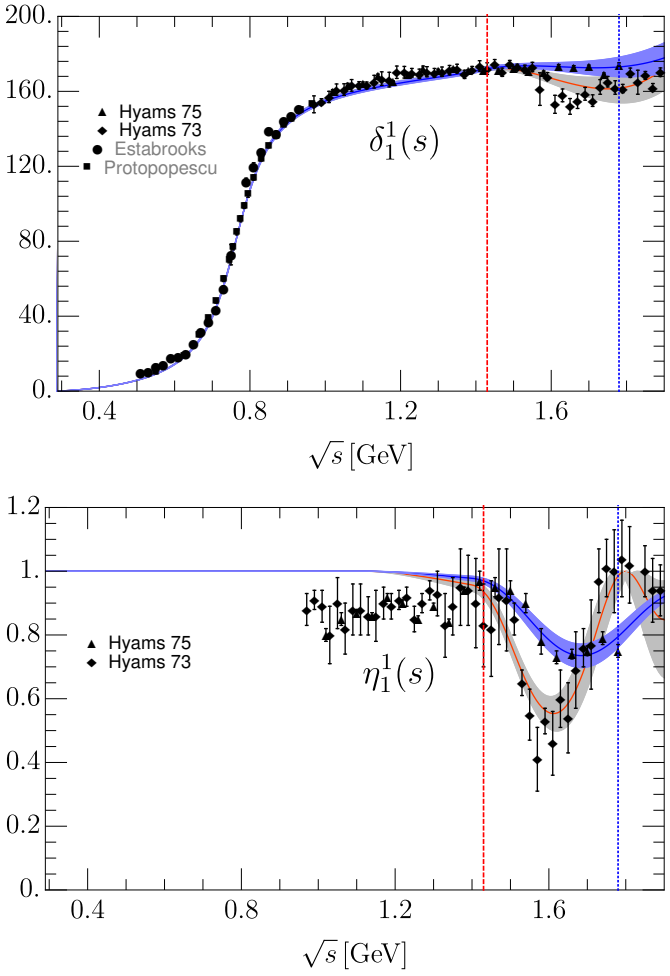

FIG. 4: Comparison of our two solutions (Table VIII) with data [5] (solid squares) and [38] (solid circles). The red dashed vertical line separates the region where the fits describe data and dispersion relation results from the region above where the parameterization is just fitted to [3] (solid diamonds). The blue dotted vertical line depicts the energy of the last data point. The gray band corresponds to the fit of solution I and the blue band is solution II.

TABLE XI: Threshold parameters in customary $m_\pi = 1$ units.

	This work	Dispersive result [12]
$a_1^1(\text{x}10^3)$	38.3±0.6	38.1±0.9
$b_1^1(\text{x}10^3)$	4.52±0.53	5.37±0.14

GeV. We have made an explicit effort to keep it relatively simple in order to be easy to implement in further phenomenological and experimental analyses (in final state interactions, isobar models, etc...).

The advantages of this parameterization are that it describes the data up to 2 GeV consistently with the dispersive representation in [12] and its uncertainties. In addition, it reproduces the dispersive results in the complex plane including the associated poles of the $\sigma/f_0(500)$, $f_0(980)$ and $\rho(770)$ resonances. Moreover, its low energy behavior is compatible with the dispersive results for scattering lengths and the Adler zero position, and therefore with the constraints due to the QCD spontaneous chiral symmetry breaking.

Actually, this new parameterization reproduces the results and uncertainties of a previous piece-wise fit that was constrained to satisfy Forward Dispersion relations up to 1.43 GeV and partial-wave dispersion relations (Roy and GKPY equations) up to 1.12 GeV. The latter were used in [12] to obtain a rigorous analytic continuation to the complex plane which, together with its uncertainties, is also described when continuing analytically our new parametrization, without the need for a numerical integration of the dispersion relations. This is why the pole positions and residue of the $\sigma/f_0(500)$, the $f_0(980)$ and the $\rho(770)$ are so well implemented. It also allows our parameterization to be used consistently in applications with isobar models, so popular in experimental analyses.

The new parameterization also reproduces the existing data from 1.43 to 2 GeV, although the dispersion relations do not reach this energies. Moreover, in this region, there are two contradictory data sets, and we thus provide two solutions that describe phenomenologically either one of the conflicting sets. Nevertheless, below 1.43 GeV these two solutions agree and are consistent with the dispersive analysis.

We hope that the simplicity and the remarkable analytic properties of this data parameterization can be of use for future phenomenological and experimental studies whenever the $\pi\pi \to \pi\pi$ interaction is needed.

ACKNOWLEDGMENTS

JRP and AR are supported by the Spanish project FPA2016-75654-C2-2-P. This project has received funding from the European Union's Horizon 2020 research and innovation programme under grant agreement No 824093. AR would also like to acknowledge the financial support of the Universidad Complutense de Madrid through a predoctoral scholarship. JRE is supported by the Swiss National Science Foundation, project No. PZ00P2_174228.

[1] B. Hyams *et al.*, Nucl. Phys. **B64**, 134 (1973).

[2] G. Grayer *et al.*, Nucl. Phys. **B75**, 189 (1974).

[3] B. Hyams *et al.*, Nucl. Phys. **B100**, 205 (1975).
[4] R. Kaminski, L. Lesniak, and K. Rybicki, Z. Phys. **C74**, 79 (1997), arXiv:hep-ph/9606362 [hep-ph].
[5] S. D. Protopopescu, M. Alston-Garnjost, A. Barbaro-Galtieri, S. M. Flatte, J. H. Friedman, T. A. Lasinski, G. R. Lynch, M. S. Rabin, and F. T. Solmitz, Phys. Rev. **D7**, 1279 (1973).
[6] L. Rosselet *et al.*, Phys. Rev. **D15**, 574 (1977).
[7] S. Pislak *et al.* (BNL-E865), Phys. Rev. Lett. **87**, 221801 (2001), [Erratum: Phys. Rev. Lett.105,019901(2010)], arXiv:hep-ex/0106071 [hep-ex].
[8] J. R. Batley *et al.* (NA48-2), Eur. Phys. J. **C70**, 635 (2010).
[9] K. M. Watson, Phys. Rev. **95**, 228 (1954).
[10] B. Ananthanarayan, G. Colangelo, J. Gasser, and H. Leutwyler, Phys.Rept. **353**, 207 (2001), arXiv:hep-ph/0005297 [hep-ph].
[11] G. Colangelo, J. Gasser, and H. Leutwyler, Nucl. Phys. **B603**, 125 (2001), arXiv:hep-ph/0103088 [hep-ph].
[12] R. García-Martín, R. Kamiński, J. R. Peláez, J. Ruiz de Elvira, and F. J. Ynduráin, Phys.Rev. **D83**, 074004 (2011), arXiv:1102.2183 [hep-ph].
[13] C. Ditsche, M. Hoferichter, B. Kubis, and U. G. Meissner, JHEP **06**, 043 (2012), arXiv:1203.4758 [hep-ph].
[14] M. Hoferichter, J. Ruiz de Elvira, B. Kubis, and U.-G. Meißner, Phys. Rept. **625**, 1 (2016), arXiv:1510.06039 [hep-ph].
[15] P. Buettiker, S. Descotes-Genon, and B. Moussallam, Eur. Phys. J. **C33**, 409 (2004), arXiv:hep-ph/0310283 [hep-ph].
[16] J. R. Pelaez and F. J. Yndurain, Phys. Rev. **D71**, 074016 (2005), arXiv:hep-ph/0411334 [hep-ph].
[17] R. Kaminski, J. R. Pelaez, and F. J. Yndurain, Phys. Rev. **D77**, 054015 (2008), arXiv:0710.1150 [hep-ph].
[18] R. Kaminski, J. R. Pelaez, and F. J. Yndurain, Phys. Rev. **D74**, 014001 (2006), [Erratum: Phys. Rev.D74,079903(2006)], arXiv:hep-ph/0603170 [hep-ph].
[19] F. J. Yndurain, R. Garcia-Martin, and J. R. Pelaez, Phys. Rev. **D76**, 074034 (2007), arXiv:hep-ph/0701025 [hep-ph].
[20] S. M. Roy, Phys.Lett. **36B**, 353 (1971).
[21] I. Caprini, G. Colangelo, and H. Leutwyler, Phys.Rev.Lett. **96**, 132001 (2006), arXiv:hep-ph/0512364 [hep-ph].
[22] R. García-Martín, R. Kaminski, J. R. Peláez, and J. Ruiz de Elvira, Phys.Rev.Lett. **107**, 072001 (2011), arXiv:1107.1635 [hep-ph].
[23] B. Moussallam, Eur. Phys. J. **C71**, 1814 (2011), arXiv:1110.6074 [hep-ph].
[24] J. R. Pelaez and F. J. Yndurain, Phys. Rev. **D68**, 074005 (2003), arXiv:hep-ph/0304067 [hep-ph].
[25] D. Atkinson, Nucl. Phys. **B8**, 377 (1968), [Erratum: Nucl. Phys.B15,331(1970)].
[26] D. Atkinson, Nucl. Phys. **B23**, 397 (1970).
[27] I. Caprini, Phys. Rev. **D77**, 114019 (2008), arXiv:0804.3504 [hep-ph].
[28] H. Q. Zheng, Z. Y. Zhou, G. Y. Qin, Z. Xiao, J. J. Wang, and N. Wu, Nucl. Phys. **A733**, 235 (2004), arXiv:hep-ph/0310293 [hep-ph].
[29] H. Becker *et al.* (CERN-Cracow-Munich), *Argonne Symp.1978:461*, Nucl. Phys. **B151**, 46 (1979).
[30] D. H. Cohen, D. S. Ayres, R. Diebold, S. L. Kramer, A. J. Pawlicki, and A. B. Wicklund, Phys. Rev. **D22**, 2595 (1980).
[31] A. D. Martin and E. N. Ozmutlu, Nucl. Phys. **B158**, 520 (1979).
[32] V. A. Polychronakos, N. M. Cason, J. M. Bishop, N. N. Biswas, V. P. Kenney, D. S. Rhines, R. C. Ruchti, W. D. Shephard, M. J. Stangl, and J. M. Watson, Phys. Rev. **D19**, 1317 (1979).
[33] A. Etkin *et al.*, Phys. Rev. **D25**, 1786 (1982).
[34] W. Wetzel, K. Freudenreich, F. X. Gentit, P. Muhlemann, W. Beusch, A. Birman, D. Websdale, P. Astbury, A. Harckham, and M. Letheren, Nucl. Phys. **B115**, 208 (1976).
[35] J. Pisut and M. Roos, Nucl. Phys. **B6**, 325 (1968).
[36] G. D. Lafferty, Z. Phys. **C60**, 659 (1993).
[37] M. Ablikim *et al.* (BESIII), Phys. Lett. **B753**, 629 (2016), arXiv:1507.08188 [hep-ex].
[38] P. Estabrooks and A. D. Martin, Nucl. Phys. **B79**, 301 (1974).
[39] L. M. Barkov *et al.*, Nucl. Phys. **B256**, 365 (1985).
[40] S. R. Amendolia *et al.* (NA7), *Proceedings, 23RD International Conference on High Energy Physics, JULY 16-23, 1986, Berkeley, CA*, Nucl. Phys. **B277**, 168 (1986).
[41] C. Hanhart, Phys. Lett. **B715**, 170 (2012), arXiv:1203.6839 [hep-ph].
[42] M. Tanabashi *et al.* (Particle Data Group), Phys.Rev. **D98**, 030001 (2018).

Chapter 3

Meson spectroscopy

It has been pointed out throughout this thesis how the determination of low-energy hadronic resonances is not only relevant for their own classification in multiplets, but also for our understanding of low-energy Chiral Perturbation Theory, and thus QCD. The study of spectroscopy has motivated several experimental collaborations in recent years, like LHCb, BaBar, BELLE, BESIII, CLAS12, GlueX, ALICE and many others. At the same time, it is a growing field within Lattice QCD practitioners.

In the first part of this chapter, in section 3.1 we will detail how a model independent extraction of resonances can be made, with particular emphasis on strange resonances. The original works are presented in sections 3.1.4 and 3.1.3. Next, in section 3.2 we will introduce the N/D and K-matrix formalisms, together with the P formalism for describing production processes in a general basis. Thus, the results obtained for the study of the hybrid meson are presented in section 3.3.3. Finally, in section 3.4 we will implement and compare some approximations of 3-body interactions, with particular emphasis on the quasi-two-body approximation applied to the decay $a_1(1260) \to 3\pi$, giving rise to the publication included in section 3.4.3.

3.1 Analytic determination of strange resonances

In section 1.3.6 the model-independent definition of a resonance pole is introduced, that is, the poles appearing in the next continuous Riemann sheet across the unitarity cut. In this section we will explore different analytical ways of reaching the next continuous sheets and identify the poles.

We start by restricting ourselves to the simple elastic case, where an algebraic formula can be written, let us call $S(s,t)$ the analytical S-matrix describing the process of interest. The Schwartz reflection principle states that $S(s+i\epsilon,t) = S^*(s-i\epsilon,t)$.

Furthermore, if one wants to continue from the first to the second Riemann sheet the unitarity cut must be crossed continuously, *i.e.*

$$S^I(s+i\epsilon,t) = S^{II}(s-i\epsilon,t), \tag{3.1}$$

therefore one gets $S^*(z,t) = S^{II}(z,t)$, where z is a complex number. Finally, by imposing the unitarity condition for the S-matrix $SS^* = \mathbb{1}$ we get

$$S^{II}(z,t) = (S^I(z,t))^{-1}. \tag{3.2}$$

Therefore a pole in the second Riemann sheet corresponds to a zero in the first.

Now, for a well-defined angular-momentum partial wave the formula above yields

$$f_\ell^{II}(z) = \frac{f_\ell^I(z)}{1+2i\sigma(z)t_\ell^I(z)}, \tag{3.3}$$

where $\sigma(z)$ is defined so that the relation $\sigma^*(z) = -\sigma(z^*)$ is fulfilled, in order to ensure that $f_\ell^{II}(z)$ respects the Schwartz reflection principle.

Even though the algebraic formula for the coupled-channel case is not that simple, it is doable as long as one has control over all relevant channels. In particular let us restrict ourselves to the well-known $\pi\pi \to \pi\pi, K\bar{K}$ system. In this case one has to take into account the unitary relation to obtain the desired branch cut discontinuity

$$Im f_\ell(s) = f_\ell(s)\Sigma(s)f_\ell^*(s), \tag{3.4}$$

where in this case $f_\ell(s)$ is now a symmetric matrix which includes all possible scattering partial waves, and $\Sigma(s)$ is the diagonal matrix whose elements are the phase spaces. For example, in the particular case of the scalar-isoscalar $\pi\pi \to \pi\pi$ partial wave the system can be described as

$$f_l(s) = \begin{pmatrix} f_{\pi\pi\to\pi\pi}(s) & f_{\pi\pi\to K\bar{K}}(s) \\ f_{K\bar{K}\to\pi\pi}(s) & f_{K\bar{K}\to K\bar{K}}(s) \end{pmatrix}, \tag{3.5}$$

with

$$\Sigma(s) = \begin{pmatrix} \sigma_{\pi\pi}(s) & 0 \\ 0 & \sigma_{K\bar{K}}(s) \end{pmatrix}. \tag{3.6}$$

With this system of equations one could extract for example the parameters of the $f_0(980)$. In section 3.3.3 such coupled systems will be applied to $\eta^{(\prime)}\pi$ in order to determine with precision the pole position of the hybrid meson (published in [171]).

Now, it was already detailed in the previous chapter how to derive an optimal set of dispersion relations, both for the real axis and the complex plane. We will take advantage of the equations already calculated in sections 2.1.1 and 2.1.2, to determine in a dispersive way the partial wave in first Riemann sheet in the elastic region. As shown above, the later is exactly equal as calculating the second Riemann sheet. Hence, as Roy-Steiner equations are a result of causality and crossing, and the input, which is

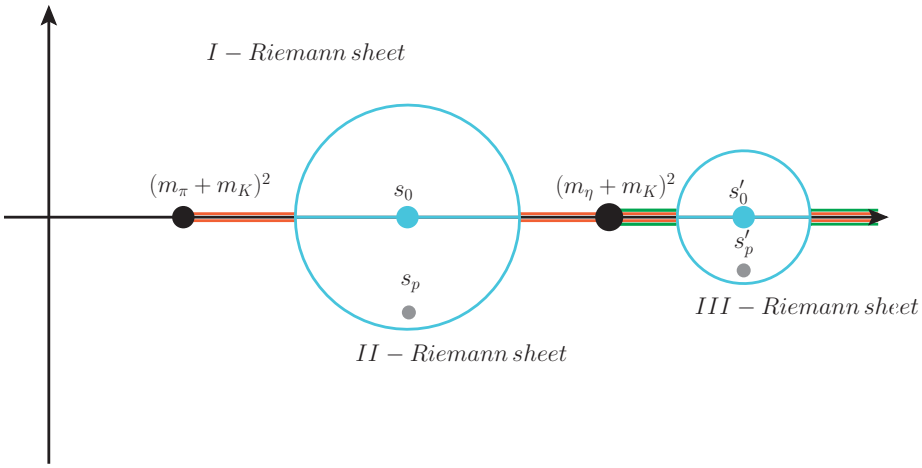

Figure 3.1: Unfolding different Riemann sheets by means of Padè approximants. The colored straight lines represent the right hand cuts produced by the πK or the ηK thresholds respectively.

constrained to described the data, is forced to be unitary, the $\kappa/K_0^*(700)$ pole can be directly extracted from first principles, as it is explained in section 3.1.4.

Unfortunately, we do not know a first-principle dispersive method for calculating inelastic resonances, the reason is that Roy-Steiner equations cannot be used in those energy regions. As a result, there are always some model dependencies, however, our approach is to implement analytic methods, at least getting rid of models for the unstable continuations into the complex plane.

There is one advantageous approach, the use of sequences of Padé approximants [172–175] ready to be used in this kind of systems. Their main advantage is that they provide a rigorous analytical continuation into the next continuous Riemann sheet. Let us review their main properties and definitions. A Padé approximant is defined as the ratio of two polynomials of a given order which together fulfill

$$P_M^N(s, s_0) = \frac{Q_N(s, s_0)}{R_M(s, s_0)} = f_\ell(s) + O((s - s_0)^{M+N+1}), \tag{3.7}$$

where N and M are the orders of the Q and R polynomials, respectively. The sequence gets closer and closer to the partial wave as we increase the orders of the polynomials. It is worth noticing that $R_M(s, s_0)$ would give rise to poles in the complex plane depending on its order, which hence cannot be free in our work. As the Padé sequence depends on the point of the expansion s_0, it should be close enough to the position of the pole we are looking for in the complex plane, as shown in Fig. 3.1. Once the region where we want to expand is known, all the analytical features of the partial wave $f_\ell(s)$ have to be controlled. To this end, before choosing the optimal point of expansion, the circle that encloses the pole from s_0 must be analyzed. As the order M will select a priori the number of poles, or non analyticities we could generate, it has to be fixed to reproduce the structures appearing in this circle.

For the simple case of a narrow isolated pole, $M = 1$ is a good choice, and hence

$$P_1^N(s,s_0) = \sum_{k=0}^{N-1} a_k (s-s_0)^k + \frac{a_N (s-s_0)^N}{1-\frac{a_{N+1}}{a_N}(s-s_0)}. \tag{3.8}$$

Thus the parameter determining the approximation is just N, which makes sense as this expansion around s_0 once the pole is removed is nothing but a Taylor expansion of order N. In this particular case $a_k = \frac{1}{k!} f_\ell^{(k)}(s_0)$ are the Taylor coefficients. Now by comparing to the customary relativistic Breit-Wigner formula

$$f_\ell(s) \simeq \frac{m\Gamma(s)}{s - m^2 - im\Gamma(s)}, \tag{3.9}$$

it is clear that it is no more than a Padé approximant of order $N = 0, M = 1$, which is a pretty naive approximation, at best. For the Nth Padé approximant the parameters and residue of the pole are

$$s_p^N = s_0 + \frac{a_N}{a_{N+1}}, \qquad Z^N = -\frac{a_N^{N+2}}{a_{N+1}^{N+1}}, \tag{3.10}$$

which converge to the physical pole position and residue as fast as the sequence converges to the partial wave [176].

Let us remark that, in many cases, the resonances are not isolated, or they are so broad that the regions that enclose them also include other structures (Fig. 3.2), like different poles, branch points or cusps, etc.... Is in these cases when Padé approximants excel, as most of the times the different structures are also described within the data, or they could be fitted from the Padé formulas. Explicit formulas for two poles are given in section 3.1.3.

The only input needed is the function in the real axis. Fortunately, all fits to data used in our work have been previously constrained with dispersion relations as seen in section 2.2.3. Thus their model dependencies are heavily suppressed.

3.1.1 Motivation

The actual situation regarding light strange mesons have been reviewed in sections 1.1.1 and 1.2.1. A reliable determination of strange resonances is relevant for hadron spectroscopy, and also for their classification in multiplets, which is crucial for our understanding of QCD at low energies, *i.e.*, the regime where Chiral Perturbation Theory is the theory describing meson interactions. In addition, as explained in detail in section 2.2, πK appears as a final state in most of the hadronic processes with net strangeness, which implies that their scattering effects contribute to the final shape of the amplitude. As expected, all relevant resonances thus play an important role in final state interactions, this is the case for example for heavy B and D meson decays. Conversely, the parameters of heavier resonances have been determined from heavy decays rather than from actual scattering processes.

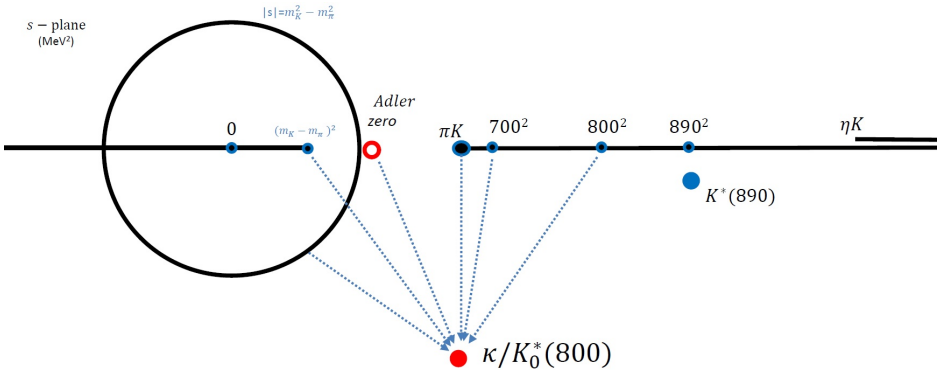

Figure 3.2: Analytic structure of the scalar $\pi K \to \pi K$ partial wave.

As explained in 3.1, the analyses of these resonances are often made using simple models, in particular specific isobar parameterizations, Breit-Wigner forms and naive modifications of the last ones. Subsequently, the parameters are usually plagued with large systematic uncertainties associated to model dependencies, although they are most of the times neglected. The situation found in the Review of Particle Physics [134] shows a clear spread of results that depend on the different models used by every experimental collaboration, not only on the statistical uncertainties of the data. Another interesting discussion is the one that arises when deciding if a resonance should be described by its Breit-Wigner parameters or the actual pole position in the complex plane. Whereas the former is customarily used within the literature, the later is actually the model-independent definition of a resonance, as Breit-Wigner formulae are not unique, and depend heavily on kinematic modifications like barrier factors. On top of all the above, there is another systematic source of uncertainty, this is, the one associated to the continuation into the complex plane itself. As shown for the $\sigma/f_0(500)$ [177], the analytic continuation, even when using standard well-behaved formulae is unstable, and produces large deviations between two fits that could be almost equal in the real axis. This situation could worsen for resonances close to thresholds, overlapping resonances, anomalous thresholds, cusps, or broad resonances like the $\kappa/K_0^*(700)$, as shown in Fig. 3.2. All in all, it is clear that a naive formula can only be used up to some degree of accuracy if the resonance is narrow and far from other analytic structures.

For the cases when this simple situation does not occur the use of partial wave dispersion relations has proved to be the most model independent, and rigorous technique. These integral equations describe all analytic structures by construction and small variations in the real axis do always produce small deviations of the pole positions, which is not the case of model descriptions. The use of such a system of equations was able to determine with high precision the parameters of the lightest resonance in QCD [120]. After several years, another dispersive determination [112] triggered a change in the denomination and the uncertainties listed in the Review of Particle Physics. The situation regarding the $\kappa/K_0^*(700)$ pole is nowadays similar to the one found for the $\sigma/f_0(500)$ some years ago. Although there are many determinations using different approximations [69, 161, 162], and even a dispersive result [178] it "still needs confirmation" according to the PDG. That is the reason why a work on this topic would be timely.

Dispersion relations offer a totally model independent calculation of the resonances lying on the complex plane, unfortunately, the region of applicability for partial-wave dispersion relations is limited. Actually it roughly concurs with the elastic region, in particular, the region for $\pi\pi \to \pi\pi$ and $\pi K \to \pi K$ is limited to roughly ~ 1 GeV. In order to overcome these complications, an alternative analytic method must be developed and several different techniques have been used in the past: conformal expansions [52, 177, 179], Laurent expansions [180–184], rational expansions [185], but in this thesis we focus on sequences of Padé approximants [172–174]. The advantage is that they do not assume any particular parameterization, while they also converge to the actual partial wave as the order of the Padé approximant is increased. The inputs used to implement this formulae are obtained from fits that describe the data and fulfill dispersion relations [52], still considered the correct description of the physical region. Hence, Padé approximants show a promising set of features to be implemented on top of our dispersive formalism, with the main goal of determining all relevant strange resonances appearing in $\pi K \to \pi K$ below 1.8 GeV [175].

3.1.2 Outline of the main results

In section 3.1.3 we present a published work based on the use of sequences of Padés approximants. This analytic method recovers all the analytic features of a given amplitude if the order of the approximant is large enough. Here we implement this technique to the study of all strange resonances decaying to πK below roughly 2 GeV. Additionally, we present in section 3.1.4 a continuation of the dispersive analysis carried out in sections 2.2.3, 2.2.4 and section 2.3 , where the hyperbolic dispersion relations are implemented in the complex plane. The main results are the following:

- We present the sequence of Padés technique and how to apply it in both the elastic and inelastic regions. The necessary input comes from the dispersive results of section 2.2.3. No further data input is needed.
- The stability against truncation in the series is calculated and we show how all systematic uncertainties associated to this approximation are smaller than the statistical ones, which are obtained through the bootstrap technique. An additional source of uncertainty, included as systematic, is the one related to the deviations that could arise in the complex plane because of small uncertainties for the derivatives in the real axis. To estimate this new source we use different parameterizations that fulfill the dispersion relations.
- We calculate with a high degree of precision the parameters of up to six strange resonances, of which 4 are inelastic and could only be obtained through models otherwise. The results for every resonance are shown together with the values listed in the PDG, just to illustrate the big spread found for all of them when using determinations relying on some models.
- The result for the $\kappa/K_0^*(700)$ resonance in section 3.1.3 is compatible with the previous result of [178], calculated by means of Hyperbolic Dispersion Relations.

This new result triggered the denomination change of the present $K_0^*(700)$ from the $K_0^*(800)$ old name.

- In section 3.1.4 we determine, in a very accurate and completely model-independent way the pole position of the $\kappa/K_0^*(700)$ and $K^*(892)$ resonances. It is done by constraining the data in a dispersive way. This prediction is based on the result of all $\pi K \to \pi K$ and $\pi\pi \to K\bar{K}$ constrained parameterizations coming from section 2.3.

- We provide two different poles for the $\kappa/K_0^*(700)$, either coming from a non-subtracted or a once-subtracted dispersion relation. Both solutions are almost equal, with very similar uncertainties, suggesting to a very stable result.

- Finally we also obtain the coupling of these resonances to πK in a model-independent way.

3.1.3 Publication: *Strange resonance poles from $K\pi$ scattering below 1.8 GeV*

Eur. Phys. J. C (2017) 77:91
DOI 10.1140/epjc/s10052-017-4668-1

THE EUROPEAN PHYSICAL JOURNAL C

Regular Article - Theoretical Physics

Strange resonance poles from $K\pi$ scattering below 1.8 GeV

J. R. Pelaez[1,a], **A. Rodas**[1], **J. Ruiz de Elvira**[2,3]

[1] Departamento de Física Teórica II, Universidad Complutense de Madrid, 28040 Madrid, Spain
[2] Helmholtz-Institut für Strahlen- und Kernphysik (Theorie) and Bethe Center for Theoretical Physics, Universität Bonn, 53115 Bonn, Germany
[3] Albert Einstein Center for Fundamental Physics, Institute for Theoretical Physics, University of Bern, Sidlerstrasse 5, 3012 Bern, Switzerland

Received: 26 December 2016 / Accepted: 30 January 2017 / Published online: 11 February 2017

Abstract In this work we present a determination of the mass, width, and coupling of the resonances that appear in kaon–pion scattering below 1.8 GeV. These are: the much debated scalar κ-meson, nowadays known as $K_0^*(800)$, the scalar $K_0^*(1430)$, the $K^*(892)$ and $K_1^*(1410)$ vectors, the spin-two $K_2^*(1430)$ as well as the spin-three $K_3^*(1780)$. The parameters will be determined from the pole associated to each resonance by means of an analytic continuation of the $K\pi$ scattering amplitudes obtained in a recent and precise data analysis constrained with dispersion relations, which were not well satisfied in previous analyses. This analytic continuation will be performed by means of Padé approximants, thus avoiding a particular model for the pole parameterization. We also pay particular attention to the evaluation of uncertainties.

1 Introduction

A reliable determination of strange resonances is by itself relevant for hadron spectroscopy and their own classification in multiplets, as well as for our understanding of intermediate energy QCD and the low-energy regime through Chiral Perturbation Theory. In addition kaon–pion scattering and the resonances that appear in it are also of interest because most hadronic processes with net strangeness end up with at least a $K\pi$ pair that contributes decisively to shape the whole amplitude through final state interactions. This is, for instance, the case of heavy B or D meson decays into kaons and pions. Actually, the parameterization of these amplitudes and their final states interaction is very frequently done in terms of simple resonance exchange models. Conversely, although many of the strange resonances were observed in $K\pi$ scattering long ago [1], most of them were later confirmed in studies of heavier meson decays, which were also used to determine their parameters.

However, very often the analyses of these resonances have been made in terms of crude models, which make use of specific parameterizations like isobars, Breit–Wigner forms or modifications, which very often assume the existence of some simple background. As a result, resonance parameters suffer a large model dependence or may even be process dependent. Thus, the statistical uncertainties in the resonance parameters should be accompanied by systematic errors that are usually ignored. This can easily be checked by looking at the Review of Particle Physics (RPP) compilation [2], where very frequently for these resonances it is only possible to provide an "estimate" of their mass or width, together with some educated guess for the uncertainty, since the central values reported by different experiments on the same resonance are inconsistent among themselves. Part of these discrepancies may definitely be due to systematic effects on data, but to a large extent they are due to the use of models in their analysis to extract resonance parameters. In some cases, as for the $K_0^*(800)$, even the very existence of the resonance is called for confirmation.

The most rigorous way of identifying the parameters of a resonance is from the position s_R of its associated pole in the complex energy-squared plane, which is related to the resonance mass M_R and width Γ_R by $\sqrt{s_R} \equiv M - i\Gamma/2$. The reason is that poles are process independent, whereas determining resonance parameters from peaks or bumps on the data depends on backgrounds as well as on the presence of thresholds or other resonance contributions specific to each process.

But even when using the pole definition there is an additional problem; the data can be equally well described in a given region by different functional forms whose analytic continuation is different. For instance, in a given energy interval, data could be fitted with a polynomial of sufficiently high degree, and such a parameterization never has a pole nor cuts. If the resonance is narrow and isolated one can use physically motivated functions like a Breit–Wigner formula

[a] e-mail: jrpelaez@fis.ucm.es

or variations. However, as soon as resonances are wide and their associated poles require an analytic continuation deep in the complex plane or if there are coupled channels with thresholds nearby or overlapping resonances, it is better to avoid models for the analytic continuation to the pole.

The most rigorous way to determine poles in the complex plane is to perform an analytic continuation of the amplitude by means of partial-wave dispersion relations [3–6]. A paradigmatic example has been the recent determination of the long debated $\sigma/f_0(500)$ pole by means of Roy [7–9] and GKPY equations [10], which triggered a radical revision of its parameters in the RPP (see for a detailed account of this progress [11]). However, although a similar dispersive analysis for the $K_0^*(800)$ in terms of Roy–Steiner equations has been performed [12], the $K_0^*(800)$ status in the RPP is that it still "Needs confirmation". These partial-wave dispersion relations are very rigorous and take into account the contributions from all the singularities in the complex plane and particularly those of the left-hand cut due to thresholds in crossed channels. The price to pay is that they are complicated sets of coupled integral equations whose convergence region in the complex plane only covers the lowest resonances. Moreover, they use as input waves beyond $J = 1$ as well as in the intermediate energy region, which typically includes the inelastic region. Therefore, in practice, the amplitudes obtained in these studies only satisfy precisely these partial-wave dispersive constraints up to energies slightly beyond the elastic regime, at best. In our case this makes them valid to study the $K_0^*(800)$ and $K_0^*(892)$, but unsuitable to determine the parameters of all the other resonances appearing in $K\pi$ scattering below 1.8 GeV. Hence, the use of dispersion relations to make rigorous analytic continuations of partial waves to the complex plane is therefore rather limited for resonances well above 1 GeV.

For the above reasons there is a growing interest in other methods based on analyticity properties to extract resonance pole parameters from data in a given energy domain. They are based on several approaches: conformal expansions to exploit the maximum analyticity domain of the amplitude [13–15], Laurent [16,17] or Laurent–Pietarinen [18–20] expansions, or Padé approximants [21–23]. They all determine the pole position without assuming a particular model for the relation between the mass, width and residue. In this sense they are model independent analytic continuations to the complex plane.

Of course, these analytic methods require as input some data description. But it is not enough that it may be a precise description: it should also be consistent with some basic principles, which usually is not the case. Actually, it has been recently shown [24] that $K\pi$ scattering data [25,26], which are the source for several determinations of strange resonances, do not satisfy well Forward Dispersion Relations up to 1.8 GeV. This means that in the process of extracting data by using models, they have become in conflict with causality. Nevertheless, in [24] the data were refitted constrained to satisfy those Forward Dispersion Relations and a careful systematic and statistical error analysis was provided. The constrained fits suffer some visible changes compared to unconstrained fits and is therefore of interest to check the resonance parameters resulting from this constrained analysis. In this work we will make use of the Padé approximants method in order to extract the parameters of all resonances appearing in those waves.

The plan of this article is as follows. In the next section we will briefly review the status of data for $K\pi$ scattering and their phenomenological description. Then, in Sect. 3, the Padé approximant method will be introduced. In Sect. 4 we present our numerical results in separated subsections dedicated to scalar, vector, and tensor resonances. Finally, in Sect. 5 we provide our conclusions.

2 $K\pi$ scattering

Data on $K\pi$ scattering were measured indirectly from $KN \to K\pi N$ reactions during the 70s and the 80s. The most widely used are those of Estabrooks et al. [25] and Aston et al. [26], which provide amplitude phases and modulus up to roughly 1.8 GeV. Note they are all extracted within an isospin limit formalism, so that charged and neutral mesons are assumed to have the same mass. Here we will use $m_\pi = 139.57$ MeV and $m_K = 496$ MeV.

Apart from the simple phenomenological parameterizations of the original experimental articles [1,25,26], the data set, or parts of it, has been described with a wide variety of approaches, also used to identify strange resonances below 1.8 GeV. For instance, already in the 80s the S-wave was described up to almost 1.3 GeV with a unitarized model of mesons coupled to quark–antiquark confined channels [27]. In the 90s, the S and P waves were described with unitarized Chiral Perturbation Theory, using the Inverse Amplitude Method first in the elastic regime [28,29] and then with coupled channels up to 1.2 GeV [30,31]. An alternative unitarization method for ChPT amplitudes described S-wave data up to 1.43 GeV [32]. In addition, data has also been described with: (i) the chiral unitary approach to next to leading order [33–35] for the S and P-waves, (ii) the N/D unitarization approach with coupled channels for the S-wave up to 1.4 GeV, (iii) unitarized chiral Lagrangians that include some resonances explicitly while others are generated dynamically for the S wave [36–40], (iv) conformal parameterizations [13] for the S-wave, (v) the explicit consideration of resonances with ad hoc pole parameterizations and very simple chiral symmetry requirements for the S-wave [41–43], or (vi) unitarized models with resonances [44] for the P-wave. Note that these models do not deal with D or F waves.

Not all those models are equally rigorous, but in all them partial-wave unitarity plays a central role. The most constrained by fundamental principles are those including chiral symmetry constraints and based on dispersion relations, although usually they have some approximation for the so-called left-hand and circular cuts, which are branch cuts due to thresholds in crossed channels or to the angular integration of Legendre polynomials. The most rigorous treatment is the Roy–Steiner equation analysis of [4,12] for the S and P-waves, where left and circular cuts are treated systematically, although it only extends to energies below $\sqrt{s} \simeq 0.97$ GeV and the amplitudes above that energy or higher angular momentum are considered input.

It is very important to remark that all the approaches above make use of the existing scattering data from [25] and [26]. However, for the extraction of those $K\pi$ scattering data from $KN \to K\pi N$, several approximations and assumptions were needed. For instance, it was assumed that the full process is dominated by one pion exchange (OPE-model), frequently neglecting final rescattering with the nucleon or the exchange of other resonances. In addition the OPE was approximated by an on-shell extrapolation. These are sources of systematic uncertainty, not directly provided in the experimental papers, which explain in part why different experiments do not always agree within their quoted uncertainties, which are of statistical nature. As a matter of fact, it has been recently shown [24] that simple fits to those data do not satisfy well Forward Dispersion Relations (FDR) up to 1.8 GeV, even when including estimates of the systematic uncertainty (typically estimated as the difference between conflicting data points). Note that, since the Roy–Steiner formalism is in practice limited to energies below $\sqrt{s} \simeq 1$ GeV, above that energy it is only possible to test two independent FDRs.

Nevertheless, the existing data was also refitted in [24], but constrained to satisfy FDRs. The resulting Constrained Fit to Data (CFD) provides a precise description of data, which is consistent within uncertainties with two FDRs, although only up to 1.6 GeV. The CFD is a rather simple set of parameterizations of the S, P, D and F partial-wave phase shifts and inelasticities in the isospin limit, for both possible isospins $I = 1/2$ and $3/2$, as well as a Regge description above 1.7 GeV. These parameterizations are given as piecewise functions. Each piece is valid in a given energy interval of real energies and is matched continuously to the next piece, typically at different energy thresholds. No model dependent assumptions are thus made.

However, these parameterizations should not be used directly to extract resonance parameters. The functional form of each piece of those parameterizations has been chosen to be simple and flexible enough to describe the amplitude in a certain interval of real energies. Of course, each piece of function by itself may be continued to the complex plane in a certain domain that depends on the analytic structure of that piece. However, that analytic extension is not necessarily a good approximation to the continuation of the whole amplitude to the complex plane, which has a definite analytic structure in terms of cuts associated to physical thresholds.

This is rather general, not just an issue with the CFD, since one could always fit peaks and dips in a finite energy interval with a polynomial, whose analytic continuation would never provide a pole in the complex plane. The same happens with a Breit–Wigner formula, which can always be fitted to a peak in an interval, with some choice of smooth background if needed. This always produces a pole, but it only has some physical meaning if the pole is close to the real axis and well isolated from other singularities. Note that this parameterization or any of its modifications (with kinetic factors or Blatt–Weisskopf barrier factors) also imposes a particular relation between the pole position and residue.

Thus, in order to extract pole parameters from the Constrained Fit to Data in [24] we will make use of the Padé method, which extracts the pole in a given interval once the analytic structure in a domain that contains the pole of the resonance is fixed, without imposing a particular relation between the position and residue of that resonance.

3 Pole determination using Padé approximants

The $P_M^N(s, s_0) = Q_N(s, s_0)/R_M(s, s_0)$ Padé approximant of a function $F(s)$ is a rational function that satisfies

$$P_M^N(s, s_0) = F(s) + O((s - s_0)^{M+N+1}), \tag{1}$$

with $Q_N(s, s_0)$ and $R_M(s, s_0)$ polynomials in s of order N and M, respectively. These approximants can be calculated easily from the derivatives of the data fit with respect to the energy squared s.

Thanks to the de Montessus de Ballore theorem these Padé approximants can be used to unfold the next continuous Riemann sheet of a scattering amplitude in order to search for resonance poles [21–23]. The relevant observation is that when they yield a pole they do not assume a model for the relation between its position and residue. Hence, in this sense the pole is model independent, although there is some residual dependence on the choice of parameterization for the data, from which the derivatives are obtained [23]. This will be taken into account into our systematic error estimation.

The choice of Padé series to be used, with more or less poles, is based on the expected analytic structure of the partial wave in a domain that includes a segment in the real axis and the pole of the resonance we study. Therefore, the series should have at least a pole to describe the resonance, but if in order to contain that pole the domain also contains another singularity, like a branch point, we will need a series with an additional pole.

For example, when the resonance is narrow and well isolated from other singularities, the amplitude $F(s)$ must be analytic inside a domain around a real s_0, except for a single pole at $s = s_p$. Note that the upper half of this domain lies on the first, or "physical", Riemann sheet and has no poles. In contrast, the lower half lies on the unphysical Riemann sheet that is connected continuously with the first when crossing the real axis and thus it can contain poles. In such case we can use the sequence

$$P_1^N(s, s_0) = \sum_{k=0}^{N-1} a_k (s - s_0)^k + \frac{a_N (s - s_0)^N}{1 - \frac{a_{N+1}}{a_N}(s - s_0)}, \tag{2}$$

which converges to $F(s)$ within the domain of analyticity excluding s_p. The constants $a_n = \frac{1}{n!}F^{(n)}(s_0)$ are given by the n^{th} derivative of the function. This is how an analytic continuation to the complex plane can be obtained just from the fit of a function $F(s)$ to the data in the physical region of the real s axis. Likewise, the pole and residue are

$$s_p^N = s_0 + \frac{a_N}{a_{N+1}}, \quad Z^N = -\frac{(a_N)^{N+2}}{(a_{N+1})^{N+1}}. \tag{3}$$

Note that the coupling of a given resonance to $K\pi$ can be obtained from the residue as follows:

$$|g_{K\pi}|^2 = \frac{16\pi(2l+1)|Z|}{(2q_{K\pi}(s_p))^{2l}}, \tag{4}$$

where

$$q_{K\pi}(s) = \frac{1}{2}\sqrt{\frac{(s - (m_K + m_\pi)^2)(s - (m_K - m_\pi)^2)}{s}}$$

is the center-of-mass momentum of the $K\pi$ system and l the angular momentum of the partial wave.

However, when the pole associated to a resonance lies near a branch cut produced by unitarity, we may need one additional pole to mimic the branch points inside the domain. In such cases we will use the following sequence with $M = 2$:

$$P_2^N(s, s_0) = \frac{\sum_{k=0}^{N} (a_k a_N^2 - a_k a_{N-1} a_{N+1} - a_{k-1} a_N a_{N+1} + a_{k-1} a_{N-1} a_{N+2} + a_{k-2} a_{N+1}^2 - a_{k-2} a_N a_{N+2})(s - s_0)^k}{a_N^2 - a_{N-1} a_{N+1} + (a_{N-1} a_{N+2} - a_N a_{N+1})(s - s_0) - (a_N a_{N+2} - a_{N+1}^2)(s - s_0)^2}, \tag{5}$$

which has similar converge properties. The explicit expression for the poles may be found in [23]. In the case of the κ, when using this $M = 2$ sequence of Padé series, we will see that one of the poles will converge to the pole associated to the resonance s_p, whereas the other will simulate a branch cut.

Let us now comment on the uncertainty estimates. From the above definitions it is clear that the calculation of pole parameters relies on the data fitting function and its derivatives at a given energy point s_0. Thus, a first source of uncertainty is inherent to the data uncertainties and we will refer to it as "statistical" error. We will estimate this uncertainty by a Monte Carlo Gaussian sampling of the fit parameters within their error bars. Note that following the $\pi\pi$-scattering analysis in [45], the gaussianity of the uncertainties in the CFD was also checked in [24], hence ensuring that the standard approach for error propagation can be used.

As a second source of uncertainty, we will have a "theoretical" uncertainty due to the numerical procedure and the fact that the sequence of Padé approximants with fixed order M, will be truncated at a given value N. de Montessus de Ballore theorem tells us that, if the amplitude in that domain and the Padé series used for the approximation have the same number of poles, the differences between the $\sqrt{s_p^N}$ should become smaller and the pole position should converge to

$$\sqrt{s_p} = M - i\Gamma/2. \tag{6}$$

We thus estimate the uncertainty in this truncation by

$$\Delta\sqrt{s_p^N} = \left|\sqrt{s_p^N} - \sqrt{s_p^{N-1}}\right|. \tag{7}$$

We will truncate the sequence at a value of N such that this error is negligible or smaller than the "statistical" error. This last $\Delta\sqrt{s_p^N}$ will then be called $\Delta_{\rm th}$. The center of the domain, s_0, is chosen as the point where this theoretical uncertainty is smaller.

Finally, we will also consider different parameterizations fitted to the very same CFD amplitudes described in the previous paragraph. Note that each parameterization is allowed to have its own s_0. Although all these parameterizations will lie within the uncertainties of the CFD in the real axis, they yield slightly different derivatives that result in different central values for the pole. Our final result will then be the average of the different values obtained with different parameterizations and we will consider an additional systematic uncertainty, defined as the variance of these results, due to the model dependence when calculating the derivatives at a given point. For example, if we obtain values M_i for the pole mass from n different models, our final value will be the averaged mass $\bar{M}$ and the systematic uncertainty will be $\Delta_{sys}M = \sqrt{\sum_i^n (M_i - \bar{M})^2/(n-1)}$. Typically we will study other conformal parameterizations with different conformal variables, or popular parameterizations like Breit–Wigner, or when these are not the most suitable choice, other parameterizations already used in the literature.

Our final uncertainty will be the quadratic combination of the theoretical, statistical and systematic errors. Similar

definitions hold for the central values and systematic uncertainties for the width and coupling of the pole.

Thus, in the next sections we will show that we can use the sequence $P_1^N(s, s_0)$ to determine the poles of all strange resonances below 1.8 GeV except for the $K_0^*(800)$. In these cases we truncate at $N = 4$. For the $K_0^*(800)$ the sequence with $M = 1$ does not converge properly to the pole position since there is a nearby threshold which is as closer to the center of the domain than the κ pole itself. In contrast, the sequence with $M = 2$ does converge rapidly to a resonance pole, while the other pole mimics the $K\eta$ threshold and cut. In this case the systematic error is small enough for $N = 3$.

As a side remark, let us note that the above Padé sequence that we will use in this work *should not be confused* with the use of a Padé approximant to restore unitarity on the Chiral Perturbation Theory (ChPT) expansion [46–48]. These uses of Padé series are completely unrelated. We have nevertheless found such a confusion often and we will try to clarify this issue here.

In the approach of this work there will be no dynamical input, only a parameterization of the data by means of different functions and the assumption that there is at least a pole in the vicinity of a certain point s_0. Using only the data description as input, in particular the derivatives of the amplitude at that point, there is a series of Padé approximants that reproduce that pole. The only analytic structure of relevance is the pole and possibly some cut nearby, but the latter would be mimicked by further poles in the Padé sequence. Note that these Padé approximants are built from a series in powers of $(s-s_0)$ that could be applied for any function describing data. The inputs are only the derivatives of the amplitude at that point. There are no requirements from any kind of dynamics, particularly chiral dynamics: it is just data. Our results in this paper will be consistent with QCD dynamics, and chiral dynamics in particular, as long as the data are consistent with it.

In contrast, in the case of Padé series for ChPT, besides the fit to data, there is an attempt to describe the dynamics from the ChPT Lagrangian, which is a low-energy expansion with the QCD symmetry constraints in terms of pions, kaons and etas. ChPT produces a series in powers of $(k/f_\pi)^2$, where f_π is the pion decay constant and k is either the meson momenta or any of their masses. Being organized basically as a polynomial in momentum/mass variables the ChPT series cannot satisfy unitarity, which is a condition on the right-hand or physical cut. However, it can be shown that unitarity fixes the imaginary part of the inverse amplitude on the physical or right-hand cut. Next, by using the ChPT expansion to calculate the real part of the inverse amplitude, one ends up *formally* with a Padé approximant in the $1/f$ expansion. But rigorously it is *not* a Padé approximant in the energy or mass expansion. Therefore the series upon which the Padé series is built is completely different from the one used in this work, and the center of the expansion is also completely different. When used up to a given order in ChPT, the Padé approximant ensures unitarity and, if re-expanded, it reproduces the chiral logarithms associated to unitary of the next order in the ChPT expansion (nor the polynomial terms or the crossing logarithms of the next order [48,49]). These Padé series built as resummations of the $1/f^2$ ChPT expansion are completely different from those used here. For further details we refer the reader to [48]. Nevertheless, the parameterizations we use for our central values also have a factor to account for the Adler zero (at leading order within ChPT) that appears below threshold in the scalar wave. This makes the parameterization consistent with Chiral Symmetry, but we could have also used here a functional form without it, as long as it describes the data, since for our method we only require input around one energy point in the data region.

In summary, the approach of this work has absolutely nothing to do with unitarized Chiral Perturbation Theory and the Padé approximants used in that case. Quite the contrary, here we do not have any dynamical input at the Lagrangian level, and this is done on purpose, to avoid as much as possible any model dependence. We only use data as input. Of course, we use a dispersive description (again, not dynamical) of data, which has been constrained to satisfy forward dispersion relations, although respecting unitarity (by being parameterized only in terms of the phase-shift and inelasticity) and respecting within uncertainties analyticity and crossing constraints. Our Padé series here is just a consequence of the analyticity of the amplitude, which allows for a Padé expansion around a point s_0 that also encloses the possible resonance pole.

4 Results

Let us then discuss our results for each channel.

4.1 Scalar resonances

In the scalar channel there are two resonances with isospin zero: the $K_0^*(800)$, which according to the RPP still "Needs confirmation", and the $K_0^*(1430)$. We start discussing the former

4.1.1 The $K_0^*(800)$ or κ resonance

This resonance appears in the low-energy region, where the scattering is still elastic. Note that the CFD parameterization describes the elastic region by means of a relatively simple conformal expansion whose explicit expression can be found in [24]. The advantage of such a conformal parameterization is that once the elastic cut is separated exactly by unitarity, it provides a rapidly convergent expansion analytic

in the whole complex plane. Of course, it only represents well the physical amplitude at low energies, but these good analytic properties already made it possible in [24] to provide the parameters of the pole that appears in this parameterization: $M = 680 \pm 15$ MeV, $\Gamma = 668 \pm 15$ MeV and $g_{K_0^*(800)K\pi} = 4.99 \pm 0.08$ GeV. If we only use input from the elastic region, the Padé approach should in principle reproduce this pole at that position and therefore the present analysis for this resonance would be of limited value. However, the fact that we already have a precise determination of the pole will be useful to calibrate and understand the uncertainties of the Padé approach due to the truncation of the series and the use of different data parameterizations to calculate the derivatives, or to illustrate how to choose the center of the expansion and the most convenient Padé series. In particular, since this resonance has such a large width, one would need to reach deep in the complex plane and it is likely that the Padé sequence will be sensitive to other singularities, particularly to thresholds nearby. Actually we will see that in this case the $M = 1$ Padé series, which only has one pole, will not converge and we will need the $M = 2$ series.

The results for $M = 1$ can be found in Fig. 1. In the upper panel we show $\Delta\sqrt{s_p^N}$ for different values of s_0. Note that the $N = 3$ curve (dashed) is nowhere smaller than that of $N = 2$ (dotted). The smallest uncertainty for each N is attained at $\sqrt{s_0} \sim 830$ MeV, and we show in the lower panel how it translates into a truncation uncertainty for the pole position, which grows from $N = 2$ (light gray circle) to $N = 3$ (darker gray circle). Note also that the central value of the darker circle lies well outside the lighter circle. We have also calculated the $N = 4, 5$ cases and there is no evidence of convergence for $M = 1$. We thus conclude that considering the Padé series with just one pole is not enough to reproduce the analytic structure in the region relevant for such a deep pole.

We then show in Fig. 2 the results for the $M = 2$ Padé series, which has two poles. Once again, in the upper panel we show $\Delta\sqrt{s_p^N}$, for different values of s_0, as dotted and dashed curves for $N = 2$ and $N = 3$, respectively. Now we see that this truncation difference decreases drastically in several s_0 regions as N increases. Actually, already at $N = 3$ it becomes smaller than the statistical uncertainties, with a minimum at $\sqrt{s_0} = 950$ MeV. Thus the P_2^3 pole will define our resonance values and $\Delta\sqrt{s_p^3}$ the theoretical uncertainty $\Delta_{\rm th}$ listed in Table 1. In the lower panel we show the pole position and its minimum truncation uncertainty for $N = 2, 3$ as the light and dark gray areas, respectively. The other pole obtained for this sequence corresponds to the ηK threshold, which is the nearest singularity to s_0.

Once a central value and a theoretical error for the pole position has been obtained, we add the statistical uncertainty

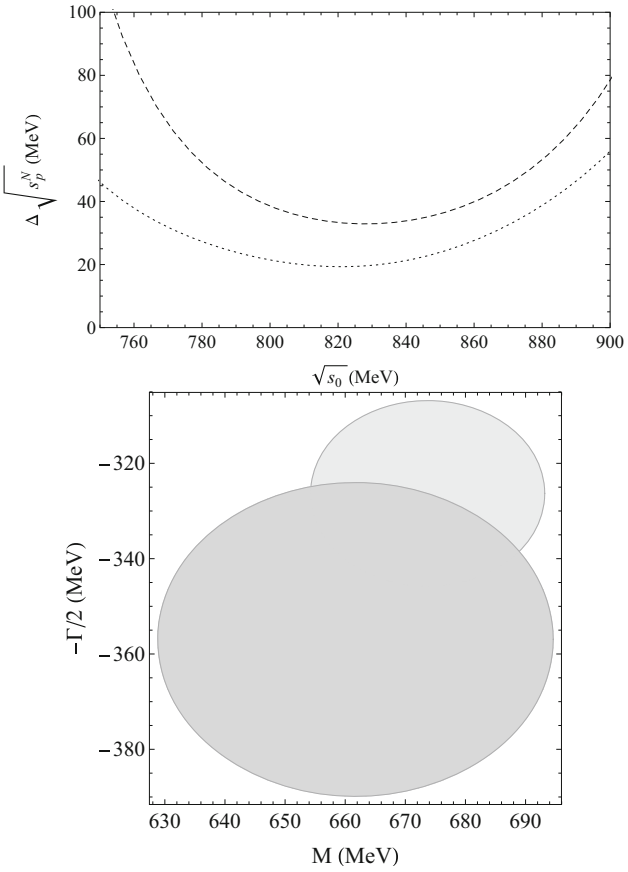

Fig. 1 *Upper panel*, uncertainty $\Delta\sqrt{s_p^N}$ for different values of $\sqrt{s_0}$ in the κ pole determination for $M = 1$. We show *dotted* and *dashed lines* for $N = 2$ and $N = 3$, respectively. It is clear that the $M = 1$ case does not converge as N increases. We have checked higher N and there is no improvement. *Lower panel*, theoretical uncertainty regions $\Delta\sqrt{s_p^N}$ for the best center $\sqrt{s_0}$ for $M = 1$, where $N = 2$ is plotted as the *light gray region* and $N = 3$ as the *gray region*

in quadrature:

$$\Delta_{s_p} = \sqrt{\Delta_{\rm th}^2 + \Delta_{\rm stat}^2}. \tag{8}$$

Recall that the statistical errors are obtained from a Monte Carlo Gaussian sampling of the parameters of the CFD parameterization within their uncertainties. Statistical uncertainties dominate the quadrature, since the theoretical error is the $\Delta\sqrt{s_p^N}$ for the N when it becomes smaller than the experimental one. In the case of the $K^*(800)$ this procedure leads to the results for the pole position and the coupling that are listed in the second column of Table 1. The central value $(680 \pm 13) - i(325 \pm 7)$ MeV obtained with the Padé approximant can now be compared with the pole position extracted analytically from the CFD parameterization in $(680 \pm 15) - i(334 \pm 7.5)$ MeV. This illustrates the remarkable accuracy of the Padé sequence to extract resonance parame-

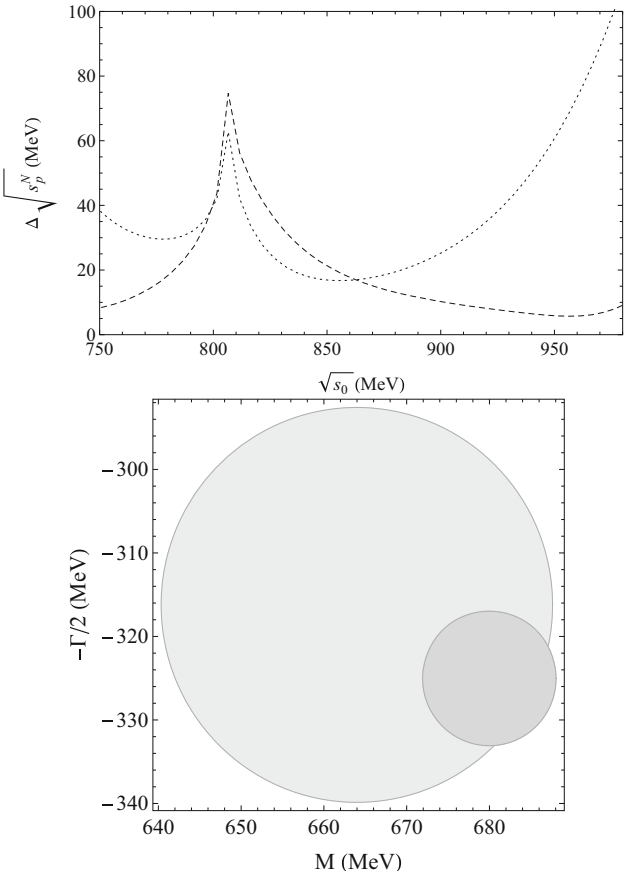

Fig. 2 *Upper panel*, uncertainty $\Delta\sqrt{s_p^N}$ for different values of $\sqrt{s_0}$ in the κ pole determination for $M = 2$. We show *dotted* and *dashed lines* for $N = 2$ and $N = 3$, respectively. *Lower panel*, theoretical uncertainty regions $\Delta\sqrt{s_p^N}$ for the best center $\sqrt{s_0}$ for $M = 2$, where $N = 2$ is plotted as the *light gray region* and $N = 3$ as the *gray region*

ters and the soundness of our method to estimate uncertainties.

In the third and fourth columns of Table 1 we also show the results obtained by following the same procedure with the Schenk [58] and Chew–Mandelstam (C-M) [59] parameterizations already used in [23] fitted to the CFD curve. For each parameterization we choose its best s_0 value. As explained above, although these parameterizations fall within the uncertainties of the CFD in the real axis, they yield slightly different derivatives, which result in somewhat different values

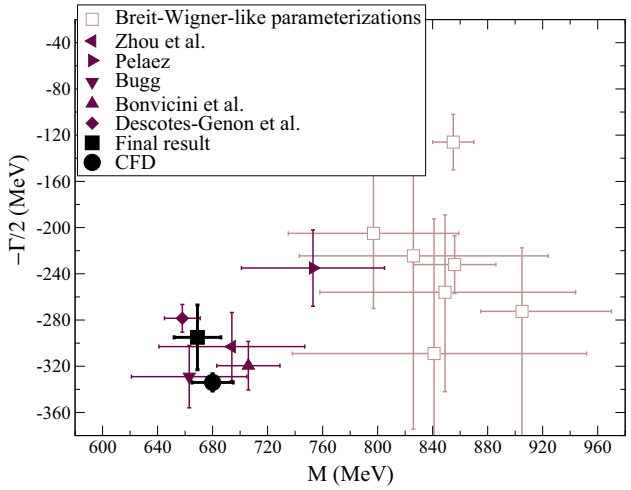

Fig. 3 Final result for the κ pole. Other references are taken from the RPP compilation [2], Descotes-Genon et al. [12], Bonvicini et al. [50], Bugg [42,43], Peláez [30,31], Zhou et al. [51], and the Breit–Wigner parameterizations [52–57] listed in the RPP

for the pole. Thus, we take as our final central result for the $K_0^*(800)$ resonance the average of these different parameterizations and consider the systematic uncertainty as explained in the introduction, combining it quadratically with the theoretical and statistical uncertainties. We thus arrive at the final result for the $K_0^*(800)$ pole and coupling:

$$\sqrt{s_{K_0^*(800)}} = (670 \pm 18) - i(295 \pm 28)\ \text{MeV}, \qquad (9)$$
$$g_{K_0^*(800)} = 4.47 \pm 0.40\ \text{GeV}.$$

This result is shown in Fig. 3 together with the other references listed in the RPP for this resonance. Note that we have highlighted with solid symbols those poles coming from analytic or dispersive approaches, whereas mass and width values obtained from models using Breit–Wigner approximations are shown with empty squares.

4.1.2 The $K_0^*(1430)$

For the heavier $K_0^*(1430)$ resonance, the elastic formalism cannot be used, although the resonance is almost elastic, since its branching ratio to πK is larger than 90%. In this case the CFD [24] makes use of and inelastic formalism parameterized through simple rational functions that fit the total

Table 1 $K_0^*(800)$ pole results for the CFD and different parameterizations fitted to the CFD. The uncertainty for $\sqrt{s_p}$ and g include statistical and theoretical errors only

	CFD Padé	Schenk Padé	C-M Padé
$\sqrt{s_p}$ (MeV)	$(680 \pm 13) - i(325 \pm 7)$	$(656) - i(283)$	$(673) - i(276)$
Δ_{th} (MeV)	6	13	10
g (GeV)	4.88 ± 0.16	4.30	4.22
Δ_{th} (GeV)	0.15	0.32	0.20
$\sqrt{s_0}$ (GeV)	0.96	0.81	0.87

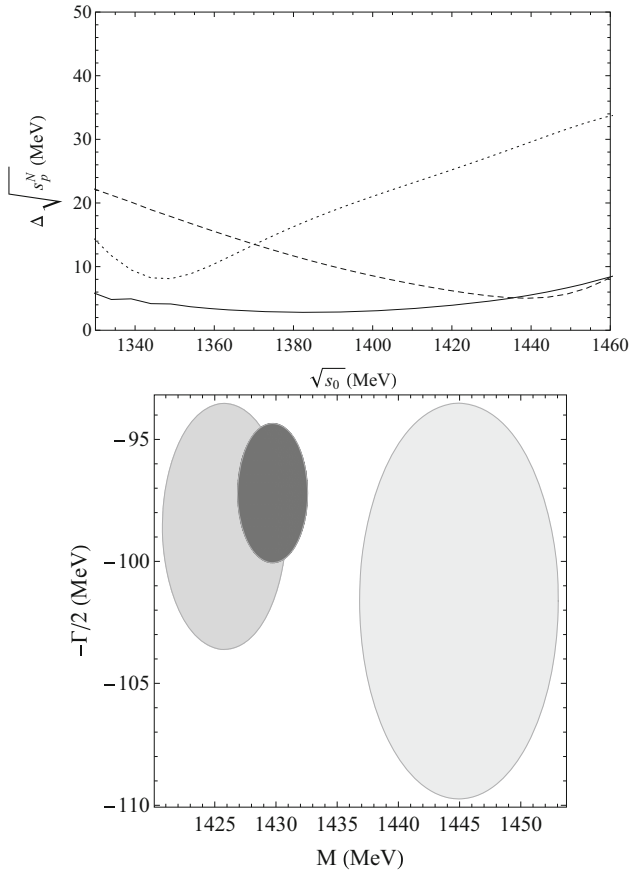

Fig. 4 *Upper panel*, uncertainty $\Delta\sqrt{s_p^N}$ for different values of $\sqrt{s_0}$ in the $K_0^*(1430)$ pole determination. The *dotted*, *dashed* and *continuous lines* correspond to the $N = 2$, 3 and 4 cases, respectively. *Lower panel*, theoretical uncertainty regions $\Delta\sqrt{s_p^N}$ for the $K_0^*(1430)$ pole. The *light gray*, *gray* and *dark gray areas* correspond to $N = 2$, 3 and 4

phase and the modulus of the partial wave. Let us remark that, even for $\pi\pi$ scattering, no partial-wave dispersion relations have been implemented up to more than 1.1 GeV, since Roy and GKPY equations reach 1.1 GeV at most in their usual formulation. Forward dispersion relations have been extended for $\pi\pi$ scattering up to 1420 MeV [5] and for $K\pi$ up to 1600 MeV [24], but they are not suitable for resonance pole extractions. Therefore, lacking these rigorous dispersive methods to extract poles, it is here where the Padé technique yields more relevant results, providing a sound analytic continuation to the next Riemann sheet.

The convergence of the P_1^N sequence, with just one pole, is fairly good this time because the resonance is not as deep in the complex plane as the $K_0^*(800)$. In particular, the truncation errors, shown in the upper panel of Fig. 4 decrease from $N = 2$ to 4 rather fast for s_0 within the 1350–1420 MeV range. We obtain a minimum for the combined Δ_{s_p} error at $\sqrt{s_0} = 1380$ MeV. Once the Padé series has been truncated at $N = 4$, where the theoretical error becomes smaller than the statistical one calculated from a Monte Carlo Gaussian

Table 2 $K_0^*(1430)$ pole results for the CFD and different parameterizations fitted to the CFD. The uncertainty for $\sqrt{s_p}$ and g include statistical and theoretical errors only

	CFD Padé	BW Padé
$\sqrt{s_p}$ (MeV)	$(1430 \pm 5) - i(97 \pm 6)$	$(1431) - i(122)$
$\Delta_{\rm th}$ (MeV)	3	7
g (GeV)	3.31 ± 0.21	4.32
$\Delta_{\rm th}$ (GeV)	0.06	0.07
$\sqrt{s_0}$ (GeV)	1.38	1.44

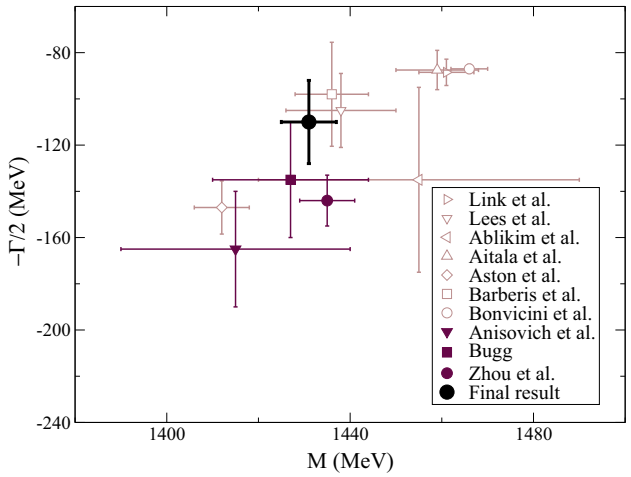

Fig. 5 Final result for the $K_0^*(1430)$ pole. Other results correspond to those listed in the RPP compilation [2], Zhou et al. [51], Bugg [42,43], Anisovich et al. [60], Bonvicini et al. [50], Barberis et al. [61], Aston et al. [26], Aitala et al. [52–57], Ablikim et al. [62], Lees et al. [63], Link et al. [64]

sampling of the CFD parameters. This truncation uncertainty translates into the light gray, gray and dark gray areas in the lower panel of Fig. 4. The darker one gives our final central value and theoretical uncertainty, whose numerical values can be read in the second column of Table 2. In addition, we have added in quadrature the statistical uncertainty in the first line.

In that table we also show the result of using a typical Breit–Wigner model, as done in most of the works listed in the RPP, to fit the CFD parameterization. As can be seen in the third column of Table 2, this leads to a sizable change in the width, but to almost an imperceptible variation of the mass. This is a source of systematic uncertainty due to model dependence. Our final result is obtained by combining the three sources of uncertainty: theoretical, statistical, and systematic. We find

$$\sqrt{s_{K_0^*(1430)}} = (1431 \pm 6) - i(110 \pm 19)\ \text{MeV}, \qquad (10)$$
$$g_{K_0^*(1430)} = 3.82 \pm 0.74\ \text{GeV}.$$

In Fig. 5 we have plotted this final result value as a black circle, which compares rather well with the references listed in the RPP.

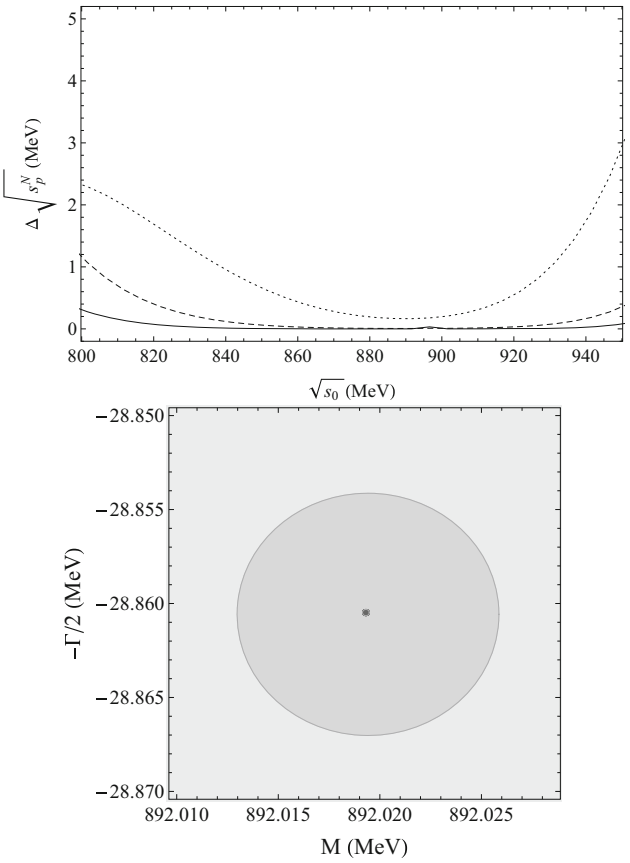

Fig. 6 *Upper panel* $\Delta\sqrt{s_p^N}$ in the $K^*(892)$ pole determination for different values of $\sqrt{s_0}$ using the P_1^N sequence. The *dotted*, *dashed* and *continuous lines* correspond to $N = 2, 3$ and 4, respectively. *Lower panel* Theoretical uncertainty regions $\Delta\sqrt{s_p^N}$ for the $K^*(892)$ pole. The *light gray* and *gray areas* correspond to $N = 2, 3$, whereas the $N = 4$ case corresponds to the *tiny dark gray spot* in the center, since the theoretical uncertainty becomes negligible

4.2 Vector resonances

Let us now discuss the vector resonances that appear in $K\pi$ scattering below 1.8 GeV. These are the $K^*(892)$ and the $K_1^*(1410)$, both of them with isospin 1/2.

4.2.1 The $K^*(892)$

The lightest one is the $K^*(892)$, which is elastic for all means and purposes. It is also very narrow compared to the $K_0^*(800)$ and therefore much closer to the real axis and well isolated from other analytic structures. Hence, as can be seen in the upper panel of Fig. 6, the P_1^N sequence, with just one pole, converges very rapidly. Actually, we estimate our theoretical error from $N = 4$ since it is when the truncation error becomes negligible compared to the statistical one (four orders of magnitude smaller), obtained as usual from a Monte Carlo Gaussian sampling of the CFD parameters. The Δ_{s_p} error is minimized for $\sqrt{s_0} = 890$ MeV, but the outcome is remarkably similar within the 870–910 MeV range. In the lower panel of Fig. 6 we see that the theoretical uncertainty on the pole becomes extremely small and that he convergence is remarkable, with the central value being almost the same from $N = 2$ to $N = 4$.

Table 3 $K^*(892)$ pole results. The uncertainty for $\sqrt{s_p}$ and g include statistical and theoretical errors only

	CFD Padé
$\sqrt{s_p}$ (MeV)	$(892 \pm 1) - i(29 \pm 1)$
Δ_{th} (MeV)	1×10^{-4}
g	6.1 ± 0.1
Δ_{th}	$\simeq 0$
$\sqrt{s_0}$ (GeV)	0.89

Concerning the systematic uncertainty due to the use of other models to fit the same data, we have found that the result, if we consider a Breit–Wigner model fitted to the CFD values, differs by less than 1 MeV. However, it is worth noting that when fitting a Breit–Wigner to the CFD result, the sequence of Padé approximants with just one pole converges rather poorly. We have also tried other conformal parameterizations with different centers. In any case, by changing the model, the systematic uncertainty is smaller than the statistical error, which dominates the uncertainty in our final result.

The final result for the $K^*(892)$ parameters is shown in Table 3. This result may appear incompatible with the determinations in the RPP. There are several reasons for this: first, because in the RPP only Breit–Wigner (BW) parameters are given and then $s_p = M_{BW}^2 - iM_{BW}\Gamma_{BW}$, so that Re $\sqrt{s_p}$ is not exactly M_{BW} and Im $\sqrt{s_p}$ is not exactly $\Gamma_{BW}/2$. Taking these different definitions into account improves slightly the agreement. Second, there is the issue of using an isospin conserving formalism when extracting the CFD parameterization and when measuring the data, so that our resonances do not correspond to the charged nor the neutral cases. Therefore, when comparing to the resonances observed in a charged or neutral channels, which are the ones listed in the PDG, a difference of about ± 2 MeV is expected to arise. However, our pole is to be understood as the pole in the isospin conserving limit. Note that this distinction between charges and neutral resonances is not done in the RPP for other resonances. Moreover, there is a third reason, which is that the BW extractions of resonance parameters are usually obtained from a fit to the amplitude in a limited region or assuming the existence of a certain background from other regions or resonances. In contrast, here the whole elastic region is described with the CFD amplitude, thus, we are giving the pole of the whole amplitude. In general we do not think that obtaining this particular resonance from scatter-

ing data is competitive with the determinations from other reactions, which much better data and statistics.

4.2.2 The $K_1^*(1410)$

Let us now turn to the $K_1^*(1410)$, which cannot be considered elastic and has a rather small 7% branching fraction to $K\pi$. Still, we will be able to obtain its pole, as we did for the $K_0^*(1430)$, since Padé approximants also provide the analytic continuation to the continuous Riemann sheet of the partial waves in the inelastic region. Once more it is enough to compute derivatives from the vector partial-wave CFD parameterization in [24].

The theoretical convergence is really fast as can be observed in Fig. 7. The theoretical error is small in the range 1280–1450 MeV, with a minimum for the total error located at $\sqrt{s_0} = 1304$ MeV. In this case the theoretical uncertainty becomes much smaller than the statistical one at $N = 4$. Partly, this is due to the fact that in this energy region there are two conflicting experiments and this leads to large uncertainties in the CFD parameterization. As a consequence, what we call "statistical" uncertainties dominate the final result for this resonance.

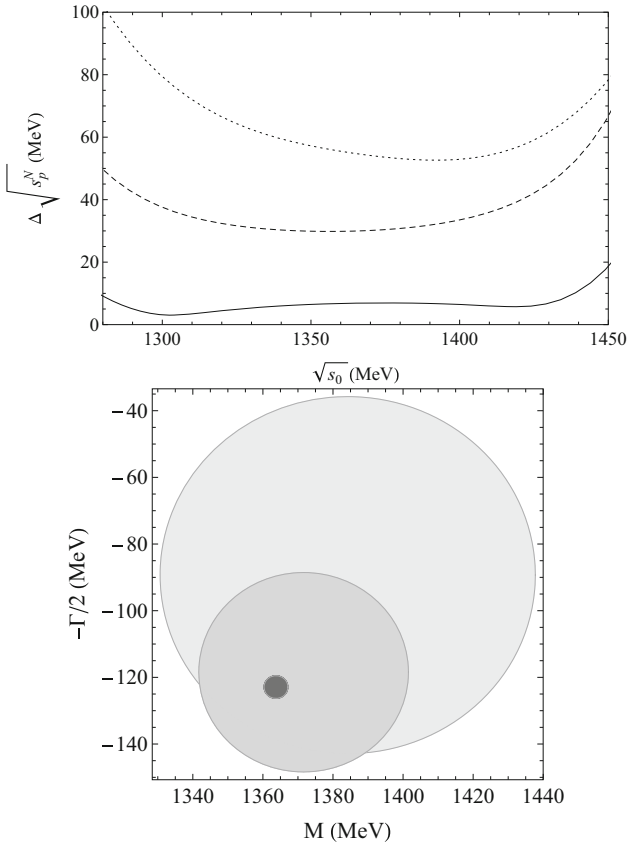

Fig. 7 *Upper panel* $\Delta\sqrt{s_p^N}$ in the $K_1^*(1410)$ pole determination for different values of $\sqrt{s_0}$ using the P_1^N sequence. The *dotted*, *dashed* and *continuous lines* correspond to $N = 2, 3$ and 4, respectively. *Lower panel* Theoretical uncertainty regions $\Delta\sqrt{s_p^N}$ for the $K_1^*(1410)$ pole. The *light gray*, *gray* and *dark gray areas* correspond to $N = 2, 3$ and 4

Table 4 $K_1^*(1410)$ pole results for the CFD and different parameterizations fitted to the CFD. The uncertainty for $\sqrt{s_p}$ and g include statistical and theoretical errors only

	CFD Padé	BW Padé
$\sqrt{s_p}$ (MeV)	$(1362^{+37}_{-37}) - i(123^{+41}_{-54})$	$(1374) - i(88)$
Δ_{th} (MeV)	3	0.7
g	$2.41^{+1.60}_{-1.11}$	1.36
Δ_{th}	0.04	0.007
$\sqrt{s_0}$ (GeV)	1.30	1.38

As with other resonances, we have also fitted other parameterizations to the CFD data to estimate the systematic uncertainty when calculating the derivatives at one given energy. In Table 4 we show the results when calculating the derivatives with a BW formalism, which is the one used by all the determinations quoted in the RPP [2]. For the final central value we thus take the average over these two determinations and we evaluate our final error as the quadrature between statistical, theoretical, and systematic uncertainties as

$$\sqrt{s_{K_1^*(1410)}} = (1368^{+38}_{-38}) - i(106^{+48}_{-59})\ \text{MeV}, \qquad (11)$$
$$g_{K_1^*(1410)} = 1.89^{+1.77}_{-1.34}.$$

This might look less precise than the averaged result of $M = 1414 \pm 15$ MeV and $\Gamma/2 = 116 \pm 10.5$ given in the RPP [2], but this is because this average is dominated by a measurement of the LASS experiment on $K^- p \to \bar{K}^0 \pi^+ \pi^- n$ [1] using a BW parameterization with simple backgrounds. It is not evident the systematic effect due to these simple backgrounds. When using the $K\pi$ scattering data obtained later by the same experiment [26] one obtains $M = 1380 \pm 21 \pm 19$ and $\Gamma/2 = 88 \pm 26 \pm 11$, very similar to our extraction, but based only on a BW formalism and without taking into account the conflicting data of Estabrooks et al. [25] in this region. In this sense we think our result is more robust and confirms the parameters of this resonance without using a specific BW functional form, nor assuming any particular background. In Fig. 8 we show how our final result compares to all other results listed in the RPP. It can be seen that the results are rather consistent with the exception of that of Etkin et al. [69].

4.3 Tensor resonances

In practice, once we reach 1.3 GeV all available channels have some measured inelasticity. Since all resonances with $J = 2$ or higher angular momentum waves are above this energy, we use the inelastic CFD parameterization of [24]

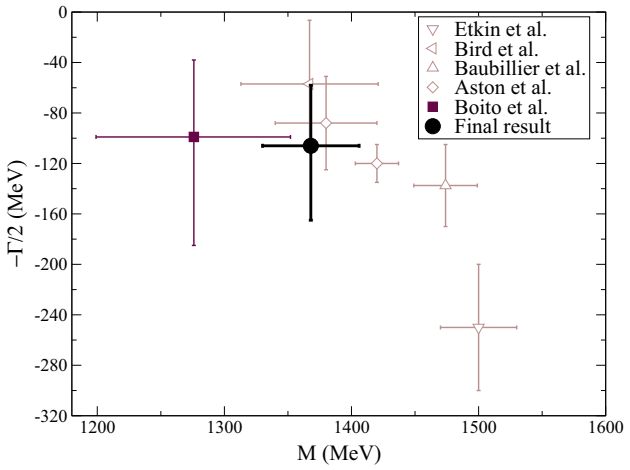

Fig. 8 Final result for the $K_1^*(1410)$ pole. Other references are taken from the RPP compilation [2], Boito et al. [65], Aston et al. [26], Baubillier et al. [66,67], Bird et al. [68], Etkin et al. [69]

and the fact that the Padé approximants perform the analytical continuation directly to the continuous Riemann sheet. We describe next how we extract the parameters of the $K_2^*(1430)$ and $K_3^*(1780)$ resonances, which have $J = 2$ and 3, respectively.

4.3.1 The $K_2^*(1430)$

This resonance appears in $K\pi$ scattering with angular momentum 2 and isospin 1/2 and shows a nice Breit–Wigner-like shape. Its branching ratio to $K\pi$ is 50%, the other relevant channels being $K^*(892)\pi$, $K^*(892)\pi\pi$ and $K\rho$.

Since there is a well isolated pole, we can use the $M = 1$ Padé sequence with one pole. The upper panel of Fig. 9 shows how the sequence converges rapidly and for $N = 4$ the truncation uncertainty is completely negligible, having a minimum at $\sqrt{s_0} = 1410$ MeV. In the lower panel we see that the area covered by the $N = 4$ Padé, almost becomes a point and that the central value of the pole position is very stable. The parameters of the resonance thus obtained are listed in Table 5.

As done with other resonances, we have tried calculating the derivatives needed for the Padé approximants by means of other parameterizations fitted to the CFD results. In particular we show in Table 5 the result when using a Breit–Wigner formula fitted to the CFD and then the Padé approximants to extract the pole. The difference is rather small, but we have taken the average with the CFD result obtained with Padé series and added the systematic uncertainty as explained in the introduction, yielding our final result:

$$\sqrt{s_{K_2^*(1430)}} = (1424 \pm 4) - i(66 \pm 2)\ \text{MeV}, \qquad (12)$$
$$g_{K_2^*(1430)} = 3.23 \pm 0.22\ \text{GeV}^{-1},$$

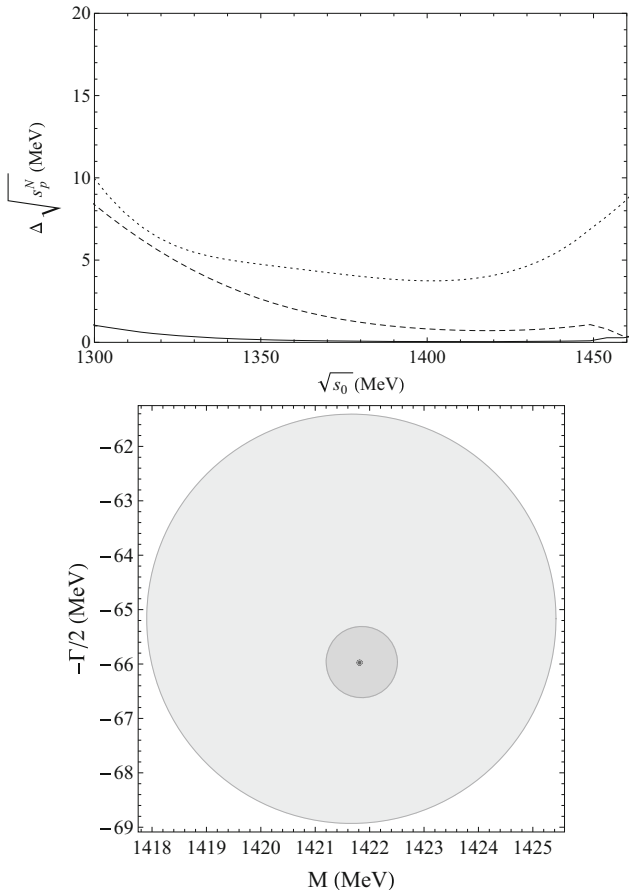

Fig. 9 *Upper panel* $\Delta\sqrt{s_p^N}$ in the $K_2^*(1430)$ pole determination for different values of $\sqrt{s_0}$ using the P_1^N sequence. The *dotted*, *dashed* and *continuous lines* correspond to $N = 2, 3$ and 4, respectively. *Lower panel* Theoretical uncertainty regions $\Delta\sqrt{s_p^N}$ for the $K_2^*(1430)$ pole. The *light gray*, *gray* and *dark gray areas* correspond to $N = 2, 3$ and 4

Table 5 $K_2^*(1430)$ pole results for the CFD and different parameterizations fitted to the CFD. The uncertainty for $\sqrt{s_p}$ and g include statistical and theoretical errors only

	CFD Padé	BW Padé
$\sqrt{s_p}$ (MeV)	$(1422 \pm 3) - i(66 \pm 2)$	$(1427) - i(66)$
Δ_{th} (MeV)	0.04	0.01
g (GeV)$^{-1}$	3.37 ± 0.07	3.08
Δ_{th} (GeV)$^{-1}$	0.001	3×10^{-5}
$\sqrt{s_0}$ (GeV)	1.41	1.51

which, as can be seen in Fig. 10, is in good agreement with other determinations quoted in the RPP [2]. The RPP average is dominated by the work of LASS [1,26], which use BW formalisms and simple backgrounds. Our result has a relatively small uncertainty, despite including estimates of systematic error, both in the pole extraction and the data, and

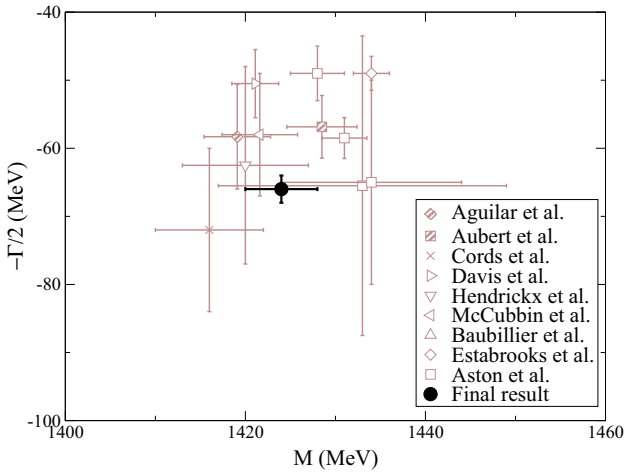

Fig. 10 Final result for the $K_2^*(1430)$ pole. The following references are taken from the RPP compilation [2], Aston et al. [26], Estabrooks et al. [25], Baubillier et al. [66,67], Mccubbin et al. [70], Hendrickx et al. [71], Davis et al. [72], Cords et al. [73], Aubert et al. [74], Aguilar et al. [75]

avoiding the use of backgrounds or other assumptions in the pole extraction.

4.3.2 *The* $K_3^*(1780)$

The heaviest strange resonance that can be studied using the CFD parameterizations is the $K_3^*(1780)$, which appears in the F-wave with isospin 1/2. Let us note that the $K_3^*(1780)$ has a branching ratio to πK of 20%, with the other three relevant channels being $K\rho$, $K^*(892)$ and $K\eta$. First of all, let us remark that its mass lies beyond 1600 MeV, the energy up to which the CFD parameterization satisfies well the Forward Dispersion Relations. Nevertheless, as explained in [24], this is most likely due to the data in other waves, since imposing FDRs up to higher energies demands deviations from the D-wave data, for instance, but the F-wave barely changes from an unconstrained fit up to larger energies. Thus we feel confident our method can be applied to this resonance.

The $K_3^*(1780)$ is well isolated from contributions from other singularities and we can use the Padé sequence with just one pole. As usual, we show in Fig. 11 the convergence of the sequence which has a very small truncation error for $N = 4$. Actually, it is about two orders of magnitude smaller than the statistical one, as seen in Table 6. As seen in the lower panel of that figure, the central value barely changes with N (Note the small scale of the axis).

Once again we have tried to estimate the uncertainty due to calculating the derivatives of the amplitude with different parameterizations, but the differences are rather small. In Table 6 we show the pole extracted with the Padé method if, instead of using the CFD parameterizations, we use a BW fit to the CFD. The mass and width barely change but the

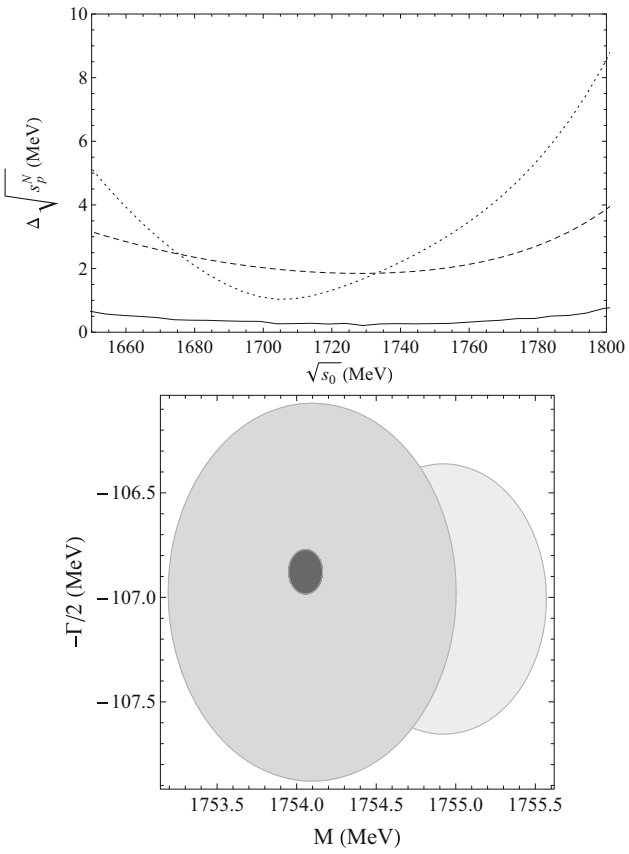

Fig. 11 *Upper panel* $\Delta\sqrt{s_p^N}$ in the $K_3^*(1780)$ pole determination for different values of $\sqrt{s_0}$ using the P_1^N sequence. The *dotted*, *dashed* and *continuous lines* correspond to $N = 2, 3.$ and 4, respectively. *Lower panel* Theoretical uncertainty regions $\Delta\sqrt{s_p^N}$ for the $K_3^*(1780)$ pole. The *light gray*, *gray* and *dark gray areas* correspond to $N = 2, 3.$ and 4

coupling is slightly different, changing by less than the statistical uncertainty. We thus take the average and enlarge the uncertainty with a systematic error combined as explained in the introduction to this section. Our result is

$$\sqrt{s_{K_3^*(1780)}} = (1754 \pm 13) - i(119 \pm 14)\ \text{MeV}, \qquad (13)$$
$$g_{K_3^*(1780)} = 1.28 \pm 0.14\ \text{GeV}^{-2},$$

which, as seen in Fig. 12, is compatible with the results quoted in the RPP [2]. It should be noted that our uncertainties are only slightly larger than the RPP average, which is dominated by the result of Aston et al. [26], but here we do not make a particular assumption for the functional form or a background in the amplitude.

5 Summary

In this work we have presented a determination of the parameters of resonances that appear in $K\pi$ scattering below

Table 6 $K_3^*(1780)$ pole results for the CFD and different parameterizations fitted to the CFD. The uncertainty for $\sqrt{s_p}$ and g include statistical and theoretical errors only

	CFD Padé	BW Padé
$\sqrt{s_p}$ (MeV)	$(1753 \pm 13) - i(119 \pm 14)$	$(1755) - i(118)$
Δ_{th} (MeV)	0.3	4.3
g (GeV)$^{-2}$	1.32 ± 0.13	1.23
Δ_{th} (GeV)$^{-2}$	0.003	0.03
$\sqrt{s_0}$ (GeV)	1.73	1.76

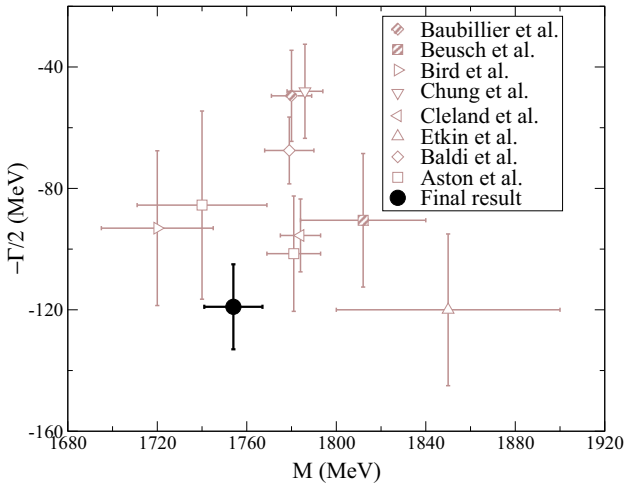

Fig. 12 Final result for the $K_3^*(1780)$ pole determination. We also show results taken from the PDG [2], Aston et al. [26], Baldi et al. [76], Etkin et al. [69], Cleland et al. [77], Chung et al. [78], Bird et al. [68], Beusch et al. [79], Baubillier et al. [66,67]

1.8 GeV. This has been achieved by means of series of Padé approximants, which should converge to the appropriate analytic structure of the amplitude in a given domain. This constitutes another instance of the applicability and usefulness of this method, which avoids specific model assumptions in the determinations of the mass, width and coupling of a resonance. As a matter of fact, these parameters are usually obtained from Breit–Wigner-like parameterizations (or slight modifications) which make a specific relation between the width and residue, and usually assume that the data contain simple backgrounds superimposed to the resonance signal. With this method we determine the pole without such assumptions. Moreover, it should be remarked that this method can be applied in the inelastic region, where the powerful partial-wave dispersion relations cannot be used in practice to obtained poles.

In addition, these determinations have been obtained using as input a recent dispersive description of all the $K\pi$ data, which is constrained to satisfy two Forward Dispersion Relations (and several crossing sum rules) up to 1600 MeV. It should also be noted that simple fits to the data, as those used in previous determinations of resonance parameters, do not fulfill these fundamental constraints. These constrained fits have also taken into account systematic uncertainties due to incompatibilities between different experiments.

Thus, we have provided determinations of the mass, width, and coupling to $K\pi$ for the conflictive $K_0^*(800)$ or κ resonance, the $K_0^*(1430)$ scalar, the $K^*(892)$ and $K_1^*(1410)$ vectors, the spin-two $K_2^*(1430)$ as well as the spin-three $K_3^*(1780)$. The results are fairly competitive with the results on the Review of Particle Properties, although it should be noted that these results contain some estimation of systematic and theoretical uncertainties usually lacking in the literature.

Acknowledgements JRP and AR are supported by the Spanish Project FPA2014-53375-C2-2 and the Spanish Excellence network HADRONet FIS2014-57026-REDT. The work of JRE was supported by the DFG (SFB/TR 16, "Subnuclear Structure of Matter") and the Swiss National Science Foundation.

References

1. D. Aston et al., Phys. Lett. B **180**, 308 (1986) [Erratum: Phys. Lett. B **183**, 434 (1987)]
2. C. Patrignani et al. (Particle Data Group), Chin. Phys. C **40**, 100001 (2016)
3. B. Ananthanarayan, G. Colangelo, J. Gasser, H. Leutwyler, Phys. Rep. **353**, 207 (2001)
4. P. Buettiker, S. Descotes-Genon, B. Moussallam, Eur. Phys. J. C **33**, 409 (2004)
5. R. Garcia-Martin, R. Kaminski, J.R. Pelaez, J. Ruiz de Elvira, F.J. Yndurain, Phys. Rev. D **83**, 074004 (2011)
6. M. Hoferichter, J. Ruiz de Elvira, B. Kubis, U.G. Meiner, Phys. Rep. **625**, 1 (2016)
7. S.M. Roy, Phys. Lett. **36B**, 353 (1971)
8. I. Caprini, G. Colangelo, H. Leutwyler, Phys. Rev. Lett. **96**, 132001 (2006)
9. B. Moussallam, Eur. Phys. J. C **71**, 1814 (2011)
10. R. Garcia-Martin, R. Kaminski, J.R. Pelaez, J. Ruiz de Elvira, Phys. Rev. Lett. **107**, 072001 (2011)
11. J.R. Pelaez, Phys. Rept. **658**, 1 (2016). arXiv:1510.00653 [hep-ph]
12. S. Descotes-Genon, B. Moussallam, Eur. Phys. J. C **48**, 553 (2006)
13. S.N. Cherry, M.R. Pennington, Nucl. Phys. A **688**, 823 (2001)
14. F.J. Yndurain, R. Garcia-Martin, J.R. Pelaez, Phys. Rev. D **76**, 074034 (2007)
15. I. Caprini, Phys. Rev. D **77**, 114019 (2008)
16. Z.H. Guo, J.A. Oller, Phys. Rev. D **93**(9), 096001 (2016)
17. J.A. Oller, Phys. Rev. D **71**, 054030 (2005)
18. A. Varc et al., Phys. Rev. C **88**(3), 035206 (2013)
19. A. Varc et al., Phys. Rev. C **89**(4), 045205 (2014)
20. A. Varc et al., Phys. Rev. C **89**(6), 065208 (2014)
21. P. Masjuan, J.J. Sanz-Cillero, Eur. Phys. J. C **73**, 2594 (2013). arXiv:1306.6308 [hep-ph]

22. P. Masjuan, J. Ruiz de Elvira, J.J. Sanz-Cillero, Phys. Rev. D **90**(9), 097901 (2014)
23. I. Caprini, P. Masjuan, J. Ruiz de Elvira, J.J. Sanz-Cillero, Phys. Rev. D **93**(7), 076004 (2016)
24. J.R. Pelaez, A. Rodas, Phys. Rev. D **93**(7), 074025 (2016)
25. P. Estabrooks et al., Nucl. Phys. B **133**, 490 (1978)
26. D. Aston et al., Nucl. Phys. B **296**, 493 (1988)
27. E. van Beveren, T.A. Rijken, K. Metzger, C. Dullemond, G. Rupp, J.E. Ribeiro, Z. Phys. C **30**, 615 (1986). arXiv:0710.4067 [hep-ph]
28. A. Dobado, J.R. Pelaez, Phys. Rev. D **47**, 4883 (1993). arXiv:hep-ph/9301276
29. A. Dobado, J.R. Pelaez, Phys. Rev. D **56**, 3057 (1997)
30. A. Gomez Nicola, J.R. Pelaez, Phys. Rev. D **65**, 054009 (2002)
31. J.R. Pelaez, Mod. Phys. Lett. A **19**, 2879 (2004)
32. H.Q. Zheng, Z.Y. Zhou, G.Y. Qin, Z. Xiao, J.J. Wang, N. Wu, Nucl. Phys. A **733**, 235 (2004)
33. J.A. Oller, E. Oset, J.R. Pelaez, Phys. Rev. Lett. **80**, 3452 (1998)
34. J.A. Oller, E. Oset, J.R. Pelaez, Phys. Rev. D **59**, 074001 (1999) [Erratum: Phys. Rev. D **60**, 099906 (1999); Erratum: Phys. Rev. D **75**, 099903 (2007)]
35. J.A. Oller, E. Oset, Phys. Rev. D **60**, 074023 (1999). arXiv:hep-ph/9809337
36. D. Black, A.H. Fariborz, F. Sannino, J. Schechter, Phys. Rev. D **58**, 054012 (1998)
37. D. Black, A.H. Fariborz, F. Sannino, J. Schechter, Phys. Rev. D **59**, 074026 (1999)
38. M. Jamin, J.A. Oller, A. Pich, Nucl. Phys. B **587**, 331 (2000). arXiv:hep-ph/0006045
39. T. Wolkanowski, M. So tysiak, F. Giacosa, Nucl. Phys. B **909**, 418 (2016)
40. T. Ledwig, J. Nieves, A. Pich, E. Ruiz Arriola, J. Ruiz de Elvira, Phys. Rev. D **90**(11), 114020 (2014)
41. S. Ishida, M. Ishida, T. Ishida, K. Takamatsu, T. Tsuru, Prog. Theor. Phys. **98**, 621 (1997)
42. D.V. Bugg, Phys. Lett. B **572**, 1 (2003) [Erratum: Phys. Lett. B **595**, 556 (2004)]
43. D.V. Bugg, Phys. Rev. D **81**, 014002 (2010)
44. P.C. Magalhaes, M.R. Robilotta, Phys. Rev. D **90**(1), 014043 (2014)
45. R. Navarro Pérez, E. Ruiz Arriola, J. Ruiz de Elvira, Phys. Rev. D **91**, 074014 (2015)
46. T.N. Truong, Phys. Rev. Lett. **61**, 2526 (1988)
47. A. Dobado, M.J. Herrero, T.N. Truong, Phys. Lett. B **235**, 134 (1990)
48. A. Dobado, J.R. Pelaez, Phys. Rev. D **47**, 4883 (1993)
49. J. Gasser, U.G. Meissner, Nucl. Phys. B **357**, 90 (1991)
50. G. Bonvicini et al. (CLEO Collaboration), Phys. Rev. D **78**, 052001 (2008)
51. Z.Y. Zhou, H.Q. Zheng, Nucl. Phys. A **775**, 212 (2006)
52. M. Ablikim et al. (BES Collaboration), Phys. Lett. B **698**, 183 (2011)
53. M. Ablikim et al., Phys. Lett. B **693**, 88 (2010)
54. M. Ablikim et al. (BES Collaboration), Phys. Lett. B **633**, 681 (2006)
55. E.M. Aitala et al. (E791 Collaboration), Phys. Rev. Lett. **89**, 121801 (2002)
56. C. Cawlfield et al. (CLEO Collaboration), Phys. Rev. D **74**, 031108 (2006)
57. J.M. Link et al. (FOCUS Collaboration), Phys. Lett. B **535**, 43 (2002)
58. A. Schenk, Nucl. Phys. B **363**, 97 (1991). doi:10.1016/0550-3213(91)90236-Q
59. G.F. Chew, S. Mandelstam, Phys. Rev. **119**, 467 (1960). doi:10.1103/PhysRev.119.467
60. A.V. Anisovich, A.V. Sarantsev, Phys. Lett. B **413**, 137 (1997)
61. D. Barberis et al. (WA102 Collaboration), Phys. Lett. B **436**, 204 (1998)
62. M. Ablikim et al. (BES Collaboration), Phys. Rev. D **72**, 092002 (2005)
63. J.P. Lees et al. (BaBar Collaboration), Phys. Rev. D **89**(11), 112004 (2014)
64. J.M. Link et al. (FOCUS Collaboration), Phys. Lett. B **653**, 1 (2007)
65. D.R. Boito, R. Escribano, M. Jamin, Eur. Phys. J. C **59**, 821 (2009)
66. M. Baubillier et al. (BIRMINGHAM-CERN-GLASGOW-MICHIGAN STATE-PARIS Collaboration), Nucl. Phys. B **202**, 21 (1982)
67. M. Baubillier et al. (Birmingham-CERN-Glasgow-Michigan State-Paris Collaboration), Z. Phys. C **26**, 37 (1984)
68. F.P. Bird, SLAC-0332, SLAC-332, UMI-89-12872, SLAC-R-0332, SLAC-R-332
69. A. Etkin et al., Phys. Rev. D **22**, 42 (1980)
70. N.A. McCubbin, L. Lyons, Nucl. Phys. B **86**, 13 (1975)
71. K. Hendrickx, P. Cornet, F. Grard, V.P. Henri, R. Windmolders, D. Vignaud, D. Burlaud, S. Tavernier, Nucl. Phys. B **112**, 189 (1976)
72. P.J. Davis, S.E. Derenzo, S.M. Flatte, M. Alston-Garnjost, G.R. Lynch, F.T. Solmitz, Phys. Rev. Lett. **23**, 1071 (1969)
73. D. Cords et al., Phys. Rev. D **4**, 1974 (1971)
74. B. Aubert et al. (BaBar Collaboration), Phys. Rev. D **76**, 012008 (2007)
75. M. Aguilar-Benitez, R.L. Eisner, J.B. Kinson, Phys. Rev. D **4**, 2583 (1971)
76. R. Baldi et al., Phys. Lett. **63B**, 344 (1976)
77. W.E. Cleland et al., Nucl. Phys. B **208**, 189 (1982)
78. S.U. Chung et al., Phys. Rev. Lett. **40**, 355 (1978)
79. E. Konigs et al., Phys. Lett. **74B**, 282 (1978)

3.1.4 Preprint: *Determination of the lightest strange resonance* $K_0^*(700)$ *or* κ*, from a dispersive data analysis*

Determination of the lightest strange resonance $K_0^*(700)$ or $\kappa/K_0^*(700)$, from a dispersive data analysis

J.R. Pelaez[1] and A. Rodas[1]

[1] *Departamento de Física Teórica and IPARCOS, Universidad Complutense de Madrid, 28040 Madrid, Spain*

In this work we present a precise and model-independent dispersive determination from data of the existence and parameters of the lightest strange resonance $\kappa/K_0^*(700)$. We use both subtracted and unsubtracted partial-wave hyperbolic and fixed-t dispersion relations as constraints on combined fits to $\pi K \to \pi K$ and $\pi\pi \to K\bar{K}$ data. We then use the hyperbolic equations for the analytic continuation of the isospin $I = 1/2$ scalar partial wave to the complex plane, in order to determine the $\kappa/K_0^*(700)$ and $K^*(892)$ associated pole parameters and residues.

Despite the fact that Quantum Chromodynamics (QCD) was formulated more than four decades ago, some of the lowest lying states of QCD still "Need confirmation" according to the Review of Particle Properties (RPP) [1]. This is the case of the lightest strange scalar resonance, traditionally known as κ, but recently renamed $K_0^*(700)$ (It was $K_0^*(800)$ until 2018).

Light scalar mesons have been a subject of debate since the σ meson (now $f_0(500)$) was proposed by Johnson and Teller in 1955 [2]. Schwinger in 1957 [3] incorporated it as a singlet in the isospin picture and pointed out that its strong coupling to two pions would make it extremely broad and hard to find. A similar situation occurs when extending this picture to include strangeness and $SU(3)$ flavor symmetry. Actually, in 1977 Jaffe [4] proposed the existence of a scalar nonet below 1 GeV including a very broad $\kappa/K_0^*(700)$ meson. Of this light-scalar nonet, the $f_0(980)$ and $a_0(980)$, were easily identified since the 60's. However, the $\sigma/f_0(500)$ and $\kappa/K_0^*(700)$ have been very controversial for decades because they are so broad that their shape is not always clearly resonant or even perceptible. Moreover, it was proposed [4, 5] that these states might not be "ordinary-hadrons", due to their inverted mass hierarchy compared to the usual quark model $quark - antiquark$ nonets. In terms of QCD it has also been shown that their dependence on the number of colors is at odds with the ordinary one [6–8]. From the point of view of Regge Theory, a dispersive analysis of both the $\sigma/f_0(500)$ and $\kappa/K_0^*(700)$ shows that they do not follow ordinary linear Regge trajectories [9, 10].

Definitely, both the $\sigma/f_0(500)$ and $\kappa/K_0^*(700)$ do not display prominent Breit-Wigner peaks, but their shape is often distorted by particular features of each reaction. Thus, it is convenient to refer to the resonance pole position, $\sqrt{s_{pole}} = M - i\Gamma/2$, which is process independent. Here M and Γ are the resonance pole mass and width. Note that poles of wide resonances lie deep into the complex plane and their determination requires rigorous analytic continuations. This is the first problem of most $\sigma/f_0(500)$ and $\kappa/K_0^*(700)$ determinations: Simple models continued to the complex plane yield rather unstable results. In addition, many models assume a particular relation between the width and coupling, not necessarily correct for broad states, or impose a threshold behavior incompatible with chiral symmetry breaking constraints. These are reasons why Breit-Wigner-like parameterizations—devised for narrow resonances— are inadequate for resonances as wide as the $\sigma/f_0(500)$ and $\kappa/K_0^*(700)$. In contrast, dispersion relations, solve this first problem by providing the required rigorous analytic continuation to the complex plane. In practice, they are more stringent and powerful for two-body scattering.

The second problem is that meson-meson scattering data are plagued with systematic uncertainties, since they are extracted indirectly from meson-nucleon to meson-meson-nucleon experiments. Inconsistencies appear both between different sets and even within a single set. Thus, for very long, a rough description of data was enough for simple models to be considered acceptable, making model-based determinations of the $\sigma/f_0(500)$ and $\kappa/K_0^*(700)$ even more unreliable. Moreover, fairly good-looking data fits come out inconsistent with dispersion relations, as shown in [11]. We will see here how they lead to very unstable $\kappa/K_0^*(700)$ pole determinations.

Once again dispersion theory helps overcoming this second problem, by providing stringent constrains between different channels and energy regions. This explains the interest on dispersive studies in the literature: for $\pi\pi$ [7, 12–16], for πN [17, 18], for $\gamma\gamma \to \pi\pi$ [19], for πK [20–22] and for $\pi\pi \to K\bar{K}$ [23] scattering. Actually, partial-wave dispersion relations implementing crossing correctly have been decisive in the 2012 major RPP revision of the $\sigma/f_0(500)$, changing its nominal mass from 600 to 500 MeV and decreasing its uncertainties by a factor of 5. In contrast, the $\kappa/K_0^*(700)$ still "Needs Confirmation" in the Review of Particle Physics.

Note that a $\kappa/K_0^*(700)$ pole is found as long as the isospin 1/2 scalar wave data is reproduced and the model respects some basic analyticity and chiral symmetry properties [24–31]. Furthermore, its pole must lie below 900 MeV [32]. However, the pole position spread is very large when using models. In Fig.1 we show with solid symbols the T-matrix poles of the $\kappa/K_0^*(700)$ listed in the RPP and as a shadowed rectangle the uncertainty

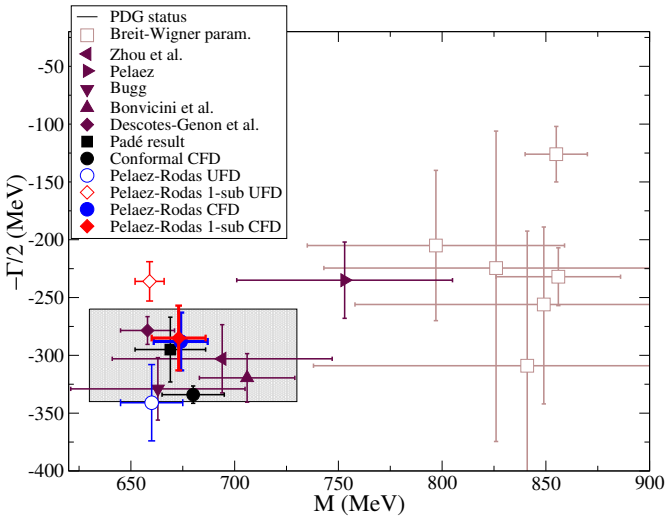

FIG. 1. $K_0^*(700)$ pole position. The Breit-Wigner parameterizations are taken from the RPP compilation [34], which also includes: Descotes-Genon et al. [22], Bonvicini et al. [35], D.Bugg [36], J.R.Peláez [31], Zhou et al. [33] and the "Padé Result" [37]. The conformal CFD is our simple analytic extrapolation of our parameterization in [11]. We also show the results using Roy-Steiner equations for the continuation to the complex plane, either when using as input our UFD or CFD parameterizations. The red points use a once-subtracted relation for F^- and the blue ones an unsubtracted one. For UFD both determinations do not agree. This illustrates how unstable pole determinations are, starting from the same parameterization of the data and even using dispersive studies. Only once Roy-Steiner Eqs. are imposed as a constraint on data, the two determinations of the pole fall on top of each other. This final pole position is the main result of this work.

estimate in the RPP. Note that the Breit-Wigner poles, shown as hollow squares, have a very large spread and differ substantially from those having some analyticity and chiral symmetry properties built in.

Some T-matrix poles in the RPP used dispersive or complex analyticity techniques, although with approximations for the so-called "unphysical" cuts below threshold, which are the most difficult to calculate. In the πK case, these are a "left" cut due to thresholds in the crossed channels and a circular one due to partial-wave integration. Thus Fig. 1 also shows results from NLO Chiral Perturbation Theory (ChPT) unitarized with the Inverse Amplitude Method [31], and [33], where the unphysical cuts are approximated with NLO ChPT or calculated with a cutoff, respectively.

The most sound determination of the $\kappa/K_0^*(700)$ pole so far is the dispersive analysis by Descotes-Genon et al. [22], also shown in Fig. 1, which uses crossing to implement rigorously the left cut. The pole is obtained using as input a numerical solution in the real axis of Roy-Steiner equations obtained from fixed-t dispersion relations. Unfortunately these fixed-t Roy-Steiner equations do not reach the $\kappa/K_0^*(700)$-pole region in the complex plane. Remarkably, in [22] it was explicitly shown that the $\kappa/K_0^*(700)$ region is accessible with partial-wave hyperbolic dispersion relations. These were then used to obtain the pole, although starting from the solutions coming from the fixed-t ones. Note that this is a "solving relations" approach, since no data was used as input in the πK elastic region around the nominal $\kappa/K_0^*(700)$ mass, but only data from other channels and other energies as boundary conditions to the integral equations. In this sense, [22] provides a model-independent *prediction*. Despite the existence of this rigorous result, the $\kappa/K_0^*(700)$ still "Needs Confirmation", and we were encouraged by RPP members to carry out an alternative dispersive analysis *using data*, as previously done by our group for the $\sigma/f_0(500)$. The present work, which follows a "constraining data" approach instead of a "solving relations" approach, provides such an analysis.

It is worth noticing that the $\kappa/K_0^*(700)$ has also been recently found in lattice calculations [38] of πK scattering. However, since their pion is still at the unphysical mass of $\sim 400\,\text{MeV}$, it appears as a "virtual" pole slightly below threshold and in the second Riemann sheet. This pole is extracted with a simple K-matrix model, but it is fairly consistent with the expectations from unitarized NLO Chiral Perturbation Theory extrapolated to higher masses [39]. However, using pion masses between 200 and 400 MeV it is shown that the extraction of the pole using simple models is rather unstable [40]. This makes the approach followed in the present work even more relevant, since in the future lattice will provide data at physical masses and energies around the $\kappa/K_0^*(700)$ region that will require a "constraining data" technique for a model-independent description and its continuation to the complex plane.

Let us then describe our approach. In [11] we first provided Unconstrained Fits to πK Data (UFD) up to 2 GeV, paying particular attention to the inclusion of systematic uncertainties. It was then shown that they did not satisfy well Forward Dispersion Relations (FDRs). However, we showed that it was possible to use these FDRs as constraints and obtain a set of Constrained Fits to Data (CFD), which at least satisfy the FDRs up to 1.6 GeV while still providing a fairly good description of data. It is worth noticing that our "conformal CFD" parameterization of the low-energy isospin 1/2 scalar-wave already contains a $\kappa/K_0^*(700)$ pole, shown in Fig. 1. This is still a model-dependent extraction, based on a particular parameterization only valid up to roughly 1 GeV.

Later on [37], we used sequences of Padé approximants built from derivatives of the CFD fit to extract a new pole. This "Padé Method" does not assume any relation between the pole position and its residue thus reducing dramatically the model dependence of the result, listed as "Padé result" in Fig. 1. The value came out consistent within uncertainties with the dispersive result in [22]

and triggered the recent change of name in the 2018 RPP edition from $K_0^*(800)$ to $K_0^*(700)$. However, this result is not fully model independent, since it assumes the existence of one pole, the Padé series have to be truncated, the cuts are mimicked by poles, etc... (see [37] for details).

Thus, we present here the $\kappa/K_0^*(700)$ pole obtained from a full analysis of the existing data constrained to satisfy not only Forward Dispersion relations as in [11], but also both the S and P partial-wave dispersion relations (Roy-Steiner equations) obtained either from fixed-t or hyperbolic dispersion relations (HDR) along the $(s-a)(u-a) = b$. As shown in [22] the latter are the ones whose convergence region in the complex plane reaches the $\kappa/K_0^*(700)$ pole.

The price to pay when using partial wave dispersion relations is that they require input from the crossed channel $\pi\pi \to K\bar{K}$, which also has the same two problems of being frequently described with models and the existence of two incompatible sets of data (see [23] for details). In addition, in this case,there is an "unphysical" region between the $\pi\pi$ and $K\bar{K}$ thresholds, where data do not exist, but is needed for the calculations. Fortunately, Watson's Theorem tells us that the phase there is the well-known $\pi\pi$ phase shift, which allows for a full reconstruction of the amplitude using the standard Mushkelishvili-Omnés method. Thus, in [23] we rederived the HDR partial-wave projection both for $\pi\pi \to K\bar{K}$ and $\pi K \to \pi K$, but choosing appropriately the center of the hyperbolas in the s, t plane to extend their applicability region up to 1.47 GeV. Once again we found that the existing data does not satisfy well the dispersive representation, but we were able to provide constrained parameterizations of the two existing sets that describe the S-wave data up to almost 2 GeV and are consistent with HDR up to 1.47 GeV within uncertainties. These are called CFD_B and CFD_C and will be part of our input for the πK HDR, although we have explicitly checked that using one or the other barely changes the $\kappa/K_0^*(700)$ pole position by 1 MeV, negligible against our final uncertainties. Note that, contrary to previous calculations, we also provide uncertainties for $\pi\pi \to K\bar{K}$. Those for the g_1^1 wave are particularly relevant for the $\kappa/K_0^*(700)$ pole.

For our purposes in this work, the most relevant partial wave is the scalar one with $I = 1/2$ whose Unconstrained Fit to Data (UFD) is shown in Fig. 2. As explained in [11] this wave is obtained by fitting the data measured in the $f_{1/2} + f_{3/2}/2$ and the $I = 3/2$ combinations [41, 42]. It is also relevant that, as shown in Fig.3, the $I = 1/2$ vector wave UFD describes well the scattering data, in contrast to the solution [22]. The rest of the unconstrained partial-waves and high-energy input parameterizations are described in [11] for πK and [23] $\pi\pi \to K\bar{K}$. Minor updates will be given in detail in a forthcoming publication [43].

However, as seen in the upper panel of Fig.4 when the

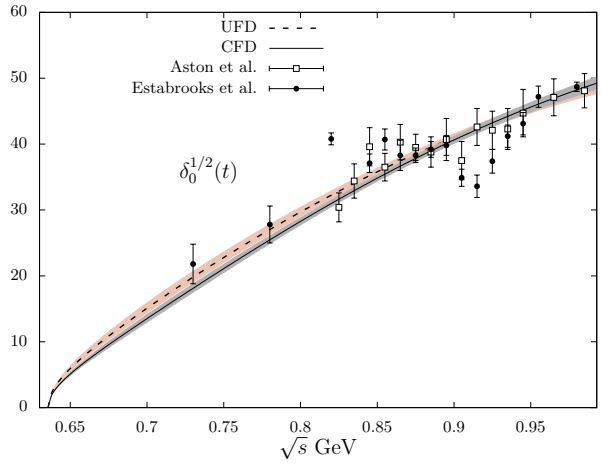

FIG. 2. CFD versus UFD $f_0^{1/2}(s)$ partial wave.

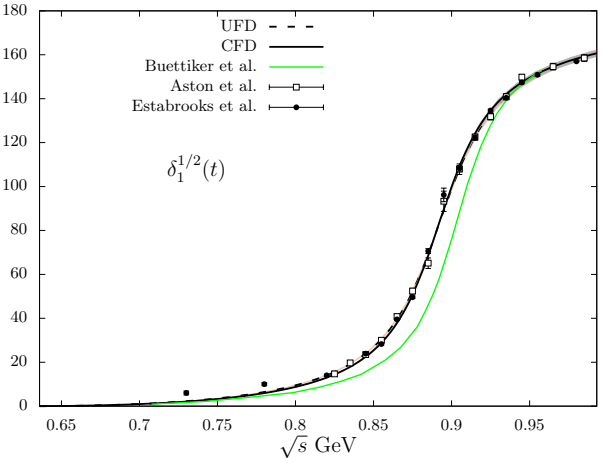

FIG. 3. CFD versus UFD $f_1^{1/2}(s)$ partial wave.

UFD is used as input of the dispersion relation, the dispersive representation is not satisfied within uncertainties. Actually, the fixed-t HDR output does not lie too far from the UFD input, but we can see that using an unsubtracted or a once-subtracted F^- HDR, their respective dispersive outputs come on opposite sides and far from the input UFD parameterization.

At this point it is very instructive to see how unstable is the extraction of the pole parameters from one fit that looks rather reasonable to the eye, as the UFD does. Thus, in Fig.1 we show the position of the $\kappa/K_0^*(700)$ pole when calculated using the hyperbolic dispersion relations without subtractions for F^- (hollow blue) or with one subtraction (hollow red). Note that *we use the same UFD input in the physical regions* but the poles are very incompatible among themselves. This is mostly due to the pseudo-physical region of the g_1^1 partial wave. This serves as illustration of how unreliable it is to determine the $\kappa/K_0^*(700)$ pole from a simple fits to data. And even

more unreliable if a simple model is used for the continuation of the fit to the complex plane

Thus, in order to obtain a rigorous and stable pole determination, we have imposed that the dispersive representation should be satisfied within uncertainties when fitting the data. To this end, we have followed our usual procedure [11, 15, 23] of defining a χ^2-like distance between the input and the output at many different energy values, which is then minimized together with the χ^2 of the data when doing the fits. We minimize simultaneously 18 dispersion relations. Two of them are the FDRs we already used in [11]. Four HDR for the $\pi\pi \to K\bar{K}$ partial waves. Once subtracted for g_0^0, g_2^0, g_1^1 and another unsubtracted for g_1^1, as we did in [23]. However, this time we also consider the once subtracted case for g_1^1. In addition we now impose three more dispersion relations within uncertainties for the four $S^{1/2}, S^{3/2}, P^{1/2}, P^{3/2}$ πK partial-waves. One comes from fixed-t relations, whereas the other two are HDR, whose applicability region in the real axis was maximized in [23] choosing $a = -13.9 m_\pi^2$. These HDR always have one-subtraction for the symmetric amplitude F^+ but either one or no subtractions for F^-. For the πK $S^{1/2}$-wave, most of the dispersive uncertainty comes from the the πK S-waves themselves when using the subtracted F^-, whereas a large contribution comes from g_1^1 for the unsubtracted.

The details of our technique have been explained several times in [11, 23]. The resulting Constrained Fits to Data (CFD) set differ slightly from the unconstrained ones, but still describe the data. This is illustrated in Fig. 3, were we see that the difference between UFD and CFD is rather small for the P-wave, both providing remarkable descriptions of the scattering data. In contrast, in Fig. 2 we see that the CFD S-wave is lower than the UFD around the $\kappa/K_0^*(700)$ nominal mass, but still describes well the experimental information. Other waves also suffer small changes, but are less relevant for the $\kappa/K_0^*(700)$ (see [43]). All in all, we can see in the lower panel of Fig.4 that when the CFD set is now used as input of the dispersion relations the curves of the input, and the three outputs agree within uncertainties.

With all dispersion relations well satisfied we can now use our CFD as input in the HDR and look for the pole of the $\kappa/K_0^*(700)$. Note that in order to ensure that our final $\kappa/K_0^*(700)$ pole and its uncertainties lie within the convergence region, we now use the HDR with $a = -9 m_\pi^2$. These results are shown in 1, this time as a solid blue and red symbols depending on whether they are obtained with the unsubtracted or the once-subtracted F^-. Contrary to the unconstrained case, the agreement between both determinations when using the CFD set is now remarkably good. The precise values of the pole position and residue for our subtracted and unsubtracted results are listed in Table I, together the dispersive result of [22] and our Padé sequence determination [10].

Now, let us recall that the unsubtracted result depends strongly on the pseudo-physical region of $\pi\pi \to K\bar{K}$. In addition under the change of a the subtracted result, both in the real axis and for the pole, barely changes, whereas the unsubtracted one changes slightly (a few MeV for the pole). Therefore although both are compatible, we consider the once-subtracted result the more robust and our final result.

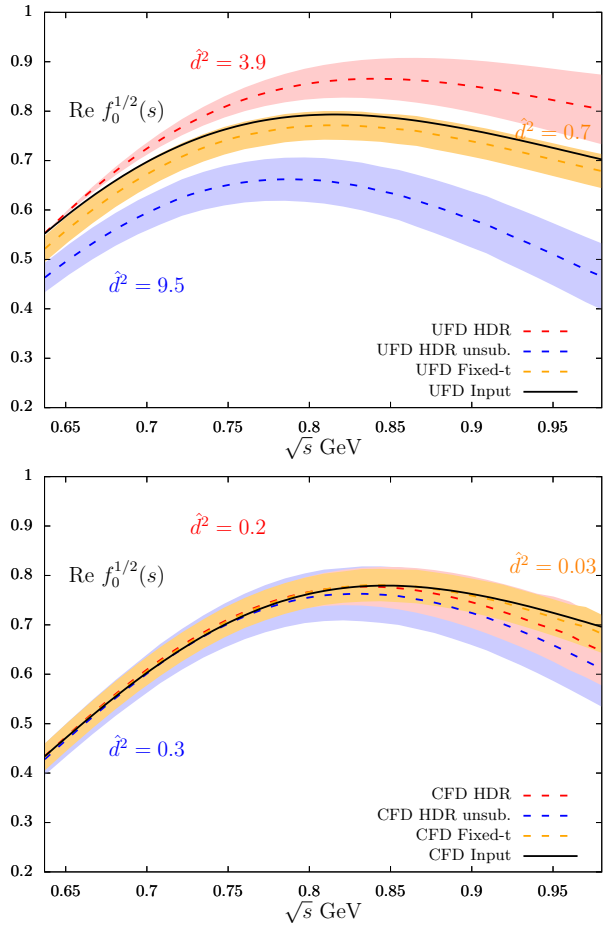

FIG. 4. Dispersive output of the $f_0^{1/2}(s)$ partial wave with the F^- amplitude dispersion relation unsubtracted or with one subtraction, versus the input from the data parameterization. Upper panel: Unconstrained Fits to Data (UFD). Note the huge discrepancies between the curves. Lower panel: Constrained Fits to Data (CFD) now all the curves agree within uncertainties.

Let us remark that our dispersive pole obtained from data also agrees with the solution in [22], although our uncertainties associated to the width are larger. In part, this is because we have estimated uncertainties for all our input.

For completeness, we have also calculated the parameters of the vector $K^*(892)$ pole, since we also describe the data there. We find: $\sqrt{s_p} = (891 \pm 2) - i(26 \pm 4)$ MeV and it dimensionless residue $|g| = 5.71 \pm 0.2$.

In summary, we have shown that simple, unconstrained

fits to the existing πK and $\pi\pi \to K\bar{K}$ data fail to satisfy hyperbolic and fixed-t dispersion relations and yield rather unreliable $\kappa/K_0^*(700)$ pole determinations. However, we have obtained fits to data constrained to satisfy those two hyperbolic dispersion relations, together with other Forward or fixed-t dispersion relations. These constrained fits provide a rigorous, precise and robust determination of its associate pole parameters. We think these results should provide the needed confirmation that, according to the Review of Particle Physics and the hadronic community, was needed to establish firmly the existence and properties of the $\kappa/K_0^*(700)$.

TABLE I. Poles and residues of the $\kappa/K_0^*(700)$. The last line is our final result.

	$\sqrt{s_{pole}}$ (MeV)	$\lvert g\rvert(GeV)$
$K_0^*(700)$ [22]	$(658 \pm 13) - i(278.5 \pm 12.0)$	—
$K_0^*(700)$ [37]	$(670 \pm 18) - i(295 \pm 28)$	4.4±0.4
$K_0^*(700)$	$(674 \pm 13) - i(288 \pm 25)$	3.95±0.22
$K_0^*(700)$ **1-sub**	$(673 \pm 13) - i(285 \pm 29)$	3.96±0.14

Acknowledgments

This project has received funding from the Spanish grant FPA2016-75654-C2-2-P and the European Union's Horizon 2020 research and innovation programme under grant agreement No 824093. AR would also like to acknowledge the financial support of the Universidad Complutense de Madrid through a predoctoral scholarship.

[1] M. Tanabashi *et al.* (Particle Data Group), Phys. Rev. **D98**, 030001 (2018).
[2] M. H. Johnson and E. Teller, Phys. Rev. **98**, 783 (1955).
[3] J. S. Schwinger, Annals Phys. **2**, 407 (1957).
[4] R. L. Jaffe, Phys.Rev. **D15**, 267 (1977).
[5] R. L. Jaffe, *Proceedings, 4th International Workshop on QCD - Theory and Experiment (QCD@Work 2007)*, AIP Conf.Proc. **964**, 1 (2007), [Prog.Theor.Phys.Suppl.168,127(2007)], arXiv:hep-ph/0701038 [hep-ph].
[6] J. R. Pelaez, Phys. Rev. Lett. **92**, 102001 (2004), arXiv:hep-ph/0309292 [hep-ph].
[7] J. R. Pelaez and F. J. Yndurain, Phys. Rev. **D71**, 074016 (2005), arXiv:hep-ph/0411334 [hep-ph].
[8] J. R. Pelaez, Phys. Rept. **658**, 1 (2016), arXiv:1510.00653 [hep-ph].
[9] J. T. Londergan, J. Nebreda, J. R. Peláez, and A. Szczepaniak, Phys.Lett. **B729**, 9 (2014), arXiv:1311.7552 [hep-ph].
[10] J. R. Peláez and A. Rodas, Eur.Phys.J. **C77**, 431 (2017), arXiv:1703.07661 [hep-ph].
[11] J. R. Peláez and A. Rodas, Phys. Rev. **D93**, 074025 (2016), arXiv:1602.08404 [hep-ph].
[12] B. Ananthanarayan, G. Colangelo, J. Gasser, and H. Leutwyler, Phys.Rept. **353**, 207 (2001), arXiv:hep-ph/0005297 [hep-ph].
[13] G. Colangelo, J. Gasser, and H. Leutwyler, Phys. Lett. **B488**, 261 (2000), arXiv:hep-ph/0007112 [hep-ph].
[14] R. Kaminski, L. Lesniak, and B. Loiseau, Phys. Lett. **B551**, 241 (2003), arXiv:hep-ph/0210334 [hep-ph].
[15] R. García-Martín, R. Kamiński, J. R. Peláez, J. Ruiz de Elvira, and F. J. Ynduráin, Phys.Rev. **D83**, 074004 (2011), arXiv:1102.2183 [hep-ph].
[16] R. García-Martín, R. Kaminski, J. R. Peláez, and J. Ruiz de Elvira, Phys.Rev.Lett. **107**, 072001 (2011), arXiv:1107.1635 [hep-ph].
[17] C. Ditsche, M. Hoferichter, B. Kubis, and U. G. Meissner, JHEP **06**, 043 (2012), arXiv:1203.4758 [hep-ph].
[18] M. Hoferichter, J. Ruiz de Elvira, B. Kubis, and U.-G. Meißner, Phys. Rept. **625**, 1 (2016), arXiv:1510.06039 [hep-ph].
[19] M. Hoferichter, D. R. Phillips, and C. Schat, Eur. Phys. J. **C71**, 1743 (2011), arXiv:1106.4147 [hep-ph].
[20] B. Ananthanarayan and P. Buettiker, Eur. Phys. J. **C19**, 517 (2001), arXiv:hep-ph/0012023 [hep-ph].
[21] P. Buettiker, S. Descotes-Genon, and B. Moussallam, Eur. Phys. J. **C33**, 409 (2004), arXiv:hep-ph/0310283 [hep-ph].
[22] S. Descotes-Genon and B. Moussallam, Eur. Phys. J. **C48**, 553 (2006), arXiv:hep-ph/0607133 [hep-ph].
[23] J. R. Pelaez and A. Rodas, Eur. Phys. J. **C78**, 897 (2018), arXiv:1807.04543 [hep-ph].
[24] E. van Beveren, T. A. Rijken, K. Metzger, C. Dullemond, G. Rupp, and J. E. Ribeiro, Z. Phys. **C30**, 615 (1986), arXiv:0710.4067 [hep-ph].
[25] J. A. Oller, E. Oset, and J. R. Pelaez, Phys. Rev. Lett. **80**, 3452 (1998), arXiv:hep-ph/9803242 [hep-ph].
[26] J. A. Oller, E. Oset, and J. R. Pelaez, Phys. Rev. **D59**, 074001 (1999), [Erratum: Phys. Rev.D75,099903(2007)], arXiv:hep-ph/9804209 [hep-ph].
[27] D. Black, A. H. Fariborz, F. Sannino, and J. Schechter, Phys. Rev. **D59**, 074026 (1999), arXiv:hep-ph/9808415 [hep-ph].
[28] D. Black, A. H. Fariborz, F. Sannino, and J. Schechter, Phys. Rev. **D58**, 054012 (1998), arXiv:hep-ph/9804273 [hep-ph].
[29] J. A. Oller and E. Oset, *Hadron spectroscopy. Proceedings, Workshop, Frascati, Italy, March 8-12, 1999*, Phys.Rev. **D60**, 074023 (1999), arXiv:hep-ph/9809337 [hep-ph].
[30] F. E. Close and N. A. Tornqvist, J. Phys. **G28**, R249 (2002), arXiv:hep-ph/0204205 [hep-ph].
[31] J. R. Pelaez, Mod. Phys. Lett. **A19**, 2879 (2004), arXiv:hep-ph/0411107 [hep-ph].
[32] S. N. Cherry and M. R. Pennington, Nucl. Phys. **A688**, 823 (2001), arXiv:hep-ph/0005208 [hep-ph].
[33] Z. Y. Zhou and H. Q. Zheng, Nucl. Phys. **A775**, 212 (2006), arXiv:hep-ph/0603062 [hep-ph].
[34] M. Tanabashi *et al.* (Particle Data Group), Phys.Rev. **D98**, 030001 (2018).
[35] G. Bonvicini *et al.* (CLEO), Phys. Rev. **D78**, 052001 (2008), arXiv:0802.4214 [hep-ex].
[36] D. V. Bugg, Phys. Lett. **B572**, 1 (2003), [Erratum: Phys. Lett.B595,556(2004)].
[37] J. R. Peláez, A. Rodas, and J. Ruiz de Elvira, Eur. Phys. J. **C77**, 91 (2017), arXiv:1612.07966 [hep-ph].
[38] J. J. Dudek, R. G. Edwards, C. E. Thomas, and D. J. Wilson (Hadron Spectrum), Phys.Rev.Lett. **113**, 182001 (2014), arXiv:1406.4158 [hep-ph].
[39] J. Nebreda and J. R. Pelaez., Phys. Rev. **D81**, 054035

(2010), arXiv:1001.5237 [hep-ph].
[40] D. J. Wilson, R. A. Briceno, J. J. Dudek, R. G. Edwards, and C. E. Thomas, (2019), arXiv:1904.03188 [hep-lat].
[41] P. Estabrooks, R. K. Carnegie, A. D. Martin, W. M. Dunwoodie, T. A. Lasinski, and D. W. G. S. Leith, Nucl. Phys. **B133**, 490 (1978).
[42] D. Aston *et al.*, Nucl. Phys. **B296**, 493 (1988).
[43] J. Peláez and A. Rodas, .

3.2 Production and decay processes

Up to this point in this chapter we have studied how to extract analytically the parameters of both elastic and inelastic resonances from scattering processes. To this end, we have first obtained a dispersive description of the second Riemann sheet, or a suitable sequence of Padé approximants to study the regions where the former method is not applicable.

In this section we will derive two different useful formalisms, the first one will be used to describe overlapping resonances, or multiple channels coupling to each other, whereas the second method will be helpful for unitarizing partial waves. In the last part of this section, the quasi-two-body approximation is presented.

Let us start by describing the situation where two resonances dominate a given partial wave. If the distance between the masses of the resonances is much larger than the width of each one of them, it is suitable to consider the following partial wave description

$$f(s) \simeq \frac{m_1\Gamma_1}{s - m_1^2 - im_1\Gamma_1} + \frac{m_2\Gamma_2}{s - m_2^2 - im_2\Gamma_2}. \tag{3.11}$$

It is worth noticing that every Breit-Wigner fulfills unitarity by construction but the sum does not obey this rule though. If the resonances are close enough a customary approach is given by the following formula

$$f(s) \simeq \frac{m_1\Gamma_1}{s - m_1^2 - im_1\Gamma_1} + \frac{m_2\Gamma_2}{s - m_2^2 - im_2\Gamma_2}\mathrm{e}^{i\phi(s)}, \tag{3.12}$$

where the new term $\mathrm{e}^{i\phi(s)}$ is introduced to fit the interference between the resonances. Unfortunately, simple models are used to describe this unknown function $\phi(s)$, which still produce a violation of unitarity. Even worse, in most modern experiments the cross sections are dominated by several overlapping resonances, decaying to different channels and producing more complicated interference patterns.

The problem of several overlapping resonances was extensively studied in nuclear interactions [186–188], although it can easily be translated into relativistic resonances [189, 190]. In potential theory, the T-matrix describing the transition between an initial (α) and a final (β) two particle state through different intermediate states is

$$T_{\alpha\beta} = g_{\alpha i} S_{ij} g_{j\beta}, \tag{3.13}$$

where, as shown in Fig. 3.3, the propagator of the resonance is given by

$$S_{ij} = (M - i\Gamma/2 - \sqrt{s})^{-1}_{ij}. \tag{3.14}$$

M and Γ are both hermitian matrices, where

$$\Gamma_{ij} = 2\rho(\sqrt{s})_\kappa g_{i\kappa} g_{\kappa j} \tag{3.15}$$

and g_{ij} are the couplings of each resonance to the initial and final states. Due to the hermiticity and time reversal properties the couplings $g_{i\kappa}$ are real and symmetric.

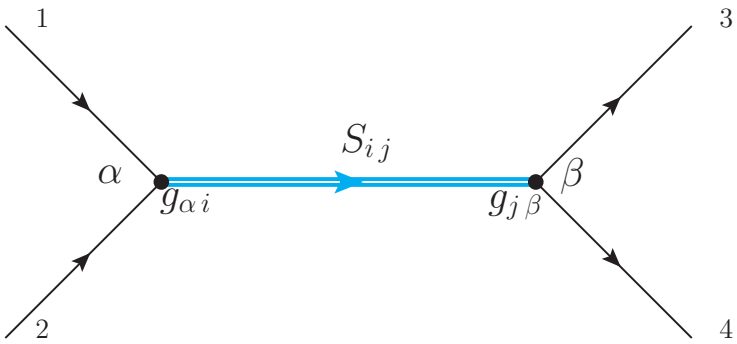

Figure 3.3: Resonance exchange between the initial and final states.

It is always possible to diagonalize the M matrix by means of a unitary matrix

$$m_i\delta_{ij} = U_{ik}M_{kt}U^{-1}_{tj}, \tag{3.16}$$

as a result, the new couplings are

$$g'_{\alpha i} = g_{\alpha k}U^{-1}_{ki}. \tag{3.17}$$

Let us now define a new transition matrix

$$S'_{ij} = S + S'\Sigma S, \tag{3.18}$$

with $S_{ij} = ((m_i - \sqrt{s})\delta_{ij})^{-1}$ and $\Sigma_{ij} = i\rho(\sqrt{s})_\kappa g_{i\kappa}g_{\kappa j}$. This expression can be iterated and in matrix form it reads $S' = S + S\Sigma S + S\Sigma S\Sigma S + ...$ By adopting this matrix form, the final formula for the T matrix after iterating the S' matrix defined above is

$$T = gSg + gS(i\rho(\sqrt{s}))Sg + gS(i\rho(\sqrt{s}))SgS(i\rho(\sqrt{s}))Sg + ..., \tag{3.19}$$

which is nothing but the expansion of

$$T = gSg(1 - i\rho(\sqrt{s})gSg)^{-1}. \tag{3.20}$$

In the case of relativistic scattering $\sqrt{s} \to s$, and by defining the K matrix

$$K_{\alpha\beta} = \sum_i \frac{g_{\alpha i}g_{i\beta}}{m_i^2 - s}, \tag{3.21}$$

the final formula reads

$$T = K(1 - i\rho(s)K)^{-1}. \tag{3.22}$$

Again, due to hermiticity and time reversal invariance K is a real symmetric matrix. The parameters m_i are the "bare masses" of the resonances we would be including in our description, and $g_{\alpha i}$ are the couplings of these resonances to every different channel.

As explained above, the K matrix approach fulfills unitarity by construction, which is not only crucial for interacting resonances, but also when studying coupled channels.

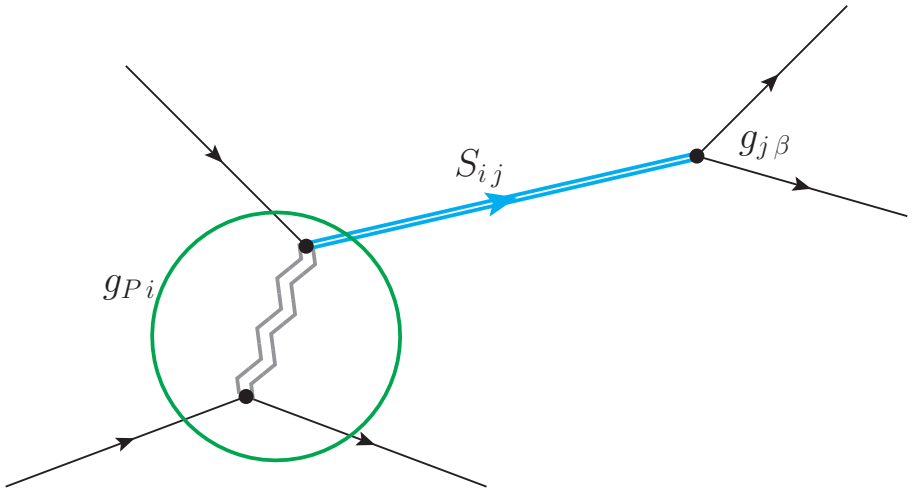

Figure 3.4: Production process dominated by a resonance exchange.

This is the reason why this technique has been gaining weight over the naive, outdated Breit-Wigner approach.

In section 3.3.3 (published in [171]) we will apply this technique to the study of a coupled-channel production process, *i.e.*, instead of having a pure $2 \to 2$ interaction, the initial state has the form depicted in Fig. 3.4. Of course, if this process is dominated by the same resonance exchange, a pole should be found in the very same position, which is actually the case as explained below. We start by defining the amplitude of the production process as

$$F_{P\beta} = g_{Pi} S_{ij} g_{j\beta}, \tag{3.23}$$

and follow the very same derivation explained above. Let us summarize it, by defining a new vector associated to the production

$$P_{\beta P} = \frac{g_{\beta i} g_{iP}}{(m_i^2 - s)}, \tag{3.24}$$

the production amplitude can be described as

$$F = (1 - i\rho(s)K)^{-1} P. \tag{3.25}$$

This formula entails that a production process shares the same analytic structures appearing in scattering and is also dominated by the same resonances.

In practice, the K matrix will be modified to include some background, *i.e.*, it will be added a suitable polynomial to describe the background seen in experiments, without modifying any of its unitarity properties.

In particular, in section 3.3.3 we will detach the lower vertex seen in Fig. 3.4. In such cases, unitary tells us that the imaginary part of that process is equal to the sum over all possible intermediate states (Fig. 3.5), that is, the sum over all possible rescattering effects. In spite of the difference between the diagrams, they share the same denominator producing again the same analytic structures from scattering.

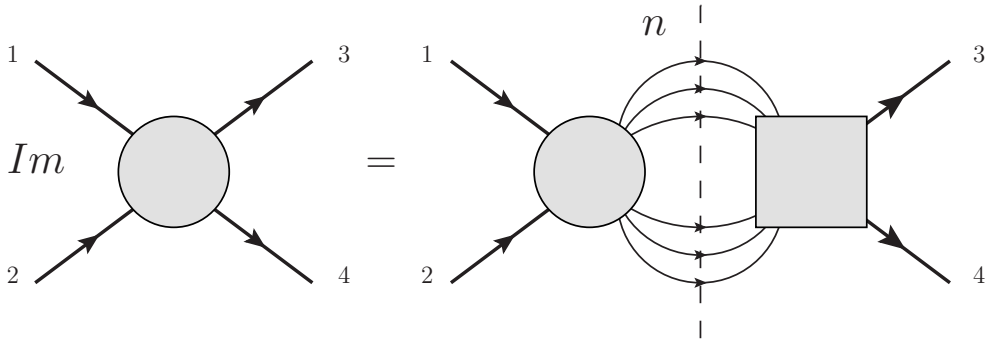

Figure 3.5: Unitarity relation in a production process (circle). The imaginary part of the amplitude is related to the sum over the possible intermediate scattering processes (square).

Another related formalism, which we will also implement on top of the former, is the N/D method, used in section 3.3.3. Therefore, we introduce a brief derivation of the method as done in [68, 191].

The analytic structure for partial waves was introduced in section 1.3.2. It is worth remembering that a partial wave will have a right hand cut produced by unitary in the s-channel, a left hand cut produced by crossed interactions, and a circular cut produced by the projection itself, where the later is a mere kinematical cut. In order to decibel this structures we first define

$$t_\ell^I(s) = \frac{N_\ell^I(s)}{D_\ell^I(s)}, \tag{3.26}$$

where $D_\ell^I(s)$ is built so that it only contains the right hand cut of the s-channel, whereas $N_\ell^I(s)$ contains the other cuts. The unitarity relations for the partial wave translates into the following set of coupled equations

$$\begin{aligned} \text{Im}\, D_\ell^I(s) &= -\sigma(s) N_\ell^I(s), & s > s_{th} \\ \text{Im}\, N_\ell^I(s) &= \text{Im}\, f_\ell^I(s) D_\ell^I(s), & s < s_L, \end{aligned} \tag{3.27}$$

where s_L denotes the branch point of the left hand cut, and both imaginary parts vanish in the rest of the real axis.

Taking into account the relations above, a dispersion relation for the numerator can be written

$$\begin{aligned} D_\ell^I(s) &= \sum_{k=0}^{N-1} c_k s^k - \frac{(s-s_0)^N}{\pi} \int_{s_{th}}^{\infty} \frac{\sigma(s) N_\ell^I(s')}{(s'-s)(s'-s_0)^N} ds', \\ N_\ell^I(s) &= \sum_{k=\ell}^{N-1} d_k s^k + \frac{(s-s_0)^N}{\pi} \int_{s_{th}}^{\infty} \frac{\text{Im}\, f_\ell^I(s') D_\ell^I(s')}{(s'-s)(s'-s_0)^N} ds', \end{aligned} \tag{3.28}$$

where N is the number of subtractions that ensures the asymptotic behavior $N_\ell^I(s)/s^N \to 0$. These equations define the N/D problem and must be solved iteratively in order to

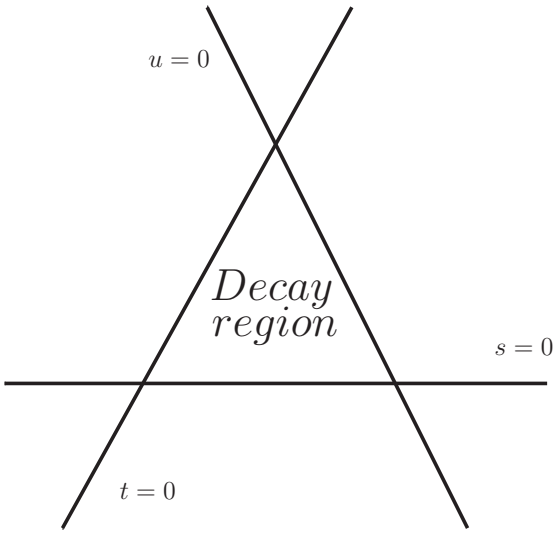

Figure 3.6: Physical region for the decay process.

respect unitarity. The inputs needed are the subtraction constants, which can be fixed from the low-energy behavior and the left-hand cut of $f_\ell^I(s)$. Most approaches, however, neglect the left-hand cut as a first approximation, solving the system of equations from a starting set of values controlled by the low-energy expansion of the partial wave. Zeros may appear in the function $f_\ell^I(s)$, in order to fulfill this requirement a given set of poles, called Castillejo-Dalitz-Dyson poles, can be explicitly included in the denominator

$$D_\ell^I(s) = \sum_{k=0}^{N-1} c_k s^k - \frac{(s-s_0)^N}{\pi} \int_{s_{th}}^{\infty} \frac{\sigma(s) N_\ell^I(s')}{(s'-s)(s'-s_0)^N} ds' + \sum_k \frac{\gamma}{s - s_k}. \tag{3.29}$$

The relevant part of this equation for our purposes relies on the denominator, as the numerator will be substituted by a smooth production function as explained in the derivation of Eq. (3.25).

Finally, we will also make use of several dispersive and unitary techniques in section 3.4.3 (published in [192]). First, let us briefly introduce the description of a massive particle decaying to lighter ones. As seen in Fig. 3.6, the region corresponding to the physical decay process lies within the Mandelstam triangle, which entails that the amplitude of a decay process can be obtained from scattering amplitudes by means of crossing and analyticity as we previously studied in section 1.3.

In the simple case of a two-body decay, considering that the initial particle has a mass M and decays to two particles with different masses we have

$$\begin{aligned} E_1 &= \frac{M^2 - m_2^2 + m_1^2}{2M}, \\ |p_1| = |p_2| &= \frac{\left[\left(M^2 - (m_1+m_2)^2\right)\left(M^2 - (m_1-m_2)^2\right)\right]^{1/2}}{2M}. \end{aligned} \tag{3.30}$$

Additionally, decay processes are customarily described in terms of the invariant amplitude $\mathcal{M}$, which obeys

$$S = 1 + i2\pi\mathcal{M}. \tag{3.31}$$

Therefore it represents the equivalent to the interaction matrix for scattering processes. If one takes into account that $\mathcal{M}$ provides the probability of the particle to decay, the differential width can be calculated as

$$d\Gamma = \frac{1}{32\pi^2}|\mathcal{M}|^2\frac{|p_1|}{M^2}d\Omega_1, \tag{3.32}$$

where $d\Omega$ is the differential solid angle of particle 1. If it is a three particle decay instead, the differential lifetime reads

$$d\Gamma = \frac{1}{(2\pi)^5}\frac{1}{16M^2}|\mathcal{M}|^2\,|p_1^*|\,|p_3|\,dm_{12}d\Omega_1^*d\Omega_3, \tag{3.33}$$

where $|p_1^*|$ is the momentum of particle 1 in the rest frame of 1 and 2, whereas ω_3 is the angle of particle 3 in the rest frame of M. Therefore, both momenta are given by

$$|p_1^*| = \frac{\left[\left(m_{12}^2 - (m_1+m_2)^2\right)\left(m_{12}^2 - (m_1-m_2)^2\right)\right]^{1/2}}{2m_{12}}, \tag{3.34}$$

and

$$|p_3| = \frac{\left[\left(M^2 - (m_{12}+m_3)^2\right)\left(M^2 - (m_{12}-m_3)^2\right)\right]^{1/2}}{2M}. \tag{3.35}$$

In section 3.4.3, however, the $a_1(1260)$ decays to three pions through the process

$$\tau \to \pi^-\pi^+\pi^-\nu_\tau, \tag{3.36}$$

which produces a four-body phase space as the final integration variable. Fortunately, the strong decay process $a_1(1260) \to 3\pi$ can be factorized out from the rest of the reaction and thus we will pay particular attention to how to simplify and describe and analytic, unitary process within a simple approximation.

Even though general 3-body formalisms do exist in the literature [109, 111, 193–206], we will restrict ourselves to a quasi-two body approximation, for simplicity. We first start by disregarding the $\pi^-\pi^-$ interaction in favor of the $\pi^-\pi^+$ one; while the former is a repulsive smooth interaction, the later is a strongly interacting system, particularly for the $I = \ell = 1$ quantum numbers, which correspond to the $\rho(770)$ resonance exchange. This system with angular momentum 1 could in principle interact with the final π^-, considered a bachelor, to produce the spin 1 $a_1(1260)$, and thus we will focus on the study of the $\rho\pi$ system instead.

This system, described by an amplitude $t(s)$, will now govern the unitarity relation of the whole decay $a(s)$. Hence, $a(s)$ can be recast in term of $t(s)$. It is worth noticing,

however, that the ρ resonance is not stable and thus a customary line shape with a dynamical width [207] will be used

$$f_\rho(s) = \mathcal{N}\frac{F_1(p(s)R)}{m_\rho^2 - s - im_\rho\Gamma_\rho(s)}, \qquad F_1^2(pR) = \frac{(pR)^2}{1+(pR)^2},$$
$$\Gamma_\rho(s) = \Gamma_\rho\frac{p(s)}{p\left(m_\rho^2\right)}\frac{m_\rho}{\sqrt{s}}\frac{F_1^2(p(s)R)}{F_1^2\left(p\left(m_\rho^2\right)R\right)}, \tag{3.37}$$

where F_1 is the customary Blatt-Weiskopf barrier factor [208] and $p(s) = \sqrt{s-4m_\pi^2}/2$ is the two-pion momentum in their center of mass.

Now, in order to get the most general answer, the amplitude of the decay process A must be symmetrized due to Bose symmetry

$$A = A^{(1)} + A^{(3)}, \tag{3.38}$$

where $A^{(i)}$ means that the π^- pion at position i has been considered the bachelor particle. Finally, by implementing all these features, together with some algebraic manipulations, one can obtain a two-body phase space as in Eq. (12a) of section 3.4.3.

Finally, a dispersive formalism will also be adopted, which is similar to the one of section 3.3.3. Let us summarize our approach, as defined earlier in this section. The formula for the K-matrix contains and imaginary part $i\rho(s)$, which appears as a direct implementation of the simple Breit-Wigner formulas it is derived from. However, if one wants to include a more precise, dispersive formula, the dispersion relation over the right-hand cut must be included, which opens at threshold, produced by the discontinuity the phase-space contains above and below the real axis. Thus, a dispersive phase space is achieved by defining

$$i\rho'(s) = \rho_0 + \frac{s}{\pi}\int_{s_{th}}^{\infty} \mathrm{d}s' \frac{\rho\left(s'\right)}{s'\left(s'-s-i\epsilon\right)}, \tag{3.39}$$

where the subtraction constant can be fixed by a suitable choice. This equation is the so-called Chew-Mandelstam phase space [209,210], which no longer contains non-desired left-hand cuts, nor does it have any singularities.

A straightforward improvement over this simplification would be to study the three-body unitarity relation through Khuri-Treimann equations [204, 211, 212]. However, although there exist several contributions to the case of spinless particles [108,110,213–215], a general formulation for particles with spin is yet unknown.

3.3 Determination of the lightest hybrid meson

3.3.1 Motivation

As explained in section 1.1.1, determining the structure of hadrons in terms of quark and gluons is of key importance to our understanding of the underlying strong interactions. Up to now, most of the studied mesons in this thesis fit within the $q\bar{q}$ picture, nonetheless, QCD has in principle a much richer spectrum. Actually, there is a growing interest in the study of mesonic resonances with exotic quantum numbers, *i.e.*, those with non-$q\bar{q}$ quantum numbers. During the last few years more and more theoretical analyses have been performed about these states [26–30], most of them in the heavy quark sector. In this next sections we focus our attention on the mesons with explicit gluonic degrees of freedom, *aka* hybrids. Whose experimental evidence have been reported by several collaborations [216, 217] and were also predicted by several different models long ago [218–223]. Since gluons are the mediators of strong interactions, QCD cannot be fully understood without addressing their role in binding hadrons.

The Review of Particle Physics [134] reports two different hybrids with the quantum numbers $J^{PC}(I^G) = 1^{-+}(1^-)$, a lighter one called $\pi_1(1400)$ whose main decay is $\eta\pi$, and a second $\pi_1(1600)$ decaying mostly to both $\eta'\pi$ and $\rho\pi$. However, this picture is not satisfactory from the phenomenological [224–228], theoretical [218–222] and Lattice QCD [229–231] points of view, where only one hybrid meson with these quantum numbers is expected. Moreover, in the $SU(3)$ limit a hybrid could not decay to $\eta\pi$ [232], and although one could try to fit the lighter state inside a tetraquark model prediction, it is heavily disfavored [233, 234].

The experimental determination of hybrid mesons is challenging, since most of the measured final states are dominated by non-exotic resonances. The determination of such quantum numbers rely on more sophisticated amplitude analyses. Unfortunately, simple model assumptions, limited statistics, and naive approximations produced non reliable results. These are the reason why there are several experiments devoted to the analysis of exotic spectroscopy, like COMPASS [235, 236], CLAS12 and GlueX [237, 238].

In particular, only one coupled channel analysis for the $\eta^{(\prime)}\pi$ system from E852 has been performed [239], and although the description of the data is satisfactory the analysis was not conclusive. Hence, the interest in a new analysis using the recent COMPASS data [136] is threefold: First we can analyze the $\eta^{(\prime)}\pi$ system as a coupled channel, indicating if there are two different resonances or just one decaying to different channels. Second, the statistics of this analysis are unmatched, which would produce a trustworthy result, and third, due to the kinematics, in particular the high energetic pion beam from COMPASS, the analysis is way easier than most production processes.

3.3.2 Outline of the main results

- We implement an analytic method for the study of production processes, which is applied for the first time for the coupled $\eta^{(\prime)}\pi$ system.
- The most recent and precise data on these channels, coming from the COMPASS collaboration [240] are fitted, including up to tensor partial waves, reaching an overall $\chi^2/d.o.f. \sim 1.3$.
- We test two different possibilities; the first one is the PDG scenario, where we have two different exotic mesons decaying to these two channels separately. In the second one we describe the whole coupled-channel system with just one exotic resonance.
- The solution with only one hybrid meson describes remarkably well the COMPASS collaboration data, in particular, it does explain the two different peaks appearing in these two channels. Therefore we conclude that there is no statistical evidence for a second resonance. Furthermore, when a second K-matrix pole is included in the fit, the result becomes unstable, and the parameters of this second state strongly depends on the starting point of the fit. In addition its coupling to the partial waves is almost negligible.
- We conclude that there is evidence of one hybrid meson in this energy region, reconciling theoretical and Lattice QCD predictions with the phenomenological analyses and disfavoring the PDG scenario.

3.3.3 Publication: *Determination of the Pole Position of the Lightest Hybrid Meson Candidate*

Determination of the Pole Position of the Lightest Hybrid Meson Candidate

A. Rodas,[1,*] A. Pilloni,[2,3,†] M. Albaladejo,[2,4] C. Fernández-Ramírez,[5] A. Jackura,[6,7] V. Mathieu,[2] M. Mikhasenko,[8] J. Nys,[9] V. Pauk,[10] B. Ketzer,[8] and A. P. Szczepaniak[2,6,7]

(Joint Physics Analysis Center)

[1]*Departamento de Física Teórica, Universidad Complutense de Madrid, E-28040 Madrid, Spain*
[2]*Theory Center, Thomas Jefferson National Accelerator Facility, Newport News, VA 23606, USA*
[3]*European Centre for Theoretical Studies in Nuclear Physics and Related Areas (ECT*) and Fondazione Bruno Kessler, I-38123 Villazzano (TN), Italy*
[4]*Departamento de Física, Universidad de Murcia, E-30071 Murcia, Spain*
[5]*Instituto de Ciencias Nucleares, Universidad Nacional Autónoma de México, Ciudad de México 04510, Mexico*
[6]*Center for Exploration of Energy and Matter, Indiana University, Bloomington, IN 47403, USA*
[7]*Physics Department, Indiana University, Bloomington, IN 47405, USA*
[8]*Universität Bonn, Helmholtz-Institut für Strahlen- und Kernphysik, 53115 Bonn, Germany*
[9]*Department of Physics and Astronomy, Ghent University, Ghent 9000, Belgium*
[10]*Institut für Kernphysik & PRISMA Cluster of Excellence, Johannes Gutenberg Universität, D-55099 Mainz, Germany*

(Received 13 October 2018; revised manuscript received 19 November 2018; published 29 January 2019)

Mapping states with explicit gluonic degrees of freedom in the light sector is a challenge, and has led to controversies in the past. In particular, the experiments have reported two different hybrid candidates with spin-exotic signature, $\pi_1(1400)$ and $\pi_1(1600)$, which couple separately to $\eta\pi$ and $\eta'\pi$. This picture is not compatible with recent Lattice QCD estimates for hybrid states, nor with most phenomenological models. We consider the recent partial wave analysis of the $\eta^{(\prime)}\pi$ system by the COMPASS Collaboration. We fit the extracted intensities and phases with a coupled-channel amplitude that enforces the unitarity and analyticity of the S matrix. We provide a robust extraction of a single exotic π_1 resonant pole, with mass and width $1564 \pm 24 \pm 86$ and $492 \pm 54 \pm 102$ MeV, which couples to both $\eta^{(\prime)}\pi$ channels. We find no evidence for a second exotic state. We also provide the resonance parameters of the $a_2(1320)$ and $a_2'(1700)$.

DOI: 10.1103/PhysRevLett.122.042002

Introduction.—Explaining the structure of hadrons in terms of quarks and gluons, the fundamental building blocks of quantum chromodynamics (QCD), is of key importance to our understanding of strong interactions. The vast majority of observed mesons can be classified as $q\bar{q}$ bound states, although QCD should have, in principle, a much richer spectrum. Indeed, several experiments have reported resonance candidates that do not fit the valence quark model template [1,2], mainly in the heavy sector [3–7]. These new experimental results, together with rapid advances in lattice gauge computations, open new fronts in studies of the fundamental aspects of QCD, such as quark confinement and mass generation. Since gluons are the mediators of the strong interaction, QCD dynamics cannot be fully understood without addressing the role of gluons in binding hadrons. The existence of states with explicit excitations of the gluon field, commonly referred to as *hybrids*, was postulated a long time ago [8–12], and has recently been supported by lattice [13–15] and phenomenological QCD studies [16–19]. In particular, a state with exotic quantum numbers $J^{PC}(I^G) = 1^{-+}(1^-)$ in the mass range 1.7–1.9 GeV is generally expected. The experimental determination of hybrid hadron properties—e.g., their masses, widths, and decay patterns—provides a unique opportunity for a systematic study of low-energy gluon dynamics. This has motivated the COMPASS spectroscopy program [20,21] and the 12 GeV upgrade of Jefferson Lab, with experiments dedicated to hybrid photoproduction at CLAS12 and GlueX [22,23].

The hunt for hybrid mesons is challenging, since the spectrum of particles produced in high energy collisions is dominated by nonexotic resonances. The extraction of exotic signatures requires sophisticated partial-wave amplitude analyses. In the past, inadequate model assumptions and limited statistics resulted in debatable results. The first

reported hybrid candidate was the $\pi_1(1400)$ in the $\eta\pi$ final state [24–28]. Another state, the $\pi_1(1600)$, was later claimed in the $\rho\pi$ and $\eta'\pi$ channels, with different resonance parameters [29,30]. The COMPASS experiment confirmed a peak in $\rho\pi$ and $\eta'\pi$ at around 1.6 GeV [31,32] and an additional structure in $\eta\pi$, at approximately 1.4 GeV [33]. A theoretical approach based on a unitarized $U(1)$-extended chiral Lagrangian predicted a π_1 state with mass of about 1400 MeV decaying mostly into $\eta'\pi$ [34]. A phenomenological unitary coupled-channel analysis of the $\eta^{(\prime)}\pi$ system from E852 data was instead not conclusive [35]. While the $\pi_1(1600)$ is close to the expectation for a hybrid, the observation of two nearby 1^{-+} hybrids below 2 GeV is surprising. This makes the microscopic interpretation of the $\pi_1(1400)$ problematic. Moreover, in the $SU(3)$ limit, Bose symmetry prevents the decay of a hybrid into $\eta\pi$ [36]. A tetraquark interpretation of the lighter state might be viable, and would explain why this state has eluded predictions in constituent gluon models. However, this interpretation would lead to the prediction of unobserved doubly charged and doubly strange mesons [37], and is unfavored in the diquark-antidiquark model [38,39]. Establishing whether there exists one or two exotic states in this mass region is thus a stringent test for the available phenomenological frameworks in the nonperturbative regime.

In Ref. [40] we analyzed the spectrum of the $\eta\pi$ D-wave extracted from the COMPASS data. In this Letter, we extend the mass dependent study to the exotic P wave, and present results of the first coupled-channel analysis of the $\eta^{(\prime)}\pi$ COMPASS data. We establish that a single exotic π_1 is needed and provide a detailed analysis of its properties. We also determine the resonance parameters of the nonexotic $a_2(1320)$ and $a_2'(1700)$.

Description of the data.—We use the mass independent analysis by COMPASS of $\pi p \to \eta^{(\prime)}\pi p$, with a 190 GeV pion beam [33]. We focus on the P- and D-wave intensities and their relative phase, in both channels. The published data are integrated over the range of transferred momentum squared $-t_1 \in [0.1, 1]$ GeV^2. However, given the diffractive nature of the reaction, most of the events are produced in the forward direction, near the lower limit in $-t_1$. The $\eta^{(\prime)}\pi$ partial-wave intensities and phase differences are given in 40 MeV mass bins, from threshold up to 3 GeV. Intensities are normalized to the number of observed events corrected by the detector acceptance. The errors quoted are statistical only; systematic uncertainties or correlations in the extraction of the partial waves were found to be negligible [41]. We thus assume that all data points are independent and normally distributed. As seen in Figs. 4(a) and 5(a) of Ref. [33], at the $\eta'\pi$ mass of 2.04 GeV there is a sharp falloff in the P-wave intensity, and a sudden change by 50° in the phase difference between the P and D wave. This behavior might be attributed to another state. The E852 experiment claimed indeed a third exotic $\pi_1(2015)$ in the $f_1(1285)\pi$ and $\omega\pi\pi$ channels [42,43]. However, this state is too broad to explain such an abrupt behavior and thus it is difficult to find a compelling explanation. Unfortunately, it is not possible to crosscheck this behavior with the $\eta\pi$ relative phase due to lack of data in the 1.8–2.0 GeV region. Moreover, fitting these features of the P wave drives the position of the a_2' to unphysical values. For these reasons, we fit data up to 2 GeV only.

Enforcing unitarity allows us to properly implement the interference among the various resonances and the background. In principle, one wishes to include all the kinematically allowed channels in a unitary analysis. Recently, COMPASS published the complete 3π partial-wave analysis [32], including the exotic 1^{-+} wave in the $\rho\pi$ final state. However, the extraction of the resonance pole in this channel is hindered by the irreducible Deck process [44], which refers to the exchange of a pion between the final state ρ and π (cf. Fig. 8 in Ref. [32]). This generates a peaking background in the exotic partial wave [45,46]. Since the Deck mechanism is not fully accounted for in the COMPASS amplitude model, we do not include the 3π data in our analysis. As discussed in Ref. [40], neglecting additional channels does not affect the pole position, as long as the resonance poles are far away from threshold, which is the case studied here.

Reaction model.—At high energies, peripheral production of $\pi p \to \eta^{(\prime)}\pi p$ is dominated by Pomeron ($\mathbb{P}$) exchange. The notion of Pomeron exchange emerges from Regge theory [47,48], and allows us to factorize the $\pi\mathbb{P} \to \eta^{(\prime)}\pi$ process. For fixed t_1 the latter resembles an ordinary helicity partial wave amplitude $a_i^J(s)$, with $i = \eta^{(\prime)}\pi$ the final channel index, J the angular momentum of the $\eta^{(\prime)}\pi$ system, and s its invariant mass squared. This amplitude, in principle, also depends on the effective spin and helicity of the Pomeron. However, the approximately constant hadron cross section at high energies implies that the effective spin of the Pomeron is near 1, which explains dominance of the partial wave components with angular momentum projection $M = \pm 1$ as seen in data [33,49,50]. Since the two are related by parity, we drop reference to the Pomeron quantum numbers (for more details, see Ref. [40]). As discussed previously, we fix an effective value $t_{\text{eff}} = -0.1$ GeV^2.

We parametrize the amplitudes following the coupled-channel N/D formalism [51],

$$a_i^J(s) = q^{J-1} p_i^J \sum_k n_k^J(s) [D^J(s)^{-1}]_{ki}, \tag{1}$$

where p_i is the $\eta^{(\prime)}\pi$ breakup momentum, and q the π beam momentum in the $\eta^{(\prime)}\pi$ rest frame. (One unit of incoming momentum q is divided out because of the Pomeron-nucleon vertex [40]). The $n_k^J(s)$'s incorporate exchange "forces" in the production process and are smooth

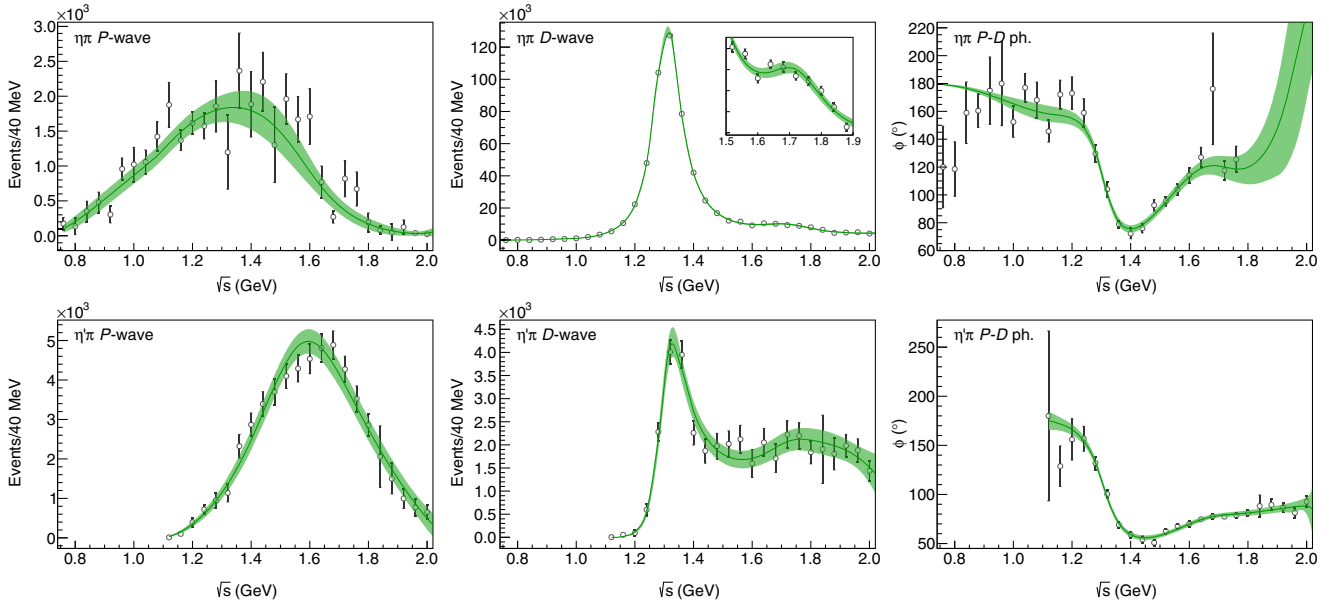

FIG. 1. Fits to the $\eta\pi$ (upper line) and $\eta'\pi$ (lower line) data from COMPASS [33]. The intensities of the P (left), D wave (center), and their relative phase (right) are shown. The inset zooms into the region of the $a_2'(1700)$. The solid line and green band show the result of the fit and the 2σ confidence level provided by the bootstrap analysis, respectively. The initialization of the fit is chosen by randomly generating $O(10^5)$ different sets of values for the parameters. The best fit has $\chi^2/\mathrm{dof} = 162/122 = 1.3$. The errors shown are statistical only.

functions of s in the physical region. The $D^J(s)$ matrix represents the $\eta^{(\prime)}\pi \to \eta^{(\prime)}\pi$ final state interactions, and contains cuts on the real axis above thresholds (right-hand cuts), which are constrained by unitarity.

For the numerator $n_k^J(s)$, we use an effective expansion in Chebyshev polynomials. A customary parametrization of the denominator is given by [52]

$$D_{ki}^J(s) = [K^J(s)^{-1}]_{ki} - \frac{s}{\pi}\int_{s_k}^{\infty} ds' \frac{\rho N_{ki}^J(s')}{s'(s'-s-i\epsilon)}, \qquad (2)$$

where s_k is the threshold in channel k and

$$\rho N_{ki}^J(s') = \delta_{ki}\frac{\lambda^{J+1/2}(s', m_{\eta^{(\prime)}}^2, m_\pi^2)}{(s'+s_L)^{2J+1+\alpha}} \qquad (3)$$

is an effective description of the left-hand singularities in the $\eta^{(\prime)}\pi \to \eta^{(\prime)}\pi$ scattering, which is controlled by the s_L parameter fixed at the hadronic scale $\simeq 1\ \mathrm{GeV}^2$. Finally,

$$K_{ki}^J(s) = \sum_R \frac{g_k^{J,R} g_i^{J,R}}{m_R^2 - s} + c_{ki}^J + d_{ki}^J s, \qquad (4)$$

with $c_{ki}^J = c_{ik}^J$ and $d_{ki}^J = d_{ik}^J$, is a standard parametrization for the K matrix. In our reference model, we consider two K-matrix poles in the D wave, and one single K-matrix pole in the P wave; the numerator of each channel and wave is described by a third-order polynomial. We set $\alpha = 2$ in Eq. (3), which has been effective in describing the single-channel case [40]. The remaining 37 parameters are fitted to data, by performing a χ^2 minimization with MINUIT [53]. As shown in Fig. 1, the result of the best fit is in good agreement with data. In particular, a single K-matrix pole is able to correctly describe the P-wave peaks in the two channels, which are separated by 200 MeV. The shift of the peak in the $\eta\pi$ spectrum to lower energies originates from the combination between final state interactions and the production process. The uncertainties on the parameters are estimated via the bootstrap method [54,55]: we generate a large number of pseudo datasets and refit each one of them. The (co)variance of the parameters provides an estimate of their statistical uncertainties and correlations. The values of the fitted parameters and their covariance matrix are provided in the Supplemental Material [56]. The average curve passes the Gaussian test in Ref. [57].

Once the parameters are determined, the amplitudes can be analytically continued to complex values of s. The $D^J(s)$ matrix in Eq. (2) can be continued underneath the unitarity cut into the closest unphysical Riemann sheet. A pole s_P in the amplitude appears when the determinant of $D^J(s_P)$ vanishes. Poles close to the real axis influence the physical region and can be identified as resonances, whereas further singularities are likely to be artifacts of the specific model with no direct physical interpretation. For any practical parametrization, especially in a coupled-channel problem, it is not possible to specify *a priori* the number of poles. Appearance of spurious poles far from

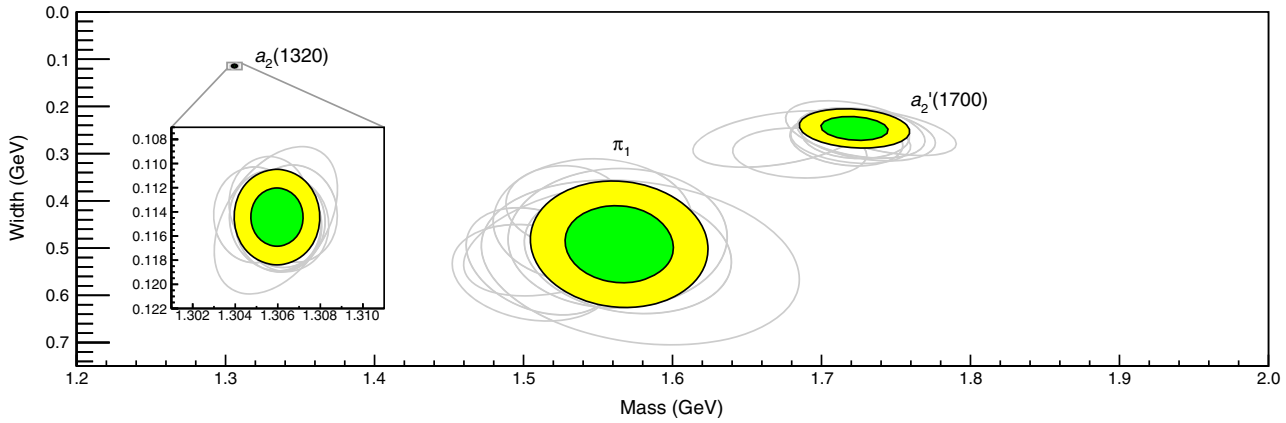

FIG. 2. Positions of the poles identified as the $a_2(1320)$, π_1, and $a_2'(1700)$. The inset shows the position of the $a_2(1320)$. The green and yellow ellipses show the 1σ and 2σ confidence levels, respectively. The gray ellipses in the background show, within 2σ, variation of the pole position upon changing the functional form and the parameters of the model, as discussed in the text.

the physical region is thus unavoidable. It is, however, possible to isolate the physical poles by testing their stability against different parametrizations and data resampling. We select the resonance poles in the $m \in [1, 2]$ and $\Gamma \in [0, 1]$ GeV region, where customarily $m = \mathrm{Re}\sqrt{s_P}$ and $\Gamma = -2\mathrm{Im}\sqrt{s_P}$. We find two poles in the D wave, identified as the $a_2(1320)$ and $a_2'(1700)$, and a single pole in the P wave, which we call π_1. The pole positions are shown in Fig. 2, and the resonance parameters in Table I. To estimate the statistical significance of the π_1 pole, we perform fits using a pure background model for the P wave, i.e., setting $g^{P,1}_{\eta^{(\prime)}\pi} = 0$ in Eq. (4). The best solution having no poles in our reference region has a χ^2 almost 50 times larger, which rejects the possibility for the P-wave peaks to be generated by nonresonant production. We also considered solutions having two isolated P-wave poles in the reference region, which would correspond to the scenario discussed in the PDG [58]. The χ^2 for this case is equivalent to the single pole solution. One of the poles is compatible with the previous determination, while the second is unstable; i.e., it can appear in a large region of the s plane depending on the initial values of the fit parameters. Moreover, the behavior of the $\eta\pi$ phase required by the fit is rather peculiar. A 180° jump (due to a zero in the amplitude) appears above 1.8 GeV, where no data exist. We conclude there is no evidence for a second pole.

TABLE I. Resonance parameters. The first error is statistical, the second systematic.

Poles	Mass (MeV)	Width (MeV)
$a_2(1320)$	$1306.0 \pm 0.8 \pm 1.3$	$114.4 \pm 1.6 \pm 0.0$
$a_2'(1700)$	$1722 \pm 15 \pm 67$	$247 \pm 17 \pm 63$
π_1	$1564 \pm 24 \pm 86$	$492 \pm 54 \pm 102$

Systematic uncertainties.—Unlike the COMPASS mass independent fit, the pole extraction carries systematic uncertainties associated with the reaction model. To assess these, we vary the parameters and functional forms which were kept fixed in the previous fits. We can separate these in two categories: (i) variations of the numerator function $n_k^J(s)$ in Eq. (1), which is expected to be smooth in the region of the data, and (ii) variations of the function $\rho N(s')$, which determines the imaginary part of the denominator in Eq. (2). As for the latter, we investigate whether the specific form we chose biases the determination of the poles. Upon variation of the parameters and of the functional forms, the shape of the dispersive integral in Eq. (2) is altered, but the fit quality is unaffected. The pole positions change roughly within 2σ, as one can see in Fig. 2. As for the numerator $n_k^J(s)$, we varied the effective value of t_{eff} and the order of the polynomial expansion. Given the flexibility of the numerator parametrization, these variations effectively absorb the model dependence related to the production mechanism. None of these cause important changes in pole locations. Our final estimate for the uncertainties is reported in Table I, while the detailed summary is given in the Supplemental Material [56].

Conclusions.—We performed the first coupled-channel analysis of the P and D waves in the $\eta^{(\prime)}\pi$ system measured at COMPASS [33]. We used an amplitude parametrization constrained by unitarity and analyticity. We find two poles in the D wave, which we identify as the $a_2(1320)$ and the $a_2'(1700)$, with resonance parameters consistent with the single-channel analysis [40]. In the P wave, we find a single exotic π_1 in the region constrained by data. This determination is compatible with the existence of a single isovector hybrid meson with quantum numbers $J^{PC} = 1^{-+}$, as suggested by lattice QCD [13–15]. Its mass and width are determined to be $1564 \pm 24 \pm 86$ and $492 \pm 54 \pm 102$ MeV, respectively. The statistical uncertainties are estimated via the bootstrap technique, while the

systematics due to model dependence are assessed by varying parameters and functional forms that are not directly constrained by unitarity. We find no evidence for a second pole that could be identified with another π_1 resonance. Solutions with two poles are possible, but do not improve the fit quality and, when present, the position of the second pole is unstable against different starting values of the fit. It is worth noting that the two-pole solutions have a peculiar behavior of the $\eta\pi$ phase in the $\gtrsim 2$ GeV mass region, where no data exist. New data from GlueX and CLAS12 experiments at Jefferson Lab in this and higher mass region will be valuable to test this behavior.

We would like to thank the COMPASS Collaboration for useful comments. A. P. thanks the Mainz Institute for Theoretical Physics (MITP) for its kind hospitality while this work was being completed. This work was supported by the U.S. Department of Energy under Grants No. DE-AC05-06OR23177 and No. DE-FG02-87ER40365, U.S. National Science Foundation under Grant No. PHY-1415459, Ministerio de Ciencia, Innovación y Universidades (Spain) Grants No. FPA2016-75654-C2-2-P and No. FPA2016-77313-P, Universidad Complutense de Madrid predoctoral scholarship program, Research Foundation–Flanders (FWO), PAPIIT-DGAPA (UNAM, Mexico) under Grants No. IA101717 and No. IA101819, CONACYT (Mexico) under Grant No. 251817, the German Bundesministerium für Bildung und Forschung (BMBF), and Deutsche Forschungsgemeinschaft (DFG) through the Collaborative Research Center [The Low-Energy Frontier of the Standard Model (SFB 1044)] and the Cluster of Excellence [Precision Physics, Fundamental Interactions and Structure of Matter (PRISMA)].

*arodas@ucm.es
†pillaus@jlab.org

[1] B. Ketzer, Proc. Sci., QNP2012 (**2012**) 025.
[2] C. A. Meyer and E. S. Swanson, Prog. Part. Nucl. Phys. **82**, 21 (2015).
[3] A. Esposito, A. Pilloni, and A. D. Polosa, Phys. Rep. **668**, 1 (2017).
[4] R. F. Lebed, R. E. Mitchell, and E. S. Swanson, Prog. Part. Nucl. Phys. **93**, 143 (2017).
[5] F.-K. Guo, C. Hanhart, U.-G. Meißner, Q. Wang, Q. Zhao, and B.-S. Zou, Rev. Mod. Phys. **90**, 015004 (2018).
[6] S. L. Olsen, T. Skwarnicki, and D. Zieminska, Rev. Mod. Phys. **90**, 015003 (2018).
[7] M. Karliner, J. L. Rosner, and T. Skwarnicki, Annu. Rev. Nucl. Part. Sci. **68**, 17 (2018).
[8] D. Horn and J. Mandula, Phys. Rev. D **17**, 898 (1978).
[9] N. Isgur and J. E. Paton, Phys. Rev. D **31**, 2910 (1985).
[10] M. S. Chanowitz and S. R. Sharpe, Nucl. Phys. **B222**, 211 (1983); **B228**, 588 (1983).
[11] T. Barnes, F. Close, F. de Viron, and J. Weyers, Nucl. Phys. **B224**, 241 (1983).
[12] F. E. Close and P. R. Page, Nucl. Phys. **B443**, 233 (1995).
[13] P. Lacock, C. Michael, P. Boyle, and P. Rowland (UKQCD Collaboration), Phys. Lett. B **401**, 308 (1997).
[14] C. Bernard, J. E. Hetrick, T. A. DeGrand, M. Wingate, C. DeTar, C. McNeile, S. Gottlieb, U. M. Heller, K. Rummukainen, B. Sugar, and D. Toussaint (MILC Collaboration), Phys. Rev. D **56**, 7039 (1997).
[15] J. J. Dudek, R. G. Edwards, P. Guo, and C. E. Thomas (Hadron Spectrum Collaboration), Phys. Rev. D **88**, 094505 (2013).
[16] A. P. Szczepaniak and E. S. Swanson, Phys. Rev. D **65**, 025012 (2001).
[17] A. P. Szczepaniak and P. Krupinski, Phys. Rev. D **73**, 116002 (2006).
[18] P. Guo, A. P. Szczepaniak, G. Galata, A. Vassallo, and E. Santopinto, Phys. Rev. D **78**, 056003 (2008).
[19] S. D. Bass and P. Moskal, arXiv:1810.12290.
[20] G. Baum *et al.* (COMPASS Collaboration), http://cds.cern.ch/record/298433 (1996).
[21] P. Abbon *et al.* (COMPASS Collaboration), Nucl. Instrum. Methods Phys. Res., Sect. A **779**, 69 (2015).
[22] A. Rizzo (CLAS Collaboration), J. Phys. Conf. Ser. **689**, 012022 (2016).
[23] S. Dobbs (GlueX Collaboration), *Proc. Sci.*, Hadron2017 (2018) 047.
[24] D. R. Thompson *et al.* (E852 Collaboration), Phys. Rev. Lett. **79**, 1630 (1997).
[25] S. U. Chung *et al.* (E852 Collaboration), Phys. Rev. D **60**, 092001 (1999).
[26] G. S. Adams *et al.* (E852 Collaboration), Phys. Lett. B **657**, 27 (2007).
[27] A. Abele *et al.* (Crystal Barrel Collaboration), Phys. Lett. B **423**, 175 (1998).
[28] A. Abele *et al.* (Crystal Barrel Collaboration), Phys. Lett. B **446**, 349 (1999).
[29] E. I. Ivanov *et al.* (E852 Collaboration), Phys. Rev. Lett. **86**, 3977 (2001).
[30] Yu. A. Khokhlov (VES Collaboration), Nucl. Phys. **A663–A664**, 596c (2000); Particles and nuclei, in *Proceedings of the 15th International Conference, PANIC '99, Uppsala, Sweden, 1999*.
[31] M. Alekseev *et al.* (COMPASS Collaboration), Phys. Rev. Lett. **104**, 241803 (2010).
[32] R. Akhunzyanov *et al.* (COMPASS Collaboration), Phys. Rev. D **98**, 092003 (2018).
[33] C. Adolph *et al.* (COMPASS Collaboration), Phys. Lett. B **740**, 303 (2015).
[34] S. D. Bass and E. Marco, Phys. Rev. D **65**, 057503 (2002).
[35] A. P. Szczepaniak, M. Swat, A. R. Dzierba, and S. Teige, Phys. Rev. Lett. **91**, 092002 (2003).
[36] F. E. Close and H. J. Lipkin, Phys. Lett. B **196**, 245 (1987).
[37] S. U. Chung, E. Klempt, and J. G. Korner, Eur. Phys. J. A **15**, 539 (2002).
[38] R. L. Jaffe and F. Wilczek, Phys. Rev. Lett. **91**, 232003 (2003).
[39] R. Jaffe, Phys. Rep. **409**, 1 (2005).
[40] A. Jackura *et al.* (COMPASS and JPAC Collaborations), Phys. Lett. B **779**, 464 (2018).
[41] T. Schlüter, The $\pi^-\eta$ and $\pi^-\eta'$ systems in exclusive 190 GeV $\pi^- p$ reactions at COMPASS, Ph.D. thesis, Munich University, 2012.

[42] J. Kuhn *et al.* (E852 Collaboration), Phys. Lett. B **595**, 109 (2004).
[43] M. Lu *et al.* (E852 Collaboration), Phys. Rev. Lett. **94**, 032002 (2005).
[44] R. T. Deck, Phys. Rev. Lett. **13**, 169 (1964).
[45] G. Ascoli, R. Cutler, L. M. Jones, U. Kruse, T. Roberts, B. Weinstein, and H. W. Wyld, Phys. Rev. D **9**, 1963 (1974).
[46] D. Ryabchikov, Analysis of $\pi^-\pi^-\pi^+$ in COMPASS data: role of $a_1(1260)$ meson and Deck process, https://indico.cern.ch/event/591374/contributions/2498368/attachments/1427728/2191292/03_ryabchikov_athos2017.pdf.
[47] G. F. Chew and S. C. Frautschi, Phys. Rev. Lett. **7**, 394 (1961).
[48] S. Donnachie, H. G. Dosch, O. Nachtmann, and P. Landshoff, *Pomeron Physics and QCD*, Cambridge Monographs on Particle Physics, Nuclear Physics and Cosmology (Cambridge University Press, Cambridge, 2005).
[49] F. E. Close and G. A. Schuler, Phys. Lett. B **458**, 127 (1999).
[50] T. Arens, O. Nachtmann, M. Diehl, and P. V. Landshoff, Z. Phys. C **74**, 651 (1997).
[51] J. D. Bjorken, Phys. Rev. Lett. **4**, 473 (1960).
[52] I. J. R. Aitchison, Nucl. Phys. **A189**, 417 (1972).
[53] F. James and M. Roos, Comput. Phys. Commun. **10**, 343 (1975).
[54] W. H. Press, S. A. Teukolsky, W. T. Vetterling, and B. P. Flannery, *Numerical Recipes: The Art of Scientific Computing*, 3rd ed. (Cambridge University Press, New York, NY, USA, 2007).
[55] B. Efron and R. Tibshirani, *An Introduction to the Bootstrap*, Chapman & Hall/CRC Monographs on Statistics & Applied Probability (CRC Press, Baco Raton, 1994).
[56] See Supplemental Material at http://link.aps.org/supplemental/10.1103/PhysRevLett.122.042002 for additional information about fit results and systematic studies.
[57] R. Navarro Pérez, E. Ruiz Arriola, and J. Ruiz de Elvira, Phys. Rev. D **91**, 074014 (2015).
[58] M. Tanabashi *et al.* (Particle Data Group), Phys. Rev. D **98**, 030001 (2018).

SUPPLEMENTAL MATERIAL

TABLE I: Parameters of the numerator $n_k^J(s) = \sum_{n=0}^{3} a_n^{J,k} T_n[\omega(s)]$, with $\omega(s) = s/(s+s_0)$, and $s_0 = 1\,\mathrm{GeV}^2$ reflects the short range nature of $\eta^{(\prime)}\pi$ production. All numbers are expressed in GeV units. The first values are obtained from the best fit, and should be used to reproduce the plots. The second values contains the mean value and standard deviation estimated with 5×10^4 bootstrapped datasets. We remark that the coefficients are $\gtrsim 95\%$ correlated, and the single error has to be taken with care.

	$\eta\pi$ channel			$\eta'\pi$ channel	
$a_0^{P,\eta\pi}$	408.75	356 ± 334	$a_0^{P,\eta'\pi}$	-47.05	-43 ± 39
$a_1^{P,\eta\pi}$	-632.57	-547 ± 534	$a_1^{P,\eta'\pi}$	65.84	59 ± 63
$a_2^{P,\eta\pi}$	281.48	240 ± 255	$a_2^{P,\eta'\pi}$	-20.96	-17 ± 30
$a_3^{P,\eta\pi}$	-57.98	-47 ± 63	$a_3^{P,\eta'\pi}$	1.20	-0 ± 8
$a_0^{D,\eta\pi}$	-247.80	-247 ± 28	$a_0^{D,\eta'\pi}$	230.92	233 ± 79
$a_1^{D,\eta\pi}$	413.91	415 ± 39	$a_1^{D,\eta'\pi}$	-290.66	-290 ± 125
$a_2^{D,\eta\pi}$	-190.94	-192 ± 39	$a_2^{D,\eta'\pi}$	176.88	177 ± 83
$a_3^{D,\eta\pi}$	59.25	61 ± 29	$a_3^{D,\eta'\pi}$	-3.82	-1 ± 62

TABLE II: Parameters of $D^J(s)$. The errors and correlations are estimated with bootstrap.

	Resonating terms			K-matrix background	
$g_{\eta\pi}^{P,1}$	-0.68	-0.55 ± 0.38	$c^P_{\eta\pi,\eta\pi}$	-15.43	-14.77 ± 7.22
$g_{\eta'\pi}^{P,1}$	-13.12	-13.12 ± 0.95	$c^P_{\eta\pi,\eta'\pi}$	-67.22	-65.28 ± 13.91
$m^2_{P,1}$	3.52	3.52 ± 0.08	$c^P_{\eta'\pi,\eta'\pi}$	-190.73	-184.19 ± 38.21
			$d^P_{\eta\pi,\eta\pi}$	1.82	1.93 ± 2.24
			$d^P_{\eta\pi,\eta'\pi}$	7.64	7.59 ± 5.09
			$d^P_{\eta'\pi,\eta'\pi}$	63.85	60.54 ± 18.59
$g_{\eta\pi}^{D,1}$	5.63	5.64 ± 0.34	$c^D_{\eta\pi,\eta\pi}$	-2402.56	-2385.05 ± 273.87
$g_{\eta'\pi}^{D,1}$	-3.77	-3.78 ± 0.10	$c^D_{\eta\pi,\eta'\pi}$	462.60	469.55 ± 55.87
$m^2_{D,1}$	1.86	1.86 ± 0.02	$c^D_{\eta'\pi,\eta'\pi}$	-86.60	-92.25 ± 28.11
$g_{\eta\pi}^{D,2}$	147.79	147.17 ± 9.88	$d^D_{\eta\pi,\eta\pi}$	-614.58	-608.35 ± 49.32
$g_{\eta'\pi}^{D,2}$	-33.39	-34.07 ± 3.41	$d^D_{\eta\pi,\eta'\pi}$	164.72	166.85 ± 17.46
$m^2_{D,2}$	8.06	8.06 ± 0.30	$d^D_{\eta'\pi,\eta'\pi}$	-42.19	-44.45 ± 11.59

TABLE III: Summary of systematic studies of the denominator. For each systematic variation, 5×10^4 bootstrapped pseudodatasets are produced, and the average is shown here. For each parameter varied, we consider the maximum deviation of the pole position from the one in the reference fit. If that is compatible with the statistical uncertainty, we neglect the effect. If larger, we assign a systematic uncertainty to it, and eventually add in quadrature all the systematic uncertainties. We vary the value of s_L and α in the reference model in Eq. (2). As an alternative model, we use $\rho N^J_{ki}(s') = \delta_{ki}\, Q_J(z_{s'})\, s'^{-\alpha}\lambda^{-1/2}(s', m^2_{\eta^{(\prime)}}, m^2_\pi)$, where $Q_J(z_{s'})$ is the second kind Legendre function, and $z_{s'} = 1 + 2s's_L/\lambda(s', m^2_{\eta^{(\prime)}}, m^2_\pi)$, with $s_L = 1\,\mathrm{GeV}^2$. Asymptotically it behaves as $s'^{-\alpha}$, has a left hand cut starting at $s' = 0$, a short cut between $(s' - m_{\eta^{(\prime)}})^2$ and $(s' + m_{\eta^{(\prime)}})^2$, and an incomplete circular cut.

Systematic	Poles	Mass (MeV)	Deviation (MeV)	Width (MeV)	Deviation (MeV)
		Variation of the function $\rho N(s')$			
	$a_2(1320)$	1306.4	0.4	115.0	0.6
$s_L = 0.8\,\mathrm{GeV}^2$	$a_2'(1700)$	1720	−3	272	26
	π_1	1532	−33	484	−8
	$a_2(1320)$	1305.6	−0.4	113.2	−1.2
$s_L = 1.8\,\mathrm{GeV}^2$	$a_2'(1700)$	1743	21	254	7
	π_1	1528	−36	410	−82
	$a_2(1320)$		0.0		0.0
Systematic assigned	$a_2'(1700)$		21		26
	π_1		36		82
	$a_2(1320)$	1305.9	−0.1	114.7	0.3
$\alpha = 1$	$a_2'(1700)$	1685	−37	299	52
	π_1	1506	−58	552	60
	$a_2(1320)$		0.0		0.0
Systematic assigned	$a_2'(1700)$		37		52
	π_1		58		60
	$a_2(1320)$	1304.9	−1.1	114.2	−0.2
$Q_J, \alpha = 1$	$a_2'(1700)$	1670	−52	269	22
	π_1	1511	−53	528	36
	$a_2(1320)$	1306.0	0.1	115.0	0.6
$Q_J, \alpha = 1.5$	$a_2'(1700)$	1717	−5	272	25
	π_1	1578	14	530	39
	$a_2(1320)$	1306.2	0.2	114.7	0.3
$Q_J, \alpha = 2$	$a_2'(1700)$	1723	1	261	15
	π_1	1570	6	508	16
	$a_2(1320)$		1.1		0.0
Systematic assigned	$a_2'(1700)$		52		25
	π_1		53		0

TABLE IV: Summary of systematic studies of the numerator. For each systematic variation, 5×10^4 bootstrapped pseudodatasets are produced, and the average is shown here. For each parameter varied, we consider the maximum deviation of the pole position from the one in the reference fit. If that is compatible with the statistical uncertainty, we neglect the effect. If larger, we assign a systematic uncertainty to it, and eventually add in quadrature all the systematic uncertainties. We vary the value of t_{eff}, and increase the order of the polynomial expansion by one unit.

Systematic	Poles	Mass (MeV)	Deviation (MeV)	Width (MeV)	Deviation (MeV)
Variation of the numerator function $n(s)$					
Polynomial expansion	$a_2(1320)$	1305.9	-0.1	114.7	0.3
	$a_2'(1700)$	1723	1	249	2
	π_1	1563	-1	479	-13
Systematic assigned	$a_2(1320)$		0.0		0.0
	$a_2'(1700)$		0		0
	π_1		0		0
$t_{\text{eff}} = -0.5\,\text{GeV}^2$	$a_2(1320)$	1306.8	0.8	114.1	-0.3
	$a_2'(1700)$	1730	8	259	13
	π_1	1546	-18	443	-49
Systematic assigned	$a_2(1320)$		0.8		0.0
	$a_2'(1700)$		0		0
	π_1		0		0

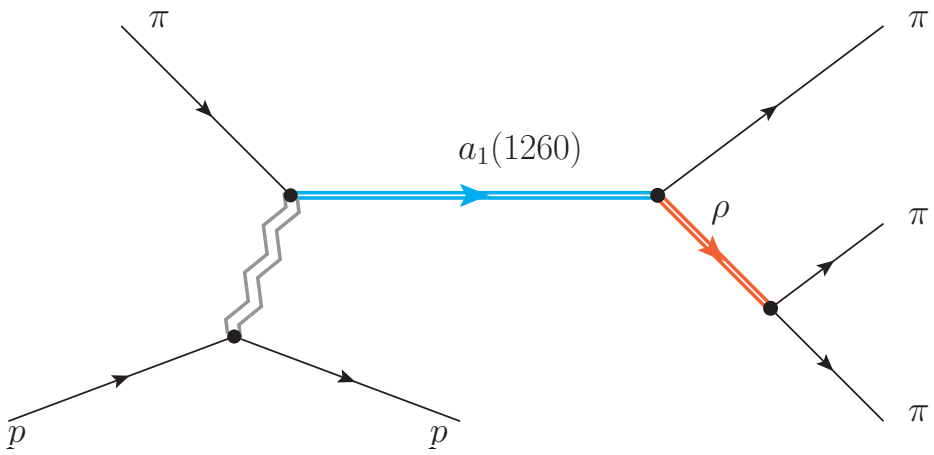

Figure 3.7: Diffractive dissociation of a pion beam on a proton target.

3.4 Decay of the $a_1(1260)$ to three pions

3.4.1 Motivation

While hadron scattering relating two-body initial and final states has been extensively studied and is well understood, there is no general framework extending it to the three-body scenario. The derivation of three-body unitarity relations mediated by isobars is been studied both on the finite volume [194–202], and in the infinite volume [109, 111, 193, 204–206].

The understanding of three-body interactions is crucial for the interpretation of many hadronic processes and of particular interest in the model-independent determination of the heavy exotic states like the X,Y,Z [27, 29, 241], or the newly observed pentaquarks, whose main decay channels are three-body final states. Not only the heavy ones, but also the enigmatic a_1, ω_2 and the π_1 have a large branching ratio to three particles.

There has been substantial progress in recent years both from the pure phenomenological point of view and from Lattice QCD, although the first works studying the difficulties of constraining $3 \to 3$ amplitudes from S-matrix principles are much older [193, 204]. Despite the efforts, simple algebraic formulations for $3 \to 3$ are not yet feasible, although there has been some recent progress on that topic [111]. All these works rely on the isobar approximation, which in the cases of interest is a fairly good assumption, for example, to a very good approximation the decay of the $a_1(1260)$ to three pions is mediated by a ρ resonance as shown in Fig. 3.7 and Fig. 3.8.

In section 3.4.3 we will pay attention to the phenomenological description of this particular axial resonance, extracting its parameters through a three-body approximation. This resonance, whose quantum numbers are $J^{PC} = 1^{++}$ appears both in $\pi p \to 3\pi p$ (Fig. 3.7) and in $\tau^- \to \pi^-\pi^+\pi^-\nu_\tau$ (Fig. 3.8). Nevertheless, although there are precise measurements of the production process, we will focus instead on the tau

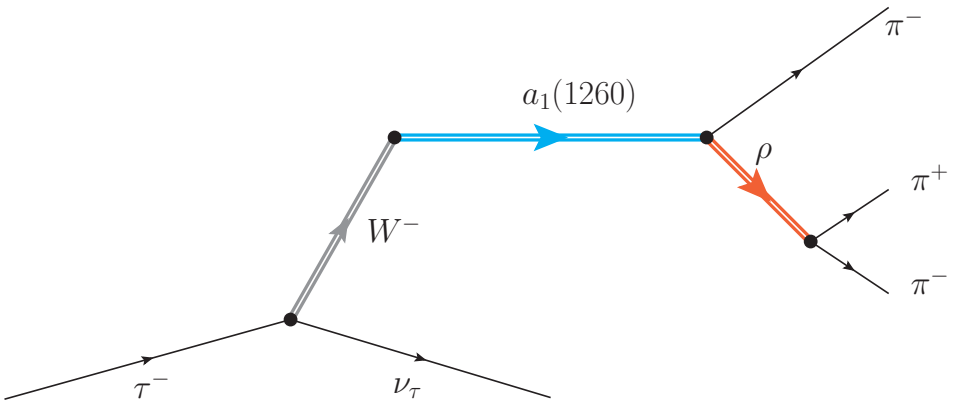

Figure 3.8: Diagram for the $a_1(1260)$ resonance dominating the $\tau^- \to \pi^-\pi^+\pi^-\nu_\tau$ decay.

decay. The reason is that the former may contain a large background effect, known as the Deck process in pion diffraction [210, 242–244], which happens to dominate in channels with this same quantum numbers. A precise determination of the parameters of the $a_1(1260)$ would hence constrain the contribution coming from this Deck process, relevant also in different quantum numbers, like the one of the $\pi_1 \to 3\pi$ decay.

On top of that, the $a_1(1260)$ is a broad resonance, whose parameters are not only affected by crude isobar implementations, but also by crude analytic continuations. Therefore, a more reliable application of the 3-body problem is needed, together with a dispersive description of the partial wave in order to extract the pole position of the resonance as model independent and precise as possible.

3.4.2 Outline of the main results

- We analyze the weak decay of the τ to three pions, which has been measured by the ALEPH collaboration. The high statistics allow us to determine with high precision the amplitude of the process.

- A three-body approximation, based on the quasi-two-body description is built. We use up to four different analytic formulas for the phase space. A first dispersive symmetrized one, and 3 different, less powerful approximations. Two of them are later disfavored due to the statistics of the fit.

- The quasi-two-body approximation is based on the use of isobars, in particular for the ρ taking into account its line shape, and symmetrizing the interaction between channels due to Bose statistics, the final formula is analytic and simple to use. We also test our approximation against the more naive approximation where the ρ is considered stable. Both results are compared, and the situation regarding the branch cut produced in the complex plane is discussed.

- Finally, we pay special attention on how to perform the analytic continuation of our approximation and determine the parameters of the $a_1(1260)$. In addition

the four different determinations of the $a_1(1260)$ are compared.

3.4.3 Publication: *Pole position of the* $a_1(1260)$ *from* τ*-decay*

Pole position of the $a_1(1260)$ from τ-decay

M. Mikhasenko,[1,*] A. Pilloni,[2,3] A. Jackura,[4,5] M. Albaladejo,[2,6] C. Fernández-Ramírez,[7] V. Mathieu,[2] J. Nys,[8] A. Rodas,[9] B. Ketzer,[1] and A. P. Szczepaniak[4,5,2]

(Joint Physics Analysis Center Collaboration)

[1]*Universität Bonn, Helmholtz-Institut für Strahlen- und Kernphysik, 53115 Bonn, Germany*
[2]*Theory Center, Thomas Jefferson National Accelerator Facility, Newport News, Virginia 23606, USA*
[3]*European Centre for Theoretical Studies in Nuclear Physics and Related Areas (ECT*) and Fondazione Bruno Kessler, I-38123 Villazzano (TN), Italy*
[4]*Center for Exploration of Energy and Matter, Indiana University, Bloomington, Indiana 47403, USA*
[5]*Physics Department, Indiana University, Bloomington, Indiana 47405, USA*
[6]*Departamento de Física, Universidad de Murcia, E-30071 Murcia, Spain*
[7]*Instituto de Ciencias Nucleares, Universidad Nacional Autónoma de México, Ciudad de México 04510, Mexico*
[8]*Department of Physics and Astronomy, Ghent University, Ghent 9000, Belgium*
[9]*Departamento de Física Teórica, Universidad Complutense de Madrid, E-28040 Madrid, Spain*

(Received 10 October 2018; published 28 November 2018)

We perform an analysis of the three-pion system with quantum numbers $J^{PC} = 1^{++}$ produced in the weak decay of τ leptons. The interaction is known to be dominated by the axial meson $a_1(1260)$. We build a model based on approximate three-body unitary and fix the free parameters by fitting it to the ALEPH data on $\tau^- \to \pi^-\pi^+\pi^-\nu_\tau$ decay. We then perform the analytic continuation of the amplitude to the complex energy plane. The singularity structures related to the $\pi\pi$ subchannel resonances are carefully addressed. Finally, we extract the $a_1(1260)$ pole position $m_p^{(a_1(1260))} - i\Gamma_p^{(a_1(1260))}/2$ with $m_p^{(a_1(1260))} = (1209 \pm 4^{+12}_{-9})$ MeV, $\Gamma_p^{(a_1(1260))} = (576 \pm 11^{+89}_{-20})$ MeV.

DOI: 10.1103/PhysRevD.98.096021

I. INTRODUCTION

The internal dynamics of the quantum chromodynamics (QCD) degrees of freedom manifests itself in the spectrum of hadron resonances. The mass of a resonance characterizes the energy of the excitation while its width reflects on the coupling to the decay channels. The meson spectrum has been qualitatively elucidated by the quark model [1] and recently, at least for some states, calculations based on first principles lattice QCD are becoming available [2,3]. For a majority of states, however, *ab initio* QCD calculations of their decay properties, e.g., decay widths, branching ratios, are not yet available. Pushing such calculations forward is important given the growing body of evidence for novel hadronic phenomena [4–10], e.g., the X, Y, Z states observed in heavy quarkonia [11–13]. Many of these new states are observed in decays to three-particle final sates.While hadron scattering involving two stable particles is rather well understood formally, the methodology for incorporating three and more particles is still being developed both in the infinite volume [14–18] and finite volume [19–24].

A large number of light meson resonances dominantly decay to three pions. This includes the enigmatic $a_1(1260)$ resonance, which is the lightest axial vector meson with $J^{PC} = 1^{++}$. The properties of the a_1 resonance are difficult to assess, due to its large width that is affected by the three-pion dynamics. The $\pi\pi$ subchannel is dominated by the ρ resonance whose finite width is expected to be important for the extraction of the a_1 resonance properties. Indeed, a large part of the $a_1(1260)$ peak seen in the invariant mass distribution of three pions lays below the nominal $\rho\pi$ threshold. However, the pole of the resonance was previously addressed in Lagrangian-based models [25,26], assuming a stable ρ-meson.

The $J^{PC} = 1^{++}$ three-pion state can be observed in the $\tau \to 3\pi\nu_\tau$ decay as well as in pion diffraction off a proton

*mikhail.mikhasenko@hiskp.uni-bonn.de

target $\pi p \to 3\pi p$. There appears to be a discrepancy in the a_1 resonance parameters extracted from the two reactions [1,27]. The problem may be related to the presence of a large, coherent, nonresonant background, known as the Deck process in pion diffraction [28–31]. This process happens to dominate in the $J^{PC} = 1^{++}$ partial wave and directly influences the extraction of the $a_1(1260)$ resonance parameters in pion diffraction. Thus, an independent determination of the $a_1(1260)$ resonance properties is not only relevant for a better understanding of this state but also to constrain the Deck process, which contributes significantly to other partial waves including the ones with the exotic quantum numbers 1^{-+} [31]. In this paper, we therefore focus on the $\tau^- \to \pi^-\pi^+\pi^-\nu_\tau$ decay with the aim of extracting the $a_1(1260)$ resonance parameters.

The paper is organized as follows. In Sec. II we present our model, we relate the differential width of $\tau^- \to \pi^-\pi^+\pi^-\nu_\tau$ to the three-pion scattering amplitude in the 1^{++} sector. In Sec. III we show how the model is constrained by the fit to ALEPH data. In Sec. IV we explore the analytic properties of our model for complex values of the 3π invariant mass squared, establishing the main singularities of the amplitude, and we determine the location of the $a_1(1260)$ pole. The studies of the systematics are described in Sec. V. Our conclusions are summarized in Sec. VI.

II. THE REACTION MODEL

We consider the reaction $\tau \to 3\pi\nu_\tau$ and derive an expression for the differential width which characterizes the 3π invariant mass spectrum [32–36]. The differential width is calculated by averaging (summing) over the τ (ν_τ) polarizations and integrating the matrix element squared over the final-state momenta,

$$\mathrm{d}\Gamma = \frac{1}{2m_\tau}\cdot\frac{1}{2}\sum_{\lambda_\tau\lambda_\nu}|A_{\lambda_\nu,\lambda_\tau}|^2\mathrm{d}\Phi_4, \tag{1}$$

where m_τ is the mass of the τ-lepton, $m_\tau = 1776$ MeV [1], the neutrino is considered massless, $\mathrm{d}\Phi_4$ is the four-body differential phase space, and λ_x are the lepton helicities of the $x = \tau, \nu$. The process is dominated by the emission of a W boson by the leptonic current,

$$\langle 3\pi\nu_\tau,\lambda_\nu|T|\tau,\lambda_\tau\rangle = -\frac{G_F}{\sqrt{2}}V^*_{ud}\bar{u}(p_\nu,\lambda_\nu)\gamma^\alpha(1-\gamma^5) \times u(p_\tau,\lambda_\tau)\langle 3\pi|J^{5-}_\alpha(0)|0\rangle, \tag{2}$$

where $\langle 3\pi\nu_\tau,\lambda_\nu|T|\tau,\lambda_\tau\rangle = A_{\lambda_\nu,\lambda_\tau}(2\pi)^4\delta^4(p_\tau - p_\nu - p_{3\pi})$, $G_F V^*_{ud}/\sqrt{2}$ is the Cabibbo-favored weak coupling, $p_{3\pi}$, p_τ, and p_ν are the four-momenta of three-pion system and the leptons, u ($\bar{u}$) are the Dirac spinors of the τ (ν_τ), see Fig. 1. Because of G-parity conservation the $\pi^-\pi^+\pi^-$ system has positive C-parity. Hence, the vector current $\bar{u}\gamma^\alpha u$ does not couple it, and can be removed. Since the W^- is heavily off-shell, one should also consider the timelike polarization, which carries $J^{PC} = 0^{-+}$. However, the corresponding helicity amplitude is suppressed by the PCAC [33,37]. This enables us to treat the off-shell W^- as purely axial. The polarization of the real W^- provides a complete basis which we use to expand the hadronic current,

$$A_{\lambda_\nu,\lambda_\tau} = \frac{G_F}{\sqrt{2}}V^*_{ud}\bar{u}(p_\nu,\lambda_\nu)\gamma^\alpha\gamma^5 u(p_\tau,\lambda_\tau)\sum_\Lambda \varepsilon_\alpha(\Lambda)A_\Lambda, \tag{3}$$

where $\varepsilon^{\alpha*}(\Lambda)\langle 3\pi|J^{5-}_\alpha(0)|0\rangle = A_\Lambda(2\pi)^4\delta^4(p_\tau - p_\nu - p_{3\pi})$ is the helicity amplitude for the decay of the axial current to three pions. The squared matrix element summed and averaged over the ν_τ and τ helicities, respectively, is

$$\frac{1}{2}\sum_{\lambda_\tau\lambda_\nu}|A_{\lambda_\nu,\lambda_\tau}|^2 = G_F^2|V_{ud}|^2(p^\alpha_\tau p^\beta_\nu + p^\beta_\tau p^\alpha_\nu - g^{\alpha\beta}(p_\tau\cdot p_\nu)) \times \sum_{\Lambda,\Lambda'}\varepsilon_\alpha(\Lambda)\varepsilon^*_\beta(\Lambda')A_\Lambda A^*_{\Lambda'}. \tag{4}$$

The explicit evaluation of the expression is performed in the τ-rest frame where $p_\tau\cdot\varepsilon(0) = (m_\tau^2 - s)/(2\sqrt{s})$, and $p_\tau\cdot\varepsilon(\pm) = 0$.

Using the recursive relation for the phase space, we split it into the $\tau^- \to W^-\nu_\tau$-phase space $\mathrm{d}\Phi_2$, and the three-pion phase space $\mathrm{d}\Phi_3$: $\mathrm{d}\Phi_4 = \int \mathrm{d}\Phi_2\mathrm{d}\Phi_3\mathrm{d}s/(2\pi)$, where $\sqrt{s}$ is the invariant mass of the hadronic system. To obtain the differential width $\mathrm{d}\Gamma/\mathrm{d}s$, we integrate explicitly over the neutrino angles,

$$\frac{\mathrm{d}\Gamma}{\mathrm{d}s} = \frac{G_F^2|V_{ud}|^2}{64\pi^2 m_\tau^3}(m_\tau^2 - s)^2 \times \int \mathrm{d}\Phi_3\left(|A_+|^2 + |A_-|^2 + \frac{m_\tau^2}{s}|A_0|^2\right). \tag{5}$$

Here, one power of the factor $(m_\tau^2 - s)$ follows from the matrix element in Eq. (4), the other is given by the $W^-\nu_\tau$ two-body phase space. The expression for the $\mathrm{d}\Phi_3$ is given in Appendix B. The integral is kept in the final expression to facilitate the further discussion on partial-wave expansion of the amplitude A_Λ.

The helicity amplitude A_Λ describes the coupling of the axial current to the three charged pions. The pions are labeled as follows, $\pi^-_1\pi^+_2\pi^-_3$ (see Fig. 1). We use the isobar model to parametrize the dynamics and explicitly incorporate the $\pi^-_1\pi^-_3$ Bose symmetry,

$$A_\Lambda = A^{(3)}_\Lambda + A^{(1)}_\Lambda, \tag{6}$$

where the isobar amplitude $A^{(k)}_\Lambda$ includes only the subchannel interaction in a pion pair leaving the pion indexed k as a bachelor. In Eq. (6), we disregard the $\pi^-\pi^-$ interaction since it is negligible compared to the dominant ρ-meson in

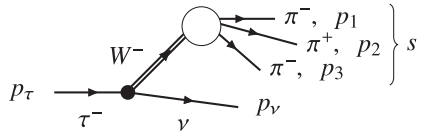

FIG. 1. Diagram for the decay $\tau^- \to \pi^-\pi^+\pi^-\nu_\tau$. The momenta of the τ lepton and ν_τ are denoted by p_τ and p_ν. The pions momenta are labeled by p_i, $i = 1, 2, 3$. s is the invariant mass of the three pions.

the $\pi^+\pi^-$ subchannel. The pion momenta are denoted by p_i where $i = 1, 2, 3$ as shown in Fig. 1 and the subchannel invariant mass squared is denoted as $\sigma_k = (p_i + p_j)^2$. Here and below we use the circular convention, i.e., the bachelor pion has index k such that the (ijk) are numbers (123), (231) or (312).

Each isobar amplitude receives different contributions, often referred to as decay channels [1]. The importance of different decay channels can be estimated by the relative branching fractions of the $a_1(1260)$ decay. The latest measurements were carried out by the CLEO experiment from τ decay [38,39] and by the COMPASS experiment in diffractive production [40]. The extraction of branching ratios is model-dependent and is influenced by the production mechanism; however, we get a rough estimate of their relative importance. The $\rho\pi S$-wave channel is dominant with a branching ratio of 60%–80%. The second most important channel, $f_0(500)\pi P$-wave, was estimated to contribute less than 20%. The combined branching ratio to the remaining channels ($\rho\pi D$-wave, $f_2\pi P$-wave, $K^*\bar{K}S, D$-waves) does not exceed 10%. We thus limit the analysis to the main $\rho\pi S$-wave channel. Including other decay channels would require the introduction of additional parameters for couplings and production strengths, which cannot be fixed by current publicly available data.

Therefore, we take the isobar amplitude to have the form,

$$A_\Lambda^{(k)} = \mathcal{C}^{(k)} a(s) f_\rho(\sigma_k) N_\Lambda(\Omega_k, \Omega_{ij}), \tag{7}$$

where $\mathcal{C}^{(k)} = \langle 1, \mu_i; 1, \mu_j | 1, 0\rangle = \pm 1/\sqrt{2}$ is the Clebsch-Gordan coefficient relating the two pion with isospin projection $\mu_{i,j} = \pm 1$ to ρ^0 isospin states, thus, the sign depends on the index k. The $a(s)$ denotes the dynamical part of the amplitude $a_1 \to \rho\pi S$-wave in the canonical basis [41,42], $f_\rho(\sigma)$ is a parametrization for the ρ-meson decay amplitude, and $N_\Lambda(\Omega_k, \Omega_{ij})$ is the angular decay function for the decay chain $a_1 \to \rho\pi$, $\rho \to \pi\pi$,

$$N_\Lambda(\Omega_k, \Omega_{ij}) = \sqrt{3} \sum_\lambda D^{1*}_{\Lambda\lambda}(\Omega_k) D^{1*}_{\lambda 0}(\Omega_{ij}). \tag{8}$$

The angles $\Omega_k = (\theta_k, \phi_k)$ are the polar and the azimuthal angles of the vector $\vec{p}_i + \vec{p}_j$ in the 3π helicity frame, i.e., the center-of-mass (CM) frame with the axis orientation fixed by the production kinematics. The $\Omega_{ij} = (\theta_{ij}, \phi_{ij})$ are the spherical angles of the pion i in the helicity frame of the isobar (ij). Detailed discussion on the decay function in Eq. (8) can be found in the Appendix B.

The line shape of the ρ-meson is given by the customary Breit-Wigner amplitude with dynamical width [40,43]

$$\begin{aligned} f_\rho(\sigma) &= \mathcal{N} \frac{F_1(p(\sigma)R)}{m_\rho^2 - \sigma - i m_\rho \Gamma_\rho(\sigma)}, \\ \Gamma_\rho(\sigma) &= \Gamma_\rho \frac{p(\sigma)}{p(m_\rho^2)} \frac{m_\rho}{\sqrt{\sigma}} \frac{F_1^2(p(\sigma)R)}{F_1^2(p(m_\rho^2)R)}, \\ F_1^2(pR) &= \frac{(pR)^2}{1 + (pR)^2}, \end{aligned} \tag{9}$$

where $p(\sigma) = \sqrt{\sigma/4 - m_\pi^2}$ is the pion break-up momentum, the function $F_1(pR)$ combines the threshold factor $p(\sigma)$ and the customary Blatt-Weisskopf barrier factor with size parameter $R = 5\ \mathrm{GeV}^{-1}$. We use in the analysis $m_\pi = 139.57$ MeV, $m_\rho = 775.26$ MeV [1]. For convenience we fix $\mathcal{N}$ so that the phase-space integral $\rho(s)$ defined below in Eq. (12a) approaches the two-body phase space asymptotic value, $1/8\pi$, in the limit $s \to \infty$, i.e.,

$$\int_{4m_\pi^2}^\infty \sqrt{1 - 4m_\pi^2/\sigma} |f_\rho(\sigma)|^2 \mathrm{d}\sigma = 16\pi^2. \tag{10}$$

The normalization for $f_\rho(\sigma)$ fixes the normalization of $a(s)$.

Using Eqs. (6) and (7) to substitute the amplitude A_Λ in Eq. (5), we get the expression for the differential width in terms of the dynamic amplitude $a(s)$.

$$\frac{\mathrm{d}\Gamma}{\mathrm{d}s} = \frac{G_F^2 |V_{ud}|^2}{64\pi^2 m_\tau^3} \left(2 + \frac{m_\tau^2}{s}\right) (m_\tau^2 - s)^2 |a(s)|^2 \rho(s). \tag{11}$$

where $\rho(s)$ is the effective $\rho\pi$ phase space. We will consider two models for $\rho(s)$'s:

$$\begin{aligned} \rho_{\mathrm{SYMM}}(s) = \frac{1}{2} \int \mathrm{d}\Phi_3 | & f_\rho(\sigma_1) N_0(\Omega_1, \Omega_{23}) \\ & - f_\rho(\sigma_3) N_0(\Omega_3, \Omega_{12})|^2, \end{aligned} \tag{12a}$$

$$\rho_{\mathrm{QTB}}(s) = \int \mathrm{d}\Phi_3 |f_\rho(\sigma_1) N_0(\Omega_1, \Omega_{23})|^2. \tag{12b}$$

The expression in Eq. (12a) strictly follows from Eqs. (6), (7), and (11). The label SYMM is introduced to emphasize the symmetrization between the decay channels, i.e., the $\rho\pi$ channels $k = 1$ and 3. The relative minus sign comes from the symmetry of the isospin coefficient in Eq. (7). The integral in Eq. (12a) is the same for all helicities Λ due to the properties of the Wigner d-functions, therefore we set $\Lambda = 0$ for simplicity. The interference term is only significant at low energy,

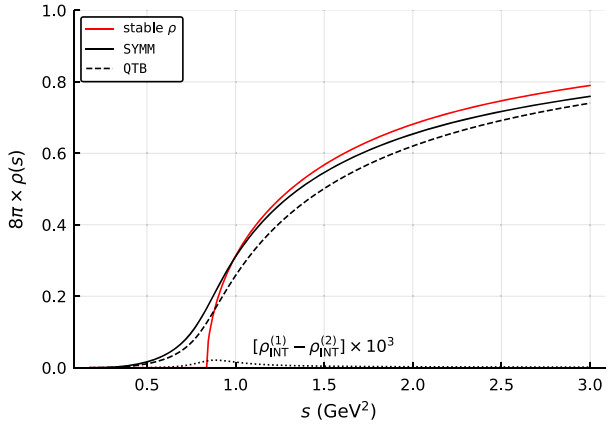

FIG. 2. The phase space $\rho(s)$ calculated for different models. The black solid line shows the symmetrized $\rho_{\rm SYMM}$ from Eq. (12a). The dashed curve represents $\rho_{\rm QTB}$ from Eq. (12b), which neglects the interference between the two $\rho\pi$ decay chains. For reference we draw the two-body $\rho\pi$ phase space given by $\sqrt{(s-(m_\rho+m_\pi)^2)(s-(m_\rho-m_\pi)^2)}/(8\pi s)$ with a solid red line. Due to the chosen normalization in Eq. (10), all functions approach the same asymptotic limit. The dotted line shows the difference in the interference terms calculated in two different ways for $s+i\epsilon$ as discussed in Sec. IV B.

where the overlapping region of the two ρ-mesons contributes to a substantial fraction of the Dalitz plot. The $\rho_{\rm QTB}$ (quasi-two-body) in Eq. (12) is a simplified phase space where the interference term is neglected. In this case, the integrals of the two decay chains squared are identical, which cancels the $1/2$ factor in front. This model treats the ρ-meson as quasistable and the interaction between the $\rho\pi$ as a two-body interaction. The simplification is suggested and discussed in Ref. [44] to treat the multiparticle final states. The same approximation is commonly used to account for 4π channel in the $\pi\pi/K\bar{K}$ coupled-channels problem [45,46]). Finally, as shown in Fig. 2, the interference is rather small. Since this model is simpler, we would like to test it as an alternative.

Our model for the decay amplitude is constrained by the approximate three-body unitary [29,44]. Turning general 3-body unitarity into some practically useful equations is cumbersome and not complete yet. A significant progress in this direction has been made in Refs. [14–17]. In particular, one can separate the genuine three-body unitary from the subchannel unitarity related to rescattering between different isobars. These processes modify the line shape of the subchannel amplitudes [47–53]. A good example is the $\rho\pi$-dynamics studied in the 1^{--} sector in the decay of ω/ϕ [48,50], where the final-state interaction were found to shift and skew the ρ-meson peak. Conversely, in our models we focus on the 3-body resonance dynamics, and simplify the problem by neglecting the effects of the rescattering on the isobar line shapes. We introduce the $\rho\pi$ elastic scattering isobar amplitude $t(s)$, to impose the unitarity constraints for the amplitude $a(s)$:

$$2{\rm Im}a(s) = t^*(s)\rho(s)a(s), \tag{13a}$$

$$2{\rm Im}t(s) = t^*(s)\rho(s)t(s), \tag{13b}$$

where $\rho(s)$ is the effective phase space given by Eq. (12a) or Eq. (12b). The factor of 2 in the left-hand side of Eq. (13) is kept for convenience.

The unitarity equations (13) can be satisfied by a certain choice of the parametrization.

$$t(s) = \frac{g^2}{m^2 - s - ig^2C(s)/2}, \qquad a(s) = \alpha(s)t(s), \tag{14}$$

where $C(s)$ is an analytic function constrained by condition ${\rm Im}iC(s) = \rho(s)$. To describe the amplitude dominated by a single resonance, we added a first order polynomial $(m^2 - s)/g^2$ to the denominator of $t(s)$, which is equivalent to have the K-matrix with a single pole [42]. The numerator function $\alpha(s)$ is supposed to incorporate the singularities specific to the production process into the amplitude $a(s)$. The final state interaction required by unitarity is accounted for by the multiplicative form of the production amplitude in Eq. (14). It diminishes the differences between different possible production mechanisms, e.g., resonant vs nonresonant production of $\rho\pi$. In the case at hand we use $\alpha = {\rm const}$. There are two common constructions for $C(s)$ which both satisfy unitarity:

(1) The models with $C(s) = \rho(s)$ will be called *nondispersive*. These models have left-hand singularities on the physical sheet inherited from the phase space, which are not motivated by physics.

(2) The *dispersive* models have $C(s) = \tilde{\rho}(s)$, with

$$i\tilde{\rho}(s) = l_0 + \frac{s}{\pi}\int_{9m_\pi^2}^{\infty} {\rm d}s' \frac{\rho(s')}{s'(s'-s-i\epsilon)}, \tag{15}$$

where the subtraction constant l_0 is chosen such that the real part of $i\tilde{\rho}(s)$ is zero at the point $(m_\rho + m_\pi)^2$. The function $i\tilde{\rho}(s)$ has no singularities other than the unitarity cut as guaranteed by the Cauchy integral theorem. It is analogous to the Chew-Mandelstam function for the two-body scattering amplitude [29].

We note that the first construction with $C(s) = \rho(s)$ resembles the Breit-Wigner amplitude with a dynamical width [1]. In contrast, the dispersive amplitudes do not have the unmotivated left-hand cut generated by ρ in Eq. (12a). For all models, the structure of $C(s)$ ensures unitarity and extends the applicability of Eq. (14) from threshold to energy regions where higher-lying resonances or/and nonelastic channels become significant.

TABLE I. Summary of the models discussed in Sec. II. The numerator and denominator refer to Eq. (16).

Model	$\rho(s)$ in the numerator	$C(s)$ in the denominator	χ^2/n.d.f.	m (GeV)	g (GeV)
SYMM-DISP	$\rho_{\mathrm{SYMM}}(s)$	$\tilde{\rho}_{\mathrm{SYMM}}(s)$	94/100	1.205	6.64
SYMM	$\rho_{\mathrm{SYMM}}(s)$	$\rho_{\mathrm{SYMM}}(s)$	663/100	1.230	6.65
QTB-DISP	$\rho_{\mathrm{QTB}}(s)$	$\tilde{\rho}_{\mathrm{QTB}}(s)$	68/100	1.223	7.45
QTB	$\rho_{\mathrm{QTB}}(s)$	$\rho_{\mathrm{QTB}}(s)$	344/100	1.236	7.42

To summarize, the final expression for the differential cross section is.

$$\frac{\mathrm{d}\Gamma}{\mathrm{d}s} = \frac{1}{s}\left(1-\frac{s}{m_\tau^2}\right)^2\left(1+\frac{2s}{m_\tau^2}\right)\frac{c\rho(s)}{|m^2-s-ig^2C(s)/2|^2}. \tag{16}$$

Equation (16) follows from Eq. (11). The constant c absorbs all energy-independent numerical factors; m, g, and c are real parameters which are fitted to data. The four models we are going to test are summarized in Table I. Our primary model is SYMM-DISP, which is the one that incorporates the most of physical arguments. The SYMM model contains additional left-hand singularities with respect to SYMM-DISP. The QTB and QTB-DISP models do not include the interference between the two decay chains, but are much simpler to calculate on the real axis and continue to the complex plane. The $C(s)$ is calculated using the same $\rho(s)$ as in the numerator of Eq. (16), which is either ρ_{QTB} or ρ_{SYMM} as given in Table I.

III. FIT RESULTS AND RESONANCE PARAMETERS

The largest public data set for $\tau \to 3\pi\nu_\tau$ was collected by the ALEPH experiment in 2005 [54].[1] The distribution $\mathrm{d}\Gamma/\mathrm{d}s$ is binned in 0.025 GeV^2 bins and normalized by the measured branching ratio. We fit 103 data points in the range 0.38 GeV$^2 \le s \le$ 2.94 GeV^2. We minimize the χ^2-function taking into account the covariance matrix provided in Ref. [54],

$$\chi^2(c,m,g) = (\vec{D}-\vec{M}(c,m,g))^T C_{\mathrm{stat}}^{-1}(\vec{D}-\vec{M}(c,m,g)), \tag{17}$$

where $\vec{D}$ is a vector of ALEPH data points, $\vec{M}(c,m,g)$ is a vector of the model predictions calculated for the centers of the bins. The matrix C_{stat} is the covariance matrix of the statistical errors. The systematic uncertainties are smaller than the statistical ones by a factor 5, and can be neglected. Nonzero correlations among different bins are introduced by the unfolding procedure. It is worth noticing the 3π spectrum does not show the expected random noise. As discussed in the follow up analysis of the ALEPH [55], the problem appears because the errors of the unfolding procedure were not correctly propagated. Hence, the absolute value of χ^2 we obtained does not have a strict statistical meaning. However, we assume that for the model characterization based on relative χ^2 values, the problem should not be critical.

The gradient minimization is performed using the `NLopt` optimizer and the `ND_MMA` algorithm [56] with the automatic differentiation provided by the `ForwardDiff.jl`-package [57]. The minimum we find is always stable and isolated, as checked by repeating the minimization from different starting values. Fits to the ALEPH data set are shown in Fig. 3, and the fit parameters and χ^2 values are shown in Table I. The nondispersive models are not consistent with the data, with χ^2 at least three times worse than we have obtained for the dispersive models. In particular, they fail to reproduce the line shape around the peak and in the threshold region, and we do not consider them any further. On the other hand, the dispersive models show a good agreement with data, obtaining $\chi^2/\mathrm{n.d.f.} = 94/100$ and $\chi^2/\mathrm{n.d.f.} = 61/100$ for the SYMM-DISP and QTB-DISP, respectively.

In the next section we will perform the analytic continuation of the amplitude to the second sheet and search for the $a_1(1260)$ resonance pole. For comparison with the PDG [1], we first provide the customary Breit-Wigner parameters, that can be extracted on the real axis. We remind the reader that these are expected to be reaction-dependent, and do not provide an unambiguous characterization of the resonance. We define the Breit-Wigner mass squared m_{BW}^2 as the value of s when the denominator of the amplitude $t(s)$ in Eq. (14) becomes purely imaginary. The value of the denominator at this point gives the Breit-Wigner width, as it is equal to $-im_{\mathrm{BW}}\Gamma_{\mathrm{BW}}$. For QTB-DISP we get the Breit-Wigner mass and width as (1246 ± 3) MeV and (394 ± 5) MeV; for SYMM-DISP, (1254 ± 3) MeV and (461 ± 8) MeV, where the errors are statistical only.

IV. ANALYTIC CONTINUATION THE POLE POSITION

Once the amplitude is fixed on the real axis, its analytic structure is unambiguously defined and can be explored. Unitarity introduces a branch cut along the real axis from

[1] An updated analysis was published in 2014 [55]. The main difference is related to the use of a new method to unfold detector effects from the mass spectra. However, the data were binned into wider bins with variable bin size, which makes it less straightforward to use. For this reason we stick to data of [54].

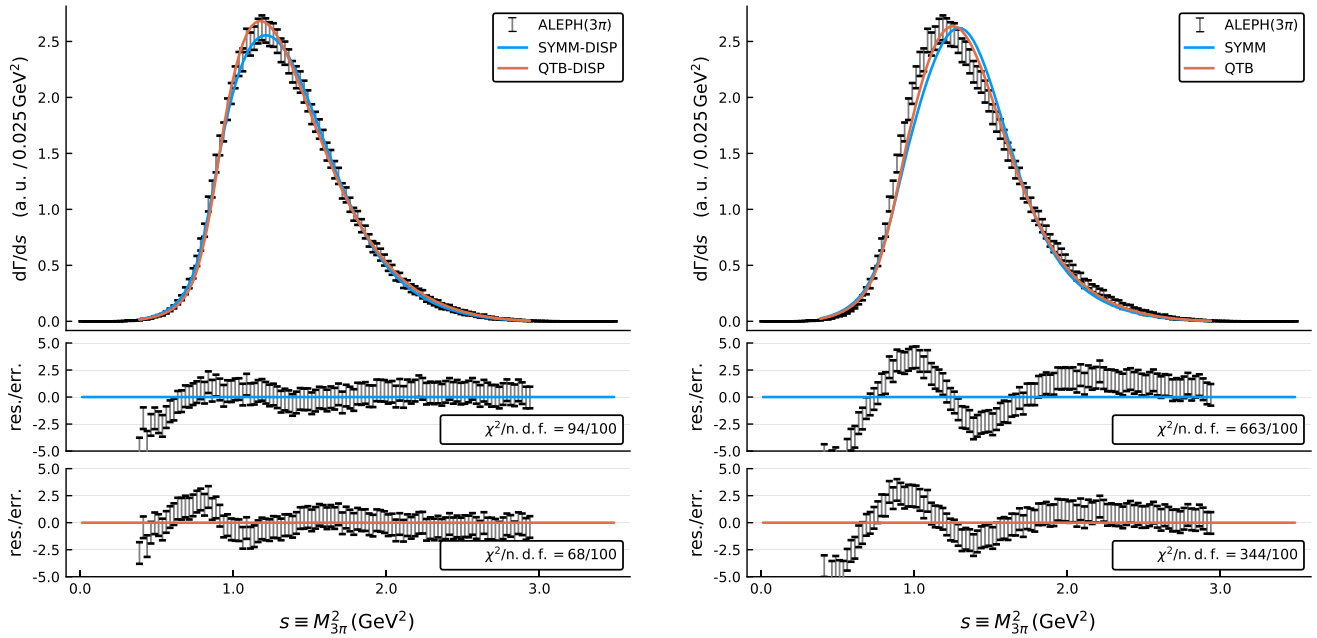

FIG. 3. Fit to ALEPH data with the four models described in the text. The models differ by either including the effect of interference between two $\rho\pi$ decay channels (SYMM) or not (QTB), and either using the dispersive integral over the phase space (DISP), or not. The lower panels show the normalized residues.

the 3π threshold to infinity, which opens a nontrivial Riemann topology or sheet structure. The first Riemann sheet is the one containing the physical values of the amplitude slightly above the real axis. By construction, the amplitudes in the dispersive models contain no other singularity on the first sheet than the unitarity cut. Resonance poles are expected to lie on the second sheet, which is connected to the physical axis from below. The unitarity condition Eq. (13b) gives us a relation on the real axis that can be used to continue the amplitude in the complex s-plane. The real-axis relation followed from Eq. (13) reads

$$t_I^{-1}(s+i\epsilon) - \Delta t^{-1}(s) = t_I^{-1}(s-i\epsilon) = t_{II}^{-1}(s+i\epsilon), \qquad (18)$$

where $\Delta t^{-1}(s) \equiv t_I^{-1}(s+i\epsilon) - t_I^{-1}(s-i\epsilon) = -i\rho(s)$ is the discontinuity across the cut, s is real, ϵ is an infinitesimal positive number, and the Roman subscript indicates the Riemann sheet. Thus, $t_{II}^{-1}(s) = t_I^{-1}(s) + i\rho(s)$ and the pole positions are determined by $t_{II}^{-1}(s) = 0$. The first sheet amplitude, $t_I^{-1}(s)$, is straightforward to calculate in the complex plane using the dispersive integral in Eq. (15). Continuation of the discontinuity, however, is more challenging since it is not explicitly analytical expression, as Eq. (12a) contains a modulus operator. Therefore, we need to find an analytic function which coincides with the discontinuity on the real axis. All singularities of the discontinuity $-i\rho(s)$ will be present in the second sheet amplitude according to Eq. (18). Among those, we expect the reflection of the $\rho\pi$ unitarity cut, which is pushed into the second sheet due to the unstable nature of the ρ-meson.

For the continuation to the complex s-plane, we need to evaluate $f_\rho(\sigma)$ and $f_\rho^*(\sigma)$ in Eqs. (12a) and (12b) for complex argument σ. Along the physical axis $f_\rho(\sigma) = f_\rho^{(I)}(\sigma+i\epsilon)$ and the analytic function $f_\rho^{(II)}(\sigma+i\epsilon)$ coincides with $f_\rho^*(\sigma)$ due to the Schwarz reflection principle and the continuity of the Riemann sheet structure, since

$$\begin{aligned} f_\rho^*(\sigma) &= f_\rho^{(I)*}(\sigma+i\epsilon) = f_\rho^{(I)}(\sigma-i\epsilon) \\ &= f_\rho^{(II)}(\sigma+i\epsilon). \end{aligned} \qquad (19)$$

A. Analytic continuation of the QTB-DISP model

We start with the QTB-DISP model, whose analytic continuation is simpler than the one of the SYMM-DISP model. The discontinuity across the unitarity cut is given by $-i\rho_{\mathrm{QTB}}$ in Eq. (12b). The angular integrals in the phase space can be solved analytically due to the properties of the Wigner D-functions. We obtain

$$\rho_{\mathrm{QTB}}(s) = \frac{1}{2\pi(8\pi)^2 s}\int_{4m_\pi^2}^{(\sqrt{s}-m_\pi)^2} f_\rho^{(II)}(\sigma_1) f_\rho^{(I)}(\sigma_1)\frac{\sqrt{\lambda_1\lambda_{s1}}}{\sigma_1}\mathrm{d}\sigma_1, \qquad (20)$$

where we used the definition $\lambda_i = \lambda(\sigma_i, m_\pi^2, m_\pi^2)$, $\lambda_{si} = \lambda(s, \sigma_i, m_\pi^2)$, with λ being the Källén triangle function $\lambda(x,y,z) = x^2+y^2+z^2-2(xy+yz+zx)$. Using Eq. (19), we replaced $|f_\rho(\sigma_1)|^2$ by the analytic expression $f_\rho^{(II)}(\sigma_1)$ $f_\rho^{(I)}(\sigma_1)$. The function $f_\rho^{(I)}(\sigma_1)$ does not have singularities

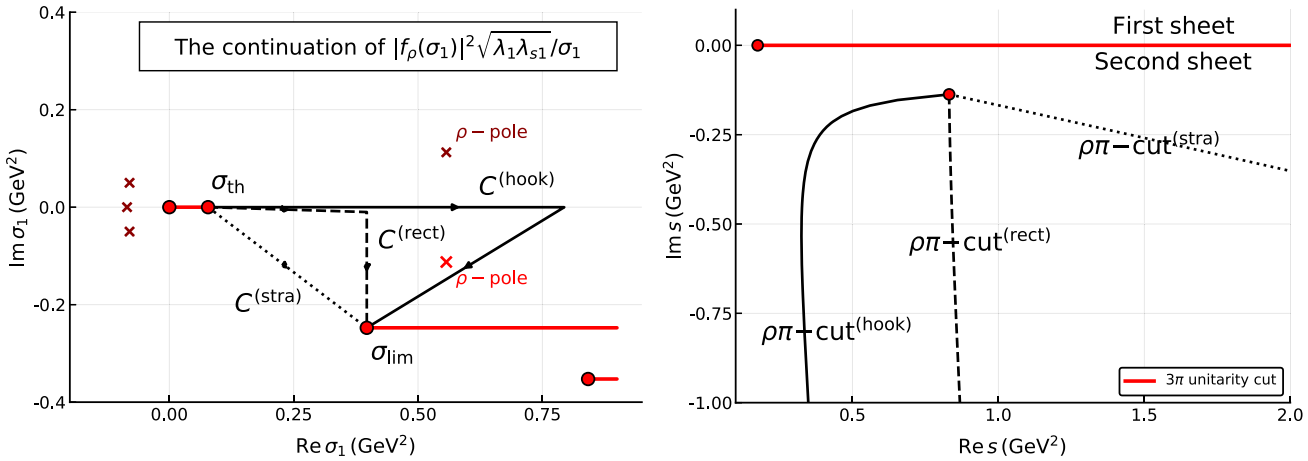

FIG. 4. The left plot shows the complex plane of the integrand of Eq. (20), for $s = 0.6 - 0.35i$ GeV^2. The red circular markers are the square-root branch points, the crosses indicate positions of the poles. The integration paths from Eq. (21) are shown by the solid lines with arrows. The right plot presents the location of the $\rho\pi$ cut for the different integration paths.

apart form cuts on the real axis, while the $f_\rho^{(II)}(\sigma_1)$ contains the pole of the ρ-meson in the complex plane. For complex values of s, the integral for the $\rho_{\rm QTB}(s)$ in Eq. (20) has the upper endpoint in the complex plane, which requires a prescription for the path of integration. The value of the integral does not depend on the path of integration, unless there are singularities of the integrand in the complex plane. The integrand is plotted for complex values of σ_1 in Fig. 4. It has four branch points in the σ_1-variable: 0, $\sigma_{\rm th} = 4m_\pi^2$, $\sigma_{\rm lim} = (\sqrt{s} - m_\pi)^2$, and $(\sqrt{s} + m_\pi)^2$, coming from the product of the Källén functions,[2] and the resonance pole of the ρ-meson at $\sigma_p = (m_\rho^{\rm (pole)} - i\Gamma_\rho^{\rm (pole)}/2)^2$.[3] Singularities of the integral arise when the upper integration endpoint touches one of the singularities of the integrand. The ρ-meson pole in the integrand transforms into a branch singularity in the integral function. We find the branch point $s_{\rho\pi}$ by checking when the upper integration endpoint touches the ρ-meson pole; $s_{\rho\pi} = (m_\rho^{\rm (pole)} + m_\pi - i\Gamma_\rho^{\rm (pole)}/2)^2$. It is indeed a branch singularity, because for every s there are several ways to connect the integration limits in Eq. (20) (see for example the solid and the dotted paths in the left panel of Fig. 4) which yield integral values differing by the residual of integrand in the ρ-meson pole. Practically, the choice of the integration path determines the location of the $\rho\pi$ branch cut in the complex s-plane as the loci of s values, for which the integration path goes through the pole. To demonstrate the evolution of the cut in the s-plane we consider the three different paths given in Eq. (21a):

$$C_\sigma^{\rm (stra)}:\ \sigma_{\rm th} \to \sigma_{\rm lim} \tag{21a}$$

$$C_\sigma^{\rm (rect)}:\ \sigma_{\rm th} \to {\rm Re}\sigma_{\rm lim} \to \sigma_{\rm lim}, \tag{21b}$$

$$C_\sigma^{\rm (hook)}:\ \sigma_{\rm th} \to 5{\rm Re}\sigma_{\rm lim} \to \sigma_{\rm lim}. \tag{21c}$$

The corresponding $\rho\pi$ cut locations are shown in the right panel of Fig. 4. The path $C_\sigma^{\rm (hook)}$ rotates the $\rho\pi$ cut such that it opens up a larger area of the closest unphysical sheet and is used in the following for finding poles and illustration purposes.

The amplitude $t(s)$ in the complex s-plane for the QTB-DISP model is shown in the left panel of Fig. 5. Naively, one would expect a single pole in the complex plane, originating from the single K-matrix pole, $g^2/(m^2 - s)$, present in Eq. (14). In contrast to this expectation, two poles are observed. Furthermore, both are rather close to the physical region. The correspondence between the K-matrix poles and the complex poles can be established by varying the coupling g. In the limit $g \to 0$ the complex poles should approach the real axis at the position of the corresponding K-matrix poles. We find

[2]The branch points are connected by cuts. Since the integral is calculated numerically it is important to make sure that the integration path does not cross any cut between the integration end points. To illustrate the cut choice shown in Fig. 4, we write

$$\sqrt{\lambda_1\lambda_{s1}} = \sqrt{\sigma_1}\sqrt{\sigma_1 - 4m_\pi^2}\sqrt{(\sqrt{s} - m_\pi)^2 - \sigma_1} \times \sqrt{(\sqrt{s} + m_\pi)^2 - \sigma_1}.$$

For real values of s, this expression has two short branch cuts on the real axis: one between 0 and $\sigma_{\rm th}$, and the other between the points $(\sqrt{s} \pm m_\pi)^2$. When s is complex the first s-independent cut remains, while the second one splits into two straight cuts to the right with the branching points $(\sqrt{s} \pm m_\pi)^2$ as shown in Fig. 4.

[3]For the ρ-meson the pole parameters are very close to the Breit-Wigner parameters $m_\rho^{\rm (pole)} \approx m_\rho$, $\Gamma_\rho^{\rm (pole)} \approx \Gamma_\rho$.

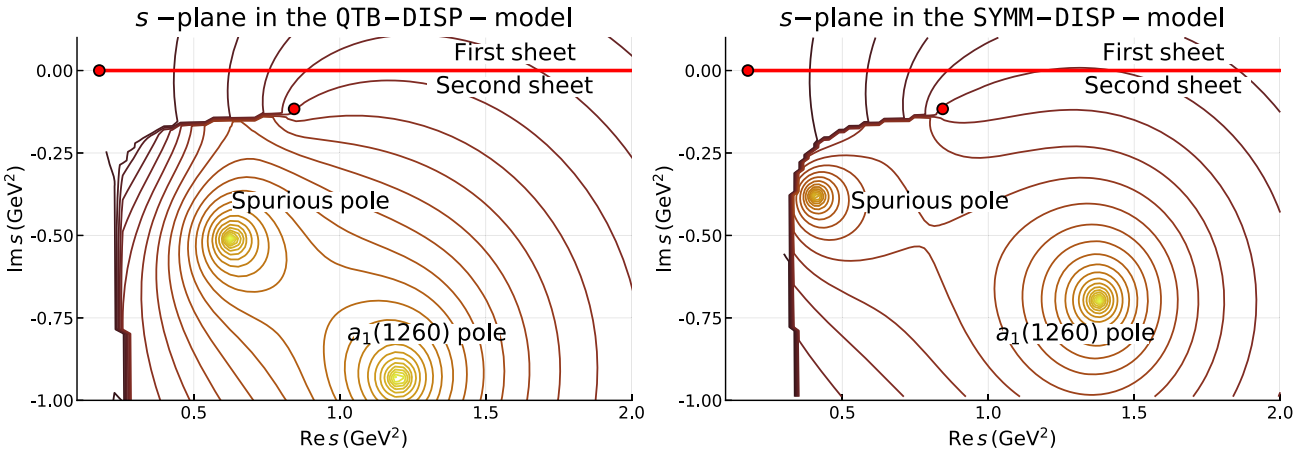

FIG. 5. Analytic continuation of the amplitude $t(s)$ in Eq. (14) for different models: QTB-DISP (Left plot), SYMM-DISP (Right plot). Lines indicate the $|t(s)|$ equipotential levels. The poles of the amplitude are the bright spots. The red dots indicate branch points corresponding to the opening of decay channels.

that the deep pole approaches the real axis at $s = m^2 = (1223\ \mathrm{MeV})^2$ (see Table I with the fit results), while the left pole goes to $s = 0$. Due to these observations, we identify the deep pole with $a_1(1260)$-pole label, i.e., corresponding to a resonance, and the left pole with a "spurious"-pole, i.e., an artifact from our parametrization in Eq. (14). This exercise also helps us to understand the origin of the spurious pole: it is the $1/s$ singularity in ρ_{QTB} [see Eq. (20)]. Clearly, this pole is an integral part of the model. In Appendix A we consider variations of the model attempting to get rid of the spurious pole. We show that its effect on the real axis is indeed required by the data. It effectively parametrizes the unphysical sheet singularities, e.g., the left-hand cuts related to the cross channel exchanges between pions in the final state. For now, we conclude by extracting the positions of the $a_1(1260)$ resonance pole in the QTB-DISP model. We use the convention $s_p = (m_p + i\Gamma_p/2)^2$, obtaining

$$\begin{aligned}\texttt{QTB}-\texttt{DISP}\colon\ m_p^{(a_1(1260))} &= (1166 \pm 6)\ \mathrm{MeV},\\ \Gamma_p^{(a_1(1260))} &= (798 \pm 26)\ \mathrm{MeV}.\end{aligned} \tag{22}$$

For the error estimation we used the bootstrap technique [58,59]: 1000 sets of pseudodata were generated using the original data and the covariance matrices, with the correlations taken into account in the Gaussian approximation. By refitting the pseudo data sets, we collect samples of the parameters, which we use to estimate their uncertainties. The distributions of the mass and width of the pole obtained from the bootstrap are Gaussian to a good approximation. The fit results and the calculated error ellipses are shown in Fig. 9. The mean values of the bootstrap sample for the pole positions differ from the real data fit results by $< 0.2\sigma$ which indicate a good consistency and negligible bias of the bootstrap method [59].

B. Analytic continuation of the SYMM-DISP model

The evaluation of the discontinuity given by Eq. (12a) for complex s is more complicated since the angular integrals cannot be solved completely, see Appendix B. We start by casting $\rho_{\mathrm{SYMM}}(s)$ in the form:

$$\rho_{\mathrm{SYMM}}(s) = \rho_{\mathrm{QTB}}(s) - \rho_{\mathrm{INT}}(s), \tag{23}$$

where the first term in the sum is the phase-space factor in the QTB-DISP model, the second term is the interference contribution given by Eq. (B16). Substituting $f_\rho \to f_\rho^{(I)}$ and $f_\rho^* \to f_\rho^{(II)}$ in Eq. (B16) we get:

$$\begin{aligned}\rho_{\mathrm{INT}}(s) = \frac{1}{2\pi(8\pi)^2 s}\int_{4m_\pi^2}^{\sigma_{\mathrm{lim}}} \mathrm{d}\sigma_1 \int_{\sigma_3^-(\sigma_1,s)}^{\sigma_3^+(\sigma_1,s)} \mathrm{d}\sigma_3 \\ \times \frac{f_\rho^{(II)}(\sigma_1)}{\sqrt{\sigma_1 - 4m_\pi^2}} \frac{f_\rho^{(I)}(\sigma_3)}{\sqrt{\sigma_3 - 4m_\pi^2}} \\ \times \frac{W(\sqrt{s},\sqrt{\sigma_1},\sqrt{\sigma_3})}{((\sqrt{s}+\sqrt{\sigma_1})^2 - m_\pi^2)((\sqrt{s}+\sqrt{\sigma_3})^2 - m_\pi^2)}.\end{aligned} \tag{24}$$

The function $W(a,b,c)$ is a multivariable polynomial defined in Eq. (B14). Omitting constant factors, the function $f_\rho(\sigma)$ is given by

$$\begin{aligned}f_\rho(\sigma) &\propto \frac{\sqrt{F(\sigma)}}{m_\rho^2 - \sigma - i m_\rho \Gamma(\sigma)}, \qquad \Gamma(\sigma) \propto \frac{i\sqrt{4m_\pi^2 - \sigma}}{\sqrt{\sigma}} F(\sigma),\\ F(\sigma) &\propto \frac{\sigma - 4m_\pi^2}{\sigma - 4m_\pi^2 + 4/R^2}.\end{aligned} \tag{25}$$

A right-hand cut is introduced by $i\sqrt{4m_\pi^2 - \sigma}$. In addition, there are two branch points: one at $\sigma = 0$ from the phase space in the width $\Gamma(\sigma)$, and another one at $\sigma = 4m_\pi^2 - 4/R^2$

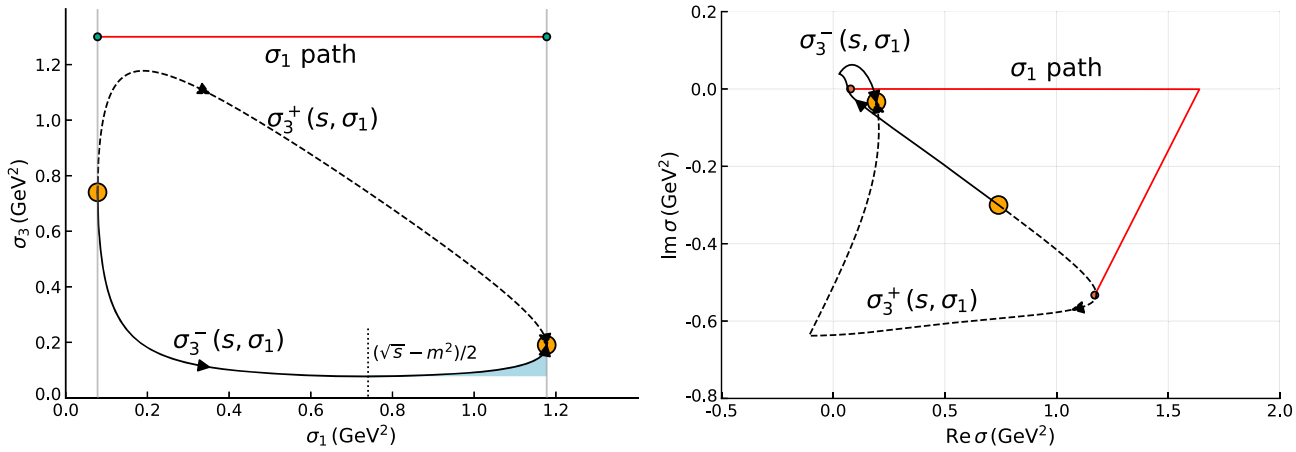

FIG. 6. Integration paths in the complex σ-plane: while σ_1 is moving along the path $\sigma_{\mathrm{th}} \to \sigma_{\mathrm{lim}}$, the integration endpoints $\sigma_3^+(s,\sigma_1)(\sigma_3^-(s,\sigma_1))$ are traveling in the complex plane along the lines shown by black solid (dashed) curve The left plot shows the integration ranges of σ_1 and σ_3 for a real value of $s = 1.5\ \mathrm{GeV}^2$. The red line is the straight integration path in σ_1. The yellow circles indicate the border of the integration domain when the integration endpoints in σ_3 coincide. In the right plot, the same lines are shown in the complex σ plane combined for σ_1 and σ_3 when $s = 1.5 - 0.6i\ \mathrm{GeV}^2$. The points $4m_\pi^2$ and $(\sqrt{s}-m_\pi)^2$ are shown by the small orange dots. While σ_1 moves along the contour $C^{(\mathrm{hook})}$ indicated by the red line, the integration limits $\sigma_3^\pm$ follow the dashed and the solid lines analogously to the left plot. The shaded area indicates the additional contribution to the phase-space integral discussed in Eq. (28).

due to the Blatt-Weisskopf factor in the numerator. The break-up momentum singularity $\sqrt{\sigma - 4m_\pi^2}$ in the numerator of $f(\sigma)$ is canceled by the same factor which arises from the angular function (see Eq. (24)). The parametrization of $f_\rho(s)$ in Eq. (25) contains 5 poles, as one can count by the order of the polynomial which would give zeros of the denominator. They correspond to the ρ-meson poles at $(m_\rho \pm i\Gamma_\rho/2)^2$, and three spurious poles lying far away from the physical region as shown in Fig. 4. The integration endpoints of the σ_3 variable, $\sigma_3^\pm(\sigma_1, s)$, describe the border of the Dalitz plot for fixed value of s (Fig. 6, left panel),

$$\sigma_3^\pm(\sigma_1, s) = \frac{s + 3m_\pi^2 - \sigma_1}{2} \pm \frac{\sqrt{\lambda_1 \lambda_{s1}}}{2\sigma_1}. \tag{26}$$

As soon as s becomes complex the endpoints depart from the real axis and move into the complex plane. The trajectories of the $\sigma_3^\pm$ as functions of σ_1 moving from $4m_\pi^2$ to $(\sqrt{s}-m_\pi)^2$ are nontrivial. As shown in Fig. 6, while σ_1 moves along the $C^{(\mathrm{hook})}$ path (see Eq. (21c)), the σ_3^- circles around the branch point $4m_\pi^2$. When σ_3 crosses the unitarity cut, the sheet, on which it is evaluated, must be changed. However, if the σ_1 path goes exactly through the point $(s - m_\pi^2)/2$, σ_3^- just touches the branch point $4m_\pi^2$, (indeed, $\sigma_3^-((s-m_\pi^2)/2, s) = 4m_\pi^2$). In that case we are allowed to stay on the same sheet. Therefore, there are two ways to calculate ρ_{INT} for a complex argument (see Appendix C for more details):

(1) $\rho_{\mathrm{INT}}^{(1)}$: We choose a special path in σ_1,

$$C_\sigma^{(\mathrm{spec})}:\ \sigma_{\mathrm{th}} \to (s - m_\pi^2)/2 \to \sigma_{\mathrm{lim}}, \tag{27}$$

the $\sigma_3^\pm$ always stay on the same sheet and can be connected with a straight (undistorted) path.

(2) $\rho_{\mathrm{INT}}^{(2)}$: We let σ_3^- circle around the branch point, changing sheets of $f(\sigma_3)$ appropriately. When $\sigma_1 = \sigma_{\mathrm{th}}$, the integration limits $\sigma_3^\pm$ coincide. For certain values of σ_1, σ_3^- changes the sheet and, therefore, when σ_1 is in its upper limit σ_{lim}, the positions of $\sigma_3^\pm$ coincide, but they are on the different sheets. The integration path must be detoured around the branch point as shown in Fig. 7.

The first option provides a unique continuation of Eq. (B16), however, the integration contour is bound to pass through $(s - m_\pi^2)/2$ which is nonanalytic point of the integrand (see Appendix C). The integrand in the second option stays analytic on the integration contour, but in the limit of real s, the function $\rho_{\mathrm{INT}}^{(2)}$ deviates from the original expression in Eq. (B16). For $s = \mathrm{Re}s + i\epsilon$, we change the sheet of σ_3^- when $\sigma_1 > (s - m_\pi^2)/2$, in contrast to the first option. The mismatch is calculated by integrating the discontinuity across the σ_3 unitarity cut over the shaded area of Fig. 6.

$$\begin{aligned}
&\rho_{\mathrm{INT}}^{(1)}(s+i\epsilon) - \rho_{\mathrm{INT}}^{(2)}(s+i\epsilon) \\
&= \int_{(s-m_\pi^2)/2}^{(\sqrt{s}-m_\pi)^2} \mathrm{d}\sigma_1 \int_{\sigma_3^-(\sigma_1,s)}^{\sigma_{\mathrm{th}}} \mathrm{d}\sigma_3 \frac{[f_\rho^{(I)}(\sigma_3+i\epsilon) - f_\rho^{(I)}(\sigma_3-i\epsilon)]}{\sqrt{\sigma_3 - 4m_\pi^2}} \\
&\times \frac{f_\rho^{(II)}(\sigma_1)}{\sqrt{\sigma_1 - 4m_\pi^2}} \frac{W(\sqrt{s}, \sqrt{\sigma_1}, \sqrt{\sigma_3})}{((\sqrt{s}+\sqrt{\sigma_1})^2 - m_\pi^2)((\sqrt{s}+\sqrt{\sigma_3})^2 - m_\pi^2)}.
\end{aligned} \tag{28}$$

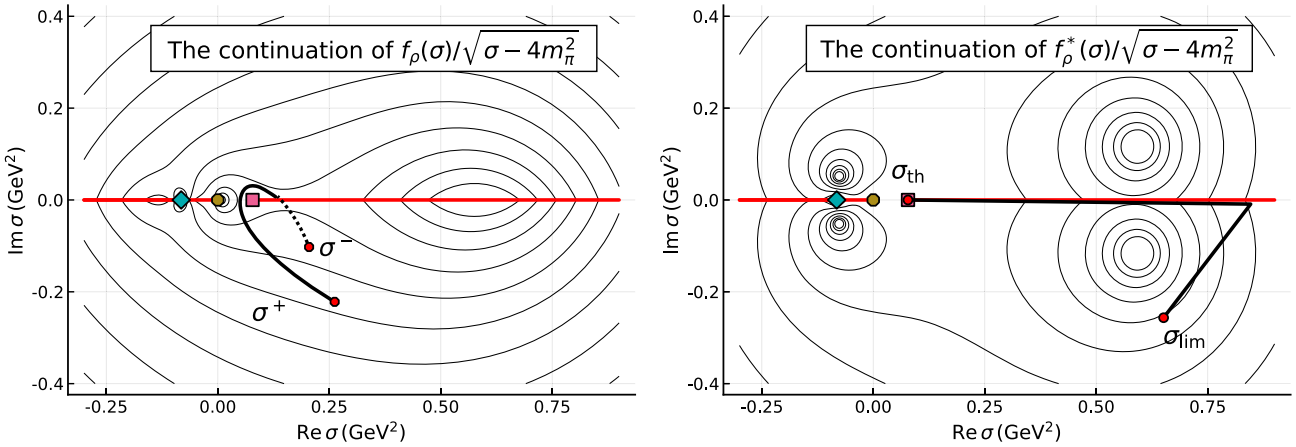

FIG. 7. The complex sheets of the isobar amplitude $f_\rho(\sigma)$ and $f^*_\rho(\sigma)$. The left plot shows the analytic continuation of the function $f_\rho(\sigma)$ above and below the real axis. The function for positive imaginary part is the same as $f^{(I)}_\rho(\sigma)$; it is continuously connected to $f^{(II)}_\rho(\sigma)$ plotted for the negative imaginary part of σ. The right plot shows the analytic continuation of $f^*_\rho(\sigma)$, where the sheets are inverted. The lines are $|f_\rho(\sigma)|$ equipotential surfaces. The circular spots are the poles (see also red crosses in the left plot of Fig. 4). The markers on the real axis are the branch points of the left-hand cuts: the square marker shows the branch point from the break-up momentum located at $\sigma = 4m_\pi^2$, the diamond marker the $\sigma = 0$ branch point, the circular marker indicates the branch point related to the Blatt-Weisskopf factors in the numerator of the $f_\rho(\sigma)$ in Eq. (25).

The difference is practically negligible as shown in Fig. 2. The impact on the fit parameters and the values of the amplitude in the complex plane is a few orders of magnitude smaller than the statistical uncertainties. For the following discussion we use $\rho^{(2)}_{\rm INT}(s)$ for the reason that the $\rho\pi$-cut can be rotated in the same way as before by using $C^{(\rm hook)}$ path in σ_1. Interestingly, an analogous problem appears in relation to the Khuri-Treiman equations (see Appendix in Ref. [14], Sec. IV in Ref. [60]). Reference [61] gives arguments in favor of the first option.

As soon as the discontinuity is known for the whole complex plane, the amplitude on the unphysical sheet can be computed according to Eq. (18). The contour plot on the right panel of Fig. 5 presents the closest unphysical sheet of the amplitude, which is smoothly connected to the real axis. We find two poles and identify them as the $a_1(1260)$ resonance pole and the left "spurious" pole as shown in Fig. 5. for the same reasoning as in Sec. IV A. The pole parameters are

$$\begin{aligned} \texttt{SYMM}-\texttt{DISP}\colon\ m_p^{(a_1(1260))} &= (1209 \pm 4)\ \text{MeV}, \\ \Gamma_p^{(a_1(1260))} &= (576 \pm 11)\ \text{MeV}. \end{aligned} \tag{29}$$

The statistical errors are obtained from a bootstrap analysis as described above in Sec. IV A. The combined results are presented in Fig. 9.

V. SYSTEMATIC UNCERTAINTIES

The description of three-particle resonances is a difficult problem because of the complicated structure of final-state interactions, which induces an interplay between different decay channels. The latter manifests itself in the

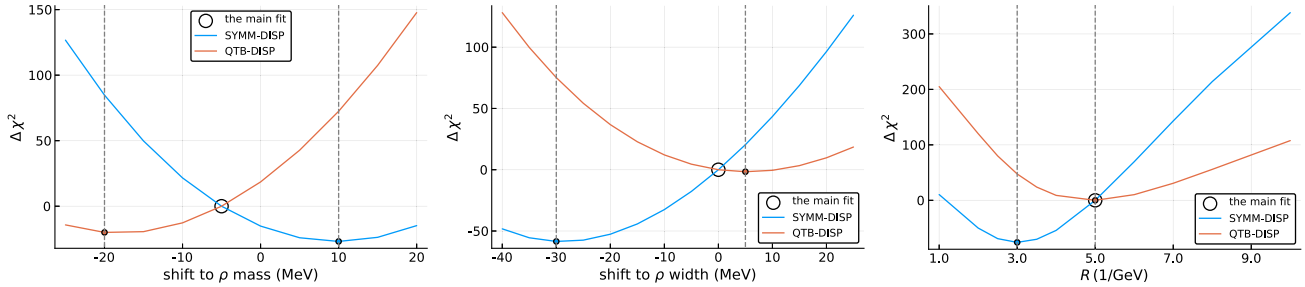

FIG. 8. The change of the χ^2 is plotted against the ρ-meson parameters in Eq. (9): the mass m_ρ, the width Γ_ρ and the Blatt-Weisskopf size parameter R. The vertical lines indicate the estimated values where the minimum is found.

TABLE II. The values m, g and χ^2 for fits described in Sec. V. For scans over parameters m_ρ, R and Γ_ρ we present the values of m, g and χ^2 obtained in the minimum in the profile χ^2 plots shown in Fig. 8.

				QTB-DISP			SYMM-DISP
#	Fit studies	m, GeV	g, GeV	χ^2/n.d.f.	m, GeV	g, GeV	χ^2/n.d.f.
1	$s < 2$ GeV^2	1.232	7.6	53/62	1.200	6.57	81/62
2	$R' = 3$ GeV^{-1}				1.211	7.00	18/100
3	$m'_\rho = m_\rho + 10$ MeV				1.207	6.85	83/100
4	$m'_\rho = m_\rho - 10$ MeV	1.204	7.23	37/100			
5	$m'_\rho = m_\rho - 20$ MeV	1.217	7.01	30/100			
6	$\Gamma'_\rho = \Gamma_\rho + 5$ MeV	1.223	7.45	66/100			
7	$\Gamma'_\rho = \Gamma_\rho - 30$ MeV				1.205	6.79	36/100

modification of the isobar line shape and the presence of interference terms. The importance of three-body effects is readily seen in the difference of SYMM-DISP and QTB-DISP pole positions, cf. Eqs. (29) and (22). Knowing that the interference between two $\rho\pi$ decay channels must be present, we now focus on systematic studies of SYMM-DISP, keeping QTB-DISP for a mere comparison. The largest systematic uncertainty is the dependence of the $a_1(1260)$ pole position on the line shape of the subchannel resonance ρ. In principle, we know that final-state interactions shift and skew the ρ peak. The scale of the ρ-meson mass shift can be estimated from the studies of ω/ϕ decays using Khuri-Treiman equations [48,50]. Figure 3 of Ref. [48] suggests a shift of the real and imaginary parts of the isobar amplitude of the order of 10 MeV before and after final-state interactions are taken into account. To estimate the effect on the $a_1(1260)$ pole position, we vary the parameters of $f_\rho(\sigma)$ in Eq. (9), i.e., the mass m_ρ, the width Γ_ρ and the Blatt-Weisskopf radius R, performing a χ^2 scan over each parameter, while keeping the others at their nominal values (Fig. 8). The new pole position obtained for the parameter value which minimizes the χ^2 for each scan is then used to estimate the systematic error for the pole position of the main fit. The results of these studies are summarized in Table II (see fit studies #2–7, were #4 was introduced as an additional intermediate point outside of the minimum). The $a_1(1260)$ pole position is extracted, the results for the pole mass and width are represented in Fig. 9 by open ellipses.

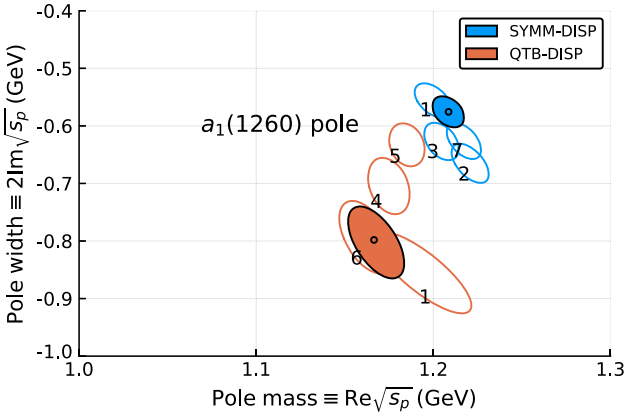

FIG. 9. Extracted $a_1(1260)$ pole positions in the models QTB-DISP and SYMM-DISP. The ellipses show the 2σ contour of the systematic uncertainties obtained by the bootstrap method. The results of the systematic tests are shown by the open ellipses. The numerical labels correspond to the indices of the studies described in Table II.

We perform an additional test of the influence of heavier resonances, as the $a_1(1640)$, by excluding the region $s > 2$ GeV^2 from the fit. The fit quality does not change substantially, but get slightly worse due to the reduction of the degrees of freedom (see #1 in Table II). The values for the pole position are shown in Fig. 9 and included to the systematic error of our final result.

The final systematic uncertainties are found by assigning the maximal deviation of the pole position in the systematic studies to the main fit SYMM-DISP:

$$m_p^{(a_1(1260))} = (1209 \pm 4^{+12}_{-9})\ \text{MeV},$$
$$\Gamma_p^{(a_1(1260))} = (576 \pm 11^{+89}_{-20})\ \text{MeV}.$$

where the first uncertainty is statistical and the second systematic.

VI. CONCLUSIONS

In this paper we have presented a new analysis of the lightest isovector axial-vector resonance $a_1(1260)$ decaying to three charged pions. Despite the fact that the corresponding $J^{PC} = 1^{++}$ partial wave dominates the hadronic weak decay of τ leptons as well as diffractive reactions of high-energy pions, the parameters of the $a_1(1260)$ are still poorly known. While the latter reactions suffer from an irreducible background due to nonresonant processes, the system of three pions produced in τ decay provides a very clean access to axial-vector resonances.

Compared to a two-particle system, however, the system of three interacting particles exhibits additional phenomena, such as 3-particle rescattering or interference between different decay chains. These 3-body effects are taken into account using reaction models constraining the dynamics in the total invariant mass, however, without imposing subchannel unitarity. We have considered four analytic models of an isolated resonance decaying to three pions via the $\rho\pi$ channel. All these models satisfied approximate three-body unitary, but differ by the left-hand singularities and the treatment of the interference between the two $\rho\pi$ decay channels. Using the $\tau^- \to \pi^-\pi^+\pi^-\nu_\tau$ data from ALEPH [54], we found that the dispersive models, having no left-hand singularities on the physical sheet, fit the data clearly better.

In order to find the pole position corresponding to the $a_1(1260)$ resonance, we have explored the analytic structure of the amplitude and performed its analytic continuation into the complex plane of the three-pion invariant mass squared, a challenging, and technically demanding task, requiring us to use a prescription for the integration paths in the two-pion invariant mass squared. We have searched for the singularities in the closest unphysical sheet, and have identified a pole as the $a_1(1260)$ resonance. The mass and width of the $a_1(1260)$ are given in terms of its pole position in the main SYMM-DISP model:

$$m_p^{(a_1(1260))} = (1209 \pm 4^{+12}_{-9})\ \text{MeV},$$
$$\Gamma_p^{(a_1(1260))} = (576 \pm 11^{+89}_{-20})\ \text{MeV}.$$

The dominant source of systematic errors is the sensitivity to the details of the subchannel interactions. The simplified QTB-DISP model, which neglects the interference between the two $\rho\pi$-channels, results in a significantly different pole position and a larger systematic uncertainty.

This analysis can be extended by further advancing the theoretical framework and constraining the model by fitting the Dalitz decay variables. This will be possible when the data from Belle II or BES III become available. In addition, the results from this analysis will help to better constrain the nonresonant background in diffractive reactions, as measured by the COMPASS experiment.

ACKNOWLEDGMENTS

This work was supported by the German Bundesministerium für Bildung und Forschung, the U.S. Department of Energy under Grants No. DE-AC05-06OR23177 and No. DE-FG02-87ER40365, Research Foundation—Flanders (FWO), PAPIIT-DGAPA (UNAM, Mexico) under Grants No. IA101717 and No. IA101819, CONACYT (Mexico) under Grant No. 251817, U.S. National Science Foundation under Grant No. PHY-1415459, Ministerio de Ciencia, Innovación y Universidades (Spain) Grants No. FPA2016-77313-P and No. FPA2016-75654-C2-2-P, and Universidad Complutense de Madrid.

APPENDIX A: STUDIES OF THE SPURIOUS POLE

Performing the analytical continuation in Sec. IV we have shown that, in addition to the expected $a_1(1260)$ pole, there is a spurious pole rather close to the physical region. At first, the spurious pole looks surprising, however, it is clearly present in every Breit-Wigner-like model of a resonance decaying to particles of different masses. Indeed, the denominator of the Breit-Wigner amplitude with energy-dependent width decaying to two scalar particles in an S-wave reads:

$$D_{\text{BW}}(s) = m^2 - s - im\Gamma(s),$$
$$\Gamma(s) = \frac{g^2}{16\pi m}\frac{\sqrt{(s-(m_1+m_2)^2)(s-(m_1-m_2)^2)}}{s}. \tag{A1}$$

When $m_1 \neq m_2$, the equation $D_{\text{BW}}(s) = 0$ has 4 complex roots, which we can identify by the order of the polynomial which gives those roots:

$$(16\pi s(m^2-s))^2 + g^4(s-(m_1+m_2)^2) \times (s-(m_1-m_2)^2) = 0 \tag{A2}$$

Since all coefficients of the polynomial are real, the poles appear in conjugated pairs above and below the real axis. The two Breit-Wigner poles below the real axis are analogous to the $a_1(1260)$ and the spurious pole. To demonstrate this further, we draw the complex plane of the $1/D_{\text{BW}}(s)$ function with $m = 1.2$ GeV, $g = 7.8$ GeV,

TABLE III. Extension of Table I with the models from Appendix A. We added the last column to present additional parameters which enter in the models.

Model	$\rho(s)$ in the numerator	$C(s)$ in the denominator	χ^2/n.d.f.	m, MeV	g, GeV	h, m'^2 GeV^2
sQTB − DISP$^{(2)}$	$\rho_{\text{QTB}}(s)$	$\tilde{\rho}_{\text{QTB}}(s)$	979/100	1.915	17.94	
sQTB − DISP$^{(3)}$	$\rho_{\text{QTB}}(s)$	$\tilde{\rho}_{\text{QTB}}(s)$	67/100	1.075	9.27	0.578
sQTB − DISP$^{(4)}$	$\rho_{\text{QTB}}(s)$	$\tilde{\rho}_{\text{QTB}}(s)$	42/100	1.229	6.01	−39.3, 0.0

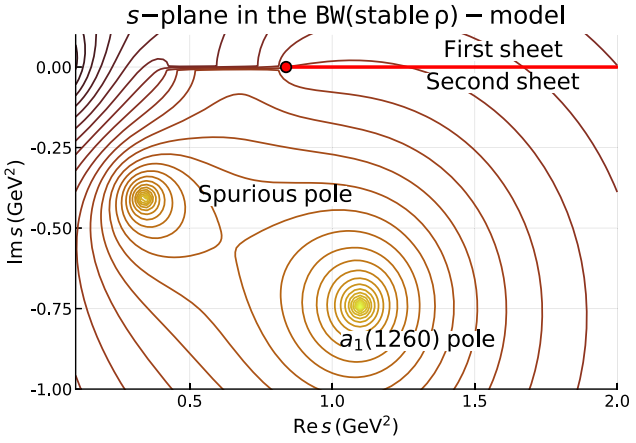

FIG. 10. Analytic continuation of the amplitude $1/D_{\rm BW}(s)$ from Eq. (A1). Lines indicate the $|D_{\rm BW}|$ equipotential levels. The poles of the amplitude are the bright spots. The red dots indicate branch points for channel openings.

$m_1 = m_\rho$, $m_2 = m_\pi$ in Fig. 10. We find that the spurious pole has no influence on the physical region as long as the resonance is far from threshold and rather narrow. Both poles become important for the real axis physics when the studied resonance is close to threshold or/and wider.

The spurious pole is a feature of Breit-Wigner-like models. It is generated by the $1/s$ singularity of the phase space in Eqs. (A1) and (20). In order to remove it, we try to exclude the $1/s$ factor from the dispersive term. Following the studies of QTB-DISP, we consider a new model for scattering and production amplitudes $\hat{t}(s) = t(s)/s$ and $\hat{a}(s) = a(s)/s$, and modify the unitarity equations accordingly.

$$2{\rm Im}\hat{t}(s) = \hat{t}^*(s)(s\rho_{\rm QTB}(s))\hat{t}(s), \tag{A3a}$$

$$2{\rm Im}\hat{a}(s) = \hat{t}^*(s)(s\rho_{\rm QTB}(s))\hat{a}(s), \tag{A3b}$$

where $s\rho(s)$ is free of the $1/s$ singularity. The parametrization which satisfies the unitarity constraints is

$$\hat{a}^{\rm sQTB-DISP^{(k)}}(s) = \frac{c'}{K_k^{-1}(s) - is\tilde{\rho}_{\rm QTB}(s)/2}, \tag{A4}$$

where the index k gives the number of parameters in the function $K_k^{-1}(s)$, the models are labeled $\texttt{sQTB}-\texttt{DISP}^{(k)}$. The function $s\rho(s)$ has a $\sim s^1$ asymptotic behavior, therefore the dispersive integral must be subtracted twice. The integrand is thus the same as in Eq. (15), but the integral is multiplied by an extra factor of s as in Eq. (A4). To make the dispersive integral independent of the subtraction points we must consider a polynomial of order $k \geq 2$. We consider three forms of functions $K_k(s)$,

$$K_2(s) = g^2/(m^2 - s), \tag{A5}$$

$$K_3(s) = g^2/(s(m^2 - s) + h) \tag{A6}$$

$$K_4(s) = g^2/(m^2 - s) + h'/(m'^2 - s) \tag{A7}$$

The $K_2(s)$ and $K_4(s)$ are inspired by the K-matrix approach with one and two poles, respectively, while $K_3(s)$ is a special two-pole model which exactly coincides with QTB-DISP when $h = 0$.

The models $\texttt{sQTB}-\texttt{DISP}^{(k)}$ are fitted to the data giving parameters presented in Table III. In Fig. 11 we show the continuation of the $\texttt{sQTB}-\texttt{DISP}^{(2)}$ model,

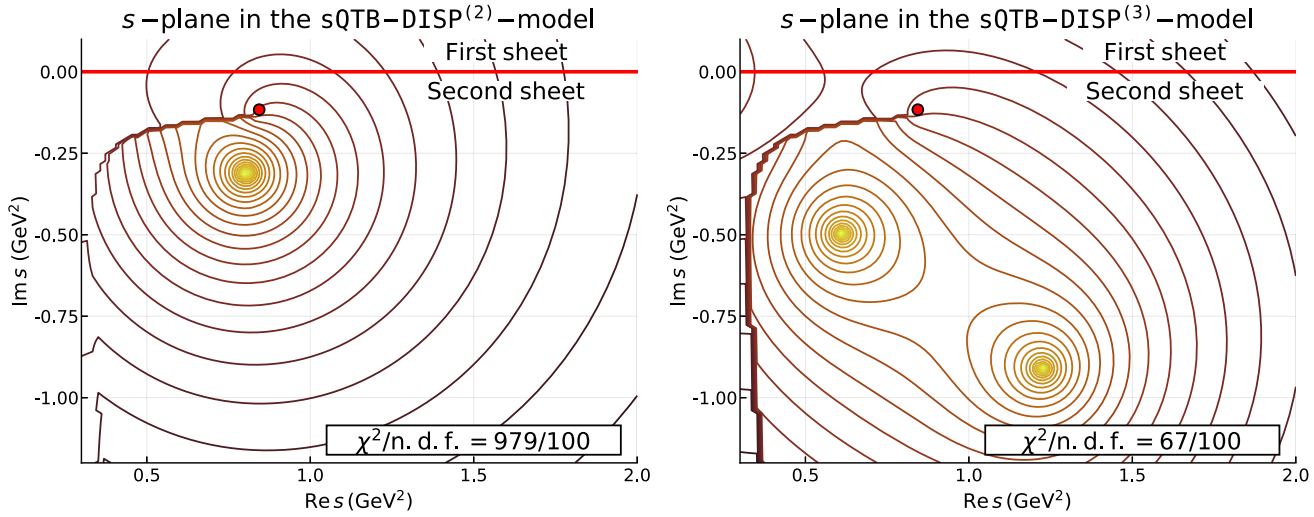

FIG. 11. $t(s)$ in the model sQTB − DISP$^{(k)}$. Lines indicate equipotential levels for the $|\hat{t}^{\rm sQTB-DISP^{(k)}}(s)|$ function from Eq. (A4). The poles of the amplitude are the yellow spots. The red dots indicate branch points for channel openings: 3π-branch point and $\rho\pi$-branch point. The complex plane for the model sQTB − DISP$^{(2)}$ (the models model sQTB − DISP$^{(3)}$) fitted to the data is shown in the left (right) plot. The quality of the fit is indicated in the legend box on the right.

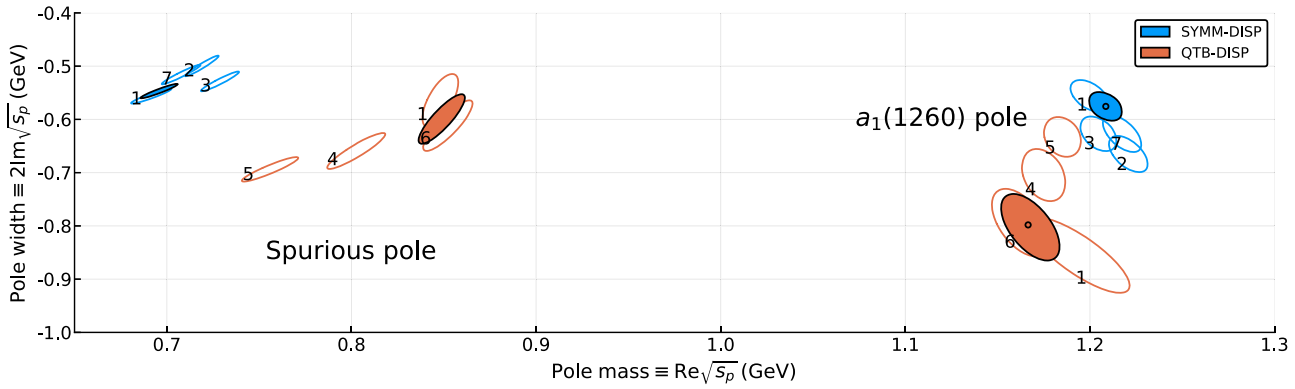

FIG. 12. Extracted pole positions in the models QTB-DISP and SYMM-DISP: the resonance poles are on the right, the spurious poles are on the left. The ellipses show the 2σ contours of the statistical uncertainties obtained by the bootstrap method. The results of the systematic tests are shown by the open ellipses. The numerical labels correspond to the indexes of the systematic tests described in Table II.

fitted to data. The spurious pole is no longer present. However, the quality of the fit is not acceptable: the best χ^2/n.d.f. is equal to 979/100. When we increase the freedom by taking the model $\mathtt{sQTB-DISP}^{(3)}$ the fit quality significantly improves to yield a $\chi^2/\text{n.d.f.} = 67/100$. Quite spectacularly, the picture of the complex plane is changed back: the place of the spurious pole is taken by the explicit pole introduced in the K-function (see the right plot of Fig. 11). The next relaxation of the setup in $\mathtt{sQTB-DISP}^{(4)}$ overfits the data and gives $\chi^2/\text{n.d.f.} = 42/100$. However, the positions of the resonance and spurious poles do not change much.

The position of the spurious pole was investigated for all systematic studies we performed in Sec. V as shown in Fig. 12.

APPENDIX B: ANALYTICAL SIMPLIFICATION OF THE PHASE-SPACE INTEGRAL

In this Appendix we demonstrate how the integrals in the phase-space factor $\rho(s)$ Eq. (12a) can be simplified using the properties of the Wigner D-functions.

$$\rho(s) = \frac{1}{2}\int \mathrm{d}\Phi_3 |f_\rho(\sigma_1)N_0(\Omega_1,\Omega_{23}) - f_\rho(\sigma_3)N_0(\Omega_3,\Omega_{12})|^2, \tag{B1}$$

We start by explicitly defining the angles in the decay functions $N_0(\Omega_k,\Omega_{ij})$ given by Eq. (8). The three-pion center-of-mass (CM) frame is oriented by the direction of W in τ decay (W helicity frame). The momentum vector of the τ defines the xz plane, a.k.a. the production plane. $\Omega_k = (\theta_k,\phi_k)$ denotes the polar and azimuthal angles of the vector $\vec{p}_i + \vec{p}_j$ in the CM-frame. The $\Omega_{ij} = (\theta_{ij},\phi_{ij})$ are the spherical angles of the pion i in the helicity frame of the isobar (ij). This helicity frame is obtained from the CM frame by active rotation $R^{-1}(\Omega_k)$ and boost along the z-axis. Equivalently, we can notice that the boost does not change azimuthal orientation, therefore, the y-axis direction $\vec{e}_y$ in the helicity frame can be found by $\vec{e}'_z \times \vec{e}_z$, where $\vec{e}'_z$ is the original orientation of the CM z-axis.

We write the phase-space differential through the two pairs of spherical angles.

$$\begin{aligned}\mathrm{d}\Phi_3 &= \frac{\mathrm{d}\sigma_1}{2\pi}\frac{1}{8\pi}\frac{\sqrt{\lambda_{s1}}}{s}\frac{\mathrm{d}\Omega_1}{4\pi}\frac{1}{8\pi}\frac{\sqrt{\lambda_1}}{\sigma_1}\frac{\mathrm{d}\Omega_{23}}{4\pi} \\ &= \frac{\mathrm{d}\sigma_3}{2\pi}\frac{1}{8\pi}\frac{\sqrt{\lambda_{s3}}}{s}\frac{\mathrm{d}\Omega_3}{4\pi}\frac{1}{8\pi}\frac{\sqrt{\lambda_3}}{\sigma_3}\frac{\mathrm{d}\Omega_{12}}{4\pi},\end{aligned} \tag{B2}$$

where we used $\lambda_i = \lambda(\sigma_i, m_\pi^2, m_\pi^2)$, $\lambda_{si} = \lambda(s,\sigma_i,m_\pi^2)$, with $\lambda(x,y,z) = x^2+y^2+z^2-2(xy+yz+zx)$ the Källén triangle function. The decay functions are conveniently normalized:

$$\int \frac{\mathrm{d}\Omega_k}{4\pi}\frac{\mathrm{d}\Omega_{ij}}{4\pi}|N_0(\Omega_k,\Omega_{ij})|^2 = 1. \tag{B3}$$

Now we can expand the squared expression in Eq. (B1), use the normalization property, and combine the squared terms,

$$\begin{aligned}\rho_{\mathrm{SYMM}}(s) = &\underbrace{\frac{1}{2\pi(8\pi)^2 s}\int |f_\rho(\sigma_1)|^2\frac{\sqrt{\lambda_1\lambda_{s1}}}{\sigma_1}\mathrm{d}\sigma_1}_{\rho_{\mathrm{QTB}}(s)} \\ &\underbrace{-\int \mathrm{d}\Phi_3 f_\rho(\sigma_1)f_\rho^*(\sigma_3)N_0(\Omega_1,\Omega_{23})N_0^*(\Omega_3,\Omega_{12})}_{\rho_{\mathrm{INT}}(s)},\end{aligned} \tag{B4}$$

where we used the observation that the last integral is real. Indeed, the term transforms to itself under complex

conjugation due to the $1 \leftrightarrow 3$ symmetry of the differential phase space and the relation $N_0(\Omega_k, \Omega_{ij}) = -N_0(\Omega_k, \Omega_{ji})$ following from

$$\begin{aligned} D^l_{\lambda 0}(\Omega_{ji}) &= d^l_{\lambda 0}(\pi - \theta_{ij}) e^{-i\lambda(\pi+\phi_{23})} \\ &= (-1)^{l+\lambda} d^l_{\lambda 0}(\theta_{ij})(-1)^{\lambda} e^{-i\lambda\phi_{23}} \\ &= (-1)^l D^l_{\lambda 0}(\Omega_{ij}), \end{aligned} \tag{B5}$$

for $l = 1$, which has to be used for both terms $N_0(\Omega_3, \Omega_{12})$ and $N_0(\Omega_1, \Omega_{23})$.

The interference term can be further simplified by integrating over three angular variables. The $N_\Lambda(\Omega_3, \Omega_{12})$ contains a product of Wigner D-functions which can be written as

$$\begin{aligned} D^{1*}_{\Lambda\lambda}(\Omega_3) D^{1*}_{\lambda 0}(\Omega_{12}) &= D^{1*}_{\Lambda\lambda}(\phi_3, \theta_3, \phi_{12}) d^1_{\lambda 0}(\theta_{12}) \\ &= \sum_{\lambda'} D^{1*}_{\Lambda\lambda'}(\phi_1, \theta_1, \phi_{23}) d^1_{\lambda'\lambda}(\hat{\theta}_{13}) d^1_{\lambda 0}(\theta_{12}), \end{aligned} \tag{B6}$$

where $\hat{\theta}_{13}$ is the angle between $\vec{p}_1$ and $\vec{p}_3$ in CM-frame. One can understand the relation in the following way. The $D^{1*}_{\Lambda\lambda}(\Omega_3) = D^{1*}_{\Lambda\lambda}(\phi_3, \theta_3, 0)$ and $D^{1*}_{\lambda 0}(\Omega_{12}) = D^{1*}_{\lambda 0}(\phi_{12}, \theta_{12}, 0)$ represent the rotations $[R_z(\phi_3) R_y(\theta_3)]^{-1}$ and $[R_z(\phi_{12}) R_y(\theta_{12})]^{-1}$. The first transformation rotates the 3π system in the CM-frame such that the momentum $\vec{p}_1 + \vec{p}_2 = -\vec{p}_3$ is aligned to the z-axis. When the system is boosted to the (12) rest frame (helicity frame), the second transformation aligns $\vec{p}_1$ to z-axis (we remind that Ω_{12} stands for the spherical angles of the particle 1 in the (12) helicity frame). Since the rotation $R_z(\phi_{12})$ commutes with the boost along z-axis, we can combine the three rotations in CM-frame, $R_z^{-1}(\phi_{12}) R_y^{-1}(\theta_3) R_z^{-1}(\phi_3)$. The combined transformation has a clear meaning: it brings the 3π system to the x-z plane such that $\vec{p}_3$ points to $-z$-direction. The transformation $R_z^{-1}(\phi_{23}) R_y^{-1}(\theta_1) R_z^{-1}(\phi_1)$ also brings the 3π system to the xz-plane while $\vec{p}_1$ is aligned with $-z$-direction. The difference between the results of the transformations is a rotation about y-axis, represented by $d^1_{\lambda'\lambda}(\hat{\theta}_{13})$. In that way, the function $D^{*1}_{\Lambda\lambda}(\phi_1, \theta_1, \theta_{23})$ appears in both decay functions in the interference term in Eq. (B4). This allows us to solve three angular integrals analytically. The expression for $\rho_{\rm INT}$ is simplified as follows:

$$\begin{aligned} \rho_{\rm INT}(s) = \frac{1}{(8\pi)^2 s} \int \frac{d\sigma_1}{2\pi} \frac{d\cos\theta_{23}}{2} f^*_\rho(\sigma_3) f_\rho(\sigma_1) \frac{\sqrt{\lambda_1 \lambda_{s1}}}{\sigma_1} \\ \times \sum_{\lambda,\lambda'} d^1_{\lambda 0}(\theta_{23}) d^1_{\lambda\lambda'}(\hat{\theta}_{13}) d^1_{\lambda' 0}(\theta_{12}). \end{aligned} \tag{B7}$$

All angles can be expressed through the invariants,

$$\begin{aligned} \cos\theta_{23} &= \frac{\sigma_1(\sigma_3 - \sigma_2)}{\sqrt{\lambda_1 \lambda_{s1}}}, \\ \sin\theta_{23} &= \frac{2\sqrt{\sigma_1}\sqrt{\phi(s, \sigma_1, \sigma_3)}}{\sqrt{\lambda_1 \lambda_{s1}}}, \end{aligned} \tag{B8}$$

$$\begin{aligned} \cos\theta_{12} &= \frac{\sigma_3(\sigma_2 - \sigma_1)}{\sqrt{\lambda_3 \lambda_{s3}}}, \\ \sin\theta_{12} &= \frac{2\sqrt{\sigma_3}\sqrt{\phi(s, \sigma_1, \sigma_3)}}{\sqrt{\lambda_3 \lambda_{s3}}}, \end{aligned} \tag{B9}$$

$$\begin{aligned} \cos\hat{\theta}_{13} &= \frac{2s(2m_\pi^2 - \sigma_2) + (s + m_\pi^2 - \sigma_1)(s + m_\pi^2 - \sigma_3)}{\sqrt{\lambda_{s1}\lambda_{s3}}}, \\ \sin\hat{\theta}_{13} &= \frac{2\sqrt{s}\sqrt{\phi(s, \sigma_1, \sigma_3)}}{\sqrt{\lambda_{s1}\lambda_{s3}}}. \end{aligned} \tag{B10}$$

where we introduced the Kibble function ϕ as it enters all $\sin\theta$ expressions [62],

$$\begin{aligned} \phi(s, \sigma_1, \sigma_3) &= \sigma_1\sigma_2\sigma_3 - m_\pi^2(s - m_\pi^2)^2, \\ \sigma_2 &= s + 3m_\pi^2 - \sigma_1 - \sigma_3. \end{aligned} \tag{B11}$$

We combined the d-functions in Eq. (B7) and get the expressions for the angular part through invariants [63]:

$$\begin{aligned} \sum_{\lambda,\lambda'} d^1_{\lambda 0}(\theta_{23}) d^1_{\lambda\lambda'}(\hat{\theta}_{13}) d^1_{\lambda' 0}(\theta_{12}) &= \cos(\theta_{12} + \hat{\theta}_{13} - \theta_{23}) \\ &= \frac{H(\sqrt{s}, \sqrt{\sigma_1}, \sqrt{\sigma_3})}{\lambda_1^{1/2} \lambda_3^{1/2} \lambda_{s1} \lambda_{s3}}, \end{aligned} \tag{B12}$$

where $H(\sqrt{s}, \sqrt{\sigma_1}, \sqrt{\sigma_3})$ is a polynomial in $\sqrt{\sigma_1}$, $\sqrt{\sigma_3}$, and $\sqrt{s}$. The expression $H(\sqrt{s}, \sqrt{\sigma_1}, \sqrt{\sigma_3})$ is further factorized [64] and cancels terms zeros of the denominator which otherwise would be pole singularities in the physical reason.

$$\begin{aligned} H(s, \sigma_1, \sigma_3) = \sqrt{\sigma_1\sigma_3}(\sqrt{s} - \sqrt{\sigma_1} - m_\pi)(\sqrt{s} - \sqrt{\sigma_1} + m_\pi) \\ \times (\sqrt{s} - \sqrt{\sigma_3} - m_\pi)(\sqrt{s} - \sqrt{\sigma_3} + m_\pi) \\ \times W(\sqrt{s}, \sqrt{\sigma_1}, \sqrt{\sigma_3}), \end{aligned} \tag{B13}$$

with the polynomial $W(\sqrt{s}, \sqrt{\sigma_1}, \sqrt{\sigma_3})$ given by

$$W(a,b,c) = -4m_\pi^6 + 4m_\pi^2 s^2 - 4m_\pi^4 ab + 4m_\pi^2 a^3 b - 4m_\pi^4 ac + 4m_\pi^2 a^3 c - 9m_\pi^4 bc + 8m_\pi^2 a^2 bc + a^4 bc + 14m_\pi^2 ab^2 c + 2a^3 b^2 c + 9m_\pi^2 b^3 c - a^2 b^3 c - 4ab^4 c - 2b^5 c + 14m_\pi^2 abc^2 + 2a^3 bc^2 + 12m_\pi^2 b^2 c^2 - 6ab^3 c^2 - 4b^4 c^2 + 9m_\pi^2 bc^3 - a^2 bc^3 - 6ab^2 c^3 - 5b^3 c^3 - 4abc^4 - 4b^2 c^4 - 2bc^5. \tag{B14}$$

The angular function from Eq. (B12) is simplified to its final form

$$\cos(\theta_{12} + \hat{\theta}_{13} - \theta_{23}) = \frac{W(\sqrt{s}, \sqrt{\sigma_1}, \sqrt{\sigma_3})}{((\sqrt{s} + \sqrt{\sigma_1})^2 - m_\pi^2)((\sqrt{s} + \sqrt{\sigma_3})^2 - m_\pi^2)\sqrt{(\sigma_1 - 4m_\pi^2)(\sigma_3 - 4m_\pi^2)}}. \tag{B15}$$

The final expression for the interference term is

$$\rho_{\mathrm{INT}}(s) = \frac{1}{2\pi(8\pi)^2 s}\int_{4m_\pi^2}^{\sigma_{\mathrm{lim}}} \mathrm{d}\sigma_1 \int_{\sigma_3^-(\sigma_1,s)}^{\sigma_3^+(\sigma_1,s)} \mathrm{d}\sigma_3 \times \frac{f_\rho^*(\sigma_1)}{\sqrt{\sigma_1 - 4m_\pi^2}} \frac{f_\rho(\sigma_3)}{\sqrt{\sigma_3 - 4m_\pi^2}} \times \frac{W(\sqrt{s}, \sqrt{\sigma_1}, \sqrt{\sigma_3})}{((\sqrt{s} + \sqrt{\sigma_1})^2 - m_\pi^2)((\sqrt{s} + \sqrt{\sigma_3})^2 - m_\pi^2)}. \tag{B16}$$

APPENDIX C: THE DALITZ PLOT INTEGRAL IN THE COMPLEX PLANE

To address the issues of the evaluation of Eq. (B16) for complex values of s, we consider a simplified version of the problem:

$$X(s) = \int_{\sigma_{\mathrm{th}}}^{\sigma_{\mathrm{lim}}} \mathrm{d}\sigma_1 \int_{\sigma_3^-(\sigma_1,s)}^{\sigma_3^+(\sigma_1,s)} \mathrm{d}\sigma_3 \frac{1}{\sqrt{\sigma_3 - 4m_\pi^2}}, \tag{C1}$$

where $\sigma_{\mathrm{th}} = 4m_\pi^2$, $\sigma_{\mathrm{lim}} = (\sqrt{s} - m_\pi)^2$, $\sigma_3^\pm(\sigma_1, s) = (s + 3m_\pi^2 - \sigma_1)/2 \pm {\lambda_1}^{1/2}{\lambda_{s1}}^{1/2}/(2\sigma_1)$. Similar to Eq. (B16) this expression contains two nested integrals with the same limits. The integrand has a branch point at $4m_\pi^2$, the integration paths have to be modified in order to avoid crossing the cut. The position of the $\sigma_3^\pm$ are shown in Fig. 13 for $s = \mathrm{Re}s + i\epsilon$. We observe that the σ_3^+ has always positive imaginary part and stays far from the branch point $\sigma_3 = 4m_\pi^2$. The σ_3^- circles around the branch point changing the sheet of the integrand. When $\sigma_1 = \sigma_{\mathrm{lim}}$, the σ_3 endpoints nearly coincide, $\sigma_3^\pm(\sigma_{\mathrm{lim}}) = m_\pi(\sqrt{s} + m_\pi) \pm i\epsilon$, however, they are on the different sides of the integrand cut. In other words, if a straight line

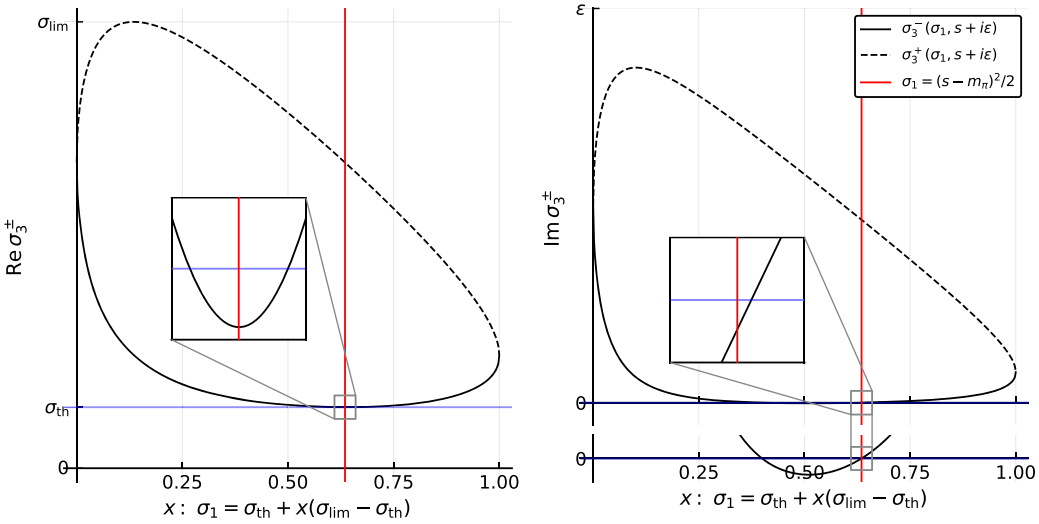

FIG. 13. The left (right) plot presents the real (imaginary) part of the $\sigma_3^\pm$ as a function of σ_1 for a fixed value of $s + i\epsilon$. The σ_1 is changed linearly between the integration limits. The zoomed plots show how the σ_3^- passes the real axis first below the branch point $\sigma_{\mathrm{th}} = 4m_\pi^2$, then returns above the branch point performing the circling. The red line indicates the closest point on the σ_1-path to the $(s-1)/2$ since it does not go exactly through it.

integration in σ_3 is done, we should observe a singularity related to the circling in the complex σ_1 plane. The inner integral can be solved analytically.

$$X(s) = 2\int_{\sigma_{\rm th}}^{\sigma_{\rm lim}} d\sigma_1 \left(\sqrt{\sigma_3^+(\sigma_1, s) - 4m_\pi^2} - \sqrt{\sigma_3^-(\sigma_1, s) - 4m_\pi^2} \right), \quad \text{(C2)}$$

where the first term does not give problems near the physical region since σ_3^+ stays away from $4m_\pi^2$. However, the second square root has two branch points at $(s - m_\pi^2)/2$ in the σ_1 plane. (Another example of a simple function with two adjoined square root branch points is $\sqrt{z^2}$.)

$$\sigma_3^+(\sigma_1, s) - 4m_\pi^2 = 0 \to (\sigma_1 - (s - m_\pi^2)/2)^2 = 0 \quad \text{(C3)}$$

Figure 14 shows the σ_1 plane, where we see that a straight connection between $\sigma_{\rm th}$ and $\sigma_{\rm lim}$ is not allowed by the presence of the cut. Here, two options arise:

(1) $X^{(1)}$: we draw the σ_1 path directly through the branch point $(s - m_\pi^2)/2$ (the point P in Fig. 13 can be aligned with the branch point $(s - m_\pi^2)/2$). The point $\sigma_1 = (s - m_\pi^2)/2$ is special because when the path goes through it, the σ_3^- does not circle the branch point but just touches it.

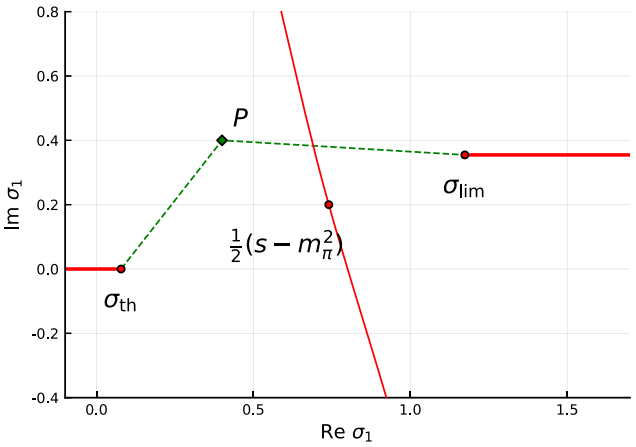

FIG. 14. Analytical structure of the integrand in Eq. (C2). The branch points are shown by the red dots with the cuts indicated by the solid red lines. The arbitrary integration path $\sigma_{\rm th} \to {\rm P} \to \sigma_{\rm lim}$ is shown by the dashed green line.

(2) $X^{(2)}$: we go analytically under the cut taking any arbitrary path. $X^{(2)}$ corresponds to the function which we would obtain connecting the points $\sigma_3^\pm$ properly, i.e., avoiding $1/\sqrt{\sigma_3 - 4m_\pi^2}$ cut.

The two options give two different analytical functions. Additional discussions on the subject can be found in Refs. [14,60].

[1] M. Tanabashi *et al.* (Particle Data Group), Phys. Rev. D **98**, 030001 (2018).
[2] S. Dürr, Z. Fodor, J. Frison, C. Hoelbling, R. Hoffmann *et al.*, Science **322**, 1224 (2008).
[3] J. J. Dudek, R. G. Edwards, M. J. Peardon, D. G. Richards, and C. E. Thomas, Phys. Rev. D **82**, 034508 (2010).
[4] C. Adolph *et al.* (COMPASS Collaboration), Phys. Rev. Lett. **115**, 082001 (2015).
[5] M. Mikhasenko, B. Ketzer, and A. Sarantsev, Phys. Rev. D **91**, 094015 (2015).
[6] M. Mikhasenko, arXiv:1507.06552.
[7] F. Aceti, L. R. Dai,, and E. Oset, Phys. Rev. D **94**, 096015 (2016).
[8] A. P. Szczepaniak, Phys. Lett. B **757**, 61 (2016).
[9] A. P. Szczepaniak, Phys. Lett. B **747**, 410 (2015).
[10] A. Pilloni, C. Fernández-Ramírez, A. Jackura, V. Mathieu, M. Mikhasenko, J. Nys, and A. P. Szczepaniak (JPAC Collaboration), Phys. Lett. B **772**, 200 (2017).
[11] A. Esposito, A. Pilloni, and A. D. Polosa, Phys. Rep. **668**, 1 (2017).
[12] F.-K. Guo, C. Hanhart, U.-G. Meißner, Q. Wang, Q. Zhao, and B.-S. Zou, Rev. Mod. Phys. **90**, 015004 (2018).
[13] S. L. Olsen, T. Skwarnicki,, and D. Zieminska, Rev. Mod. Phys. **90**, 015003 (2018).
[14] I. J. R. Aitchison and R. Pasquier, Phys. Rev. **152**, 1274 (1966).
[15] W. J. Holman, Phys. Rev. **138**, B1286 (1965).
[16] G. N. Fleming, Phys. Rev. **135**, B551 (1964).
[17] R. J. Eden, P. V. Landshoff, D. I. Olive, and J. C. Polkinghorne, *The Analytic S-Matrix* (Cambridge University Press, Cambridge, England, 1966).
[18] M. Mai, B. Hu, M. Doring, A. Pilloni, and A. Szczepaniak, Eur. Phys. J. A **53**, 177 (2017).
[19] M. T. Hansen and S. R. Sharpe, Phys. Rev. D **95**, 034501 (2017).
[20] R. A. Briceño, M. T. Hansen, and S. R. Sharpe, Phys. Rev. D **95**, 074510 (2017).
[21] R. A. Briceño, M. T. Hansen, and S. R. Sharpe, Phys. Rev. D **98**, 014506 (2018).
[22] Y. Meng, C. Liu, U.-G. Meißner, and A. Rusetsky, Phys. Rev. D **98**, 014508 (2018).
[23] F. Romero-López, A. Rusetsky, and C. Urbach, Eur. Phys. J. C **78**, 846 (2018).
[24] M. Mai and M. Döring, Eur. Phys. J. A **53**, 240 (2017).
[25] L. Roca, E. Oset, and J. Singh, Phys. Rev. D **72**, 014002 (2005).
[26] H. Nagahiro, K. Nawa, S. Ozaki, D. Jido, and A. Hosaka, Phys. Rev. D **83**, 111504 (2011).

[27] S. Eidelman (Particle Data Group), Phys. Lett. B **592**, 1 (2004).
[28] G. Ascoli, L. Jones, B. Weinstein, and H. Wyld, Phys. Rev. D **8**, 3894 (1973).
[29] J. L. Basdevant and E. L. Berger, Phys. Rev. D **16**, 657 (1977).
[30] R. T. Deck, Phys. Rev. Lett. **13**, 169 (1964).
[31] M. Aghasyan *et al.* (COMPASS Collaboration), Phys. Rev. D **98**, 092003 (2018).
[32] M. G. Bowler, Phys. Lett. B **182**, 400 (1986).
[33] J. H. Kuhn and E. Mirkes, Z. Phys. C **56**, 661 (1992); **67**, 364(E) (1995).
[34] N. Isgur, C. Morningstar, and C. Reader, Phys. Rev. D **39**, 1357 (1989).
[35] D. G. Dumm, P. Roig, A. Pich, and J. Portoles, Phys. Lett. B **685**, 158 (2010).
[36] I. M. Nugent, T. Przedzinski, P. Roig, O. Shekhovtsova, and Z. Was, Phys. Rev. D **88**, 093012 (2013).
[37] G. Colangelo, M. Finkemeier, E. Mirkes, and R. Urech, Nucl. Phys. B, Proc. Suppl. **55C**, 325 (1997).
[38] D. Asner *et al.* (CLEO Collaboration), Phys. Rev. D **61**, 012002 (1999).
[39] R. A. Briere *et al.* (CLEO Collaboration), Phys. Rev. Lett. **90**, 181802 (2003).
[40] C. Adolph *et al.* (COMPASS Collaboration), Phys. Rev. D **95**, 032004 (2017).
[41] P. Collins, *An Introduction to Regge Theory & High Energy Physics*, 1st ed. (Cambridge University Press, Cambridge, England, 1977).
[42] A. Martin and T. Spearman, *Elementary Particle Theory*, 1st ed. (North-Holland, Amsterdam, 1970).
[43] J. Pisut and M. Roos, Nucl. Phys. **B6**, 325 (1968).
[44] J. L. Basdevant and E. L. Berger, Phys. Rev. D **19**, 239 (1979).
[45] D. V. Bugg, B. S. Zou,, and A. V. Sarantsev, Nucl. Phys. **B471**, 59 (1996).
[46] A. V. Anisovich, V. A. Nikonov, A. V. Sarantsev, V. V. Anisovich, M. A. Matveev, T. O. Vulfs, K. V. Nikonov, and J. Nyiri, Phys. Rev. D **84**, 076001 (2011).
[47] I. Aitchison and J. Brehm, Phys. Lett. B **84**, 349 (1979).
[48] F. Niecknig, B. Kubis, and S. P. Schneider, Eur. Phys. J. C **72**, 2014 (2012).
[49] F. Niecknig and B. Kubis, J. High Energy Phys. 10 (2015) 142.
[50] I. V. Danilkin, C. Fernandez-Ramirez, P. Guo, V. Mathieu, D. Schott, M. Shi, and A. P. Szczepaniak, Phys. Rev. D **91**, 094029 (2015).
[51] M. Albaladejo and B. Moussallam, Eur. Phys. J. C **77**, 508 (2017).
[52] G. Colangelo, S. Lanz, H. Leutwyler, and E. Passemar, Phys. Rev. Lett. **118**, 022001 (2017).
[53] I. Lorenz and E. Passemar, Proc. Sci. ICHEP2016 (**2016**) 539.
[54] S. Schael *et al.* (ALEPH Collaboration), Phys. Rep. **421**, 191 (2005).
[55] M. Davier, A. Hcker, B. Malaescu, C.-Z. Yuan, and Z. Zhang, Eur. Phys. J. C **74**, 2803 (2014).
[56] K. Svanberg, SIAM J. Optim. **12**, 555 (2006).
[57] J. Revels, M. Lubin, and T. Papamarkou, arXiv:1607.07892.
[58] W. H. Press, S. A. Teukolsky, W. T. Vetterling, and B. P. Flannery, *Numerical Recipes in FORTRAN: The Art of Scientific Computing* (Press Syndicate of the University of Cambridge, Cambridge, England, 1992).
[59] B. Efron and R. J. Tibshirani, *An Introduction to the Bootstrap*, Monographs on Statistics and Applied Probability No. 57 (Chapman & Hall/CRC, Boca Raton, Florida, USA, 1993).
[60] R. Pasquier and J. Y. Pasquier, Phys. Rev. **170**, 1294 (1968).
[61] R. C. Hwa, Phys. Rev. **130**, 2580 (1963).
[62] T. W. B. Kibble, Phys. Rev. **117**, 1159 (1960).
[63] A. Meurer, PeerJ Comput. Sci. **3**, e103 (2017).
[64] W. R. Inc, *Mathematica*, Version 11.3 (Wolfram Research, Inc., Champaign, IL, 2018).

Chapter 4

Regge pole trajectories

The relevance of the Regge theory has been shown in several sections of this thesis, however, despite its application in the previous sections to meson-meson scattering 2.2.3, 2.2.4, 2.3 and 3.3.3 we introduced only one of its main features. In next sections we will detail how Regge physics, together with dispersion relations, are capable of determining the Regge trajectory of an isolated resonance from first principles and the parameters of the associated pole. We thus do not rely on fits to several resonances of the same family, or in simple models. In section 4.1 we will detail the main features of such application, just to present the original result in section 4.1.3. This will be the last chapter of this thesis before the conclusions and the Appendixes.

4.1 Regge phenomenology

In section 1.4 we introduced the reader to the general concepts and formulas of Regge theory used throughout several sections of this thesis. In this chapter we will focus on the application of Regge theory, together with dispersion relations, to the determination of the Regge trajectories of the resonances of interest. In particular we will study two light scalar mesons.

If we have an isolated pole, its Regge contribution to the partial wave is of the form

(Eq.(1.105))

$$\begin{aligned} f_\ell(t) &= \frac{1}{32\pi}\int_{-1}^{1} dz_t P_\ell(z_t) T(s,t) \\ &= \frac{1}{32\pi}\int_{-1}^{1} dz_t P_\ell(z_t)(P_\alpha(-z_t) \pm P_\alpha(z_t))\frac{-\pi(2\alpha(t)+1)}{2\sin\pi\alpha(t)}\beta(t) \\ &= -\frac{1}{32\pi}(1\pm(-1)^\ell)\beta(t)\frac{2\alpha(t)+1}{(\alpha(t)-\ell)(\alpha(t)+\ell+1)}. \end{aligned} \tag{4.1}$$

Let us call t_r the value of t where $\alpha(t_r)=\ell$, so that if we are close enough to t_r the trajectory can be expanded as $\alpha(t)\approx \ell + (t-t_r)\alpha'_R(t_t) + i\alpha_I(t_r)$. Substituting this approximation into the above equation one gets

$$f_\ell(t) \approx \frac{\beta(t_r)/\alpha'_R(t_r)}{t_r - t - i\alpha_I(t_r)/\alpha'_R(t_r)}, \tag{4.2}$$

which compared to the customary Breit-Wigner formula entails $M=\sqrt{t_r}$ and $\Gamma = \alpha_I(t_r)/(\alpha'_R(t_r)M)$. When t_r is below threshold, $\alpha_I(t_r)=0$ and we recover the behavior of a bound state. Hence it is clear now how bound states and resonances relate with Regge poles. As shown in Eq. (4.1), depending on the signature the resonance is produced when $\mathrm{Re}\,\alpha$ crosses an even or an odd integer ℓ value for mesons, or half-integer value for baryons.

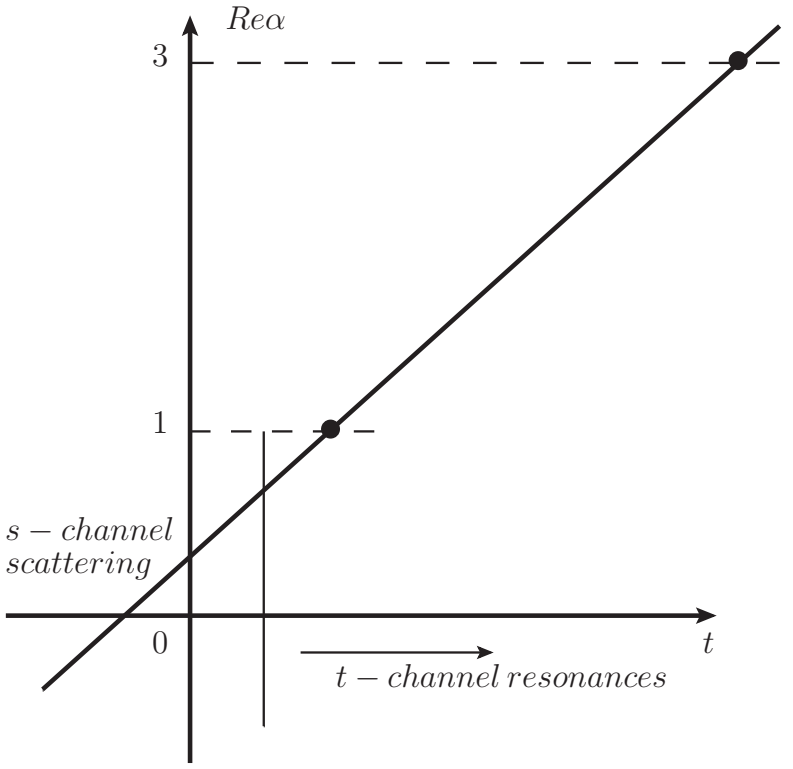

Figure 4.1: A Chew-Frautschi plot describing an ordinary Regge trajectory.

Let us focus for a moment on the ordinary behavior of Regge trajectories for relativistic scattering. Even though there is no rigorous proof, phenomenologically,

its os observed that almost all Regge trajectories have a real part which increases as a straight line of the energy squared t. This behavior is distinctive of both mesons and baryons, which also share the same slopes (~ 1 GeV^{-2}). These straight lines will connect families of resonances of the same signature, every 2 integer values of the total angular momentum or every integer if the trajectories are degenerated.

It is worth noticing that for large values of s, t becomes negative, is in this region, where the resonance with the largest value of $\mathrm{Re}\,\alpha$ will be the one dominating the exchange (Fig. 4.1), and hence the one describing the asymptotic behavior. This translates into a simple property for mesons, usually, the asymptotic behavior is controlled by the lightest relevant resonances, as it is the case for the $\rho(770)$ family (see Fig. 4.2).

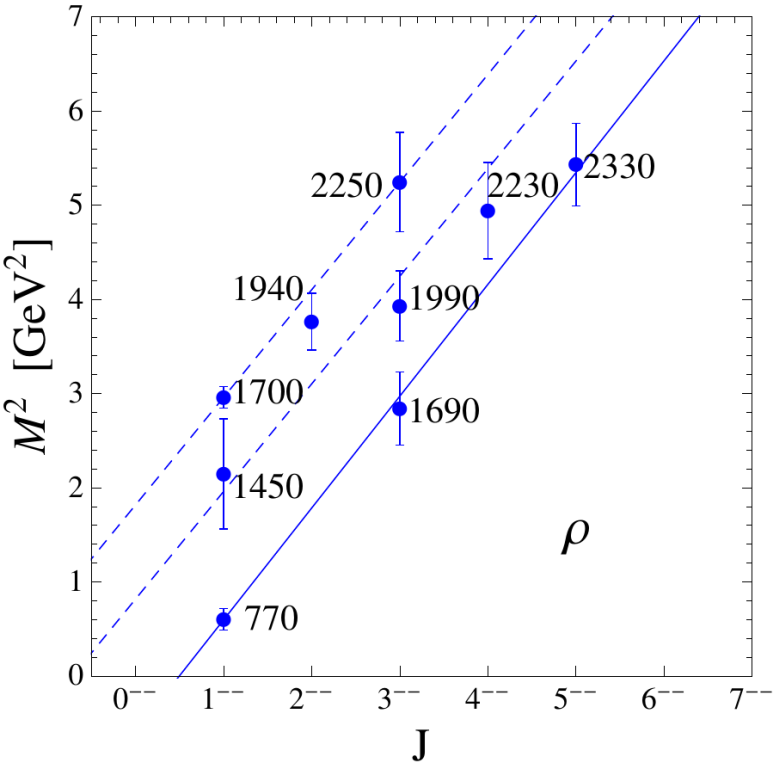

Figure 4.2: Figure from [245] (P. Masjuan et al.). A Chew-Frautschi plot describing the trajectory of the $\rho(770)$ (continuous line) together with other ρ resonances (dashed lines).

In what follows next, we focus on the properties of Regge trajectories described by an isolated pole. Let us start by choosing a given signature, and change the t channel for the s channel, so that the formula derived above can be written as

$$f_\ell(s) \simeq \frac{\beta(s)}{\ell - \alpha(s)}. \tag{4.3}$$

Actually, a partial wave would be described by several resonances, plus some background, but in this case we will restrict ourselves to the vicinity of the resonance of interest, so

that the final formula reads

$$f_\ell(s) = \frac{\beta(s)}{\ell - \alpha(s)} + f_{back}(s). \tag{4.4}$$

Now, one can make use of the properties derived in section 1.3.2 to obtain the analytic structure of the functions $\beta(s)$ and $\alpha(s)$. For meson-meson scattering, the partial wave has three singular structures in the first Riemann sheet, the right hand cut created by s-channel unitarity, the left hand cut produced by crossed channel interactions, and a circular cut in the unequal mass case due to the projection formula. It can be rigorously proven however [87] that the Regge trajectory and residue are only producing the first one, and thus have only a right hand cut, starting at their threshold, until infinity. On top of that, if one demands elastic unitarity hence, then

$$\mathrm{Im}\,\alpha(s) = \rho(s)\beta(s), \tag{4.5}$$

where $\rho(s) = \frac{2q(s)}{\sqrt{s}}$ is the two-particle phase space. By making use now of the Schwarz reflection principle one gets $\alpha^*(s) = \alpha(s^*)$ and $\beta^*(s) = \beta(s^*)$; These relations are useful when manipulating the dispersion relations. Taking into account all formulas above we can write a once-subtracted dispersion relation for $\alpha(s)$ as

$$\mathrm{Re}\,\alpha(s) = \alpha(0) + \frac{s}{\pi}\int_{s_{th}}^{\infty} \frac{\mathrm{Im}\,\alpha(s')}{s'(s'-s)} ds', \tag{4.6}$$

where we have factorized out explicitly the intercept of the trajectory. It is then clear from these two equations that obtaining a dispersive description for both $\alpha(s)$ and $\beta(s)$ requires solving a coupled system of integral equations. As for the $\beta(s)$ function, one first defines the reduced residue $\gamma(s) = \beta(s)\hat{s}^{-\alpha(s)}\Gamma(\alpha(s)+3/2)$ which is a real function and hence can be solved dispersively by using an Omnès function like those studied in Appendix C, yielding the final set of formulas of section 4.1.3.

The last requirement is that the pole that this Regge formula is producing in the partial wave should be compatible with the pole obtained from dispersive or phenomenological analyses. Let us first recall the relation between the partial wave in the first and second Riemann sheets

$$f_\ell^{II}(s) = \frac{f_\ell^I(s)}{1 + 2i\rho(s) f_\ell^I(s)}, \tag{4.7}$$

which, together with Eq.(4.3) yields

$$f_\ell^{II}(s) = \frac{\beta(s)}{\ell - \alpha(s) + 2i\rho(s)\beta(s)}, \tag{4.8}$$

so that the pole is at $\alpha(s_r) + 2i\rho(s_r)\beta(s_r) = \ell$. Note that it is displaced from the $\mathrm{Re}\,\alpha(s_r) = \ell$ region depending on how broad the resonance is.

Even though all this formulas were derived for spinless particles, the formalism still holds in the case where one or several particles have spin. However, the extra analytic structures arising from the spin, together with the fact that particles with spin must obey the MacDowell symmetry [246] (Fig. 4.3) produces a complicated coupled system with no easy phenomenological application.

4.1.1 Motivation

As reviewed in section 3.3 there is a growing interest on the study of mesons that do not fit within the $q\bar{q}$ model. We ascertain here whether the much debated $\kappa/K_0^*(700)$ resonance can fit this picture from the Regge theory point of view. In section 1.4 and in the previous section we explained how an ordinary hadron should be described by its linear Regge trajectory, and hence it could be classified together with a whole tower of partners who share the same parity and quantum numbers. These trajectories have all compatible slopes, with a value of roughly 1 GeV^{-2} in the angular-momentum versus mass-squared plane. Let us remark that this trajectories can be well described by several models, like flux tubes, or string dynamics, and were the original motivation for string models in Hadron Physics. On top of that, the degeneracy between different families of baryons also gives a hint on their super-symmetric relations.

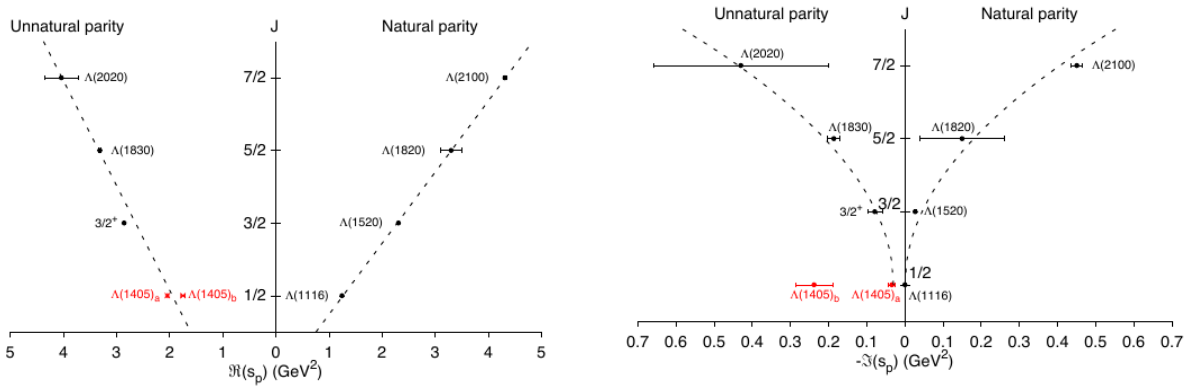

Figure 4.3: Figure from [247] (C. Fernández-Ramírez et al. [JPAC collab.]). Regge trajectory for the baryon family of Λ resonances.

We already introduced how the whole Regge theory emerges as an application of analytic constraints in the complex angular momentum plane. Even though there are clear hints that all $q\bar{q}$ meson trajectories should be explained unambiguously from Regge theory principles, it is still not possible to deduce one general formula for all of them. Furthermore, the lightest scalars are not included in the most well known fitted Regge trajectories for several reasons [245, 248] . However, Regge trajectories can be calculated from the properties of an isolated resonance [5, 249] (Fig. 4.4), or tested against the nature of a complete family [247, 250] (Fig. 4.3). This procedure relies on the analytic behavior of partial waves and Regge trajectories [87, 251, 252], which makes it a fundamental property arising from first principles. Actually, it just uses as input the parameters of the resonance of interest, which in the case of the broad $\sigma/f_0(500)$ and $\kappa/K_0^*(700)$ can be accurately determined from different dispersive approaches [112, 120, 178, 253].

We summarized in section 1.2.1 how different approaches, from determinations relying on large N_c, sum rules, and two-loop ChPT calculations lead to the same result, both the $\sigma/f_0(500)$ and $\kappa/K_0^*(700)$ are not ordinary $q\bar{q}$ mesons [70, 254–259], they look instead like quasi-bound states with a predominant meson-meson component.

From the Regge theory point of view, this behavior is illustrated by the similarity between the $\sigma/f_0(500)$ trajectory calculated in [5] and those of Yukawa potentials at low energies [260–262], as shown in Fig. 4.4. This is why a calculation of the Regge trajectory of the $\kappa/K_0^*(700)$ within this dispersive formalism is not only appropriate in order to compare both results, but also timely.

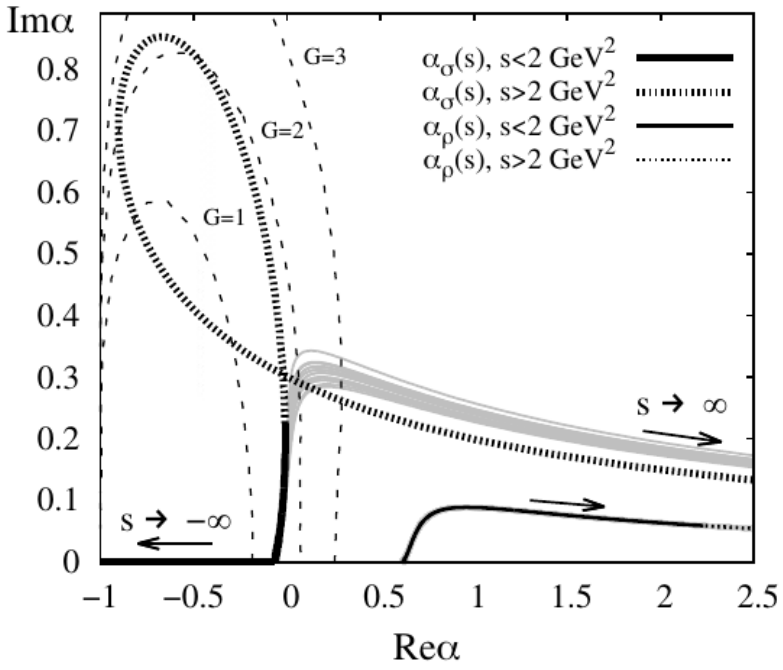

Figure 4.4: Figure from [5] (J.T. Londergan et al.). Comparison of the $\sigma/f_0(500)$ Regge trajectory versus various Yukawa potentials.

4.1.2 Outline of the main results

- We derive the original dispersive calculation of Regge trajectories for $\pi K \to \pi K$ scattering.
- As the $\kappa/K_0^*(700)$ and the $K_0^*(1430)$ resonances are well separated and do not interfere with each other, we can approximate the wave by one pole closer to their mass energy region. Provided the approximation is good enough, the calculation of the Regge trajectory for the elastic channel is model independent.
- We first study the heavy $K_0^*(1430)$, which decays almost only to πK. As expected an ordinary $q\bar{q}$-meson behavior is found and the dispersive calculated slope is perfectly compatible with the universal one. Note that in this case the trajectory is not fitted, but predicted from dispersion relations and unitarity.
- Finally, we study in detail the Regge trajectory of the $\kappa/K_0^*(700)$, which comes out non-ordinary, with a much smaller slope than expected and a non negligible curvature. At low energy it is compared with several Yukawa potentials, suggesting

clear similarities with them, and with the behavior of the $\sigma/f_0(500)$ [5]. The reduced mass of both systems are of the same order, and the ratio is directly related to the ratio of the masses of the scattering processes that creates them. We thus conclude that there is a clear indication of a non-ordinary $\kappa/K_0^*(700)$ behavior, whose trajectory better suits some kind of πK quasi-molecular behavior.

4.1.3 Publication: *The non-ordinary Regge behavior of the* $K_0^*(800)$ *or* κ*-meson versus the ordinary* $K_0^*(1430)$

Eur. Phys. J. C (2017) 77:431
DOI 10.1140/epjc/s10052-017-4994-3

THE EUROPEAN PHYSICAL JOURNAL C

Regular Article - Theoretical Physics

The non-ordinary Regge behavior of the $K_0^*(800)$ or κ-meson versus the ordinary $K_0^*(1430)$

J. R. Pelaez[a], **A. Rodas**

Departamento de Física Teórica II and UPARCOS, Universidad Complutense de Madrid, Madrid 28040, Spain

Received: 24 March 2017 / Accepted: 15 June 2017 / Published online: 28 June 2017

Abstract The Regge trajectory of an elastic resonance can be calculated from dispersion theory, instead of fitted phenomenologically, using only its pole parameters as input. This also provides a correct treatment of resonance widths in Regge trajectories, essential for very wide resonances. In this work we first calculate the $K_0^*(1430)$ Regge trajectory, finding the ordinary almost real and linear behavior, typical of $q\bar{q}$ resonances. In contrast, for the $K_0^*(800)$ meson, the resulting Regge trajectory is non-linear and has a much smaller slope than ordinary resonances, being remarkably similar to that of the $f_0(500)$ or σ meson. The slope of these unusual Regge trajectories seems to scale with the meson masses rather than with scales typical of quark degrees of freedom. We also calculate the range of the interaction responsible for the formation of these resonances. Our results strongly support a non-ordinary, predominantly meson–meson-like, interpretation for the lightest strange and non-strange resonances.

1 Introduction

There is growing evidence for the existence of hadrons that do not follow the ordinary quark–antiquark classification of mesons or the three quark classification of baryons. One of the most remarkable features of these ordinary resonances is the observation that, to a very good approximation, most hadrons can be *fitted* into linear Regge trajectories with an almost universal slope of about 0.9 GeV^{-2} in the spin versus mass squared plane. Regge trajectories are due to the analytic constraints of amplitudes in the complex angular momentum plane. Always subject to these constraints, different dynamics give rise to different Regge trajectories relating the angular momentum and the parameters of poles associated to resonances. In particular, linear relations between the squared mass and the angular momentum are characteristic of relativistic confining interactions like a relativistic rotating rigid bar, flux tubes, string dynamics, etc. or those between quarks in QCD. The slope of such linear trajectories is related to the "string tension" or energy density of the tube connecting the various quarks in the hadron. However, different dynamics do not necessarily lead to linear Regge trajectories.

Let us remark that, due to the analytic properties of amplitudes in the complex plane, in certain cases Regge trajectories can be *calculated* from the properties of just one resonance [1,2], *instead of fitted* to several resonances assuming that a straight line should describe them. This approach relies on dispersion relations and unitarity constraints for Regge trajectories and residues [3–7] and is more fundamental and predictive than a pure straight line fit. Actually, it does not assume a priori a particular functional form for the trajectories. In addition, it includes a consistent treatment of resonance widths, which are usually neglected in the usual phenomenological fits of Regge trajectories. This allows for a clear identification of wide resonances, instead of using, incorrectly, the width as a source of uncertainty in the fits.

The method has been described and applied recently in [1,2]. On the one hand, four ordinary linear Regge trajectories were found from the $\rho(770)$, $f_2(1270)$, $f_2'(1525)$ and $K^*(892)$ resonance poles. The slopes obtained are fairly close to 0.9 GeV^{-2}, expected to be universal for all ordinary trajectories. This is just a confirmation of their well-established ordinary nature, although the observed partners in their Regge trajectories can be understood as predictions of the approach, since the input only comes from the above four particles. On the other hand, for the controversial $f_0(500)$ or σ meson, whose position has recently been determined accurately in [8,9] using rigorous and model-independent dispersive formalisms, a non-linear Regge behavior with a much smaller slope and a much larger imaginary part was found [1]. Its Regge trajectory was strikingly similar to that of a Yukawa potential, at least below 2 GeV^2. Moreover, by imposing a linear Regge trajectory on the σ pole position the dispersion relations yielded an amplitude that was at odds with the

[a] e-mail: jrpelaez@fis.ucm.es

scattering data, even qualitatively. This justified the omission of $f_0(500)$ from (J, M^2) "quarkonia" linear fits in [10], and provided strong support for the generally accepted non-ordinary nature of this meson, which may contain a large, or even dominant, meson–meson component (see [11] for a recent review).

In this work, after briefly reviewing the method in the next section, we extend this research further into the scalar strange sector in Sect. 3. As a further check of the reliability of the approach in the strange sector, we study first the $K_0^*(1430)$ in Sect. 3.1. The elastic formalism is a good approximation because, following the Review of Particle Properties (RPP) [12], the $K_0^*(1430)$ branching ratio to $K\pi$ is $(93 \pm 10)\%$. Our calculation gives rise to an almost real and linear Regge trajectory, with a slope very consistent with the universal value.

In contrast, in Sect. 3.2 we show that the controversial κ or $K^*(800)$ meson results in a non-ordinary trajectory, whose imaginary part is larger than the real part, which is not linear and whose slope is much smaller than the universal slope of ordinary trajectories. This is a new piece of evidence supporting the non-quark–antiquark nature of this state (tetraquark, meson–meson "molecule", different admixtures of these, etc.) which has been suggested from many other approaches [13–22]. The existence of this state has been the subject of a long debate and it is still listed under "Needs confirmation" in the RPP. However, by means of a rigorous dispersive analysis in [23], based on Roy–Steiner partial wave dispersion relations, it has been confirmed that a pole associated to that state exists. This pole, below 800 MeV, is found by many other approaches based on chiral symmetry and/or dispersion relations [15–19,22,24], in analytic extractions of poles without model-dependent assumptions [25,26] or very recently on the lattice [27] (although given the high quark masses used in the calculation it appears as a virtual state, as suggested in [28] from dispersion theory and effective chiral Lagrangians).

Moreover, in Sect. 3.2 we will discuss the striking similarities of the κ trajectory calculated at low energies with the trajectory of the σ meson as well as with Yukawa potentials. In particular, we show that the range of a Yukawa potential that would mimic the trajectories of this resonances seems to scale with the reduced mass of the system, suggesting an important role for meson–meson dynamics in the formation of these resonances. The range of this Yukawa potential is a well-defined and intuitive measure of the scale involved in the σ and κ formation, in contrast to the conventional mean-squared radius, which is ill-defined for resonances since they are non-normalizable states. The spatial scale of a resonance is of interest to discuss its nature as a composite or compact object, and the scales we find are somewhat smaller but comparable to typical meson–meson scattering lengths. In Sect. 4 we will present our conclusions.

2 Dispersive calculation of Regge trajectories

Following [1,2], let us briefly recall the notation and the derivation of the dispersion relations that determine the Regge trajectory and residue of an elastic resonance just from its pole parameters. The partial wave expansion of the kaon–pion scattering amplitude $T(s,t)$ is

$$T(s,t) = 32\pi \sum_l (2l+1) t_l(s) P_l(z_s(t)), \tag{1}$$

where $z_s(t)$ is the cosine of the s-channel scattering angle. In the elastic region the partial waves can be parameterized as

$$t_l(s) = e^{i\delta_l(s)} \sin\delta_l(s)/\rho(s), \quad \rho(s) = 2q(s)/\sqrt{s}, \tag{2}$$

$$q(s) = \sqrt{(s-(m_K+m_\pi)^2)(s-(m_K-m_\pi)^2)/4s}, \tag{3}$$

where l is the angular momentum, $\delta_l(s)$ is the phase shift and $q(s)$ is the center-of-mass momentum. Thus the partial wave has a branch cut from threshold to infinity. Near the pole of a resonance with spin l the partial wave reads

$$t_l(s) = \frac{\beta(s)}{l-\alpha(s)} + f(l,s), \tag{4}$$

where $f(l,s)$ is an analytic function around $l = \alpha(s)$. The complex function $\alpha(s)$ is called the Regge trajectory of the resonance and $\beta(s)$ its residue. Both functions satisfy the Schwartz reflection symmetry also satisfied by the partial wave, *i.e.*, $\alpha(s^*) = \alpha^*(s)$ and $\beta(s^*) = \beta^*(s)$. If we now consider a region where the pole dominates the partial wave behavior, then the unitarity condition $\mathrm{Im}t_l(s) = \rho(s)|t_l(s)|^2$ implies that

$$\mathrm{Im}\,\alpha(s) = \rho(s)\beta(s). \tag{5}$$

Moreover, the elastic unitarity condition determines the analytic continuation of $t_l(s)$ through the cut to the second Riemann sheet, where resonance poles may occur. Similarly, Eq. (5) determines the analytic continuation of $\alpha(s)$ [6,7].

Let us now recall that near threshold partial waves behave as $t_l(s) \propto q^{2l}$, therefore if the resonance pole dominates the partial wave, then $\beta(s) \propto q^{2\alpha(s)}$ in that region. Moreover, the Regge contribution to the amplitude is proportional to $(2\alpha+1)P_\alpha(z_s)$, hence, in order to cancel the spurious pole of the Legendre function $P_\alpha(z_s) \propto \Gamma(\alpha+1/2)$. The residue must vanish in that region of energy whenever $\alpha(s)+3/2$ is a negative integer, *i.e.*, it is convenient to write

$$\beta(s) = \gamma(s)\hat{s}^{\alpha(s)}/\Gamma(\alpha(s)+3/2), \tag{6}$$

where $\hat{s} = 4q^2/s_0$ and in order to have the right dimensions, we have introduced a scale s_0, which we conveniently set to $s_0 = 1$ GeV^2 without losing generality. The so-called

reduced residue, $\gamma(s)$, is a real analytic function. Hence, on the real axis above threshold, since $\beta(s)$ is real, the phase of γ is

$$\arg\gamma(s) = -\mathrm{Im}\alpha(s)\log(\hat{s}) + \arg\Gamma(\alpha(s)+3/2). \tag{7}$$

Consequently, we can write for $\gamma(s)$ a dispersion relation using an Omnés function:

$$\gamma(s) = P(s)\exp\left(c_0 + c's + \frac{s}{\pi}\int_{(m_K+m_\pi)^2}^{\infty} \mathrm{d}s' \frac{\arg\gamma(s')}{s'(s'-s)}\right), \tag{8}$$

where $P(s)$ is an entire function. The large-s behavior is not determined from first principles, but linear Regge trajectories are expected for ordinary mesons and thus we allow α to behave as a first order polynomial at large-s. Thus we only need to use two subtractions to obtain a dispersion relation [3–5]:

$$\alpha(s) = \alpha_0 + \alpha' s + \frac{s}{\pi}\int_{(m_K+m_\pi)^2}^{\infty} \mathrm{d}s' \frac{\mathrm{Im}\alpha(s')}{s'(s'-s)}. \tag{9}$$

Let us remark that in [2] it was shown that considering three subtractions lead to almost indistinguishable results. Therefore linear trajectories are not imposed a priori and, actually, a non-linear behavior was found for the $f_0(500)$ resonance [1].

From Eq. (5) it then follows that $c' = \alpha'(\log(\alpha' s_0) - 1)$ and that $P(s)$ can only be a constant. Therefore, we arrive at the following equations [1,2,6,7] describing the Regge trajectory of a resonance pole when it dominates a partial wave as in Eq. (4):

$$\mathrm{Re}\,\alpha(s) = \alpha_0 + \alpha' s + \frac{s}{\pi} PV \int_{(m_K+m_\pi)^2}^{\infty} \mathrm{d}s' \frac{\mathrm{Im}\alpha(s')}{s'(s'-s)}, \tag{10}$$

$$\begin{aligned}\mathrm{Im}\,\alpha(s) = {} & \frac{\rho(s) b_0 \hat{s}^{\alpha_0+\alpha' s}}{|\Gamma(\alpha(s)+\frac{3}{2})|} \\ & \times \exp\left(-\alpha' s[1-\log(\alpha' s_0)] + \frac{s}{\pi} PV \int_{(m_K+m_\pi)^2}^{\infty} \right. \\ & \left. \times \mathrm{d}s' \frac{\mathrm{Im}\alpha(s')\log\frac{\hat{s}}{\hat{s}'} + \arg\Gamma\left(\alpha(s')+\frac{3}{2}\right)}{s'(s'-s)}\right),\end{aligned} \tag{11}$$

$$\begin{aligned}\beta(s) = {} & \frac{b_0 \hat{s}^{\alpha_0+\alpha' s}}{\Gamma(\alpha(s)+\frac{3}{2})} \exp \\ & \times \left(-\alpha' s[1-\log(\alpha' s_0)] + \frac{s}{\pi}\int_{(m_K+m_\pi)^2}^{\infty} \right. \\ & \left. \times \mathrm{d}s' \frac{\mathrm{Im}\alpha(s')\log\frac{\hat{s}}{\hat{s}'} + \arg\Gamma\left(\alpha(s')+\frac{3}{2}\right)}{s'(s'-s)}\right),\end{aligned} \tag{12}$$

where PV denotes the principal value. For real s, the last two equations reduce to Eq. (5).

The dispersive approach to calculating Regge trajectories consists on solving those three equations numerically with the free parameters fixed by demanding that the pole on the second sheet of the amplitude in Eq. (4) reproduces the position and residue of the pole associated to the resonance under study. As already commented in the introduction this procedure yields almost real and linear Regge trajectories with a universal slope of $\sim 0.9\,\mathrm{GeV}^{-2}$ for the $\rho(770)$ [1] $f_2(1270)$, $f_2'(1525)$ and $K^*(892)$ resonances [2]. In contrast it leads to a very unusual non-linear trajectory for the $f_0(500)$ or σ meson.

For scalars like $f_0(500)$, studied in [1], or $K_0^*(800)$ and $K_0^*(1430)$, which will be studied here, the method is slightly modified [1] to factor out explicitly in the residue the Adler-zero of the partial wave required by chiral symmetry, namely, $\beta(s) \propto (s - s_A)$. For our purposes here it is enough to place it at its leading order position within Chiral Perturbation Theory, which for kaon–pion scattering is at $s_A = 0.236\ \mathrm{GeV}^2$. Then, since we do not want to spoil the large s-behavior, we need to replace $\Gamma(\alpha + 3/2)$ by $\Gamma(\alpha + 5/2)$. A spurious pole appears now at $\alpha = -3/2$, but this is far away from the resonance region and hence becomes irrelevant from the calculation. In summary, for $K_0^*(800)$ and $K_0^*(1430)$ the right hand side of Eq. (12) should contain an $(s - s_A)$ factor and all instances of $3/2$ in the Γ functions should be replaced by $5/2$. Then b_0 has GeV^{-2} dimensions.

Before discussing our numerical results let us recall the relation between the coupling g of the resonance to its dominant decay channel and the residue of the pole $|Z|$:

$$|g|^2 = \frac{16\pi(2l+1)|Z|}{|2q(s_p)|^{2l}}. \tag{13}$$

Note that by calculating $\alpha(s)$ from the pole of one elastic resonance, we are not only obtaining the real part of the trajectory, which predicts the mass of the next partner in the trajectory, but also the imaginary part, which can be naively converted into a prediction of the width. In particular, for Breit–Wigner resonances that have just a single dominant decay mode, their width can be related to their Regge trajectory as $\Gamma = \mathrm{Im}\alpha/(M\mathrm{Re}\alpha')$. There are several caveats here: first, that we have assumed a Breit–Wigner form. Second, that the next partner of the linear trajectory found for the $K_0^*(1430)$ is heavy enough to lie beyond the strict applicability limits of our approach (the elastic or almost elastic region). Thus, being obtained from the extrapolation of our results to high energies, this Γ can only be considered as an estimate. Third, that, being in the inelastic region, the partner does not have to decay predominantly into a single mode, so that the Γ above should only be interpreted as the partial width to $K\pi$. With these caveats

in mind we will see that the partial-width estimate is fairly reasonable.

In practice, it is the full elastic amplitude, including the background, the one that satisfies elastic unitarity. Therefore, our approximation that the pole contribution alone satisfies elastic unitarity is only valid in the region where the pole dominates the partial wave. However, dispersion relations are integrated from threshold to infinity. There are two possibilities now: to restrict the integrals to the region where the resonance pole dominates, or to use the one-pole approximation in the whole energy region. In the results we describe in the next section we have opted for the second one but we have checked that the results change little if we use the first option. In particular, about 90% of the integral comes from s' within roughly one width of the resonance in the s region of interest (again within roughly one width of the resonance). We will then compare our results in the surroundings of each resonance, where they are to be trusted, and cover with a mesh the areas where our approximation is not expected to hold.

3 Numerical results

Strictly speaking, the method described in the previous section is suitable for resonances appearing in the elastic scattering of two mesons. In the strange sector this is fulfilled by the vector $K^*(892)$, already studied in [2], and the $K_0^*(800)$ to be studied below in Sect. 3.2, since in practice both have a 100% branching ratio to $K\pi$. However, it was shown in [2] that the method is also able to reproduce the ordinary behavior of the $f_2(1270)$, $f_2'(1525)$ resonances, which are almost elastic, each with a dominant decay whose branching ratio is larger than 84%. For this reason, we are confident to extend the approach here to $K_0^*(1430)$, whose branching ratio to $K\pi$ is $(93 \pm 10)\%$ according to the RPP [12]. Thus, we will consider this small inelasticity as a source of systematic error and include an additional 7% uncertainty in the $K_0^*(1430)$ residue.

For each resonance we obtain the best values for α_0, α' and b_0 by fitting the pole in Eq. (4) to the parameters of the observed associated pole, where $\alpha(s)$ and $\beta(s)$ are numerical solutions of Eqs. (10) and (12). Hence, the inputs to calculate each Regge trajectory are just the pole position s_p and residue $|g^2|$ of a single resonance.

In practice, at each step in the fitting procedure a set of α_0, α' and b_0 parameters is chosen and the system of Eqs. (10) and (11) is solved iteratively. The resulting Regge amplitude for each α_0, α' and b_0 is then continued to the complex plane to find a pole. From this pole we define a χ^2 function by calculating the differences between the mass, width and coupling observed values of the pole under study and the pole obtained from the above equation, divided by the uncertainties. The best values for α_0, α' and b_0 are obtained by minimizing this χ^2 function.

3.1 $K_0^*(1430)$ resonance

According to the RPP, $K_0^*(1430)$ is a well-established resonance, whose parameters are obtained both from $K\pi$ scattering and decay from production processes. Note, however, that our formalism is based on scattering amplitudes (particularly due to the use of the unitarity condition in Eq. (5), and when looking at scattering data the nearest peak to 1430 MeV actually occurs at a somewhat lower energy. In addition, even taking into account that it is only approximately elastic, the amplitude does not follow a typical isolated Breit–Wigner shape. These two features can be seen in both panels of Fig. 1, where we have represented as a dotted line the modulus of the amplitude obtained in a recent reanalysis [29] of scattering data [30,31] constrained to satisfy Forward Dispersion Relations (FDR). The reason for such a behavior can be attributed to the presence of backgrounds, possibly from other resonances. In particular they may come from the still controversial $K_0^*(800)$, whose width is of the order of 600 MeV, and maybe also from another still disputed $K_0^*(1950)$ resonance, with a with of the order of 200 MeV. Thus, in this case, although the presence of the resonance is undisputed, there is some spread in its parameters, particularly on the width.

Thus, we are going to deal with the pole of the $K_0^*(1430)$ resonance following two different approaches. Within the first, more conservative approach, we will use a very simple description using a Breit–Wigner (BW) functional form. The parameters of this "BW-pole" are obtained from the RPP and read

$$\sqrt{s_{K_0^*}} = M - i\Gamma/2 = (1431 \pm 50) - i(135 \pm 40)\ \text{MeV},$$
$$|g_{K_0^*}|^2 = 22.0 \pm 6.2\ \text{GeV}^2. \quad (14)$$

The resulting BW line shape is shown on the left panel of Fig. 1 as a dashed line. Note that, despite dominating the amplitude in that region, this BW form does not describe the data accurately, which implies the existence of a background. Fortunately, for our approach only the pole parameters are needed.

Within the second approach we will use a recent pole determination [26] that does not assume a particular functional form or model for the pole, but uses a sequence of Padé approximants with powerful convergence properties in the complex plane. This sequence is calculated from the values of the amplitude and its derivatives at an energy point near the resonance. The values of the amplitude are taken from the recent analysis of scattering data [29] constrained with forward dispersion relations. This approach is meant to minimize the model dependence. In this case the "PFDR-pole" parameters are:

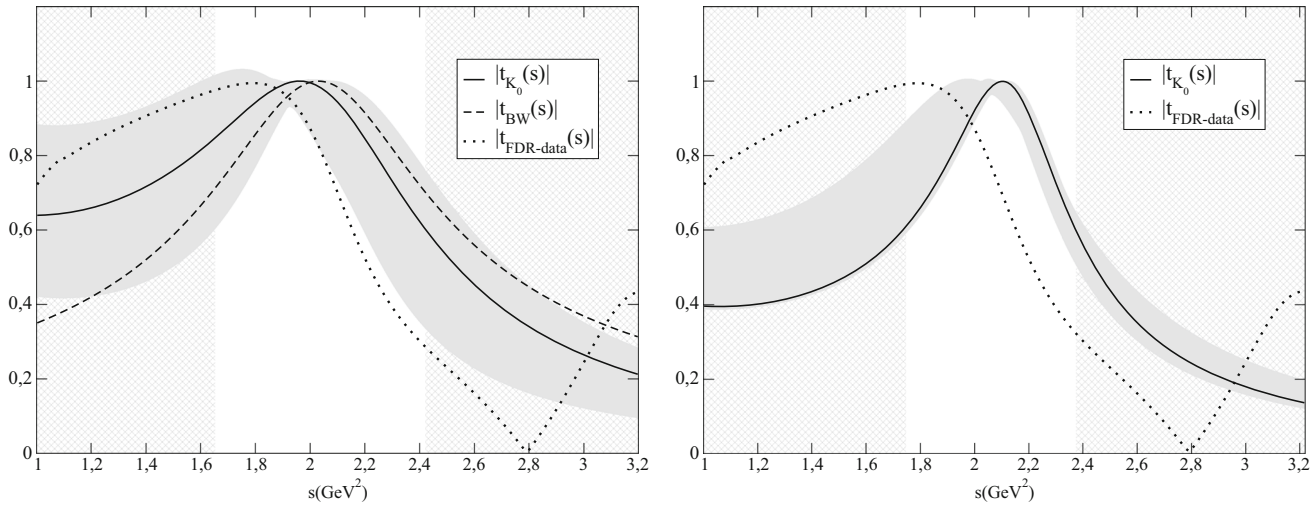

Fig. 1 The *dotted line*, labeled "FDR-data", corresponds to the modulus of the $K\pi$ scattering partial wave in the scalar–isospin 1/2 channel, obtained from a fit to data constrained with forward dispersion relations [29]. On the *left panel*, the *dashed line* is the Breit–Wigner shape obtained using the resonance parameters in the RPP. Note that the Breit–Wigner peak is displaced from the peak in the data. The continuous line is the result of our method, with a Regge pole consistent with that of the Breit–Wigner parameterization, but satisfying the dispersive constraints on the Regge trajectory Eqs. (10) to (12). On the *right panel* we show similar results, but avoiding a Breit–Wigner or other particular model. The resulting Regge-pole shape is also somewhat displaced with respect to data but slightly narrower than when assuming a Breit–Wigner formalism. In both cases the *gray bands* cover the uncertainties due to the errors in the input pole parameters. The regions covered with a mesh correspond to $s < (M - \Gamma/2)^2$ and $s > (M + \Gamma/2)^2$

$$\sqrt{s_{K_0^*}} = (1431 \pm 6) - i(110 \pm 19)\ \text{MeV},$$
$$|g_{K_0^*}|^2 = 14.6 \pm 5.6\ \text{GeV}^2. \quad (15)$$

Still, one might be concerned about the description of data and try to get a more accurate parameterization in terms of more Regge poles. Actually, the parameterizations in [29] do have several poles [26] and describe the data very accurately. However, if one tries to implement a dispersive formalism with more Regge poles, each one has three more functions to determine ($\text{Re}\,\alpha$, $\text{Im}\,\alpha$ and β), but still just one elastic unitarity condition for the whole partial wave. Thus, one does not obtain a closed system of integral equations. It is only because we assume that elastic unitarity is good for each pole separately that we can derive the powerful system of two integral relations provided in Sect. 2, relating the real and imaginary parts of each pole trajectory.

Therefore the input for our equations are just the pole parameters of each resonance, and these have to be extracted by isolating each pole contribution, as we have just done in the previous paragraphs. The pole itself does not have to describe the data perfectly, since there is a background to complete the description. For the trajectory of a given resonance only its own pole is relevant, everything else is background, no matter whether it comes from another resonance. In particular, $K_0^*(800)$ and the $K_0^*(1430)$ are fairly well separated. Thus, when extracting the parameters of one of them, the contributions of the other one should be considered background.

Hence, we assume that β and α are related by elastic unitarity. For this approximation to hold, elastic unitarity should be a good approximation for t_l (which is indeed the case as shown in [29]) and the pole *should dominate* the partial wave in a certain region. The method is then valid in that same region. This is why we provided the curves in Fig. 1, just to show that the pole contribution (extracted in [26] from a parameterization that describes the data accurately) dominates the amplitude in that same region. One might be worried that the peak is somewhat displaced, but we will also make the calculation with a Breit–Wigner functional form, which by construction satisfies unitarity, and we will check that the results are compatible with those obtained from the pole extracted in [26].

We then apply the method explained in the previous section to these two determinations of the pole. For the "BW-pole" approach, its values Eq. (14) are well fitted, resulting in $\sqrt{s_{K_0^*}} = (1431 \pm 51) - i(139 \pm 65)$ MeV and a coupling of $|g_{K_0^*}|^2 = 21.6 \pm 9.1\ \text{GeV}^2$. The larger errors obtained for the width and the coupling are caused mostly by the systematic uncertainties included for the branching ratio, since it has a 7% inelasticity. Then, on the left panel of Fig. 1, we show as a continuous line the Regge-pole amplitude resulting from our method. We see that even though we have just fitted the pole, which is the only relevant feature for the Regge trajectory, this amplitude is rather similar to the Breit–Wigner form. The gray bands cover the uncertainties in the Regge-pole amplitude arising from the errors of the input.

We follow the same steps for the "PFDR-pole". Its values in Eq. (15) are well fitted, resulting in $\sqrt{s_{K_0^*}} = (1431 \pm 6) - i(110 \pm 22)$ MeV and a coupling of $|g_{K_0^*}|^2 = 15.0^{+5.3}_{-1.96}$ GeV^{-2}. Once again the larger errors obtained for the width and the coupling are caused mostly by the estimation of systematic uncertainties due to the 7% inelasticity. This time we show on the right panel of Fig. 1 the resulting Regge-pole amplitude, whose peak is somewhat narrower than that of the Breit–Wigner shape in the left panel. The gray bands cover the uncertainties in the Regge-pole amplitude arising from the errors of the input.

In the process of fitting to the observed values the pole in Eq. (4), with the constraints in Eqs. (10)–(12), we obtain the b_0, α_0 and α' parameters. For the BW-pole they are

$$\alpha_0 = -1.10^{+0.04}_{-0.21}; \quad \alpha' = 0.78^{+0.07}_{-0.13}\ \text{GeV}^{-2};$$
$$b_0 = 4.08^{+1.08}_{-3.19}\ \text{GeV}^{-2}, \tag{16}$$

whereas for the PFDR-pole trajectory we find

$$\alpha_0 = -1.28^{+0.01}_{-0.17}; \quad \alpha' = 0.81^{+0.01}_{-0.04}\ \text{GeV}^{-2};$$
$$b_0 = 2.5^{+1.1}_{-0.4}\ \text{GeV}^{-2}. \tag{17}$$

With these parameters the trajectory $\alpha(s)$ is fully determined as a solution of the integral equations. Thus, in Fig. 2 we show the resulting trajectories for the BW-pole (thick lines) and the PFDR-pole (thin lines). The real part of the trajectories is shown as a continuous line and the imaginary part as a dashed line. Both pole determinations yield very similar trajectories. In the figure we have covered with a light mesh the regions that lie beyond three half-widths of the $K_0^*(1430)$ mass, where we do not expect our method to give accurate results and the curves should be considered a qualitative extrapolation. Within the applicability region, we find that the real part of the trajectory is almost linear and bigger in modulus than the imaginary part above the resonance mass. In other words, it comes out as expected for Regge trajectories of ordinary mesons.

Nevertheless, in Fig. 2 we show the resulting Regge trajectory up to $s = 5$ GeV^2. The reason for such an extrapolation is to show the position of the $K_2^*(1980)$ mass at $M_{K_2^*(1980)} = (1973 \pm 8 \pm 25)$ MeV [12], which could be the next state in the Regge trajectory. It should be noted that this resonance is listed in the RPP, but omitted from the summary tables, because it "Needs confirmation" [12]. No other $J^P = 2^+$ candidate is found nearby in the RPP, particularly not with a slightly higher mass. This resonance is fairly close to our extrapolated trajectory. This can be considered as further support for its existence. However, it should be noted that it is somewhat lighter than expected from our results, although one should take into account that the mass listed in the RPP is not the pole mass that we use in our calculations.

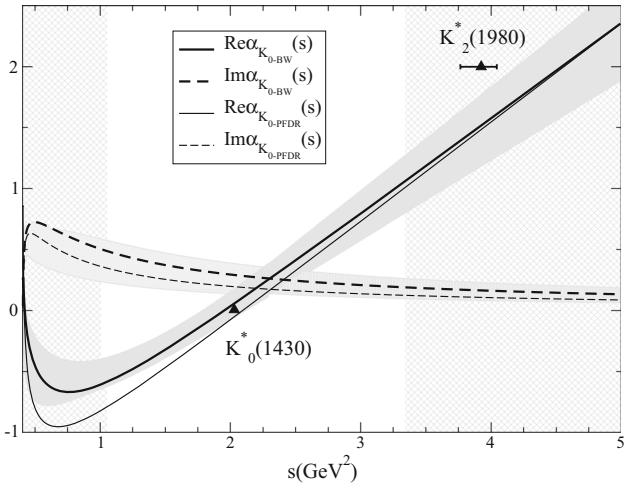

Fig. 2 Real (*solid*) and imaginary (*dashed*) parts of the $K_0^*(1430)$ Regge trajectory. The *gray bands* cover the uncertainties due to the errors in the input pole parameters for the Breit–Wigner pole, which central values are the *thick lines*, the values obtained for the PFDR-pole are the *thin lines*. The area covered with a mesh is the mass region starting three half-widths above and below the resonance mass, where our approximation that $K\pi$ is elastic and dominated by $K_0^*(1430)$ does not longer hold and where our approach should be considered only as a mere extrapolation. We show the $K_0^*(1980)$ resonance listed in the RPP that seems a good candidates for a $K_0^*(1430)$ partner in this trajectory

It is worth remarking that $K_2^*(1980)$ is not only slightly off our trajectory, but also off from standard linear trajectories. In particular since forcing $K_0^*(1430)$ and the $K_2^*(1980)$ to lie on the same straight trajectory $J = \alpha_0 + \alpha' M^2$, yields a slope $\alpha' \simeq 1.07\,\text{GeV}^{-2}$, which is somewhat larger than the usual value of $0.9\,\text{GeV}^{-2}$. This small tension with the universal slope could be due to the fact that, although $K_0^*(1430)$ is generally accepted as an ordinary quark–antiquark meson, it might also have some small mixing with other meson configurations [32–36]. This would be rather natural since such non-ordinary mesons candidates, which as commented in the introduction include the $K_0^*(800)$, are relatively close. In particular, $K_0^*(800)$, having a width of the order of 600 MeV and a pole mass around 700 MeV, is less than one width and a half away from the $K_0^*(1430)$.

Moreover, since $K_2^*(1980)$ seems to be a good candidate for the next partner of $K_0^*(1430)$, we can estimate $\Gamma_{K_2^*(1980)\to K\pi} \simeq 97$ MeV by approximating the width as $\Gamma = \text{Im}\alpha/(M\text{Re}\alpha')$, assuming $K_2^*(1980)$ can be described by a Breit–Wigner form. Unfortunately, no estimate of this partial width is given in the RPP, but at least our result is smaller than the total width $\Gamma_{tot} = (373 \pm 33 \pm 60)$ MeV.

As a final remark on Fig. 2, we want to comment on the apparent cusp seen at threshold in the $K_0^*(1430)$ trajectory, even if it lies beyond the strict applicability region of our method (since it lies in the area covered with a mesh). It is just an artifact of our approximation due to our assumption that the Regge pole dominates the amplitude. But as

seen in Fig. 1, for $K_0^*(1430)$ this dominance is only a good approximation in an energy region of the order of the resonance width around the nominal mass. Being a Regge pole in the complex-l plane $\beta(s)$ must carry a $q^{2\alpha(s)}$ factor. Right at the pole this becomes exactly q^{2l}, as expected from partial wave kinematics. However, the pole does not dominate at threshold, where $\alpha(s_{th}) \neq l$. Therefore at threshold the approximation $q^{2l} \sim q^{2\alpha}$ is not so good.

Now, for trajectories of scalar particles $\mathrm{Re}\,\alpha$ is negative between threshold and the pole. Consequently, in the first step of the calculation, $q^{2\alpha}$ diverges at threshold and so does $\beta(s)$. If $0 > \mathrm{Re}\,\alpha > -0.5$ this spurious divergence is compensated in $\mathrm{Im}\alpha = \rho(s)\beta(s)$ by the $\rho(s) \sim q$ factor. Thus the artifact due to extending our approximation to threshold goes unnoticed. This will be the case of the light $K_0^*(800)$ (or the σ resonance studied in [1]). However, for $K_0^*(1430)$, $\mathrm{Re}\,\alpha$ can become close or smaller than -0.5 at threshold, making $\mathrm{Im}\,\alpha \to +\infty$ there. But recall that our equations are solved iteratively. Then, if at any step of the calculation we feed in the equations a huge positive $\mathrm{Im}\,\alpha(s')$ near threshold, the resulting $\mathrm{Re}\,\alpha(s)$ changes sign becoming positive near threshold. With further iterations the solution at threshold always stabilizes at values of $\mathrm{Re}\,\alpha(s) > -0.5$. Beyond threshold it can be negative until it reaches the value of $\alpha = 0$ at the resonance mass. Therefore the spurious behavior of the trajectory around $s = s_{th}$ is not due to the presence of another Regge pole like $K_0^*(800)$, but just to assuming that at threshold the amplitude is dominated by the $K_0^*(1430)$ pole.

One might then worry that this artifact may spoil our calculation, but we have also checked explicitly that the part of the integral around threshold is negligible for the result of the trajectory in the applicability region. As explained above we could have restricted the integrals to the region around the resonance and the result would have changed little.

3.2 $K_0^*(800)$ resonance

This is a very interesting state, because, as commented in the introduction, it is a firm candidate to be a non-ordinary meson together with the other members of the light scalar nonet. There is also a longstanding debate on its parameters and even its very existence, and in the RPP it is still listed as "Needs Confirmation". However, all sensible implementations of chiral symmetry and unitarity obtain a pole for this state, which is also necessary for the understanding of several heavy meson decays (see, for instance [37]). Within unitarized chiral perturbation theory it was shown that this state does not follow the N_c behavior of ordinary mesons [21,22] and that for heavy quark masses it would become a virtual state [28], which has been recently confirmed on the lattice [27]. The most rigorous determination of its parameters was obtained from the dispersive analysis in [23] using the Roy–Steiner equations with unitarity and low-energy chiral constraints. In that work the pole position is given explicitly, but unfortunately not the residue, which is needed for our approach. For this reason we will use the parameters obtained in [29], in which a conformal expansion with the correct analytic properties was fitted to $K\pi$ scattering data constrained to satisfy forward dispersion relations up to 1.6 GeV. The pole parameters we will use are thus

$$\sqrt{s_\kappa} = (680 \pm 15) - i(334 \pm 8)\ \mathrm{MeV},$$
$$|g_\kappa|^2 = 25.0 \pm 0.6\ \mathrm{GeV}^2, \tag{18}$$

which are fairly consistent with the position provided in [23] and the RPP.

As in previous sections, the pole parameters above are then fitted with our Regge amplitude in Eq. (4), neglecting the background and with the Regge slope and residue satisfying the dispersive representation in Eqs. (10)–(12). The pole obtained from this fit is located at $\sqrt{s_\kappa} = (680 \pm 15) - i(334 \pm 8)$ MeV, with a coupling $|g_\kappa|^2 = 25.1 \pm 0.5\ \mathrm{GeV}^2$, very consistent with the input values. The parameters of the fit are

$$\alpha_0 = 0.28 \pm 0.02; \quad \alpha' = 0.15 \pm 0.03\ \mathrm{GeV}^{-2};$$
$$b_0 = 0.44 \pm 0.04,\ \mathrm{GeV}^{-2}, \tag{19}$$

and the corresponding trajectory $\alpha(s)$ is shown in the left panel of Fig. 3. It is clearly not an ordinary Regge trajectory, since it is not predominantly real, the real part is non-linear and the slope (at the $K_0^*(800)$ mass) is almost one order of magnitude smaller than the usual $\alpha' \simeq 0.9\ \mathrm{GeV}^{-2}$ slope for ordinary mesons.

In Fig. 4 we compare the one-pole partial wave of Eq. (4), when the pole follows this non-ordinary trajectory (continuous line and dark error band), with the dispersive data fit from [29] (dashed line). It can be seen that the non-ordinary Regge-pole amplitude consistently dominates the amplitude in that region, even though we have only fitted the pole position and residue deep in the complex plane.

To check the robustness of our results we have performed some further tests. First, we have also used the pole obtained in a recent work [26], which also used the constrained data analysis of [29], although the pole was not obtained from the conformal fit there, but from a sequence of Padé approximants. The pole parameters thus obtained were

$$\sqrt{s_\kappa} = (670 \pm 18) - i(295 \pm 28)\ \mathrm{MeV},$$
$$|g_\kappa|^2 = 20.0^{+3.7}_{-3.4}\ \mathrm{GeV}^2. \tag{20}$$

Note that the uncertainties in these parameters are more conservative than those in Eq. (18). Once again we fit this pole with our single-Regge-pole amplitude. The resulting pole is at $\sqrt{s_\kappa} = (670 \pm 18) - i(295 \pm 28)$ MeV, with $|g_\kappa|^2 = 20.0^{+3.7}_{-2.2}\ \mathrm{GeV}^2$, almost identical to the input. The parameters obtained for the Regge trajectory associated to this pole are

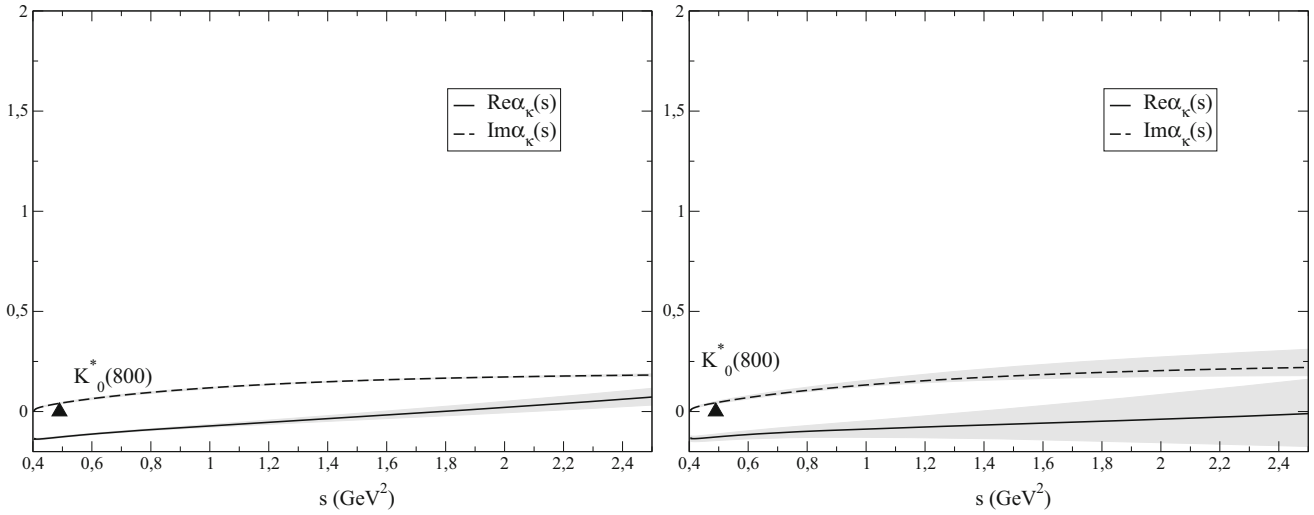

Fig. 3 Real (*solid*) and imaginary (*dashed*) parts of the $K_0^*(800)$ Regge trajectory for both FDR [29] and PFDR [26] results. The real part is smaller than the imaginary part in the whole energy region. The *slope* of the Regge trajectory is almost one order of magnitude smaller than the usual ones. In addition there cannot be any candidate for this resonance since the real part is below 0.25 up to $s = 5\ \text{GeV}^{-2}$

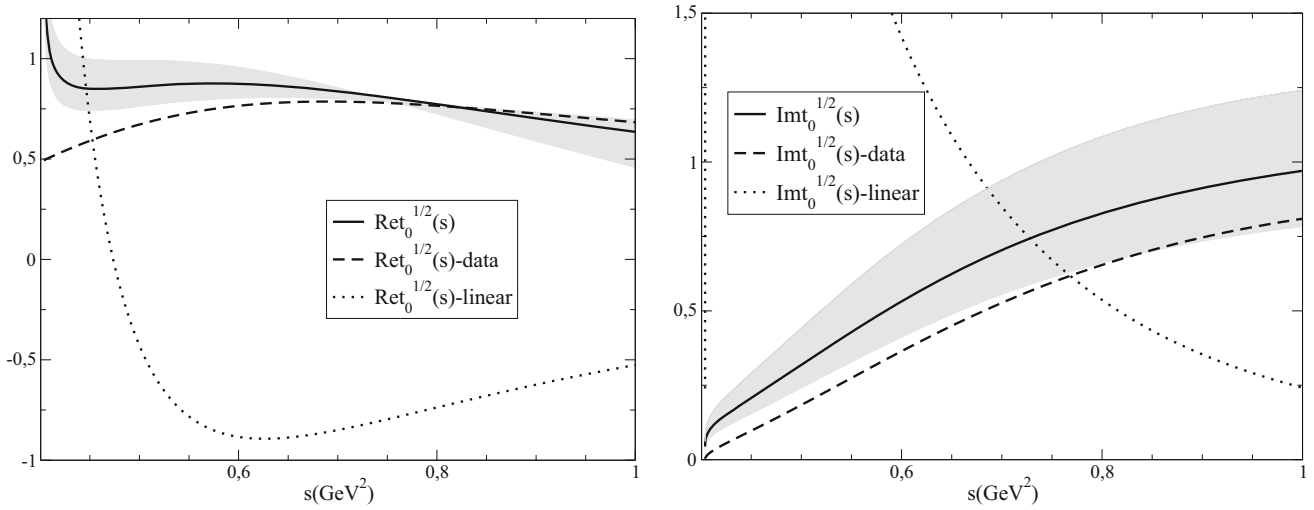

Fig. 4 Real and imaginary parts of the partial wave $t_0^{1/2}(s)$. *Dashed lines* represent the constrained fit to data in [29]. The *solid curves* represent the single Regge-pole partial wave determined using the dispersive representation of the Regge trajectory. The estimated uncertainties are shown as *gray bands*. The *dotted lines*, which are completely at odds with the data curve, represent the single Regge-pole partial wave when imposing an ordinary linear Regge trajectory with $\alpha' \simeq 0.9\ \text{GeV}^{-2}$, as a solution from the dispersive equations of $\alpha(s)$ and $\beta(s)$

$$\alpha_0 = 0.27 \pm 0.03; \quad \alpha' = 0.11 \pm 0.9\ \text{GeV}^{-2};$$
$$b_0 = 0.45^{+0.11}_{-0.8},\ \text{GeV}^{-2}, \tag{21}$$

very consistent with the determination in Eq. (19), although more conservative. Once again we see on the right panel of Fig. 3 that the resulting trajectory is very different from that expected for an ordinary meson and very consistent with the trajectory in the left panel, although with more conservative error bands.

As a second test, we have performed the same analysis but imposing an ordinary slope $\alpha' = 0.9\ \text{GeV}^{-2}$. Despite having one less free parameter for the fit, it is still possible to fit the pole position fairly well, finding $\sqrt{s_\kappa} = 683 - i331$ MeV, with the coupling $|g_\kappa|^2 = 25.1\ \text{GeV}^2$. With α' fixed we now find a linear Regge trajectory and one could be tempted to think that we could also consider κ to lie in an ordinary Regge trajectory. However, the resulting amplitude may describe the pole, but fails completely to describe in the real axis the amplitude fitted to data. This can be seen in Fig. 4, where we show as dotted lines the real and imaginary parts of the resulting amplitude when imposing an ordinary linear Regge trajectory for $K_0^*(800)$, versus the partial wave fitted

to data. Therefore the linear Regge trajectory with universal slope does not yield a pole that dominates the observed amplitude.

Moreover, if one was to assume an ordinary linear Regge trajectory $J = \alpha_0 + \alpha' M^2$ for $K_0^*(800)$ with the universal value $0.9\,\mathrm{GeV}^{-2}$, then taking $M_\kappa \simeq 0.68\,\mathrm{GeV}$, one finds $\alpha_0 \simeq -0.42$. Hence the first partner with $J = 2$ in this trajectory would appear at 1.64 GeV. No $J^P = 2^+$ resonance is identified in the RPP with such a mass. The closest one is the $K_2^*(1430)$, but that would require $\alpha' = 1.26\ \mathrm{GeV}^{-2}$, very inconsistent with the universal slope. The second closest $J^P = 2^+$ resonance is $K_2^*(1980)$, but we have already seen in the previous section that this one would fit better in the $K_0^*(1430)$ trajectory. Actually, to make it the partner of the $K_0^*(800)$ in a linear trajectory, a value of $\alpha' \simeq 0.58\,\mathrm{GeV}^{-2}$ is required, also rather different from the universal value. A $K(1630)$ resonance is listed in the RPP with unknown J^P, but it is not confirmed by more than one experiment, it is omitted from the summary tables and has a surprisingly small width of 16^{+19}_{-16} MeV, which makes its existence very questionable. Furthermore, even in QCD-inspired quark models [38], only two $J^P = 2^+$ states are listed below 2 GeV and they can be nicely identified with $K_2^*(1430)$ and $K_2^*(1980)$. Therefore, even from more familiar phenomenology there is no natural candidate for a partner of $K_0^*(800)$ if it lies in an ordinary trajectory.

A third test is that we have also tried to fit the pole without factorizing the Adler zero, but once again the result is at odds with the data.

These results strongly support the non-ordinary nature of the $K_0^*(800)$ resonance, or κ meson. Furthermore, a rather similar non-ordinary Regge behavior has been recently observed [1] for the $f_0(500)$ resonance, formerly known as the σ meson. As commented in the introduction, there is a rather general agreement in the literature that these two resonances would belong to the same light scalar multiplet. The similarities between the trajectories of these two states is shown in Fig. 5 where we plot $\mathrm{Im}\alpha(s)$ versus $\mathrm{Re}\alpha(s)$ for $K_0^*(800)$ together with the results obtained for σ in [1]. It should be noted that for $f_0(500)$ a very robust behavior below 2 GeV^2 was found, which is qualitatively similar to the one we also find for $K_0^*(800)$. Namely, both $f_0(500)$ and $K_0^*(800)$ trajectories in this plane are almost exactly real up to a value of $\mathrm{Re}\alpha(s)$ between -0.5 and 0, where both curves rise almost vertically developing an imaginary part up to slightly above 0.2, without barely changing the real part. This happens for values of $s < 2\,\mathrm{GeV}^2$, where we expect our method to be valid, and we have plotted this part of the curves with thick lines. It is worth noting that this is the typical behavior of Regge trajectories of Yukawa potentials $V(r) = Ga\exp(-r/a)/r$ at low energies [39–41], which we have plotted as dashed lines for different values of G. Therefore, it seems that both the σ and the κ mesons have a Regge trajectory at low energies that is qualitatively similar to Yukawa potential trajectories.

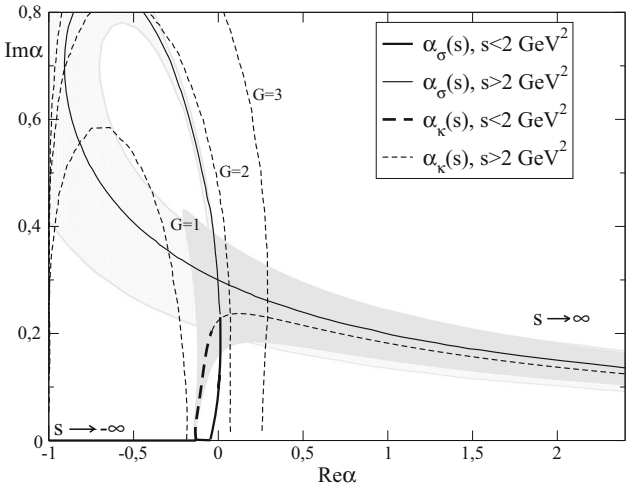

Fig. 5 At low and intermediate energies (*thick lines*), the trajectories of σ and κ are similar to those of Yukawa potentials [39–41] $V(r) = Ga\exp(-r/a)/r$ (*thin dashed lines* labeled with different values of G). Beyond 2 GeV^2, we plot our results as *thin lines* because they should be considered just as extrapolations

Above 2 GeV^2 our method becomes less reliable, but we still show the results as thin curves for completeness. It should be considered just a mere extrapolation. Moreover, given the high energies under consideration, the comparison with non-relativistic Yukawa potential does not make sense any longer. The sigma presents two possible behaviors, in one of them $\mathrm{Im}\alpha$ reaches a value between 0.2 and 0.4 and then decreases slowly while the real part starts increasing again. This is the same behavior we find for the $K_0^*(800)$. However, within uncertainties, $f_0(500)$ has another possible behavior which still follows the Yukawa trajectory above 2 GeV^2. In any case, at those high energies these trajectories are still non-ordinary as seen in Fig. 3 for $K_0^*(800)$.

Once the semiquantitative analogy with Yukawa potentials has been established, it is possible to estimate the Yukawa parameters that mimic best the σ and κ trajectories. The trajectory of $f_0(500)$ is almost equal to a $G = 2$ curve up to $s = 2$ GeV^2, while the curve with $G = 1.4$ is rather similar to the $K_0^*(800)$ trajectory. Using the parameterizations of Yukawa Regge trajectories in [39–41] we can estimate the effective ranges of the Yukawa potential in the σ case [1]: $a_{\pi\pi} = 0.5\ \mathrm{GeV}^{-1} \simeq 0.1$ fm, as well as in the κ case: $a_{\pi K} \simeq 0.36\ \mathrm{GeV}^{-1} \simeq 0.07$ fm.

The range of the interaction is a relevant quantity because there is some interest in the literature in determining the size of resonances and whether they are compact or extended objects. If they are extended the "molecular" interpretation, i.e. predominantly formed from a two-meson interaction,

would be preferred over the interpretation where the binding force is between quarks. Unfortunately, the concept of size is poorly defined for resonances, since the spatial part of their wave-function is non-normalizable. In particular, the simple extrapolation of methods that can determine the compositeness of bound states [42–44] is not directly translatable to resonances. Some efforts to generalize the concept of size, radius or some compositeness criteria can be found in [45–50]. For instance, in [50], the scalar radius was generalized to a complex number finding: $\langle r^2\rangle_s^\sigma = (0.19 \pm 0.02) - i(0.06 \pm 002)\,\mathrm{fm}^2$, i.e., close in modulus but smaller than a typical meson radius. In contrast, in our case the range of the Yukawa potential that mimics the Regge trajectory is a well-defined quantity, giving a very intuitive picture of the range of the interactions responsible for the formation of the resonance.

Returning to our values, the interaction range we have found is somewhat smaller but of the order of typical values of meson–meson observables like the scalar scattering lengths $a_0^{(I)}$, where I is the isospin in $\pi\pi$ or πK. Their values are $a_0^{(0)} \simeq a_0^{(1/2)} \simeq 1.6\ \mathrm{GeV}^{-1} \simeq 0.3\,\mathrm{fm}$. Therefore the range of interactions producing κ and σ seem comparable but somewhat smaller than meson–meson interactions themselves. Keeping in mind that the range of the interaction is not directly the "size" of a resonance our interaction ranges compare rather well with the modulus of the radius $\sqrt{|\langle r^2\rangle_s^\sigma|} \simeq 0.45\,\mathrm{fm}$ obtained in [50]. Very naively one would expect the interaction range to be smaller than any generalization of the radius, since after all the resonance is a quasi-bound state that escapes from the typical interaction range.

Moreover, if the interactions is of the meson–meson type, a rather natural mass scale for the system is the reduced mass of the two mesons. If a naive $a \sim 1/\mu$ proportionality is assumed for the range, one would expect: $a_{\pi\pi}/a_{\pi K} \approx \mu_{\pi K}/\mu_{\pi\pi} = 1.56$. Remarkably, from our previous estimates of the effective range we find $a_{\pi\pi}/a_{\pi K} \simeq 1.39$, i.e. within a 10% from that expectation. This would also be consistent with the interpretation that both σ and κ are predominantly meson–meson resonances.

4 Conclusions

In contrast to the usual phenomenological approach of fitting the spin and squared mass of hadrons into linear trajectories, in this work we have applied a method *to calculate* Regge trajectories without assuming a priori their functional form. In addition, instead of using as input the parameters of several resonances, the only input is the position and residue of the pole associated to a single resonance. The method applies to elastic meson resonances, i.e., those resonances that decay almost completely into a single two-meson channel. In particular, the method has been previously shown to predict that the $\rho(770)$, $f_2(1270)$, $f_2'(1525)$ and $K^*(892)$ Regge trajectories are almost real and linear with a constant slope of roughly $0.9\ \mathrm{GeV}^{-2}$, in good agreement with the expectations for a confining interaction between a constituent quark and an antiquark, i.e. for ordinary mesons. In contrast, the Regge trajectory of the controversial $f_0(500)$ or σ meson, was found to be non-real, not linear and with a much smaller slope than ordinary trajectories.

Here we have applied this method to the controversial $K_0^*(800)$ or κ meson and to the almost elastic and scalar strange $K_0^*(1430)$ resonance. For the latter we have found a rather ordinary trajectory which suggests that its nature is largely dominated by confining quark–antiquark interactions. The $K_2^*(1980)$ is even a fairly reasonable candidate to be its next trajectory partner with $J = 2$, although with some tension in the parameters, so that it would not be too surprising if the $K_0^*(1430)$ had other subdominant, but sizable, non-$q\bar{q}$ components.

Of course, the most interesting result of this work is the trajectory of the controversial $K_0^*(800)$, which for long has been considered a non-ordinary meson candidate. The Regge trajectory we find for this resonance is not predominantly real and its real part is not linear. This clearly supports the identification of this state as a non-ordinary meson. Moreover, its Regge trajectory slope at the physical mass is much smaller than the universal slope of ordinary trajectories. This also seems to suggest that meson physics, more than interquark interactions, might be responsible for its formation.

In addition, the trajectory of $K_0^*(800)$ is very similar to that already found for the $f_0(500)$ or σ meson, thus supporting the widely extended view that both belong to the same light scalar nonet. Furthermore, at low energies the trajectories of these two resonances have very significant similarities with the trajectories of Yukawa potentials between two mesons, whose range has been estimated here: $\sim 0.36\ \mathrm{GeV}^{-1}$ for κ and $\sim 0.5\ \mathrm{GeV}^{-1}$ for σ. This is of interest because, being non-normalizable states, it is very hard to define the concept of "size" for resonances, whereas the range of the interaction that produces the resonance is a well-defined and intuitive concept. Incidentally, the interaction range seems compatible with a scaling inversely proportional to the reduced mass of the meson system, which also seems relatively natural if the meson–meson interactions plays a dominant role in the resonance formation.

Altogether, our results seem to support a predominantly non-ordinary nature for $K_0^*(800)$ and suggest that its formation is mainly due to meson–meson dynamics.

Acknowledgements Work supported by the Spanish Projects FPA2014-53375-C2-2, FPA2016-75654-C2-2-P and the group UPARCOS and the Spanish Excellence network HADRONet FIS2014-57026-REDT. A. Rodas would also like to acknowledge the financial support of the Universidad Complutense de Madrid through a predoctoral scholarship.

Funded by SCOAP[3].

References

1. J.T. Londergan, J. Nebreda, J.R. Pelaez, A. Szczepaniak, Phys. Lett. B **729**, 9 (2014)
2. J.A. Carrasco, J. Nebreda, J.R. Pelaez, A.P. Szczepaniak, Phys. Lett. B **749**, 399 (2015)
3. P.B.D. Collins, *An Introduction to Regge Theory and High Energy Physics* (Cambride Univerity Press, Cambridge, 1977)
4. V.M. Gribov, *The Theory of Complex Angular Momenta* (Cambride Univerity Press, Cambridge, 2003)
5. P.D.B. Collins, R.C. Johnson, E.J. Squires, Phys. Lett. B **26**, 223 (1968)
6. G. Epstein, P. Kaus, Phys. Rev. **166**, 1633 (1968)
7. S.-Y. Chu, G. Epstein, P. Kaus, R.C. Slansky, F. Zachariasen, Phys. Rev. **175**, 2098 (1968)
8. I. Caprini, G. Colangelo, H. Leutwyler, Phys. Rev. Lett. **96**, 132001 (2006). arXiv:hep-ph/0512364
9. R. Garcia-Martin, R. Kaminski, J.R. Pelaez, J. Ruiz de Elvira, Phys. Rev. Lett. **107**, 072001 (2011)
10. A.V. Anisovich, V.V. Anisovich, A.V. Sarantsev, Phys. Rev. D **62**, 051502 (2000)
11. J.R. Pelaez, Phys. Rept. **658**, 1 (2016)
12. C. Patrignani et al. (Particle Data Group), Chin. Phys. C **40**, 100001 (2016)
13. R.L. Jaffe, Phys. Rev. D **15**, 267 (1977)
14. E. van Beveren et al., Z. Phys. C **30**, 615 (1986)
15. J.A. Oller, E. Oset, J.R. Pelaez, Phys. Rev. Lett. **80**, 3452 (1998)
16. J.A. Oller, E. Oset, J.R. Pelaez, Phys. Rev. D **59**, 074001 (1999) [Erratum-ibid. D **60**, 099906 (1999)] [Erratum-ibid. D **75**, 099903 (2007)]
17. D. Black, A.H. Fariborz, F. Sannino, J. Schechter, Phys. Rev. D **58**, 054012 (1998)
18. D. Black, A.H. Fariborz, F. Sannino, J. Schechter, Phys. Rev. D **59**, 074026 (1999)
19. J.A. Oller, E. Oset, Phys. Rev. D **60**, 074023 (1999)
20. F.E. Close, N.A. Tornqvist, J. Phys. G **28**, R249 (2002)
21. J.R. Pelaez, Phys. Rev. Lett. **92**, 102001 (2004)
22. J.R. Pelaez, Mod. Phys. Lett. A **19**, 2879 (2004)
23. S. Descotes-Genon, B. Moussallam, Eur. Phys. J. C **48**, 553 (2006)
24. T. Wolkanowski, M. Soltysiak, F. Giacosa, Nucl. Phys. B **909**, 418 (2016)
25. S.N. Cherry, M.R. Pennington, Nucl. Phys. A **688**, 823 (2001)
26. J.R. Pelaez, A. Rodas, J. Ruiz de Elvira, Eur. Phys. J. C **77**(2), 91 (2017)
27. J.J. Dudek et al. [Hadron Spectrum Collaboration], Phys. Rev. Lett. **113**(18), 182001 (2014)
28. J. Nebreda, J.R. Pelaez, Phys. Rev. D **81**, 054035 (2010)
29. J.R. Pelaez, A. Rodas, Phys. Rev. D **93**(7), 074025 (2016)
30. P. Estabrooks et al., Nucl. Phys. B **133**, 490 (1978)
31. D. Aston et al., Nucl. Phys. B **296**, 493 (1988)
32. A.H. Fariborz, R. Jora, J. Schechter, Phys. Rev. D **72**, 034001 (2005)
33. A.H. Fariborz, R. Jora, J. Schechter, Phys. Rev. D **76**, 014011 (2007)
34. A.H. Fariborz, R. Jora, J. Schechter, Phys. Rev. D **77**, 034006 (2008)
35. A.H. Fariborz, R. Jora, J. Schechter, M.N. Shahid, Phys. Rev. D **84**, 113004 (2011)
36. F. Giacosa, Phys. Rev. D **75**, 054007 (2007)
37. M. Ablikim et al. [BES Collaboration], Phys. Lett. B **698**, 183 (2011)
38. S. Godfrey, N. Isgur, Phys. Rev. D **32**, 189 (1985)
39. C. Lovelace, D. Masson, Nuovo Cimento **26**, 472 (1962)
40. A.O. Barut, F. Calogero, Phys. Rev. **128**, 1383 (1962)
41. A. Ahamadzadeh, P.G. Burke, C. Tate, Phys. Rev. **131**, 1315 (1963)
42. S. Weinberg, Phys. Rev. **130**, 776 (1963)
43. S. Weinberg, Phys. Rev. **131**, 440 (1963)
44. S. Weinberg, Phys. Rev. B **137**, 672 (1965)
45. V. Baru, J. Haidenbauer, C. Hanhart, Y. Kalashnikova, A.E. Kudryavtsev, Phys. Lett. B **586**, 53 (2004)
46. J. Yamagata-Sekihara, J. Nieves, E. Oset, Phys. Rev. D **83**, 014003 (2011)
47. T. Hyodo, D. Jido, A. Hosaka, Phys. Rev. C **85**, 015201 (2012)
48. F. Aceti, L.R. Dai, L.S. Geng, E. Oset, Y. Zhang, Eur. Phys. J. A **50**, 57 (2014)
49. Z.H. Guo, J.A. Oller, Phys. Rev. D **93**(9), 096001 (2016)
50. M. Albaladejo, J.A. Oller, Phys. Rev. D **86**, 034003 (2012)

Chapter 5

Conclusions

How can I be so bad at everything I try, and still be so great?

– Bender Bending Rodríguez

Throughout this thesis we studied a wide range of applications of dispersion relations and S-matrix principles, with special attention to those related to πK and $\pi\pi \to K\bar{K}$ scattering. In particular, our main goals, which were to determine with high precision and in a model independent way the parameters of meson resonances, with particular emphasis in the long time debated $\kappa/K_0^*(700)$ and the hybrid meson $\pi_1(1600)$, was achieved.

In the second chapter we obtained consistent, precise and model-independent parameterizations for all $\pi\pi \to \pi\pi$, $\pi K \to \pi K$ and $\pi\pi \to K\bar{K}$ scattering processes. In order to do so we first took into account the systematic effects, discarding data points that violate unitarity, or that do not follow the normal distribution, finally obtaining a set of fits that respect gaussianity. We carefully took into account all partial waves with relevant angular momenta, which correspond to $\ell \leq 4$ for $\pi K \to \pi K$ and $\ell \leq 3$ for $\pi\pi \to K\bar{K}$ scattering. Hence, we tested the fulfillment of different dispersion relations, finding important deviations. After imposing these equations we obtained the desired set of parameterizations, which describe both the data and the dispersive equations, while at the same time the most relevant low-energy parameters were predicted with high accuracy.

In the case of $\pi K \to \pi K$ scattering, the solutions of section 2.2.3 describe well the data up to 1.8 GeV, where the amplitudes can then be approximated by Regge theory as explained in section 1.4. Besides the low-energy region, we were able to fulfill dispersion relations up to the matching point where Regge theory is introduced, providing a new dispersive constraint also for the factorization constants. The accurate determination of the scattering lengths is obtained through the use of three sum rules

and the extrapolation of the anti-symmetric amplitude below the $(m_\pi + m_K)$ threshold. Our result for $\pi K \to \pi K$ scattering describes the data up to 1.7 GeV, while it fulfils analyticity, which is the first dispersive determination of the inelastic region. Finally, although part of our results in the low-energy region are compatible with [2], our vector partial wave describes the data, contrary to the previous work.

As for the $\pi\pi \to K\bar{K}$ scattering proccess, we analyzed in a dispersive way the physical region for the first time, finding many caveats and two possible solutions within the literature. We also determined a new dispersive solution of the phase for the g_0^0 wave after fixing some inconsistencies in the experimental analysis of [263]. Finally, a precise description of all relevant partial waves, which also describes the Muskhelishvili–Omnès solution in the unphysical region is provided in 2.2.4.

In addition, the combined analysis of $\pi K \to \pi K$ and $\pi\pi \to K\bar{K}$ scatterings is first presented in 2.3. After updating some previously defined parameterizations we solved the whole system of equations for the first time. The result was obtained using a total of 18 dispersion relations, which are all well satisfied within uncertainties once the fits are constrained. The low-energy parameters of several partial waves are calculated and the tension with Lattice QCD calculations is solved.

Finally, an extension of the successful $\pi\pi \to \pi\pi$ scattering analysis of [3] is performed in section 2.4.3. We performed a set of global fits for the scalar and vector partial waves that describe simultaneously the central value and its uncertainties of the low-energy expansion, the elastic and inelastic dispersion relations, and their whole convergence region in the complex plane. Finally, the new fits also accommodate the poles of the relevant resonances appearing in this process, in particular the $\sigma/f_0(500)$, $f_0(980)$ and $\rho(770)$, which are perfectly compatible with the dispersive result in [112].

In the third chapter focused on the model-independent, robust determination of resonance parameters appearing in scattering and production processes. There are a wide variety of results to be summarized, the first one is the precise extraction of the $\kappa/K_0^*(700)$ and some other strange resonance poles by means of an analytic extrapolation using sequences of Padé approximants, which provide a stable and very accurate determination of the parameters of every state studied. This result triggered the denomination change of the $\kappa/K_0^*(700)$ from the old $\kappa/K_0^*(800)$ name. Additionally, for the $\kappa/K_0^*(700)$ pole we obtained a second determination, the most rigorous one, coming from two different sets of hyperbolic dispersion relations. We think this result may conclude its long debated existence, also proving that if the descriptions are obtained respecting S-matrix principles the uncertainty in the pole position is fairly small. Besides the $\kappa/K_0^*(700)$, we were also able to exploit the Padé approximants in the inelastic region for the first time, giving rise to the precise calculation of 5 more resonances, whose parameters are compared against the ones listed by the PDG, just to show how unreliable model calculations are for higher angular momentum, or wide resonances.

These analytic principles may also be implemented for production processes, where we studied the $\eta^{(\prime)}\pi$ system looking for the poles of two different hybrid mesons as

listed in the PDG [4]. However, no statistical evidence for the lighter one is found, thus disfavoring the widely considered PDG hypothesis. This result also reconciles the predictions coming from Lattice QCD, where only one state is found. Also, by using a coupled-channel dispersive formalism we were not only able to describe all data with only one resonance, but also to extract its parameters in a precise and robust way. This is the most precise and reliable determination of the $\pi_1(1600)$ up to date.

In order to extract information of many upcoming data analyses, particularly on exotic resonances, one needs to control 3-body interactions. Although no perfect general formalism is found, there are several reliable approximations in the literature. In the last section of the third chapter we studied a quasi-two-body dispersive formalism with which we were able to extract the parameters of the axial $a_1(1260)$, using the data of the ALEPH collaboration [264]. The method was more reliable and stable than more naive approximations, and thus was tested against them in the paper. A detailed extraction and calculation of both systematic and statistic uncertainties is provided.

Finally, in the last chapter we studied the nature of two scalar strange resonances, the heavier $K_0^*(1430)$ and the lighter $\kappa/K_0^*(700)$. The analysis was performed by dispersively calculating their Regge trajectories, which is an accurate determination that does not rely on models nor in fits. As expected, the $K_0^*(1430)$ appears as an ordinary $q\bar{q}$ meson, with a straight, customary Regge trayectory. However, the trajectory of the $\kappa/K_0^*(700)$ is clearly not ordinary, with a much smaller slope than the one expected for mesons. Furthermore, it is compatible with a Yukawa-like potential at low energies, suggesting a quasi-molecular behavior. Finally, we compared our result with that of the $\sigma/f_0(500)$ [5], and both look similar, with effective ranges whose ratio behaves like the ratio between the reduced mass of the πK and $\pi\pi$ systems, respectively, also supporting a molecular picture.

As a final remark, we have seen how our results shed light upon several fields of hadronic physics. Even more, we were able to perform precise calculations in areas that have been a long-standing field of debate. We thus expect that our works provide enough evidence to clarify some confusions, and that they become a reliable source of information for all phenomenologists working on low-energy physics. Finally, most of our determinations may be of help for the experimental community, hereby, all the code developed during this thesis is openly provided upon request.

Appendix A

Derivation of Roy-Steiner like equations

In this appendix we present an explicit derivation of the Roy-Steiner-like equations used in sections 2.2.4, 2.3, 2.4.3 and 3.1.4. We will first start with the derivation of the Roy-like equations, but with one less subtraction than the ones in [114]. They are called GKPY equations and were first introduced in [3, 129].

Let us start by writing down a once-subtracted dispersion relation for $\pi\pi \to \pi\pi$ scattering

$$\begin{aligned}\mathrm{Re}\, T^I(s,t) = \mathrm{Re}\, T^I(s_0,t) + \frac{s-s_0}{\pi} PV \int_{4m_\pi^2}^{\infty} ds' \frac{\mathrm{Im}\, T^I(s',t)}{(s'-s_0)(s'-s)} \\ + \frac{s-s_0}{\pi} PV \int_{-t}^{-\infty} ds' \frac{\mathrm{Im}\, T^I(s',t)}{(s'-s_0)(s'-s)},\end{aligned} \tag{A.1}$$

where now we recast the dummy variable s' as $u' \to 4m_\pi^2 - t - s'$and we set $s_0 = 0$, so that we can group both integrals and get:

$$\mathrm{Re}\, T^I(s,t) = \mathrm{Re}\, T^I(0,t) + \frac{s}{\pi} PV \int_{4m_\pi^2}^{\infty} ds' \left[\frac{\mathrm{Im}\, T^I(s',t)}{s'(s'-s)} - \frac{\mathrm{Im}\, T^I(u',t)}{u'(u'-s)} \right]. \tag{A.2}$$

In order to rewrite the contribution of the u-channel we will make use of the crossing matrices defined in section 2.1, Eq. (2.7), which related the crossed channels as

$$\begin{aligned} T^I(u',t) &= T^I\left(4m_\pi^2 - s' - t, t\right) = \sum_{I'} C_{su}^{II'} T^{I'}(s',t), \\ T^I(0,t) &= \sum_{I''} C_{st}^{II''} T^{I''}(t,0). \end{aligned} \tag{A.3}$$

We can now write a dispersion relation for the crossed amplitude $T^{I''}(t,s)$ with the

subtraction point t_0 and evaluated at $s = 0$

$$T^{I''}(t,0) = T^{I''}(t_0,0) + \frac{t-t_0}{\pi}\int_{4m_\pi^2}^{\infty} ds' \left[\frac{\operatorname{Im} T^{I''}(s',0)}{(s'-t)(s'-t_0)} - \frac{\sum_{I'''} C_{su}^{I''''} \operatorname{Im} T^{I'''}(s',0)}{(4m_\pi^2 - t - s')(4m_\pi^2 - s' - t_0)}\right]. \tag{A.4}$$

Finally, by setting $t_0 = 4m_\pi^2$ we get the scattering length as $T^I(4m_\pi^2, 0) = a_0^I$, so that we can rewrite Eq. (A.1) as:

$$\operatorname{Re} T^I(s,t) = \sum_{I'} C_{st}^{II'} a_0^{I'} + \frac{s}{\pi} PV\int_{4m_\pi^2}^{\infty} ds' \left[\frac{\operatorname{Im} T^I(s',t)}{s'(s'-s)} - \frac{\sum_{I'} C_{su}^{II'} \operatorname{Im} T^{I'}(s',t)}{(s'+t-4m_\pi^2)(s'+s+t-4m_\pi^2)}\right]$$
$$+ \frac{t-4m_\pi^2}{\pi} PV\int_{4m_\pi^2}^{\infty} ds' \sum_{I''} C_{st}^{II''} \left[\frac{\operatorname{Im} T^{I'}(s',0)}{(s'-t)(s'-4m_\pi^2)} - \frac{\sum_{I''} C_{su}^{I''I'''} \operatorname{Im} T^{I'''}(s',0)}{s'(s'+t-4m_\pi^2)}\right]. \tag{A.5}$$

In order to project this expression into partial waves we must first define

$$t = \frac{(s-4M_\pi^2)(x-1)}{2}, \quad u = s + t - 4M_\pi^2,$$
$$u' = s' + t - 4M_\pi^2, \quad y = \frac{u'+t}{u'-t}. \tag{A.6}$$

The projections will produce different kernels inside the integrals, they are defined as:

$$K_{\ell\ell'}(s,s') = \frac{s}{\pi s'(s-s')}\int_0^1 dx P_\ell(x) P_{\ell'}(y), \quad L_{\ell\ell'}(s,s') = \frac{s}{\pi}\int_0^1 dx \frac{P_\ell(x) P_{\ell'}(y)}{u'(u+s')}, \tag{A.7}$$
$$M_\ell(s,s') = \frac{1}{\pi(s'-4M_\pi^2)}\int_0^1 dx P_\ell(x)\frac{t-4M_\pi^2}{s'-t}, \quad N_\ell(s,s') = \frac{1}{\pi s'}\int_0^1 dx P_\ell(x)\frac{4M_\pi^2 - t}{u'}.$$

Finally, we include these expressions into Eq. (A.5) and project the amplitudes into partial waves. The final result reads

$$\operatorname{Re} f_\ell^I(s) = \xi_\ell \sum_{I'} C_{st}^{II'} a_0^{I'} + \sum_{\ell'=0}^{\infty} (2\ell'+1)\, PV \int_{4M_\pi^2}^{\infty} ds' \Big[K_{\ell\ell'}(s,s') \operatorname{Im} f_{\ell'}^I(s')$$
$$- L_{\ell\ell'}(s,s') \sum_{I'} C_{su}^{II'} \operatorname{Im} f_{\ell'}^{(I')}(s') + \sum_{I''} C_{st}^{II''} M_\ell(s,s') \operatorname{Im} f_{\ell'}^{(I'')}(s')$$
$$- N_\ell(s,s') \sum_{I''}\sum_{I'''} C_{st}^{II''} C_{su}^{I''I'''} \operatorname{Im} f_{\ell'}^{(I''')}(s')\Big]. \tag{A.8}$$

This expression and its derivation is similar to how the system of Roy equations is obtained in [114]. These were implemented in [3], which will be our input for section 2.2.4.

For $\pi K \to \pi K$ and $\pi\pi \to K\bar{K}$ scattering however, the derivation of the dispersion relations for the amplitudes is more complicated, as one cannot cross the s and t channels without going from $\pi K \to \pi K$ to $\pi\pi \to K\bar{K}$ scattering. Therefore the partial waves of both processes will appear inside our system of dispersion relations. The first application to this processes was carried out by Johannesson and Nilsson in 1978 [132], where they mixed fixed-t and Hyperbolic Dispersion Relations to relate the subtraction constants with low-energy parameters. Let us sketch the derivation for $a \neq 0$ and T^+. We start by writing down two different once-subtracted dispersion relations

$$T^+(s,t) = c^+(t) + \frac{1}{\pi}\int_{m_+^2}^{\infty} ds' \frac{\mathrm{Im}\, T^+(s',t)}{s'^2}\left(\frac{s^2}{s'-s} + \frac{u^2}{s'-u}\right), \tag{A.9}$$

$$T^+(t,b,a) = h^+(b,a) + \frac{t}{\pi}\int_{4m_\pi^2}^{\infty} \frac{\mathrm{Im}\, T^{I_t=0}(t',s'_b)}{\sqrt{6}\, t'(t'-t)} dt' + \frac{1}{\pi}\int_{m_+^2}^{\infty} ds' \frac{\mathrm{Im}\, T^+(s',t'_b)}{s'}\left(\frac{s}{s'-s} + \frac{u}{s'-u}\right), \tag{A.10}$$

where the first one is a fixed-t dispersion relation and the second is a hyperbolic one, with the customary definition of the Mandesltam variables over the hyperbola

$$s'_b \equiv s_b(t'), \quad u'_b \equiv u_b(t'), \quad t'_b = 2\Sigma - s' - \frac{b}{s'-a} + a. \tag{A.11}$$

As shown in Eq. (A.10), the subtraction constant of the fixed-t dispersion relation depends only on t, so that by equating both amplitudes at a given $b = b_0$ we get

$$\begin{aligned} c^+(t) = {} & h^+(b_0,a) + \frac{t}{\pi}\int_{4m_\pi^2}^{\infty} \frac{\mathrm{Im}\, T^{I_t=0}(t',s'_{b_0})}{\sqrt{6}\, t'(t'-t)} dt' + \frac{1}{\pi}\int_{m_+^2}^{\infty} ds' \frac{\mathrm{Im}\, T^+(s',t'_{b_0})}{s'}\left(\frac{s_{b_0}}{s'-s_{b_0}} + \frac{u_{b_0}}{s'-u_{b_0}}\right) \\ & - \frac{1}{\pi}\int_{m_+^2}^{\infty} ds' \frac{\mathrm{Im}\, T^+(s',t)}{s'^2}\left(\frac{s_{b_0}^2}{s'-s_{b_0}} + \frac{u_{b_0}^2}{s'-u_{b_0}}\right), \end{aligned} \tag{A.12}$$

where the values of s and u of the first line lie in the hyperbola $(s-a)(u-a) = b$ and thus s, u are defined through

$$\begin{aligned} s_b \equiv s_b(t) &= \frac{1}{2}\left(2\Sigma - t + \sqrt{(t+2a-2\Sigma)^2 - 4b}\right), \\ u_b \equiv u_b(t) &= \frac{1}{2}\left(2\Sigma - t - \sqrt{(t+2a-2\Sigma)^2 - 4b}\right). \end{aligned} \tag{A.13}$$

We can now evaluate $h(b,a)$ in a simple way, first, it is worth noticing that at $t = 0$ and $b = b_0 = a^2 - 2\Sigma a + \Delta^2$ we get

$$\begin{aligned} s_b = s_{th} &= (m_\pi + m_K)^2, \\ u_b = u_{th} &= (m_\pi - m_K)^2. \end{aligned} \tag{A.14}$$

Now, according to our normalization, the value of the amplitude at threshold is $T^+(s_{th},0) = 8\pi m_+ a_0^+$, where $m_+ = (m_\pi + m_K)$, so if we set $t = 0$ and $b = b_0$ we get

$$h(b_0,a) = 8\pi m_+ a_0^+ - \frac{1}{\pi}\int_{m_+^2}^{\infty} ds' \frac{\mathrm{Im}\, T^+(s',t'_b)}{s'}\left(\frac{s_{b_0,t=0}}{s'-s_{b_0,t=0}} + \frac{u_{b_0,t=0}}{s'-u_{b_0,t=0}}\right). \tag{A.15}$$

As a result, the value of $c^+(t)$ obtained is

$$\begin{aligned} c^+(t) = 8\pi m_+ a_0^+ &+ \frac{t}{\pi}\int_{4m_\pi^2}^{\infty} \frac{\mathrm{Im}\, T^{I_t=0}(t', s'_{b_0})}{\sqrt{6}\, t'(t'-t)} dt' \\ &+ \frac{1}{\pi}\int_{m_+^2}^{\infty} ds' \frac{\mathrm{Im}\, T^+(s', t'_{b_0})}{s'} \left[\left(\frac{s_{b_0}}{s'-s_{b_0}} + \frac{u_{b_0}}{s'-u_{b_0}} \right) - \left(\frac{s_{b_0,t=0}}{s'-s_{b_0,t=0}} + \frac{u_{b_0,t=0}}{s'-u_{b_0,t=0}} \right) \right] \\ &- \frac{1}{\pi}\int_{m_+^2}^{\infty} ds' \frac{\mathrm{Im}\, T^+(s', t)}{s'^2} \left(\frac{s_{b_0}^2}{s'-s_{b_0}} + \frac{u_{b_0}^2}{s'-u_{b_0}} \right). \end{aligned} \tag{A.16}$$

In the same way, by equating both amplitudes first at $t = 0$, and calculating $c^+(0)$ in terms of a_0^+ we get

$$\begin{aligned} h(b,a) = 8\pi m_+ a_0^+ &+ \frac{1}{\pi}\int_{m_+^2}^{\infty} ds' \frac{\mathrm{Im}\, T^+(s', 0)}{s'^2} \left[\left(\frac{s^2}{s'-s} + \frac{u^2}{s'-u} \right) - \left(\frac{s_{th}^2}{s'-s_{th}} + \frac{u_{th}^2}{s'-u_{th}} \right) \right] \\ &- \frac{1}{\pi}\int_{m_+^2}^{\infty} ds' \frac{\mathrm{Im}\, T^+(s', t'_b)}{s'} \left(\frac{s_{b,t=0}}{s'-s_{b,t=0}} + \frac{u_{b,t=0}}{s'-u_{b,t=0}} \right). \end{aligned} \tag{A.17}$$

These two subtraction constants can be simplified taking into account that $(s-a)(u-a) = (s'-a)(u'-a) = b$ in all hyperbolic integrals, using Eq. (A.13) and the relation between Mandelstam variables $s+t+u = 2(m_K^2 + m_\pi^2)$. The final result for both the fixed-t and hyperbolic dispersion relations is:

$$\begin{aligned} T^+(s,t) = 8\pi m_+ a_0^+ &+ \frac{1}{\pi}\int_{m_+^2}^{\infty} ds' \frac{\mathrm{Im}\, T^+(s', t)}{s'^2} \left[\left(\frac{s^2}{s'-s} + \frac{u^2}{s'-u} \right) - k(s', t) \right] \\ &+ \frac{t}{\pi}\int_{4m_\pi^2}^{\infty} \frac{\mathrm{Im}\, T^{I_t=0}(t', s'_b)}{\sqrt{6}\, t'(t'-t)} dt' + \frac{1}{\pi}\int_{m_+^2}^{\infty} ds' \mathrm{Im}\, T^+(s', t_{\Delta^2}) \left(h(s', t, \Delta^2, 0) - h(s', 0, \Delta^2, 0) \right), \\ T^+(s_b,t) = 8\pi m_+ a_0^+ &+ \frac{t}{\pi}\int_{4m_\pi^2}^{\infty} \frac{\mathrm{Im}\, T^{I_t=0}(t', s'_b)}{\sqrt{6}\, t'(t'-t)} dt' \\ &+ \frac{1}{\pi}\int_{m_+^2}^{\infty} ds' \frac{\mathrm{Im}\, T^+(s', t_b)}{s'} \left[h(s', t, b, a) - h(s', 0, b, a) \right] \\ &+ \frac{1}{\pi}\int_{m_+^2}^{\infty} ds' \frac{\mathrm{Im}\, T^+(s', 0)}{s'^2} \left[g(s', b, a) - g(s', \Delta^2, 0) \right], \end{aligned} \tag{A.18}$$

where the kernels are defined as

$$\begin{aligned} h(s', t, b, a) &= \frac{s'(2\Sigma - t) - 2[b - a^2 + (2\Sigma - t)a]}{s'^2 - s'(2\Sigma - t) + [b - a^2 + (2\Sigma - t)a]}, \\ g(s', b, a) &= \frac{s'(2\Sigma)^2 - 2[b - a^2 + 2\Sigma a](s' + \Sigma)}{s'^2 - s'2\Sigma + [b - a^2 + 2\Sigma a]}, \\ k(s', t) &= \frac{1}{s'^2} \frac{s'(2\Sigma - t)^2 - 2\Delta^2 s' - \Delta^2(2\Sigma - t)}{s'^2 - s'(2\Sigma - t) + \Delta^2}. \end{aligned} \tag{A.19}$$

One can follow the same steps for the derivation of the subtraction constant of the once-subtracted $T^-/(s-u)$ dispersion relation. After using the projecting formulas

Eqs (1.48) and (1.49) we get Eqs.(2.27) and (2.28). However, in this case the kernels read

$$d(s',t,b,a) = \frac{1}{s'^2 - s'(2\Sigma - t) + [b - a^2 + (2\Sigma - t)a]},$$
$$f(s',b,a) = \frac{1}{s'^2 - s'2\Sigma + [b - a^2 + 2\Sigma a]}. \tag{A.20}$$

Appendix B

Roy-Steiner range of validity

We have made use of different kinds of Roy-Steiner dispersion relations in sections 2.2.4, 2.3 and 2.4.3. Although there are several works explaining their region of applicability [114, 120, 163, 167, 178, 265], we will briefly review their applicability domain in the complex plane in this appendix.

B.1 Fixed-t dispersion relations

Fixed-t dispersion relations have been shown to be very effective in the study of both equal mass and different mass particles. In the s-channel, they usually offer a bigger applicability region over the more complicated Hyperbolic Dispersion Relations, with a physical region that goes up to $s_{max} \sim 1.1\text{GeV}$ for both $\pi\pi \to \pi\pi$ and $\pi K \to \pi K$ scattering.

In order to calculate the applicability domain in the complex plane we must first evaluate the double-spectral boundaries for each process. These are obtained from the singularities arising from the box diagrams of Appendix D in 2.2.4, which appears at the energies for which the inner particlescan be on-shell according to the Landau-Kutkowski rules. In the case of $\pi\pi \to \pi\pi$ scattering the only relevant boundary, called ρ_{st} is defined by [80]

$$b_I(s,t) : t\,(s - 4m_\pi^2) - 16s\,m_\pi^2 = 0, \tag{B.1}$$
$$b_{II}(s,t) : t\,(s - 16m_\pi^2) - 4s\,m_\pi^2 = 0, \tag{B.2}$$

which produces the following maximum values allowed for t

$$T_{st}(s) = \frac{16s\,m_\pi^2}{s-4m_\pi^2}, \quad \forall s \leq s_0, \tag{B.3}$$

$$T_{st}(s) = \frac{4s\,m_\pi^2}{s-16m_\pi^2}, \quad \forall s \geq s_0, \tag{B.4}$$

where $s_0 = 20m_\pi^2$.

Now, let us recall that this fixed-t value, appearing inside the Roy-Steiner equations will be related with the internal variable of the integral s', not s, which is the external energy variable at which we are evaluating the amplitudes. Taking into account the large Lehmann-Martin ellipse [83, 266, 267], the t variable must be contained in an ellipse with foci at $t = -\lambda_{s'}/s'$ and $t = 0$, with right extremity at $T_{st}(s')$.

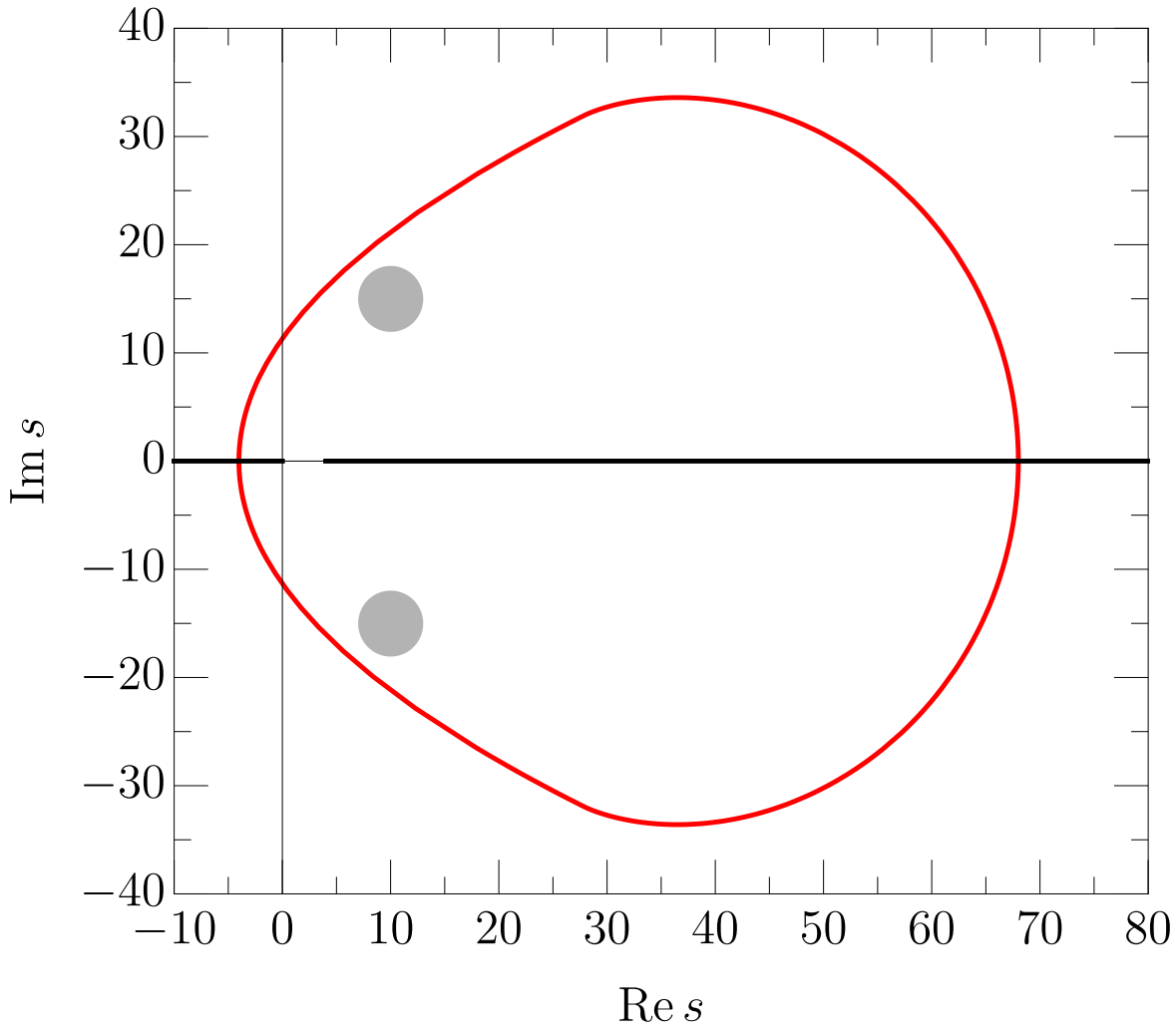

Figure B.1: Domain of validity in the complex s-plane of the fixed-t dispersion relations for $\pi\pi \to \pi\pi$ scattering, in m_π units. The shadowed areas represent the typical region where the $\sigma/f_0(500)$ pole could lie at.

Such an ellipse can be obtained in a very simple way if we use polar coordinates

over the fixed foci at $t = 0$. Producing the following result for the radius

$$T(s', \theta) = \frac{T_{st}(s')(\lambda_{s'} + s' T_{st}(s'))}{\lambda_{s'} \cos^2 \frac{\theta}{2} + s' T_{st}(s')}. \tag{B.5}$$

This equation defines the maximum allowed value for the modulus of t for a given value of the integration variable s'. Now, the t variable will be considered inside the applicability region if it lies inside all possible ellipses, so that the allowed radius is

$$T(\theta) = \min_{s_{th} \leq s' \leq \infty} T(s', \theta). \tag{B.6}$$

Finally, the external s variable will only be inside the domain of validity if the partial wave projection can be performed without touching any boundary. Thus taking into account the s-channel projection formula:

$$f_\ell(s) = \frac{1}{32\pi N} \int_{-1}^{1} dz_s P_\ell(x) T\left(s, t\left(z_s\right), u\right), \tag{B.7}$$

and using the relation

$$z_s = 1 + \frac{2st}{\lambda_s}, \tag{B.8}$$

we can obtain the allowed values for s in the complex plane throughout the equation

$$\lambda_s + sT(\theta) \exp(i\theta) = 0. \tag{B.9}$$

Finally, the equation above defines the region of validity for both $\pi\pi \to \pi\pi$ (Fig. B.1) and $\pi K \to \pi K$ (Fig. B.2) scattering, respectively.

A simple evaluation of the $\sigma/f_0(500)$ and $\kappa/K_0^*(700)$ parameters with large uncertainties in the s plane entails that while fixed-t dispersion relations are suitable to determine the $\sigma/f_0(500)$ pole in the complex plane (see Fig. B.1), the $\kappa/K_0^*(700)$ cannot be obtained with high precision from fixed-t dispersion relations, as it is outside their applicability region (see Fig. B.2). This is the main reason why we have to resort to this very same analytic features for the Hyperbolic Dispersion Relations in the next section.

B.2 Hyperbolic Dispersion Relations

While the region of validity of the fixed-t dispersion relations is easily calculated, the one of the Hyperbolic Dispersion Relations is way more complicated. It involves first the equation over the hyperbola $(s - a)(u - a) = b$, and second it involves both the s-channel ellipse and the t-channel one. Fortunately, almost all needed equations are provided in appendix D of section 2.2.4. In this section we will follow the derivation of [124].

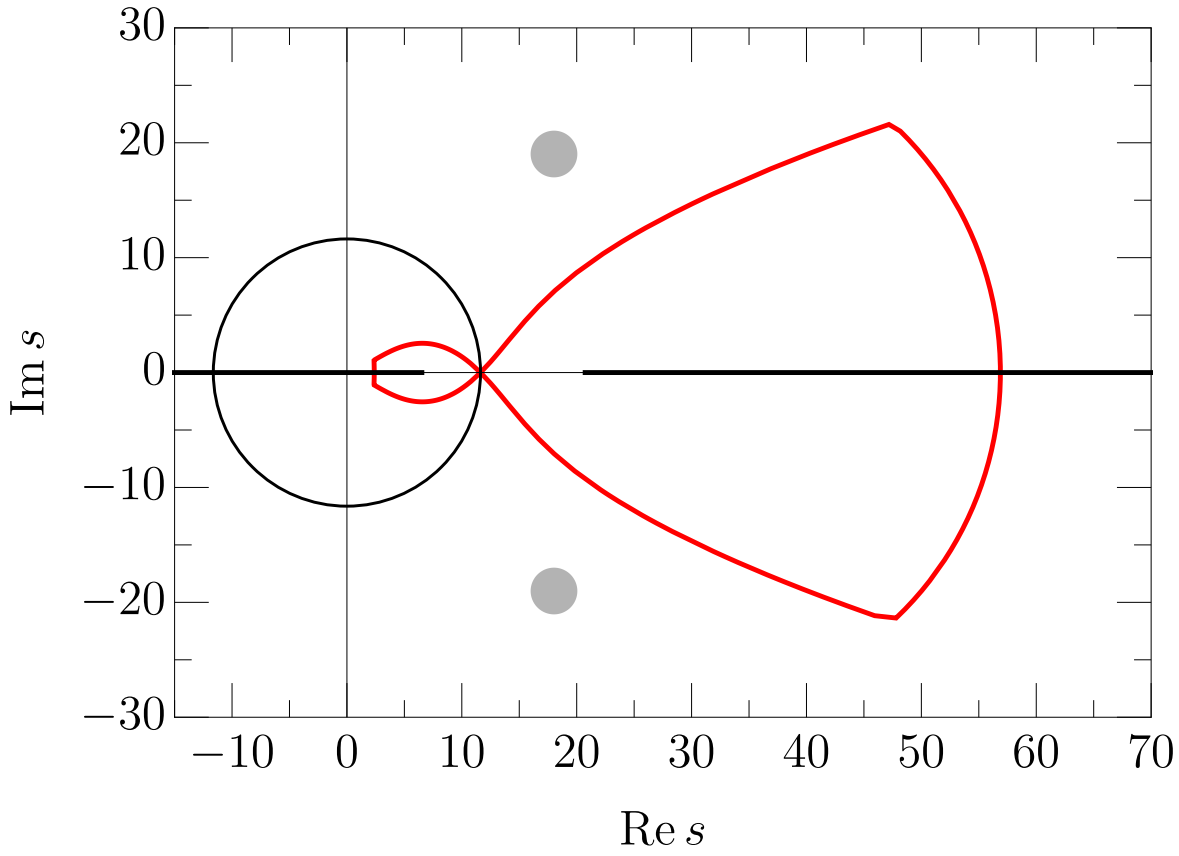

Figure B.2: Domain of validity in the complex s-plane of the fixed-t dispersion relations for $\pi K \to \pi K$ scattering, in m_π units. The shadowed areas represent the typical region where the $\kappa/K_0^*(700)$ pole is found.

Let us start with the simpler derivation of the range of validity over the s-channel Lehmann-Martin ellipse, which is again defined throughout the ellipse with foci at $t = -\lambda_{s'}/s'$ and $t = 0$. However, we shall now use the hyperbolic relation for the b variable

$$b_s(s,t) = (s-a)(2\Sigma - s - t - a), \tag{B.10}$$

so that we end up with an ellipse over b with foci at $b_s = (s-a)(2\Sigma - s' - a)$ and $b_s = (s-a)(2\Sigma - s' + \lambda_{s'}/s' - a)$. This ellipse does not have any fixed foci, which makes the calculation a bit more complicated. Given the value $b_s(s',\theta)$ over the boundary, calculated from the origin of coordinates, the value b inside all possible ellipses is

$$b_s(\theta) = \min_{s_{th} \le s' \le \infty} b_s(s',\theta). \tag{B.11}$$

Finally, the t-channel Lehmann-Martin ellipse must be addressed carefully, as it is fairly more complicated, first, the ellipse must be defined by modifying its original axis, from an ellipse in z_t to a new one in z_t^2 as

$$\frac{\left(\mathrm{Re}\left\{z_t'^2\right\} - \frac{1}{2}\right)^2}{\tilde{A}_t^2} + \frac{\left(\mathrm{Im}\left\{z_t'^2\right\}\right)^2}{\tilde{B}_t^2} = 1, \tag{B.12}$$

where $\tilde{A}_t$ and $\tilde{B}_t$ are related to the original semi-major and semi-minor axis obtained from the boundaries as

$$\tilde{A}_t = \frac{A_t^2 + B_t^2}{2} = A_t^2 - \frac{1}{2}, \qquad \tilde{B}_t = A_t B_t = A_t\sqrt{A_t^2 - 1}, \tag{B.13}$$

next, we use the linear relation

$$z_t'^2 = \frac{(t' - \Sigma + 2a)^2 - 4b\,(s', t'; a)}{16 p_t'^2 q_t'^2}, \tag{B.14}$$

in order to define the left and right extremities for the ellipse in the b variable, which read

$$b_t^-\,(t', a) = \frac{1}{4}\,(t' - \Sigma + 2a)^2 - 4m^2 N_{st}\,(t')^2\,, \tag{B.15}$$

$$b_t^+\,(t', a) = \frac{1}{4}\,(t' - \Sigma + 2a)^2 - 4p_t'^2 q_t'^2 + 4m^2 N_{st}\,(t')^2 = (t' - \Sigma)\,a + a^2 + \Sigma_-^2 + 4m^2 N_{st}\,(t')^2\,,$$

where the $N_{st}(t')$ formula is given in the appendix of section 2.2.4. Again, this formula provides a family of ellipses in t', of which the minimum value will be the b contained inside all of them

$$b_t(\theta) = \min_{4m_\pi^2 \le t' \le \infty} b(t', \theta). \tag{B.16}$$

Finally, the s variable will remain inside the boundary anytime the b values needed for the s-channel partial-wave projection are inside their limits. We use again the partial wave projection formula of Eq. (B.7) and perform the corresponding change of variables from t to b. We finally get that the more restrictive equation for s is

$$(2\Sigma - s - a)(s - a) + b(\theta)\exp(i\theta) = 0. \tag{B.17}$$

The regions of applicability corresponding to both ellipses in Eqs. (B.11) and (B.16) are shown in Fig. B.3, where we have used $a = -9m_\pi^2$ in order to maximize the real axis for which the $\kappa/K_0^*(700)$ pole and its uncertainties lie within the boundaries. Note that as explained in section 2.2.4 the maximum analyticity domain in the real axis is reached for $a = -13.9m_\pi^2$, but it narrows the domain of validity in the complex plane so that the $\kappa/K_0^*(700)$ gets out of the region. Notice that the $\kappa/K_0^*(700)$ pole parameters $\sqrt{s_{pole}} \sim 670 + i290$MeV lie well inside both ellipses.

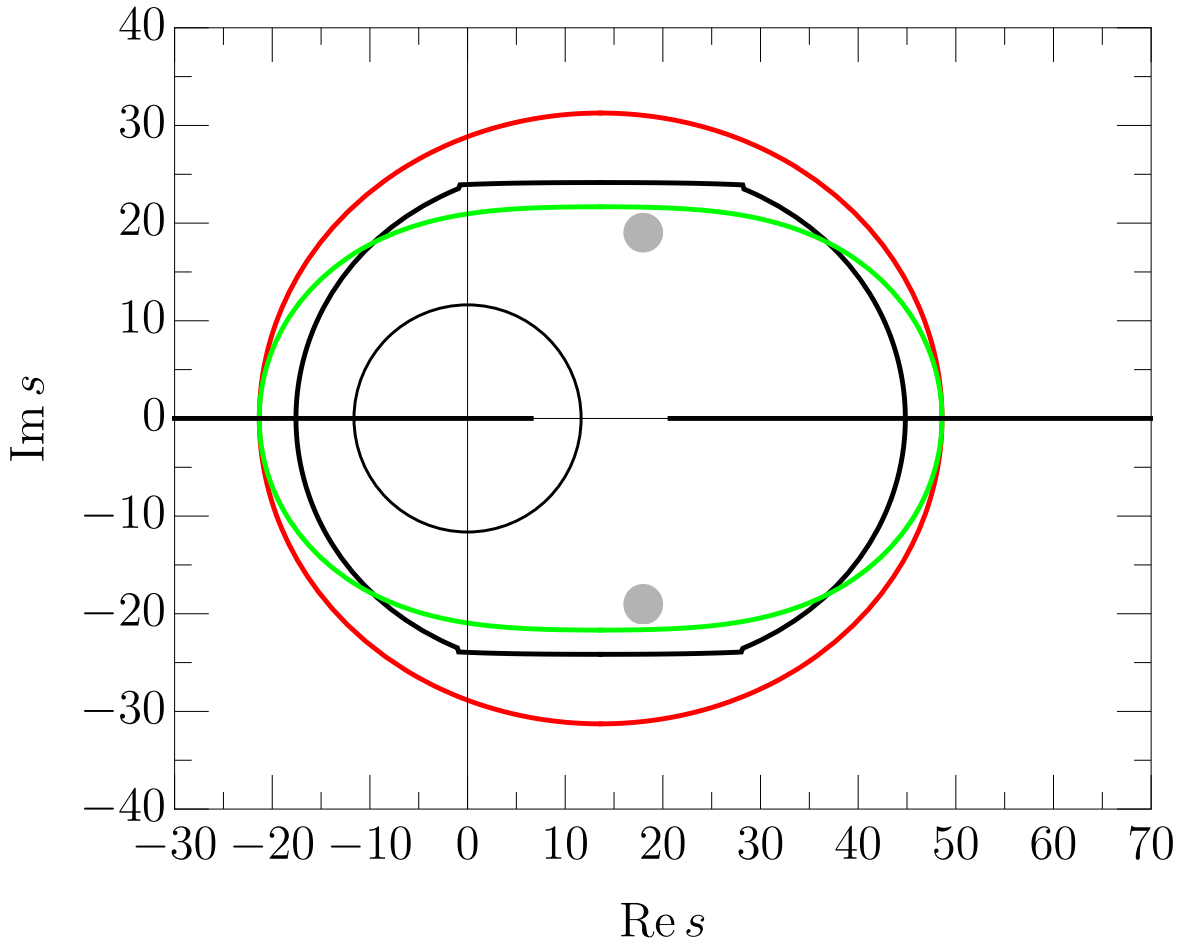

Figure B.3: Domain of validity in the complex s-plane of Hyperbolic Dispersion Relations for $\pi K \to \pi K$ scattering, in m_π units. The red curve depicts the allowed region due to the s-channel contributions, while the green line encloses the very same region for the t-channel contributions, both for $a = -9m_\pi^2$. The black line represents the most restrictive allowed area for $a = 0$ [178]. The shadowed areas represent the region where the $\kappa/K_0^*(700)$ pole is found. Although the applicability region in the real axis can be extended by taking $a = -13.9m_\pi^2$, we find that with this value the $\kappa/K_0^*(700)$ pole lies out of the boundary in the complex plane, so that $a = -9m_\pi^2$ will be used instead to obtain its parameters.

Appendix C

Muskhelishvili-Omnès problem

In this section the solution for the dispersive system of the crossed $\pi\pi \to K\bar{K}$ partial waves $g_\ell^I(t)$ is reviewed in more detail that in section 2.2.4. We derive the general analytic solution, and apply it to our particular case. Finally, a remark on the numerical treatment and continuity of the solution is discussed.

As can be seen in Eq. (2.28), in order to solve the $\pi\pi \to K\bar{K}$ system of dispersion relations, the integrals must be calculated from the $\pi\pi$ threshold. However, the physical region of this process starts at the $K\bar{K}$ threshold and thus an extrapolation to the pseudo-physical region must be performed without any guidance from data. Nevertheless, below the inelastic threshold we can neglect any channel but $\pi\pi$ and then Watson's Theorem implies that the g_ℓ^I phase below $K\bar{K}$ threshold is just that of $\pi\pi$ scattering. Thus we can write $\phi_\ell^I(t) = \delta^I_{\ell,\pi\pi\to\pi\pi}(t)$. Unfortunately, Watson's Theorem does not constrain the modulus of the partial wave in any way, so that an alternative approach to an ordinary dispersive calculation must be performed. Determining the modulus in the unphysical region once the phase is fixed is known as the standard Muskhelishvili-Omnès (MO) problem [268, 269]. Starting from the original partial-wave dispersion relation

$$g_\ell^I(t) = \Delta_\ell^I(t) + \frac{1}{\pi}\int_{t_\pi}^{t_{\rm m}} \mathrm{d}t' \frac{T\,(t')^*\, g_\ell^I\,(t')}{t'-t} + \frac{1}{\pi}\int_{t_{\rm m}}^{\infty} \mathrm{d}t' \frac{\mathrm{Im}\, g_\ell^I\,(t')}{t'-t}, \tag{C.1}$$

where we know the discontinuity up to t_m

$$\frac{\mathrm{Disc}\, g_\ell^I(t)}{2i} = \mathrm{Im}\, g_\ell^I(t) = T(t)^* g_\ell^I(t)\theta\left(t-t_\pi\right), \tag{C.2}$$

the solution can be obtained following the same approach as in [2, 122, 124, 132, 133]. We first start by rewriting the dispersive equations as

$$g_\ell^I(t) = \Delta_\ell^I(t) + \frac{1}{\pi}\int_{4m_\pi^2}^{\infty} dt' \frac{\mathrm{Im}\, g_\ell^I(t)}{t'-t}, \tag{C.3}$$

where we have assumed that no subtractions are necessary for simplicity, although we will include them later depending on the behavior of each partial wave. The function $\Delta_\ell^I(t)$, known as the inhomogeneity, contains all contributions coming from the rest of the partial waves, both from $\pi K \to \pi K$ and $\pi\pi \to K\bar{K}$ scattering, and produces only the left and circular cuts. The right-hand cut is the integral over the discontinuity of the partial wave itself.

Now we define the so-called Omnès function

$$\Omega_\ell^I(t) = \exp\left(\frac{t}{\pi}\int_{4m_\pi^2}^{t_m}\frac{\phi_\ell^I(t')dt'}{t'(t'-t)}\right), \tag{C.4}$$

which satisfies

$$\Omega_\ell^I(t) \equiv \Omega_{l,R}^I(t)e^{i\phi_\ell^I(t)\theta(t-4m_\pi^2)\theta(t_m-t)}, \tag{C.5}$$

where, in the real axis, $\Omega_{l,R}^I(t)$ can be written as:

$$\begin{aligned}\Omega_{l,R}^I(t) &= \left|\frac{t_m}{t_\pi}(t-t_\pi)^{-\phi_\ell^I(t)/\pi}(t_m-t)^{\phi_\ell^I(t)/\pi}\right|\exp\left(\frac{t}{\pi}\int_{4m_\pi^2}^{t_m}dt'\frac{\phi_\ell^I(t')-\phi_\ell^I(t)}{t'(t'-t)}\right)\\ &= \overline{\Omega_l^I}(t)|t_m-t|^{\phi_\ell^I(t)/\pi}.\end{aligned} \tag{C.6}$$

It is worth noticing that, by construction, the Omnès function contains the very same phase shift as the partial wave up to t_m and hence they share the same right-hand cut. We thus define a new function, containing only a right-hand cut starting above t_m as

$$F_\ell^I(t) = \frac{g_\ell^I(t)-\Delta_\ell^I(t)}{\Omega_\ell^I(t)}, \tag{C.7}$$

where the analytic structure is as follows, there is a finite cut from $4m_\pi^2$ up to t_m due to $\Delta_\ell^I(t)/\Omega_\ell^I(t)$, and an infinite cut from t_m up to infinity due to $g_\ell^I(t)/\Omega_\ell^I(t)$. Hence, by assuming that no subtractions are needed for $F_\ell^I(t)$, as we did for $g_\ell^I(t)$ we get

$$F_\ell^I(t) = \frac{1}{\pi}\int_{4m_\pi^2}^{t_m}dt'\frac{\Delta_\ell^I(t')\sin\phi_\ell^I(t')}{\Omega_{\ell,R}^I(t')(t'-t)} + \frac{1}{\pi}\int_{t_m}^{\infty}dt'\frac{|g_\ell^I(t')|\sin\phi_\ell^I(t')}{\Omega_{\ell,R}^I(t')(t'-t)}. \tag{C.8}$$

The equation above then produces the following result for the partial wave

$$g_\ell^I(t) = \Delta_\ell^I(t) + \Omega_\ell^I(t)\left[\frac{1}{\pi}\int_{4m_\pi^2}^{t_m}dt'\frac{\Delta_\ell^I(t')\sin\phi_\ell^I(t')}{\Omega_{\ell,R}^I(t')(t'-t)} + \frac{1}{\pi}\int_{t_m}^{\infty}dt'\frac{|g_\ell^I(t')|\sin\phi_\ell^I(t')}{\Omega_{\ell,R}^I(t')(t'-t)}\right], \tag{C.9}$$

or more conveniently, in terms of a principal value integral

$$\begin{aligned}g_\ell^I(t) = \Bigg\{\Delta_\ell^I(t)\cos\delta_\ell^I(t) + |\Omega_\ell^I(t)|\Bigg[&\frac{1}{\pi}PV\int_{4m_\pi^2}^{t_m}dt'\frac{\Delta_\ell^I(t')\sin\phi_\ell^I(t')}{\Omega_{\ell,R}^I(t')(t'-t)}\\ &+\frac{1}{\pi}\int_{t_m}^{\infty}dt'\frac{|g_\ell^I(t')|\sin\phi_\ell^I(t')}{\Omega_{\ell,R}^I(t')(t'-t)}\Bigg]\Bigg\}\mathrm{e}^{i\delta_\ell^I(t)}.\end{aligned} \tag{C.10}$$

There are two different kinds of subtractions that may be included depending on the behavior of the partial wave. One the one hand, there are are the genuine subtractions necessary to ensure the convergence of the original dispersion relation Eq. (2.28). As a result, this new equation turns out to be

$$g_\ell^I(t) = \Delta_\ell^I(t) + t^n \Omega_\ell^I(t) \left[\frac{1}{\pi} \int_{4m_\pi^2}^{t_m} dt' \frac{\Delta_\ell^I(t') \sin \phi_\ell^I(t')}{\Omega_{\ell,R}^I(t') t'^n (t'-t)} + \frac{1}{\pi} \int_{t_m}^{\infty} dt' \frac{|g_\ell^I(t')| \sin \phi_\ell^I(t')}{\Omega_{\ell,R}^I(t') t'^n (t'-t)} \right]. \tag{C.11}$$

On the other hand, the second kind of subtractions depend on the behavior of $\Omega_\ell^I(t)$ when $t \to t_m$. If for example $\phi_\ell^I(t_m) > \pi$, then according to Eq. (C.6) the singularity produced by the Omnés function is not integrable. Another subtraction should be included to ensure the integrability of the MO equations when $t' \to t_m$. Thus, by defining a new function

$$\hat{F}_\ell^I(t) = \frac{(g_\ell^I(t) - \Delta_\ell^I(t))(t_m - t)}{\Omega_\ell^I(t)}, \tag{C.12}$$

the singularity is now integrable, and we can thus write a dispersion relation for $g_\ell^I(t)$. However, one subtraction needs to be included to ensure that the dispersion relation for $\hat{F}_\ell^I(t)$ converges. The final result reads:

$$\begin{aligned} g_\ell^I(t) = \Delta_\ell^I(t) + t^n \frac{\Omega_\ell^I(t)}{(t_m - t)} \Bigg[\alpha + \frac{t}{\pi} \int_{4m_\pi^2}^{t_m} dt' \frac{(t_m - t') \Delta_\ell^I(t') \sin \phi_\ell^I(t')}{\Omega_{\ell,R}^I(t') t'^{n+1} (t'-t)} \\ + \frac{t}{\pi} \int_{t_m}^{\infty} dt' \frac{(t_m - t') |g_\ell^I(t')| \sin \phi_\ell^I(t')}{\Omega_{\ell,R}^I(t') t'^{n+1} (t'-t)} \Bigg]. \end{aligned} \tag{C.13}$$

Taking into account all these results we can finally calculate the complete system of equations for $\pi\pi \to K\bar{K}$ scattering, which read

$$\begin{aligned} g_0^0(t) &= \Delta_0^0(t) + \frac{t \Omega_0^0(t)}{t_m - t} \left[\alpha + \frac{t}{\pi} \int_{4m_\pi^2}^{t_m} dt' \frac{(t_m - t') \Delta_0^0(t') \sin \phi_0^0(t')}{\Omega_{0,R}^0(t') t'^2 (t'-t)} \right. \\ &\quad \left. + \frac{t}{\pi} \int_{t_m}^{\infty} dt' \frac{(t_m - t') |g_0^0(t')| \sin \phi_0^0(t')}{\Omega_{0,R}^0(t') t'^2 (t'-t)} \right], \\ g_1^1(t) &= \Delta_1^1(t) + \Omega_1^1(t) \left[\frac{1}{\pi} \int_{4m_\pi^2}^{t_m} dt' \frac{\Delta_1^1(t') \sin \phi_1^1(t')}{\Omega_{1,R}^1(t') (t'-t)} + \frac{1}{\pi} \int_{t_m}^{\infty} dt' \frac{|g_1^1(t')| \sin \phi_1^1(t')}{\Omega_{1,R}^1(t') (t'-t)} \right], \\ g_1^1(t) &= \hat{\Delta}_1^1(t) + t \Omega_1^1(t) \left[\frac{1}{\pi} \int_{4m_\pi^2}^{t_m} dt' \frac{\hat{\Delta}_1^1(t') \sin \phi_1^1(t')}{\Omega_{1,R}^1(t') t' (t'-t)} + \frac{1}{\pi} \int_{t_m}^{\infty} dt' \frac{|g_1^1(t')| \sin \phi_1^1(t')}{\Omega_{1,R}^1(t') t' (t'-t)} \right], \\ g_2^0(t) &= \Delta_2^0(t) + t \Omega_2^0(t) \left[\frac{1}{\pi} \int_{4m_\pi^2}^{t_m} dt' \frac{\Delta_2^0(t') \sin \phi_2^0(t')}{\Omega_{2,R}^0(t') t' (t'-t)} + \frac{1}{\pi} \int_{t_m}^{\infty} dt' \frac{|g_2^0(t')| \sin \phi_2^0(t')}{\Omega_{2,R}^0(t') t' (t'-t)} \right]. \end{aligned} \tag{C.14}$$

Note that we have written two dispersion relations for $g_1^1(t)$: In the second line with no genuine subtractions and in the third line with one genuine subtraction. In section 2.3 we explained why we are interested in studying these two cases.

Even though all analytic MO expressions are manifestly integrable, the divergent nature of the Omnès function produces a large cusp at t_m that cannot be handled by standard integration subroutines. The solution of a standard algorithm will largely depend on the grid of points and the integration time taken to perform the evaluation. In order to avoid these drawbacks we will perform a suitable change of variables following [2] which ensures a much smoother behavior close to t_m. We start by splitting the integrals below and above t_m by a small value τ, for simplicity we will study the case of a non subtracted MO equation

$$g_\ell^I(t) = \Delta_\ell^I(t) + \frac{\Omega_\ell^I(t)}{\pi}\left[\int_{4m_\pi^2}^{t_m-\tau} dt' \frac{\Delta_\ell^I(t')\sin\phi_\ell^I(t')}{\Omega_{\ell,R}^I(t')(t'-t)} + \int_{t_m-\tau}^{t_m} dt' \frac{\Delta_\ell^I(t')\sin\phi_\ell^I(t')}{\Omega_{\ell,R}^I(t')(t'-t)}\right.$$
$$\left. + \int_{t_m+\tau}^{\infty} dt' \frac{|g_\ell^I(t')|\sin\phi_\ell^I(t')}{\Omega_{\ell,R}^I(t')(t'-t)} + \int_{t_m}^{t_m+\tau} dt' \frac{|g_\ell^I(t')|\sin\phi_\ell^I(t')}{\Omega_{\ell,R}^I(t')(t'-t)}\right]. \tag{C.15}$$

If τ is small enough, we can approximate $\Omega_\ell^I(t)$ by its asymptotic form

$$\left|\Omega_\ell^I\left(t \approx t_{\rm m}\right)\right| \approx \left|\overline{\Omega_\ell^I}\left(t_{\rm m}\right)\right| \left|t_{\rm m} - t\right|^{\phi_\ell^I(t)/\pi}, \tag{C.16}$$

so that, after defining the new integration variable as $v(t') = (t'-t_m)/(t_m-t)$ one obtains

$$\frac{\Omega_\ell^I(t)}{\pi}\int_{t_m-\tau}^{t_m} dt' \frac{\Delta_\ell^I(t')\sin\phi_\ell^I(t')}{\Omega_{\ell,R}^I(t')(t'-t)} = \frac{\Delta_\ell^I(t_m)\exp(i\phi_\ell^I(t_m))\sin\phi_\ell^I(t_m)}{\pi}\int_0^{\tau(t)} \frac{dv}{v^{\phi_\ell^I(t_m)/\pi}(1-v)},$$
$$\frac{\Omega_\ell^I(t)}{\pi}\int_{t_m}^{t_m+\tau} dt' \frac{|g_\ell^I(t')|\sin\phi_\ell^I(t')}{\Omega_{\ell,R}^I(t')(t'-t)} = \frac{g_\ell^I(t_m)\sin\phi_\ell^I(t_m)}{\pi}\int_0^{\tau(t)} \frac{dv}{v^{\phi_\ell^I(t_m)/\pi}(1+v)}. \tag{C.17}$$

Now this equations can be easily evaluated by any standard integration subroutine, and the numerical problem is gone.

Apart from this behavior, the equations above also imply that at t_m, the modulus of the input coming from the partial wave and the output provided by the MO equations match each other. Explicitly, if we take into account that $\tau(t_m) = \infty$ the equations above read

$$\frac{1}{\pi} PV \int_0^\infty \frac{dv}{v^{\phi_1^1(t_m)/\pi}(1-v)} = -\frac{\cos(\phi_\ell^I(t_m))}{\sin(\phi_\ell^I(t_m))},$$
$$\frac{1}{\pi}\int_0^\infty \frac{dv}{v^{\phi_\ell^I(t_m)/\pi}(1+v)} = \frac{1}{\sin(\phi_\ell^I(t_m))}, \tag{C.18}$$

which, if included in Eq. (C.10) produce the desired result

$$|g_\ell^I(t_m)|_{out} = \left\{\Delta_\ell^I(t_m)\cos\delta_\ell^I(t_m) - \Delta_\ell^I(t_m)\cos\delta_\ell^I(t_m) + |g_\ell^I(t_m)|_{in}\right\} = |g_\ell^I(t_m)|_{in}. \tag{C.19}$$

The matching condition of Eq. (C.19) must be carefully studied. Let us assume that the MO input and output do not agree well in the region surrounding the energy point t_m, where the method imposes the output to be exactly the same as the input. This would be a clear indication that the data parameterization does not satisfy well the dispersion relations in that region. However the equations would be forcing the output to describe the modulus at t_m. This will thus provoke a deviation across the whole energy region, propagating a systematic effect that cannot be fixed. In order to avoid this problem, several values of t_m will be tested, an we will fix t_m to be the value where input and output lie close to each other.

The MO formalism presented above is applied in this thesis to meson-meson scattering only. However, MO like equations have recently been successfully applied to many other interesting processes, like $\eta \to 3\pi$ decays [108, 110, 214], heavy meson decays [270–272], form factors [103] and even to the study of XYZ states [273].

Appendix D

Kernels

In the previous Appendix A we detailed the derivation of several Roy-Steiner like equations, which, after projecting into partial waves, provide us with the necessary tools to perform a rigorous and model-independent analysis of several scattering processes. Even though some integral kernels of the partial-wave dispersion relations are included in section 2.2.4, we will present here the whole system of integrands we have used to perform a coupled study of both $\pi\pi \to K\bar{K}$ and $\pi K \to \pi K$ scattering. Namely, we present kernels for fixed-t and Hyperbolic Dispersion Relations in the s- and t-channels. Only those corresponding to the t-channel T^+ and T^- with one and no subtractions, respectively, were already given in section 2.2.4.

Let us recall that the hyperbolae we use for our dispersion relations are defined through the equation $(s-a)(u-a) = b$, as well as some previous useful definitions

$$z_s = 1 + \frac{2st}{\lambda_s}, \quad \lambda_s = (s - m_+^2)(s - m_-^2) = s^2 - 2s\Sigma + \Delta^2 = 4s\, q_{K\pi}^2(s)\,.$$

In addition, in order to further simplify our equations we will now define

$$\begin{aligned} x(t,s') &= \frac{4q_K(t)q_\pi(t)}{2s'+t-2\Sigma}, \quad A(t,s') = \text{Arcth}\Big(x(t,s')\Big), \\ B(s,s') &= \frac{s}{\lambda_s}\left[\log\left(s'+s-2\Sigma\right) - \log\left(s' - \frac{\Delta^2}{s}\right)\right], \\ C(s,s') &= 1 - \frac{2s(s'+s-2\Sigma)}{\lambda_s}. \end{aligned} \tag{D.1}$$

Note that $C(s,s') \neq C(s',s)$, and both cases will appear below.

D.0.1 Fixed-t

In this subsection we provide the explicit expressions for the $L^{I}_{\ell\ell'}(s,s')$ and $L^{\pm}_{\ell\ell'}(s,t')$ kernels needed in the partial-wave dispersion relations in Eq. (2.19), only up to the vector resonance, as no tensor resonance will be studied within this thesis, although they will be included as input. Let us recall that s corresponds to the "output" partial wave, while s' and t' correspond to the "input". At the same time, ℓ and ℓ' stand for the "output" and "input" angular momenta respectively. Finally, the s-channel kernels read

$$
\begin{aligned}
L^{+}_{0,0}(s,s') &= \frac{s^2}{s'^2(s'-s)} - \frac{2\Sigma s' - 2\Delta^2}{s'\lambda_{s'}} + \frac{\Delta^2 + s's + 2\Sigma s}{s'^2 s} + B(s,s'),\\
L^{+}_{0,1}(s,s') &= 3\frac{(s'^3 + s'^2 s - s's^2 + s\Delta^2)}{s'^2\lambda_{s'}} + 3C(s',s)B(s,s'),\\
L^{+}_{1,0}(s,s') &= -\frac{2s}{\lambda_s} + C(s,s')B(s,s'),\\
L^{+}_{1,1}(s,s') &= \frac{s\lambda_s}{\lambda_{s'}s'(s'-s)} + \frac{\lambda_s}{s'\lambda_{s'}} + \frac{-6s'^3 s + 6s's\Delta^2 + 12s'^2 s(\Sigma - s)}{s'\lambda_{s'}\lambda_s} + C(s',s)\Big(C(s,s')B(s,s')\Big),\\
L^{-}_{0,0}(s,s') &= \frac{1}{s'-s} - B(s,s'),\\
L^{-}_{0,1}(s,s') &= 3\left[\frac{1}{s'-s} - \frac{2s'}{\lambda_{s'}} - \frac{s'\lambda_s}{(s'-s)s\lambda_{s'}} - C(s',s)B(s,s')\right],\\
L^{-}_{1,0}(s,s') &= -C(s,s')B(s,s') - 2\frac{s}{\lambda_s},\\
L^{-}_{1,1}(s,s') &= \frac{s'\lambda_s}{(s'-s)s\lambda_{s'}} - 3C(s',s)\left(C(s,s')B(s,s') + 2\frac{sC(s',s)}{\lambda_s}\right),
\end{aligned}
\tag{D.2}
$$

In addition, the t-channel contribution kernels are way simpler

$$
\begin{aligned}
L^{0}_{0,2\ell}(s,t') &= \frac{2(2\ell)+1}{\sqrt{3}}(q_\pi(t')q_K(t'))^{(2\ell)}\frac{s}{\lambda_s}\left[\log\left(1+\frac{\lambda_s}{st'}\right) - \frac{\lambda_s}{st'}\right],\\
L^{0}_{1,2\ell}(s,t') &= \frac{2(2\ell)+1}{\sqrt{3}}(q_\pi(t')q_K(t'))^{(2\ell)}\frac{s}{\lambda_s}\left[\left(1+\frac{2st'}{\lambda_s}\right)\log\left(1+\frac{\lambda_s}{st'}\right) - 2\right].
\end{aligned}
\tag{D.3}
$$

D.0.2 Hyperbolic

t-channel projection

In this subsection we provide the explicit expressions for the $G^{I}_{\ell\ell'}(t,t')$ and $G^{\pm}_{\ell\ell'}(t,s')$ kernels needed in the partial-wave dispersion relations in Eq. (2.28). Let us recall that $\ell \leq 2$ corresponds to the angular momentum of the partial-wave dispersion relation, i.e. the "output" partial wave, whereas ℓ' corresponds to the angular momentum of the "input" wave inside the integral of the dispersion relation. Similarly, s' and t' are the integration variables, whereas t is the variable of the "output" partial wave coming out

of the dispersion relation. Note that, in the input, partial waves with $\ell' > 2$ can be safely neglected, except for the $\ell' = 4$ partial wave needed for the g_2^0 equation, which nevertheless gives a rather small contribution.

We start by listing the kernels appearing in the $g_1^1(t)$ dispersion relation. As in the main text of section 2.1, for the antisymmetric case, those with a hat correspond to one-subtraction and those without to the unsubtracted case

$$
\begin{aligned}
G^1_{1,3}(t,t') &= \hat{G}^1_{1,3}(t,t') = \frac{7}{48}(t'+t-4\Sigma+10a), \qquad \text{(D.4)}\\
G^-_{1,0}(t,s') &= 4\sqrt{2}\left[\frac{(2s'-2\Sigma+t)A(t,s')-4q_K(t)q_\pi(t)}{16(q_K(t)q_\pi(t))^3}\right],\\
G^-_{1,1}(t,s') &= 12\sqrt{2}\left[P_1(z_{s'})\frac{(2s'-2\Sigma+t)A(t,s')-4q_K(t)q_\pi(t)}{16(q_K(t)q_\pi(t))^3}-\frac{2s'}{3(s'-a)\lambda_{s'}}\right],\\
G^-_{1,2}(t,s') &= 20\sqrt{2}\left[P_2(z_{s'})\frac{(2s'-2\Sigma+t)A(t,s')-4q_K(t)q_\pi(t)}{16(q_K(t)q_\pi(t))^3}-\frac{2s'z'_s}{(s'-a)\lambda_{s'}}\right.\\
&+ \left.\frac{s'^2(2s'+t-2\Sigma)^2}{2(s'-a)^2\lambda^2_{s'}}-\frac{24s'^2(q_K(t)q_\pi(t))^2}{5(s'-a)^2\lambda'^2_s}\right],\\
\hat{G}^-_{1,0}(t,s') &= 4\sqrt{2}\left[(s'-\Sigma+t/2)\frac{A(t,s')-4q_K(t)q_\pi(t)}{16(q_K(t)q_\pi(t))^3}-\frac{1}{3\lambda_{s'}}\right],\\
\hat{G}^-_{1,1}(t,s') &= 12\sqrt{2}\left[(s'-\Sigma+t/2)P_1(z_{s'})\frac{A(t,s')-4q_K(t)q_\pi(t)}{16(q_K(t)q_\pi(t))^3}-\frac{1}{3\lambda_{s'}}\right],\\
\hat{G}^-_{1,2}(t,s') &= 20\sqrt{2}\left[(s'-\Sigma+t/2)P_2(z_{s'})\frac{A(t,s')-4q_K(t)q_\pi(t)}{16(q_K(t)q_\pi(t))^3}-\frac{1}{3\lambda_{s'}}-\frac{2s'^2t}{\lambda^2_{s'}(s'-a))}\right],
\end{aligned}
$$

where $P_l(z_{s'})$ are the Legendre polynomials. For the symmetric case we find

$$
\begin{aligned}
G^0_{2,4}(t,t') &= \frac{3}{8}(t+t'-4\Sigma+7a), \qquad \text{(D.5)}\\
G^+_{2,0}(t,s') &= \frac{\sqrt{3}(2s'+t-2\Sigma)^2}{32q_K(t)^5q_\pi(t)^5}\left[(3-x(t,s')^2)A(t,s')-3x(t,s')\right],\\
G^+_{2,1}(t,s') &= \frac{3\sqrt{3}(2s'+t-2\Sigma)^2}{32q_K(t)^5q_\pi(t)^5}P_1(z_{s'})\left[(3-x(t,s')^2)A(t,s')-3x(t,s')\right],\\
G^+_{2,2}(t,s') &= 5\sqrt{3}\left[\frac{(2s'+t-2\Sigma)^2}{32q_K(t)^5q_\pi(t)^5}P_2(z_{s'})\Big((3-x(t,s')^2)A(t,s')-3x(t,s')\Big)\frac{16s'^2t}{5(s'-a)^2\lambda^2_{s'}}\right].
\end{aligned}
$$

Finally, for the $g_0^0(t)$ dispersion relation the kernels we need are

$$\begin{aligned}
G^0_{0,2}(t,t') &= \frac{5}{16}(t+t'-4\Sigma+6a),\\
G^+_{0,0}(t,s') &= \sqrt{3}\left[\frac{A(t,s')}{q_K(t)q_\pi(t)}+\frac{2(\Sigma-s')}{\lambda_{s'}}\right],\\
G^+_{0,1}(t,s') &= 3\sqrt{3}\left[\frac{A(t,s')}{q_K(t)q_\pi(t)}P_1(z_{s'})-\frac{(2s'+2t-2\Sigma)}{\lambda_{s'}}-\frac{2at}{(s'-a)\lambda_{s'}}\right],\\
G^+_{0,2}(t,s') &= 5\sqrt{3}\left[\frac{A(t,s')}{q_K(t)q_\pi(t)}P_2(z_{s'})-\frac{2s-2\Sigma}{\lambda_{s'}}-\frac{6st(\Delta^2+s'(3s'+2t-4\Sigma)}{(s'-a)\lambda^2_{s'}}\right.\\
&+ \left.\frac{3s'^2t(2s'+t-2\Sigma)^2}{2(s'-a)^2\lambda'^2_s}-\frac{8s'^2t(q_K(t)q_\pi(t))^2}{(s'-a)^2\lambda^2_{s'}}\right].
\end{aligned} \tag{D.6}$$

s-channel projection

Finally, we provide the $K^\pm_{\ell,\ell'}(s,s')$ kernels that are needed for the dispersive contributions of Eq. (2.27). Let us recall that in this case we neglect $\ell \geq 2$, since their contribution to the partial waves of interest is very small. The conventions regarding the variables and angular momenta are the ones explained above. The s-channel kernels of the unsubtracted antisymmetric amplitude thus read

$$K^+_{0,0}(s,s') = \frac{2((s'+\Sigma)\Delta^2-2s'\Sigma)}{s'^2\lambda_{s'}}-\frac{s'^2+2s'(\Sigma-s)-2s\Sigma}{s'^2(s'-s)}+B(s,s'), \tag{D.7}$$

$$\begin{aligned}
K^-_{0,0}(s,s') &= \frac{1}{s'-s}-B(s,s'),\\
K^+_{0,1}(s,s') &= 3\left[\frac{s(s'+2\Sigma)-\Delta^2}{\lambda_{s'}s}-\frac{s'\lambda_s}{(a-s')\lambda_{s'}s}+C(s',s)B(s,s')\right],\\
K^-_{0,1}(s,s') &= -3\left[\frac{(s's+\Delta^2)}{\lambda_{s'}s}-\frac{s'(3s^2-2\Sigma s+\Delta^2)}{(a-s')\lambda_{s'}s}+C(s',s)B(s,s')\right],\\
K^+_{1,0}(s,s') &= -K^-_{1,0}(s,s') = C(s,s')B(s,s')+2\frac{s}{\lambda_s},\\
K^+_{1,1}(s,s') &= 3C(s',s)\left[C(s,s')B(s,s')+2\frac{s}{\lambda_s}\right]+\frac{s'(a-s)\lambda_s}{(s'-s)s(a-s')\lambda_{s'}},\\
K^-_{1,1}(s,s') &= -3C(s',s)\left[C(s,s')B(s,s')+2\frac{s}{\lambda_s}\right]+\frac{s'(a-s)\lambda_s}{(s'-s)s(a-s')\lambda_{s'}},
\end{aligned} \tag{D.8}$$

whereas the once-subtracted kernels for the antisymmetric case read

$$\begin{aligned}
\hat{K}^{-}_{0,0}(s,s') &= \frac{1}{s'-s} - B(s,s') + \frac{\lambda_s}{2s\lambda_{s'}} - 2\frac{(s-\Sigma)}{\lambda_{s'}},\\
\hat{K}^{-}_{0,1}(s,s') &= 3\left[\frac{1}{s'-s} - 2\frac{(s'+s-\Sigma)}{\lambda_{s'}} - \frac{\lambda_s(s'+s)}{2(s'-s)s\lambda_{s'}} - C(s',s)B(s,s')\right],\\
\hat{K}^{-}_{1,0}(s,s') &= -C(s,s')B(s,s') - \frac{2s}{\lambda_s} - \frac{\lambda_s}{6s\lambda_{s'}},\\
\hat{K}^{-}_{1,1}(s,s') &= -3C(s',s)\left[C(s,s')B(s,s') + \frac{2s}{\lambda_s}\right] + \frac{(s'+s)\lambda_s}{2s(s'-s)\lambda_{s'}}.
\end{aligned} \tag{D.9}$$

Next, we provide the kernels for the t-channel contribution, which read

$$\begin{aligned}
K^{0}_{0,0}(s,t') &= \frac{1}{\sqrt{3}}\frac{s}{\lambda_s}\left[\log\left(1+\frac{\lambda_s}{st'}\right) - \frac{\lambda_s}{st'}\right],\\
K^{0}_{0,2}(s,t') &= \frac{5}{\sqrt{3}}(q_\pi(t')q_K(t'))^2\frac{s}{\lambda_s}\left[\log\left(1+\frac{\lambda_s}{st'}\right) - \frac{\lambda_s}{st'}\right] + \frac{\sqrt{3}\lambda_s(s-a)}{16st'},\\
K^{0}_{1,0}(s,t') &= \frac{1}{\sqrt{3}}\frac{s}{\lambda_s}\left[P_1(z_s)\log\left(1+\frac{\lambda_s}{st'}\right) - 2\right],\\
K^{0}_{1,2}(s,t') &= \frac{5}{\sqrt{3}}\frac{s}{\lambda_s}(q_\pi(t')q_K(t'))^2P_1(z_s)\left[\log\left(1+\frac{\lambda_s}{st'}\right) - 2\right] + \frac{5\lambda_s(s-a)}{16\sqrt{3}st'},\\
K^{1}_{0,1}(s,t') &= \frac{3}{4\sqrt{2}}\frac{s(t'+2s-2\Sigma)}{\lambda_s}\left[\log\left(1+\frac{\lambda_s}{st'}\right) - \frac{\lambda_s}{s(t'+2s-2\Sigma)}\right],\\
K^{1}_{1,1}(s,t') &= \frac{3}{4\sqrt{2}}\frac{s(t'+2s-2\Sigma)}{\lambda_s}\left[P_1(z_s)\log\left(1+\frac{\lambda_s}{st'}\right) - 2\right],\\
\hat{K}^{1}_{0,1}(s,t') &= \frac{3}{4\sqrt{2}}\frac{s(t'+2s-2\Sigma)}{\lambda_s}\left[\log\left(1+\frac{\lambda_s}{st'}\right) - \frac{2\lambda_s}{t's} + \frac{\lambda_s^2}{t's^2(t'+2s-2\Sigma)}\right],\\
\hat{K}^{1}_{1,1}(s,t') &= \frac{3}{4\sqrt{2}}\frac{s(t'+2s-2\Sigma)}{\lambda_s}\left[P_1(z_s)\log\left(1+\frac{\lambda_s}{st'}\right) - 2\right] - \frac{\lambda_s}{8\sqrt{2}t's},
\end{aligned} \tag{D.10}$$

where once again we have used a hat for the once-subtracted kernels of the T^- amplitude.

All these kernels produce smooth integrable inputs in the physical region, they are suppressed at higher energies and match the kinematic behavior of every partial wave. They also produce the left and circular cut structures required by partial-wave projection.

Bibliography

[1] S. Weinberg, "Phenomenological Lagrangians," *Physica*, vol. A96, no. 1-2, pp. 327–340, 1979.

[2] P. Buettiker, S. Descotes-Genon, and B. Moussallam, "A new analysis of πK scattering from Roy and Steiner type equations," *Eur. Phys. J.*, vol. C33, pp. 409–432, 2004.

[3] R. García-Martín, R. Kamiński, J. R. Peláez, J. Ruiz de Elvira, and F. J. Ynduráin, "The Pion-pion scattering amplitude. IV: Improved analysis with once subtracted Roy-like equations up to 1100 MeV," *Phys.Rev.*, vol. D83, p. 074004, 2011.

[4] M. Tanabashi *et al.*, "Review of Particle Physics," *Phys. Rev.*, vol. D98, no. 3, p. 030001, 2018.

[5] J. T. Londergan, J. Nebreda, J. R. Pelǵaez, and A. Szczepaniak, "Identification of non-ordinary mesons from the dispersive connection between their poles and their Regge trajectories: The $f_0(500)$ resonance," *Phys.Lett.*, vol. B729, pp. 9–14, 2014.

[6] N. Kemmer, "Field Theory of Nuclear Interaction," *Phys. Rev.*, vol. 52, pp. 906–910, 1937.

[7] M. Gell-Mann, *The Eightfold Way: A Theory of strong interaction symmetry.* 1961.

[8] Y. Ne'eman, "Derivation of strong interactions from a gauge invariance," *Nucl. Phys.*, vol. 26, pp. 222–229, 1961. [,34(1961)].

[9] M. Gell-Mann, "A Schematic Model of Baryons and Mesons," *Phys.Lett.*, vol. 8, pp. 214–215, 1964.

[10] S. Godfrey and N. Isgur, "Mesons in a Relativized Quark Model with Chromodynamics," *Phys.Rev.*, vol. D32, pp. 189–231, 1985.

[11] J. J. Dudek, R. G. Edwards, M. J. Peardon, D. G. Richards, and C. E. Thomas, "Toward the excited meson spectrum of dynamical QCD," *Phys. Rev.*, vol. D82, p. 034508, 2010.

[12] D. Morgan, "Is the 0+ Nonet Respectable?," *Phys. Lett.*, vol. 51B, pp. 71–78, 1974.

[13] N. A. Tornqvist, "Scalar Mesons in the Unitarized Quark Model," *Phys. Rev. Lett.*, vol. 49, pp. 624–627, 1982.

[14] N. A. Tornqvist and M. Roos, "Resurrection of the sigma meson," *Phys. Rev. Lett.*, vol. 76, pp. 1575–1578, 1996.

[15] N. A. Tornqvist, "Understanding the scalar meson q anti-q nonet," *Z. Phys.*, vol. C68, pp. 647–660, 1995.

[16] R. Jaffe and F. Low, "The Connection Between Quark Model Eigenstates and Low-Energy Scattering," *Phys.Rev.*, vol. D19, pp. 2105–2118, 1979.

[17] J. D. Weinstein and N. Isgur, "Do Multi-Quark Hadrons Exist?," *Phys. Rev. Lett.*, vol. 48, p. 659, 1982.

[18] J. D. Weinstein and N. Isgur, "The q q anti-q anti-q System in a Potential Model," *Phys. Rev.*, vol. D27, p. 588, 1983. [,261(1983)].

[19] J. D. Weinstein and N. Isgur, "K anti-K Molecules," *Phys. Rev.*, vol. D41, p. 2236, 1990.

[20] G. Janssen, B. C. Pearce, K. Holinde, and J. Speth, "On the structure of the scalar mesons f0 (975) and a0 (980)," *Phys. Rev.*, vol. D52, pp. 2690–2700, 1995.

[21] N. N. Achasov and V. V. Gubin, "Search for the scalar a0 and f0 mesons in the reactions e+ e- —> gamma pi0 pi0 (eta)," *Phys. Rev.*, vol. D56, pp. 4084–4097, 1997.

[22] P. Minkowski and W. Ochs, "Identification of the glueballs and the scalar meson nonet of lowest mass," *Eur. Phys. J.*, vol. C9, pp. 283–312, 1999.

[23] E. van Beveren and G. Rupp, "Modified Breit-Wigner formula for mesonic resonances describing OZI decays of confined q anti-q states and the light scalar mesons," *Eur. Phys. J.*, vol. C22, pp. 493–501, 2001.

[24] J. Vijande, A. Valcarce, F. Fernandez, and B. Silvestre-Brac, "Nature of the light scalar mesons," *Phys. Rev.*, vol. D72, p. 034025, 2005.

[25] C. J. Morningstar and M. J. Peardon, "The Glueball spectrum from an anisotropic lattice study," *Phys.Rev.*, vol. D60, p. 034509, 1999.

[26] A. Esposito, A. Pilloni, and A. D. Polosa, "Multiquark Resonances," *Phys.Rept.*, vol. 668, pp. 1–97, 2016.

[27] R. F. Lebed, R. E. Mitchell, and E. S. Swanson, "Heavy-Quark QCD Exotica," *Prog.Part.Nucl.Phys.*, vol. 93, pp. 143–194, 2017.

[28] F.-K. Guo, C. Hanhart, U.-G. Meißner, Q. Wang, Q. Zhao, and B.-S. Zou, "Hadronic molecules," *Rev.Mod.Phys.*, vol. 90, no. 1, p. 015004, 2018.

[29] S. L. Olsen, T. Skwarnicki, and D. Zieminska, "Nonstandard heavy mesons and baryons: Experimental evidence," *Rev.Mod.Phys.*, vol. 90, no. 1, p. 015003, 2018.

[30] M. Karliner, J. L. Rosner, and T. Skwarnicki, "Multiquark States," *Ann.Rev.Nucl.Part.Sci*, vol. 68, no. 1, 2018.

[31] D. J. Gross and F. Wilczek, "Ultraviolet Behavior of Nonabelian Gauge Theories," *Phys.Rev.Lett.*, vol. 30, pp. 1343–1346, 1973.

[32] D. J. Gross and F. Wilczek, "Asymptotically Free Gauge Theories - I," *Phys. Rev.*, vol. D8, pp. 3633–3652, 1973.

[33] D. J. Gross and F. Wilczek, "ASYMPTOTICALLY FREE GAUGE THEORIES. 2.," *Phys. Rev.*, vol. D9, pp. 980–993, 1974.

[34] H. D. Politzer, "Reliable Perturbative Results for Strong Interactions?," *Phys.Rev.Lett.*, vol. 30, pp. 1346–1349, 1973.

[35] Y. Nambu, "Axial vector current conservation in weak interactions," *Phys. Rev. Lett.*, vol. 4, pp. 380–382, 1960. [,107(1960)].

[36] Y. Nambu and G. Jona-Lasinio, "DYNAMICAL MODEL OF ELEMENTARY PARTICLES BASED ON AN ANALOGY WITH SUPERCONDUCTIVITY. II," *Phys. Rev.*, vol. 124, pp. 246–254, 1961. [,141(1961)].

[37] Y. Nambu and G. Jona-Lasinio, "Dynamical Model of Elementary Particles Based on an Analogy with Superconductivity. 1.," *Phys. Rev.*, vol. 122, pp. 345–358, 1961. [,127(1961)].

[38] J. Goldstone, "Field Theories with Superconductor Solutions," *Nuovo Cim.*, vol. 19, pp. 154–164, 1961.

[39] J. Goldstone, A. Salam, and S. Weinberg, "Broken Symmetries," *Phys. Rev.*, vol. 127, pp. 965–970, 1962.

[40] S. L. Adler and W. A. Bardeen, "Absence of higher order corrections in the anomalous axial vector divergence equation," *Phys. Rev.*, vol. 182, pp. 1517–1536, 1969. [,268(1969)].

[41] W. A. Bardeen, "Anomalous Ward identities in spinor field theories," *Phys. Rev.*, vol. 184, pp. 1848–1857, 1969.

[42] K. Fujikawa, "Path Integral for Gauge Theories with Fermions," *Phys. Rev.*, vol. D21, p. 2848, 1980. [Erratum: Phys. Rev.D22,1499(1980)].

[43] J. F. Donoghue, C. Ramirez, and G. Valencia, "The Spectrum of QCD and Chiral Lagrangians of the Strong and Weak Interactions," *Phys. Rev.*, vol. D39, p. 1947, 1989.

[44] G. Ecker, J. Gasser, A. Pich, and E. de Rafael, "The Role of Resonances in Chiral Perturbation Theory," *Nucl. Phys.*, vol. B321, pp. 311–342, 1989.

[45] D. Espriu, E. de Rafael, and J. Taron, "The QCD Effective Action at Long Distances," *Nucl. Phys.*, vol. B345, pp. 22–56, 1990. [Erratum: Nucl. Phys.B355,278(1991)].

[46] M. Knecht, B. Moussallam, J. Stern, and N. H. Fuchs, "Determination of two loop $\pi\pi$ scattering amplitude parameters," *Nucl.Phys.*, vol. B471, pp. 445–470, 1996.

[47] M. Knecht, B. Moussallam, J. Stern, and N. H. Fuchs, "The Low-energy $\pi\pi$ amplitude to one and two loops," *Nucl.Phys.*, vol. B457, pp. 513–576, 1995.

[48] G. Amoros, J. Bijnens, and P. Talavera, "Low-energy constants from K(lepton-4) form-factors," *Phys. Lett.*, vol. B480, pp. 71–76, 2000.

[49] J. Bijnens, G. Colangelo, and G. Ecker, "The Mesonic chiral Lagrangian of order p**6," *JHEP*, vol. 02, p. 020, 1999.

[50] J. Bijnens, N. Hermansson-Truedsson, and S. Wang, "The order p^8 mesonic chiral Lagrangian," *JHEP*, vol. 01, p. 102, 2019.

[51] S. Weinberg, "Dynamical approach to current algebra," *Phys. Rev. Lett.*, vol. 18, pp. 188–191, 1967.

[52] J. R. Peláez and A. Rodas, "Pion-kaon scattering amplitude constrained with forward dispersion relations up to 1.6 GeV," *Phys. Rev.*, vol. D93, no. 7, p. 074025, 2016.

[53] J. Bijnens and G. Ecker, "Mesonic low-energy constants," *Ann. Rev. Nucl. Part. Sci.*, vol. 64, pp. 149–174, 2014.

[54] C. Miao, X.-i. Du, G.-w. Meng, and C. Liu, "Lattice study on kaon pion scattering length in the I = 3/2 channel," *Phys. Lett.*, vol. B595, pp. 400–407, 2004.

[55] S. R. Beane, P. F. Bedaque, T. C. Luu, K. Orginos, E. Pallante, A. Parreno, and M. J. Savage, "pi K scattering in full QCD with domain-wall valence quarks," *Phys. Rev.*, vol. D74, p. 114503, 2006.

[56] J. M. Flynn and J. Nieves, "Elastic s-wave $B\pi$, $D\pi$, DK and $K\pi$ scattering from lattice calculations of scalar form-factors in semileptonic decays," *Phys. Rev.*, vol. D75, p. 074024, 2007.

[57] Z. Fu, "Lattice study on πK scattering with moving wall source," *Phys. Rev.*, vol. D85, p. 074501, 2012.

[58] K. Sasaki, N. Ishizuka, M. Oka, and T. Yamazaki, "Scattering lengths for two pseudoscalar meson systems," *Phys. Rev.*, vol. D89, no. 5, p. 054502, 2014.

[59] C. Helmes, C. Jost, B. Knippschild, B. Kostrzewa, L. Liu, F. Pittler, C. Urbach, and M. Werner, "Hadron-Hadron Interactions from $N_f = 2 + 1 + 1$ Lattice QCD: $I = 3/2$ πK Scattering Length," *Phys. Rev.*, vol. D98, no. 11, p. 114511, 2018.

[60] J. R. Peláez, "From controversy to precision on the σ meson: a review on the status of the non-ordinary $f_0(500)$ resonance," *Phys.Rept.*, vol. 658, p. 1, 2016.

[61] A. Dobado, M. J. Herrero, and T. N. Truong, "Study of the Strongly Interacting Higgs Sector," *Phys. Lett.*, vol. B235, p. 129, 1990.

[62] A. Dobado, M. J. Herrero, and T. N. Truong, "Unitarized Chiral Perturbation Theory for Elastic Pion-Pion Scattering," *Phys. Lett.*, vol. B235, pp. 134–140, 1990.

[63] R. Rosenfeld, "Resonances in the Higgs Sector for Large, Finite Higgs," *Phys. Rev.*, vol. D42, pp. 126–137, 1990.

[64] K.-i. Hikasa and K. Igi, "Strongly interacting WW sector with a scalar resonance," *Phys. Lett.*, vol. B261, pp. 285–288, 1991. [Erratum: Phys. Lett.B270,128(1991)].

[65] T. N. Truong, "Radiative corrections to W(L) W(L) scattering in the standard model," *Phys. Lett.*, vol. B258, pp. 402–408, 1991.

[66] A. Dobado and J. R. Pelaez, "The Inverse amplitude method in chiral perturbation theory," *Phys. Rev.*, vol. D56, pp. 3057–3073, 1997.

[67] J. A. Oller, E. Oset, and J. R. Pelaez, "Nonperturbative approach to effective chiral Lagrangians and meson interactions," *Phys. Rev. Lett.*, vol. 80, pp. 3452–3455, 1998.

[68] J. A. Oller and E. Oset, "N/D description of two meson amplitudes and chiral symmetry," *Phys.Rev.*, vol. D60, p. 074023, 1999.

[69] J. A. Oller, E. Oset, and J. R. Pelaez, "Meson meson interaction in a nonperturbative chiral approach," *Phys. Rev.*, vol. D59, p. 074001, 1999. [Erratum: Phys. Rev.D75,099903(2007)].

[70] J. R. Pelaez, "Light scalars as tetraquarks or two-meson states from large N(c) and unitarized chiral perturbation theory," *Mod. Phys. Lett.*, vol. A19, pp. 2879–2894, 2004.

[71] J. A. Oller and E. Oset, "Chiral symmetry amplitudes in the S wave isoscalar and isovector channels and the σ, $f_0(980)$, $a_0(980)$ scalar mesons," *Nucl. Phys.*, vol. A620, pp. 438–456, 1997. [Erratum: Nucl. Phys.A652,407(1999)].

[72] D. Jido, J. A. Oller, E. Oset, A. Ramos, and U. G. Meissner, "Chiral dynamics of the two Lambda(1405) states," *Nucl. Phys.*, vol. A725, pp. 181–200, 2003.

[73] E. Oset and A. Ramos, "Nonperturbative chiral approach to s wave anti-K N interactions," *Nucl. Phys.*, vol. A635, pp. 99–120, 1998.

[74] J. A. Oller and U. G. Meissner, "Chiral dynamics in the presence of bound states: Kaon nucleon interactions revisited," *Phys. Lett.*, vol. B500, pp. 263–272, 2001.

[75] C. Hanhart, J. R. Pelaez, and G. Rios, "Quark mass dependence of the rho and sigma from dispersion relations and Chiral Perturbation Theory," *Phys. Rev. Lett.*, vol. 100, p. 152001, 2008.

[76] J. Ruiz de Elvira, J. R. Pelaez, M. R. Pennington, and D. J. Wilson, "Chiral Perturbation Theory, the $1/N_c$ expansion and Regge behaviour determine the structure of the lightest scalar meson," *Phys. Rev.*, vol. D84, p. 096006, 2011.

[77] C. Hanhart, J. R. Peláez, and G. Ríos, "Remarks on pole trajectories for resonances," *Phys.Lett.*, vol. B739, pp. 375–382, 2014.

[78] R. J. Eden, P. V. Landshoff, D. I. Olive, and J. C. Polkinghorne, *The analytic S-matrix*. Cambridge: Cambridge Univ. Press, 1966.

[79] A. Martin and T. Spearman, *Elementary particle theory*. North-Holland Pub. Co., 1970.

[80] B. R. Martin, D. Morgan, and G. Shaw, *Pion Pion Interactions in Particle Physics*. 1976.

[81] S. Mandelstam, "Determination of the pion - nucleon scattering amplitude from dispersion relations and unitarity. General theory," *Phys. Rev.*, vol. 112, pp. 1344–1360, 1958.

[82] S. Mandelstam, "Analytic properties of transition amplitudes in perturbation theory," *Phys. Rev.*, vol. 115, pp. 1741–1751, 1959.

[83] H. Lehmann, "Analytic properties of scattering amplitudes as functions of momentum transfer," *Nuovo Cim.*, vol. 10, p. 579, 1958.

[84] V. N. Gribov, *Strong interactions of hadrons at high energies: Gribov lectures on Theoretical Physics*. Cambridge University Press, 2012.

[85] G. Breit and E. Wigner, "Capture of Slow Neutrons," *Phys. Rev.*, vol. 49, pp. 519–531, 1936.

[86] T. Regge, "Introduction to complex orbital momenta," *Nuovo Cim.*, vol. 14, p. 951, 1959.

[87] P. D. B. Collins, *An Introduction to Regge Theory and High-Energy Physics*. Cambridge Monographs on Mathematical Physics, Cambridge, UK: Cambridge Univ. Press, 2009.

[88] V. N. Gribov, *The theory of complex angular momenta: Gribov lectures on theoretical physics*. Cambridge Monographs on Mathematical Physics, Cambridge University Press, 2007.

[89] J. R. Pelaez and F. J. Yndurain, "Regge analysis of pion pion (and pion kaon) scattering for energy $s^{1/2} > 1.4$ GeV," *Phys. Rev.*, vol. D69, p. 114001, 2004.

[90] I. Caprini, G. Colangelo, and H. Leutwyler, "Regge analysis of the $\pi\pi$ scattering amplitude," *Eur. Phys. J.*, vol. C72, p. 1860, 2012.

[91] G. Veneziano, "Construction of a crossing-symmetric, Regge behaved amplitude for linearly rising trajectories," *Nuovo Cim.*, vol. A57, pp. 190–197, 1968.

[92] C. Lovelace, "A novel application of regge trajectories," *Phys. Lett.*, vol. 28B, pp. 264–268, 1968.

[93] J. A. Shapiro, "Narrow-resonance model with regge behavior for pi pi scattering," *Phys. Rev.*, vol. 179, pp. 1345–1353, 1969.

[94] K. Kawarabayashi, S. Kitakado, and H. Yabuki, "Veneziano's model and nonet scheme for 1-minus and 2-plus mesons," *Phys. Lett.*, vol. 28B, pp. 432–435, 1969.

[95] G. F. Chew and S. C. Frautschi, "Principle of Equivalence for All Strongly Interacting Particles Within the S Matrix Framework," *Phys.Rev.Lett.*, vol. 7, pp. 394–397, 1961.

[96] J. Hanlon *et al.*, "The Inclusive Reactions $p + n \to p + X$ and $\pi^+ + n \to p + X$ at 100-GeV/c," *Phys. Rev. Lett.*, vol. 37, p. 967, 1976.

[97] W. Hoogland *et al.*, "Measurement and Analysis of the pi+ pi+ System Produced at Small Momentum Transfer in the Reaction pi+ p —> pi+ pi+ n at 12.5-GeV," *Nucl. Phys.*, vol. B126, pp. 109–123, 1977.

[98] D. H. Cohen, T. Ferbel, P. Slattery, and B. Werner, "STUDY OF pi pi SCATTERING IN THE ISOTOPIC SPIN-2 CHANNEL," *Phys. Rev.*, vol. D7, p. 661, 1973.

[99] P. B. Johnson *et al.*, "COMPILATION OF pi- p DATA AT 4-GeV/c: BACKWARD RESONANCE PRODUCTION AND pi pi SCATTERING," *Phys. Rev.*, vol. 176, pp. 1651–1661, 1968.

[100] W. J. Robertson, W. D. Walker, and J. L. Davis, "High-energy pi pi collisions," *Phys. Rev.*, vol. D7, pp. 2554–2564, 1973.

[101] C. Itzykson and J. B. Zuber, *Quantum Field Theory.* International Series In Pure and Applied Physics, New York: McGraw-Hill, 1980.

[102] D. J. Wilson, R. A. Briceno, J. J. Dudek, R. G. Edwards, and C. E. Thomas, "The quark-mass dependence of elastic πK scattering from QCD," 2019.

[103] S. Ropertz, C. Hanhart, and B. Kubis, "A new parametrization for the scalar pion form factors," *Eur. Phys. J.*, vol. C78, no. 12, p. 1000, 2018.

[104] G. Colangelo, M. Hoferichter, M. Procura, and P. Stoffer, "Dispersive approach to hadronic light-by-light scattering," *JHEP*, vol. 09, p. 091, 2014.

[105] G. Colangelo, M. Hoferichter, B. Kubis, M. Procura, and P. Stoffer, "Towards a data-driven analysis of hadronic light-by-light scattering," *Phys. Lett.*, vol. B738, pp. 6–12, 2014.

[106] G. Colangelo, M. Hoferichter, M. Procura, and P. Stoffer, "Dispersion relation for hadronic light-by-light scattering: theoretical foundations," *JHEP*, vol. 09, p. 074, 2015.

[107] G. Colangelo, M. Hoferichter, M. Procura, and P. Stoffer, "Dispersion relation for hadronic light-by-light scattering: two-pion contributions," *JHEP*, vol. 04, p. 161, 2017.

[108] M. Albaladejo and B. Moussallam, "Extended chiral Khuri-Treiman formalism for $\eta \to 3\pi$ and the role of the $a_0(980)$, $f_0(980)$ resonances," *Eur.Phys.J.*, vol. C77, p. 508, 2017.

[109] A. Jackura, C. Fernández-Ramírez, V. Mathieu, M. Mikhasenko, J. Nys, A. Pilloni, K. Saldaña, N. Sherrill, and A. P. Szczepaniak, "Phenomenology of Relativistic $\mathbf{3} \to \mathbf{3}$ Reaction Amplitudes within the Isobar Approximation," *Eur. Phys. J.*, vol. C79, no. 1, p. 56, 2019.

[110] G. Colangelo, S. Lanz, H. Leutwyler, and E. Passemar, "Dispersive analysis of $\eta \to 3\pi$," *Eur. Phys. J.*, vol. C78, no. 11, p. 947, 2018.

[111] M. Mikhasenko, Y. Wunderlich, A. Jackura, V. Mathieu, A. Pilloni, B. Ketzer, and A. P. Szczepaniak, "Three-body scattering: Ladders and Resonances," 2019.

[112] R. García-Martín, R. Kaminski, J. R. Peláez, and J. Ruiz de Elvira, "Precise determination of the $f_0(600)$ and $f_0(980)$ pole parameters from a dispersive data analysis," *Phys.Rev.Lett.*, vol. 107, p. 072001, 2011.

[113] M. Froissart, "Asymptotic behavior and subtractions in the Mandelstam representation," *Phys.Rev.*, vol. 123, pp. 1053–1057, 1961.

[114] S. M. Roy, "Exact integral equation for pion pion scattering involving only physical region partial waves," *Phys.Lett.*, vol. 36B, pp. 353–356, 1971.

[115] F. Steiner, "Partial wave crossing relations for meson-baryon scattering," *Fortsch. Phys.*, vol. 19, pp. 115–159, 1971.

[116] J. Gasser and G. Wanders, "One channel Roy equations revisited," *Eur. Phys. J.*, vol. C10, pp. 159–173, 1999.

[117] G. Wanders, "The Role of the input in Roy's equations for pi pi scattering," *Eur. Phys. J.*, vol. C17, pp. 323–336, 2000.

[118] B. Ananthanarayan, G. Colangelo, J. Gasser, and H. Leutwyler, "Roy equation analysis of $\pi\pi$ scattering," *Phys.Rept.*, vol. 353, pp. 207–279, 2001.

[119] G. Colangelo, J. Gasser, and H. Leutwyler, "$\pi\pi$ scattering," *Nucl. Phys.*, vol. B603, pp. 125–179, 2001.

[120] I. Caprini, G. Colangelo, and H. Leutwyler, "Mass and width of the lowest resonance in QCD," *Phys.Rev.Lett.*, vol. 96, p. 132001, 2006.

[121] B. Ananthanarayan and P. Buettiker, "Comparison of pion kaon scattering in SU(3) chiral perturbation theory and dispersion relations," *Eur. Phys. J.*, vol. C19, pp. 517–528, 2001.

[122] M. Hoferichter, D. R. Phillips, and C. Schat, "Roy-Steiner equations for gamma gamma -> pi pi," *Eur. Phys. J.*, vol. C71, p. 1743, 2011.

[123] I. Danilkin and M. Vanderhaeghen, "Dispersive analysis of the $\gamma\gamma^* \to \pi\pi$ process," *Phys. Lett.*, vol. B789, pp. 366–372, 2019.

[124] C. Ditsche, M. Hoferichter, B. Kubis, and U. G. Meissner, "Roy-Steiner equations for pion-nucleon scattering," *JHEP*, vol. 06, p. 043, 2012.

[125] M. Hoferichter, J. Ruiz de Elvira, B. Kubis, and U.-G. Meißner, "Roy–Steiner-equation analysis of pion–nucleon scattering," *Phys. Rept.*, vol. 625, pp. 1–88, 2016.

[126] J. R. Pelaez and F. J. Yndurain, "The Pion-pion scattering amplitude," *Phys. Rev.*, vol. D71, p. 074016, 2005.

[127] R. Kaminski, J. R. Pelaez, and F. J. Yndurain, "The pion-pion scattering amplitude. II. Improved analysis above bar K anti-K threshold," *Phys. Rev.*, vol. D74, p. 014001, 2006. [Erratum: Phys. Rev.D74,079903(2006)].

[128] R. Kaminski, J. R. Pelaez, and F. J. Yndurain, "The Pion-pion scattering amplitude. III. Improving the analysis with forward dispersion relations and Roy equations," *Phys. Rev.*, vol. D77, p. 054015, 2008.

[129] R. Kaminski, R. Garcia-Martin, P. Grynkiewicz, J. R. Pelaez, and F. J. Yndurain, "New dispersion relations in the description of pi pi scattering amplitudes," *Int. J. Mod. Phys.*, vol. A24, pp. 402–409, 2009.

[130] G. E. Hite and F. Steiner, "New dispersion relations and their application to partial-wave amplitudes," *Nuovo Cim.*, vol. A18, pp. 237–270, 1973.

[131] N. O. Johannesson and J. L. Petersen, "Coupled channel study of the S-wave $\pi\pi \to K\bar{K}$ interaction," *Nucl. Phys.*, vol. B68, pp. 397–412, 1974.

[132] N. Johannesson and G. Nilsson, "An Analysis of Low-Energy πK Scattering," *Nuovo Cim.*, vol. A43, p. 376, 1978.

[133] B. Ananthanarayan, P. Buettiker, and B. Moussallam, "πK sum rules and the SU(3) chiral expansion," *Eur. Phys. J.*, vol. C22, pp. 133–148, 2001.

[134] M. Tabanashi *et al.*, "Review of Particle Physics," *Phys.Rev.*, vol. D98, no. 03, p. 030001, 2018.

[135] I. Bediaga, T. Frederico, and O. Lourenço, "CP violation and CPT invariance in $B^{\pm}$ decays with final state interactions," *Phys. Rev.*, vol. D89, no. 9, p. 094013, 2014.

[136] C. Adolph *et al.*, "Resonance Production and $\pi\pi$ S-wave in $\pi^- + p \to \pi^-\pi^-\pi^+ + p_{recoil}$ at 190 GeV/c," *Phys.Rev.*, vol. D95, no. 3, p. 032004, 2017.

[137] M. Ablikim *et al.*, "Confirmation of the $X(1835)$ and observation of the resonances $X(2120)$ and $X(2370)$ in $J/\psi \to \gamma\pi^+\pi^-\eta'$," *Phys. Rev. Lett.*, vol. 106, p. 072002, 2011.

[138] M. Ablikim *et al.*, "Amplitude Analysis of the $D^+ \to K^0_S\pi^+\pi^0$ Dalitz Plot," *Phys. Rev.*, vol. D89, no. 5, p. 052001, 2014.

[139] B. Aubert *et al.*, "Measurements of branching fractions and CP-violating asymmetries in $B^0 \to \pi^+\pi^-$, $K^+\pi^-$, K^+K^- decays," *Phys. Rev. Lett.*, vol. 89, p. 281802, 2002.

[140] B. Aubert *et al.*, "Study of the $B \to J/\psi K^-\pi^+\pi^-$ decay and measurement of the $B \to X(3872)K^-$ branching fraction," *Phys.Rev.*, vol. D71, p. 071103, 2005.

[141] B. Aubert *et al.*, "Observation of direct CP violation in $B^0 \to K^+\pi^-$ decays," *Phys. Rev. Lett.*, vol. 93, p. 131801, 2004.

[142] Y. Cho *et al.*, "Study of k- pi- scattering using the reaction k- d —> k- pi- p p(s)," *Phys. Lett.*, vol. 32B, pp. 409–412, 1970.

[143] A. M. Bakker *et al.*, "A determination of the I=3/2 $K\pi$ elastic-scattering cross section from the reaction $K^-n \to pK^-\pi^-$ at 3 gev/c," *Nucl. Phys.*, vol. B24, pp. 211–220, 1970.

[144] B. Jongejans, R. A. van Meurs, A. G. Tenner, H. Voorthuis, P. M. Heinen, W. J. Metzger, H. G. J. M. Tiecke, and R. T. Van de Walle, "STUDY OF THE I = 3/2 K- pi- ELASTIC SCATTERING FROM THE REACTION K- p —> K- pi- p pi+ AT 4.25-GeV/c INCIDENT K- MOMENTUM," *Nucl. Phys.*, vol. B67, pp. 381–394, 1973.

[145] D. Linglin *et al.*, "K- pi- elastic scattering cross-section measured in 14.3 gev/c k- p interactions," *Nucl. Phys.*, vol. B57, pp. 64–76, 1973.

[146] P. Estabrooks, R. K. Carnegie, A. D. Martin, W. M. Dunwoodie, T. A. Lasinski, and D. W. G. S. Leith, "Study of $K\pi$ Scattering Using the Reactions $K^\pm p \to K^\pm\pi^+ n$ and $K^\pm p \to K^\pm\pi^-\Delta^{++}$ at 13 GeV/c," *Nucl. Phys.*, vol. B133, pp. 490–524, 1978.

[147] D. Aston *et al.*, "A Study of $K^-\pi^+$ Scattering in the Reaction $K^-p \to K^-\pi^+ n$ at 11 GeV/c," *Nucl. Phys.*, vol. B296, pp. 493–526, 1988.

[148] D. H. Cohen, D. S. Ayres, R. Diebold, S. L. Kramer, A. J. Pawlicki, and A. B. Wicklund, "Amplitude Analysis of the K^-K^+ System Produced in the Reactions $\pi^-p \to K^-K^+n$ and $\pi^+n \to K^-K^+p$ at 6 GeV/c," *Phys. Rev.*, vol. D22, p. 2595, 1980.

[149] A. Etkin *et al.*, "Amplitude Analysis of the $K^0(s)K^0(s)$ System Produced in the Reaction $\pi^-p \to K^0(s)K^0(s)n$ at 23-GeV/c," *Phys. Rev.*, vol. D25, p. 1786, 1982.

[150] R. S. Longacre *et al.*, "A Measurement of $\pi^- p \to K^0(s)\ K^0(s)\ n$ at 22-GeV/c and a Systematic Study of the 2++ Meson Spectrum," *Phys. Lett.*, vol. B177, pp. 223–227, 1986.

[151] S. J. Lindenbaum and R. S. Longacre, "Coupled channel analysis of J(PC) = 0++ and 2++ isoscalar mesons with masses below 2-GeV," *Phys. Lett.*, vol. B274, pp. 492–497, 1992.

[152] B. Hyams *et al.*, "$\pi\pi$ Phase Shift Analysis from 600-MeV to 1900-MeV," *Nucl. Phys.*, vol. B64, pp. 134–162, 1973.

[153] G. Grayer *et al.*, "High Statistics Study of the Reaction pi- p –> pi- pi+ n: Apparatus, Method of Analysis, and General Features of Results at 17-GeV/c," *Nucl. Phys.*, vol. B75, pp. 189–245, 1974.

[154] B. Hyams *et al.*, "A Study of All the pi pi Phase Shift Solutions in the Mass Region 1.0-GeV to 1.8-GeV from pi- p –> pi- pi+ n at 17.2-GeV," *Nucl. Phys.*, vol. B100, pp. 205–224, 1975.

[155] P. del Amo Sanchez *et al.*, "Analysis of the $D^+ \to K^-\pi^+e^+\nu_e$ decay channel," *Phys. Rev.*, vol. D83, p. 072001, 2011.

[156] M. Ablikim *et al.*, "Study of $D^+ \to K^-\pi^+e^+\nu_e$," *Phys. Rev.*, vol. D94, no. 3, p. 032001, 2016.

[157] J. Bijnens, P. Dhonte, and P. Talavera, "pi K scattering in three flavor ChPT," *JHEP*, vol. 05, p. 036, 2004.

[158] D. J. Wilson, R. A. Briceno, J. J. Dudek, R. G. Edwards, and C. E. Thomas, "Coupled $\pi\pi, K\bar{K}$ scattering in P-wave and the ρ resonance from lattice QCD," *Phys.Rev.*, vol. D92, no. 9, p. 094502, 2015.

[159] E. M. Aitala *et al.*, "Model independent measurement of S-wave K- pi+ systems using D+ —> K pi pi decays from Fermilab E791," *Phys. Rev.*, vol. D73, p. 032004, 2006. [Erratum: Phys. Rev.D74,059901(2006)].

[160] J. P. Lees *et al.*, "Measurement of the I=1/2 $K\pi$ $\mathcal{S}$-wave amplitude from Dalitz plot analyses of $\eta_c \to K\bar{K}\pi$ in two-photon interactions," *Phys. Rev.*, vol. D93, p. 012005, 2016.

[161] H. Q. Zheng, Z. Y. Zhou, G. Y. Qin, Z. Xiao, J. J. Wang, and N. Wu, "The kappa resonance in s wave pi K scatterings," *Nucl. Phys.*, vol. A733, pp. 235–261, 2004.

[162] D. V. Bugg, "An Update on the Kappa," *Phys. Rev.*, vol. D81, p. 014002, 2010.

[163] J. R. Pelaez and A. Rodas, "$\pi\pi \to K\bar{K}$ scattering up to 1.47 GeV with hyperbolic dispersion relations," *Eur. Phys. J.*, vol. C78, no. 11, p. 897, 2018.

[164] R. Navarro Perez, J. E. Amaro, and E. Ruiz Arriola, "Statistical error analysis for phenomenological nucleon-nucleon potentials," *Phys. Rev.*, vol. C89, no. 6, p. 064006, 2014.

[165] R. Navarro Pérez, E. Ruiz Arriola, and J. Ruiz de Elvira, "Self-consistent statistical error analysis of $\pi\pi$ scattering," *Phys.Rev.*, vol. D91, p. 074014, 2015.

[166] J. R. Peláez and A. Rodas, "Dispersive analysis tools for $\pi\pi$ and πK scattering," in *17th International Conference on Hadron Spectroscopy and Structure (Hadron 2017) Salamanca, Spain, September 25-29, 2017*, vol. Hadron2017, p. 139, 2018.

[167] P. Buettiker, S. Descotes-Genon, and B. Moussallam, "pi K scattering inputs to ChPT," *Nucl. Phys. Proc. Suppl.*, vol. 133, pp. 223–226, 2004. [,223(2003)].

[168] Yu. S. Surovtsev, P. Bydzovsky, R. Kaminski, V. E. Lyubovitskij, and M. Nagy, "Can parameters of f_0 mesons be determined correctly analyzing only $\pi\pi$ scattering?," *Phys. Rev.*, vol. D86, p. 116002, 2012.

[169] P. Bydžovský, R. Kamiński, and V. Nazari, "Modified $\pi\pi$ amplitude with σ pole," *Phys. Rev.*, vol. D90, no. 11, p. 116005, 2014.

[170] L.-Y. Dai, X.-W. Kang, T. Luo, and U.-G. Meißner, "A study on the correlation between poles and cuts in $\pi\pi$ scattering," 2019.

[171] A. Rodas *et al.*, "Determination of the pole position of the lightest hybrid meson candidate," *Phys. Rev. Lett.*, vol. 122, no. 4, p. 042002, 2019.

[172] P. Masjuan and J. J. Sanz-Cillero, "Pade approximants and resonance poles," *Eur. Phys. J.*, vol. C73, p. 2594, 2013.

[173] P. Masjuan, J. Ruiz de Elvira, and J. J. Sanz-Cillero, "Precise determination of resonance pole parameters through Padé approximants," *Phys. Rev.*, vol. D90, no. 9, p. 097901, 2014.

[174] I. Caprini, P. Masjuan, J. Ruiz de Elvira, and J. J. Sanz-Cillero, "Uncertainty estimates of the σ-pole determination by Padé approximants," *Phys. Rev.*, vol. D93, no. 7, p. 076004, 2016.

[175] J. R. Peláez, A. Rodas, and J. Ruiz de Elvira, "Strange resonance poles from $K\pi$ scattering below 1.8 GeV," *Eur. Phys. J.*, vol. C77, no. 2, p. 91, 2017.

[176] R. de Montessus de Ballore, "Sur les fractions continues algébriques," *Bull. Soc. Math. France*, vol. 30, pp. 28–36, 1902.

[177] I. Caprini, "Finding the sigma pole by analytic extrapolation of pi pi scattering data," *Phys. Rev.*, vol. D77, p. 114019, 2008.

[178] S. Descotes-Genon and B. Moussallam, "The $K_0^*(800)$ scalar resonance from Roy-Steiner representations of πK scattering," *Eur. Phys. J.*, vol. C48, p. 553, 2006.

[179] F. J. Yndurain, R. Garcia-Martin, and J. R. Pelaez, "Experimental status of the pi pi isoscalar S wave at low energy: f(0)(600) pole and scattering length," *Phys. Rev.*, vol. D76, p. 074034, 2007.

[180] Z.-H. Guo and J. A. Oller, "Resonance on top of thresholds: the $\Lambda_c(2595)^+$ as an extremely fine-tuned state," *Phys. Rev.*, vol. D93, no. 5, p. 054014, 2016.

[181] J. A. Oller, "Final state interactions in hadronic D decays," *Phys. Rev.*, vol. D71, p. 054030, 2005.

[182] A. Švarc, M. Hadzimehmedovic, H. Osmanovic, J. Stahov, L. Tiator, and R. L. Workman, "Introducing the Pietarinen expansion method into the single-channel pole extraction problem," *Phys. Rev.*, vol. C88, no. 3, p. 035206, 2013.

[183] A. Švarc, M. Hadžimehmedović, H. Osmanović, J. Stahov, L. Tiator, and R. L. Workman, "Pole positions and residues from pion photoproduction using the Laurent-Pietarinen expansion method," *Phys. Rev.*, vol. C89, no. 6, p. 065208, 2014.

[184] A. Švarc, M. Hadžimehmedović, R. Omerović, H. Osmanović, and J. Stahov, "Poles of Karlsruhe-Helsinki KH80 and KA84 solutions extracted by using the Laurent-Pietarinen method," *Phys.Rev.*, vol. C89, no. 4, p. 045205, 2014.

[185] R.-A. Tripolt, I. Haritan, J. Wambach, and N. Moiseyev, "Threshold energies and poles for hadron physical problems by a model-independent universal algorithm," *Phys. Lett.*, vol. B774, pp. 411–416, 2017.

[186] H. Feshbach, "Unified theory of nuclear reactions," *Annals Phys.*, vol. 5, pp. 357–390, 1958.

[187] H. Feshbach, "A Unified theory of nuclear reactions. 2.," *Annals Phys.*, vol. 19, pp. 287–313, 1962. [Annals Phys.281,519(2000)].

[188] H. Feshbach, "The unified theory of nuclear reactions: III. Overlapping resonances," *Annals Phys.*, vol. 43, pp. 410–420, 1967.

[189] L. Rosenfeld, "Unitarity of the collision matrix and interdependence of resonance parameters," *Acta Phys. Polon.*, vol. A38, pp. 603–619, 1970.

[190] I. J. R. Aitchison, "K-matrix formalism for overlapping resonances," *Nucl.Phys.*, vol. A189, pp. 417–423, 1972.

[191] J. A. Oller, *A Brief Introduction to Dispersion Relations*, vol. 9783030135829 of *SpringerBriefs in Physics*. Springer, 2019.

[192] M. Mikhasenko, A. Pilloni, M. Albaladejo, C. Fernández-Ramírez, A. Jackura, V. Mathieu, J. Nys, A. Rodas, B. Ketzer, and A. P. Szczepaniak, "Pole position of the $a_1(1260)$ from τ-decay," *Phys. Rev.*, vol. D98, no. 9, p. 096021, 2018.

[193] G. N. Fleming, "Recoupling Effects in the Isobar Model. 1. General Formalism for Three-Pion Scattering," *Phys.Rev.*, vol. 135, pp. B551–B560, 1964.

[194] M. T. Hansen and S. R. Sharpe, "Relativistic, model-independent, three-particle quantization condition," *Phys.Rev.*, vol. D90, no. 11, p. 116003, 2014.

[195] M. T. Hansen and S. R. Sharpe, "Expressing the three-particle finite-volume spectrum in terms of the three-to-three scattering amplitude," *Phys.Rev.*, vol. D92, no. 11, p. 114509, 2015.

[196] M. T. Hansen and S. R. Sharpe, "Applying the relativistic quantization condition to a three-particle bound state in a periodic box," *Phys. Rev.*, vol. D95, no. 3, p. 034501, 2017.

[197] M. Mai and M. Döring, "Three-body Unitarity in the Finite Volume," *Eur.Phys.J.*, vol. A53, no. 12, p. 240, 2017.

[198] Y. Meng, C. Liu, U.-G. Meißner, and A. Rusetsky, "Three-particle bound states in a finite volume: unequal masses and higher partial waves," *Phys. Rev.*, vol. D98, no. 1, p. 014508, 2018.

[199] R. A. Briceño, M. T. Hansen, and S. R. Sharpe, "Relating the finite-volume spectrum and the two-and-three-particle S matrix for relativistic systems of identical scalar particles," *Phys.Rev.*, vol. D95, no. 7, p. 074510, 2017.

[200] R. A. Briceño, M. T. Hansen, and S. R. Sharpe, "Three-particle systems with resonant subprocesses in a finite volume," *Phys. Rev.*, vol. D99, no. 1, p. 014516, 2019.

[201] R. A. Briceño, M. T. Hansen, and S. R. Sharpe, "Numerical study of the relativistic three-body quantization condition in the isotropic approximation," *Phys. Rev.*, vol. D98, no. 1, p. 014506, 2018.

[202] M. T. Hansen and S. R. Sharpe, "Lattice QCD and Three-particle Decays of Resonances," 2019.

[203] G. 't Hooft and M. J. G. Veltman, "Regularization and Renormalization of Gauge Fields," *Nucl.Phys.*, vol. B44, pp. 189–213, 1972.

[204] I. J. R. Aitchison and R. Pasquier, "Three-Body Unitarity and Khuri-Treiman Amplitudes," *Phys.Rev.*, vol. 152, no. 4, p. 1274, 1966.

[205] M. Mai, B. Hu, M. Döring, A. Pilloni, and A. Szczepaniak, "Three-body Unitarity with Isobars Revisited," *Eur.Phys.J.*, vol. A53, p. 177, 2017.

[206] T. D. Blanton, F. Romero-López, and S. R. Sharpe, "Implementing the three-particle quantization condition including higher partial waves," *JHEP*, vol. 03, p. 106, 2019.

[207] J. Pisut and M. Roos, "The rho meson shape," *Nucl. Phys.*, vol. B6, pp. 325–352, 1968.

[208] J. M. Blatt and V. F. Weisskopf, *Theoretical Nuclear Physics*. New York: Wiley, 1952.

[209] G. F. Chew and S. Mandelstam, "Theory of low-energy pion pion interactions," *Phys.Rev.*, vol. 119, pp. 467–477, 1960.

[210] J. L. Basdevant and E. L. Berger, "Unitary Coupled-Channel Analysis of Diffractive Production of the a1 Resonance," *Phys. Rev.*, vol. D16, p. 657, 1977.

[211] N. N. Khuri and S. B. Treiman, "Pion-Pion Scattering and $K^{\pm} \to 3\pi$ Decay," *Phys.Rev.*, vol. 119, pp. 1115–1121, 1960.

[212] I. J. R. Aitchison, "Dispersion Theory Model of Three-Body Production and Decay Processes," *Phys.Rev.*, vol. 137, pp. B1070–B1084, 1965.

[213] J. Kambor, C. Wiesendanger, and D. Wyler, "Final state interactions and Khuri-Treiman equations in $\eta \to 3\pi$ decays," *Nucl.Phys.*, vol. B465, pp. 215–266, 1996.

[214] G. Colangelo, S. Lanz, H. Leutwyler, and E. Passemar, "$\eta \to 3\pi$: Study of the Dalitz plot and extraction of the quark mass ratio Q," *Phys.Rev.Lett.*, vol. 118, no. 2, p. 022001, 2017.

[215] M. Albaladejo, N. Sherrill, C. Fernández-Ramírez, A. Jackura, V. Mathieu, M. Mikhasenko, J. Nys, A. Pilloni, and A. P. Szczepaniak, "Khuri-Treiman equations for $\pi\pi$ scattering," *Eur.Phys.J.*, vol. C78, no. 7, p. 574, 2018.

[216] B. Ketzer, "Hybrid Mesons," in *Proceedings, 6th International Conference on Quarks and Nuclear Physics (QNP 2012): Palaiseau, France, April 16-20, 2012*, vol. QNP2012, p. 025, 2012.

[217] C. A. Meyer and E. S. Swanson, "Hybrid Mesons," *Prog.Part.Nucl.Phys.*, vol. 82, pp. 21–58, 2015.

[218] D. Horn and J. Mandula, "A Model of Mesons with Constituent Gluons," *Phys.Rev.*, vol. D17, p. 898, 1978.

[219] N. Isgur and J. E. Paton, "A Flux Tube Model for Hadrons in QCD," *Phys.Rev.*, vol. D31, p. 2910, 1985.

[220] M. S. Chanowitz and S. R. Sharpe, "Hybrids: Mixed States of Quarks and Gluons," *Nucl.Phys.*, vol. B222, pp. 211–244, 1983. [Erratum: Nucl. Phys.B228,588(1983)].

[221] T. Barnes, F. Close, F. de Viron, and J. Weyers, "$q\bar{q}g$ Hermaphrodite Mesons in the MIT Bag Model," *Nucl.Phys.*, vol. B224, p. 241, 1983.

[222] F. E. Close and P. R. Page, "The Production and decay of hybrid mesons by flux tube breaking," *Nucl.Phys.*, vol. B443, pp. 233–254, 1995.

[223] I. J. General, S. R. Cotanch, and F. J. Llanes-Estrada, "QCD Coulomb gauge approach to hybrid mesons," *Eur. Phys. J.*, vol. C51, pp. 347–358, 2007.

[224] S. D. Bass and E. Marco, "Final state interaction and a light mass 'exotic' resonance," *Phys.Rev.*, vol. D65, p. 057503, 2002.

[225] A. P. Szczepaniak and E. S. Swanson, "Coulomb gauge QCD, confinement, and the constituent representation," *Phys.Rev.*, vol. D65, p. 025012, 2002.

[226] A. P. Szczepaniak and P. Krupinski, "Energy spectrum of the low-lying gluon excitations in the Coulomb gauge," *Phys.Rev.*, vol. D73, p. 116002, 2006.

[227] P. Guo, A. P. Szczepaniak, G. Galata, A. Vassallo, and E. Santopinto, "Heavy quarkonium hybrids from Coulomb gauge QCD," *Phys.Rev.*, vol. D78, p. 056003, 2008.

[228] S. D. Bass and P. Moskal, "η' and η Mesons with Connection to Anomalous Glue." 2018.

[229] P. Lacock, C. Michael, P. Boyle, and P. Rowland, "Hybrid mesons from quenched QCD," *Phys.Lett.*, vol. B401, pp. 308–312, 1997.

[230] C. W. Bernard *et al.*, "Exotic mesons in quenched lattice QCD," *Phys.Rev.*, vol. D56, pp. 7039–7051, 1997.

[231] J. J. Dudek, R. G. Edwards, P. Guo, and C. E. Thomas, "Toward the excited isoscalar meson spectrum from lattice QCD," *Phys.Rev.*, vol. D88, no. 9, p. 094505, 2013.

[232] F. E. Close and H. J. Lipkin, "New Experimental Evidence for Four Quark Exotics: The Serpukhov $\phi\pi$ Resonance and the Gams $\eta\pi$ Enhancement," *Phys.Lett.*, vol. B196, p. 245, 1987.

[233] R. L. Jaffe and F. Wilczek, "Diquarks and exotic spectroscopy," *Phys.Rev.Lett.*, vol. 91, p. 232003, 2003.

[234] R. Jaffe, "Exotica," *Phys.Rept.*, vol. 409, pp. 1–45, 2005.

[235] G. Baum *et al.*, "COMPASS: A Proposal for a Common Muon and Proton Apparatus for Structure and Spectroscopy." 1996.

[236] P. Abbon *et al.*, "The COMPASS Setup for Physics with Hadron Beams," *Nucl.Instrum.Meth.*, vol. A779, pp. 68–115, 2015.

[237] A. Rizzo, "The hybrid mesons quest: the MesonEx experiment at Jefferson Laboratory," *J.Phys.Conf.Ser.*, vol. 689, no. 1, p. 012022, 2016.

[238] S. Dobbs, "Searching for Hybrid Mesons with GlueX," *PoS*, vol. Hadron2017, p. 047, 2018.

[239] A. P. Szczepaniak, M. Swat, A. R. Dzierba, and S. Teige, "Study of the $\eta\pi$ and $\eta'\pi$ spectra and interpretation of possible exotic $J^{PC} = 1^{-+}$ mesons," *Phys.Rev.Lett.*, vol. 91, p. 092002, 2003.

[240] C. Adolph *et al.*, "Odd and even partial waves of $\eta\pi^-$ and $\eta'\pi^-$ in $\pi^- p \to \eta^{(\prime)}\pi^- p$ at 191 GeV/c," *Phys.Lett.*, vol. B740, pp. 303–311, 2015.

[241] A. Esposito, A. Pilloni, and A. D. Polosa, "Hybridized Tetraquarks," *Phys.Lett.*, vol. B758, pp. 292–295, 2016.

[242] R. T. Deck, "Kinematical interpretation of the first $\pi\rho$ resonance," *Phys.Rev.Lett.*, vol. 13, pp. 169–173, 1964.

[243] G. Ascoli, R. Cutler, L. M. Jones, U. Kruse, T. Roberts, B. Weinstein, and H. W. Wyld, "Deck-model calculation of $\pi^- p \to \pi^-\pi^+\pi^- p$," *Phys.Rev.*, vol. D9, pp. 1963–1979, 1974.

[244] R. Akhunzyanov *et al.*, "Light isovector resonances in $\pi^- p \to \pi^-\pi^-\pi^+ p$ at 190 GeV/c." 2018.

[245] P. Masjuan, E. Ruiz Arriola, and W. Broniowski, "Systematics of radial and angular-momentum Regge trajectories of light non-strange $q\bar{q}$-states," *Phys. Rev.*, vol. D85, p. 094006, 2012.

[246] S. W. MacDowell, "Analytic Properties of Partial Amplitudes in Meson-Nucleon Scattering," *Phys.Rev.*, vol. 116, pp. 774–778, 1959.

[247] C. Fernández-Ramírez, I. V. Danilkin, V. Mathieu, and A. P. Szczepaniak, "Understanding the Nature of $\Lambda(1405)$ through Regge Physics," *Phys.Rev.*, vol. D93, no. 7, p. 074015, 2016.

[248] A. V. Anisovich, V. V. Anisovich, and A. V. Sarantsev, "Systematics of q anti-q states in the (n, M**2) and (J, M**2) planes," *Phys. Rev.*, vol. D62, p. 051502, 2000.

[249] J. A. Carrasco, J. Nebreda, J. R. Peláez, and A. P. Szczepaniak, "Dispersive calculation of complex Regge trajectories for the lightest f_2 resonances and the $K^*(892)$," *Phys.Lett.*, vol. B749, pp. 399–406, 2015.

[250] J. A. Silva-Castro, C. Fernandez-Ramirez, M. Albaladejo, I. V. Danilkin, A. Jackura, V. Mathieu, J. Nys, A. Pilloni, A. P. Szczepaniak, and G. Fox, "Regge phenomenology of the N^* and Δ^* poles," *Phys. Rev.*, vol. D99, no. 3, p. 034003, 2019.

[251] P. D. B. Collins, R. C. Johnson, and E. J. Squires, "Heavy bosons, Regge trajectories and dynamical theories," *Phys.Lett.*, vol. 26B, pp. 223–225, 1968.

[252] S.-Y. Chu, G. Epstein, P. Kaus, R. C. Slansky, and F. Zachariasen, "Crossing-symmetric rising regge trajectories," *Phys. Rev.*, vol. 175, pp. 2098–2105, 1968.

[253] J. R. Peláez, A. Rodas, and J. Ruiz de Elvira, "Dispersive analysis of the $\kappa/K_0^*(700)$ meson and other light strange resonances," *EPJ Web Conf.*, vol. 212, p. 03003, 2019.

[254] J. R. Pelaez, "On the Nature of light scalar mesons from their large N(c) behavior," *Phys. Rev. Lett.*, vol. 92, p. 102001, 2004.

[255] J. R. Pelaez and G. Rios, "Nature of the f0(600) from its N(c) dependence at two loops in unitarized Chiral Perturbation Theory," *Phys. Rev. Lett.*, vol. 97, p. 242002, 2006.

[256] J. Nebreda and J. R. Pelaez., "Strange and non-strange quark mass dependence of elastic light resonances from SU(3) Unitarized Chiral Perturbation Theory to one loop," *Phys. Rev.*, vol. D81, p. 054035, 2010.

[257] Z.-H. Guo, J. A. Oller, and J. Ruiz de Elvira, "Chiral dynamics in form factors, spectral-function sum rules, meson-meson scattering and semi-local duality," *Phys. Rev.*, vol. D86, p. 054006, 2012.

[258] T. Wolkanowski, M. Sołtysiak, and F. Giacosa, "$K_0^*(800)$ as a companion pole of $K_0^*(1430)$," *Nucl. Phys.*, vol. B909, pp. 418–428, 2016.

[259] Z.-H. Guo and J. A. Oller, "Probabilistic interpretation of compositeness relation for resonances," *Phys. Rev.*, vol. D93, no. 9, p. 096001, 2016.

[260] C. Lovelace and D. Masson, "Calculation of Regge poles," in *High-energy physics. Proceedings, 11th International Conference, ICHEP'62, Geneva, Switzerland, Jul 4-11, 1962*, pp. 510–512, 1962.

[261] A. O. Barut and F. Calogero, "Singularities in Angular Momentum of the Scattering Amplitude for a Class of Soluble Potentials," *Phys. Rev.*, vol. 128, no. 3, p. 1383, 1962.

[262] A. Ahmadzadeh, P. G. Burke, and C. Tate, "Regge Trajectories for Yukawa Potentials," *Phys. Rev.*, vol. 131, no. 3, p. 1315, 1963.

[263] A. Etkin *et al.*, "Evidence for Two New 0++ Mesons and a Possible Scalar Decuplet," *Phys. Rev.*, vol. D25, p. 2446, 1982.

[264] S. Schael *et al.*, "Branching ratios and spectral functions of tau decays: Final ALEPH measurements and physics implications," *Phys. Rept.*, vol. 421, pp. 191–284, 2005.

[265] G. Mahoux, S. M. Roy, and G. Wanders, "Physical pion pion partial-wave equations based on three channel crossing symmetry," *Nucl.Phys.*, vol. B70, pp. 297–316, 1974.

[266] H. Lehman, "Extension of the axiomatic analyticity domain of scattering amplitudes by unitarity-I," *Nuovo Cim.*, vol. 42, p. 930, 1966.

[267] H. Lehman, "Extension of the axiomatic analyticity domain of scattering amplitudes by unitarity.—II," *Nuovo Cim.*, vol. 44, p. 1219, 1966.

[268] N. I. Muskhelishvili, *Singular Integral Equations*. 1953.

[269] R. Omnes, "On the Solution of certain singular integral equations of quantum field theory," *Nuovo Cim.*, vol. 8, pp. 316–326, 1958.

[270] M. Albaladejo, J. T. Daub, C. Hanhart, B. Kubis, and B. Moussallam, "How to employ $\overline{B}_d^0 \to J/\psi\left(\pi\eta, \overline{K}K\right)$ decays to extract information on $\pi\eta$ scattering," *JHEP*, vol. 04, p. 010, 2017.

[271] D. L. Yao, P. Fernandez-Soler, M. Albaladejo, F. K. Guo, and J. Nieves, "Heavy-to-light scalar form factors from Muskhelishvili–Omnès dispersion relations," *Eur. Phys. J.*, vol. C78, no. 4, p. 310, 2018.

[272] D.-L. Yao, P. Fernandez-Soler, F.-K. Guo, and J. Nieves, "New parametrization of the form factors in $\bar{B} \to D\ell\bar{\nu}_\ell$ decays," 2019.

[273] Y.-H. Chen, L.-Y. Dai, F.-K. Guo, and B. Kubis, "Nature of the $Y(4260)$: A light-quark perspective," *Phys. Rev.*, vol. D99, no. 7, p. 074016, 2019.